

DISS. ETH NO. 24324

Field-induced chirality in a frustrated quantum spin ladder

A thesis submitted to attain the degree of
DOCTOR OF SCIENCES of ETH ZURICH

(Dr. sc. ETH Zurich)

presented by

MAREK PIKULSKI

MSc ETH Physik, ETH Zürich

born on 17.11.1985

citizen of
Poland

accepted on the recommendation of

Prof. Dr. J. F. Mesot, examiner

Prof. em. Dr. H.-R. Ott, co-examiner

Prof. Dr. T. C. Schulthess, co-examiner

2017

DOI: 10.3929/ethz-b-000204120

20171201b3i+

Abstract

This work focuses on the magnetism of spin- $\frac{1}{2}$ moments in BiCu_2PO_6 , which is believed to be described by an effectively one-dimensional frustrated spin-ladder model. In accordance with this model, magnetic order is induced by externally-applied magnetic fields. This phenomenon is studied both experimentally, using nuclear-magnetic resonance (NMR) in high magnetic fields, and theoretically, through numerical calculations. The corresponding methods, as well as other relevant concepts, are introduced in chapter 1. The subsequent presentation is divided into two parts.

Part I concerns selected developments related to NMR instrumentation. Besides serving as an illustration of certain technical aspects of the method, these topics are considered interesting in their own right.

- In chapter 2, the development of an NMR spectrometer is reported. The design attempts to perform a majority of the required signal processing in the digital domain. This simplifies the experimental setup and allows for the use of general-purpose hardware. A firmware-defined solution, based on a commercially-available radio-processor device, is adopted. The spectrometer is implemented by writing suitable application software and extending the firmware of a field-programmable gate array (FPGA). This approach is advantageous in terms of flexibility and reproducibility. Tests demonstrate the suitability for typical condensed-matter NMR experiments.
- Chapter 3 concerns the construction of NMR probes for measurements at low temperatures. After describing a more conventional probe, intended to be used in a ^4He -flow cryostat, the design of an NMR probe for a top-loading “cryogen-free” dilution refrigerator is presented. Selected aspects of the accomplished work are reported, with a particular emphasis on the heat-sinking of the coaxial transmission lines used for the high-frequency signals. Finally, remaining challenges and possible solutions are discussed.

The main part of this work (part II) is dedicated to the aforementioned field-induced magnetic phases of BiCu_2PO_6 . A detailed introduction to this material is given in chapter 4.

Chapters 5 and 6 reconsider and extend previous estimates of the parameters (hyperfine couplings and g -tensors) required for a quantitative description of the ^{31}P -NMR spectra in BiCu_2PO_6 . Moreover, the effect of various parameters of the frustrated-ladder model on the magnetic susceptibility and specific heat is examined through exact-diagonalization calculations. This includes possible Dzyaloshinskii-Moriya (DM) interactions and site-dependent g -factors.

Chapter 7 presents density-matrix renormalization group (DMRG) calculations performed for the frustrated spin-ladder model. Numerical and physical consequences of ground-state degeneracy are considered in detail. The previously-reported appearance of long-range chiral correlations is confirmed, and additional calculations clarify that the onset of chiral order coincides with the closing of a gap in the magnetic-excitation spectrum (spin gap). The dependence of the chiral phase on the exchange couplings is studied. The results suggest that, consistently with previous results for the related zigzag-chain model, field-induced chiral order is generally observed in the frustrated spin ladder, provided magnetic frustration is strong enough to induce incommensurate correlations. Furthermore, the chiral phase is stabilized with increasing rung coupling, and its occurrence is robust against symmetry-allowed DM interactions

and site-dependent g -factors. Chiral order is known to be a precursor of spiral magnetic order (helical magnetic order). By considering suitable correlation functions, the details of the expected spiral structure, including the distortions induced by various DM interactions, are studied.

Quantitative comparison between calculation results and published experimental data indicates that the one-dimensional frustrated spin-ladder model is incomplete. In particular, only one field-induced phase transition is predicted in the relevant range of magnetizations, whereas at least two transitions are observed experimentally. While part of the discrepancies may be related to the neglect of interladder couplings, it is argued that magnetoelastic effects are likely to play a decisive role in BiCu_2PO_6 .

The results of ^{31}P -NMR experiments performed in the field-induced phases of BiCu_2PO_6 are presented in chapter 8. To my knowledge, these data represent the first microscopic local-probe measurements of the field-induced magnetic order realized above approximately 35 T (for magnetic fields applied along the b -axis of the crystal). Symmetry arguments and quantitative considerations show that the NMR data are consistent with a spiral magnetic structure. Combined with other experimental reports, and the numerical calculations performed in this work, this is interpreted as persuasive evidence for a previously-proposed field-induced spiral order, and hence field-induced chirality, in BiCu_2PO_6 .

Note that this work benefited from contributions from many individuals and sources (see Acknowledgments for details).

Zusammenfassung

Diese Arbeit befasst sich mit dem Magnetismus der lokalen Spin- $\frac{1}{2}$ -Momente in BiCu_2PO_6 , welche als quasi-eindimensionale, frustrierte Spinleiter beschrieben werden, deren quantenmechanischer Grundzustand eine Spinflüssigkeit ist. Externe Magnetfelder induzieren Phasenübergänge mit einhergehender magnetischer Ordnung. In der vorliegenden Arbeit wird dieses Phänomen sowohl theoretisch, mittels numerischer Berechnungen, als auch experimentell, mittels Kernspinresonanzspektroskopie (NMR-Spektroskopie) in hohen Magnetfeldern, untersucht. Die entsprechenden Methoden werden in Kapitel 1 erläutert. Die darauffolgende Arbeit ist in zwei Teile untergliedert.

In Teil I werden ausgewählte technische Entwicklungen rund um die NMR-Spektroskopie beschrieben. Im Hinblick auf den wissenschaftlichen Teil dieser Arbeit (Teil II), können diese auch als Veranschaulichung diverser praktischer Aspekte der Methode aufgefasst werden.

- Kapitel 2 beschreibt die Entwicklung eines NMR-Spektrometers, welches im Gegensatz zu den meisten konventionellen Systemen, die Aus- und Eingangssignale direkt abtastet, sodass ein Großteil der Signalverarbeitung digital erfolgen kann. Der Einsatz leistungsfähiger Komponenten ermöglicht eine Überabtastung bei typischen Signalfrequenzen. Dieser Ansatz erlaubt zudem die Verwendung generischer, kommerziell erhältlicher Hardware. Somit werden sämtliche NMR-spezifischen Funktionen mittels Software und programmierbarer Logik (field-programmable gate array, FPGA) festgelegt, wodurch etwaige zukünftige Erweiterungen, sowie eine mögliche Replikation des Aufbaus, vereinfacht werden. Auch wenn es sich hierbei nicht um die erste Implementierung eines Systems dieser Art handelt, belegen die beschriebenen Testmessungen, dass die entwickelte Lösung den speziellen Anforderungen der NMR-Spektroskopie in der Festkörperphysik gerecht werden kann.
- Kapitel 3 behandelt NMR-Probenstäbe für den Einsatz bei tiefen Temperaturen. Die kurze Vorstellung eines Probenstabes für einen ^4He -Flusskryostaten dient dabei auch als Kontrast zum anschließend beschriebenen Entwurf eines Probenstabes für einen ^3He - ^4He -Mischungskryostaten. Eine Besonderheit des letzteren Projektes besteht darin, dass es sich um ein System mit "Toploading"-Fähigkeit handelt, bei welchem kein direkter Kontakt zwischen Probe und Mischung vorgesehen ist. Auf die Beschreibung der bereits umgesetzten Arbeit, mit besonderem Augenmerk auf der Kühlung der Innenleiter der Hochfrequenzsignalleitungen zur NMR Spule, folgt ein Überblick über die noch verbleibenden Herausforderungen sowie mögliche Lösungen.

Der Hauptteil dieser Arbeit (Teil II) ist den eingangs erwähnten feldinduzierten magnetischen Phasen von BiCu_2PO_6 gewidmet. Kapitel 4 enthält eine detaillierte Beschreibung dieses Materials.

In den anschließenden Kapiteln 5 und 6 werden vormals beschriebene Analysen der für eine quantitative Interpretation der ^{31}P -Hochfeld-NMR-Spektren benötigten Kopplungsparameter (g -Tensoren und Hyperfeinkopplungskonstanten) nachvollzogen und erweitert. Des Weiteren wird der Einfluss der verschiedenen Austauschkonstanten des frustrierten Spinleitermodells auf die magnetische Suszeptibilität und die spezifische Wärmekapazität numerisch, mittels exakter Diagonalisierung untersucht. Diese Berechnungen beziehen mögliche Anisotropien, wie Dzyaloshinskii-Moriya-Wechselwirkung (DM) und

positionsabhängige g -Tensoren, mit ein.

In Kapitel 7 werden die Ergebnisse von Dichte-Matrix-Renormierungs-Gruppen-Berechnungen (DMRG) für das frustrierte Spinleitermodell vorgestellt. Der durch ein externes Magnetfeld induzierte Grundzustand ist zweifach entartet, was wichtige numerische und physikalische Auswirkungen hat. Die Rechnungen bestätigen das zuvor beobachtete Auftreten langreichweitiger chiraler Korrelationen und zeigen, dass dieses zeitgleich mit dem Schließen der Energielücke im Anregungsspektrum erfolgt. Die Untersuchung des Einflusses der Austauschkonstanten auf die chirale Phase deutet auf das Vorhandensein einer solchen Phase in allen frustrierten Spinleitern mit ausreichend starker Frustration hin, im Einklang mit früheren Ergebnissen für das verwandte Zickzack-Spinleiter-Modell. Der Stabilitätsbereich dieser Phase wächst zudem mit der Sprosskopplung. Des Weiteren ist die chirale Ordnung robust gegen schwache bis mittelstarke DM-Wechselwirkungen sowie positionsabhängige g -Faktoren. Im Zusammenspiel mit Zwischenleiter-Kopplungen impliziert die chirale Ordnung im idealisierten, eindimensionalen Modell üblicherweise die Entstehung klassischer Spiralstrukturen. Durch Berechnung geeigneter Korrelationsfunktionen werden die erwarteten Spiralstrukturen, einschließlich der Auswirkungen der DM-Wechselwirkung, im Detail untersucht.

Der quantitative Vergleich zwischen den Modellrechnungen und veröffentlichten Daten weist darauf hin, dass das Modell unvollständig ist. Insbesondere prognostiziert das Modell nur einen Phasenübergang, wohingegen experimentell mindestens zwei Phasengrenzen beobachtet werden. Auch wenn möglicherweise relevante Zwischenleiter-Kopplungen nicht in den Rechnungen berücksichtigt werden konnten, werden diese Diskrepanzen als indirektes Indiz für eine wesentliche Rolle magnetoelastischer Kopplungen in BiCu_2PO_6 interpretiert.

Die Ergebnisse der im Rahmen dieser Arbeit durchgeführten ^{31}P -Hochfeld-NMR-Experimente an BiCu_2PO_6 werden schlussendlich in Kapitel 8 vorgestellt. Dabei handelt es sich, soweit bekannt, um die ersten mikroskopisch-aufgelösten lokalen Messungen in der oberhalb von etwa 35 T auftretenden feldinduzierten magnetischen Phase (für entlang der b -Kristallrichtung angelegte Magnetfelder). Symmetriebetrachtungen, sowie phänomenologische, quantitative Modellierung zeigen, dass die NMR-Spektren mit einer magnetischen Spiralstruktur konsistent sind. Unter Hinzunahme der o. g. numerischen Berechnungen, sowie unabhängiger experimenteller Ergebnisse, rechtfertigen diese Beobachtungen die Schlussfolgerung, dass BiCu_2PO_6 , wie in vorausgehenden Arbeiten vorgeschlagen, in der entsprechenden Hochfeldphase tatsächlich eine magnetische Spiralstruktur annimmt, welche aus der in den Modellrechnungen untersuchten feldinduzierten chiralen Phase erwächst.

Zuletzt sei an dieser Stelle noch ausdrücklich auf die sich am Ende dieser Arbeit befindenden Danksagungen (Acknowledgments) hingewiesen.

Formal conventions

Citations

- No strict distinction between “cf.” and “see” (cf. , e. g. , [84]) is made in this work, and either word, or none, can refer to similar, related, or underlying works. In particular, this includes cases in which arguments developed, reenacted, or extended; or conclusions made in this work are similar to, equivalent to, influenced by, or based on a given reference.
- Irrespectively of any possibly associated citation signals, references to sections, figures, equations, or other elements of this work generally imply any sources directly or indirectly referenced within these elements or within the context of these elements, even if explicit remarks like “and references therein” are omitted for the sake of readability.
- For readability, citations (except footnotes) are typeset within punctuation, including citations which apply to an entire sub-clause or sentence.

General notation Most of the notation used in this work should adhere to common conventions. Potentially particular symbols are listed below.

- The canonical basis vector along a spatial direction k is denoted as e_k .
- Unit vectors are denoted by $\hat{v} = \|v\|^{-1}v$.
- The notation ∂_x is used as a short-hand for $\partial/\partial x$.

Dates Numerical dates are formatted in either day-month-year or year-month-day formats.

Contents

Abstract	i
Zusammenfassung	iii
Formal conventions	v
1 Introduction	1
1.1 Spin Hamiltonians	1
1.1.1 Effective Hamiltonians	1
1.1.2 Dzyaloshinskii-Moriya (DM) interaction	2
1.1.3 Symmetric anisotropies	2
1.2 Quantum spin liquids	2
1.3 Model systems	3
1.3.1 Spin chain	3
1.3.2 Spin ladder	3
1.3.3 Zigzag chain	3
1.3.4 Frustrated ladder	4
1.4 Numerical methods	6
1.4.1 Exact diagonalization	6
1.4.2 Monte Carlo	6
1.4.3 Density-matrix renormalization group	7
1.4.4 Symmetries	7
1.4.5 Site-dependent g-tensors	8
1.5 Pulsed nuclear-magnetic resonance	8
1.5.1 Nuclear moments	9
1.5.2 Magnetic resonance	9
1.5.3 Nuclear magnetization	9
1.5.4 Dynamics of nuclear magnetization	10
1.5.5 Experimental aspects	12
1.5.6 Spectrum	12
1.5.7 Basic experiments	13
1.5.7.1 Single-pulse experiment	13
1.5.7.2 Spin-echo experiment	13
1.5.8 Relaxation	14
1.5.9 Hyperfine interactions and g-tensor	14

I	Development of NMR instrumentation	17
2	A firmware-defined direct-sampling NMR spectrometer	19
2.1	Introduction	19
2.2	Motivation	19
2.2.1	Signal conversion	19
2.2.2	Hardware aspects	20
2.3	Design	21
2.3.1	Interface, software and pulse programming	23
2.3.2	Data transfer and averaging	24
2.3.3	Transmitter	24
2.3.4	Receiver	25
2.3.5	Implementation	25
2.4	Testing	26
2.4.1	Synthetic tests	26
2.4.2	Magnetic resonance experiments	27
2.5	Discussion and Conclusions	28
3	NMR probes	29
3.1	Introduction	29
3.2	Tuning	29
3.3	Thermal aspects	30
3.4	Improved NMR probe with two-axis rotator	31
3.5	Towards an NMR probe for a “cryogen-free” dilution refrigerator	33
3.5.1	Motivation	33
3.5.2	Design	34
3.5.3	Heat-sinking of coaxial lines	35
3.5.3.1	Design	36
3.5.3.2	Fabrication and Testing	37
3.5.3.3	Overall signal transmission	37
3.5.4	Considerations regarding sample holder	37
3.6	Summary and Outlook	38
II	BiCu₂PO₆: Field-induced magnetic order in a frustrated spin ladder	41
4	BiCu₂PO₆: General aspects	43
4.1	Introduction	43
4.2	Structural aspects	44
4.2.1	Crystal structure	44
4.2.2	Crystal symmetry	46
4.2.3	Site symmetries	46
4.2.4	Exchange mechanism	47
4.2.5	Local environment of the Cu sites	48
4.3	Theoretical model for BCPO	49
4.3.1	Heisenberg Hamiltonian and g-tensor	49
4.3.2	Symmetry-allowed Dzyaloshinskii-Moriya interactions	50

4.3.3	Model parameters	51
4.4	Related compounds	52
4.5	Field-induced phases	52
4.6	Outline and relation to previous work	53
5	BiCu₂PO₆: Low-field thermodynamic properties	55
5.1	Introduction	55
5.2	Results for representative parameters	55
5.2.1	Susceptibility and g-tensors	55
5.2.2	Magnetic specific heat and entropy	58
5.2.3	Energy gap and finite-size effects	59
5.2.4	Inhomogeneous system	60
5.3	Interladder coupling	62
5.4	Influence of coupling parameters	63
5.4.1	Magnetic susceptibility	63
5.4.2	Specific heat	64
5.4.3	Phase diagram	64
5.4.4	Parameter set <i>B</i> and influence of symmetric anisotropies	70
5.4.5	Discussion	71
5.5	Conclusions	73
6	BiCu₂PO₆: Interactions between electronic and nuclear moments	75
6.1	Introduction	75
6.2	Notation	75
6.3	Dipolar coupling	76
6.3.1	Formalism	76
6.3.2	Convergence and uniqueness	77
6.3.3	Order of magnitude	77
6.3.4	Demagnetization lineshape	78
6.3.5	Paramagnetic phase	78
6.4	Hyperfine couplings	79
6.5	Model for NMR shift	79
6.5.1	Pristine compound	79
6.5.2	Weakly-doped compound	80
6.6	Estimation of hyperfine couplings from angular dependence of NMR frequencies	82
6.6.1	Data	82
6.6.2	Method	82
6.6.3	Results for full model	84
6.6.4	Results for uniform model	86
6.7	Uncertainties	87
6.8	Discussion	88
7	Field-induced magnetic order in the frustrated spin ladder	91
7.1	Previous knowledge	91
7.1.1	Spin ladder	91
7.1.2	Zigzag chain	91
7.1.2.1	Phase diagram	92

7.1.3	Frustrated ladder	94
7.1.4	Frustrated ladder with reduced symmetry	95
7.2	Introduction	96
7.3	Ground-state degeneracy	97
7.3.1	Symmetry associated with degeneracy	97
7.3.2	Uniqueness of measurements	98
7.3.3	Consequences for correlation functions	100
7.4	Convergence	101
7.5	Notation	101
7.6	Spin textures	102
7.6.1	Triplon density	102
7.6.2	Short-period oscillations and fits	103
7.6.3	Nature of short-period oscillations	105
7.6.4	Discussion	106
7.7	Pertinent observables	107
7.7.1	Definitions	107
7.7.2	Structure factors	108
7.7.3	Asymptotic behavior of correlation functions	109
7.7.4	Number of required measurements	109
7.8	Degeneracy, chirality and spiral structures	109
7.8.1	Chirality and degenerate ground states	109
7.8.2	Symmetry breaking	110
7.9	Results	111
7.9.1	Magnetization	111
7.9.2	Spin correlations	111
7.9.3	Dimerization	112
7.9.4	Chirality	113
7.10	Interpretation	120
7.10.1	Chiral order	120
7.10.2	Onset of chiral order	120
7.10.3	Spin canting	122
7.11	Influence of model parameters	123
7.11.1	Effect of the rung exchange	123
7.11.2	Role of frustration	125
7.11.3	Relevance of reduced symmetry associated with inequivalent Cu sites	127
7.12	Intermediate summary	129
7.13	Influence of individual DM interactions	132
7.14	Special case: DM interaction on nearest-neighbor leg bond	133
7.14.1	Field-induced chirality	135
7.14.2	Transverse component	136
7.14.3	Longitudinal component	140
7.14.4	Inferred magnetic structure	141
7.15	Discussion and conclusions	141
7.16	Open questions regarding BiCu_2PO_6	143
8	BiCu_2PO_6: High-field nuclear magnetic resonance experiments	147

8.1	Introduction and previous results	147
8.2	Experimental details	149
8.3	Results	150
8.4	Phase boundaries	151
8.5	Analysis of NMR shift	152
8.6	Interpretation of NMR spectra in the high-field phase	154
8.6.1	Phenomenology	155
8.6.2	General spiral structures	156
8.6.2.1	General symmetry considerations	156
8.6.2.2	Proposed magnetic structure for individual ladder	157
8.6.2.3	Structural chirality	158
8.6.2.4	Specialization to symmetric spiral	158
8.6.2.5	Symmetry considerations for linear coupling	159
8.6.3	Explicit models	161
8.6.3.1	Possible spiral structure	161
8.6.3.2	Long-range order along the a -direction	162
8.6.3.3	Long-range order along the a -direction: Quantitative model	162
8.6.3.4	Long-range order along the a -direction: Candidate solutions	163
8.6.3.5	Long-range order along the a -direction: Parameter uncertainties	164
8.6.3.6	Short-range order along the a -direction: Random walk	166
8.6.3.7	Short-range order along the a -direction: Range of dipolar couplings	167
8.6.3.8	Short-range order along the a -direction: Results	167
8.6.4	High-temperature line shape	168
8.6.5	Multiferroicity	169
8.6.6	Discussion	171
8.7	Intermediate-field phase	173
8.7.1	Phenomenology of NMR spectra for $H_{c1} \leq H \leq H_{c2}$	173
8.7.2	Models for the NMR spectrum	173
8.7.3	Solitons	174
8.7.4	The limit $H \gtrsim H_{c2}$	175
8.7.5	Magnetoelastic couplings	177
9	Conclusions and Outlook	179
	Acknowledgments	183
A	Appendix	185
A.1	Technical aspects of calculations	185
A.1.1	Units	185
A.1.2	Additional details	185
A.1.3	Exact-diagonalization performance	185
A.1.4	Site-dependent g -tensors	186
A.1.5	DMRG calculations	187
A.1.6	Notes for ALPS users	187
A.1.7	Convergence measures for spin texture	187
A.1.8	Calculation of structure factors	188

A.1.9	Useful identities for correlation functions	189
A.1.10	Convergence problems with longitudinal DM vectors	189
A.1.11	Computing resources	190
A.2	Dipole sums	191
A.2.1	Magnetic field inside a uniformly-magnetized volume	191
A.2.2	Efficient evaluation	192
A.3	Angular dependence of NMR shift	193
A.3.1	Experimental details	193
A.3.2	Hyperfine-coupling parameter fits	194
A.4	High-field NMR experiments	194
A.4.1	Thermometry	201
A.4.2	Sample alignment	201
A.4.3	Post-experiment checks	203
A.4.4	Additional data	206
A.4.5	Field calibration	206
A.4.6	Effect of signal compression on NMR spectrum	207
A.5	Derivations	208
A.5.1	Formal derivation of superexchange interaction	208
A.5.2	Transformation properties of DM vectors	209
A.5.3	Method to account for site-dependent g -tensors	210
A.5.4	Empirical model for specific heat	214
A.5.5	Mean-field description of interladder couplings	215
A.5.6	Derivation of (A.1)	216
A.5.7	Derivation of (A.5)	217
A.5.8	Weighted linear regression	218
A.5.9	Discrete spin-space symmetries	219
A.5.10	Longitudinal chirality and degenerate ground states	219
A.6	Miscellaneous	220
A.6.1	Goodness-of-fit measures	220
	Bibliography	223
	Curriculum vitae	253

1 Introduction

This chapter introduces well-known general concepts required for this work. Section 1.1 illustrates how strong electron correlations give rise to effective spin-Hamiltonians and anisotropic interactions. Relevant model Hamiltonians are presented in section 1.3 and selected numerical methods are discussed in section 1.4. The chapter concludes with an introduction to the experimental technique of nuclear magnetic resonance (section 1.5).

Since the first part of this work (part I, chapters 2-3) describes selected technical developments, the introduction of BiCu₂PO₆, which is at the focus of the scientific part of this work (part II), is postponed to chapter 4.

1.1 Spin Hamiltonians

1.1.1 Effective Hamiltonians

Note that, while this introduction was initially motivated by reading the advanced discussions in [68, 179, 196, 275, 276, 359, 451], the arguments and definitions below are considered general knowledge these days. Nonetheless, it is remarkable that essentially all aspects of what follows have already been described by P. W. Anderson over fifty years ago [31]. Strongly correlated electron materials are typically described within the tight-binding framework, using variants of the Hubbard Hamiltonian [178] (see also [31, eqs. 6 and 9] and [68, eq. 2])

$$\mathcal{H} = - \underbrace{\sum_{\langle i,j \rangle, \sigma} (t_{ij} c_{i\sigma}^\dagger c_{j\sigma} + \text{H.c.})}_{\mathcal{V}} + U \underbrace{\sum_i n_{i\uparrow} n_{i\downarrow}}_{\mathcal{H}_0}, \quad (1.1)$$

with hopping integrals $t_{ij} = t_{ji}^*$ and on-site repulsion U . The sum runs over pairs of sites $\langle i, j \rangle$, without double counting. The fermionic creation (annihilation) operators are denoted as $c_{i\sigma}^\dagger$ ($c_{i\sigma}$) and $n_{i\sigma} = c_{i\sigma}^\dagger c_{i\sigma}$. In the study of magnetic insulators, one considers the large- U limit, $U \gg |t_{ij}|$, and half filling, i. e., exactly one electron per lattice site. Then, \mathcal{V} can be treated as a perturbation to \mathcal{H}_0 .

The Hilbert space can be decomposed into eigenspaces Ω_e of \mathcal{H}_0 with energies e . Here, $e = nU$ with $n \in \mathbb{N}_0$ denoting the number of doubly-occupied sites [68]. At half filling, for a lattice with N sites, a basis of Ω_0 is given by

$$|\{\sigma_i\}_i\rangle = \left(\prod_{i=1}^N c_{i\sigma_i}^\dagger \right) |0\rangle, \quad ,$$

where $|0\rangle$ denotes the state containing no conduction-band electrons (vacuum). Thus, each basis state is fully specified by the choice of the spin configuration $\{\sigma_i\}_i$, which allows the states to be reinterpreted as S_z -basis states of an *effective spin model* [68]. Using spin operators $S_i^\alpha = c_{i\beta}^\dagger \sigma_\alpha^{\beta\gamma} c_{i\gamma}$,¹ second-order

¹This standard definition (see, e. g., [68, eq. 3]) is a straightforward reformulation of [31, eq. 16].

perturbation theory yields the well-known *anti-ferromagnetic Heisenberg super-exchange* Hamiltonian [31, eq. 21],

$$\mathcal{H}_{\text{eff}} = \sum_{\langle i,j \rangle} \frac{4|t_{ij}|^2}{U} (\mathbf{S}_i \cdot \mathbf{S}_j)|_{\Omega_0} + \text{const.} \quad .$$

Despite being essentially identical to the established calculation [31], the derivation of the effective Hamiltonian using the formalism of Ref. [374] is considered instructive and is therefore provided in the appendix (section A.5.1). In particular, the above notation was chosen for consistency with [374]. As already noted in [31, p. 7], at higher orders, energy sectors Ω_{nU} with $n > 1$ and multiple virtual states can contribute to a single process. For example, this gives rise to a four-spin interaction of order t_{ij}^4/U for the Hubbard model on the square lattice (e. g., [451]).

1.1.2 Dzyaloshinskii-Moriya (DM) interaction

In a tight-binding description, the spin-orbit interaction [276]

$$\mathcal{H}_{\text{SOI}} = \frac{\hbar}{2m^2c^2} \mathbf{S} \cdot (\nabla V(r) \times \mathbf{p}) \quad ,$$

leads to a spin-dependent hopping integral [179], which can be treated using the perturbative approach illustrated in section 1.1.1 (and A.5.1) [276]. To leading order, this gives rise to anisotropic spin-spin interactions of the form [179, 196, 359, 451]

$$\mathbf{D} \cdot (\mathbf{S}_1 \times \mathbf{S}_2) + \mathbf{S}_1 \cdot \mathbf{\Gamma} \cdot \mathbf{S}_2 \quad .$$

The first term is antisymmetric and known as the Dzyaloshinskii-Moriya (DM) interaction [117, 275, 276]. The symmetric tensor $\mathbf{\Gamma}$ is given by [359, 451]

$$\mathbf{\Gamma} = \frac{\mathbf{D} \otimes \mathbf{D}}{2J} - \frac{\mathbf{D}^2}{4J} \quad . \quad (1.2)$$

Although $\mathbf{\Gamma}$ is often neglected (e. g. in [15]), this approximation is not valid in general [119, 359, 451]. The transformation properties of \mathbf{D} are reviewed in the appendix (section A.5.2).

1.1.3 Symmetric anisotropies

To lowest order in the spin operators, spin-spin (dipolar) and spin-orbit interactions also give rise to magnetic anisotropies of the form $\mathbf{S}_i \cdot \mathbf{V}_{ij} \cdot \mathbf{S}_j$, where \mathbf{V}_{ij} is a symmetric tensor [403, p. 61]. While the so-called *one-ion* anisotropy terms with $i = j$ are trivial (constant) for quantum spin-1/2 operators, *bond* anisotropies corresponding to $i \neq j$ are generally allowed (cf. [403, ch. 2]). However, in order to limit the number of model parameters, no such terms—besides (1.2)—are considered in this work.

1.2 Quantum spin liquids

A spin liquid is an intrinsically disordered phase without long-range magnetic correlations [32]. To emphasize that low-dimensional systems consisting of interacting entities with small spin are strongly

influenced by quantum fluctuations, one usually speaks of quantum-spin liquids (QSLs) in these cases (e. g. , [42]). This work focuses on spin- $\frac{1}{2}$ systems. Quite generally, an energy gap towards magnetic excitations (a so-called *spin gap*) implies short-ranged, i. e. , exponentially-decaying spin correlations, much like the forces mediated by massive bosons are described by short-ranged Yukawa-type potentials [247, pp. 19-20] (see, e. g. , [101]). Accordingly, the gapped phases of the models discussed below can be considered QSLs (e. g. , [333]). External magnetic fields can suppress the excitation gap, which typically gives rise to *field-induced magnetic order* [437].

1.3 Model systems

1.3.1 Spin chain

The simplest model system is the Heisenberg spin- $\frac{1}{2}$ chain [53], whose Hamiltonian is (e. g. , [93])

$$\mathcal{H} = J \sum_i \mathbf{S}_i \cdot \mathbf{S}_{i+1} \quad . \quad (1.3)$$

The ideal system does not order magnetically [233, 296], but is in critical regime with quasi long-ranged, i. e. , algebraically-decaying (power-law) correlations [239]. The gapless spin-1 excitations [92, 93] fractionalize into spin- $\frac{1}{2}$ *spinons* corresponding to defects (domain walls) in the Néel-type correlations [128, 137]. Quite intuitively, residual interchain couplings induce attractive interactions between spinons, leading to the formation of bound states [225, 412]. Lastly, it should be noted that spin chains consisting of integer spins are fundamentally different from the half-integer case described here [14, 351].

1.3.2 Spin ladder

An n -leg Heisenberg spin ladder is a finite array of n coupled Heisenberg spin chains [102]. A two-leg ladder is depicted in Fig. 1.1. Typically, spin- $\frac{1}{2}$ ladders with antiferromagnetic exchange interactions are considered. Similarly to spin chains with half-integer and integer spin, spin- $\frac{1}{2}$ ladders with an odd number of legs differ fundamentally from ladders with an even number of legs, the former being gapless whereas the latter exhibit a spin gap [102, 333, 440]. For this work, the case $n = 2$ is relevant. The ground state of this model is a non-degenerate [381] singlet [246] with purely antiferromagnetic and short-ranged spin-spin correlations [360].

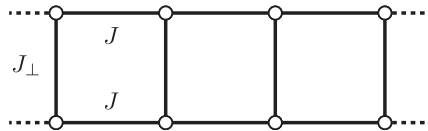


Figure 1.1: A finite-length segment of a simple two-leg spin ladder. Circles represent localized spins and solid black edges correspond to exchange interactions.

1.3.3 Zigzag chain

Magnetic frustration can also give rise to a spin gap. An important member of this class of models is the so-called zigzag chain shown in Fig. 1.2(a), which is also known as the Majumdar-Ghosh (MG)

model [241, 242]. It consists of a spin- $\frac{1}{2}$ chain with nearest-neighbor (NN) interaction J_1 and next-nearest neighbor (NNN) interaction J_2 . Note that frustration of the NNN interaction clearly requires antiferromagnetic J_2 .

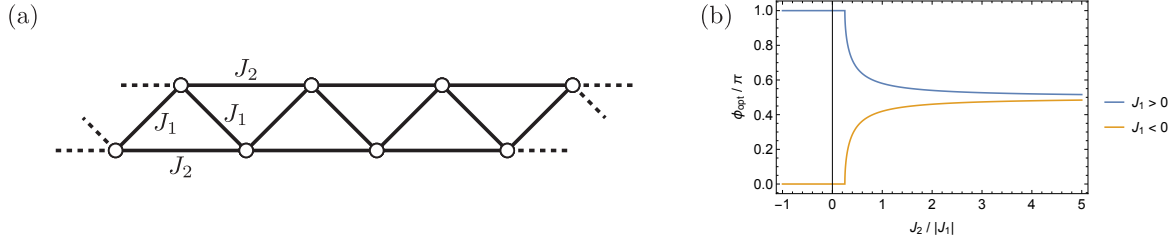


Figure 1.2: (a): A finite-length segment of a zigzag chain (frustrated spin chain). Circles represent localized spins and solid black edges correspond to exchange interactions. (b): Optimal pitch angle for classical zigzag chain.

For a sinusoidal magnetic structure formed by classical unit-length spins, the energy is $J_1 \cos \phi + J_2 \cos 2\phi$ per site (e. g. , [419]) and optimization w. r. t. the pitch angle ϕ yields Fig. 1.2(b). Thus, beyond a critical frustration ratio $J_2/|J_1| = \frac{1}{4}$, the classical ground-state is an incommensurate spiral (see, e. g. , [164, 419]). In the absence of external magnetic fields, the models with exchange couplings (J_1, J_2) and $(-J_1, J_2)$ are obviously related by a gauge symmetry, so that $J_1 > 0$ without loss of generality. While the quantum model resembles the unfrustrated spin chain for small frustration J_2/J_1 (e. g. , [69]), a spin gap appears for $J_2/J_1 > 0.2411(1)$ [69, 358] and the ground-state becomes dimerized² [69, 443]. The elementary excitations are spinons [227, 375]. Another important point is the so-called *disorder point* [69] $J_2/J_1 = 0.5$, at which the model is exactly solvable [242] (see [459] for a modern derivation). Beyond the disorder point, frustration induces incommensurate real-space correlations [24, 69, 86].³ The influence of single-axis bond anisotropies on the ground state was studied in the literature [295], as was the effect of extrinsic dimerization terms [86].

1.3.4 Frustrated ladder

The zigzag-chain (section 1.3.3) and ladder (section 1.3.2) models can be combined to obtain the frustrated spin ladder [228, 412]. For the present work, the two-leg frustrated spin ladder depicted in Fig. 1.3 is relevant. Its zero-field phase diagram and excitations were studied in [228, 385, 412].

The ground state of the model is a spin singlet (e. g. , [228]). Any such state can be represented as a superposition of so-called valence-bond states, i. e. , product states consisting of pairs of spins bound into singlets [230], which constitutes the resonating valence-bond (RVB) picture [32]. For example, the ground-state doublet of the zigzag chain (section 1.3.3) at the disorder point $J_2/J_1 = 0.5$ [69] is given exactly by two valence-bond states corresponding to the two possible dimerization patterns [242]. Because the valence-bond configuration of the dimerized ground state does not exhibit quantum fluctuations at the disorder point [242], the corresponding states qualify as a valence-bond solid (VBS) [16]. An application of the RVB picture to the simple spin ladder can be found in [440]. For the frustrated

²Note that the latter is required by the Lieb-Schultz-Mattis theorem [88, 233, 440].

³Sometimes, correlations are represented in Fourier space and considered incommensurate as soon as there is a splitting of the peak in the spin-structure factor. Since the peaks have an intrinsic width, this results in a slightly larger threshold [69] (see also [348]). However, unlike many scattering techniques, NMR is sensitive to the real-space correlations, such that this subtlety can be safely ignored.

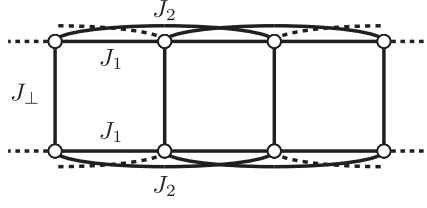


Figure 1.3: A finite-length segment of a two-leg frustrated spin ladder. Circles represent localized spins and solid black edges correspond to exchange interactions.

ladder, two different regimes are observed [228] (cf. Fig. 1.4). At low rung coupling, the system behaves essentially like a zigzag chain, except that J_{\perp} provides a confining potential binding the spinons into triplons [228, 412]. Frustration gives rise to a dimerized phase (columnar-dimer phase) which closely resembles the dimerized state of the zigzag chain [228]. Larger rung couplings yield a non-degenerate and more ladder-like ground-state with dominant contributions from singlet bonds along the rungs (rung-singlet phase) [228]. In all cases, sufficient frustration J_2/J_1 gives rise to incommensurate real-space correlations [228].

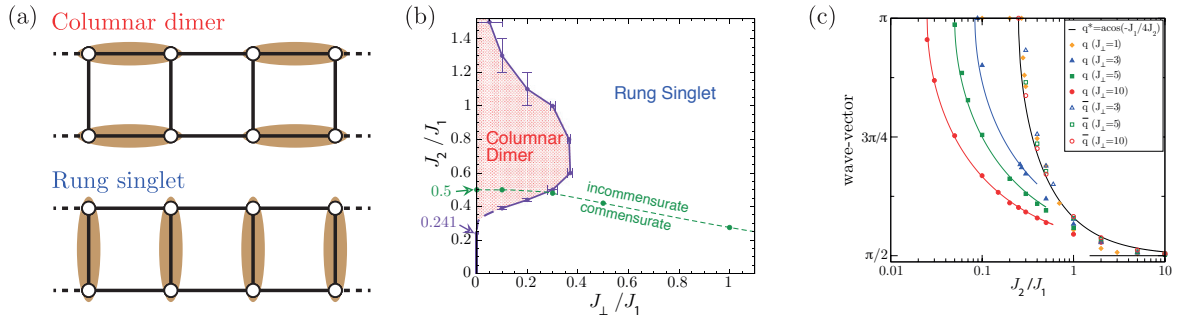


Figure 1.4: (a): Schematic representation of the dominant valence-bond configurations in the ground-state of the frustrated spin ladder in the columnar-dimer (CD) and rung-singlet (RS) phases (redrawn after [228]). (b): Phase diagram of the frustrated ladder as function of rung coupling J_{\perp}/J_1 and frustration J_2/J_1 ($J_1 > 0$) [228]. The green dashed line separates commensurate and incommensurate real-space correlations. (c): Evolution of wavevector with model parameters [228]. The authors of [228] distinguish real-space correlations (q), momentum-space correlations (position of peak in spin-structure factor, \bar{q}), and the location of the spin gap (q^*). (Reprinted figures (b) and (c) with permission from Ref. [228]. Copyright 2011 by the American Physical Society.)

A singlet-excitation gap closes at the Ising-like second-order transition from the rung-singlet (RS) to the columnar-dimer (CD) phase, whereas the spin gap persists [228, 412]. Correspondingly, the dimer-dimer correlation length diverges at the transition, while the spin-spin correlation length does not [228]. The low-energy singlet excitations in the vicinity of the CD phase should be visible in the specific heat, but not in the magnetic response [228].

1.4 Numerical methods

1.4.1 Exact diagonalization

The most direct approach consists in the numerical diagonalization of the matrix representing the Hamiltonian in a suitable basis. This standard method is known as *exact diagonalization* (ED) and two variants are usually distinguished (see, e. g. , [130, ch. 18] for details).

Full diagonalization, or *full-spectrum ED*, calculations determine a complete eigensystem of the Hamiltonian. The results enable the evaluation of various finite-temperature properties. Full-spectrum ED typically requires $\mathcal{O}(d^2)$ memory (for matrix and eigenbasis storage) and $\mathcal{O}(d^3)$ (worst-case; see, e. g. , [168, p. 42-22]) time, where d denotes the dimension of the Hilbert space which increases exponentially with system size.

In this work, full diagonalization was found impracticable for systems consisting of more than 20 spin- $1/2$ entities. However, Hamiltonians are often sparse—the Heisenberg interaction in the S_z -basis being a good example. Matrix-vector products with a sparse Hamiltonian can be computed efficiently, making iterative diagonalization algorithms an attractive alternative. The associated methods are called *sparse diagonalization*. Typical algorithms calculate the extremal, i. e. , lowest- or highest-energy, eigenpairs of a system using $\mathcal{O}(d)$ memory and time. A popular choice is the Lanczos algorithm (e. g. , [130, ch. 18]), which is also used by the software employed in this work [49]. Unfortunately, this algorithm does not allow for a reliable determination of the eigenvalue multiplicities [130, p. 542], which are required for the correct prediction of ground-state degeneracy and finite-temperature properties. For this purpose, the application would need to be modified to make use of, e. g. , the block-Lanczos or the Jacobi-Davidson method (e. g. , [130, ch. 18]). Another interesting algorithm is FEAST [222, 321]. It may seem tempting to use sparse diagonalization to extract a part of the spectrum, in order to obtain low-temperature approximations to various finite-temperature properties. However, the density-of-states in the quasi-continuous regions of the spectrum usually still scales exponentially with system size.⁴ Together with the orthogonalization step required by most algorithms, the resulting complexity becomes comparable to full-spectrum ED. Therefore, as is well-known, sparse diagonalization is mainly useful for determining a few spectrally-isolated (or extremal) eigenpairs.

1.4.2 Monte Carlo

The application of Monte-Carlo techniques to classical models is well-known [261]. Several extensions to quantum models exist, the related techniques being known as *Quantum Monte Carlo* (QMC) (see [344] for an introduction). In general, QMC is a very efficient method for calculating various finite-temperature properties. However, negative sampling weights are known to arise for frustrated quantum spin systems.⁵ This so-called sign problem results in exponential scaling and thus inhibits large-scale simulations of frustrated spin models at low temperatures (e. g. , [130]). Although the sign problem is basis dependent, it is NP hard, making the existence of a generic polynomial-time solution highly unlikely [400].

⁴This was seen explicitly for the calculations reported in chapter 5.

⁵For the stochastic-series expansion (SSE) representation (see, e. g. , [390]), this problem appears whenever the interaction graph contains cycles of magnetic bonds with an odd number of anti-ferromagnetic (transverse) couplings (this is a straightforward consequence of, e. g. , [390, eq. 11] and the surrounding discussion in [390]).

1.4.3 Density-matrix renormalization group

One of the few techniques capable of simulating large frustrated systems is density-matrix renormalization group (DMRG). While the method owes its name to the original formulation using a real-space decimation procedure [441], it can be equivalently understood as a variational method acting on a specific class of trial states called matrix-product states (MPS), which enables the application to a variety of models [350]. The DMRG code used in this work (see section A.1.5 for details) is based on the MPS formulation and can handle degenerate ground states [49, 111]. Degenerate and excited states are obtained iteratively, by projection onto the orthogonal complement of the previously-found (approximate) eigenstates [111].

For a system consisting of N subsystems (e. g., spins) with internal states $|\sigma_i\rangle$, a global state $|\psi\rangle$ is an MPS⁶ if it can be represented as

$$|\psi\rangle = \sum_{\sigma_1, \dots, \sigma_N} A^{\sigma_1} A^{\sigma_2} \dots A^{\sigma_{N-1}} A^{\sigma_N} |\sigma_1, \dots, \sigma_N\rangle ,$$

with matrices A^{σ_i} [350, section 4.1.3]. The approximation made in the DMRG method consists in restricting the dimension of these matrices such that it does not exceed a so-called *bond dimension* m [111, 350].

The optimization of the variational ansatz $|\psi\rangle$ relies on an iterative procedure, which adjusts the matrices associated with individual sites or pairs of sites, one at a time [111]. Typically, the lattice is traversed in an ordered fashion during each optimization sweep, with alternating left-to-right and right-to-left sweeps [111]. As the number of sweeps s increases, the MPS ansatz is assumed to converge towards a good approximation of the ground state ([350, p. 149] and [111]). However, it can happen that the optimization procedure gets trapped in a local minimum or advances very slowly ([350, p. 149] and [111]). Therefore, the convergence of the results clearly needs to be checked in practice.

The computational complexity is $\mathcal{O}(N)$ (e. g., [314]) and $\mathcal{O}(m^3)$ [111, 349]. However, it should be noted that any long-range entanglement in the system requires an increase of m along with N to maintain a given accuracy (see [349, p. 16.4]). It seems to be established that finite-system DMRG works best with open boundary conditions [444]. Typically, the entanglement structure of the ground state of a periodic system requires much larger values of m for a given degree of approximation [380]. On the other hand, open boundary conditions often give rise to boundary effects, such as Friedel oscillations, which can make it difficult to draw reliable conclusions about the properties of the bulk (see, e. g., [111, 112]). At least for specific models, so-called soft boundary conditions can reduce such effects [361]. In the present work, open boundary conditions are used and boundary effects are excluded by checking that the conclusions do not depend on the system size.

1.4.4 Symmetries

Whenever a system with Hamiltonian \mathcal{H} exhibits a symmetry described a group G whose representation on the Hilbert space satisfies $[g, \mathcal{H}] = 0 \forall g \in G$, the Hamiltonian can be block-diagonalized by decomposing the Hilbert space into irreducible representations of G . In practice, this can greatly reduce the computational effort needed to diagonalize \mathcal{H} (see, e. g., [130, ch. 18] for details). The following standard symmetries are relevant for this work.

⁶Normalization conventions and other details are neglected here, see [350] for more information.

- Lattice models with periodic boundary conditions are invariant under the group of lattice translations. Since this group factorizes into subgroups corresponding to translations along each lattice dimension, the one-dimensional case is considered without loss of generality. As is well known, this abelian and cyclic group yields one-dimensional irreducible representations labeled by $k = \frac{2\pi n}{L}$ ($n = 0, 1, \dots, L-1$), with L the extent of the lattice. Denoting the lattice translation by j unit cells as T_j , a state $|s_k\rangle$ transforms according to representation k if $\forall j : T_j |s_k\rangle = \exp(-i k j) |s_k\rangle$.
- Rotation symmetries in spin-space can result in additional conserved quantities, like magnitude and/or z -component of total spin $\mathbf{S}_{\text{tot}} = \sum_i \mathbf{S}_i$. Whenever the system is rotation-invariant about the z -axis (without loss of generality), $[S_{\text{tot}}^z, \mathcal{H}] = 0$ and the Hamiltonian is block-diagonal in the S_z -basis. It is easy to see that, for the $S_{\text{tot}}^z = k - \frac{L}{2}$ sector of a system consisting of L spin- $1/2$ entities, this reduces the Hilbert space dimension from 2^L to $\frac{L!}{k!(L-k)!}$.

Symmetries are generally represented by unitary (or anti-unitary) operators [446, pp. 251-254] (see also [43]), which implies that traces and hence quantum-statistical averages of local observables are invariant under G . Thus, exact calculations will never directly reveal any symmetry breaking. This well-known fact is already manifest in classical systems like the Ising ferromagnet and is usually circumvented by inclusion of an external symmetry-breaking field, certain Monte-Carlo techniques (see, e. g. , [55]), or the indirect study of the symmetry-breaking tendency through correlations.

1.4.5 Site-dependent g-tensors

The magnetic moment created by a spin $\mathbf{S}_{i,p}$ is given by $\boldsymbol{\mu}_{i,p} = -\mu_B g_i \mathbf{S}_{i,p}$, where p denotes the lattice position of the spin and g_i the g-tensor (see section 1.5.9). As is well known (see, e. g. , [15]), the presence of different g-tensors in a material, as suggested by the additional sub-lattice index i , can have important effects on the low-temperature magnetic susceptibility (see appendix for details, section A.5.3).

Consider a generic spin system with internal magnetic interactions described by a Hamiltonian \mathcal{H}_0 . Including the Zeeman interaction with an external magnetic field \mathbf{B} , the full Hamiltonian \mathcal{H} takes the form

$$\mathcal{H} = - \sum_{i,p} \mathbf{B} \cdot \boldsymbol{\mu}_{i,p} + \mathcal{H}_0 \quad .$$

The local magnetic susceptibility $\chi_{i,p}$ is then

$$\chi_{i,p}^{\alpha\beta} = \frac{\partial \langle \mu_{i,p}^\alpha \rangle}{\partial B^\beta} = \sum_i \frac{\mu_B^2}{N} (g_i C_{ij} g_j^T)^{\alpha\beta} \quad , \quad (1.4)$$

where $\langle A \rangle$ denotes the thermal and quantum-mechanical average of the observable A . For the sake of brevity, equation (A.5.3) and the machinery required to calculate C_{ij} are developed in the appendix (section A.5.3).

1.5 Pulsed nuclear-magnetic resonance

Most atomic nuclei have a nuclear spin \mathbf{I} [229, p. 12], which interacts with its environment. These interactions determine the energy levels of the nucleus. Nuclear-magnetic resonance (NMR) is a spectroscopic technique which probes the transitions between these nuclear-spin energy levels. If the nucleus

is embedded in a solid, the data provide information about the magnetic and electric fields at the site of the nucleus, which is why NMR is commonly classified as a *microscopic local probe*.

The purpose of this section is to provide a brief introduction to NMR by illustrating the basic concepts. For the sake of simplicity, the treatment is not the most general. In particular, the primary focus is on $I = 1/2$ nuclei in a strong external magnetic field, since this case is relevant for part II of this work. For more complete discussions, the reader is referred to the topical literature. The following, standard introduction to nuclear magnetic resonance is based on [8, 229, 422] and [74, ch. 2], as well as general knowledge corresponding to graduate-level physics courses (e. g. , [96, 343]).

1.5.1 Nuclear moments

The nuclear magnetic moment is [74, p. 15]

$$\boldsymbol{\mu}_N = h \gamma \mathbf{I} \quad ,$$

with the Planck constant h and the nuclear gyromagnetic ratio γ . Typically, γ is specified in MHz/T to ensure the correct units of the nuclear Zeeman energy

$$\mathcal{H}_Z = -\boldsymbol{\mu}_N \cdot \mathbf{B} \quad .$$

Here, \mathbf{B} denotes the magnetic field at the position of the nucleus, which can be applied externally and/or be created by the sample. Furthermore, nuclei with spin $I > 1/2$ feature an electric quadrupole moment Q , which couples to the electric-field gradient tensor \mathbf{V} ($V_{ij} = \partial_i \partial_j E$ with the electric field \mathbf{E}) through the nuclear quadrupole interaction [229, p. 208] (see also [95])

$$\mathcal{H}_Q = \frac{eQ}{2I(2I-1)\hbar} \mathbf{I} \cdot \mathbf{V} \cdot \mathbf{I} \quad .$$

Higher moments with corresponding interactions arise for nuclei with higher spin [8], but are usually neglected.

1.5.2 Magnetic resonance

In general, the interactions \mathcal{H}_Z and \mathcal{H}_Q lift the degeneracy of the $2I + 1$ nuclear-spin levels. Resonant radio-frequency (RF) magnetic fields can then be used to drive transitions between these energy levels, as exemplified below for the case $I = 1/2$ (section 1.5.4). In the following, the term *nuclear magnetic resonance* (NMR) will be used generically for resonances arising due to arbitrary combinations of \mathcal{H}_Z and \mathcal{H}_Q . In addition, the expression *nuclear quadrupole resonance* (NQR) is commonly used to emphasize the contribution of \mathcal{H}_Q . Although this discussion focuses on nuclear magnetic moments, similar resonance effects can be observed in other systems; e. g. , electron spins give rise to electron spin resonance (ESR) (e. g. , [9]), or the related ferromagnetic resonance (FMR) (e. g. , [204]).

1.5.3 Nuclear magnetization

Real applications involve finite temperatures and macroscopic numbers of nuclear spins, which is why a formulation using density matrices is appropriate [229, pp. 259 ff.]. The macroscopic nuclear magnetization created by a set of nuclei is then given by $\mathbf{M}_N = \langle \boldsymbol{\mu}_N \rangle = h \gamma \text{Tr} \rho \mathbf{I}$ (up to normalization), where

ρ denotes the density matrix, whose time evolution is described by the Liouville-von Neumann equation [353, p. 16]

$$i\hbar \frac{\partial \rho}{\partial t} = [\mathcal{H}, \rho] \quad . \quad (1.5)$$

While most of the concepts can be extended to nuclear spins $I > 1/2$ [229], the discussion is restricted to $I = 1/2$ hereafter (cf. section 1.5.1).

Consider the standard basis ($|+\rangle, |-\rangle$) corresponding to the quantization axis z . Since ρ is Hermitian, positive semi-definite, and $\text{Tr } \rho = 1$ [343, pp. 181-182], there exists $\mathbf{a} \in \mathbb{R}^3$ with $\|\mathbf{a}\|^2 \leq 1$, such that $\rho = \frac{1}{2}(1 + \mathbf{a} \cdot \boldsymbol{\sigma})$ (cf. [343, eq. 3.2.38 and p. 182]). Here, $\boldsymbol{\sigma}$ denotes the vector formed by the Pauli matrices [434]. Thus, any mixed state represented by the density matrix ρ can be identified with a point inside the unit sphere. The surface of the sphere corresponds to the pure states, for which $\rho^2 = \rho$ [343, p. 182]. This is the so-called *Bloch sphere* representation (see, e. g., [12] for further details) depicted in Fig. 1.5. Note that the *Bloch vector* \mathbf{a} corresponds to the macroscopic nuclear magnetization (cf. [74, p. 16]), since $\mathbf{M}_N = \frac{\hbar}{2}\gamma \mathbf{a}$.⁷

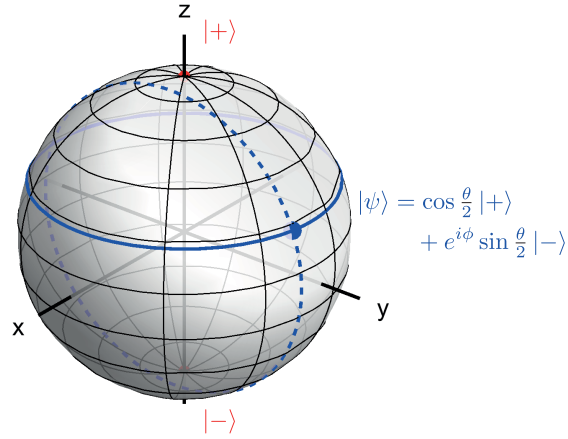


Figure 1.5: Bloch sphere representation of quantum states. The poles (red points) correspond to $|\pm\rangle$. A generic (pure) state $|\psi\rangle$ is depicted by a blue point. Blue solid and dashed lines illustrate precession and nutation, respectively. See text for details.

1.5.4 Dynamics of nuclear magnetization

For a time-independent Hamiltonian \mathcal{H} , it is easy to check that the solution of (1.5) is given by $\rho(t) = e^{-i\mathcal{H}t/\hbar} \rho e^{i\mathcal{H}t/\hbar}$. The particular case $\mathcal{H} = \frac{\hbar}{2}\omega \mathbf{n} \cdot \boldsymbol{\sigma}$, with $\|\mathbf{n}\| = 1$, yields⁸

$$\rho(t) = \frac{1}{2} \{ 1 + [(\mathbf{a} \cdot \mathbf{n})\mathbf{n} + \cos(\omega t)(\mathbf{a} - (\mathbf{a} \cdot \mathbf{n})\mathbf{n}) + \sin(\omega t)(\mathbf{n} \times \mathbf{a})] \cdot \boldsymbol{\sigma} \} \quad . \quad (1.6)$$

⁷This is easy to see using the identities in footnote 8.

⁸The following identities are useful [343, p. 170]

$$\begin{aligned} \exp(i\alpha \mathbf{n} \cdot \boldsymbol{\sigma}) &= \cos \alpha + i(\mathbf{n} \cdot \boldsymbol{\sigma}) \sin \alpha \\ (\mathbf{a} \cdot \boldsymbol{\sigma})(\mathbf{b} \cdot \boldsymbol{\sigma}) &= \mathbf{a} \cdot \mathbf{b} + i\boldsymbol{\sigma} \cdot (\mathbf{a} \times \mathbf{b}) \quad . \end{aligned}$$

Thus, the time evolution corresponds to a rotation of the Bloch vector \mathbf{a} by an angle ωt about the axis \mathbf{n} , which simplifies the following discussion.

Consider first the effect of a static magnetic field $\mathbf{B}_0 = B_0 \mathbf{e}_z$. The corresponding Zeeman Hamiltonian is $\mathcal{H}_0 = \frac{\hbar}{2}\omega_0\sigma_z$, with $\omega_0 = -2\pi\gamma B_0$. The resulting time evolution of an arbitrary Bloch vector is *precession* around the z -axis (blue solid trajectory in Fig. 1.5). If B_0 corresponds to an external magnetic field, this motion is called Larmor precession and ω_0 is the (angular) Larmor frequency. Moreover, if the external magnetic field is dominant, it is clear that only the longitudinal component of the internal magnetic field created by the sample contributes to the precession frequency ω to leading order (see [74, p. 162]).

As mentioned in section 1.5.2, resonant radio-frequency (RF) pulses are an important building block of any NMR experiment. The frequency ω_r of the pulses is called *reference frequency*. It will be convenient to decompose the Hamiltonian according to $\mathcal{H} = \mathcal{H}_0 + \mathcal{H}_1$ with $\mathcal{H}_0 = \frac{\hbar}{2}\omega_r\sigma_z$, and to work in the interaction picture [343, pp. 336-339] corresponding to \mathcal{H}_0 . The transformed density matrix $\rho_I = e^{i\mathcal{H}_0 t/\hbar} \rho e^{-i\mathcal{H}_0 t/\hbar}$ [343, p. 338] satisfies a modified Liouville-von Neumann equation,

$$i\hbar \frac{\partial \rho_I}{\partial t} = [\mathcal{H}_I, \rho_I] \quad , \quad (1.7)$$

with $\mathcal{H}_I = e^{i\mathcal{H}_0 t/\hbar} \mathcal{H}_1 e^{-i\mathcal{H}_0 t/\hbar}$ (cf. [8, p. 105]). Intuitively, this represents a transformation into a *rotating reference frame*, i. e. , a Bloch sphere which is following the precession induced by \mathcal{H}_0 (see [229, pp. 241 ff.]). This standard modification is very helpful when dealing with time-dependent magnetic fields, as described below.

In a typical NMR experiment, the sample is placed in a strong external magnetic field $\mathbf{B}_{\text{ext}} = B_{\text{ext}} \mathbf{e}_z$. As mentioned before, the transverse components of the magnetic field created by the sample are usually negligible, such that the average field at the nucleus is written as $\mathbf{B}_0 = B_0 \mathbf{e}_z$. This field gives rise to the free precession frequency ω . In addition, a small oscillating magnetic field $\mathbf{B}_{\text{rf}}(t)$ is applied perpendicular to \mathbf{B}_{ext} . Without loss of generality, $\mathbf{B}_{\text{rf}}(t) = B_1 \cos(\omega_r t - \varphi) \mathbf{e}_x$. Almost-resonant pulses are assumed, i. e. , $\omega_r \approx \omega$. After defining $\omega_1 = -2\pi\gamma B_1/2$,

$$\mathcal{H}_1 = \frac{\hbar}{2}(\omega - \omega_r)\sigma_z + \hbar\omega_1 \cos(\omega_r t - \varphi) \sigma_x \quad .$$

The interaction-picture Hamiltonian is then obtained analogously to, or by re-using, equation (1.6), followed by some standard trigonometric manipulations,

$$\begin{aligned} \mathcal{H}_I &= e^{i\frac{\hbar}{2}\omega_r\sigma_z t/\hbar} \mathcal{H}_1(t) e^{-i\frac{\hbar}{2}\omega_r\sigma_z t/\hbar} \\ &= \frac{\hbar}{2}\omega_1 [\cos(\varphi)\mathbf{e}_x + \sin(\varphi)\mathbf{e}_y + \cos(2\omega_r t - \varphi)\mathbf{e}_x + \sin(2\omega_r t - \varphi)\mathbf{e}_y] \cdot \boldsymbol{\sigma} + \frac{\hbar}{2}(\omega - \omega_r)\sigma_z \quad . \end{aligned}$$

In most cases $B_1 \ll B_0$ and the non-resonant components with frequency $2\omega_r$ can be neglected [229, p. 247], yielding the so-called *rotating wave approximation* (see [229, eq. 10.26] and, e. g. , [96, pp. 357 ff.]),⁹

$$\mathcal{H}_I = \frac{\hbar}{2}(\omega_1 \cos(\varphi), \omega_1 \sin(\varphi), \omega - \omega_r) \cdot \boldsymbol{\sigma} \quad . \quad (1.8)$$

The radio-frequency magnetic field B_1 is usually pulsed, and pulse durations are generally long compared to ω^{-1} . It is therefore justified to integrate the equation of motion (1.7) with piecewise-constant, i. e. , time-independent, \mathcal{H}_I . However, (1.7) is formally equivalent to (1.5), whose solution is (1.6). The two experimentally relevant cases are described below.

⁹Similarly, any longitudinal components of the oscillating field are negligible. The factor 2 in the definition of ω_1 arises because half the amplitude of the oscillating field corresponds to the non-resonant component.

1. If the driving field is off, $B_1 = 0$, the time evolution of the Bloch vector \mathbf{a}_I , representing the state ρ_I in the rotating reference frame, corresponds to *precession* (see [229, pp. 245 ff.]) around the z -axis with an angular frequency $\omega - \omega_r$ (blue solid trajectory in Fig. 1.5).
2. To visualize the effect of an RF pulse, it is sufficient to consider the *hard-pulse* limit $|\omega_1| \gg |\omega - \omega_r|$. In this case, \mathbf{a}_I rotates around the axis $(\cos \varphi, \sin \varphi, 0)$ at frequency ω_1 . This motion is known as *nutaton* (see [229, p. 251]), and corresponds to the blue dashed trajectory in Fig. 1.5 (in the case $\varphi = 0$). The pulse widths τ are generally measured in units of the nutation angles, e. g. , for a $\pi/2$ -pulse the length τ is chosen such that $\omega_1\tau = \pi/2$. Similarly, the phase settings $\varphi = 0, \frac{\pi}{2}, \pi$, and $\frac{3\pi}{2}$ are often denoted by the resulting rotation axes x, y, \bar{x} , and \bar{y} , respectively.

1.5.5 Experimental aspects

Typically, the sample is placed inside a coil, which is used to generate the radio-frequency (RF) field B_1 (see section 1.5.4). The precession of the Bloch vector \mathbf{a} observed in the absence of B_1 corresponds to a precession of the macroscopic nuclear magnetization (section 1.5.3). The resulting oscillating magnetic field generates an electromotive force in the coil (e. g. , [175]), which can be detected and recorded electronically. The setup typically involves (i) a magnet which creates the longitudinal magnetic field \mathbf{B}_{ext} (see section 1.5.4), (ii) a sample environment (cryostat) with an *NMR probe* which supports the sample with the surrounding RF coil, and (iii) a *spectrometer* which generates RF-pulses and records the electronic signal induced by the precessing nuclear magnetization. Some of these elements are covered in greater detail in part I of this work.

Conceptually, standard NMR experiments consist of two building blocks: (i) pulses which manipulate the nuclear magnetization, and (ii) periods during which the nuclear magnetization evolves freely and is observed passively. The nuclear-spin system is assumed to be in thermal equilibrium before each pulse sequence. The time required for the approximate realization of this initial state depends on the internal dynamics of the sample and ultimately limits the rate at which measurements can be performed. The static magnetic field \mathbf{B}_0 induces a net nuclear magnetization in thermal equilibrium [229, eqs. 11.18 and 11.22]. It is the Bloch vector $\mathbf{a}_0 = (0, 0, -a_0)$ corresponding to this equilibrium magnetization which is manipulated and observed during the NMR experiment.

1.5.6 Spectrum

In real samples, the distribution of magnetic fields \mathbf{B} is non-uniform. This can either be caused by the properties of the sample, or be due to experimental aspects such as inhomogeneity of the external magnetic field. The resulting distribution $p(\omega)$ of precession frequencies ω for a certain type of nucleus is called the *NMR spectrum* (see also [74, p. 20]), and entails a distribution of Bloch vectors (cf. isochromatic magnetic moments in [155]). Since the detection procedure outlined in section 1.5.5 is linear, the distribution $p(\omega)$ corresponds to the real-part of the Fourier transform of the detected signal (cf. [74, pp. 22-23]), for a suitable choice of reference phase (see, e. g. , [229, pp. 102 ff.]). In practice, the detection bandwidth is limited by the bandwidth of the pulses (cf. hard-pulse condition in section 1.5.4). Therefore, broad spectra are often measured by scanning the reference frequency and combining the partial spectra during post-processing of the data [91].

1.5.7 Basic experiments

1.5.7.1 Single-pulse experiment

As explained in section 1.5.5, NMR detects the precession of the nuclear magnetization. However, a non-trivial time-evolution only arises if the Bloch vector \mathbf{a} has a component orthogonal to z . The corresponding off-diagonal entries of the density matrix are called *coherences* [229, p. 261]. The simplest way to generate such components is by applying an individual RF pulse. The result of applying a $\frac{\pi}{2}$ -pulse is illustrated in Fig. 1.6(a). The pulse creates a transverse nuclear-magnetization component which precesses about the z -axis and thus can be detected inductively.

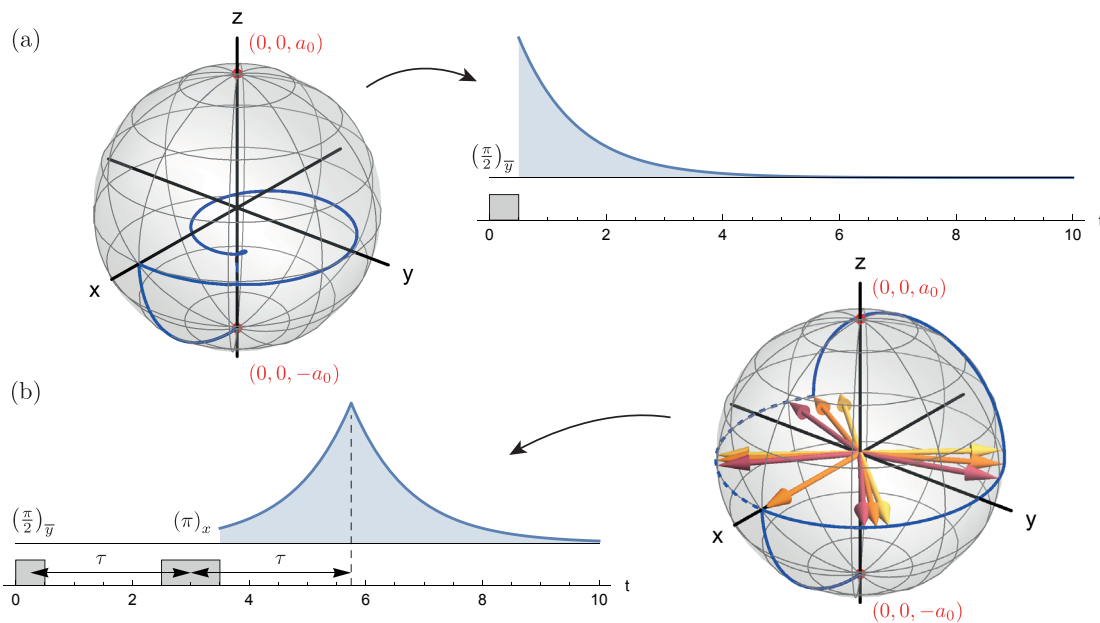


Figure 1.6: Schematic timing diagrams and trajectories on the Bloch sphere (cf. Fig. 1.5), corresponding to a single-pulse (a) and a spin-echo experiment (b) (figure inspired by [74, Fig. 2.3(a-b)]). In the timing diagrams, gray blocks represent resonant pulses $(\alpha)_k$ with pulse width α and phase k (see section 1.5.4 for notation), while the blue curves show the envelope of the acquired radio-frequency signals (section 1.5.5). The radius of the spheres corresponds to a_0 (section 1.5.5) and hard pulses are assumed for simplicity. See text for details.

1.5.7.2 Spin-echo experiment

Since some nuclei precess faster than others (cf. section 1.5.6), the distribution of Bloch vectors spreads along the equator of the Bloch sphere. This *dephasing* is illustrated by differently-colored arrows in Fig. 1.6(b) and contributes to the decay of the signal amplitude shown in Fig. 1.6(a). The central idea of the *spin-echo* experiment [155] is to apply a second pulse after a time delay τ . As shown in Fig. 1.6(b), this so-called refocusing pulse places the slowly-precessing nuclei before the faster ones, such that the distribution of Bloch vectors shrinks upon subsequent time evolution [dashed trajectory in Fig. 1.6(b)] (see also [74, p. 23]). Neglecting the effects of the finite pulse lengths, a spin echo forms at a time τ after the second pulse.

1.5.8 Relaxation

As illustrated in Fig. 1.6(a), the transverse nuclear magnetization decays with time. As discussed in section 1.5.7.2, the effect of static inhomogeneities can be circumvented by using a spin-echo sequence. However, there exist other dephasing mechanisms which cannot be refocused in general. Clearly, besides random fluctuations of the longitudinal magnetic-field component, dephasing can occur due to redistribution of angular momentum within the nuclear-spin population, e. g. , through direct nuclear-nuclear couplings or indirectly via interactions with other (electronic) magnetic moments (see [422, pp. 19-20], and also [74, p. 17]). Therefore, the intensity of the spin echo decays with τ in practice. Often, the decay is Gaussian and the associated time constant is called spin-spin relaxation rate T_{2g}^{-1} (e. g. , [422, p. 20]).

While dephasing yields an evolution towards the z -axis of the Bloch sphere, the decay towards the thermal equilibrium requires an exchange of energy with the environment and usually occurs on longer time scales [cf. Fig. 1.6(a)]. The decay is typically exponential¹⁰ and the associated time constant is called spin-lattice relaxation rate T_1^{-1} (e. g. , [422, p. 23]). The decay can be measured in a pump-probe fashion: First, a single pulse is applied to create a non-equilibrium population of the energy levels and then the longitudinal magnetization is detected after a time delay t , e. g. , by means of a spin-echo sequence. If the nuclear Zeeman interaction \mathcal{H}_Z is dominant, spin-lattice relaxation mainly occurs through magnetic-dipole transitions driven by fluctuations of the transverse component of the magnetic field at the nucleus (see, e. g. , [422, pp. 24-25]). Being analogous to controlling the populations of the nuclear-spin energy levels using transverse RF fields (section 1.5.4), the relaxation-process is most effective if the fluctuations are resonant. Typical NMR frequencies are of order 100 MHz and hence correspond to energies on the μeV scale. Since most electron dynamics involve higher energies, an adiabatic approximation is thus justified for the nuclei (cf. , e. g. , [372]).¹¹ Hence, under the above assumptions which are representative for the scientific part of the present work, the spin-lattice relaxation rate is predominantly sensitive to *slow* fluctuations of the transverse component of the magnetic field at the site of the nucleus.¹²

1.5.9 Hyperfine interactions and g-tensor

The effective magnetic field B_e created by an itinerant electron at relative position \mathbf{r} can be calculated ([67, 329] and [8, pp. 170 ff.]),

$$B_e = -\frac{\mu_0\mu_B}{4\pi} \left\{ \frac{g_L\mathbf{L}}{r^3} + \left[\frac{3(g_s\mathbf{S} \cdot \hat{\mathbf{r}})\hat{\mathbf{r}} - g_s\mathbf{S}}{r^3} + \frac{8\pi}{3}\delta(\mathbf{r})g_s\mathbf{S} \right] \right\}, \quad (1.9)$$

where \mathbf{L} and \mathbf{S} denote the orbital and spin angular momenta, and corresponding g-factors $g_L \approx 1$ and $g_s \approx 2$ were added. The first term, called *orbital* term [67], arises due to the minimal-coupling substitution $\mathbf{p} \mapsto \mathbf{p} + e\mathbf{A}$ (cf. [8, p. 171]). The second, *spin-dipolar* term [67] corresponds to the usual Zeeman interaction of the electrons, with the *Fermi-contact* term [67] proportional to $\delta(\mathbf{r})$ ensuring correct behavior in the limit $r \rightarrow 0$ [8, pp. 171-172]. Note that the orbital angular momentum of the Cu^{2+} ions relevant for part II of this work is typically mostly quenched by crystal-field effects ([371, pp. 89-91] and [114, p. 49]).

¹⁰Neglecting correlations between nuclei, a first-order treatment based on Fermi's golden rule results in a system of coupled first-order differential equations (detailed balance), whose general solution is a linear combination of exponential functions. For $I = 1/2$, only a single non-trivial exponential component appears. See, e. g. , [422, pp. 25-26] for details.

¹¹Conversely, the effect of the manipulations of the nuclear magnetization during an NMR experiment upon the electronic system is usually neglected.

¹²This is easy to see and discussed, e. g. , in [74, appendix C].

For localized moments with average position \mathbf{r}_0 , it is customary to write (e. g. , [74, 409])

$$\mathbf{B}_e = (A + D) \boldsymbol{\mu} \quad ,$$

with the magnetic moment $\boldsymbol{\mu} = -\mu_B g_s \mathbf{S}$. Here, the *dipolar coupling* is written separately,

$$D = \frac{\mu_0}{4\pi r_0^3} (3\hat{\mathbf{r}}_0 \hat{\mathbf{r}}_0^T - 1) \quad ,$$

whereas the *hyperfine coupling* A accounts for all remaining effects. If the electronic wavefunction factorizes into a spatial and a spin component, i. e. , orbital and spin-degrees of freedom are not entangled, the matrix A can in principle be obtained from (1.9). In this case, A is clearly symmetric. However, this assumption breaks down if spin-orbit interactions are present. In this case, \mathbf{S} is replaced by an effective angular momentum [10] and g_s is promoted to a matrix, the so-called *g-tensor* [428, ch. 4 and p. 113]. Although the g-tensor is not symmetric in general [104, 149, 366], it is often approximated as such [366].¹³ Similarly, the hyperfine coupling A is not symmetric in general [149, 366]. In principle, the hyperfine field \mathbf{B}_e may also involve interactions of higher order in \mathbf{S} after integrating out the spatial degrees of freedom [60, 216]. However, in the case $I = 1/2$ and $S = 1/2$ relevant for part II of this work, only bi-linear hyperfine interactions of the form $I^\alpha S^\beta$ arise [150]. With regard to the discussion of the high-field experiments presented later, it is emphasized that this does not exclude the possibility of a field-dependent coupling matrix $A + D$ (cf. [150]).

¹³Note that the resonance frequency in electron-spin resonance (ESR) is typically determined by the symmetric tensor $\sqrt{g_s g_s^T}$ [428, p. 93].

Part I

Development of NMR instrumentation

2 A firmware-defined direct-sampling NMR spectrometer

Remark The bulk of the work presented in the following chapter was performed by the author of the present work and subsequently published as a research article, written jointly with T. Shiroka, H.-R. Ott, and J. Mesot [311] (copyrighted by AIP Publishing LLC). Text, ideas, figures, and tables from the pre-print version of said publication [311] are reused in this chapter. To credit the contributions of all co-authors, the form 'we' is preserved in the corresponding sections of the text.

2.1 Introduction

As described in section 1.5, typical pulsed magnetic-resonance experiments require a spectrometer. Despite the focus on nuclear magnetic resonance (NMR), most of the following considerations also apply to related techniques, such as those mentioned in section 1.5.2, or even ultrasound measurements [1].

The spectrometer (i) generates the radio-frequency (RF) pulses used to manipulate the nuclear spins and (ii) records the resulting time evolution of the nuclear magnetic moment (see sections 1.5.4 and 1.5.5). Time-domain signal averaging improves the signal to noise ratio (SNR) (e. g. , [229, p. 86]), and allows for cancellation of certain undesired contributions by suitable variations of the signal phases (phase cycling) [106, 175]. This requires phase coherence, i. e. , a well-defined phase relation between the excitation pulses and the recorded signal (see, e. g. , [327]).

A laboratory NMR spectrometer should handle frequencies up to about 500 MHz (cf. , e. g. , [398]). Moreover, special requirements arise in typical condensed-matter physics applications: (i) Wide NMR spectra require a broad signal bandwidth [26]. (ii) In addition, efficient measurements of rapidly-relaxing nuclei require short receiver dead time and fast averaging rates [26].

2.2 Motivation

2.2.1 Signal conversion

Even for wide NMR lines, NMR signals are narrow-band compared to typical spectrometer reference frequencies (cf. section 1.5.4). Thus, the modern understanding of the Cardinal Theorem of Interpolation Theory [445] (also known as the Sampling Theorem, see [238]) implies that relatively low sampling rates are sufficient to describe the information content of such signals (see, e. g. , [148]). Typically, the signal is explicitly *down-converted* to a lower frequency by multiplication with a reference signal and subsequent filtering [197].

Since the continuous Fourier transform of a periodic lattice is a lattice (cf. , e. g. , [397]), the (idealized) sampling process itself corresponds, by virtue of the convolution theorem for the Fourier transform, to an implicit down-conversion which motivates the so-called undersampling (or super-Nyquist sampling) [148, 197, 310, 369]. An application of this idea to phase-coherently digitize NMR signals at 180 MHz

was demonstrated in [393, p. 365]. However, this places high requirements on the employed analog-to-digital converters (ADCs) and, unless an external analog bandpass filter is added to constrain the signal, the resulting data are ambiguous [197], which can be problematic when searching for signals in the presence of unknown spurious response and environmental noise.

By contrast, a fixed analog low-pass filter before the ADC is sufficient if the sampling rate satisfies the limits imposed by the sampling theorem [197]. In addition, even higher sampling rates (oversampling) are generally expected to improve the signal-to-noise ratio [416] (see also [74, p. 26]).¹ In particular, the analog down-conversion used by most conventional NMR spectrometers [197] can be completely avoided if the sampling rate of the ADCs is sufficiently high [197]. This *direct sampling* results in what is known as a direct-digital receiver [369, 395]. It is obvious that very similar considerations apply to the transmitter section of the spectrometer, where the corresponding approach is known as direct-digital synthesis (DDS) [231, 273].

Finally, NMR signals are usually down-converted to zero intermediate frequency for analysis and *quadrature detection* is employed in order to distinguish positive and negative frequencies (e. g., [197, 416]). Although typically implemented using analog components, this can also be achieved in the digital domain, by using a complex-valued local-oscillator signal in the explicit down-conversion scheme outlined above [197, 369, 416], resulting in a process known as digital down-conversion (DDC) (e. g., [341, 395]). An important advantage of DDC is the absence of artifacts created by low-frequency noise and mixer imbalance [197, 416].

2.2.2 Hardware aspects

Based on the preceding discussion, an NMR spectrometer employing direct-sampling in transmission and reception without undersampling appears conceptually most appealing. In particular, such a design avoids the cumbersome and error-prone manual routing of analog and digital signals associated with the construction of most conventional NMR spectrometers [cf., e. g., Fig. 2.1(a)].

Among the previous reports on NMR and magnetic-resonance imaging (MRI) instrumentation involving digital signal processing known to me [7, 148, 197, 231, 232, 264, 288, 310, 327, 341, 369, 391, 394, 395, 398, 454], which include demonstrations of direct sampling and DDC, the maximal sampling rate appears limited to 100 MS/s (1 MS = 10^6 samples).² On the other hand, signal-processing hardware with sampling rates up to several GS/s was available at the time of the work reported in this chapter.

For a typical width of 2 bytes per sample, a sampling rate of 1 GS/s yields data rates of about 2 GB/s. Although pulsing, DDS, and DDC can be performed in software (e. g., [369, 398]), implementations based on digital-logic circuits are generally preferred since they allow for real-time data processing and correspondingly accurate timing control. Each of the aforementioned functions can be provided by dedicated integrated circuits (e. g., [232, 394]), or programmable logic like field-programmable gate arrays (FPGAs) (e. g., [391]). FPGAs are a well-established platform for digital signal processing, and several applications to NMR, including FPGA-based spectrometers, were reported [7, 231, 232, 341, 391, 394]. Their main advantages (see, e. g., [391, 393]) are (i) parallel data processing, (ii) code portability (see below), and (iii) the possibility to simulate and test the design prior to implementation. Besides generic

¹Note, however, that in practice the SNR is usually limited by noise picked up by the external NMR circuit, as well as the noise figure of the pre-amplifier (see [165, 416]).

²Note that [310] used incoherent detection.

logic units providing combinatorial logic gates and memory elements (flip-flops), modern FPGAs contain specialized circuits such as multipliers (e. g. , [420]). The configuration of the programmable interconnects linking these elements is described by a binary file called *firmware*, which can be changed as often as desired [391]. The firmware is programmed using high-level hardware description languages (HDLs), like VHDL or Verilog (e. g. , [391]), and typically organized in modules (see, e. g. , [393, p. 358]). Thus, the same code can be re-used with different FPGA hardware. In addition, highly-optimized implementations of commonly-used circuits are available, e. g. , through the Xilinx CORE Generator System used in this work.

From a hardware perspective, an NMR spectrometer requires a transmitter (TX) output, a receiver (RX) input, and possibly a few digital general-purpose input/output (GPIO) lines for controlling auxiliary components. There exists a large variety of computer-controllable hardware products offering these rather generic features—sometimes even in a single device, as in the case of the product used in this work [see Fig. 2.1(b)]. By employing such general-purpose hardware, the implementation of the spectrometer reduces to manipulating the digital data and ensuring correct timing. This usually corresponds to developing suitable application software and, possibly, FPGA firmware, resulting in what is known as a *software-defined* or *firmware-defined instrument*, respectively. An early application of the software-defined design paradigm to NMR was reported in [167]. Furthermore, a firmware-defined NMR spectrometer based on general-purpose hardware was described in [7], but not demonstrated as part of a real experimental setup or at high frequencies.

In summary, knowledge about the practical feasibility of a direct-sampling digital NMR spectrometer capable of operating, without undersampling, at frequencies corresponding to the magnetic fields created by typical superconducting magnet systems appeared limited at the time, despite the commercial availability of suitable radio transceivers.

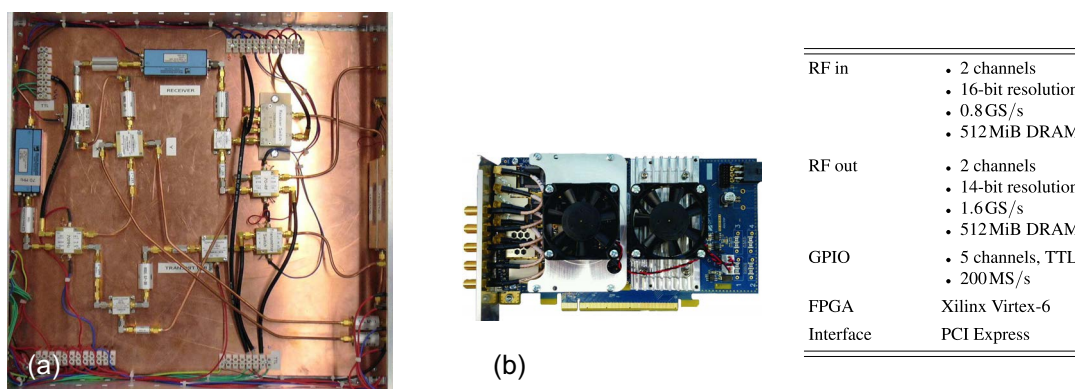


Figure 2.1: (a): Internals of a conventional hard-wired NMR spectrometer. (b): The radio-processor board used in this work (SDR14, Signal Processing Devices AB, Sweden), alongside with an overview of its key features (see text for details). The device is reproduced at a two-fold magnification with respect to the scale of panel (a).

2.3 Design

Following the considerations in section 2.2.2, a firmware-defined direct-sampling NMR spectrometer was implemented in the context of this work. It relies on a commercially-available general-purpose radio-processor device with user-programmable FPGA [see Fig. 2.1(b) for details]. Note that similar hardware

is available from various manufacturers and the implementation described here could, in principle, be easily adapted to a different device. In electrical and telecommunications engineering, the firmware-based approach is also known as *software-defined radio* (SDR) (e. g. , [57, 160]), which also explains the variety of corresponding hardware. However, SDRs typically process input and output data in streams (e. g. , [160]). Although SDR-based NMR spectrometers were reported, e. g. , recently in [160], the synchronization of transmitter and receiver usually requires work-arounds like loopback analog signals (cf. [160]). An implementation of an SDR transceiver based on the hardware used in the work was reported in [57]. While this previous work [57] inspired certain design choices in this work,³ dedicated FPGA firmware components were developed instead, in order to have direct control over the timing of the relevant signals inside the FPGA.

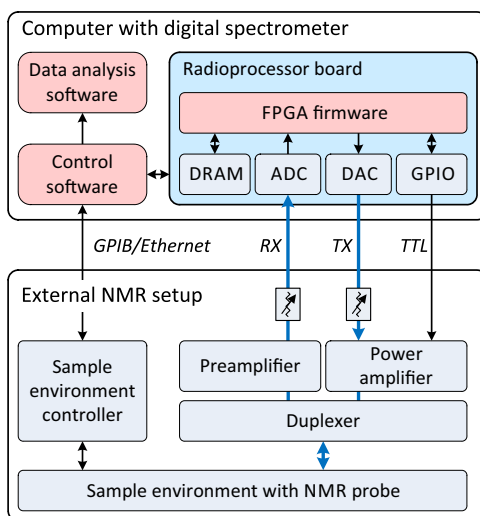


Figure 2.2: Hardware components of the NMR setup (see text for details). Firm- and software components are marked in red. Lines and arrows indicate signal and information flow; high-frequency analog signals are highlighted using thick blue lines.

Before describing the details, we show how the spectrometer integrates into the NMR setup (Fig. 2.2) (cf. [7, 197]). As discussed in section 2.2.2, the spectrometer can be considered a black box with three ports: (i) RX, (ii) TX, and (iii) amplifier unblank (TTL). The unblank signal is used to shut off the external power amplifier⁴, needed to generate sufficiently-strong excitation pulses, in order to reduce the noise while receiving (see, e. g. , [26]). Modern NMR probes use a single coil for excitation and reception, necessitating an additional routing device called duplexer [94]. Signal levels in condensed matter NMR experiments can be as low as -100 to -85 dBm, which is why one or more wideband pre-amplifiers are inserted into the receive path of the NMR setup (cf. , e. g. , [197]). Computer-controlled attenuators are placed between the spectrometer and the power amplifier, as well as between the pre-amplifier and the spectrometer. They allow for the scaling of the input signals to make the most effective use of the receiver’s dynamic range, as well as for the adjustment of the excitation-pulse amplitude (cf. , e. g. , [26]).

³This was primarily the use of half-band FIR filters (see section 2.3.4). Note that same choice of hardware and baseband sampling rate entails other similarities between the DDC units. For instance, a sample width of 24 bits allows for efficient use of the 48-bit DSP elements of the employed FPGA [57, 395, 420] and the need to process several samples in parallel is mandated by the system clock, which is imposed by the hardware manufacturer.

⁴65 dB gain with up to 60 dBm output in our case.

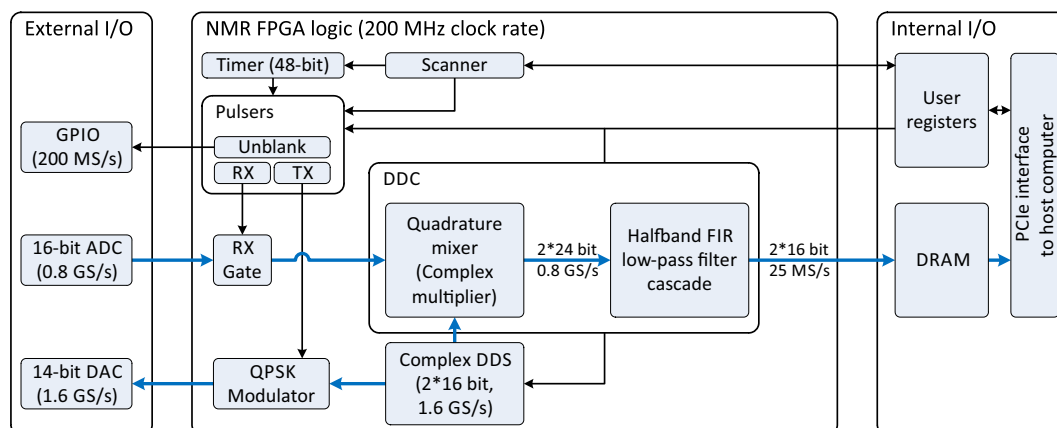


Figure 2.3: FPGA firmware block diagram of the digital spectrometer (see text for details). *External* and *internal I/O* refer to input/output connections to hardware outside and inside the measurement computer, respectively (cf. Fig. 2.2). Lines and arrows indicate information propagation; the flow of waveform data towards and from the radio-frequency front-end is highlighted using thick blue lines.

The layout of the FPGA logic developed in order to implement the NMR spectrometer is shown in Fig. 2.3. Its individual sub-components are described in the following subsections.

2.3.1 Interface, software and pulse programming

The radio-processor board used in this work provides a PCI express (PCIe) interface, enabling fast data transfers to and from the host computer. Drivers for Windows and Linux operating systems, an application programming interface (API) for the C programming language, and an FPGA development kit built around the Xilinx ISE FPGA development package are supplied by the hardware manufacturer. Hardware initialization, data acquisition, and data transfers are handled by the manufacturer's firmware and drivers. A set of user-programmable registers is provided to communicate with the user-defined logic components. These registers can be accessed at rates of over 80 000 reads/writes per second and are used to program, reset, and trigger the NMR experiments.

On the software side, a shared library (written in C++) controls the NMR logic implemented inside the FPGA and handles the acquired data. The library provides a high-level interface for performing NMR experiments. Currently, MathWorks MATLAB is used to both control and monitor the execution of the experiments. The data are analyzed following standard methods, implemented through a set of MATLAB scripts routinely used in our laboratory and originally developed by G. Allodi.

Timing relies on a 48-bit timer counting the number of clock cycles elapsed since the start of the NMR pulse sequence. Given the 200 MHz clock frequency of the firmware, this yields a time granularity of 5 ns and a maximum sequence duration of about 16 days, which is sufficient for our purposes. The pulser units are very simplistic: Each one stores a zero-terminated program table, containing pulse start and pulse duration (along with auxiliary data like TX phase, as applicable), and thus defining the time intervals during which the pulser output should be asserted (i. e., set to logical '1'). Currently, three such pulsers are responsible for RX gating, TX gating, and amplifier blanking, respectively.

2.3.2 Data transfer and averaging

The recorded signals are down-converted in real-time. Therefore, the memory required for storing the complex baseband data (two channels at 25 MS/s, 2 bytes per sample, records of typically 1 ms duration) is small and many records can be stored in the 512 MiB (1 MiB = 2^{20} bytes) DRAM (dynamic random-access memory) of the radio-processor device. Typical data transfer rates for the hardware used in this work are of the order of 100 to 400 MiB/s, which is of the order of the output data rate and therefore may represent a significant overhead. Our solution, inspired by common computer-science knowledge, is to divide the receiver DRAM into segments and to implement an on-device looping feature within our NMR logic (scanner block in Fig. 2.3). One memory segment can be read out while the other segment is being written to. This interleaved read-out process enables a simultaneous measurement and data transfer, such that the repetition rate of the NMR experiment is effectively only limited by the relaxation time of the studied nuclei.

On-device averaging would require simultaneous read and write access to the receiver DRAM by the FPGA, which is not supported by the hardware used in this work (according to the manufacturer). Instead, we use the interleaved read-out technique and perform averaging in software. The employed data types are 16-bit signed integer for the raw data, 32-bit integer for the average (1st moment), and 64-bit integer for a variance estimate (2nd moment). Tests have shown that the averaging speed is solely limited by the memory bandwidth of the host computer, most of which is required for loading and updating the aggregated data (sums and sums of squares). Following standard practice, subsequent chunks of records are therefore split into pages, in order to improve the locality of reference and hence make better use of the processor cache. Different pages are averaged in parallel. This optimized implementation can average over 2 GS/s on our test system (Intel Xeon E3-1240 with dual-channel DDR3-1333 memory), which is sufficient even for raw-data acquisition without DDC. The performance could be improved yet further by optimizing chunk and page sizes, upgrading the host computer hardware, or delegating the task to a suitable co-processor device. Finally, although not implemented in this work, on-device averaging of short waveforms is possible using memory cells within the FPGA [35].

2.3.3 Transmitter

The transmitter section of the spectrometer uses direct-digital synthesis (DDS, see section 2.2.1 and references therein). Due to the FPGA clock frequency of 200 MHz, eight phase-offset complex DDS cores are used in parallel in order to generate data at the DAC (digital-to-analog converter) sampling rate of 1.6 GS/s (such a design was previously evaluated in [57, pp. 45-46,53] in the more general context of digital up-conversion). These data also serve as a local oscillator (LO) signal for the receiver described below. The quadrature phase-shift keying (QPSK) modulator is needed for phase cycling.⁵ The 32-bit width of the phase accumulator results in a frequency resolution of less than 0.5 Hz, enough for our application. Fast phase-switching is possible, and frequency switching (see, e. g. [341]) or additional DDS units could be added with little effort. The latter are especially interesting for spin-lattice relaxation experiments using different nuclear transitions for excitation and detection [422, p. 26].⁶ If required, soft pulses [138] and arbitrary waveform generation could be included as well (cf., e. g., [232]).

⁵Note that changing the phase in steps of 90° simply amounts to selecting the right quadrature and negating it as needed.

⁶In principle, such experiments can already be performed by disabling the firmware-based DDC function, which essentially yields the software-based DDC approach described in [369], with all its associated performance challenges.

2.3.4 Receiver

The receiver uses the DDC technique reviewed in section 2.2.1. The DDC unit consists of a complex multiplier and a digital low-pass filter which removes the mixing image and reduces the data rate from 800 MS/s to 25 MS/s per quadrature. The baseband sampling rate was chosen to coincide with the maximal sampling rate of the conventional spectrometers used in our laboratory, which has proven sufficient in the past. Following [57], a filter chain consisting of five half-band finite impulse response (FIR) decimation filters (see, e. g. , [263, p. 172]) is used. The filter coefficients were obtained using the MathWorks MATLAB DSP System Toolbox. Some of the filters require the processing of several samples per clock cycle, which prevents the use of automatic code-generation tools (see also [57, p. 65]). The internal data processing is performed with 24-bit precision. Whenever truncation is required, convergent rounding to even (unbiased rounding) with saturation is used. Each filter stage reduces the sample rate by a factor of two. Therefore, for a given sample rate f_s before the filter, spectral components in a frequency interval $[\frac{f_s}{2} - \nu, \frac{f_s}{2}]$ will give rise to aliases [416] in the range $[0, \nu]$.⁷ Our filters are designed for a 10 MHz bandwidth (for each quadrature). The filter parameters have been chosen such that aliases within this band are suppressed by at least 70 dB. The passband ripple is less than 0.01 dB for the combined filter chain. While these values are sufficient for our application, they could be improved further if required.

Clock jitter [392] is a lesser concern given the large line widths typically encountered in condensed-matter NMR experiments. Moreover, as supported by the hardware used in this work and already noted in [392], such problems can obviously be solved with little effort by using an external sampling-clock source. Likewise, an external clock reference may be used whenever a higher frequency accuracy is desired.

Finally, we included an option to bypass the mixer, which is useful for experiments at very low frequencies (below about 7 MHz), where the mixer images are no longer rejected by the decimation filters. In order to ensure phase-coherent averaging also in this case, the DDS phase accumulators are reset before every single scan.

2.3.5 Implementation

The FPGA logic modules have been implemented in Verilog. Most of the modules use an AXI4-stream interface to simplify data-flow management [36]. Due to the large amount of data processed per clock cycle, register slices [37] had to be added in order to ensure timing closure. The resource usage of the final design is summarized in Table 2.1. Given the total resources available, the requirements of the NMR-specific logic are very reasonable and leave plenty of room for future extensions.

	NMR logic	Manufacturer's logic	Available
Slices	2862	16457	37680
BRAM	44	277	416
DSP48	69	151	768

Table 2.1: Overview of the resources used by the spectrometer logic and the manufacturer's firmware, as well as the total resources available on the FPGA chip. We distinguish logic slices, block random-access memory (BRAM) and 48-bit multipliers (DSP48).

⁷Aliasing is equivalent to Brillouin zone folding upon doubling the lattice constant in a crystal.

2.4 Testing

2.4.1 Synthetic tests

To demonstrate the performance of the digital receiver, we applied a fixed-frequency test signal to the receiver. In Fig. 2.4, we plot the power of the strongest spectral component in the recorded signal as a function of the spectrometer reference frequency, excluding frequencies outside the ± 10 MHz pass-band of the digital quadrature detector. The results are in very good agreement with the filter response simulated using MATLAB.

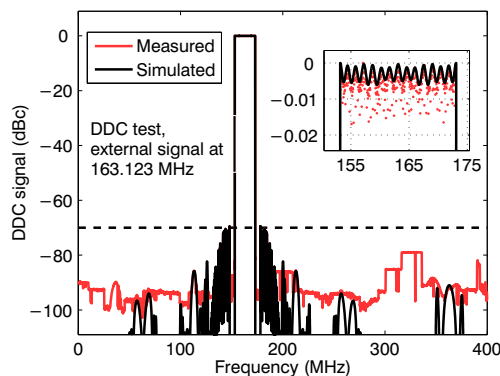


Figure 2.4: DDC gain over ± 10 MHz bandwidth for a 163.123 MHz input signal. The data have been normalized such that the maximum coincides with 0 dBc. Inset: Zoom-in showing negligible ripple inside the passband.

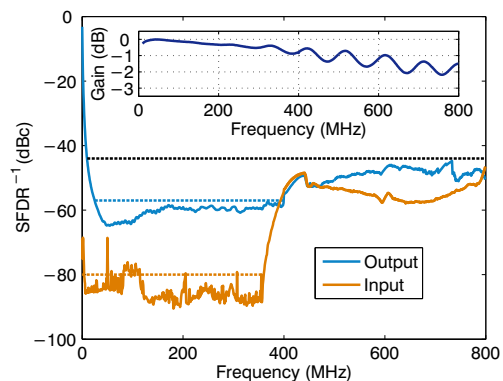


Figure 2.5: Measured SFDR of inputs and outputs of the radioprocessor device (see text). The dotted lines mark 80 dB (orange), 57 dB (turquoise), and 44 dB (black). Inset: Loop-back gain, normalized to its maximum. Oscillations are due to standing waves in the test setup.

The spurious-free dynamic range (SFDR), defined as the intensity ratio (in dB) between the strongest spurious signal and a given signal, was chosen as a figure of merit for the RF properties of the hardware and is shown in Fig. 2.5.⁸ The hardware used in this work employs interleaved sampling and a proprietary technique is used to compensate for imperfections of the ADCs [236]. These circuits were configured for the first Nyquist band, which explains the deterioration of the otherwise excellent input SFDR upon approaching 400 MHz. Since the noise floor of the radio-processor board is lower than the one of our oscilloscope, we use a loopback measurement to characterize the output-signal quality. Therefore, the output SFDR values above 390 MHz are worst-case estimates only. Finally, the combined gain of output and input (see inset of Fig. 2.5) is found to be reasonably flat up to 800 MHz.

The construction of a conventional spectrometer resembling the one depicted in Fig. 2.1(a) was part of a Master's thesis supervised by the author [212]. For this conventional spectrometer, the SFDRs of the transmitter and the receiver were of the order of 30 dBc and 50 dBc, respectively [212]. Although the corresponding parameters are better for the digital spectrometer, the practical relevance of this is limited, since the relatively narrow-band nature of nuclear-magnetic *resonance* implies that in most cases only spurious signals close to the resonance frequency need to be small, which is the case for both spectrometer designs. Still, direct sampling of the high-frequency signal has the conceptual advantage

⁸Harmonic distortion, known to originate from the test-signal source, has been excluded in the data analysis.

that spurious harmonics typically fall outside the passband of the digital receiver (e. g. , [323, point 3.2]).

2.4.2 Magnetic resonance experiments

Several NMR experiments were made to assess the performance of the new spectrometer. The results are compared with data obtained using a conventional spectrometer under the same experimental conditions (magnet, probe, and sample). All measurements were carried out at room temperature.

Figure 2.6 shows the spectrum of ^2H in heavy water in a magnetic field of 7 T. The spectrum was obtained by averaging two free-induction decay signals following a $\pi/2$ pulse. The linewidth of 0.7 kHz (FWHM) results from imperfect shimming of our magnet. The reference frequencies of both spectrometers were set to 46.155 MHz and the resulting data are in good agreement. In addition, the comparison also illustrates the absence of artifacts caused by low-frequency noise (“video” noise) and mixer imbalance (“ghost”) [197, 416].

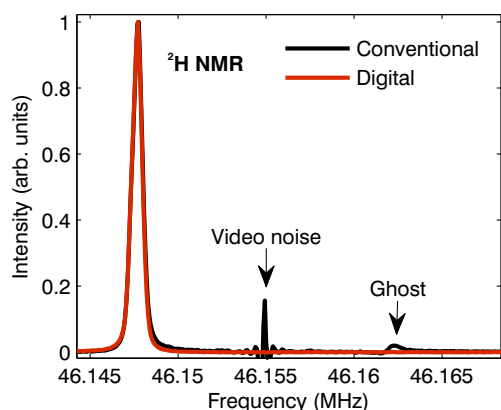


Figure 2.6: Comparison of ^2H NMR spectra in heavy water at 7.06 T recorded using a conventional and the digital NMR spectrometer (see text for details).

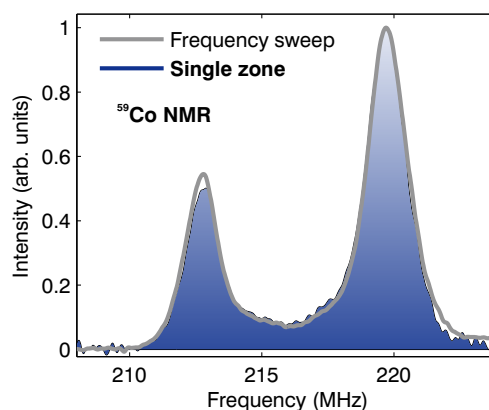


Figure 2.7: Zero-field ^{59}Co NMR spectrum of cobalt powder, recorded using the digital spectrometer (see text for details).

As a test case complementary to the slowly-relaxing, narrow-band deuterium resonance, NMR measurements were made on ^{59}Co in ferromagnetic cobalt powder in zero external magnetic field. The internal magnetic field gives rise to a rather broad spectrum spanning the range of 210-225 MHz, with two dominant peaks originating from different crystallographic phases [153, 376]. Because both, the detected signal as well as the driving RF field, are dramatically enhanced due to the magnetic order [334] (cf. also [376]), very short pulses can be used, which increases the excitation bandwidth. Figure 2.7 shows the ^{59}Co spectrum recorded with the digital spectrometer using a spin-echo sequence with 50 ns pulse duration and 20 μs pulse separation. The gray trace was obtained by varying the frequency in steps of 1 MHz and combining the individual spectra [91]. The shaded curve instead was recorded at a fixed reference frequency of 216.123 MHz. After correcting for the finite spectral width of the refocusing RF pulse⁹, the two spectra are in good agreement. Although such short pulses are rather exceptional in NMR, the data confirm the broad bandwidth of the spectrometer.

⁹Instead of the expected shape [155], for short pulses, we observe a linear relation between pulse width and signal amplitude.

2.5 Discussion and Conclusions

Motivated by the availability of suitable hardware, a digital NMR spectrometer adapted to the needs of condensed matter research was realized. The instrument relies on a commercially-available general-purpose radio-processor device with user-programmable FPGA, such that most NMR functionality is defined through the FPGA firmware and the application software. By adopting this firmware-defined approach [7], the amount of NMR-specific hardware is reduced (cf. Fig. 2.2) and the replication of an experimental setup is simplified. Also, additional functions can be implemented and tested without risk, since previous “known-to-work” configurations can be quickly restored at any time. Possible future extensions include soft pulses [138], multi-frequency operation [369] (see section 2.3.3), or even stochastic excitation [122, 195] (see also [62, 166]). Maintenance is reduced by relying on specified and well-tested hardware, which can be used for non-NMR purposes as well. As a side effect, the spectrometer is very compact and hence can in principle be easily transported (cf. [394]).

The use of direct sampling in both transmitter and receiver results in an SFDR which is superior to that of typical conventional spectrometers (section 2.4.1). Moreover, artifacts caused by low-frequency noise and mixer imbalance are absent in the digital receiver [197, 416] (section 2.4.2). Note that the absence of the aforementioned artifacts is known to be a general advantage of heterodyne over homodyne detection [416].¹⁰ The passband of the digital down-conversion filter is 20 MHz wide (± 10 MHz) and extremely flat. A comparable filter based on analog components would be difficult to realize (cf. [416]).

NMR nuclei are usually divided into two groups according to their gyromagnetic ratio: *Low-frequency* nuclei, up to and including ^{31}P , and the *high-frequency* nuclei $^{203,205}\text{Tl}$, ^3He , ^{19}F , and $^1,^3\text{H}$. The 400 MHz Nyquist frequency of the presented spectrometer corresponds to a magnetic field of over 23 T for the low-frequency nuclei (cf. [308]), which are the ones most commonly studied in condensed matter physics. This is comparable to the maximum fields of the best superconducting laboratory-NMR magnets available at the time of this writing [355]. Moreover, as shown in section 2.4.1, performance in undersampling mode is good up to 800 MHz. External analog filters need only to be changed when switching between undersampling and direct sampling. Furthermore, extending the firmware (Fig. 2.3) to handle quadrature input and output signals requires almost no modifications, so that external mixers for frequency up- and down-conversion could easily be incorporated in order to access frequencies beyond 800 MHz. Such configurations could be interesting, e. g., for measurements in pulsed magnetic fields.

Besides presenting and discussing synthetic benchmarks, we have shown that the spectrometer performs well in typical laboratory NMR experiments, which demonstrates the suitability of the chosen design for applications at signal frequencies well above 100 MHz (see section 2.2.2). Moreover, the considered test cases demonstrate that such a setup can compete with and even outperform conventional spectrometers. With regard to condensed-matter physics [26], a low dead-time (effectively solely limited by the recovery time of the external components shown in Fig. 2.2) and the ability to sustain fast repetition rates are emphasized (see section 2.3.2). Since the publication of the developments presented in this chapter [311], other spectrometer designs based on FPGAs have been described (e. g., [80, 382]). New software-defined solutions were also reported, e. g., in [287] (using components manufactured by National Instruments) and [160] (using the open-source SDR framework GNU Radio and a commercial SDR transceiver).

¹⁰For instance, similar observations were reported previously in [264] (unclear if direct sampling has been used) and independently in the context of an evaluation of transceivers for magnetic-resonance imaging [158].

3 NMR probes

3.1 Introduction

The NMR probe is an integral part of any NMR setup (cf. sections 1.5.5 and 2.3). Despite the existence of related literature (see, e. g., [98, 113] for introductions), there is no universal agreement regarding the technical details of probe construction, partly because the requirements differ from case to case. In our case, the NMR probe has three primary functions: (i) Supporting the sample and the surrounding radio-frequency (RF) coil, (ii) thermalizing the sample to the cooling apparatus, and (iii) providing an electrical connection to the coil.

Two NMR probes were developed within the context of this work. The first probe is intended to be used in conjunction with a ^4He flow cryostat, whereas the second is designed for a “cryogen-free” $^4\text{He}/^3\text{He}$ dilution refrigerator. The first one represents an evolution of an earlier design [74, 364]. Nevertheless, it is believed that a brief discussion of the differences to the previous version should be interesting for other researchers in the field. Furthermore, the basic design of this probe provides a good starting point for explaining the particular challenges associated with the development of an NMR apparatus based on the particular type of dilution refrigerator used in this work.

3.2 Tuning

In order to efficiently exchange energy with the NMR coil, the electrical circuit must be impedance-matched to the spectrometer [98]. This is usually achieved by incorporating the coil into a resonant circuit (“tank circuit”). Since impedances are complex-valued, the circuit must possess at least two adjustable parameters. Two standard technical approaches are particularly relevant for this work. The first approach, commonly referred to as *bottom tuning* (e. g., [220, p. 22] and [74, p. 31]), places the resonant circuit close to the coil and involves two adjustable capacitors [Fig. 3.1(a-b)]. While this typically allows for a high quality factor, the accessible frequency range is limited by the tuning range of the adjustable capacitors. Furthermore, the high signal levels used for exciting the nuclear spins (amplifiers with a radio-frequency output level of 1 kW are not uncommon) necessitate mechanically-adjustable capacitors, which must be supported by the design of the NMR probe. The alternative approach, called *top tuning* [Fig. 3.1(c)] (e. g., [74, p. 31]; cf. also [220, p. 22]), uses an adjustable-length coaxial line and one adjustable capacitor, which can be connected in parallel [as shown in Fig. 3.1(c)] or in series [2]. The main advantage of top tuning is that all adjustable elements of the circuit can be located outside the cryostat. Therefore, no practical limitations of the accessible frequency range arise, which is why this approach is often preferred when the magnetic fields are varied, e. g., during measurements in high magnetic fields.

The mathematical analysis of the circuits shown in Fig. 3.1(a-b) is straightforward. These two arrangements are sometimes called *high-* and *low-frequency configuration*, respectively (e. g., [74, Fig. 2.7]). In practice, the former arrangement is preferable, since it tends to yield larger accessible frequency intervals

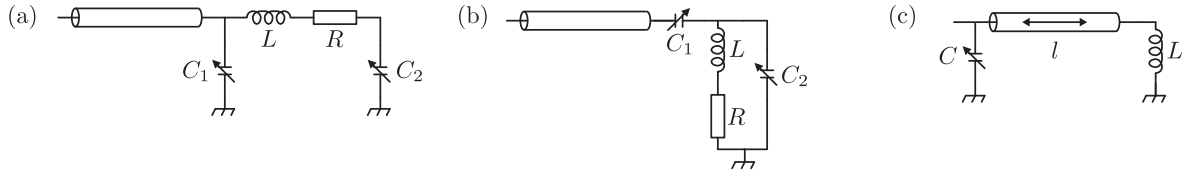


Figure 3.1: Examples of resonant electrical circuits commonly used to impedance-match NMR probes (e. g. , [176, Fig. 5], [220, Fig. 2.7], [74, Fig. 2.7], [98, Fig. 6]). The symbol used for the coaxial transmission line should be self-explanatory. The outer conductor of the coaxial line is connected to ground.

for a given type of capacitor (i. e. , frequency intervals $[\nu_{lo}, \nu_{hi}]$ with larger ν_{hi}/ν_{lo}). Moreover, only C_2 needs to handle very high voltages in this case. The top-tuning circuit [Fig. 3.1(c)] can be studied in a similar way, e. g. , by using the well-known result for the effective impedance of a device connected to a transmission line (e. g. , [324, p. 60]). However, since coil inductance L and variable capacitance C represent discontinuities of the transmission line, a formulation based on the reflection and interference of directional radio-frequency signals (see, e. g. , [324, Fig. 5.13 and eq. 5.40]) is considered more intuitive.

Finally, as has been seen by explicit calculation, the mathematical expressions corresponding to the circuits depicted in Fig. 3.1 only yield solutions for a non-zero resistance R [Fig. 3.1(a-b)], or a non-zero attenuation of the coaxial line [Fig. 3.1(c)]. Indeed, energy conservation clearly requires a dissipative element, since the circuits do not reflect any power once adjusted to the characteristic impedance of the signal source (power amplifier). Thus, besides the aforementioned mechanical aspects, an important difference between bottom and top tuning is the location where the energy of the high-power RF pulses is dissipated.

3.3 Thermal aspects

A special challenge when designing NMR probes for condensed-matter physics is that typically a trade-off between electrical characteristics (signal loss) and low-temperature performance (heat load) needs to be made (see, e. g. , [98]). Three main mechanisms for heat transport are considered: Radiative transfer, thermal conduction of the solid components, and convection. In this section, a brief reminder of the corresponding general cryogenics knowledge is given in order to provide a context for the subsequent discussion (see [320] for a more complete introduction).

Convection For this work, convection is only relevant in section 3.4, which deals with an NMR probe for a ^4He flow cryostat. In this case, convective heat transfer provides the main cooling mechanism. The effective cooling power depends on various operation parameters of the cryostat, like mass flow and pressure of the gas. Although, e. g. , the effective surface area of a probe may clearly affect the heat-transfer and thus the cooling efficiency, such effects are neglected in the following discussion.

Radiation The radiative heat flow $Q_{1 \rightarrow 2}^{(\text{rad})}$ between two surfaces with temperatures T_1 and T_2 , emissivities ϵ_1 and ϵ_2 , and equal areas A is given by the Stefan-Boltzmann equation,

$$Q_{1 \rightarrow 2}^{(\text{rad})} = \sigma \frac{\epsilon_1 \epsilon_2}{\epsilon_1 + \epsilon_2 - \epsilon_1 \epsilon_2} A (T_1^4 - T_2^4) \quad ,$$

where $\sigma \approx 5.67 \cdot 10^{-8} \text{ W m}^{-2} \text{ K}^{-4}$ (e. g. , [320, pp. 117-118]). Most low-temperature apparatus involves cylindrical probes with long and narrow support structures. It is common to interrupt such structures by *baffles* [320, pp. 118 ff.] [see Fig. 3.2(a) for an example]. Assuming predominantly radiative heat transfer and N thermally-floating baffles with areas A and emissivities ϵ , energy conservation implies¹

$$Q = \frac{1}{N+1} \frac{\epsilon \sigma A}{2-\epsilon} (T_1^4 - T_2^4) \quad .$$

Thus, even in the absence of any other heat-transport mechanisms, the baffles help reducing the radiative heat load. This effect is used heavily in cryogenics, especially in the form of so-called *superinsulation* materials consisting of thermally weakly-coupled stacks of metallized plastic foil with low emissivity (see [320, p. 123]). In case of a flow cryostat, the gas flow provides additional cooling of the baffles, such that the radiative heat load is reduced even further.

Conduction Thermal conduction is described by Fourier's law $\mathbf{q} = -\kappa \nabla T$ (see, e. g. , [213, p. 236]), with heat flux density \mathbf{q} , temperature T , and thermal conductivity κ . It is instructive to consider an approximately one-dimensional geometry following a curve γ with constant cross-sectional area A . If the endpoints are held at temperatures T_0 and T_1 , and the structure is thermally isolated, the net heat load flowing from point 0 to point 1 is easily found,

$$Q_{0 \rightarrow 1}^{(\text{cond})} = \frac{A}{L} \int_{T_1}^{T_0} \kappa(T) dT = \frac{A}{L} K_{\text{int}, T_1}(T_0) \quad , \quad (3.1)$$

where the thermal-conductivity integral K_{int, T_1} was introduced and L denotes the arc length of γ . The standard expression (3.1) can also be used to obtain the temperature distribution along γ .

3.4 Improved NMR probe with two-axis rotator

In the following, an NMR probe designed to work with a ^4He flow cryostat (Oxford Instruments Spectrostat CF) is presented. The probe is based on an earlier design, whose distinguishing feature is a two-axis rotator mechanism enabling *in-situ* control over the sample orientation [74, 364]. The previous probe was built for a shorter cryostat, which is inserted into the magnet with the sample pointing up. This configuration poses problems for operation below 4 K. In order to improve low-temperature operation, a longer cryostat loaded from the top of the magnet has to be used. With the acquisition of a suitable cryostat, the construction of a corresponding probe became necessary. Thus, one of the goals was to improve the thermal design of the probe. Other changes were motivated by the experience collected while working with the previous NMR probe.

The project was carried out in close collaboration with W. Bachmann, mechanical engineer at the physics department of ETH Zürich, who was also involved in the construction of the original probe. He was responsible for the detailed mechanical design and manufacturing, which included the pre-assembly of the mechanical components. The authors contributions consisted in the provision and continuous adjustment of detailed specifications for the required changes, the acquisition and installation of the electrical components, as well as the commissioning of the final device. A part of the associated test runs were carried out by T. Shiroka and L. Korosec.

¹ $Q = Q_{i \rightarrow i+1}^{(\text{rad})} = \frac{1}{N+1} \sum_{i=0}^N Q_{i \rightarrow i+1}^{(\text{rad})} = \dots$

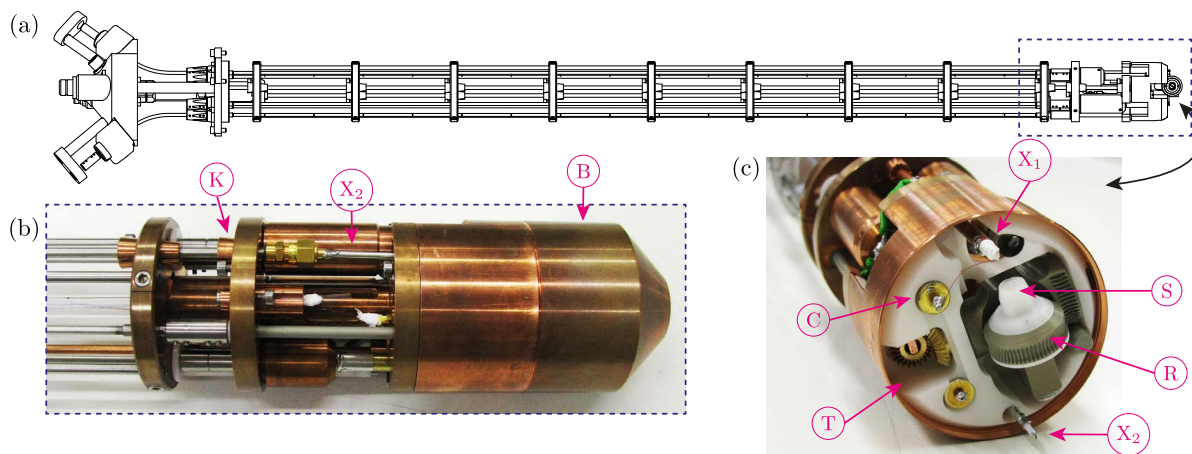


Figure 3.2: Overview drawing (a) and photographs (b-c) of NMR probe for ^4He flow cryostat. The part of the probe depicted in (b) is indicated by the dashed rectangle in (a). Image (c) shows a bottom view of the probe, as indicated by the black double arrow. The shielding cup ‘B’ visible in (b) is not shown in (a) and (c). Magenta leader lines are explained in the text.

Relevant aspects of the probe are shown in Fig. 3.2. It consists of a long structure [Fig. 3.2(a)], which is delimited by a top flange with electrical and rotary feed-throughs [Fig. 3.2(a), left], and the probe head [Fig. 3.2(a), right]. Since most aspects of the original probe were already described elsewhere [74, 364], I restrict myself to briefly presenting a few selected² differences of the revised version.

- Since the longer cryostat accommodates wider probes, it was possible to increase the range of the pitch angle to $\pm 100^\circ$ (the roll angle is unrestricted). Note that despite the resulting off-center position of the rotator mechanism (‘R’) [Fig. 3.2(c)], the field homogeneity at the sample (‘S’) is sufficient for our application. In addition, several parts of the mechanism, such as the transmission ‘T’ [Fig. 3.2(c)], were redesigned to eliminate friction-based joints and increase the torsional rigidity of the driving mechanisms of the tuning capacitors and the two-axis rotator. These changes are expected to minimize the hysteresis of the mechanism.
- A shielding can (‘B’) was added. Besides preventing temperature gradients across the sample, it limits the extent of the RF magnetic field. By reciprocity [176, 180], this also avoids pickup of unwanted signals and electromagnetic interference. In order to check for any adverse effects, the model depicted in Fig. 3.3 has been solved for frequencies ranging from 10 Hz to 1 GHz, using a finite-element software (COMSOL Multiphysics). The geometry approximates that of the actual NMR probe, whereas temperature and RF magnetic field are chosen such that the calculations yield an upper bound on the Joule heating. The simulations show that (i) Joule heating remains below 60 mW, (ii) magnetic shielding becomes effective around approximately 1 MHz (balance between skin depth and wall thickness), and (iii) the RF magnetic field inside the coil is affected to less than 1%.
- To improve the electrical characteristics, two semi-rigid coaxial lines (‘X₁’ and ‘X₂’) are used, which extend to their targets without impedance discontinuities. In combination with moving the tuning capacitors [‘C’, only one annotated in Fig. 3.2(c)] closer to the coil and providing conductive capacitor bases, this minimizes the additional wiring required to realize the tuning

²Several additional aspects have been improved, but are considered less interesting for the reader.

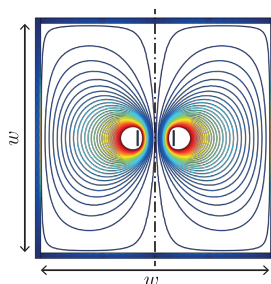


Figure 3.3: Axisymmetric model used to estimate the effects of the shielding can. The geometry consists of a 6-turn coil made from 0.3 mm dia. Cu wire, the coil dimensions being 3 mm \times 2.7 mm (inner radius by length). The excitation is chosen such that the coil generates a RF-field of 0.1 T at its center. The surrounding shield has inner dimension $w = 40$ mm and is made from 1 mm thick Cu. Room temperature is assumed. Closed curves indicate the flux lines of the magnetic field, whereas the shading of the walls represents the induced current density.

circuits shown in Figs. 3.1(a) and 3.1(c) and thus reduces noise pickup.

- The coaxial lines are thermally anchored to the structure of the probe using conical clamps (‘K’). Note that the PTFE dielectric of the cables shrinks significantly upon cooling (linear expansion of 2% in the relevant temperature range [99]), such that thermalization of the center conductor in fact relies on convection. Moreover, following standard practice, the support structure of the probe was optimized by using thin-walled stainless-steel tubes. As a result, the effective cross sectional area has decreased by an order of magnitude, which reduces the conductive heat load.

The coaxial lines are mounted such that they can easily be replaced or removed. The two cables depicted in Fig. 3.2 were supplied by Coax Co. Ltd., Japan, and fabricated from two different conductor-material combinations: Oxygen-free high-conductivity copper (OFHC) for low electrical losses (‘X₁’), as well as a combination of a silver-plated beryllium-copper center conductor with a stainless-steel outer conductor for reduced heat load (‘X₂’). A temperature of 1.9 K was reached with both cables and the shielding can (‘B’) installed.³ In subsequent tests without cable ‘X₁’ and shielding can ‘B’, performed by L. Korosec, temperatures below 1.5 K were achieved.

3.5 Towards an NMR probe for a “cryogen-free” dilution refrigerator

3.5.1 Motivation

A considerable part of this work was related to the development of an NMR apparatus intended to be used with a “cryogen-free” dilution refrigerator (Leiden Cryogenics CF-650). The term “cryogen free” is commonly used to advertise systems in which the cryogenic gases circulate through a completely closed system. In principle, such systems can be operated indefinitely, as long as electrical power and cooling water for the auxiliary components are provided. A section through this system is shown in Fig. 3.4(a). The refrigerator has five stages: The topmost two stages are cooled by a closed-cycle refrigerator (CCR), whereas the remaining three stages are refrigerated by a mixture of ³He and ⁴He. The details of the refrigeration techniques are beyond the scope of this work, the interested reader is referred to the wide

³The temperature was measured using calibrated temperature sensors on cryostat and probe, and further confirmed through measurements of the ²⁷Al-NMR spin-lattice relaxation-rate in aluminum foil (cf. section A.4.1).

body of literature existing on this topic (e. g. , [320]). The system is equipped with a superconducting magnet capable of producing magnetic fields up to 10.5 T (Cryogenic Ltd. , UK) and is designed to be *top loading*, i. e. , to allow for extracting and re-installing the probe without having to warm up the entire system. The thermal connection between probe and refrigerator is established via a clamping mechanism (proprietary, Leiden Cryogenics) visible in Fig. 3.4(b).

Early tests using the probe supplied with the refrigerator and a custom sample holder, developed together with F. Casola, T. Shiroka and W. Bachmann, were unsatisfactory. Even individual short NMR pulses induced temperature responses of the order of 50 mK at the sample holder (for sample-holder base temperatures around 0.3 K). Two primary problems were identified. First, the metal parts on the probe were susceptible to Joule heating due to currents induced by the radio-frequency (RF) magnetic field created by the NMR coil. Secondly, the probe was designed for top tuning (cf. section 3.2), but the electrical properties of the installed RF wiring were insufficient. In particular, already at moderate frequencies around 150 MHz the signal attenuation of the cold probe exceeded 6 dB (one-way) and spurious electrical resonances hindered efficient top tuning.

As discussed in section 3.2, all input RF-power is dissipated within the tuned circuit of the probe. The Joule heating of surrounding metal parts, as well as the power dissipated within the coil, only depend on the strength of the RF magnetic field (B_1 field in section 1.5.4). However, the quality factor of the tuning circuit affects the total power required to drive the coil and hence the associated heat release (e. g. , [113, eq. 21]). In top tuning, standing waves form within the RF cables, such that a good top-tuning setup requires: (i) Low overall attenuation to minimize total heat load, and (ii) current antinodes and dominant electrical losses in locations with high cooling power (cf. [98, p. 258]). Neither requirement was satisfied by the original probe and mechanical actuators required for bottom tuning were not provisioned.

It was therefore decided to rebuild the sample holder and parts of the probe. The new probe should support frequencies ranging from a few MHz to 0.5 GHz and allow for top and bottom tuning, without compromising the top-loading capability.

3.5.2 Design

A traditional approach to NMR in dilution refrigerators is to install the sample inside the mixing chamber or in a separate experimental cell filled with liquid He. A representative design with top-loading capability, which has influenced this work, is described in [223]. Typically, the sample is thermalized via the liquid, while the NMR coil is primarily heat-sunk through its leads [3].

In general, Joule heating of the NMR coil is unavoidable. Unless immersed in liquid He, the coil is therefore typically thermally decoupled from the sample [18, 72, 223]. The need to thermally separate the sample from the coil was also pointed out by V. Mitrović (Brown University, Providence; private communication). Rough estimates⁴ made by the author confirm that RF-induced heating is a concern. The design choice to follow the literature (e. g. , [223]) and thermally anchor the coil to the still stage

⁴Field-generation and field-screening are equivalent. The coil is approximated as densely-wound and infinite, to admit use of the results from [184, pp. 221,782]. The RF-field is $B_1 = 1/(8gT)$ with $g = f/B_0$, f the frequency, B_0 the external field, and T the duration of a $\frac{\pi}{2}$ -pulse. Assuming Cu wire with residual-resistivity-ratio (RRR) 300, the classical skin depth $\delta \approx 1 \mu\text{m}$ at $f = 20 \text{ MHz}$ and low temperature. For $T = 5 \mu\text{s}$ and $B_0 = 10 \text{ T}$, the energy dissipated by a $\frac{\pi}{2}$ -pulse is 0.25 J/m^2 . For an NMR coil with linear dimensions of 5 mm (diameter and length), this yields $20 \mu\text{J}$. Assuming thermalization to 1 kg of Cu at 80 mK, a temperature rise of 20 mK would arise (see [320, Tab. 10.1] for material data). Note that the anomalous skin effect [135, 313] is expected to further increase dissipation.

of the probe is finally brought about by the long thermal link between the center-of-field and the mixing chamber [cf. Fig. 3.4(a)]. Note that superconducting coils may be an option to consider in the future [33, 58, 156, 427], as are superconducting coaxial cables [25, 224, 322, 338, 453] for connecting the low-temperature stages of the probe. It is emphasized that neither of these options is excluded by the aforementioned design choice.

A major part of the reverse-engineering, design, construction, and assembly work was performed by the author. This included wiring of most thermometers and heaters, and the development of temperature-monitoring software. Valuable technical assistance was provided by other members of the group, in particular Prof. H.-R. Ott, T. Shiroka, N. Barbero, and F. Casola. Note that the following list is not exhaustive. Prof. Ott took care of the operation of the dilution refrigerator during the test runs. T. Shiroka was responsible for maintaining and repairing the resistance bridges used for thermometry, as well as for building various external cables. The heater units were characterized by T. Shiroka and N. Barbero, and a part of them was installed by N. Barbero. Mechanical parts were machined by the mechanical workshop of the ETH Zürich physics department. In a first step, the entire section of the probe above the 2nd CCR stage [Fig. 3.4(a)] was rebuilt in order to accommodate the mechanical controls required for bottom tuning. Associated modifications to the driving mechanism of the clamps used for establishing the thermal link between probe and refrigerator [sub-assembly ‘M’ in Fig. 3.4(a)] were devised by W. Bachmann, mechanical engineer at the physics department of ETH Zürich, and a new sliding-seal assembly was developed by his colleague M. Baer. The entire project, including the work described in the rest of this chapter, was supported by the expert advice of Dr. Marek Bartkowiak (PSI) in various cryogenics questions. Although representing a considerable effort, the technical aspects of constructing a vacuum-tight top end [Fig. 3.4(a)], as well as the thermal anchoring of wires carrying low-frequency signals are well understood (see, e. g. , [320]) and therefore not described in detail.

The main challenges of the project can be summarized as follows: (i) Transporting high-frequency signals down to the still stage in a manner suitable for top-tuning (see section 3.5.1), and (ii) designing a sample holder for NMR. The solutions proposed to these two problems are described in more detail in the following.

3.5.3 Heat-sinking of coaxial lines

As mentioned in section 3.4, thermal expansion produces a gap between the dielectric and the outer conductor of a semi-rigid coaxial line. Combined with the already low thermal conductivity of the PTFE dielectric [354], this renders approaches resembling the one used for the flow cryostat (section 3.4) ineffective at heat-sinking the center conductor of the coaxial line [1] (cf. [223]). The problem can be solved by replacing a section of the coaxial line with another type of transmission line which allows for better heat-sinking (e. g. , [27]). The microstrip transmission line [154, 244, 245, 339, 439] depicted in Fig. 3.4(c) has a particularly well-suited geometry. Its high thermal conductivity [52, 170, 320, 357] and good dielectric properties [109] make sapphire a predestined substrate for such applications. In addition, sapphire has a high dielectric strength [109] and, unlike quartz, is not piezoelectric (e. g. , [44, 50]), which is important given the high voltages occurring in NMR apparatus, especially in conjunction with top tuning. This solution to heat-sinking was already applied in low-temperature apparatus, including low-temperature NMR [162, 223], and has been suggested by V. Mitrović (Brown University, Providence; private communication). However, most NMR signals fall outside the range of typical design frequencies of microstrip lines. Since no literature discussing design details and electrical characteristics of finite-

size microstrip heat-sinks in the low-frequency regime is known to the author, selected considerations made in this work are presented in the following.

3.5.3.1 Design

Many aspects need to be considered when designing an actual heat-sink, like the one depicted in Fig. 3.4(d). The overall layout of the device is inspired by previous work by M. Bartkowiak and coworkers [1]. The tolerances of the packaging, made from gold-plated Cu, must accommodate the low thermal expansion of the sapphire [39, 109]. Therefore, the pins providing the electrical contact to the microstrip line are not fixed. Mechanical stresses are avoided by thermalizing the sapphire chip through a layer of grease (Apiezon N) [1]. Although indium could be used for that purpose [1], the large contact area reduces the importance of the thermal connection between chip and packaging. The thickness of the grease layer is minimized through flat machining of the contact surface and the addition of CuBe springs [4]⁵ [Fig. 3.4(d)]. Finite-element heat-transfer simulations confirm the effectiveness of the heat-sink design.⁶

As explained in section 3.5.1, top tuning requires very low loss and a well-defined characteristic impedance. Hence, efforts were made to ensure good electrical properties of the heat sinks. As mentioned before, dielectric losses and dielectric strength are no concern. Neither are spark gaps, given the high vacuum environment in which the system is operated [98, p. 257] (cf. [223]). Electromigration of the electroplated Au conductors [41, 201] due to high circulating currents should not be relevant, unless the microstrip line is heated to high temperatures under abusive power conditions.

Regarding the RF design of the transmission lines, it is noted that the conductor thickness generally affects the characteristic impedance [129, 206, 330]. A rather large thickness of 10 μm is used in order to improve power handling. The parameters of the transmission line were obtained using the TX-LINE software (formerly AWR, now National Instruments), targeting an average characteristic impedance of 49 Ω , which corresponds to the estimated impedance of a cold coaxial cable with PTFE dielectric (see [99, 421] for material properties). The design frequency range is 10 MHz to 0.5 GHz and the low-temperature material parameters [221, 254] were used. Although the anisotropic dielectric constant of sapphire can be accounted for [23, 173, 205, 307, 413–415], an isotropic dielectric constant can be assumed by aligning the microstrip with the anisotropy axis of the substrate and assuming quasi-TEM propagation. Non-TEM effects [40, 100, 172, 202, 203, 362] are negligible in the considered case. As an alternative to analytical results [118, 159], the effect of the conductive walls of the packaging is evaluated by two-dimensional quasi-TEM finite-element calculations using COMSOL Multiphysics (following the procedure outlined in [282, 283, 368]).

The transition from coaxial to microstrip transmission line deserves special attention [335, 337]. Special RF connectors (Southwest Microwave, Inc., USA) are used to progressively reduce the radius of the coaxial line until it matches the thickness of the substrate [337]. In addition, the microstrip is tapered at the ends [337]. The resulting design was checked by performing a three-dimensional full-wave finite-elements calculation using COMSOL Multiphysics.

⁵CuBe is known to remain elastic down to very low temperatures [1].

⁶Calculations performed with Simulia Abaqus (Dassault Systèmes). The grease layer is modeled pessimistically by a 100 μm thick layer of PTFE [354]. Assuming the temperatures of the corresponding stages of the probe as 3 K and 1 K, with respective center-conductor heat loads of 7 mW and 9 μW , the simulations show that the center conductors are thermalized to within 0.5 K and 50 mK, respectively. Anisotropic thermal conductivity of the substrate is considered negligible [109, p. 110].

3.5.3.2 Fabrication and Testing

The sapphire wafers (525 μm thick A-cut sapphire, Roditi International Corporation Ltd., UK) were processed by S. Loosli at the FIRST clean-room facility of ETH Zürich. The resulting microstrip lines had a width of 550 μm and 24 μm thickness (measured by S. Loosli). One of the four devices built is depicted in Fig. 3.4(d) (with lid removed). The room-temperature RF characteristics of the devices are shown in Fig. 3.4(e). The signal attenuation (insertion loss) and the impedance mismatch (return loss) are both very good throughout the relevant frequency range.⁷ Although very difficult to measure, by design, both parameters should improve further upon cooling. Furthermore, signal transmission was checked to remain linear for traveling RF waves with up to 1 kW peak power. In air, the breakdown voltage of the entire assembly is limited to slightly above 3 kV by the air gaps surrounding the launch pin. No such limitations are expected in the envisaged low-temperature and high-vacuum operation [98, p. 257] (cf. [223]).

3.5.3.3 Overall signal transmission

The heat sinks described in the preceding subsections are anchored to the 2nd CCR and the still stages [heat sinks ‘H’ in Fig. 3.4(a)].⁸ The connection towards the top of the probe is established through a combination of Cu (Huber + Suhner AG, Switzerland) and BeCu (Coax Co. Ltd., Japan) semi-rigid coaxial lines.⁹ The BeCu wiring is also used to connect the heat-sinks at the 2nd CCR and still stages. The RF characteristics of the signal transmission path from room temperature to the still stage are shown in Fig. 3.4(f). As expected, the total signal attenuation (insertion loss) is significantly reduced compared to the original probe. The return loss (RL) is below -20 dB throughout the relevant range of frequencies, which is usually considered sufficient.

The return loss of the old probe may not seem too bad. However, it should be noted that top tuning is based on the interference of the partial waves reflected at the matching capacitor C and the NMR coil L [see section 3.2 and Fig. 3.1(c)]. For the old wiring, the round-trip signal attenuation (twice the insertion loss) was comparable to the amplitude of spurious reflections arising at various locations of the probe (return loss). This gave rise to additional tuning resonances which did not correspond to an efficient (reactive) power transfer to the NMR coil.

3.5.4 Considerations regarding sample holder

As mentioned in sections 3.5.1 and 3.5.2, heating of metallic parts by RF-induced eddy currents is a concern. With respect to the NMR coil, the problem can be avoided by thermally decoupling the coil from the sample or using superconducting materials (see section 3.5.2). However, the same problem arises in any metallic parts present on the sample holder. In many reports, the samples are immersed in, or consist of, liquid He [18, 72, 177, 223]. In other cases, continuous-wave (CW) NMR has been used successfully [30, 388]. Note that NMR is also used for thermometry in nuclear demagnetization refrigerators, where the sample holders must be metallic in order to ensure thermalization (e. g., [66]).

⁷The CuBe springs, as well as the grease between sapphire chip and packaging, have no measurable effects.

⁸For the still stage, the corresponding components are also visible in Fig. 3.4(b).

⁹The latter type of cable represents a good trade-off between thermal and electrical properties and is therefore a common choice for low-temperature NMR apparatus.

While eddy-current heating can be reduced by using low frequencies (e. g. , [66, 123, 177, 267, 322]), this is clearly not an option in our application.

Based on the design choice of a thermally decoupled coil (section 3.5.1), a tentative sample holder has been devised [Fig. 3.4(g)]. The coaxial lines (red) should be made of Cu to provide a strong thermal link to the still stage of the probe and their outer conductors could be used to heat-sink the tuning capacitors if bottom tuning is used (orange). Since bottom tuning is scheduled for a later development stage, the orange parts can be ignored in a first version of the sample holder. The estimates made in section 3.5.2 imply that the sample cannot be directly attached to a metallic sample holder.¹⁰ Note that, according to her description, V. Mitrović (Brown University, Providence) is using a similar sample-holder design and has pointed out to the author that, unless liquid He (mixture) is to be used, GaAs (cf. [19, 20, 54, 115, 171, 183, 309, 399]) is a suitable non-metallic material with high phononic thermal conductivity (private communication).

There is a trade-off regarding the design of the sample holder. The tentative design depicted in Fig. 3.4(f) tries to reduce the length of the GaAs sample support in order to reduce the thermal relaxation time τ_{th} of the sample. Note that besides limiting the rate at which NMR experiments can be repeated, τ_{th} can also affect the apparent relaxation behavior of the nuclear magnetization if $T_1 \lesssim \tau_{\text{th}}$ (e. g. , [402]). The drawback of the proposed arrangement is the necessity for a split RF coil, like a suitably-adapted birdcage resonator [18], saddle coil [113, 223], or solenoid pair. The radiative heat load from the coil is generally not expected to be a problem.¹¹ The sample could be mounted on the GaAs support, e. g. , using Stycast 1266 (see [303] for thermal properties).

Two remaining engineering challenges related to the sample holder remain. First, the split coil must be positioned precisely w. r. t. the sample while avoiding heat leaks into the sample support. The use of superconductors (see section 3.5.1) might be advantageous in this respect. In particular, such coils could be thermally linked to the sample holder and coupled inductively to the remaining RF circuit (through a transformer, e. g. , see [408]). Secondly, RF-induced heating of the cold metal parts of the sample holder must be avoided.¹² For the proposed split-coil geometry, this implies that field-leakage between the two parts of the RF coil must be minimized. Then, heating due to the stray field emanating from the outwards-pointing ends of the coil pair (“return field”) can be avoided using a simple metallic shield, as done previously in [223].

3.6 Summary and Outlook

An NMR probe for use in a ^4He flow cryostat was designed and implemented. Selected aspects were improved with respect to previous versions, as described in section 3.4. The discussion also serves as an

¹⁰As remarked by V. Mitrović (Brown University, Providence), a metallic sample holder would also perturb the RF field generated by the coil (private communication).

¹¹Tests suggest that the base temperature of the mixing-chamber stage of the *probe* is around 50 mK. Extrapolating from [183], the thermal conductivity of GaAs at this temperature is $\kappa \approx 1.6 \text{ mW m}^{-1} \text{ K}^{-1}$. Taking the effective thermalization path as 5 mm wide, 650 μm thick, and 10 mm long, the maximum heat load giving rise to a temperature change of no more than 10 mK is 5 nW. Meanwhile, the radiation emitted by a black surface of 4 cm^2 at 2 K is 0.4 nW. Yet, if the thermal conductivity of the sample is small, additional precautions might become necessary.

¹²Note that, for metallic samples, the electrons of the bulk limit the increase of the average (electronic) temperature (e. g. , [123, 124]). Also, the magnitude of the nuclear magnetization is unaffected by Joule heating on time scales short compared to T_1 [322]. Similarly, measurements might be possible before the RF heating of the electrons in the sample holder has propagated to the sample. However, relying on such effects exclusively is not an option if relaxation measurements are to be performed.

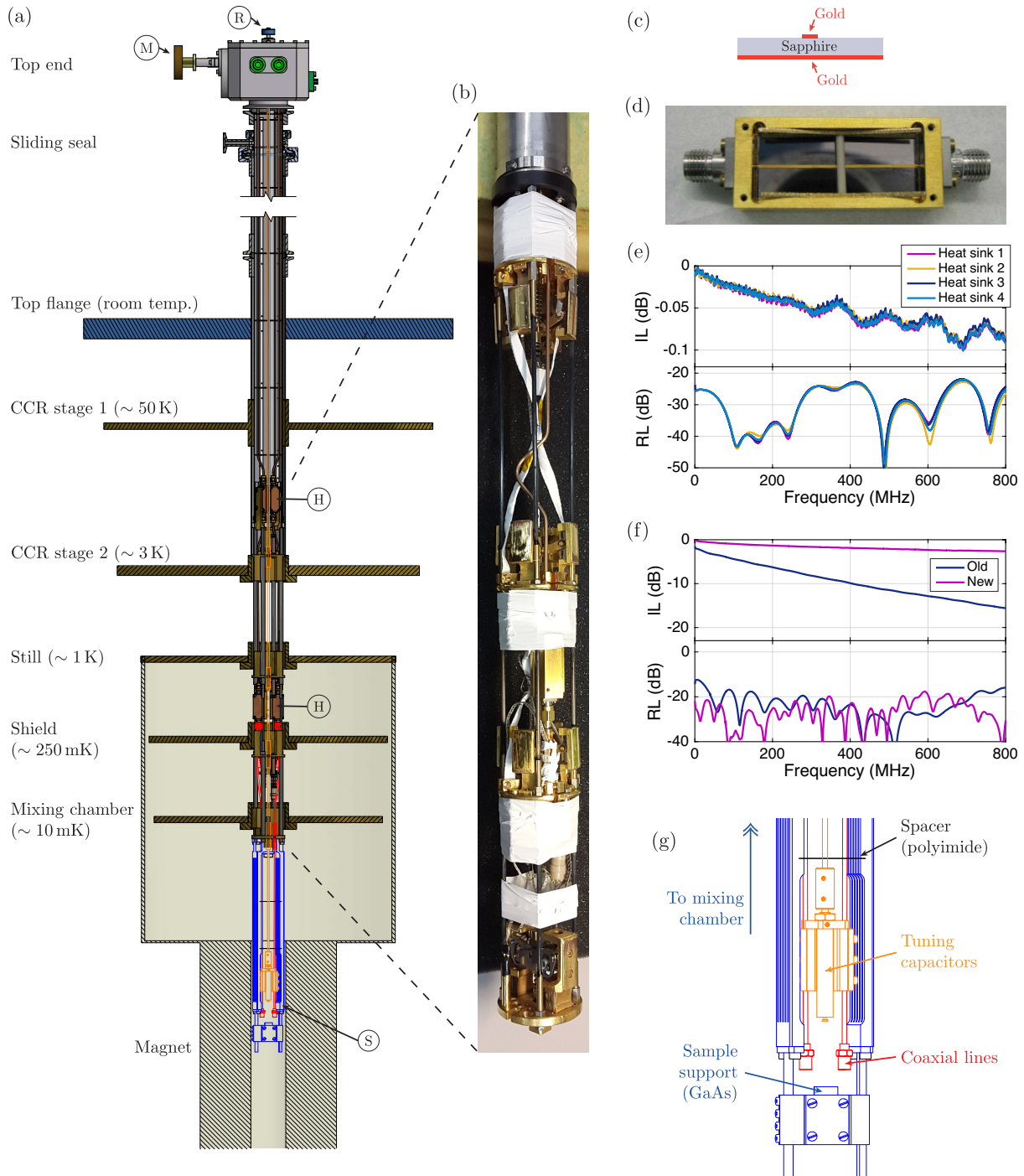


Figure 3.4: (a): Partial-section view of “cryogen-free” dilution refrigerator with loaded NMR probe (Leiden Cryogenics CF-650, probe diameter 50 mm). Unshaded parts correspond to the proposed design of the sample holder (‘S’). The temperatures of the individual stages are examples only. The walls of the vacuum chambers, as well as the radiation shield extending from the shield-stage into the magnet are omitted for clarity. (b): Photograph of the actual probe. (c): Schematic cross-section view of a microstrip line used for heat-sinking of the radio-frequency signals. (d): Photograph of final heat-sinking device (top lid removed). (e),(f): Electrical characteristics of the four heat sinks built (e) and the complete RF-signal path from the top end to the still stage of the probe (f). RL and IL stand for return loss and insertion loss, respectively. (g): Tentative sample holder design. Blue parts are anchored to the mixing chamber stage, whereas red and orange parts are anchored to the still stage of the probe. See text for details and credits.

introduction to section 3.5, which concerns the challenges associated with the design of an NMR apparatus for modern (i. e., “cryogen-free”) dilution refrigerators. In this case, sections of the probe had to be rebuilt in order to accommodate the specific requirements formulated in section 3.5.1. Furthermore, following established practice, a solution for the heat-sinking of the radio-frequency signal lines was developed and implemented (section 3.5.3). Special care was taken to ensure good signal propagation in order to allow for top tuning (cf. section 3.2). Finally, a partial design for a sample holder is presented. The remaining engineering challenges associated with the sample holder are described, together with possible solutions, in section 3.5.4. The author acknowledges private communication with V. Mitrović (Brown University, Providence), who is operating a similar NMR setup (cryogen-free dilution refrigerator, but without top-loading probe), and whose helpful suggestions have clearly inspired several design choices made in this work (see sections 3.5.2, 3.5.3, and 3.5.4). Note also the many other contributors and collaborators mentioned throughout this chapter and in the Acknowledgments. Future work should aim at developing the described ideas further in order to obtain a complete sample-holder design which can then be implemented.

Part II

BiCu₂PO₆: Field-induced magnetic order in a frustrated spin ladder

4 BiCu₂PO₆: General aspects

4.1 Introduction

The literature on BiCu₂PO₆ available at the time of writing has been summarized in Tab. 4.1, where only directly relevant works were included. Rather than trying to mention each of the publications in this introduction, I will refer to and discuss the previous works listed in Tab. 4.1, as well as additional literature, along with the presentation of the results whenever applicable.

The structure of BiCu₂PO₆ (see section 4.2.1) was first reported in [11]. The exponential suppression of various response functions, such as magnetic susceptibility [258] and specific heat [217], at low temperature suggested a gapped spin-liquid ground state [217, 258]. Together with the crystal structure, this led to the proposition of a spin-ladder model [217, 258]. The holes of the Cu²⁺ ions are assumed to be localized due to strong correlations, yielding an effective model (cf. section 1.1.1) based on antiferromagnetically-coupled spin- $\frac{1}{2}$ moments (e. g. , [401]). A large Curie-Weiss temperature (181(1) K) [401] and the observation of incommensurate correlations [257] suggested that frustration plays an important role in BiCu₂PO₆, ultimately resulting in the frustrated spin-ladder model described in section 4.3.1 [401].¹ The exchange couplings were estimated based on first-principles calculations [217, 257, 401] and experimental data [257, 316, 318, 401] (see section 4.3.3). Moreover, Dzyaloshinskii-Moriya interactions (section 1.1.2) and interladder couplings are believed to be important (see sections 4.2.4 and 4.3.3). These additional interactions are likely to be responsible for the highly orientation-dependent magnetic-field induced phases observed in BiCu₂PO₆ [207, 208] (see section 4.5).

An interesting aspect of BiCu₂PO₆ is its chemical flexibility [74, p. 96]. The spin- $\frac{1}{2}$ Cu ions can be replaced by non-magnetic Zn [217] (cf. section 5.2.4) or spin-1 Ni [218]. The Zn-doped compounds, including pure BiZn₂PO₆, share the orthorhombic *Pnma* space group of BiCu₂PO₆ [218]. Also, Ca and Pb can be substituted for Bi, giving rise to localized holes with non-vanishing spin [218]. Moreover, P can be replaced by V which induces an incommensurate modulation of the crystal structure along the *b*-direction [258].

¹Nevertheless, some early works (Tab. 4.1) neglected frustration in order to make use of quantum Monte Carlo techniques (section 1.4.2).

Property/Method	References
Crystal growth and thermal stability	[423, 424] ^c
X-ray diffraction	[11] ^a , [258] ^{b,a} , [218] ^{c,a} , [423, 424] ^{c,a}
Neutron diffraction	[424] ^c , [259] ^c
Inelastic neutron scattering	[257] ^a , [259] ^c , [316], [318], [319]
Raman scattering	[34],[87]
³¹ P NMR	[22, 63, 218] ^{c,e,a} , [74, 76] ^{c,a} , [74, 78] ^{c,d}
μ SR	[63] ^{c,a}
Magnetization/susceptibility	[258] ^{a,b} , [217] ^a , [257] ^a , [218] ^{c,a,e} , [423], [401] ^{c,d} , [207, 208] ^d , [74] ^{c,d}
Magnetostriction	[207] ^d
Calorimetric measurements	[217] ^a , [218] ^{c,a,e,f} , [455] ^g , [424] ^c , [207, 208] ^d
Heat transport	[284], [187, 189, 190] ^d , [325]
Electric polarization	[188] ^d
First-principles calculations	[217], [257], [401]
Exact diagonalization	[257], [74, 76], [401]
DMRG	[401], [74, 77, 78, 131] ^{c,d}
Quantum Monte-Carlo	[217], [22, 63] ^c , [74, 76] ^c
Bond-operator mean-field theory	[179, 318, 319]
Continuous unitary transformations	[377]

^aPolycrystalline sample.

^bV substituted for P.

^cZn (spin-0) substituted for Cu (spin- $\frac{1}{2}$).

^dWork related to field-induced phases.

^eNi (spin-1) substituted for Cu (spin- $\frac{1}{2}$).

^fCa and Pb substituted for Bi.

^gExperiments under pressure.

Table 4.1: Overview of published works directly relevant for BiCu_2PO_6 .

4.2 Structural aspects

4.2.1 Crystal structure

The crystal structure of BiCu_2PO_6 is depicted in Fig. 4.1. The sites contained in each unit cell are listed in Tab. 4.2. The conventions, especially regarding choice and naming of generating sites and lattice directions, adhere to Ref. [11] and, unless otherwise noted, the $(\mathbf{a}, \mathbf{b}, \mathbf{c})$ basis is used in this work.

Site	Multiplicity	Site (contd.)	Multiplicity
Cu(1)	4	O(1)	8
Cu(2)	4	O(2)	8
P	4	O(3)	4
Bi	4	O(4)	4

Table 4.2: Multiplicities of crystallographically inequivalent sites in BiCu_2PO_6 [11].

The framework of the crystal consists of CuO_5 and PO_4 polyhedra [11]. From a structural point of view, the CuO_4 plaquettes, which constitute the bases of the CuO_5 pyramids and have been depicted

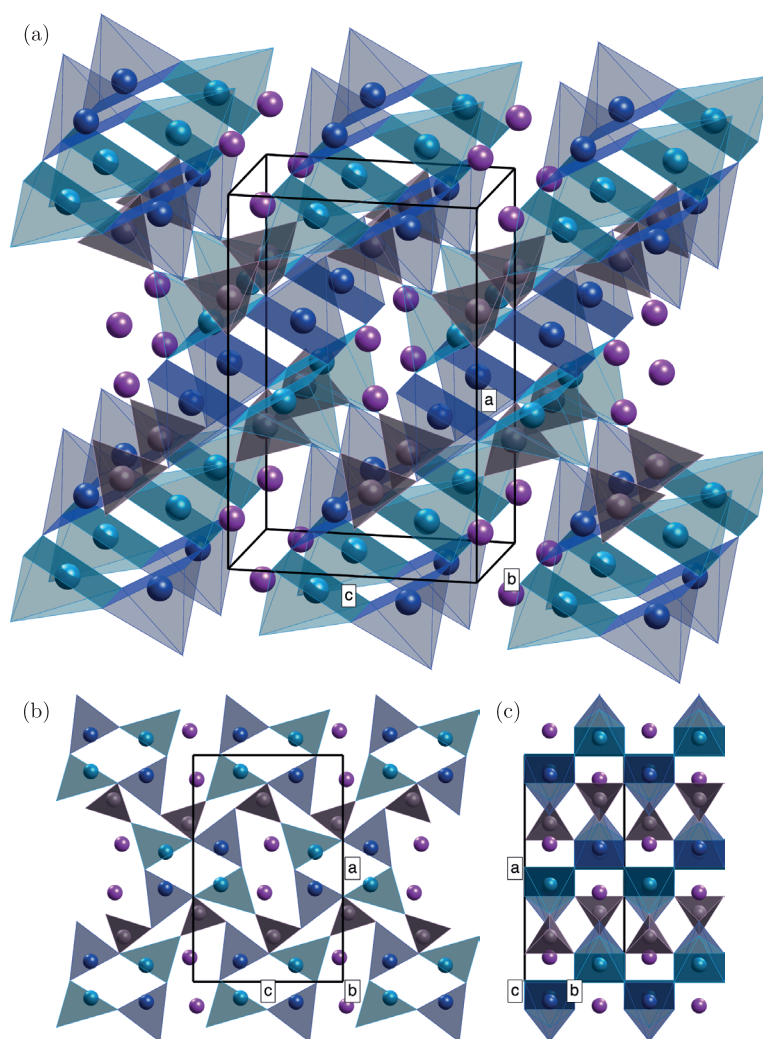


Figure 4.1: Crystal structure of BiCu_2PO_6 [11], showing positions of Cu(1) and Cu(2) (dark and light blue), P (gray) and Bi (purple) sites; the vertices of the polyhedra surrounding the Cu and P sites represent O positions. The crystallographic unit cell is shown using black lines. Panels (a), (b), and (c) correspond to different viewing angles.

with a higher opacity in Fig. 4.1, form ribbons running along the b axis [401]. The structure is clearly anisotropic, with the Cu sites arranged in layers parallel to the bc plane, which are separated by scaffolds formed by the PO_4 tetrahedra [74, p. 96]. Each unit cell cuts through two such layers. The CuO_5 and PO_4 polyhedra are coupled through steric constraints due to the shared O sites. They exhibit a buckling distortion, resulting in two inequivalent Cu sites [11].

4.2.2 Crystal symmetry

BiCu_2PO_6 crystallizes in the non-symmorphic orthorhombic $Pnma$ space group [11]. The point group is obtained by factoring out the subgroup of lattice translations. It consists of symmetry operations of the form $\bar{W}_i = (W_i, \Delta_{W_i})$, where W_i denotes an orthogonal matrix and Δ_{W_i} a fractional translation vector, i. e. \bar{W}_i maps $\mathbf{x} \mapsto W_i \mathbf{x} + \Delta_{W_i}$. The point-group symmetry operations are [38] (see also [11, p. 318])

$$\begin{aligned} E &= \begin{pmatrix} 1 & 0 & 0 \\ 0 & 1 & 0 \\ 0 & 0 & 1 \end{pmatrix}, & \Delta_E &= \begin{pmatrix} 0 \\ 0 \\ 0 \end{pmatrix} & C_2^a &= \begin{pmatrix} 1 & 0 & 0 \\ 0 & -1 & 0 \\ 0 & 0 & -1 \end{pmatrix}, & \Delta_{C_2^a} &= \begin{pmatrix} 1/2 \\ 1/2 \\ 1/2 \end{pmatrix} \\ \sigma_a &= \begin{pmatrix} -1 & 0 & 0 \\ 0 & 1 & 0 \\ 0 & 0 & 1 \end{pmatrix}, & \Delta_{\sigma_a} &= \begin{pmatrix} 1/2 \\ 1/2 \\ 1/2 \end{pmatrix} & C_2^b &= \begin{pmatrix} -1 & 0 & 0 \\ 0 & 1 & 0 \\ 0 & 0 & -1 \end{pmatrix}, & \Delta_{C_2^b} &= \begin{pmatrix} 0 \\ 1/2 \\ 0 \end{pmatrix} \\ \sigma_b &= \begin{pmatrix} 1 & 0 & 0 \\ 0 & -1 & 0 \\ 0 & 0 & 1 \end{pmatrix}, & \Delta_{\sigma_b} &= \begin{pmatrix} 0 \\ 1/2 \\ 0 \end{pmatrix} & C_2^c &= \begin{pmatrix} -1 & 0 & 0 \\ 0 & -1 & 0 \\ 0 & 0 & 1 \end{pmatrix}, & \Delta_{C_2^c} &= \begin{pmatrix} 1/2 \\ 0 \\ 1/2 \end{pmatrix} \\ \sigma_c &= \begin{pmatrix} 1 & 0 & 0 \\ 0 & 1 & 0 \\ 0 & 0 & -1 \end{pmatrix}, & \Delta_{\sigma_c} &= \begin{pmatrix} 1/2 \\ 0 \\ 1/2 \end{pmatrix} & I &= \begin{pmatrix} -1 & 0 & 0 \\ 0 & -1 & 0 \\ 0 & 0 & -1 \end{pmatrix}, & \Delta_I &= \begin{pmatrix} 0 \\ 0 \\ 0 \end{pmatrix}. \end{aligned}$$

In addition to identity E and inversion I , the group contains three glide-planes σ_α and three two-fold screw-axes C_2^α . The point group is isomorphic to $Z_2 \times Z_2 \times Z_2$ via the mapping $\sigma_\alpha \mapsto e_\alpha \in \{0, 1\}^3$.

The layers formed by the CuO_4 ribbons (see sec. 4.2.1) are transformed onto themselves by E , I , σ_b , and C_2^b . The remaining symmetries, i. e., σ_a , σ_c , C_2^a , and C_2^c interchange the two layers. The same decomposition of the point group is obtained by classifying the symmetry operations depending on whether they leave a general pseudo-vector (axial vector) pointing along b invariant or revert its orientation. This means that the structure of the Cu layers is *chiral* when viewed along the b direction, as can be seen in Fig. 4.1(b). This aspect will be reconsidered in chapter 8 (section 8.6.2.3).

4.2.3 Site symmetries

Among the non-trivial symmetries presented in the preceding section, only σ_b has fixed points which correspond to crystallographic sites. As a result, the ac planes formed by the Cu and P sites have site-symmetry groups $\{E, \sigma_b\} \simeq C_{1h}$ [11, p. 319] (see also [75, p. 3]).

4.2.4 Exchange mechanism

The Cu ions adopt a Cu^{2+} configuration in BiCu_2PO_6 [258]. Their unpaired hole is localized due to correlation effects, making BiCu_2PO_6 a magnetic insulator [401]. First-principles studies of the magnetic interactions using band-structure calculations yield the dominant exchange couplings depicted in Fig. 4.2 [217, 257, 401].² Given the quasi two-dimensional network of exchange interactions, the fact that BiCu_2PO_6 remains a spin-liquid down to very low temperatures (see references in section 4.5) corroborates a dominant Heisenberg symmetry of the exchange couplings.³

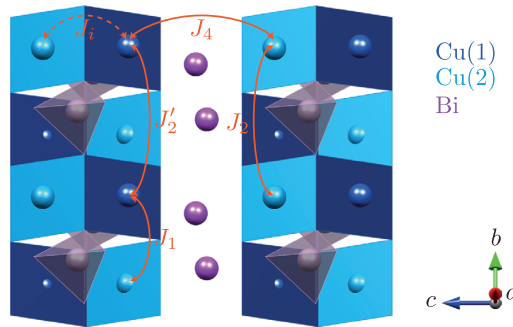


Figure 4.2: Two Cu ribbons [401]. The vertices of the Cu plaquettes and the PO_4 tetrahedra correspond to O positions. Intraladder (interladder) exchange couplings [401] are represented using orange solid (dashed) double-arrows. Figure redrawn after [401, Fig. 1], using crystal structure from [11].

Somewhat counter-intuitively, the dominant coupling in the c -direction is J_4 , which connects different ribbons and is attributed to the Cu-O-O-Cu superexchange paths [257, 401]. The intra-ribbon coupling J_i is weaker because the antiferromagnetic (AFM) Cu-O-Cu superexchange is canceled by a ferromagnetic (FM) contribution due to the almost 90° bond angle (92° , cf. Kanamori-Goodenough rules [151]) [401]. By contrast, the angle of the Cu-O-Cu superexchange path along the b direction is 112.2° , resulting in a sizable nearest-neighbor (NN) coupling J_1 [401]. Finally, two Cu-O-O-Cu paths give rise to exchange couplings J'_2 and J_2 between next-nearest neighbor (NNN) Cu(1) and Cu(2) sites, respectively [401]. While the path along the outer edge of the ribbon has very similar geometries for the two Cu sites, the other path, involving the PO_4 tetrahedron, is very sensitive to the orientation of this ligand (cf. [144]), resulting in $J'_2 \neq J_2$ [401]. All couplings are AFM, except for J_i , which is too weak for its sign to be determined unambiguously from the calculations [401].

The phase diagram of BiCu_2PO_6 as function of temperature and magnetic field is highly anisotropic [207]. DM interactions are therefore an obvious candidate to consider and have been suggested throughout the literature [74, 75, 78, 87, 179, 190, 207, 316, 318, 401]. As pointed out in [317], atomic Bi is known for strong spin-orbit interaction (SOI) [447]. Early first-principles calculations reported an admixture of its orbitals with those of Cu [217]. Meanwhile, more recent calculations indicate that Bi does not contribute directly to the magnetic Cu states, but is rather responsible for the chemical bonds between the Cu ribbons (cf. section 4.2.1) [401]. Unfortunately, none of the first-principles studies seem to have considered SOI explicitly. Even though SOI and inversion symmetry give rise to degenerate Kramers doublets [127] and thereby preserve the spin-degeneracy of the band structure, the SOI alters the nature of the eigenstates by coupling spatial and spin degrees of freedom. For instance, a doublet of

²Ref. [217] finds $J_i > J_4$; this issue has been discussed in [401], which we follow in this work.

³In zero field, the partition functions of the two-dimensional quantum and classical Ising models coincide, and the latter is well-known to exhibit magnetic order.

single-electron wave functions can be represented as [127]

$$\begin{aligned}\psi_{\mathbf{k},n,1} &= [a_{\mathbf{k},n}(\mathbf{r}) |\uparrow\rangle + b_{\mathbf{k},n}(\mathbf{r}) |\downarrow\rangle] e^{i\mathbf{k}\cdot\mathbf{r}} \\ \psi_{\mathbf{k},n,2} &= [-b_{\mathbf{k},n}^*(\mathbf{r}) |\uparrow\rangle + a_{\mathbf{k},n}^*(\mathbf{r}) |\downarrow\rangle] e^{i\mathbf{k}\cdot\mathbf{r}} \quad ,\end{aligned}$$

with lattice momentum \mathbf{k} and band index n . Clearly, no linear combination of these two wave functions factorizes into a spatial and a spin component, such that the electronic states acquire a “mixed-spin” character. The Bi-O bonds [401] are likely to influence other orbitals involving the same O sites, giving them a mixed-spin character as well. In a tight-binding description for the Cu sites, this would give rise to spin-dependent hopping, which is why strong DM interactions are expected in BiCu_2PO_6 (see sections 1.1.2 and 4.3.3).

4.2.5 Local environment of the Cu sites

The structural ribbons consist of two inequivalent CuO_4 plaquettes, which involve the O(1) and O(2) sites [401]. Together with an additional O site, CuO_5 pyramids are obtained [11], as illustrated in Fig. 4.3.

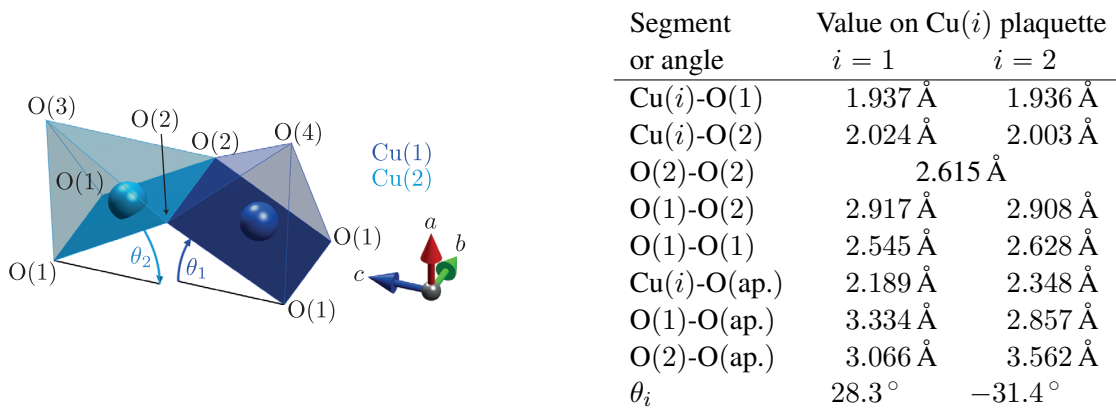


Figure 4.3: Two isolated Cu pyramids. The data are a subset of Fig. 4.1 and correspond to the generating Cu positions reported in [11]. The table lists various distances between the sites. O(ap.) denotes the oxygen at the apex of the pyramid, i. e., O(4) [O(3)] for Cu(1) [Cu(2)]. The distances and angles were obtained using [191] and the crystal structure reported in [11]. Note that the angles θ_i (cf. [74, p. 105]) are oriented according to the mathematically positive rotations about the b axis.

As reviewed in section 4.2.3, these pyramids have symmetry C_{1h} . Moreover, the CuO_4 plaquettes are approximately C_{2v} -symmetric [74, p. 105] to within 5%⁴. Taking into account the apical oxygen reduces the accuracy of this approximation to $\lesssim 10\%$ for Cu(1) and $\lesssim 20\%$ for Cu(2). Comparing the two inequivalent CuO_4 plaquettes, the Cu-O distances differ by less than 1%, and the O-O distances by less than 3.5%. The distances to the apical oxygen differ by $\lesssim 15\%$. Thus, the main difference between the two Cu sites consists in the relative position of the apical oxygen.

The square-pyramid CuO_5 coordination arises from an imbalance of the Cu $d_{x^2-y^2}$ and d_{z^2} orbitals [11]. An approximate C_{2v} -symmetry of the Cu site is corroborated by first-principles calculations, which indicate that the bands formed at the Fermi level⁵ by the $3d^9$ Cu^{2+} ions have planar $d_{x^2-y^2}$ -character

⁴Fractions refer to real-space distances.

⁵In the local-density approximation, i. e., neglecting strong correlations, the band structure of BiCu_2PO_6 is metallic [217].

[217, 401], with $pd\sigma$ -type bonds within the CuO_4 plaquettes [217]. This confirms the statements made in [74, p. 105] and hence justifies the neglect of the apical oxygen (see [74, p. 105]). Therefore, the approximate C_{2v} -symmetry of the $\text{Cu}(i)$ site assumed in [74] is also adopted in this work.

4.3 Theoretical model for BCPO

4.3.1 Heisenberg Hamiltonian and g-tensor

First-principles calculations reveal a quasi two-dimensional band structure [217, 401] and suggest the dominant exchange interactions depicted in Fig. 4.2, as discussed in section 4.2.4. The strongest exchange interactions J_1 , J'_2 , J_2 , and J_4 form frustrated spin ladders (cf. section 1.3.4) running along the b direction (e. g., [401]). Surprisingly, the two legs of a given ladder reside on different Cu ribbons [401]. Their arrangement within the crystal is shown in Fig. 4.4. Each ladder consists of two coupled zigzag chains with alternating next-nearest neighbor (NNN) couplings [401]. The ladders are arranged in layers parallel to the bc plane which are separated by PO_4 layers [74, p. 96]. As mentioned in section 4.2.2 and indicated by the black arrows in Fig. 4.4(a), two types of layers with different chirality w. r. t. the b axis exist.

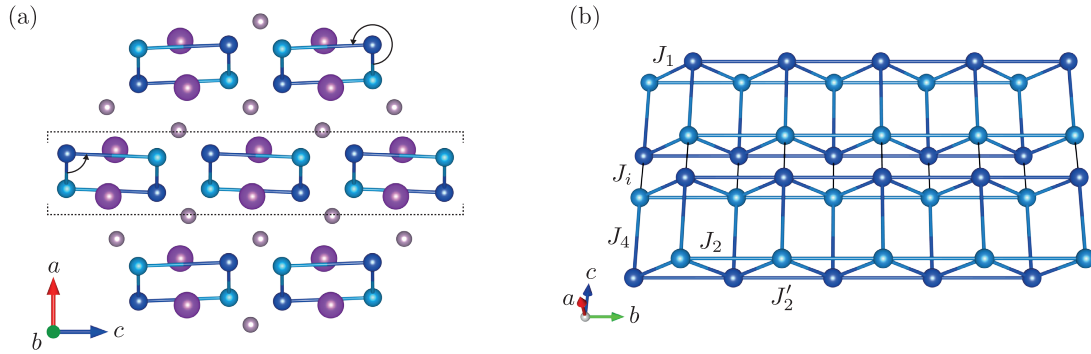


Figure 4.4: Crystal structure of BiCu_2PO_6 [11], showing positions of $\text{Cu}(1)$ and $\text{Cu}(2)$ (dark and light blue, respectively), P (gray), and Bi (purple) sites; O sites have been omitted for clarity. Exchange interactions [401] (J_1 , J'_2 , J_2 , J_4 , and J_i) are depicted by blue cylinders (intraladder couplings) and solid black lines (interladder couplings). (a): View along b direction, illustrating the two different ladder orientations (subfigure reused from [312]). An isolated magnetic layer is delimited by dotted brackets. (b): Two isolated ladder units. Crystal structure visualized using VESTA [272].

Since the interladder couplings J_i are weaker than the remaining couplings [401], consider a single ladder containing the generating Cu positions reported in [11]. Let $\text{Cu}(i, r)$ denote the $\text{Cu}(i)$ site on the r 'th rung of this ladder, and $\mathbf{S}_{i,r}$ the corresponding spin operator. In addition to the Heisenberg exchange terms, each spin couples to the external magnetic field \mathbf{H} through the Zeeman energy $-\mu_0 \mathbf{H} \cdot \boldsymbol{\mu}_{i,r}$, where $\boldsymbol{\mu}_{i,r} = -\mu_B g_{i,r} \mathbf{S}_{i,r}$ denotes the corresponding magnetic moment. The g-tensor $g_{i,r}$ is site-dependent and asymmetric in general (see section 1.5.9). Since $g_{i,r}$ relates two pseudo-vectors, it transforms as a regular matrix. The C_{1h} symmetry of the Cu site (see section 4.2.5) then implies that b is a principal axis of the g-tensor [74, p. 96]. Moreover, the $\text{Cu}(i, r)$ and $\text{Cu}(i, r + 1)$ sites are related by C_2^b , which implies

that $g_{i,r} = g_i$. The resulting frustrated-ladder Hamiltonian reads (cf. [74, eq. 5.1])

$$\mathcal{H} = \sum_r \left[\sum_{i \in \{1,2\}} \mu_0 \mathbf{H} \cdot \mu_B g_i \mathbf{S}_{i,r} + J_4 \mathbf{S}_{1,r} \cdot \mathbf{S}_{2,r} + J_1 (\mathbf{S}_{1,r} \cdot \mathbf{S}_{2,r+1} + \mathbf{S}_{2,r} \cdot \mathbf{S}_{1,r+1}) \right. \\ \left. + J'_2 \mathbf{S}_{1,r} \cdot \mathbf{S}_{1,r+2} + J_2 \mathbf{S}_{2,r} \cdot \mathbf{S}_{2,r+2} \right] \quad . \quad (4.1)$$

The fact that the expression does not distinguish between odd and even rungs r , reflects that the ladder graph can be transformed into a one-dimensional lattice with only two sites per unit cell [401]. This smaller unit-cell is advantageous when performing calculations with periodic boundary conditions [401].

4.3.2 Symmetry-allowed Dzyaloshinskii-Moriya interactions

The transformation properties of the DM vectors are described in section A.5.2 [equation (A.8)] and their application to analyze the symmetry-allowed DM vectors and their arrangement within a crystal is standard practice. In particular, the following results and the chosen notation are fully consistent with other works ([401], [259, p. 127], [74, p. 132], [319, Fig. 6.1b], and [75, 179, 377]). The symmetry σ_b constrains the allowed DM vectors in BiCu_2PO_6 . The most general DM vectors on the intraladder bonds have the form (see [319, Fig. 6.1b])

$$\begin{aligned} \mathbf{D}_1 &= (D_1^a, D_1^b, D_1^c) & \mathbf{D}_2 &= (D_2^a, 0, D_2^c) \\ \mathbf{D}'_2 &= (D_2^a, 0, D_2^c) & \mathbf{D}_4 &= (0, D_4^b, 0) \end{aligned} \quad .$$

The staggering patterns of these DM interactions are indicated in Fig. 4.5. Note that, while the model without DM interactions has a hidden translation symmetry (see section 4.3.1 and references therein), the DM interactions preclude such simplifications (cf. [401, p. 9]).

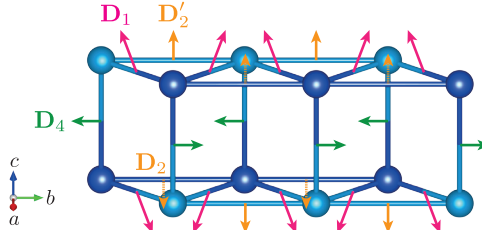


Figure 4.5: Staggering pattern of DM vectors within one frustrated-ladder unit of BiCu_2PO_6 . The magnetic bonds are oriented from top to bottom and from left to right. The out-of-plane a -components of \mathbf{D}_1 , \mathbf{D}'_2 , and \mathbf{D}_2 exhibit the same staggering pattern as the c -components of the corresponding vectors. Crystal structure visualized using VESTA [272]. Note that similar results and illustrations were reported in [259, Fig. 5.16], [75, Fig. 21], and [319, Fig. 6.1b]. (Extended version of a figure previously used in [312].)

There are two types of ladder units per unit cell, which are arranged in layers parallel to the bc plane [Fig. 4.4(a)] and related by a mirror symmetry. Up to a translation by half a unit cell along the b -direction, the interaction graphs of the two types of ladder units have the same form, i. e., same site types and same bond orientations w. r. t. the crystal axes. In a corresponding notational convention, equivalent bonds of the interaction graphs are related by the mirror symmetry σ_a . Since σ_a does not reverse any

bonds, the DM vectors transform as $(D^a, D^b, D^c) \mapsto (D^a, -D^b, -D^c)$ upon moving from one ladder layer to the next.⁶

DM terms can be eliminated by local unitary (i. e., gauge) transformations of the spin operators (see [15, 157, 196, 359]) whenever the DM interactions are unfrustrated, i. e., the sum of the DM vectors vanishes along every cycle of (oriented) magnetic bonds in the interaction graph [157, 359]. Inspection of Fig. 4.5 reveals that all components of all DM vectors are frustrated in this sense. An explicit consideration of the case $\mathbf{H} \parallel b$ confirms this general result. In this case, the only possible simplification appears to be the elimination of one of the parameters $D_{1a}, D_{1c}, D_{2a}, D_{2c}, D'_{2a}, D'_{2c}$ by a global spin-space rotation about b .

In principle, the DM vectors D_2 and D'_2 are unrelated by crystal symmetry. Still, in order to reduce the number of free parameters when discussing the effects of the DM terms it is assumed, as done in [377] and apparently also [319, Fig. 6.1b], that the J_2 and J'_2 bonds on opposite legs of the ladder are approximately related by the reflection symmetry σ_c , which transforms $(D^a, 0, D^c) \mapsto (-D^a, 0, D^c)$. The resulting staggering pattern is consistent with [319, Fig. 6.1b] and agrees with [377, Tab. 1]. In Fig. 4.5, the DM vectors D_2 and D'_2 were drawn parallel on each leg, and antiparallel on opposite legs. Under the approximate σ_c -symmetry, this corresponds to the staggering pattern of D_2^c . By contrast, the component D_2^c alternates along each leg, with the two legs in phase. This situation is different from D_1^a and D_1^c , which both exhibit the same staggering pattern.

4.3.3 Model parameters

The frustrated-ladder model described in section 4.3.1 is primarily motivated by first-principles calculations [217, 257, 401] and inelastic neutron-scattering (INS) data [257, 316]. A large negative Curie-Weiss temperature [401], as well as an overall reduction of the magnetic response compared to a simple ladder or a two-dimensional Heisenberg antiferromagnet [217], further corroborate the importance of frustration [217, 401].

The ranges of exchange couplings deduced from early INS experiments [257] are consistent with the estimates obtained from first-principles calculations (parameter set *A*) [401]. Subsequent INS studies revealed a splitting of the triplet excitations in BiCu_2PO_6 , which was attributed to DM interactions [316]. By combining additional INS data with a bond-operator mean-field theory (BOMF) for the single-triplon excitations [179], a parameter set capable of reproducing the measured dispersion was obtained (parameter set *B*) [318]. The same data have also been analyzed using the method of continuous unitary transformations (CUTs), yielding parameter set *C* [377].⁷ The three aforementioned parameter sets are summarized below.

Set	J_1/k_B	J_4/J_1	J'_2/J_1	J_2/J_1	D_1^{ac}/J_1	D_1^b/J_1	J_i/J_1
<i>A</i> [401]	140 K	0.75	0.5	1	0	0	~ 0
<i>B</i> [179, 318]	116 K	1	1	1	0.3	0.3	0.2
<i>C</i> [377]	131 K	0.83	0.9	0.9	0.48	0.61	0.13

The main difference between parameter sets *A* and *B-C* is the inclusion of DM interactions (cf. section 4.2.4). However, despite $J_2 \neq J'_2$ being strongly suggested by first-principles calculations [401], the

⁶This convention actually appears to correspond to the situation depicted in [259, Fig. 5.16].

⁷The authors of [377] also suggest $D_2^c = -0.018 J_1$, which is considered negligible.

INS data have been analyzed under the assumption $J_2 = J'_2$ [318, 377] and neglecting the possible g-tensor staggering [179, 377]. Furthermore, the uniqueness of parameter set B has not been discussed in detail (unlike in earlier work, see, e. g., [259, Figs. 5.26-5.27]), such that other parameter sets consistent with the INS data may exist. The analysis leading to parameter set B augments the BOMF by one-loop corrections [179]. Without these corrections, the estimated DM couplings are large [318], as is the case for parameter C which treats DM and interladder interactions at the mean-field level only [377]. Parameter set C is therefore not considered further. Note that, even at the one-loop level, features of the measured dispersion remain unexplained by the theory [318].

4.4 Related compounds

BiCu_2PO_6 is closely related to BiZn_2PO_6 and BiMn_2PO_6 . While all compounds share the same crystal structure [289], the CuO_5 pyramids in BiCu_2PO_6 exhibit a Jahn-Teller-type distortion (4+1 coordination) [289], which is less pronounced in BiZn_2PO_6 and BiMn_2PO_6 [289]. BiZn_2PO_6 is non-magnetic [217]. By contrast, magnetic-entropy data on BiMn_2PO_6 are consistent with localized spin- $\frac{5}{2}$ moments [289]. First-principle calculations show that the dominant couplings are J_i and J_1 , followed by J_4 [289]. Thus, frustration is less important than in BiCu_2PO_6 [289]. Furthermore, smaller hybridization of Mn with O results in overall reduced exchange interactions, which are also more three-dimensional than in BiCu_2PO_6 [289]. All these factors yield a very small spin gap (below approximately 1 K) and long-range collinear Néel-type order below $T_N \approx 30$ K [289].

Pure BiCu_2VO_6 , the endpoint of the solid-solution line $\text{BiCu}_2\text{P}_{1-x}\text{V}_x\text{O}_6$ [258], is monoclinic [328] and has a tripled unit cell (along b) [258], resulting in the observation of three ^{51}V -NMR lines [237]. The experimental evidence corroborates a spin- $\frac{1}{2}$ ladder model with three inequivalent rung couplings and thus three different effective gaps [237, 248]. Neutron-scattering experiments [248] could not determine the nature of the spin-correlations (commensurate or incommensurate), leaving the relevance of frustration in BiCu_2VO_6 as an open question.

Finally, the unit cell of BiCu_2PO_6 also closely resembles that of BiMg_2XO_6 with $\text{X} = \text{P, V, As}$ [11]. The space group of the latter is $Bbmm$, which is similar to the $Pnma$ space group of BiCu_2PO_6 [11]. Both have one inequivalent X-site, but $Bbmm$ has only one inequivalent Mg site (unlike BiCu_2PO_6 , which has two Cu sites, cf. section 4.2.1) [11].

4.5 Field-induced phases

No evidence for magnetic order is observed in BiCu_2PO_6 down to $T \sim 0.1$ K [78, 318] (cf. also [319, p. 60]), indicating that the quantum spin-liquid (QSL) ground state (cf. section 1.2) is robust against residual interactions. Therefore, field-induced magnetic order is expected (see section 1.2). The phase diagram of BiCu_2PO_6 as function of temperature and magnetic field is depicted in Fig. 4.6(a) [207]. Indeed, several field-induced phases are observed, and magnetization measurements suggest that additional phase transitions occur at even higher magnetic fields [208] [Fig. 4.6(b)]. The orientation-dependence of the phase diagram indicates the importance of anisotropies like DM interactions or non-trivial g-tensors [207].

This work focuses on the case $\mathbf{H} \parallel b$. As indicated in the bottom panel of Fig. 4.6(a), the corresponding

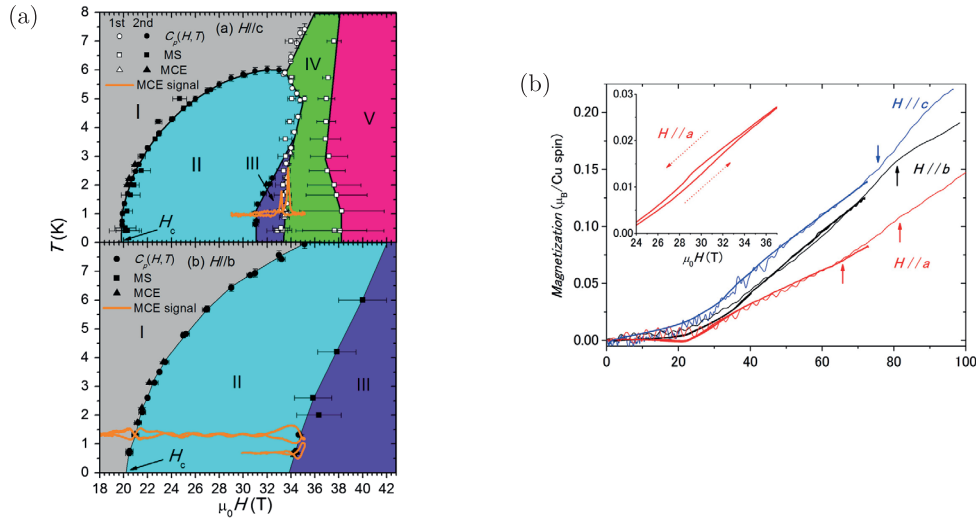


Figure 4.6: (a): Thermodynamic phase diagram of BiCu_2PO_6 as function of temperature T and magnetic field $\mu_0 H$. Open (closed) symbols correspond to first (second) order transitions. Top and bottom panels correspond to different orientations of the applied magnetic field. (Reprinted figure with permission from Ref. [207]. Copyright 2012 by the American Physical Society.) (b): High-field magnetization measured in BiCu_2PO_6 at $T \sim 2$ K (exact temperature not specified). (Reprinted figure with permission from Ref. [208]. Copyright 2014 by the American Physical Society.)

phase transitions are of second order [207]. Consistently with [74, 78, 208], the critical fields corresponding to the phase transitions towards phases II and III will be designated as H_{c1} and H_{c2} from here on. Furthermore, the terms *intermediate-field phase* and *high-field phase* (cf. [74, 208]) shall refer to phases II and III, respectively.

4.6 Outline and relation to previous work

The primary aim of the present work is to improve the understanding of the high-field field-induced phase observed in magnetic fields $\mathbf{H} \parallel b$ (cf. section 4.5).

The hyperfine couplings and g-tensors, later required to quantitatively describe the ^{31}P -NMR spectra, are estimated in chapters 5 (section 5.2.1) and 6. These analyses closely follow previous work by F. Casola [74, 75] and, in fact, rely on the same data [74]. Still, the discussion presented herein is believed to clarify certain aspects and extend the previous considerations, e. g. , by accounting for the presence of crystallographically inequivalent magnetic sites and doping-induced effects (see section 6.8 for details).

In addition, various proposed choices of model parameters (cf. section 4.3.3) are compared with previous magnetic-susceptibility and specific-heat data in section 5.4. This attempt to reproduce the experimental data using the model Hamiltonian (4.1) also considers the effect of DM interactions. The corresponding results are discussed in section 5.4.5.

The results of comprehensive numerical calculations performed for the frustrated-ladder model are presented in chapter 7, which also includes a review of previous theoretical and numerical work (section 7.1). Note that going beyond these previous results first requires their reproduction. Ultimately, the presented results are believed to clarify several aspects of the field-induced phases expected in this model.

Finally, the results of the high-field ^{31}P -NMR experiments performed in this work are presented and analyzed in chapter 8. This involves comparisons with previous ^{31}P -NMR data obtained in the intermediate-field phase, as well as other experimental reports.

5 BiCu₂PO₆: Low-field thermodynamic properties

5.1 Introduction

The considerations presented in this chapter target two goals: First, by comparing the simulated magnetic response of the model described in section 4.3.1 with the measured magnetization, the g -tensors are estimated (section 5.2.1). In combination with calculations for doped models (section 5.2.4), this serves as a preparation for analyzing the ³¹P nuclear hyperfine couplings in the following chapter (chapter 6). Secondly, the behavior of the frustrated-ladder model, as well as systematic deviations between calculations and published data, are illustrated.

Parameter set A is considered a representative choice and hence used throughout section 5.2, as well as in chapter 6. This choice is motivated by three arguments: (i) Parameter set A is rigorously-motivated, (ii) DM interactions are not expected to be important at high temperature (cf. [74, p. 109]), (iii) this choice maintains consistency with previous work [74, 76, 78], and, lastly, (iv) the analyses leading to parameter sets B and C did not consider quantitative consistency with bulk measurements like specific heat and magnetic susceptibility (see section 4.3.3 and references therein).

After a brief discussion of interladder couplings (section 5.3), the influence of the individual model parameters is examined (section 5.4), before discussing the results (section 5.5).

5.2 Results for representative parameters

5.2.1 Susceptibility and g -tensors

The temperature-dependent susceptibility calculated using parameter set A with $g_1 = g_2 = 2.16$ [401] is shown in Fig. 5.1(a). This reproduction of previous work on BiCu₂PO₆ [401] also serves for checking the technical soundness of the methods used in this work (see sections 1.4 and A.1 for details).

The measured susceptibility¹ [Fig. 5.1(b)] exhibits a residual magnetic response at low temperature,^{2,3} $\lim_{T \rightarrow 0} \chi \neq 0$, whose intrinsic nature is corroborated by a residual ³¹P-NMR shift [22, 74, 218]. As

¹In principle, each Cu site experiences the dipole fields created by all the remaining, approximately uniformly-polarized Cu moments. For a spherical sample, the largest eigenvalue of the matrix describing this coupling (cf. section 6.3.1) is smaller than $0.3 \text{ T}/\mu_B$. For BiCu₂PO₆, $|\chi^{\alpha\beta}(T)| \ll \chi_{\text{max}} = 5 \cdot 10^{-3} \mu_B/\text{T}$ (per Cu site), such that the resulting relative change in magnetic induction is less than $1.5 \cdot 10^{-3}$. The demagnetizing field (section 6.3.2) gives rise to a relative correction of at most $8 \mu_0 \chi_{\text{max}}/(474.6 \text{ \AA}^3) \approx 10^{-3}$ [11] (section 6.3). Both contributions are considered negligible.

²As previously in [74, p. 108], the small upturn at the lowest temperatures is attributed to impurity moments [424, p. 59 and Fig. 4.17a], the typical defect concentration being $\sim 0.15\%$ [423, p. 118].

³Temperature-independent contributions like core diamagnetism and Van-Vleck paramagnetism (see [217, 289]) are neglected based on the Curie-Weiss fit reported in [401].

noted in [179], the limiting value is orientation dependent,⁴

$$\lim_{T \rightarrow 0} \chi^{cc} > \lim_{T \rightarrow 0} \chi^{bb} > \lim_{T \rightarrow 0} \chi^{aa} > 0 \quad . \quad (5.1)$$

A non-zero low-temperature susceptibility can arise due to interactions which break S_{tot}^z -conservation, such as DM interactions (e. g. , [74, pp. 134-135] and [207]) (section 1.1.2), whose effects are considered later (section 5.4). Another possibility raised in previous work is g-tensor anisotropy [207]. Since the alternation of the two inequivalent Cu sites is compatible with the dominant antiferromagnetic (AFM) exchange couplings in BiCu_2PO_6 , the site-dependent g-tensors also give rise to a uniform magnetization at low temperature (see section 1.4.5 and example in appendix A.5.3; cf. [15]).

The crystal structure of BiCu_2PO_6 involves two types of ladders which are related by the mirror symmetry σ_c (see section 4.3.1). Thus, the total susceptibility of the crystal is diagonal in the (a, b, c) basis, reflecting the orthorhombic symmetry of the crystal. I specialize to Heisenberg symmetry, which should represent a good approximation at high temperatures, since the energy scales associated with any anisotropies are believed to be $\ll 100$ K (cf. , e. g. , [74, p. 109]). Assuming that the set of functions $\{C_{11}^{zz}(T), C_{12}^{zz}(T), C_{22}^{zz}(T)\}$ is linearly independent, eq. (A.15) [in section A.1.4] implies that a measurement of the longitudinal susceptibilities $\chi^{aa}(T)$, $\chi^{bb}(T)$, and $\chi^{cc}(T)$ constrains the nine values $\text{diag}(g_1 g_1^T)$, $\text{diag}(g_1 g_2^T + g_2 g_1^T)$, and $\text{diag}(g_2 g_2^T)$. The C_{1h} -symmetry of the Cu sites (section 4.2.3) implies that g_i^{bb} can be estimated rather robustly using $\chi^{bb}(T)$. However, the remaining six constraints are insufficient to fully constrain the other eight g-tensor components.

A standard assumption is $g_i^T = g_i$ which—even though not rigorously motivated (see section 1.5.9)—resolves the underconstrained nature of the model. The resulting “maximal” g-tensor model \mathcal{A} provides the best possible fit for a given Hamiltonian. In principle, the exchange energy scale J_1 can also be fitted. However, the gap is generally overestimated due to residual interactions [401] (see also [74, p. 98]), so that the fit range has to be restricted to temperatures at which the Heisenberg Hamiltonian represents a good approximation (cf. [74, Fig. 5.9b]). Since the resulting fit does not constrain the parameters very well, $J_1 = 140$ K is fixed instead [401]. Moreover, the relative uncertainties of the g-tensor components are of the order of 100%, indicating strong covariance of the corresponding fit parameters. To resolve this ambiguity, I follow [74, p. 105] and assume that the g-tensors reflect the approximate C_{2v} -symmetry of the CuO_4 plaquettes (see section 4.2.5),

$$g_i = \begin{pmatrix} g_i^{(x)} \cos^2 \theta_i + g_i^{(z)} \sin^2 \theta_i & 0 & (g_i^{(z)} - g_i^{(x)}) \cos \theta_i \sin \theta_i \\ 0 & g_i^{(b)} & 0 \\ (g_i^{(z)} - g_i^{(x)}) \cos \theta_i \sin \theta_i & 0 & g_i^{(z)} \cos^2 \theta_i + g_i^{(x)} \sin^2 \theta_i \end{pmatrix} . \quad (5.2)$$

Thus, $g_i = \text{diag}(g_i^{(x)}, g_i^{(b)}, g_i^{(z)})$ in the (x, b, z) basis which is obtained by rotating the (a, b, c) basis by θ_i about b (see Fig. 4.3). I further demand $g_i^{(\alpha)} \geq 0$ (without loss of generality) and call the resulting fit model \mathcal{B} . As discussed in section 4.2.5, the local environment of the two Cu sites is very similar, suggesting that $g_1^{(\alpha)} \approx g_2^{(\alpha)}$. To determine which g-tensor parameters differ significantly between the two sites, additional models \mathcal{B}_{bz} , \mathcal{B}_b , and \mathcal{B}_0 , obtained by augmenting \mathcal{B} by the constraints $g_1^{(x)} = g_2^{(x)}$, $g_1^{(x)} = g_2^{(x)} \wedge g_1^{(z)} = g_2^{(z)}$, and $g_1^{(x)} = g_2^{(x)} \wedge g_1^{(b)} = g_2^{(b)} \wedge g_1^{(z)} = g_2^{(z)}$, respectively, are considered. For each model, two least-squares fits, corresponding to two different data ranges, are reported in Tab. 5.1.

⁴In principle, this behavior could be accidental given that each curve has been measured on a different, specifically cut sample. However, the same ordering sequence was observed in other measurements ([424, Fig. 7.2 (p. 119)] and [207]).

Model	Data range	\bar{R}^2	$g_1^{(x)}$	$g_2^{(x)}$	$g_1^{(b)}$	$g_2^{(b)}$	$g_1^{(z)}$	$g_2^{(z)}$
\mathcal{A}	$T > 150$ K	0.999 39	–	–	–	–	–	–
\mathcal{B}	$T > 150$ K	0.999 36	2.250(14)	2.11(2)	1.88(2)	2.09(2)	1.84(3)	2.34(3)
\mathcal{B}_{bz}	$T > 150$ K	0.999 31	2.1955(7)		1.88(2)	2.09(2)	1.88(2)	2.28(2)
\mathcal{B}_b	$T > 150$ K	0.998 58	2.2012(8)		1.88(3)	2.09(3)		2.0672(7)
\mathcal{B}_0	$T > 150$ K	0.998 45	2.2012(8)			1.9767(8)		2.0672(7)
\mathcal{A}	$T > 100$ K	0.999 69	–	–	–	–	–	–
\mathcal{B}	$T > 100$ K	0.999 65	2.213(6)	2.166(9)	1.783(11)	2.186(10)	1.807(12)	2.364(11)
\mathcal{B}_{bz}	$T > 100$ K	0.999 64	2.1948(4)		1.783(11)	2.186(11)	1.827(9)	2.341(9)
\mathcal{B}_b	$T > 100$ K	0.997 02	2.1996(11)		1.78(3)	2.19(3)		2.0608(11)
\mathcal{B}_0	$T > 100$ K	0.995 80	2.1996(13)			1.9680(12)		2.0608(13)
\mathcal{C}_0	$T > 100$ K	0.998 96	2.2150(7)			1.9810(6)		2.0679(7)

Table 5.1: Results of fits to measured susceptibility [see Fig. 5.1(b) for data source and details]. Uncertainties are estimates reported by the regression routine [256]. The corresponding calculations were performed for a system size $L = 8$. The selected model is highlighted in blue color. See text for details.

The reduced R^2 values (cf. section A.6.1) listed in Tab. 5.1 show that model \mathcal{B}_{bz} results in only marginally worse a fit than the “maximal” model \mathcal{A} . The fact that $g_1 \neq g_2$ is supported by the fits. However, the degree of staggering, i. e., e. g., the difference $|g_1^{bb} - g_2^{bb}|$, seems to increase as the data range used for the fits is extended towards lower temperatures. Clearly, the estimated g -tensors will in general depend on the choice of the spin-Hamiltonian. Extending the fit range towards lower temperature represents a trade-off between a more robust fit due to clearer linear independence of the fit components and an increased systematic error resulting from interactions neglected in the model Hamiltonian \mathcal{H} . I will use model \mathcal{B}_{bz} fitted to data in the range $T > 100$ K in the following, since it provides a decent fit [cf. Fig. 5.1(b)] without introducing too many additional parameters. The aforementioned systematic uncertainties are discussed later (section 6.7).

The selected model yields $g_1^{aa} = 2.11$ and $g_2^{aa} = 2.23$, which agrees to within 10% with the value 2.27 estimated from electron-spin resonance (ESR) [258]. The results are also in reasonable agreement with previous work using a simpler g -tensor model (cf. [74, Fig. 5.9]). In principle, model-free estimates of the g -tensor can be obtained from measurements above the saturation field (e. g., [409]). However, the large saturation field of BiCu_2PO_6 [401] makes this experimentally impractical. The results are compatible with a predominantly uniaxial anisotropy of the $\text{Cu}(i)$ sites, $g_i^{(b)} \simeq g_i^{(z)}$. The similarity of the out-of-plane components, $g_1^{(x)} \simeq g_2^{(x)}$, indicates that the position of the apical oxygen does not have a significant effect, thereby corroborating the assumption of approximate C_{2v} -symmetry [cf. eq. (5.2), [74, p. 105], and section 4.2.5]. While g -factors smaller than two can arise for t_{2g} ions (e. g., [198]), principal-axis components $g_i^{(\alpha)} \geq 2$ are expected for Cu^{2+} moments ([10] and [235, pp. 92 ff.]; see also [377]). However, deviations from this prediction might be possible in BiCu_2PO_6 due to admixture of Bi orbitals (see section 4.2.4, cf. [377]).⁵

Two exemplary fits of the b -axis susceptibility are shown in Fig. 5.2, along with the corresponding sublattice susceptibilities (cf. section 1.4.5). For a site-independent g -factor, the inequivalent NNN exchange couplings $J'_2 = \frac{1}{2}J_2 < J_2$ [401] lead to $\chi_1 > \chi_2$.⁶ By contrast, the fit with site-dependent g -factor

⁵Note that, as pointed out in [317], a spin-orbit coupling of 1.25 eV is predicted for atomic Bi [447]—to be compared with 0.1 eV for Cu^{2+} [9, p. 399].

⁶This simple fact was also remarked in previous (zero-temperature) DMRG work [77, p. 8].

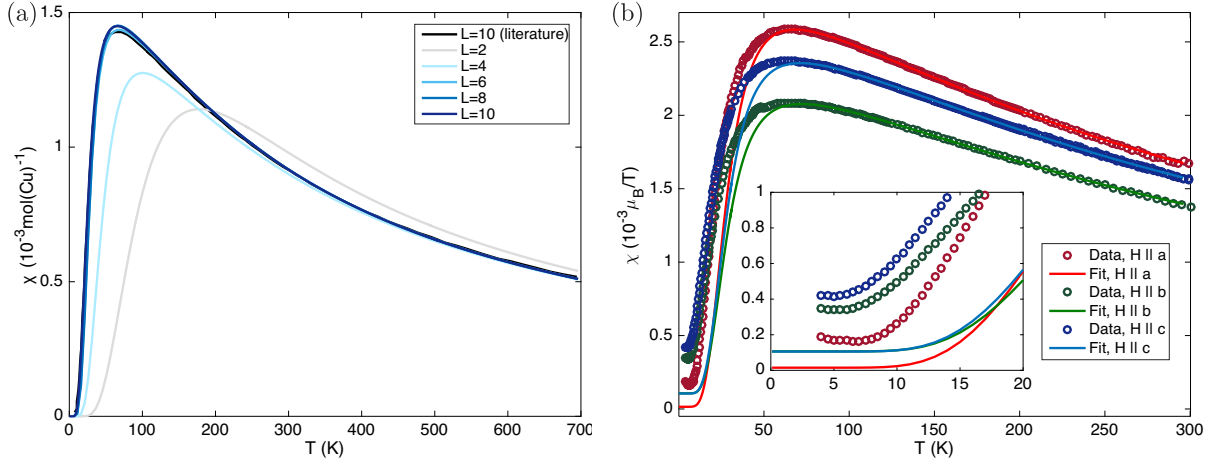


Figure 5.1: (a): Susceptibility calculated using full-spectrum exact diagonalization, along with published results sampled from [401]. (b): Best fit to measured susceptibility (see Tab. 5.1 and text). The inset shows an enlarged subset of the main figure. The data were measured by T. Shiroka using a Quantum Design MPMS XL DC SQUID magnetometer and coincide with those analyzed in previous work [75, Fig. 5] (but cf. [74, Fig. 5.9]). Measurements were taken in $\mu_0 H = 0.5$ T after zero-field cooling.

overcompensates for this difference by choosing $g_2^{(b)} > g_1^{(b)}$ to yield $\chi_1 < \chi_2$. Thus, the possibility that $g_1^{(\alpha)} \approx g_2^{(\alpha)}$, as is suggested by similarities in the crystal structure (section 4.2.5), cannot be clearly rejected using the susceptibility analysis. Therefore, a relative error of 10% is assumed in the analyses of the high-field NMR data, in order to include the possibility that $g_1^{(\alpha)} \approx g_2^{(\alpha)}$.

Lastly, since the two g -tensors are not tightly constrained by the fits, a simplified model \mathcal{C}_0 , based on full-spectrum ED calculations with $J'_2 = J_2 = 0.75J_1$ and assuming $g_1^{(\alpha)} = g_2^{(\alpha)}$, has been considered. The fit results (Tab. 5.1) show that the average g -tensor parameters are rather well determined, whereas the dominant uncertainties pertain to the differences between the Cu(1) and Cu(2) sites.

5.2.2 Magnetic specific heat and entropy

The magnetic contribution C_M to the specific heat is easy to calculate from full-spectrum ED results by using the well-known relation,

$$C_M = \frac{\partial \langle H \rangle}{\partial T} = \frac{1}{k_B T^2} \left(\langle H^2 \rangle - \langle H \rangle^2 \right) . \quad (5.3)$$

Comparing this with experimental data is useful, since $C_M(H = 0)$ only depends on the exchange Hamiltonian and no auxiliary parameters like g -tensors. Measurements of the specific heat of BiCu_2PO_6 were published in [217, 218, 424].⁷ The calculated C_M is contrasted with published data in Fig. 5.3. The main observations are discussed in the following.

As in the case of the susceptibility (see [401]), the model (4.1) overestimates the energy gap. Accordingly, this is attributed to residual interactions, such as interladder coupling and/or DM interactions (see,

⁷There were also attempts to perform AC-calorimetry measurements on BiCu_2PO_6 under pressure [455].

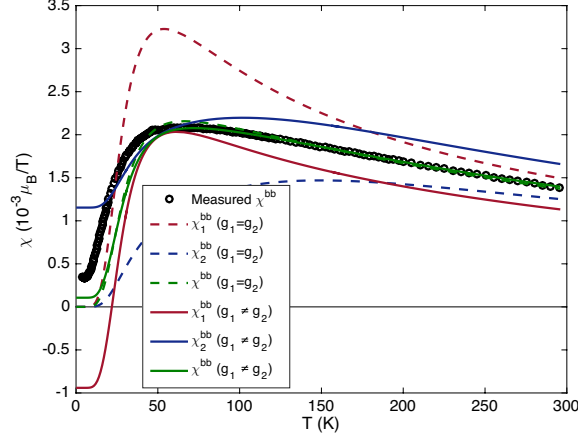


Figure 5.2: Fits to measured susceptibility [see Fig. 5.1(b) for data source and details], corresponding to models \mathcal{B}_0 and \mathcal{B}_{bz} in Tab. 5.1 (fitted over the range $T > 100$ K).

e. g., [401]). A toy model can be obtained by assuming that these additional interactions uniformly redistribute the spectral weight of all states except the ground state over a characteristic energy scale \tilde{D} . Such an approach (see section A.5.4 for details) yields the dashed curve shown in Fig. 5.3 and, indeed, this empirical model reproduces the reduced gap.

Yet, the calculated peak value of C_M is much larger than the measured one. Note that the order of magnitude of the calculated C_M is consistent with results obtained for other ladder systems [47]. To further corroborate the correctness of the calculations, I consider the magnetic entropy S_M which satisfies $S_M(T) = \int_0^T \frac{C_M}{T'} dT'$ [218].⁸ In the high-temperature limit, the magnetic entropy per Cu spin must clearly satisfy $\lim_{T \rightarrow \infty} S_M(T) = k_B \log 2$, which is indeed obeyed by the calculations, but not by the published data [see Fig. 5.3(b)]. Besides [218], the reduced saturation entropy was also noted in [424], for independent measurements, and attributed to magnetic frustration in both cases [218, 424]. However, the fact that the ED calculations [Fig. 5.3(b)] reproduce the correct limit raises questions regarding this explanation. In fact, upon closer inspection of the experimental data shown in Fig. 5.3(c), the curves for BiCu_2PO_6 and its non-magnetic counterpart BiZn_2PO_6 appear to cross at around 50 K, suggesting that $C_M < 0$ for $T \geq 50$ K, which is unexpected. As long as the aforementioned discrepancies remain unresolved, comparisons between calculated and measured C_M are therefore restricted to $T \lesssim 25$ K.

5.2.3 Energy gap and finite-size effects

The energy gap calculated for systems with different sizes and boundary conditions is shown in Fig. 5.4(a). The full-spectrum exact-diagonalization (ED) results are consistent earlier results [401], reporting a singlet ground state ($k = 0$, $S_{\text{tot}}^z = 0$) and a triplet of lowest-energy excited states with incommensurate k and $S_{\text{tot}}^z \in \{-1, 0, 1\}$. As already described in [401], there is also a $k = \pi$ singlet related to a nearby soft-mode dimerization transition [228, 412], which is slightly lower in energy for certain system sizes and periodic boundary conditions. This singlet state is also the reason why the specific heat [Fig. 5.3(a)] appears to converge slightly more slowly with system size than the susceptibility [Fig. 5.1(a)] (cf. [228,

⁸Ignoring any spin-lattice couplings, the entropy is simply the sum of S_M and a lattice contribution. The ground state is a singlet, such that $S_M(T = 0) = 0$.

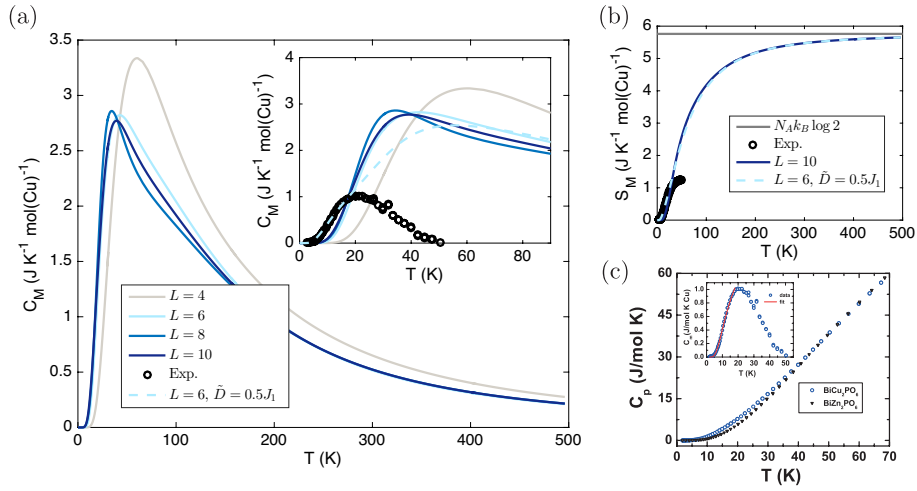


Figure 5.3: (a): Calculated magnetic specific heat C_M , along with measured data sampled from [217]. (b): Corresponding magnetic entropy, obtained by numerical integration of the data shown in (a). (c): Measured data [217]. (Reprinted figure (c) with permission from Ref. [217]. Copyright 2007 by the American Physical Society.)

p. 9]).

As pointed out in the original numerical (and experimental) work for parameter set A [401, pp. 10-11], the calculations suggest a spin gap of order 70 K for BiCu_2PO_6 [see previous results [401, p. 10 and Figs. 10-12] or Fig. 5.4(a)], whereas high-field magnetization [401], ^{31}P NMR shift [22], ^{31}P spin-lattice relaxation rate [22] (see also [76] and [74, p. 116]),⁹ and specific heat [217], suggest an energy gap of 35(5) K. Inelastic neutron-scattering experiments found an approximately doubly-degenerate excitation branch with spin gap 22 K and a non-degenerate branch with spin gap 46 K, whose weighted average of 30 K is consistent with the other experimental estimates [316]. Possible explanations for this discrepancy [401] between model calculations and experiments are reviewed at the end of this chapter.

5.2.4 Inhomogeneous system

Following [74, 75], nuclear-magnetic resonance data collected previously on weakly Zn-doped samples [74] will be used to estimate the hyperfine couplings in BiCu_2PO_6 (section 6.6). Substitution of a $\text{Cu}(i)$ site generally alters the local susceptibilities of the Cu sites in the vicinity of the dopant [76] (see section 6.5.2). While previous work [22, 63, 76] mainly reported quantum Monte Carlo calculations for doped ladders (an exception are preliminary DMRG results presented in [74, Fig. 5.13(c-d) and pp. 113-114], cf. also [76]), such calculations cannot account for frustration [76] (cf. section 1.4.2). Hence, in order to assess the importance of doping-induced effects and thus pave the way for the later estimation of the hyperfine couplings, full-spectrum ED calculations were performed for finite frustrated spin ladders with periodic boundary conditions, where one $\text{Cu}(i)$ spin ($i \in \{1, 2\}$) is substituted by a non-magnetic Zn.

Equation (1.4) can be applied to calculate the local susceptibilities for arbitrary g -tensors.¹⁰ Selected

⁹Note that the energy scales describing the thermally activated behavior of the spin-lattice relaxation rate and the NMR shift are related by a factor $\frac{3}{2}$ due to spin diffusion [22, 76, 342].

¹⁰In the formalism of section 1.4.5, the indices i, j then denote individual spins. However, only sums $\sum_{j \in J} C_{ij}(T)$ over actual sublattices J are ultimately required, yielding a straightforward and efficient extension of equation (A.13) [in section

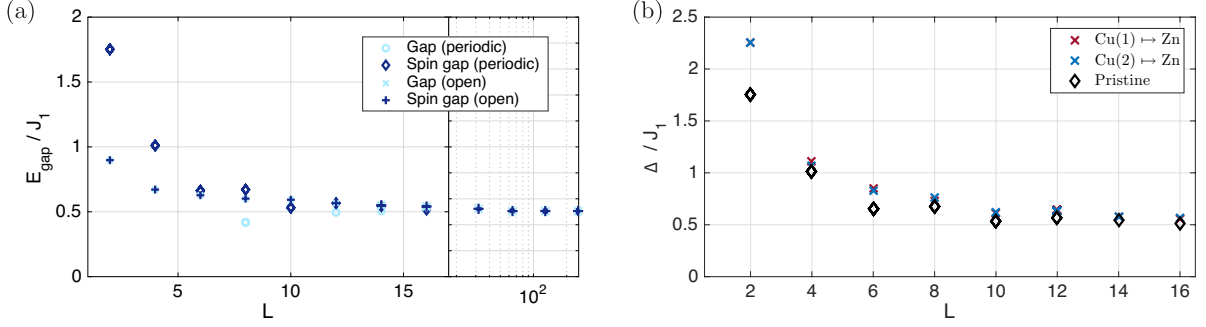


Figure 5.4: (a): Energy difference to first excited state (gap) and energy difference to first magnetic excitation (spin gap), for frustrated-ladder systems with L rungs and different boundary conditions (periodic/open). Note the discontinuity of the abscissa at $L = 17$. Results for $L \leq 16$ were obtained using ED, whereas DMRG was used to solve the larger systems ($s \geq 16$, $m \geq 512$, see sec. 7.5 for notation; error bars from energy variance are smaller than symbol size) and checked to coincide with ED data for $14 \leq L \leq 16$. (b): Spin gap Δ between ground state and first excited spin multiplet for inhomogeneous systems.

results of this procedure are shown in Fig. 5.5. Clearly, finite-size effects are negligible at temperatures $T \gtrsim 200$ K for system sizes $L \geq 8$. Since the doped system consists of an odd number of spins, the ground-state is a spin- $\frac{1}{2}$ doublet and the first excited state a spin- $\frac{3}{2}$ multiplet,¹¹ which results in a $1/T$ -divergence¹² of the susceptibility in the limit $T \searrow 0$, despite the presence of a spin gap. The effects on the magnetic response at temperatures well above the spin gap are less striking (see also section 6.5.2).¹³ As discussed previously, due to $J'_2 < J_2$, the magnetization prefers to reside on the Cu(1) sublattice [77, p. 8] and the impurity-induced spin- $\frac{1}{2}$ moment extends further into the Cu(1) sublattice [74, p. 114], which explains the different magnitudes of the diverging low-temperature local susceptibilities in Fig. 5.5. Note that the temperature dependence of the the local Cu(2) susceptibility nicely illustrates the trade-off between the $1/T$ -divergence due to ground-state polarization and the thermal suppression of the magnetic response caused by the spin gap. Reassuringly, this is in qualitative agreement with the macroscopic susceptibility measurements reported in [218, Fig. 5], [22, Fig. 4], and [423, Fig. 7]. Far from the defect, the local susceptibility remains essentially unchanged, which is consistent with previous conclusions drawn from the behavior of the ^{31}P -NMR shift [22, sec. IV.A].

The system-size dependence of the spin gap (equal to the excitation gap) is shown in Fig. 5.4(b). Clearly, no change in the spin gap is expected in the limit of dilute doping, since magnetization of the system beyond $S_{\text{tot}}^z = \pm \frac{1}{2}$ still requires the formation of a triplon by breaking of a rung bond. Further, site depletion (Zn-doping) intuitively impedes the triplon motion, which is why a larger spin gap is anticipated for the doped system [259, p. 188] (see also [77, p. 3] and experimental confirmation in [259, p. 186]). Both expectations are consistent with the calculations.

Interactions between impurity-induced moments are expected to give rise to in-gap [347] excitations ([266] and references therein; see also [74, p. 94]). Such behavior has been experimentally demonstrated

A.5.3].

¹¹The half-integer total spin is a simple consequence of the addition rules for angular momenta, whereas the level structure follows from ED and is consistent with previous anticipations (see, e. g., [218, p. 7] and references therein).

¹²As discussed in section A.1.4, full-spectrum ED in finite magnetic field only yields meaningful susceptibilities as long as the linear-response regime is preserved. If the ground-state has non-zero spin, this assumption breaks down at sufficiently low temperature. To make sure that the results are correct, only points with $R^2 \geq 0.99$ were included in Fig. 5.5.

¹³This is in accordance with the discussion in [22, p. 8] and the data in [218, Fig. 5].

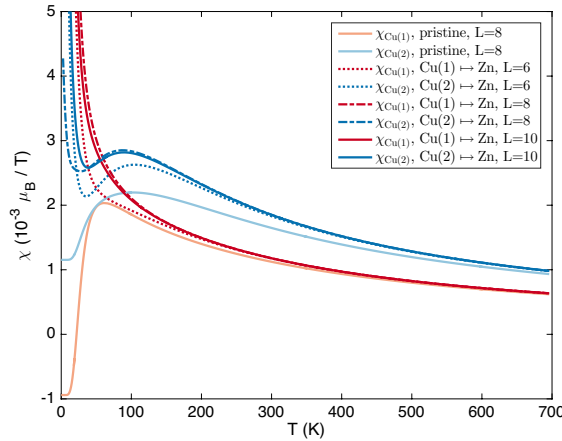


Figure 5.5: Local longitudinal susceptibilities for magnetic fields applied along the b -direction, computed using the g -tensor model obtained in section 5.2.1. Calculations were performed for the undoped system, as well as the two possible configurations with one Cu site replaced by non-magnetic Zn. The system size is parametrized by the number of rungs L . Red color indicates local susceptibilities of Cu(1) sites, whereas blue color is used for Cu(2) sites. The local susceptibilities correspond to sites two rungs away from the dopant and on the same leg as the dopant [i. e., $\chi_{\text{Cu}(i)} = \tilde{\chi}_i(i, 2)$ in the notation of section 6.5.2].

in a strong-leg Heisenberg-ladder system through inelastic neutron scattering [347]. The above works also demonstrate how numerical calculations can be used to calculate the effective interactions between the doping-induced “spin islands” [266, 347]. No such calculations were attempted for BiCu_2PO_6 , since the doping-induced phases are considered beyond the scope of the present work. Generally, doping induces glassiness [218] and magnetic order [259, p. 189] in BiCu_2PO_6 , which has been studied using ^{31}P -NMR [22, 63, 76], quantum Monte Carlo [63]¹⁴ and neutron diffraction [259].

5.3 Interladder coupling

Residual interladder couplings are generally present, as can be seen from the fact that the system exhibits field-induced magnetic order despite its quasi one-dimensional nature (cf. section 7.8.2). Recent first-principles calculations suggest that the interladder coupling $|J_i| \lesssim 0.15 J_1$ [401]. A similar estimate has been given in [63]. However, the calculations rely on numerical cancellation of large ferro- and antiferromagnetic contributions [401], so that the relative uncertainties are important. Indeed, previous DFT calculations obtained $J_i/J_1 \sim 0.3 - 0.5$ [257].¹⁵ Experimentally, Raman scattering suggests $J_i \approx 0.35 J_1$ [87]. Inelastic neutron-scattering (INS) experiments corroborate $J_i \ll J_4$ and clearly antiferromagnetic [316] (see also [259, p. 133]), the best estimate being $J_i \approx 0.2 J_1$ [318] (cf. section 4.3.3).

Clearly, the system sizes accessible with exact diagonalization (section 1.4.1) are insufficient to study coupled ladders. DMRG calculations for coupled ladders were attempted, but deemed impracticable within the context of this work, because the required bond dimensions (see section 1.4.3) grow expo-

¹⁴Although frustration is important in a single zigzag chain [297], the calculations reported in [63] explain the qualitative behavior of the frustrated-ladder system, despite its neglect (see also [218]).

¹⁵Since the corresponding assignment of interladder and intraladder couplings is inconsistent with the remaining literature (e. g., [401]), the strong interladder coupling suggested in [217] is not considered in this work.

nentially with the number of ladders (see, e. g., [111]). An instructive discussion of this problem can be found in [349, p. 16.29]. At the same time, simple mean-field descriptions appear insufficient to capture the effect of the interladder coupling (see appendix A.5.5 for an attempt).¹⁶ Thus, no further quantitative treatments of interladder couplings are attempted in this work.

As pointed out in [63] (see also [22, 218]), for unfrustrated coupled ladders with $J_1 = J_\perp$, an interladder coupling of 0.314 is sufficient to destroy the spin gap [253]. Thus, interladder couplings are generally expected to reduce the spin gap (see also [257]), as shown explicitly in [401, p. 11]. Meanwhile, strong frustration stabilizes the spin gap [228, 257, 401], also in the loosely-related case of an isotropic two-dimensional NNN-frustrated Heisenberg model [73] (cf. [218, 257]). Therefore, as previously argued in [218] and [257], the observation of a sizable spin gap despite allegedly non-negligible interladder couplings underlines the importance of magnetic frustration in BiCu_2PO_6 .

5.4 Influence of coupling parameters

As discussed in section 4.3.3, the parameters of the spin Hamiltonian (4.1) proposed in the literature are not free from uncertainties (see also [401, p. 8]). While interladder couplings are difficult to account for in finite-temperature calculations (section 5.3), DM interactions can in principle be included in exact-diagonalization (ED) calculations. Since DM interactions were repeatedly proposed to be relevant in BiCu_2PO_6 (see sections 4.2.4 and 4.3.3), the effects of altering parameter set A by either changing one exchange-coupling parameter or adding one DM term deserve consideration. Variations of the exchange couplings were mentioned previously in [401, p. 8] (see also fitting procedure in [257] for the case $J_2 = J'_2$), but without showing detailed results. The exchange couplings are parametrized by J_1 , J_4/J_1 , $(J_2 + J'_2)/(2J_1)$, and $(J_2 - J'_2)/J_1$. When varying $(J_2 + J'_2)/(2J_1)$, the ratio J'_2/J_2 is kept fixed, whereas $(J_2 + J'_2)/(2J_1)$ is kept fixed while varying $(J_2 - J'_2)/J_1$. Note that these one-parameter variations only represent a subset of all possible parameter sets. However, an exhaustive search would require computational efforts which are beyond the scope of this work, due to the high dimension of the parameter space. To restrict the number of degrees of freedom, D'_2 is linked to D_2 using the approximate symmetry described in section 4.3.2. The DM interactions on the next-nearest neighbor (NNN) bonds are thus parametrized by D_2^a and D_2^c . Full-spectrum ED calculations were performed for finite ladders with $L = 8$ rungs and periodic boundary conditions. As expected [228], the magnitude of the gap is mainly determined by the strength of the rung bond, as well as the average frustration. The effect of the difference between J_2 and J'_2 is found to be weak.

5.4.1 Magnetic susceptibility

The calculated b -axis susceptibilities were fitted to the data by adjusting the site-dependent g -factors¹⁷ g_1 and g_2 , as well as the energy scale J_1 . The results are shown in Figs. 5.6 and 5.7. Low-temperature artifacts in the curves calculated for $J_4 \leq 0.25 J_1$ are due to the combined effect of ground-state degeneracy and numerical errors. Regarding the DM interactions, the effect of D_1^b and D_4^b is negligible (Fig. 5.7). By contrast, D_1^{ac} and D_2^a mix singlet and triplet states, which reduces the spin gap and results

¹⁶Note that an expression for the first-order effect of the interladder coupling on the single-triplon dispersion was given in [401].

¹⁷Remember that b is a principal axis of the g -tensor (see section 4.3.1).

in a non-vanishing susceptibility in the limit of zero temperature (see, e. g., [401]). Interestingly, the effect of D_2^c appears much weaker than that of D_2^a (Fig. 5.7).

Except for the models including the DM interactions D_1^{ac} and D_2^a , the overall agreement is unsatisfactory, especially considering the estimated g-factors. While inclusion of D_1^{ac} or D_2^a results in significantly improved fits, some of which even yield plausible g-factors, all models systematically overestimate the low-temperature susceptibility. Most likely this is because the calculations neglect interladder couplings, which are expected to reduce the spin gap (see [401] and section 5.3).

Restricting the data range to $T \geq 100$ K, where interladder couplings should be less important, does not improve the situation. Only after fixing $J_1/k_B = 140$ K [401] in addition, the stability of the fits improves and the g-factors appear more reasonable (Fig. 5.8). These results corroborate the energy scale of the coupling J_1 proposed in [401] (see also [74, pp. 98,109]). Again, setting D_1^{ac} or D_2^a to values around $0.4 J_1$ significantly improves the fits. In particular, the results for $D_1^{ac} = 0.4 J_1$ approximate the measured susceptibility quite well, except for a slightly overestimated gap which is attributed to interladder couplings (see above), and yield plausible g-values [i. e., $g_1 \sim g_2 \sim 2$, cf. Fig. 5.8(f)].

Repeating the preceding analysis with the additional constraint $g_1 = g_2$ yields qualitatively similar susceptibility curves (not shown). It is worth mentioning that $g_1 \approx g_2 \approx 2$ with $\frac{1}{2}(g_1 + g_2) \approx 2$ is only realized for $0.75 \lesssim J_4/J_1 \lesssim 1$ and $(J_2 + J_2')/2 \gtrsim 0.75 J_1$, which compares favorably with parameter set *A*. By contrast, neither (low-to-moderate) DM interactions nor the difference $J_2 - J_2'$ have a strong influence upon the (average) g-factor.

5.4.2 Specific heat

To complement the preceding subsection, the magnetic specific heat $C_M(T)$ was calculated. The results are summarized in Figs. 5.9 and 5.10. As seen for the magnetic susceptibility, the difference $J_2 - J_2'$, as well as the DM terms D_1^b , D_4^b , and D_2^c have very little influence.¹⁸ Low-temperature features appear for small frustration (average value of J_2 and J_2') and/or strong rung coupling (J_4). These features have no counterpart in the calculated magnetic response, suggesting that they are due to singlet excitations (cf. [228, p. 9]).

The fact that no low-temperature features are observed in the experimental data (cf. section 5.2.2) suggests $J_4/J_1 \geq 0.5$, $(J_2 - J_2')/(2 J_1) \geq 0.25$, and $D_1^{ac}/J_1 \leq 0.35$. However, these conclusions need to be taken with a grain of salt, since at least the low-temperature features caused by D_1^{ac} might be masked once the reduction of the spin gap due to the interladder coupling (see section 5.3) is taken into account.

5.4.3 Phase diagram

First, the effect of J_4 deserves additional attention. Low-temperature features are observed in the magnetic specific heat $C_M(T)$ for $0.25 \lesssim J_4/J_1 \lesssim 0.5$. The dimer-dimer correlations shown in Fig. 5.11(b) clearly indicate that the system is dimerized for the considered cases with $J_4/J_1 < 0.5$. This is consistent with the appearance of the columnar-dimer (CD) phase reported earlier [228] (cf. Fig. 1.4). As anticipated in the initial numerical study of parameter set *A* [401, p. 10], this transition between the

¹⁸Note that the different effects of D_1^{ac} and D_1^b , as well as D_2^a and D_2^c , are related to the different staggering patterns of the corresponding DM vectors (section 4.3.2).

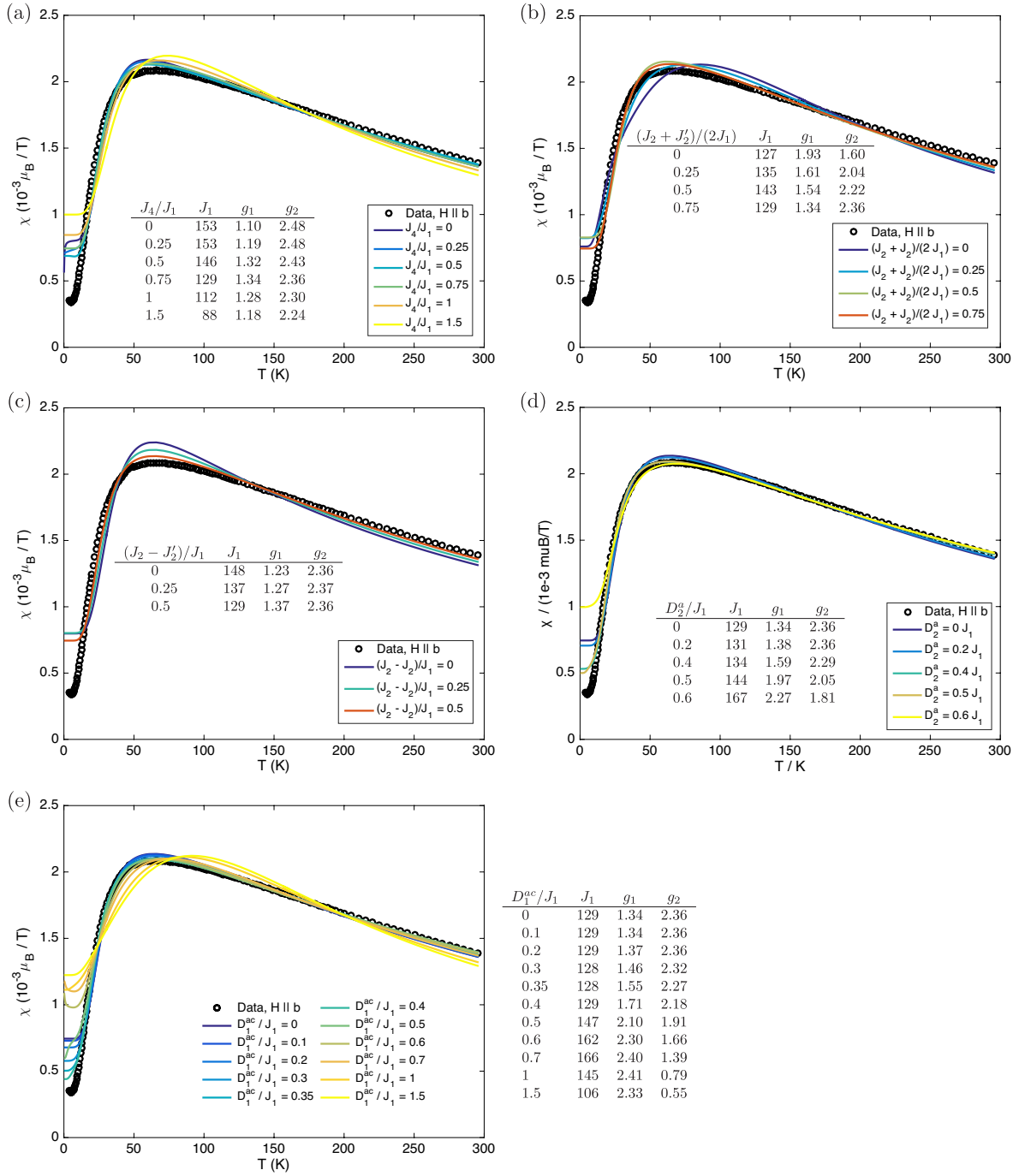


Figure 5.6: Fits of the magnetic susceptibility [see Fig. 5.1(b) for data source and details] using Hamiltonian (4.1) and variations of parameter set A (see text for details). The energy scale J_1 , as well as the g-factors g_1 and g_2 are adjusted to fit the data. The tabulated values for J_1 correspond to J_1/k_B in K. The temperature range of the fits is restricted to $T \geq 9$ K in order to exclude impurity contributions at low temperature (see section 5.2.1).

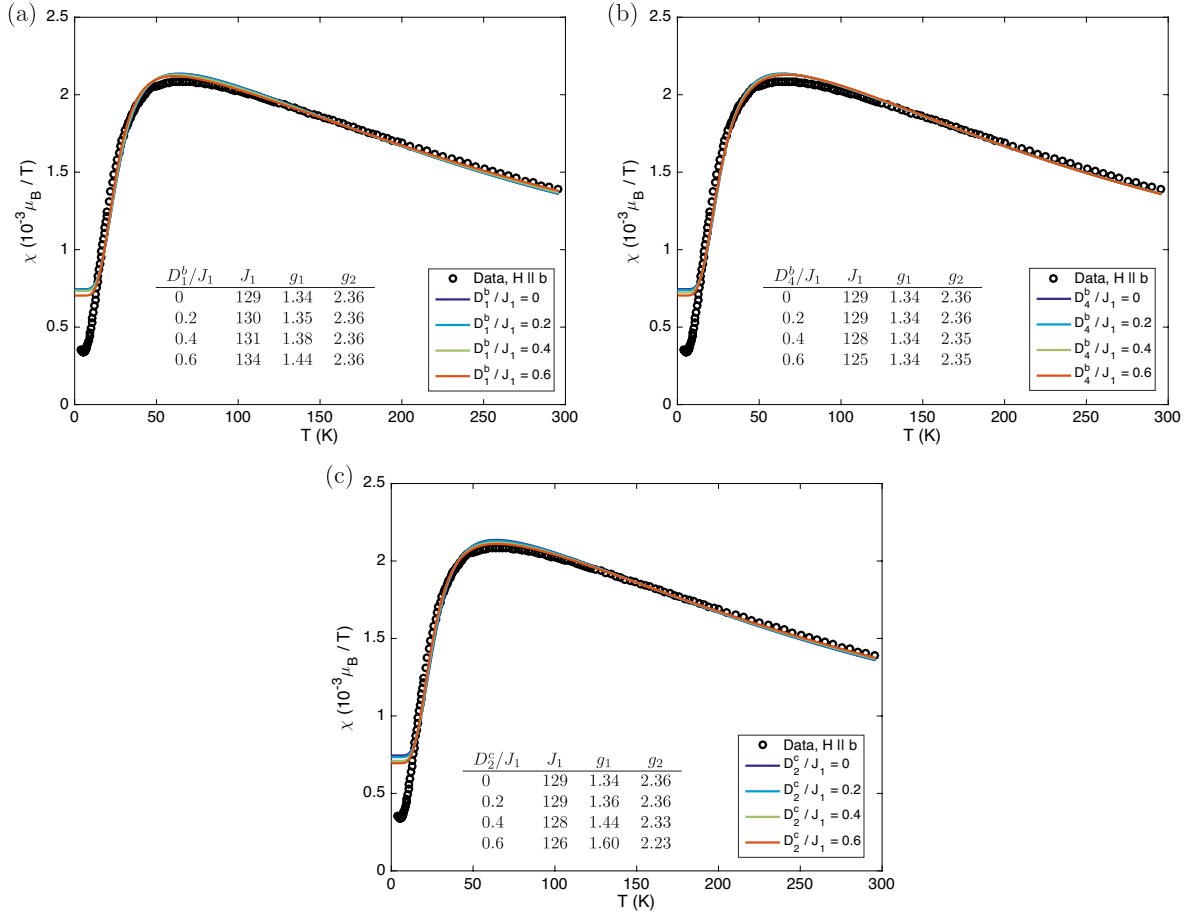


Figure 5.7: Fits of the magnetic susceptibility [see Fig. 5.1(b) for data source and details] using Hamiltonian (4.1) and variations of parameter set A (see text for details). The energy scale J_1 , as well as the g-factors g_1 and g_2 are adjusted to fit the data. The tabulated values for J_1 correspond to J_1/k_B in K. The temperature range of the fits is restricted to $T \geq 9$ K in order to exclude impurity contributions at low temperature (see section 5.2.1).

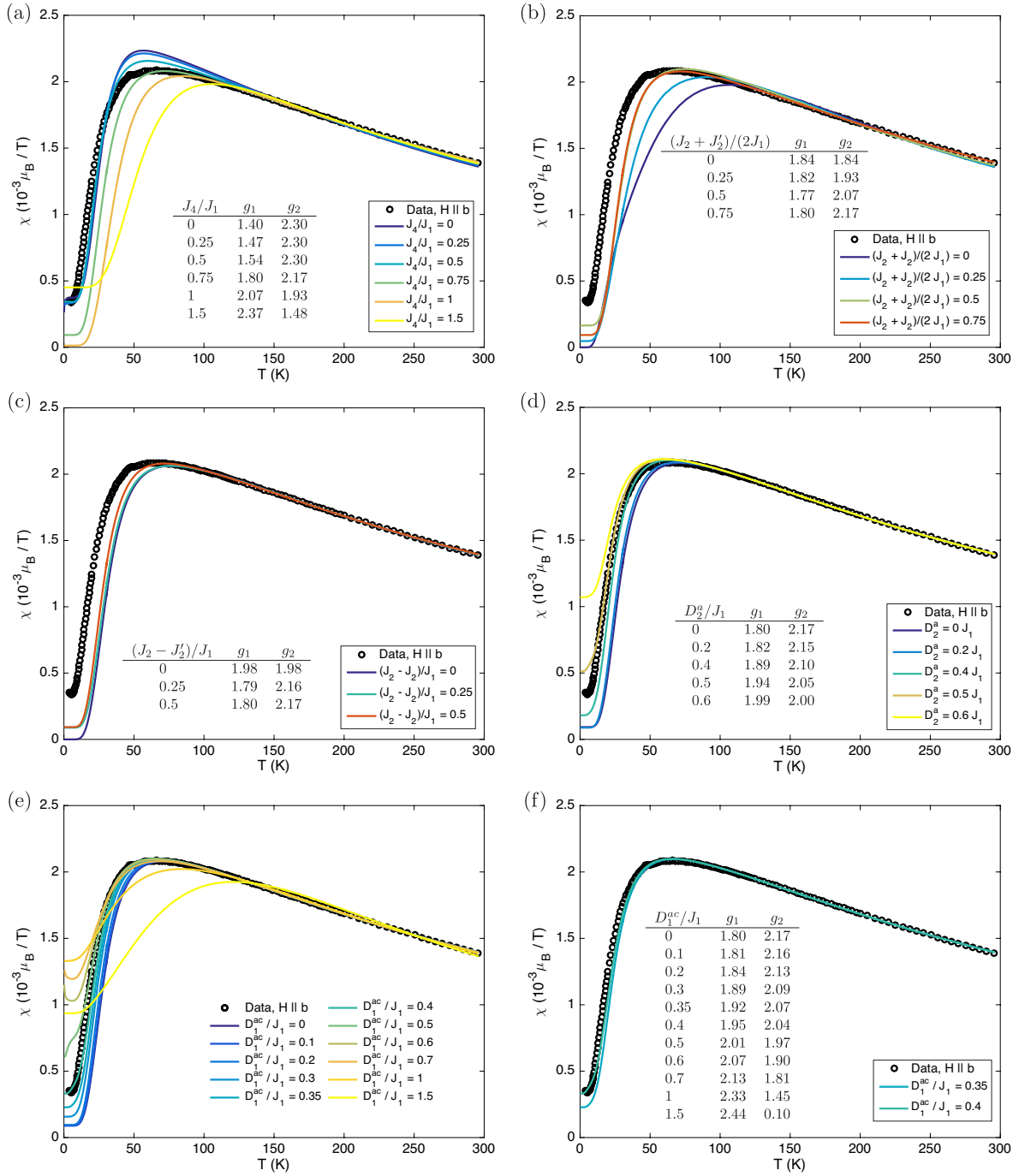


Figure 5.8: Fits of the magnetic susceptibility [see Fig. 5.1(b) for data source and details] using Hamiltonian (4.1) and variations of parameter set A (see text for details). The g -factors g_1 and g_2 are adjusted to fit the data, whereas $J_1/k_B = 140$ K [401] is fixed. The temperature range of the fits is restricted to $T \geq 100$ K in order to reduce the influence of residual interactions. Panel (f) shows a subset of data from (e).

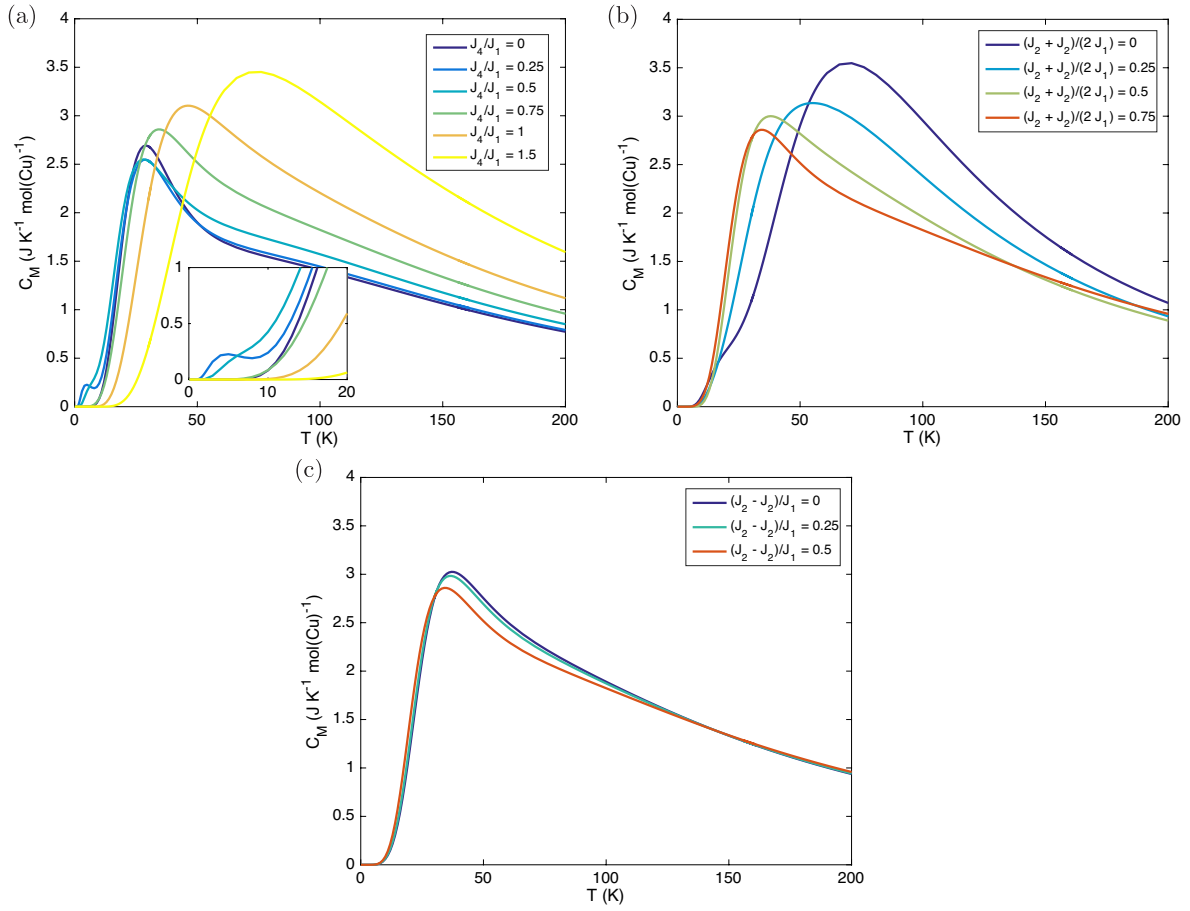


Figure 5.9: Magnetic specific heat calculated using Hamiltonian (4.1) and variations of parameter set A (see text for details). The exchange energy scale $J_1/k_B = 140$ K [401]. The inset of panel (a) shows a magnified copy of the plot. To avoid low-temperature artifacts, numerically-exact ground-state degeneracy was enforced during post-processing of the exact-diagonalization results for $J_4 \leq 0.25 J_1$.

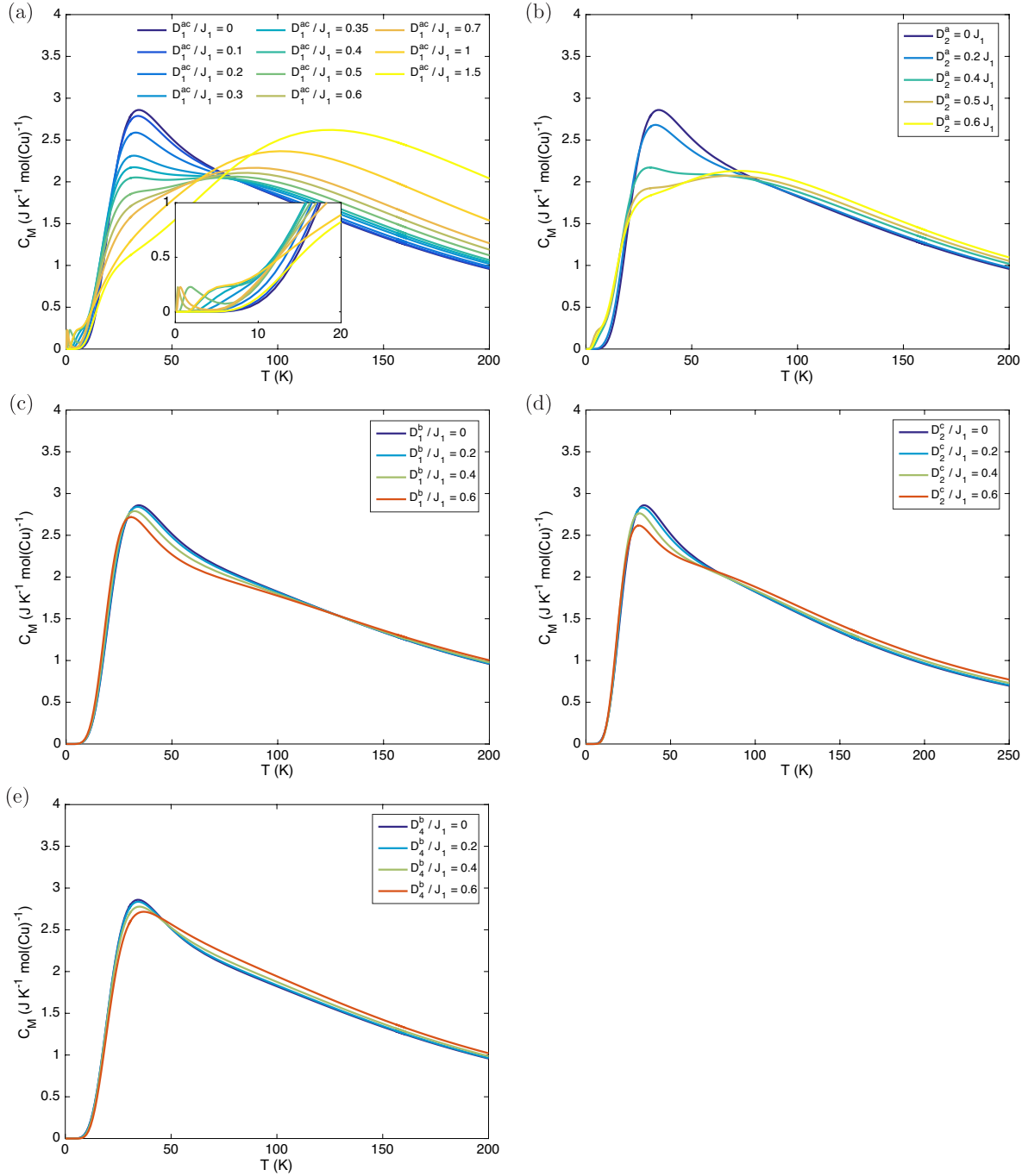


Figure 5.10: Magnetic specific heat calculated using Hamiltonian (4.1) and variations of parameter set A (see text for details). The exchange energy scale $J_1/k_B = 140$ K [401]. The inset of panel (a) shows a magnified copy of the plot.

rung-singlet (RS) and CD phases is driven by a singlet soft mode like in the case $J'_2 = J_2$ [228, 412], which is confirmed by the results shown in Fig. 5.11(a). The phase boundary between the CD and RS phases is consistent with literature [228] [cf. Fig. 1.4 and dashed line in Fig. 5.11(a)]. Having established from the dimer correlations that the system adopts the CD phase for $J_4/J_1 = 0.25$, the ground-state must be doubly-degenerate for periodic boundary conditions [412]. This is used to deduce a numerical uncertainty of $0.02 J_1$ for the energies shown in Fig. 5.11(a). Within this uncertainty, the ground-state is doubly-degenerate for $J_4/J_1 = 0.25$ and 4-fold degenerate for $J_4/J_1 = 0$, as expected for two isolated, dimerized frustrated spin chains [412] (cf. section 1.3.3). The degeneracy is fully lifted at larger values of J_4/J_1 . Note that the ground-state degeneracy affects the excitations as well: For $J_4/J_1 = 0$, the first excitation is a $k \sim \pi/2$ triplet¹⁹. Since there are three branches of triplet excitations associated with each of the degenerate ground states, this mode is 12-fold degenerate. For $J_4/J_1 = 0.25$, the first excitation is a $k = \pi$ singlet [412], which is doubly degenerate, as expected from the degeneracy of the CD ground state [412]. By contrast, the lowest-energy excitation for $J_4/J_1 = 0.5$ is a non-degenerate $k = \pi$ singlet [412], since there is no ground-state degeneracy in the RS phase [412].

The effect of the frustration $J_F = (J_2 + J'_2)/2$ is illustrated in Fig. 5.11(c). Clearly, the spin correlations become incommensurate between $J_F = 0.25$ and $J_F = 0.5$. This is again consistent with the phase diagram of the frustrated ladder [228] shown in Fig. 1.4.

Finally, it should be mentioned that the unit-cell doubling associated with the DM interactions generally results in stronger finite-size effects, as can be seen by comparing Figs. 5.4(a) and 5.11(d)—especially regarding the influence of the boundary conditions. Thus, while the gap value for $L = 8$ accidentally appears to be close to the result for large system sizes, the results presented above are likely to be affected by finite-size effects to some extent.

5.4.4 Parameter set B and influence of symmetric anisotropies

In the preceding subsections, only the DM terms themselves have been considered for simplicity. However, as suggested by the publication proposing parameter set B [318] and discussed in section 1.1.2, a symmetric anisotropy tensor Γ should be considered as well. I have therefore repeated a subset of the calculations taking this additional term into account. The results are shown in Fig. 5.12. The effect of Γ is generally small, and considered negligible for all DM interactions except D_2^a . Yet, even for D_2^a , the changes are very subtle.²⁰

As mentioned in section 5.1, no calculations of the temperature dependences of magnetic susceptibility²¹

¹⁹Lattice-momenta are given relative to the NN bond length. Since the doubled (crystallographic) unit cell is used in the calculations, the results are determined modulo π (aliasing/zone folding). In the absence of explicit dimerization, no two-spinon bound states occur in the zigzag chain for frustrating couplings $J_2/J_1 \leq 0.5$ [375]. The minimum of the single-spinon dispersion shifts continuously from $\pm k = \pi/2$ to $\pm k = \frac{1}{4}\pi, \frac{3}{4}\pi$ for J_2/J_1 beyond the MG point [227]. The two minima of the two-spinon continuum therefore shift from $k = 0, \pi$ towards $k = -\pi/2, 0, \pi/2, \pi$ [227]. Recent exact diagonalization calculations find the $\pm k = \pi/2$ state to have lowest energy at large J_2/J_1 [227, Fig. 3], which is consistent with the present results and hence indicates the formation of a two-spinon bound state (cf. [227]).

²⁰Note that for the special case of parameter set B , equation (1.2) implies $\Gamma_1^{ab} = 0.045 J_1$, $\Gamma_1^{aa} = \Gamma_1^{bb} = 0$, and $\Gamma_1^{cc} = -0.045 J_1$ [318], which are particularly small and have indeed been found to have negligible influence upon susceptibility and specific heat (data not shown).

²¹Recently-reported calculations of the magnetization reproduce the sequence of zero-temperature susceptibilities (5.1) [179]. Meanwhile, $\lim_{T \rightarrow 0} \chi^{bb} \approx 0.18 \cdot 10^{-3} \mu_B/T$ [179, Fig. 5] (bond-operator mean-field theory) is not in quantitative agreement with the DMRG calculations [neglecting interladder couplings, cf. Fig. 7.31(a)], nor with the measured data [cf. Fig. 5.13(b)].

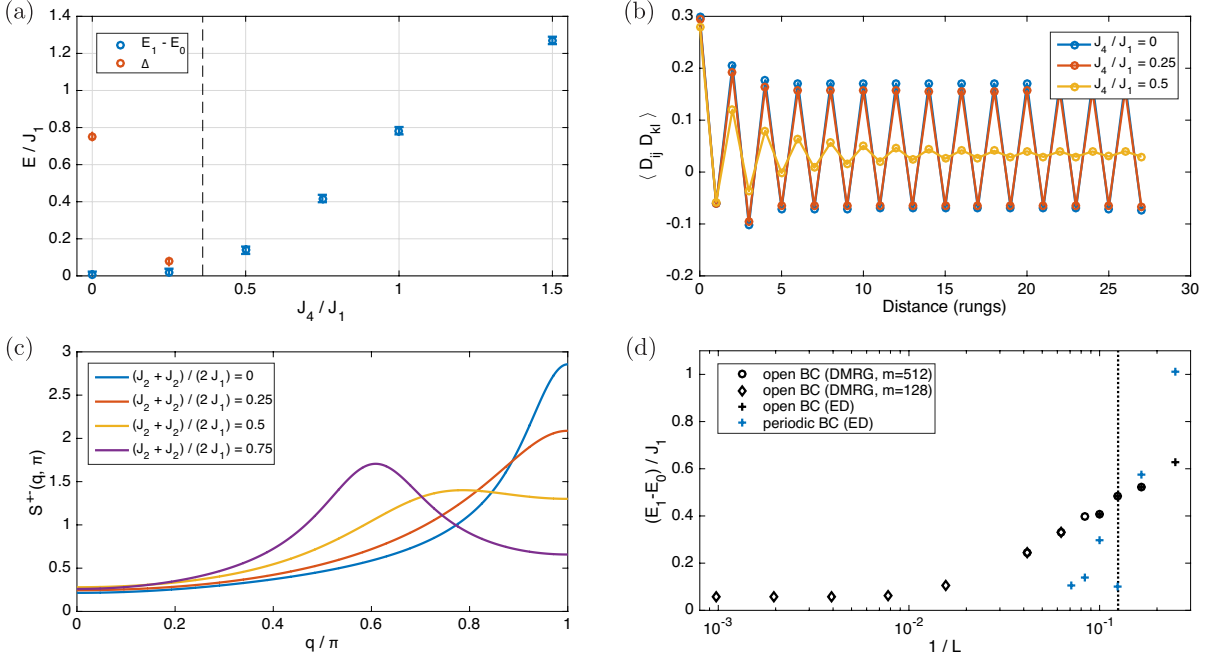


Figure 5.11: (a): Energy difference $E_1 - E_0$ between the two lowest-energy states, as well as excitation gap Δ between ground-state energy and first excited state for parameter set *A* with varying rung couplings [exact diagonalization (ED)]. The dashed line indicates the phase boundary between the columnar-dimer and rung-singlet phases ($J_4/J_1 \approx 0.36$) reported in [228]. The error bars correspond to $0.02 J_1$ (see text for details). (b): Dimer-dimer correlations on NN bonds located on one ladder leg, calculated using DMRG (bond dimension $m = 512$, averaged over $a = 8$ reference rungs, system size $L = 64$; see section 7.5 for further details) for a subset of the models considered in (a). (c): Transverse spin structure factor $S^{+-}(q, q_\perp)$ in the $q_\perp = \pi$ sector, calculated using DMRG ($m = 512$, $a = 8$, $L = 64$) for parameter set *A* with varying frustration strength. (d): Energy difference $E_1 - E_0$ between the two lowest-energy states as function of system size L (measured in rungs) for parameter set *A* with $D_1^{ac} = 0.4 J_1$. Different boundary conditions (BC) were assumed in the calculations (see plot legend). The dashed line indicates $L = 8$. Details regarding the calculation of structure factors and correlation functions are given in chapter 7.

or magnetic specific heat have been reported for parameter set *B*. The results of corresponding calculations are shown in Fig. 5.13. For comparison, selected results obtained with parameter set *A* are also included in the figure. As expected [228], the stronger rung bonds and stronger frustration of parameter set *B* result in an even larger spin gap. Clearly, parameter set *B* fails to provide a good fit to the considered quantities. It remains an open question whether the proposed [318] interladder coupling (see section 5.3) can explain the remaining differences between measured and calculated response functions.

5.4.5 Discussion

From a theoretical perspective, the consistency of the results presented in section 5.4.3 with published works [228, 412] indicates that the phase diagram of the frustrated ladder (Fig. 1.4) is largely unaffected by the presence of two inequivalent NNN couplings ($J_2 \neq J_2'$). Meanwhile, the remainder of this discussion focuses on BiCu_2PO_6 and the possibility to constrain the model parameters using susceptibility and specific-heat data.

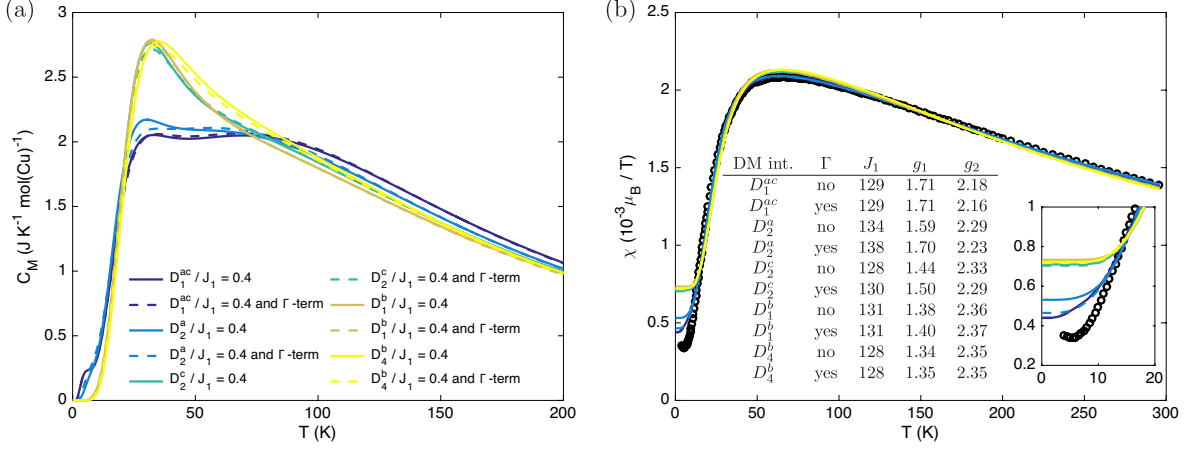


Figure 5.12: (a): Magnetic specific heat calculated using variations of parameter set A , with and without the symmetric anisotropy term parametrized by the tensor Γ . The exchange energy scale $J_1/k_B = 140$ K [401]. (b): Fits of the magnetic susceptibility [see Fig. 5.1(b) for data source and details] using variations of parameter set A , with and without the symmetric anisotropy term parametrized by the tensor Γ . The energy scale J_1 , as well as the g-factors g_1 and g_2 are adjusted to fit the data. The tabulated values for J_1 correspond to J_1/k_B in K. The temperature range of the fits is restricted to $T \geq 9$ K in order to exclude impurity contributions at low temperature (see section 5.2.1). The inset shows a magnified view of the plot. The legend is the same as in (a).

For parameter set A , the energy scale J_1 and the couplings J_4 and $J_F = (J_2 + J'_2)/2$ are indirectly corroborated by requiring agreement with the high-temperature susceptibility for (average) g-factors $g_i \approx 2$ (see section 5.4.1; see also [74, pp. 98,109]). The same is the case for parameter set B and the energy scale J_1 . Similarly, the absence of low-temperature features in the magnetic specific heat, imposes lower bounds on J_4 and J_F , which are satisfied by both parameter sets (see section 5.4.2). Note that this is also consistent with Raman scattering experiments [87], which have not reported any singlet modes below energies corresponding to 34.5 K.

By contrast, the interactions $(J_2 - J'_2)$, D_1^b , D_4^b , and D_2^c produce weaker effects, which are generally hard to resolve in the measured data. For parameter set A , agreement with the measured susceptibility can be significantly improved by including $D_1^{ac} \sim 0.35 J_1$ or $D_2^a \sim 0.4 J_1$. Remarkably, the order of magnitude is compatible with the conclusions drawn from inelastic neutron scattering (INS) (parameter set B) [318]. For the specific heat, the situation is less clear. The aforementioned DM interactions improve agreement with the data by reducing the energy gap. They also give rise to a double-peak structure in $C_M(T)$, which is not necessarily inconsistent with experiment given the reservations regarding the literature data for elevated temperatures (see discussion in section 5.2.2).²² The interactions D_1^{ac} and D_2^a also give rise to low-temperature features in $C_M(T)$, indicating the emergence of singlet excitations which become soft at very large values of D_1^{ac} . These modes are reminiscent of the transition to the CD phase (cf. [228]). It is therefore not surprising that they are not observed for parameter set B , which would place the system deeper within the RS phase in the absence of DM couplings [228] (cf. Fig. 1.4). However, as mentioned in section 5.4.2, such singlet modes may anyways be shadowed by magnetic excitations once interladder couplings (see section 5.3) are taken into account.

In the end, no fully satisfactory fit to the specific-heat and susceptibility data could be obtained for the

²²In fact, the data reported in [424, Fig. 7.9b] show similar features.

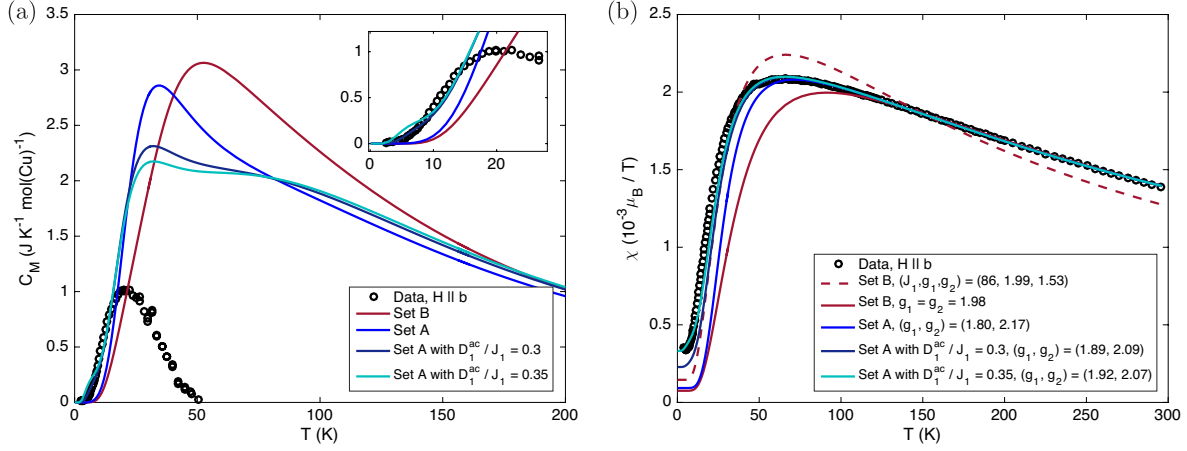


Figure 5.13: Results of exact-diagonalization calculations performed for variations of parameter set A and parameter set B (with and without the symmetric anisotropy term parametrized by the tensor Γ , respectively). (a): Magnetic specific heat (data sampled from [217]). The exchange energy scale J_1 was fixed to the values given in section 4.3.3. The inset shows a magnified view of the plot. (b): Fits of the magnetic susceptibility [see Fig. 5.1(b) for data source and details]. Models including the energy J_1 as a fit parameter are indicated by dashed lines, in the other cases the value of J_1 corresponds to (a). The fit constraints and fitted parameter values are stated in the plot legend, the values for J_1 corresponding to J_1/k_B in K. The temperature range of the fits is restricted to $T \geq 9$ K in order to exclude impurity contributions at low temperature (see section 5.2.1).

considered models, which strongly suggests that additional interactions like interladder couplings [401] and/or magneto-elastic effects (see section 8.7.5) play an important role in BiCu_2PO_6 . Nonetheless, this conclusion is not rigorous, since the parameter space could not be sampled exhaustively for practical reasons (see section 5.4, beginning). Note that the one-parameter variations considered for parameter set A correspond to a first-order expansion. In principle, numerical results can be used to expand observables, such as magnetic susceptibility or specific heat, in the coupling parameters. However, a first-order expansion is unlikely to be sufficiently accurate to refine the model parameters, which is why this approach has not been pursued further. Higher order semi-analytical methods like high-temperature expansion might be interesting to consider in the future (e. g., [161]). Also, finite-temperature DMRG [133, 442] could help avoiding finite-size effects. However, the weak effects of many model parameters imply that not all parameters can be estimated from macroscopic measurements alone. Ultimately, it appears that only a global analysis of magnetic susceptibility, magnetic specific heat, and INS data might resolve this issue.

5.5 Conclusions

Besides allowing for the estimation of the g -tensors (note the related previous works mentioned in section 6.8), the comparison of calculations performed using the model Hamiltonian (4.1) to previous measurements of magnetic susceptibility (section 5.2.1) and specific heat (section 5.2.2) confirms (see previous works referenced in the aforementioned sections and in chapter 4) that the model is able to capture the salient qualitative features of the data. Nonetheless, quantitative differences remain. The most obvious discrepancy is the overestimated spin gap (see [401] and section 5.2.3). While in principle, the exchange couplings could be adjusted to achieve better agreement, it has been shown in [257] that such a procedure

systematically underestimates the intraladder interactions and results in a model which contradicts the dispersion relations of the magnetic excitations probed with INS.

Multiple works have suggested that the deviations are due to DM interactions and interladder couplings (e. g. , [228, 401]; see sections 4.2.4 and 5.3). Nonetheless, no reported calculations of the macroscopic finite-temperature response functions appear to have considered the combined effects of frustration and these additional interactions. As shown in section 5.4, neither parameter set B (neglecting interladder couplings), nor any one-parameter variation of parameter set A , reproduces the measured data. While it cannot be excluded that a multi-parameter variation providing a good fit exists, the preceding results strongly suggest that additional interactions need to be considered. Interladder coupling is a promising candidate for reconciling experimental data and model calculations [401] (section 5.3). Unfortunately, its effects cannot be accounted for using naive mean-field theory, and corresponding DMRG calculations would require considerable computational resources (see section 5.3).

6 BiCu₂PO₆: Interactions between electronic and nuclear moments

6.1 Introduction

This chapter addresses the interaction between the ³¹P nuclei and the Cu²⁺ magnetic moments in BiCu₂PO₆. Based on previous work [74, 75] and the considerations presented in chapter 5, the hyperfine couplings are estimated. While this analysis is clearly guided by earlier work [74, 75], certain aspects are treated differently. A detailed account of the differences is given in the discussion concluding this chapter (section 6.8). A secondary motivation consists in providing a self-consistent notation for later use (in chapter 8).

6.2 Notation

The local magnetic field created at each ³¹P nucleus by the Cu magnetic moments consists of two contributions: The long-ranged dipole fields and the transferred hyperfine coupling [74, p. 106] (see section 1.5.9).

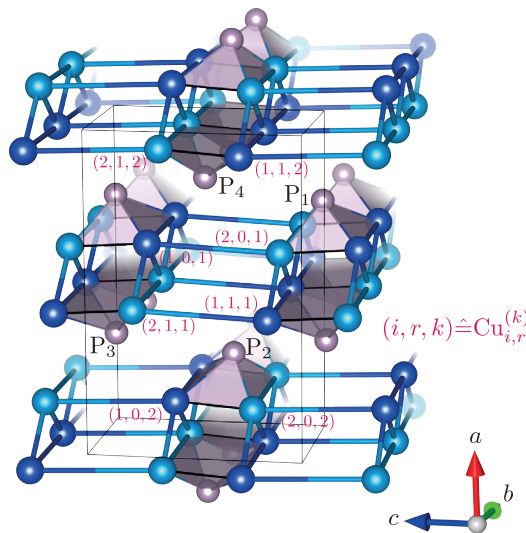


Figure 6.1: Crystal structure of BiCu₂PO₆ [11], showing positions of Cu(1) and Cu(2) (dark and light blue, respectively), and P (gray) sites; Bi and O sites have been omitted for clarity. Exchange interactions [401] (J_1 , J'_2 , J_2 , J_4 , and J_i) are depicted by blue cylinders (intraladder couplings) and solid black lines (interladder couplings) (cf. also Fig. 4.4). Transparent gray polyhedra indicate the hyperfine couplings between ³¹P nuclei and Cu spins ([22] and [74, p. 105]). The unit cell is depicted in black and the P and Cu positions are labeled in black and magenta, respectively. Crystal structure visualized using VESTA [272].

Precise knowledge of these interactions is clearly essential for a quantitative analysis of the NMR spectra.

It is useful to define an indexing convention for the Cu and P sites (cf. [74, Figs. 5.1a, 5.4(c,e), 6.6]). As illustrated in Fig. 6.1, there are four P sites and eight Cu sites in each unit cell. I denote the Cu sites as $\text{Cu}_{i,r}^{(k)}(x, y, z)$, where the index $i \in \{1, 2\}$ distinguishes the two crystallographically inequivalent Cu sites. The index $k \in \{1, 2\} \simeq \mathbb{Z}/(2\mathbb{Z})$ corresponds to the two different types of ladder layers [cf. Fig. 4.4(a)], and $r \in \{0, 1\}$ is the rung parity (cf. [74, p. 140]), which is chosen such that sites with $r = 0$ have hyperfine couplings with P_1 and P_2 . Finally, each unit cell is identified by a lattice index $(x, y, z) \in \mathbb{Z}^3$.

6.3 Dipolar coupling

Although the concepts introduced in this section are well-known in principle, derivations of the relevant results are provided in an attempt to give a concise but self-consistent discussion of dipole-lattice sums and their application to NMR.

6.3.1 Formalism

The dipolar coupling was introduced in section 1.5.9. In a crystal, one has to sum the contributions from all Cu sites. Due to the superposition principle (linearity of Maxwell's equations, e. g. , [184]), it is sufficient to consider magnetic structures of the form,

$$\begin{aligned} \boldsymbol{\mu}_{j,r}^{(k)}(x, y, z) &= \sum_{\mathbf{q}} \left[\cos(\mathbf{q} \cdot (x, y, z)) \mathbf{c}_{\mathbf{q},j,r,+}^{(k)} + \sin(\mathbf{q} \cdot (x, y, z)) \mathbf{c}_{\mathbf{q},j,r,-}^{(k)} \right] \\ &= \text{Re} \sum_{\mathbf{q}} \exp(i \mathbf{q} \cdot (x, y, z)) \left(\mathbf{c}_{\mathbf{q},j,r,+}^{(k)} - i \mathbf{c}_{\mathbf{q},j,r,-}^{(k)} \right) \quad , \end{aligned}$$

where $\boldsymbol{\mu}_{j,r}^{(k)}(x, y, z)$ is the magnetic moment at the $\text{Cu}_{j,r}^{(k)}(x, y, z)$ site with real-space position $\boldsymbol{\rho}_{j,r}^{(k)}(x, y, z)$. The magnetic moments $\boldsymbol{\mu}_{j,r}^{(k)}(x, y, z)$ are related with the corresponding spin-operators $\mathbf{S}_{j,r}^{(k)}(x, y, z)$ via the g-tensors $g_{j,k}$ (see section 1.5.9), which satisfy

$$g_{j,k+1} = \sigma_a g_{j,k} \sigma_a \quad .$$

where $g_{j,1} = g_j$ is parametrized according to (5.2) (section 5.2.1). The dipolar field at the position $\boldsymbol{\rho}_0^{(l)}$ of the P_l site in unit cell $(0, 0, 0)$ is then given by

$$\mathbf{B}_d^{(l)} = \sum_{j,r,k} \sum_{x,y,z} \frac{\mu_0}{4\pi\rho^3} (3\hat{\boldsymbol{\rho}}\hat{\boldsymbol{\rho}}^T - 1) \boldsymbol{\mu}_{j,r}^{(k)}(x, y, z) \quad , \quad (6.1)$$

with $\boldsymbol{\rho} = \boldsymbol{\rho}_{j,r}^{(k)}(x, y, z) - \boldsymbol{\rho}_0^{(l)}$. Define $\mathbf{C}_{\mathbf{q},j,r}^{(k)} = \mathbf{c}_{\mathbf{q},j,r,+}^{(k)} - i \mathbf{c}_{\mathbf{q},j,r,-}^{(k)}$ and

$$\mathbf{M}_{j,r,k,\mathbf{q}}^{(l)} = \sum_{x,y,z} \frac{\mu_0}{4\pi\rho^3} (3\hat{\boldsymbol{\rho}}\hat{\boldsymbol{\rho}}^T - 1) \exp(i \mathbf{q} \cdot (x, y, z)) \quad . \quad (6.2)$$

Then,

$$\mathbf{B}_d^{(l)} = \text{Re} \sum_{j,r,k,\mathbf{q}} \mathbf{M}_{j,r,k,\mathbf{q}}^{(l)} \mathbf{C}_{\mathbf{q},j,r}^{(k)} \quad . \quad (6.3)$$

6.3.2 Convergence and uniqueness

The calculation of the matrices $M_{j,r,k,\mathbf{q}}^{(l)}$ involves a lattice summation over the entire crystal. In practice, this is usually approximated by a summation over \mathbb{Z}^3 . However, the three-dimensional lattice sum (6.2) is only conditionally convergent [438]. In general, the limiting values of such sums depend on the summation order [436]. While this may seem disturbing at first, the physical reason is that the dipolar field inside a sample depends on the *shape* of that sample [438].

Consider two samples, represented by domains $\Omega_i \subset \mathbb{R}^3$ ($i = 1, 2$) and corresponding reference sites \mathbf{x}_i at which the dipole fields $\mathbf{B}_{d,i}$ created by Ω_i are to be calculated. Without loss of generality (cf. section 6.3.1), a single Fourier component and a single magnetic sub-lattice are considered. Further, $\mathbf{x}_1 = \mathbf{x}_2 = \mathbf{x}$ without loss of generality. Let Ω_1 and Ω_2 be topologically equivalent to a sphere for simplicity. If \mathbf{x} is sufficiently far away from the surfaces of Ω_1 and Ω_2 , a continuum magnetostatics description is valid within the domain $\Omega_2 \setminus \Omega_1$. Hence, the results re-derived in section A.2.1 (note references therein) can be invoked to obtain

$$\mathbf{B}_{d,2} = -\mu_0 (\mathcal{M}^{\Omega_2}(\mathbf{x}) - \mathcal{M}^{\Omega_1}(\mathbf{x})) \mathbf{M} \quad ,$$

with the average magnetization $\mathbf{M} = \mathbf{C}_{\mathbf{q}=0,j,r}^{(k)}/V$ if $\mathbf{q} \equiv 0 \pmod{2\pi}$ and zero otherwise, V the unit-cell volume, and the demagnetization tensors $\mathcal{M}^{\Omega_i}(\mathbf{x})$ as defined in section A.2.1. Comparison with (6.2) finally yields (cf. , e. g. , [438])

$$M_{j,r,k,\mathbf{q}}^{(l)}(\Omega_2) = M_{j,r,k,\mathbf{q}}^{(l)}(\Omega_1) - \begin{cases} \frac{\mu_0}{V} (\mathcal{M}^{\Omega_2}(\mathbf{x}) - \mathcal{M}^{\Omega_1}(\mathbf{x})) & \text{if } \mathbf{q} \equiv 0 \pmod{2\pi} \\ 0 & \text{otherwise} \end{cases} \quad , \quad (6.4)$$

where $M_{j,r,k,\mathbf{q}}^{(l)}(\Omega_i)$ denotes the result of evaluating the sum in (6.2) over the lattice domain $\Omega_i \cap \mathbb{Z}^3$. Because the demagnetization tensors do not change upon symmetric rescaling of the domain (see section A.2.1), the transformation rule (6.4) generalizes to geometrically-inspired lattice-summation schemes, such as those relevant for this work. The advantage of (6.4) is that the lattice sums can be performed in a computationally efficient order and adjusted afterwards in order to account for the actual shape of the sample used in the experiment [438].

In a later chapter (chapter 8), the dipole couplings between individual magnetic layers (*bc* planes) in BiCu_2PO_6 are considered. Direct computation of the corresponding lattice sums is particularly inefficient. Fortunately, ideas similar to Ewald summation [126] can be applied to recast the slowly-converging sums into rapidly-converging ones by means of a discrete Fourier transform [292, 438]. Although this approach is well known, the relevant publications [292, 438] employ a rather bulky formalism, which is partially owed to the fact that they treat more generic cases. In order to ensure a coherent notation and allow future readers to retrace the analyses described in this work, the required results are therefore briefly re-derived in the appendix (section A.2.2).

6.3.3 Order of magnitude

In order to check the importance of dipolar couplings it is instructive to construct an upper bound on the dipole field (6.3). For magnetic fields applied along the *b*-direction,

$$\left| \mathbf{e}_b \cdot \mathbf{B}_d^{(l)} \right| \leq \sum_{j,r,k,\mathbf{q}} \left\| \mathbf{e}_b \cdot M_{j,r,k,\mathbf{q}}^{(l)} \right\|_2 \left\| \mathbf{C}_{\mathbf{q},j,r}^{(k)} \right\|_2 \quad ,$$

where $\|\cdot\|_2$ denotes the 2-norm on \mathbb{C}^3 and the induced matrix norm on $\mathbb{C}^{3 \times 3}$ (spectral norm) [433]. For a spin-1/2 moment, $\|g_{j,k} \mathbf{C}_{\mathbf{q},j,r}^{(k)}\|_2 \lesssim \mu_B$. Numerical evaluation for the BiCu₂PO₆ lattice and $\mathbf{q} = (0, q_b, 0)$ with $q_b \in [0, 2\pi)$, yields $|e_b \cdot \mathbf{B}_d^{(l)}| \leq 0.6$ T. This indicates that, although occasionally done in previous work [74, pp. 133,139] (see also [74, pp. 145]), dipolar coupling cannot be neglected in the magnetically-ordered phases of BiCu₂PO₆.

6.3.4 Demagnetization lineshape

The transformation rule (6.4) can be applied to all nuclei which are sufficiently far away from the surface of the sample. For a macroscopic sample Ω , this condition is satisfied for essentially all nuclei. Hence, as is well known, the dipole fields created by distant magnetic moments give rise to a line broadening which is proportional to the uniform magnetization and the corresponding lineshape reflects the spatial distribution of the demagnetization tensors $\mathcal{M}^\Omega(\mathbf{r})$ for $\mathbf{r} \in \Omega$.¹ While the demagnetizing tensor $\mathcal{M}(\mathbf{r})$ is uniform inside ellipsoidal samples [277], this does not hold for samples with arbitrary geometries (see, e. g., [51]). Box-shaped samples with faces cut approximately perpendicular to the crystal directions are used throughout this work, and analytical expressions for the demagnetization tensors are known in this case [194] (cf. section A.2.1).

6.3.5 Paramagnetic phase

In order to estimate the hyperfine couplings from the angular dependence of the NMR shift later on, a model of the dipole-field contributions to the shift in the paramagnetic state is required. Using the indexing scheme introduced in sections 6.2 and 6.3.1, the Hamiltonian (4.1) and the resulting susceptibility model (section 5.2.1) imply

$$\boldsymbol{\mu}_{j,r}^{(k)}(x, y, z) = -\mu_B g_{j,k} \langle \mathbf{S}_{j,r}^{(k)}(x, y, z) \rangle = \chi_j^{(k)} \mu_0 \mathbf{H} = \boldsymbol{\mu}_j^{(k)},$$

where $\chi_j^{(k+1)} = \sigma_a \chi_j^{(k)} \sigma_a$, since the two types of magnetic layers in BiCu₂PO₆ are related by the symmetry σ_a (see section 4.3.2). Introducing $D_{j,k}^{(l)} = \sum_r M_{j,r,k,q=0}^{(l)}$ (cf. [74, p. 105]),²

$$\mathbf{B}_d^{(l)} = \sum_{j,k} D_{j,k}^{(l)} \boldsymbol{\mu}_j^{(k)}.$$

The four P sites are related by the crystal symmetries $\sigma_b \sigma_c$, $\sigma_a \sigma_c$, and $\sigma_a \sigma_b$ (see also [74, p. 105] and [75, p. 10]). Moreover, the site-symmetry of the P site (section 4.2.3) implies $M_{j,r,k,q=0}^{(l)} = \sigma_b M_{j,r,k,q=0}^{(l)} \sigma_b$,

¹The effect of the demagnetizing field on the sample magnetization is negligible in this work (see footnote 1 in chapter 5).

²The sample used in the measurements [74] analyzed in this chapter was approximately cubic [74, p. 97], which is why the matrices $D_{j,k}^{(l)}$ were obtained by brute-force summation over spherical lattice regions, in accordance with the previous work [74, p. 106]. Even so, they agree with the more sophisticated summation method of [292, 438] (see section A.2.2) to within $5 \cdot 10^{-9}$ relative deviation [after applying eq. (6.4)]. Moreover,

$$\sum_{j,k} D_{j,k}^{(l)} \approx \begin{pmatrix} 0.0333 & 0 & 0.0213 \\ 0 & 0.0145 & 0 \\ 0.0213 & 0 & -0.0478 \end{pmatrix} \frac{T}{\mu_B}$$

compares favorably with [75, eq. 13] (deviations of the order of 1% arise due to a less strict convergence criterion used in the previous work, see [75, p. 10] and [74, p. 106]).

such that

$$\begin{aligned} D_{j,k}^{(3)} &= D_{j,k}^{(1)} \\ D_{j,k}^{(4)} &= D_{j,k}^{(2)} = \sigma_a D_{j,k+1}^{(1)} \sigma_a \quad . \end{aligned}$$

6.4 Hyperfine couplings

The hyperfine coupling was introduced in section 1.5.9 and its contribution to the effective magnetic field at the site of the nucleus is written as $\mathbf{B}_h = A \boldsymbol{\mu}$. As already pointed out in [74, p. 107], the matrices A do not need to be symmetric (cf. section 1.5.9). Nonetheless, it is common to assume $A = A^T$ (e. g., [74, 409]), as is done in the following, for two reasons: (i) To maintain consistency with previous work [74, p. 107], and (ii) because not all elements of A are constrained by measurements of the NMR shift in the paramagnetic phase. To illustrate the second point, which was also noted in [74, p. 107], let $\boldsymbol{\mu} = \chi \mu_0 \mathbf{H}$. If \mathbf{B}_h is small compared to the external field $\mu_0 \mathbf{H}$, the NMR shift is proportional to $\mathbf{H} \cdot A \chi \mathbf{H}$, which depends only on the symmetric part of $K = A \chi$.³ If χ is known, the shift provides six constraints for the nine unknown elements of A and the assumption $A = A^T$ represents one possibility to obtain a determined system of equations (cf. [74, p. 107]). Note that a symmetric A is also expected if magnetic moments are localized and the effects of spin-orbit coupling are restricted to the g-tensor [see section 1.5.9, equation (1.9)].

The dominant transferred hyperfine coupling is mediated through the P – O(2) – Cu(*i*) bonds [22], resulting in the hyperfine couplings depicted in Fig. 6.1 ([22] and [74, p. 105]). The hyperfine field $\mathbf{B}_h^{(l)}$ at the P_{*l*} site in unit cell (0, 0, 0) (see section 6.2 for notation) is thus given by⁴ (cf. [74, eq. 5.13]).

$$\begin{aligned} \mathbf{B}_h^{(1)} &= A_1 \boldsymbol{\mu}_{1,0}^{(1)}(0, 0, -1) + \sigma_b A_1 \sigma_b \boldsymbol{\mu}_{1,0}^{(1)}(0, -1, -1) + A_2 \boldsymbol{\mu}_{2,0}^{(1)}(0, 0, 0) + \sigma_b A_2 \sigma_b \boldsymbol{\mu}_{2,0}^{(1)}(0, -1, 0) \\ \mathbf{B}_h^{(2)} &= \sigma_c A_1 \sigma_c \boldsymbol{\mu}_{1,0}^{(2)}(0, 0, 0) + \sigma_a A_1 \sigma_a \boldsymbol{\mu}_{1,0}^{(2)}(0, -1, 0) + \sigma_c A_2 \sigma_c \boldsymbol{\mu}_{2,0}^{(2)}(0, 0, 0) + \sigma_a A_2 \sigma_a \boldsymbol{\mu}_{2,0}^{(2)}(0, -1, 0) \\ \mathbf{B}_h^{(3)} &= A_1 \boldsymbol{\mu}_{1,1}^{(1)}(0, 0, 1) + \sigma_b A_1 \sigma_b \boldsymbol{\mu}_{1,1}^{(1)}(0, 1, 1) + A_2 \boldsymbol{\mu}_{2,1}^{(1)}(0, 0, 0) + \sigma_b A_2 \sigma_b \boldsymbol{\mu}_{2,1}^{(1)}(0, 1, 0) \\ \mathbf{B}_h^{(4)} &= \sigma_c A_1 \sigma_c \boldsymbol{\mu}_{1,1}^{(2)}(0, 0, 0) + \sigma_a A_1 \sigma_a \boldsymbol{\mu}_{1,1}^{(2)}(0, 1, 0) + \sigma_c A_2 \sigma_c \boldsymbol{\mu}_{2,1}^{(2)}(0, 0, 0) + \sigma_a A_2 \sigma_a \boldsymbol{\mu}_{2,1}^{(2)}(0, 1, 0) \quad . \end{aligned} \quad (6.5)$$

6.5 Model for NMR shift

6.5.1 Pristine compound

Using the results of sections 6.3.5 and 6.4, the internal fields $\mathbf{B}_{\text{int}}^{(l)} = \mathbf{B}_d^{(l)} + \mathbf{B}_h^{(l)}$ generated in addition to the external field $\mathbf{B}_{\text{ext}} = \mu_0 \mathbf{H}$ in the translation-invariant paramagnetic state of pristine BiCu₂PO₆ are given by

$$\mathbf{B}_{\text{int}}^{(l)} = M_0^{(l)} \mathbf{B}_{\text{ext}} \quad ,$$

³ $\mathbf{H} \cdot K \mathbf{H} = \mathbf{H} \cdot K^T \mathbf{H} \Rightarrow \dots$

⁴When comparing these expressions with Fig. 6.1, it is important to keep in mind that the P₁ and P₂ sites depicted there belong to the next unit cell along *b*. By definition, A_i describes the hyperfine coupling between the P₁ site and the closest Cu(*i*) site obtained by applying space-group translations along *c* to the generating positions reported in [11].

where (cf. [74, eqs. 5.13 and 5.14])

$$M_0^{(1)} = \bar{A}_1 \chi_1^{(1)} + \bar{A}_2 \chi_2^{(1)} + \sum_j D_{j,1}^{(1)} \chi_j^{(1)} + \sum_j D_{j,2}^{(1)} \sigma_a \chi_j^{(1)} \sigma_a \quad \text{and} \quad M_0^{(2)} = \sigma_a M_0^{(1)} \sigma_a \quad ,$$

and $\bar{A}_i = (A_i + \sigma_b A_i \sigma_b)$ (cf. [74, p. 105]). The sublattice susceptibilities $\chi_j^{(k)}$ were defined in section 6.3.5 and crystal symmetry implies $M_0^{(l+2)} = \sigma_b M_0^{(l)} \sigma_b = M_0^{(l)}$. Hence, two distinct NMR frequencies are expected in general [75, p. 12] (see also [74, p. 163]) and, indeed, observed [74, Fig. 5.10]. For $B_{\text{ext}} \gg B_{\text{int}}$, the relative NMR shift $\Delta_0^{(l)}$ of the P_l site is given by⁵ $\Delta_0^{(l)} = \hat{\mathbf{B}}_{\text{ext}} \cdot M_0^{(l)} \hat{\mathbf{B}}_{\text{ext}}$ (cf. section 1.5.4).

6.5.2 Weakly-doped compound

Consider a system where one Cu site has been replaced by a non-magnetic Zn (cf. section 5.2.4). As in previous work [74], I assume that the substitution has only local effects, i. e., all hyperfine couplings, g-tensors, and exchange interactions not involving the Zn site are unchanged. Following [74], I only consider the effect upon P sites which have hyperfine couplings with the substituted site. Since the four P_l sites are related by crystal symmetries (cf. section 6.3.5), I focus on the P_1 site without loss of generality. The corresponding situation is illustrated in Fig. 6.2. The substitution of Cu sites to the left of the depicted P_1 site can be treated by applying the site-symmetry σ_b (section 4.2.3) to the configurations resulting from substitution of the Cu sites to the right [74, p. 106]. Thus, it is sufficient to discuss the situation depicted in Fig. 6.2.

The main change of the internal field $\mathbf{B}_{\text{int}}^{(1)}$ at the P_1 site depicted in Fig. 6.2 is caused by the absence of the substituted $\text{Cu}(i)$ moment ([22] and [74, p. 106]). If χ_i denotes the corresponding susceptibility in the undoped system, this change is of the order of $(A_i + D_i) \chi_i$, where D_i is the corresponding dipolar coupling. I neglect the interladder exchange coupling, such that substitution of the encircled $\text{Cu}(1)$ [$\text{Cu}(2)$] site only affects the local susceptibilities of the lower [upper] ladder in Fig. 6.2. The next-to-leading-order correction to $\mathbf{B}_{\text{int}}^{(1)}$ is then due to the remaining $\text{Cu}(i)$ site with hyperfine coupling to P_1 . According to the numbers given in Fig. 6.2, this correction amounts to 5% [12%] of the leading-order correction for substitution of $\text{Cu}(1)$ [$\text{Cu}(2)$]. The smallest absolute value of the eigenvalues of the matrices $A_i + D_i$ being $0.11 \text{ T}/\mu_B$, the corrections arising through dipolar couplings between P_1 and the two Cu sites below (see Fig. 6.2) are of comparable magnitude and correspond to at most 6% of the leading-order effect. The next-smaller corrections are at most $20\% \cdot 6\% = 1.2\%$ of the leading order and are therefore neglected.

Let the dipolar coupling between the $\text{Cu}_{j,r}^{(k)}(x, y, z)$ and the P_1 site (see Fig. 6.2) be given by $\hat{D}_{j,r}^{(k)}(x, y, z)$ (cf. [74, eq. B.4]). Let further $\tilde{\chi}_i(j, r)$ denote the local susceptibility of the ladder with one substituted $\text{Cu}(i)$ site, at the $\text{Cu}(j)$ site r rungs away from the defect. The four local susceptibilities required to apply the aforementioned corrections are annotated in Fig. 6.2(b). Analogous to the preceding discussion of

⁵As in [74], shifts will be measured relative to the resonance frequency of ^{31}P in non-magnetic BiZn_2PO_6 , such that other contributions to the shift can be neglected (cf. [74, pp. 99-100] and section 6.6.1).

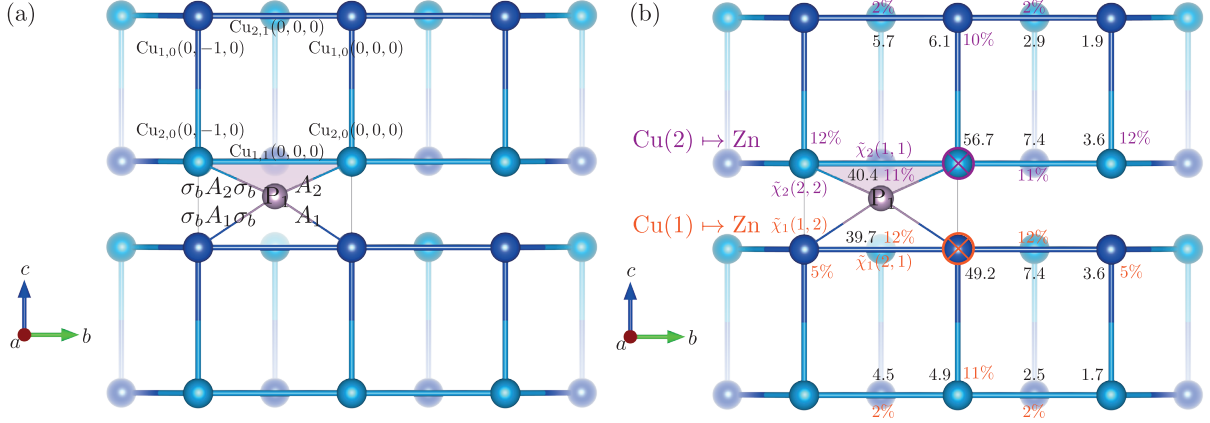


Figure 6.2: Crystal structure of BiCu_2PO_6 [11], showing positions of Cu(1) and Cu(2) (dark and light blue, respectively), and P (gray) sites; Bi and O sites have been omitted for clarity. Intraladder exchange interactions [401] are depicted by blue cylinders (cf. also Fig. 4.4). A gray pyramid indicates the hyperfine couplings ([22] and [74, p. 105]) between the P_1 site in the reference unit cell $(0, 0, 0)$ and the surrounding Cu spins (cf. Fig. 6.1). (a) Illustrates the notation used for the Cu positions and hyperfine couplings (cf. Fig. 6.1; superscript layer index is equal one and therefore omitted). Black numbers in (b) quantify the dipolar couplings between the corresponding Cu site and P_1 . The values correspond to the spectral norm of the respective coupling matrices in $10^{-3} \text{ T}/\mu_B$. Orange and purple labels indicate the relative change in local susceptibility (at $T = 296 \text{ K}$) resulting from substitution of the respective (encircled) Cu site by non-magnetic Zn, as obtained using full-spectrum exact diagonalization (see section 5.2.4). If the susceptibility before and after doping is χ and $\tilde{\chi}$, respectively, this relative change is given by $\|\tilde{\chi} - \chi\|_2/\|\chi\|_2$. Crystal structure visualized using VESTA [272].

the undoped compound the relative NMR shift is given by $\Delta_{i,+}^{(l)} = \hat{\mathbf{B}}_{\text{ext}} \cdot \mathbf{M}_{i,+}^{(1)} \hat{\mathbf{B}}_{\text{ext}}$, where

$$\begin{aligned} \mathbf{M}_{1,+}^{(1)} = & M_0 - \left(A_1 + \hat{D}_{1,0}^{(1)}(0, 0, -1) \right) \chi_1^{(1)} \\ & + \sigma_b \left(A_1 + \hat{D}_{1,0}^{(1)}(0, 0, -1) \right) \sigma_b \left(\tilde{\chi}_1(1, 2) - \chi_1^{(1)} \right) + \hat{D}_{2,1}^{(1)}(0, 0, -1) \left(\tilde{\chi}_1(2, 1) - \chi_2^{(1)} \right) \end{aligned}$$

and

$$\begin{aligned} \mathbf{M}_{2,+}^{(1)} = & M_0 - \left(A_2 + \hat{D}_{2,0}^{(1)}(0, 0, 0) \right) \chi_2^{(1)} \\ & + \sigma_b \left(A_2 + \hat{D}_{2,0}^{(1)}(0, 0, 0) \right) \sigma_b \left(\tilde{\chi}_2(2, 2) - \chi_2^{(1)} \right) + \hat{D}_{1,1}^{(1)}(0, 0, 0) \left(\tilde{\chi}_2(1, 1) - \chi_1^{(1)} \right) . \end{aligned}$$

Let $M_{i,-}^{(l)} = \sigma_b M_{i,+}^{(l)} \sigma_b$ describe the NMR shift for configurations where the dopant is located in the negative b direction from the P_l site (see Fig. 6.2). The crystal symmetries relating the various P_l sites imply $M_{i,\pm}^{(l+2)} = M_{i,\mp}^{(l)}$ and $M_{i,\pm}^{(2)} = \sigma_a M_{i,\mp}^{(1)} \sigma_a$. Hence, the sixteen possible local configurations give rise to eight different NMR shifts (cf. [74, p. 108]) described by the matrices $M_{i,\pm}^{(1)}$ and $M_{i,\pm}^{(2)}$ (with $i \in \{1, 2\}$).

6.6 Estimation of hyperfine couplings from angular dependence of NMR frequencies

6.6.1 Data

The angular dependence of the ^{31}P -NMR shift in pristine and weakly-doped BiCu_2PO_6 was measured and discussed by F. Casola in Ref. [74]. Relevant experimental details are summarized in appendix A.3.1. The resulting NMR shifts are reproduced in Fig. 6.3.

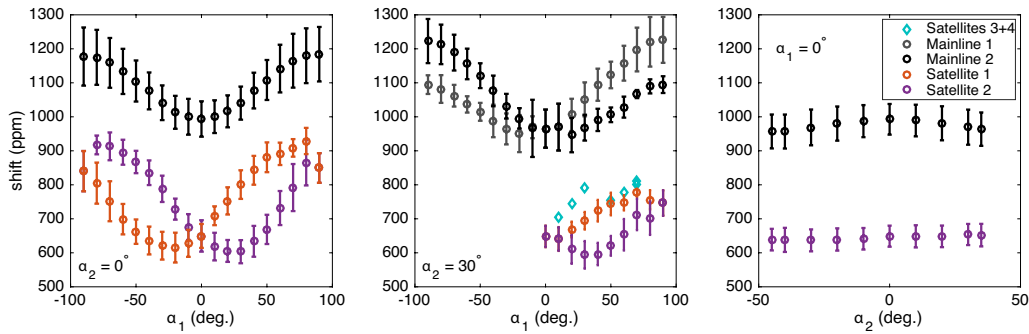


Figure 6.3: Angular dependences of relative ^{31}P -NMR shifts measured at $\mu_0 H = 3.9385 \text{ T}$ [75, p. 4] and $T \approx 296 \text{ K}$ in pristine and weakly-doped BiCu_2PO_6 (data from [74, Fig. 5.10]; see section A.3.1 for details). In addition to the “mainline” peaks of the undoped sample, dilute doping gives rise to satellite peaks (see section 6.5.2). Two satellite peaks are clearly resolved. The data acquired in low-symmetry orientations (middle panel) show possible additional satellite peaks [74, p. 108] (cf. section A.3.1), the tentative positions of which were added to the figure. All shifts are reported w. r. t. the resonance frequency of ^{31}P in polycrystalline [74, p. 99] BiZn_2PO_6 [74, Fig. 5.5] (67.8749 MHz [75, p. 5]; cf. section A.3.1).

For low doping concentrations $x \ll 1$ (fraction of Cu atoms substituted by Zn), configurations with two adjacent or next-nearest neighbor (cf. [74, Fig. 5.6c]) Zn atoms are negligibly rare. As detailed in section 6.5.2, doping gives rise to satellite peaks with different NMR shifts [22, 76]. Since each Zn atom has hyperfine couplings to two P sites (see Fig. 6.2), and the multiplicity of the P site is half that of the Cu site [11], the fraction of affected P sites is $4x$ (cf. previous derivation in [74, pp. 100-101]). This has been used to estimate the doping level in previous work, yielding $x \approx 1\%$ for the data reproduced in Fig. 6.3 [74, p. 101]. As already noted in [74, p. 100], this estimate is unaffected by a preferential substitution of one of the two inequivalent Cu sites.

6.6.2 Method

As seen in section 6.5.1, and previously described in [74, p. 105], the NMR shift in pristine BiCu_2PO_6 is fully determined by the coupling matrices \bar{A}_i . Therefore, data measured on undoped BiCu_2PO_6 cannot constrain the σ_b -odd components of A_i . Substitution of a $\text{Cu}(i)$ by non-magnetic Zn induces a satellite peak, which explicitly depends on A_i (cf. [74, p. 106] and section 6.5.2). Therefore, the resonance frequencies of satellite peaks associated with the substitution of *both* Cu sites are needed to fully constrain the hyperfine couplings A_1 and A_2 . Note that this analysis follows previous work [74, 75], the differences to the present work are discussed in section 6.8.

The NMR shifts are given by $\Delta = \hat{\mathbf{B}}_{\text{ext}} \cdot M \hat{\mathbf{B}}_{\text{ext}}$. In general, there are two distinct mainline frequency shifts $\Delta_0^{(l)}$ described by the matrices $M = M_0^{(l)}$ (section 6.5.1) and eight satellite-peak frequency shifts $\Delta_{i,\pm}^{(l)}$ corresponding to $M = M_{i,\pm}^{(l)}$ (section 6.5.2) with $i, l \in \{1, 2\}$.⁶ For the orientations sampled in the left panel of Fig. 6.3, $\sigma_c \mathbf{B}_{\text{ext}} = \mathbf{B}_{\text{ext}}$.⁷ Then, the symmetry properties of the matrices M imply essential degeneracies $\Delta_0^{(1)} = \Delta_0^{(2)}$ and $\Delta_{i,\pm}^{(1)} = \Delta_{i,\pm}^{(2)}$. Similarly, orientations sampled in the right panel of Fig. 6.3 satisfy $\sigma_a \mathbf{B}_{\text{ext}} = \mathbf{B}_{\text{ext}}$, resulting in essential degeneracies $\Delta_0^{(1)} = \Delta_0^{(2)}$ and $\Delta_{i,\pm}^{(1)} = \Delta_{i,\mp}^{(2)}$.⁸

Whereas the phenomenology of the mainline frequencies is consistent with the preceding paragraph, only half as many satellite peaks as expected are observed in Fig. 6.3 [74, p. 101]. There are three possible explanations (see [74, pp. 100-102, 106-108]):

1. There is an accidental degeneracy of the satellite peaks induced by substitution of Cu(1) and Cu(2) [74, pp. 101,107].
2. The Zn substitution is fully site-selective [74, p. 101].
3. The quadruplet of satellite peaks induced by substitution of one of the two inequivalent Cu sites has not been observed, because it overlaps with the main resonance (cf. [74, p. 108]) or has a very different resonance frequency. This would imply that the actual doping concentration is twice as large as estimated using the argument re-enacted in section 6.6.1.

As discussed above, the first scenario is the only one allowing for the extraction of all required hyperfine-coupling parameters, which is why I follow [74] and adopt this assumption in the following.

Since first-principles calculations corroborate $J'_2 \neq J_2$ in BiCu₂PO₆ [401], the local susceptibilities of the two inequivalent Cu sites differ (cf. section 5.2.1 and Fig. 5.5). Accidental degeneracy of the satellite peaks therefore requires a compensating imbalance of the hyperfine-coupling tensors A_i (cf. [74, p. 101]), which is not inconceivable given the low-symmetry configuration of the PO₄ tetrahedra (see, e. g., Fig. 4.2). Still, the ultimate answer to this question would require either a microscopic determination of the doping distribution, or first-principles calculations of g-tensors and/or hyperfine couplings.

The third and fourth satellite peaks (middle panel of Fig. 6.3) are only vaguely resolved and therefore not directly included in the fitting procedure. Instead, candidate models are accepted based on whether or not they are approximately consistent with these additional satellite peaks. An additional constraint results from the observation that the integrated satellite-peak intensity in the orientation (90°, 30°) is half of that measured in the orientation (0°, 30°) [74, Fig. 5.7 and p. 107], implying that the third and fourth satellite peaks do not merge with the other two satellite peaks at the boundary of the middle panel of Fig. 6.3 [74, p. 108].

In order to perform an actual fit, a mapping between observed shifts and a subset of the model shifts $\Delta_0^{(l)}$ and $\Delta_{i,\pm}^{(l)}$ is required (cf. [74, pp. 106-107]). There are 144 possible peak assignments, resulting from the following considerations:

- There are two possible assignments of the mainline shifts in the middle panel of Fig. 6.3.
- There are three possible choices for the accidental degeneracy of the satellite-frequency shifts,

⁶The terminology (“mainline” and “satellite” peaks) follows previous work [74, 75].

⁷Note that σ_c is not a symmetry of the combined system of sample and magnetic field, because the magnetic field transforms as a pseudo-vector. However, the equation holds as a mathematical identity when treating \mathbf{B}_{ext} like a polar vector.

⁸See [74, p. 106, and Tabs. 5.1 and B.2] for corresponding results in previous work.

$\Delta_{2,\pm}^{(l)} \approx \Delta_{1,\pm}^{(l)}$, $\Delta_{2,\pm}^{(l)} \approx \Delta_{1,\pm}^{(p(l))}$, or $\Delta_{2,\pm}^{(l)} \approx \Delta_{1,\mp}^{(p(l))}$, where $p(2) = 1$ and $p(1) = 2$. The accidental degeneracy is assumed to persist for all sample orientations. In particular, it appears highly unlikely that the accidental degeneracy in the left and middle panels of Fig. 6.3 would differ.

- For a given choice of accidental degeneracy, there are 4·3 possible mappings between the frequency-shifts of the first two satellites shown in the middle panel of Fig. 6.3 and the four doubly-degenerate satellite-frequency pairs of the model.
- An additional factor of two arises because each satellite shift in the left panel of Fig. 6.3 can correspond to either of the two satellite shifts in the middle panel.
- Finally, the right panel of Fig. 6.3 suggests that all eight satellite-peak shifts are degenerate within the experimental resolution.

The model is a linear function of twelve independent elements of A_1 and A_2 . The model predictors are sample orientations $(\alpha_{i,1}, \alpha_{2,i})$, whereas the peak assignment is taken to be an auxiliary parameter. Thus, for each peak assignment, the hyperfine-coupling parameters and their uncertainties can be estimated using a weighted least-squares linear regression (cf. section A.5.8), the weights being inversely proportional to the squared experimental uncertainties of the data points. The weights of the mainline data are empirically increased by a factor of four⁹. In addition, a global frequency offset (isotropic shift) of the satellite peaks needs to be assumed for a good fit [74, p. 107].

The linear-regression procedure described above is used to fit the data for each of the 144 possible peak assignments. Since statistical quantities like the weighted R^2 are similar for all fits, visual inspection is used to reject implausible fits (see discussion of third and fourth satellite peak earlier in this subsection).

6.6.3 Results for full model

Using the g-tensors obtained in section 5.2.1 and the calculations presented in section 5.2.4,¹⁰ the hyperfine-coupling parameters can be estimated using the procedure outlined in section 6.6.2. After visual inspection of all possible peak assignments (see section 6.6.2), twelve plausible solutions remain. These solutions are summarized in Tab. 6.1, which also contains references to figures showing the actual fits (appendix, section A.3.2). The plausible fits separate into two clusters (groups 1 and 2 in Tab. 6.1). Therefore, the hyperfine-coupling parameters are averaged for each group, yielding the results stated in Tab. 6.2. The parameter uncertainties were enlarged to encompass all individual estimates belonging to each group. The models corresponding to the averaged parameters listed in Tab. 6.2 are shown in Fig. 6.4. Reassuringly, the *predicted* positions of the other two satellite peaks are reasonably consistent with the data (cf. [74, p. 108]).

In the following chapter, the magnetic field is applied along the b -direction, so that the b -rows of the matrices $\Lambda_i = A_i g_i$ are of particular relevance. Fortunately, their values are rather well constrained by the fits (Tab. 6.2). I define the anisotropy a_i of the tensor A_i as $a_i = (\max \lambda_i - \min \lambda_i) / (\frac{1}{3} \sum_i \lambda_i)$, with λ_i the eigenvalues of A_i . Using the parameters given in Tab. 6.2, I obtain $(a_1, a_2) = (0.61, 0.48)$ for fit group 1 and $(a_1, a_2) = (1.07, 1.15)$ for fit group 2. Their generally smaller anisotropy makes the parameter estimates of fit group 1 appear more “plausible”. Meanwhile, the principal axes of the averaged solutions do not reveal a clear relation with the local structure of the crystal for neither of the

⁹Two for essential degeneracy $\Delta_0^{(l+2)} = \Delta_0^{(l)}$ and two to account for one doped and one undoped sample (see [74, p. 106]).

¹⁰I use results obtained for $L = 8$ rungs system size.

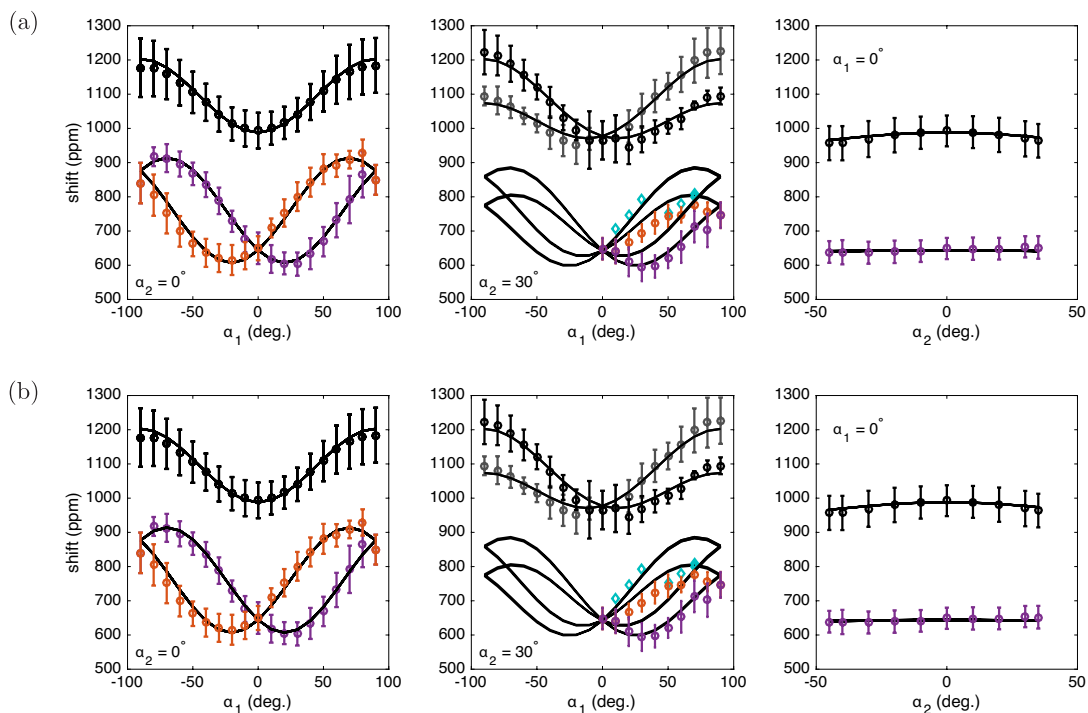


Figure 6.4: Fit models corresponding to averaged hyperfine parameters stated in Tab. 6.2. See section 6.6.3 for details. Panels (a) and (b) correspond to fit groups 1 and 2, respectively. Experimental data from [74] (see section 6.6.1).

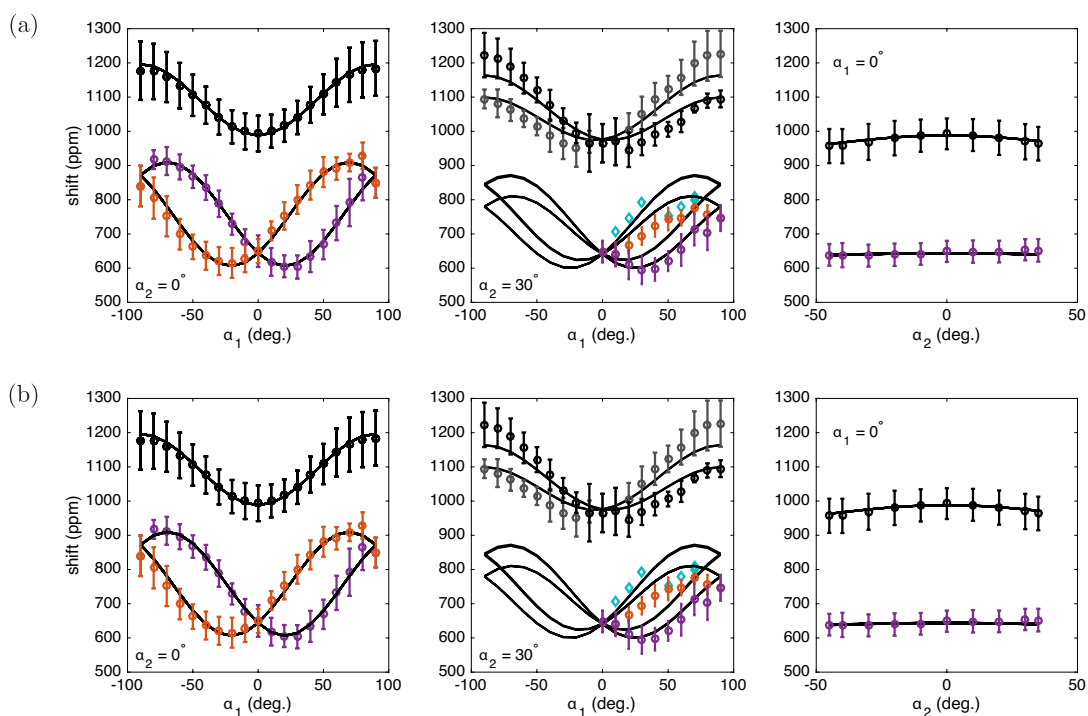


Figure 6.5: Fit models corresponding to averaged hyperfine parameters stated in Tab. 6.3. See section 6.6.4 for details. Panels (a) and (b) correspond to fit groups 1 and 2, respectively. Experimental data from [74] (see section 6.6.1).

Fit	Mainline 1	Acc. degeneracy	Sats. 1+2 for $\alpha_2 = 30^\circ$	Sats. cross	R^2
A.3(a)	$\Delta_0^{(2)}$	$\Delta_{1,\pm}^{(k)} = \Delta_{2,\pm}^{(k)}$	$\Delta_{1,-}^{(1)}, \Delta_{2,-}^{(1)}, \Delta_{1,+}^{(1)}, \Delta_{2,+}^{(1)}$	no	0.9953
A.3(b)	$\Delta_0^{(1)}$	$\Delta_{1,\pm}^{(k)} = \Delta_{2,\pm}^{(k)}$	$\Delta_{1,-}^{(2)}, \Delta_{2,-}^{(2)}, \Delta_{1,+}^{(2)}, \Delta_{2,+}^{(2)}$	no	0.9943
A.3(c)	$\Delta_0^{(2)}$	$\Delta_{1,\pm}^{(k)} = \Delta_{2,\pm}^{(p(k))}$	$\Delta_{1,-}^{(1)}, \Delta_{1,+}^{(1)}, \Delta_{2,-}^{(2)}, \Delta_{2,+}^{(2)}$	no	0.9937
A.3(d)	$\Delta_0^{(2)}$	$\Delta_{1,\pm}^{(k)} = \Delta_{2,\pm}^{(p(k))}$	$\Delta_{1,-}^{(1)}, \Delta_{1,+}^{(1)}, \Delta_{2,-}^{(2)}, \Delta_{2,+}^{(2)}$	no	0.9942
A.3(e)	$\Delta_0^{(1)}$	$\Delta_{1,\pm}^{(k)} = \Delta_{2,\pm}^{(p(k))}$	$\Delta_{1,-}^{(1)}, \Delta_{1,+}^{(1)}, \Delta_{2,-}^{(2)}, \Delta_{2,+}^{(2)}$	no	0.9951
A.3(f)	$\Delta_0^{(1)}$	$\Delta_{1,\pm}^{(k)} = \Delta_{2,\pm}^{(p(k))}$	$\Delta_{1,-}^{(1)}, \Delta_{1,+}^{(1)}, \Delta_{2,-}^{(2)}, \Delta_{2,+}^{(2)}$	no	0.9947
A.3(g)	$\Delta_0^{(2)}$	$\Delta_{1,\pm}^{(k)} = \Delta_{2,\pm}^{(k)}$	$\Delta_{1,-}^{(1)}, \Delta_{2,-}^{(1)}, \Delta_{1,+}^{(1)}, \Delta_{2,+}^{(1)}$	yes	0.9953
A.3(h)	$\Delta_0^{(1)}$	$\Delta_{1,\pm}^{(k)} = \Delta_{2,\pm}^{(k)}$	$\Delta_{1,-}^{(2)}, \Delta_{2,-}^{(2)}, \Delta_{1,+}^{(2)}, \Delta_{2,+}^{(2)}$	yes	0.9943
A.3(i)	$\Delta_0^{(2)}$	$\Delta_{1,\pm}^{(k)} = \Delta_{2,\pm}^{(p(k))}$	$\Delta_{1,-}^{(1)}, \Delta_{1,+}^{(1)}, \Delta_{2,-}^{(2)}, \Delta_{2,+}^{(2)}$	yes	0.9937
A.3(j)	$\Delta_0^{(2)}$	$\Delta_{1,\pm}^{(k)} = \Delta_{2,\pm}^{(p(k))}$	$\Delta_{1,-}^{(1)}, \Delta_{1,+}^{(1)}, \Delta_{2,-}^{(2)}, \Delta_{2,+}^{(2)}$	yes	0.9942
A.3(k)	$\Delta_0^{(1)}$	$\Delta_{1,\pm}^{(k)} = \Delta_{2,\pm}^{(p(k))}$	$\Delta_{1,-}^{(1)}, \Delta_{1,+}^{(1)}, \Delta_{2,-}^{(2)}, \Delta_{2,+}^{(2)}$	yes	0.9951
A.3(l)	$\Delta_0^{(1)}$	$\Delta_{1,\pm}^{(k)} = \Delta_{2,\pm}^{(p(k))}$	$\Delta_{1,-}^{(1)}, \Delta_{1,+}^{(1)}, \Delta_{2,-}^{(2)}, \Delta_{2,+}^{(2)}$	yes	0.9947

Group 1

Group 2

Table 6.1: Overview of plausible fit variants. See text (section 6.6.3) for details. For each fit, a reference to the actual fit, the peak assignment, as well as the weighted R^2 value are listed. ‘‘Sats. cross’’ indicates whether or not the frequency shifts of the first two satellite peaks cross when changing from $\alpha_2 = 0^\circ$ to $\alpha_2 = 30^\circ$ (for fixed α_1).

two fit groups.

6.6.4 Results for uniform model

As discussed in section 5.2.1, the experimental data are not incompatible with a site-independent g-tensor. Consistently, one would expect $J'_2 \approx J_2$. I therefore repeated the analysis¹¹ presented in the preceding section 6.6.3 using model \mathcal{C}_0 of section 5.2.1, which neglects the inequivalence of the two Cu sites. Except for the R^2 -values, the plausible solutions coincide with those listed in Tab. 6.1. The corresponding individual fits are shown in Fig. A.4 (appendix, section A.3.2). The fits are analyzed in complete analogy to section 6.6.3, yielding the results summarized in Fig. 6.5 and Tab. 6.3.

The anisotropies are $(a_1, a_2) = (0.57, 0.43)$ and $(a_1, a_2) = (1.05, 1.14)$ for the two fit groups, respectively. The fact that the principal axes of the averaged tensors do not coincide with any obvious geometrical features of the crystal, favors the more isotropic solutions of the first group, consistently with the results of section 6.6.3. On the other hand, the approximate local symmetry of the ladder (cf. Fig. 6.2) suggests that $A_1 \sim \sigma_c A_2 \sigma_c$. While this is reasonably consistent with all parameter estimates obtained in this work, the relative deviations from this expectation are smallest for the solutions obtained using fit group 2.

In the end, none of the two fit groups can be clearly rejected. Also, the fits obtained in this subsection (Fig. 6.5) agree similarly well with the data as those presented in section 6.6.3 (Fig. 6.4). Assuming that the inequivalence $J'_2 \neq J_2$ considered in the latter case represents an upper bound for the real material, a comparison of the parameter estimates listed in Tabs. 6.2 and 6.3 can be used to estimate the parameter uncertainties. For the b -row entries of the matrices Λ_i , which are of particular interest for this work (see

¹¹As before, calculations are performed for systems of size $L = 8$.

Group	$A_i/\frac{\text{T}}{\mu_B}$	$\Lambda_i/\frac{\text{T}}{\hbar}$
1	$A_1 = \begin{pmatrix} 0.16(2) & -0.047(2) & 0.00(8) \\ -0.047(2) & 0.213(6) & 0.022(6) \\ 0.00(8) & 0.022(6) & 0.18(5) \end{pmatrix}$	$\Lambda_1 = \begin{pmatrix} 0.34(5) & -0.084(9) & -0.02(15) \\ -0.103(11) & 0.38(4) & 0.049(13) \\ -0.03(17) & 0.039(11) & 0.34(10) \end{pmatrix}$
	$A_2 = \begin{pmatrix} 0.176(11) & -0.022(2) & 0.00(6) \\ -0.022(2) & 0.145(4) & -0.026(4) \\ 0.00(6) & -0.026(4) & 0.15(3) \end{pmatrix}$	$\Lambda_2 = \begin{pmatrix} 0.39(4) & -0.048(6) & -0.01(14) \\ -0.047(8) & 0.317(33) & -0.058(10) \\ -0.01(14) & -0.057(10) & 0.35(7) \end{pmatrix}$
2	$A_1 = \begin{pmatrix} 0.16(2) & 0.090(2) & 0.00(8) \\ 0.090(2) & 0.213(6) & 0.036(6) \\ 0.00(8) & 0.036(6) & 0.18(5) \end{pmatrix}$	$\Lambda_1 = \begin{pmatrix} 0.34(5) & 0.160(16) & -0.02(15) \\ 0.185(14) & 0.38(4) & 0.055(18) \\ -0.03(17) & 0.064(12) & 0.34(10) \end{pmatrix}$
	$A_2 = \begin{pmatrix} 0.176(11) & 0.085(2) & 0.00(6) \\ 0.085(2) & 0.145(4) & -0.024(4) \\ 0.00(6) & -0.024(4) & 0.15(3) \end{pmatrix}$	$\Lambda_2 = \begin{pmatrix} 0.39(4) & 0.186(19) & -0.01(14) \\ 0.191(14) & 0.317(33) & -0.061(17) \\ -0.01(14) & -0.052(10) & 0.35(7) \end{pmatrix}$

Table 6.2: Hyperfine couplings A_i and $\Lambda_i = A_i g_i$ estimated using the fits listed in Tab. 6.1. The satellite-peak offset is $-91(2)$ ppm in both cases. Uncertainties for A_i are estimates reported by the regression procedure (see section A.5.8). A 10% uncertainty was assumed for the parameters of the g-tensors when calculating Λ_i .

Group	$A_i/\frac{\text{T}}{\mu_B}$	$\Lambda_i/\frac{\text{T}}{\hbar}$
1	$A_1 = \begin{pmatrix} 0.169(14) & -0.039(2) & 0.00(7) \\ -0.039(2) & 0.178(5) & 0.027(4) \\ 0.00(7) & 0.027(4) & 0.16(4) \end{pmatrix}$	$\Lambda_1 = \begin{pmatrix} 0.37(4) & -0.077(9) & -0.01(15) \\ -0.087(10) & 0.35(4) & 0.059(10) \\ -0.01(15) & 0.053(10) & 0.34(9) \end{pmatrix}$
	$A_2 = \begin{pmatrix} 0.169(12) & -0.029(2) & 0.00(7) \\ -0.029(2) & 0.170(5) & -0.022(4) \\ 0.00(7) & -0.022(4) & 0.17(3) \end{pmatrix}$	$\Lambda_2 = \begin{pmatrix} 0.37(4) & -0.057(7) & 0.01(15) \\ -0.065(8) & 0.34(4) & -0.048(9) \\ 0.01(15) & -0.044(9) & 0.36(7) \end{pmatrix}$
2	$A_1 = \begin{pmatrix} 0.169(14) & 0.082(2) & 0.00(7) \\ 0.082(2) & 0.178(5) & 0.032(4) \\ 0.00(7) & 0.032(4) & 0.16(4) \end{pmatrix}$	$\Lambda_1 = \begin{pmatrix} 0.37(4) & 0.162(17) & -0.01(15) \\ 0.177(14) & 0.35(4) & 0.062(16) \\ -0.01(15) & 0.063(10) & 0.34(9) \end{pmatrix}$
	$A_2 = \begin{pmatrix} 0.169(12) & 0.092(2) & 0.00(7) \\ 0.092(2) & 0.170(5) & -0.028(4) \\ 0.00(7) & -0.028(4) & 0.17(3) \end{pmatrix}$	$\Lambda_2 = \begin{pmatrix} 0.37(4) & 0.182(19) & 0.01(15) \\ 0.198(15) & 0.34(4) & -0.053(17) \\ 0.01(15) & -0.055(10) & 0.36(7) \end{pmatrix}$

Table 6.3: Hyperfine couplings A_i and $\Lambda_i = A_i g_i$ estimated using the uniform model \mathcal{C}_0 of section 5.2.1, as described in section 6.6.4. The satellite-peak offset is $-90(2)$ ppm in both cases. Uncertainties for A_i are estimates reported by the regression procedure (see section A.5.8). A 10% uncertainty was assumed for the parameters of the g-tensors when calculating Λ_i .

section 6.6.3), I estimate relative uncertainties of $\sim 25\%$ for all entries but the ba -elements of fit group 2, which exhibit smaller variations $\sim 10\%$.

6.7 Uncertainties

In principle, the hyperfine couplings and g-tensors obtained in sections 6.6.3 and 5.2.1 can be used to calculate the ^{31}P -NMR spectrum expected for any hypothetical magnetic structure (see, e. g., [78]). Accordingly, the intrinsic parameters of a given magnetic-structure model can be constrained by measured NMR data. However, such analyses crucially depend on the accuracy of the g-tensors and hyperfine couplings.

The relative uncertainty of the g-tensors is discussed in section 5.2.1. Meanwhile, the estimation of the hyperfine couplings relies on a model for the local magnetic susceptibility. This model depends on the g-tensors and the internal magnetic interactions, including interladder and DM interactions. In

the following, I will therefore attempt to obtain an upper bound on the uncertainty using more general considerations.

Assuming effective $SU(2)$ -symmetry of the Hamiltonian at temperatures $T \sim 300$ K, the local susceptibility depends on the g-tensors and the three parameters $C_{ij}^{zz}(T)$ (see section 1.4.5). At high temperature, a mean-field approximation¹² can be used to eliminate $C_{12}^{zz}(T) = C_{21}^{zz}(T) \approx -C_{11}^{zz}(T) C_{22}^{zz}(T) (2 + 2J_4/J_1) \frac{J_1}{\mu_B}$.¹³ I expect $C_{11}^{zz}(T)$ and $C_{22}^{zz}(T)$ not to differ by more than 20%¹⁴ and use $\theta_1 \approx -\theta_2$ in the parametrization (5.2) of the g-tensor (section 5.2.1). I assume that the corresponding g-tensor parameters are positive and do not differ by more than 20% between the two sites. Since BiCu_2PO_6 is a strongly frustrated magnet, I further assume that $C_{ii}^{zz}(T)$ is bounded by the susceptibility of a free spin,¹⁵ $C_{ii}^{zz}(T) \leq \mu_B S(S+1)/(3k_B T)$ (e. g., [401]). Enforcing this constraint and requiring the site-averaged g-tensor parameters not to exceed 2.4 (cf., e. g., [377, p. 14]), the set of all local-susceptibility tensors consistent with the magnetization data can be obtained. With $J_1/k_B = 140$ K [401] and $J_4/J_1 \leq 2$, the diagonal elements of these tensors vary by up to 100%. The uncertainties of the off-diagonal entries are even larger. Since these uncertainties propagate linearly into the NMR shifts, they would induce comparable errors in the estimated hyperfine couplings. The situation is worsened even further by the additional assumptions required by the analysis described in section 6.6.

Unfortunately, the upper bound estimated in the preceding paragraph is too coarse for being practical. Taking a pragmatic approach, the hyperfine-coupling uncertainties obtained at the end of section 6.6.4 are adopted instead in the following.

6.8 Discussion

The data used in this chapter were acquired and published in [74]. The previous works [74, 75] also include similar analyses of local magnetization, g-tensors, and hyperfine couplings. The results presented in this chapter extend the previous treatment in several ways: (i) A formalism for dealing with site-dependent g-tensors is developed (section 1.4.5) and applied (section 5.2.1), whereas orthorhombic and site-independent g-tensors were assumed in [74, Fig. 5.9]. (ii) Calculations are performed with $J'_2 = J_2$ for model C_0 in section 5.2.1 for self-consistency and the g-tensor model respects the (approximate) local symmetry of the crystal. (iii) The local-magnetization model used to estimate the hyperfine couplings is derived from the fitted g-tensors and the calculated spin-susceptibility. This is an improvement over the phenomenological magnetization model used in previous work [74, p. 105], which also neglected the magnetic inequivalence of the two Cu sublattices suggested by first-principles calculations [401]. (iv) The effect of site depletion upon the local magnetization of nearby Cu sites is taken into account. (v) The hyperfine-coupling fits are performed systematically using linear regression and all possible peak assignments are considered.¹⁶ (vi) The uncertainties of the estimated parameters are discussed and accounted for in the analysis of the high-field NMR data.

Besides peak assignment, as well as assumed accidental degeneracy and symmetry of the coupling ten-

¹²No self-consistency condition is imposed for simplicity.

¹³For the calculations presented in section 5.2.1, this is correct to within 6.5% at $T = 296$ K.

¹⁴For the calculations presented in section 5.2.1, the difference is $\lesssim 14\%$.

¹⁵The NNN couplings are antiferromagnetic couplings within each sublattice and thus reduce the sublattice susceptibility, whereas the couplings J_1 and J_4 connect different sublattices and therefore tend to increase $C_{ii}^{zz}(T)$ (cf. mean-field).

¹⁶The results given in [74, Tab. 5.2] roughly correspond to fit group 1 (Tab. 6.3), except for the sign of the ac -elements which is likely due to a different notational convention.

sors (see section 6.6.2 and references therein), the dominant uncertainty in the hyperfine couplings is related to the local magnetization model (see section 6.7). Whereas the sum of the diagonals of the local magnetization tensors is constrained by macroscopic magnetization measurements (section 5.2.1), a *model* for spin-susceptibility and g-tensors is required to estimate (extrapolate) the off-diagonal terms, as well as the distribution of the magnetization between the two Cu sublattices. This model is also used to predict the effect of site depletion in the doped compound.

Additional constraints are needed to reduce the rather significant uncertainties in the coupling parameters (g-tensors and hyperfine couplings). Density-functional calculations capable of predicting these parameters are a possibility. Experimentally, electron-spin resonance (ESR) at high temperature might be capable of determining the g-tensors of the Cu sites (see, e. g., [185, 258]). Yet, despite first results [258] and ongoing experimental efforts (see Acknowledgments), no comprehensive studies were reported for BiCu₂PO₆. In principle, the g-tensors and hyperfine couplings can also be determined from the saturation values of magnetization and ³¹P-NMR shift (cf. [409]). However, the large saturation field [401] precludes such experiments for BiCu₂PO₆. Lastly, the g-tensors and hence the local magnetization could also be determined through Cu-NMR (see [74, p. 156]), provided that the on-site hyperfine coupling is not significantly perturbed by the crystal environment. A ⁶³Cu resonance was reported in BiCu₂PO₆, but not investigated in detail [74, p. 156]. Corresponding measurements on doped samples might also allow checking for site-selective chemical substitution (cf. section 6.6.2 and references therein). Regarding this particular question, already raised in [74, p. 101], it is worth noting that X-ray diffraction on 50%-doped samples did not reveal any additional diffraction peaks [218], indicating that—at least at high doping levels—the substitution is not site selective.

7 Field-induced magnetic order in the frustrated spin ladder

This chapter summarizes the results of a numerical study of the field-induced phases of the model Hamiltonian (4.1). Previous results for relevant model Hamiltonians are reviewed first (section 7.1). This includes previous calculations for (4.1) [77, 78, 131, 401], which clearly provided inspiration and initial guidance for this work. The presentation of the results obtained in this work begins with section 7.2.

7.1 Previous knowledge

7.1.1 Spin ladder

The spin- $\frac{1}{2}$ ladder is described in section 1.3.2. Its elementary excitations are triplons with antiferromagnetic wavevector [360]. An external magnetic field H is known to lift the degeneracy between the three triplon branches (corresponding to $S_z = -1, 0, 1$) (see, e. g., [146]). At a critical field value H_c , one of the branches softens, giving rise to a magnetic phase transition [437]. Due to the analogy between field-induced triplons and a lattice gas of bosonic particles with hard-core repulsion (see [251]), the field-induced order in the spin ladder is often described as a Bose-Einstein condensation (BEC) of triplons [146]. The transverse spin correlations in the field-induced state are quasi long-ranged, indicating an instability towards antiferromagnetic ordering of the transverse spin component¹ [145] (in the presence of suitable interladder couplings, see [64, 145, 169, 340]). A famous example (see [146]) is the field-induced magnetic order in TlCuCl_3 [252, 293]. Thermal fluctuations can inhibit the development of long-range order. If the temperature is not too high, the resulting disordered regime is gapless with critical correlations and can be described as a (spin) Luttinger Liquid [85] (see [340] for an experimental realization).

7.1.2 Zigzag chain

The (spin- $\frac{1}{2}$) zigzag chain is presented in section 1.3.3. For $J_2 > 0.5 J_1$, correlations are incommensurate and spiral-like (e. g., [291])². The “twist” associated with the spiral correlations can be quantified using the *chirality* $\kappa_{ij} = \mathbf{S}_i \times \mathbf{S}_j$ (e. g., [88]), whose properties will be considered in more detail in the following sections (e. g., sections 7.7.1 and 7.8.1).

Spiral (helical) magnetic structures are not a recent concept [116, 452]. Classical considerations suggest the formation of spiral structures in the zigzag chain [88, 164, 419]. However, such ordering is

¹The exact expressions are given in [145]. According to these, the longitudinal spin correlations asymptotically also decay like power laws. However, the transverse spin correlations decay more slowly. In particular, they decay slower than the inverse distance, whereas the longitudinal spin correlations do not (cf. section 7.7.3).

²This can be seen, e. g., from equation (15) in [291], which states that $\langle S_i^+ S_{i+d}^- \rangle \sim (-1)^d / |d|^{1/4} \exp(-i k d)$. Since $S_i^+ S_j^- + S_i^- S_j^+ \sim S_i^x S_j^x + S_i^y S_j^y$ and $S_i^+ S_j^- - S_i^- S_j^+ \sim S_i^x S_j^y - S_i^y S_j^x$, this implies $\langle S_j^x \rangle \sim \cos k d$ and $\langle S_j^y \rangle \sim \sin k d$ for a classical ordered state with $\langle S_i^y \rangle = 0$ (without loss of generality).

forbidden in low-dimensional systems at finite temperature [45, 97, 260]. It has been therefore proposed that effectively one-dimensional systems could develop a finite chirality without ordered magnetic moments [419]. In real systems, such a phase would exist at temperatures which are high enough to prevent spiral order, while low enough not to destroy the *chiral order*³ [419]. It has been proposed that such a phase can indeed be stabilized by certain types of four-spin exchange or magneto-elastic effects involving DM interactions [304]. Theoretical evidence of a chiral phase was also obtained for classical spins with easy-axis (XY) anisotropy [90]. A corresponding experimental realization was reported in $\text{Gd}(\text{hfac})_3\text{NITR}$, a compound hosting coupled zigzag chains with alternating spin- $\frac{1}{2}$ and spin- $\frac{7}{2}$ moments with XY anisotropy [89].

The emergence of chiral order corresponds to a symmetry-breaking in spin space. It is therefore not surprising that such ordering is favored by anisotropic interactions [291] which lower the symmetry group of the magnetic moments from $SU(2)$ to $U(1) \times Z_2$ [164]. In such anisotropic systems, chiral order breaks the discrete Z_2 symmetry [291] (see also [419]). For spin- $\frac{1}{2}$ moments, magnetic field [211] (cf. following subsection) and exchange anisotropies (see section 1.1.3 and below) are obvious candidates. The effect of an XXZ-type anisotropy is illustrated in Fig. 7.1 [142] (see also [141, 300]). Whereas a mild XXZ anisotropy is sufficient to induce chiral order for ferromagnetic nearest-neighbor (NN) coupling J_1 , the situation for antiferromagnetic J_1 is very different. Most importantly, these results suggest that the zero-field ground-state of BiCu_2PO_6 is not chiral. The effects of an additional explicit dimerization, i. e., alternation of the NN exchange J_1 , were considered in [405, 406]. However, no dimerization is expected in BiCu_2PO_6 (see section 1.3.4).

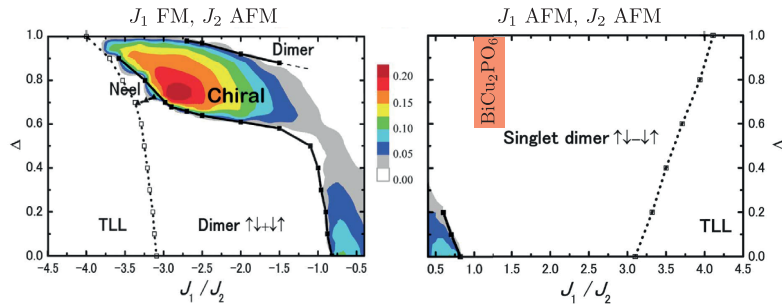


Figure 7.1: Ground-state phase diagram of the zigzag chain with XXZ anisotropy Δ [142]. The exchange interactions on the nearest-neighbor (NN) and next-nearest neighbor (NNN) bonds are assumed to be of the form $S_i^x S_j^x + S_i^y S_j^y + \Delta S_i^z S_j^z$. Results for ferromagnetic (FM) and antiferromagnetic (AFM) NN coupling J_1 are shown. The shading corresponds to the magnitude of the chiral order parameter κ_{ij}^z on the NN bonds. The parameter range corresponding to BiCu_2PO_6 (see parameter sets *A-C* in section 4.3.3, the extent in Δ is purely speculative) has been marked in orange. (Figure adapted with permission from Ref. [142]. Copyright 2010 by the American Physical Society.)

7.1.2.1 Phase diagram

The phase diagram of the zigzag chain in a magnetic field is shown in Fig. 7.2 [164, 383]. Without loss of generality, the external field is assumed to be parallel to the spin-quantization axis z . The dimer phase has been discussed in section 1.3.3, whereas the vector-chiral phase was introduced earlier in this section and will be at the main focus of this work.

³Other names for this order include “ p -type spin nematic” [240], “ $O(2)$ chiral spin nematic” [304], “ $O(2)$ spin cholesteric” [304], “vector-chiral phase” [164], or “vector-chiral spin liquid” [90].

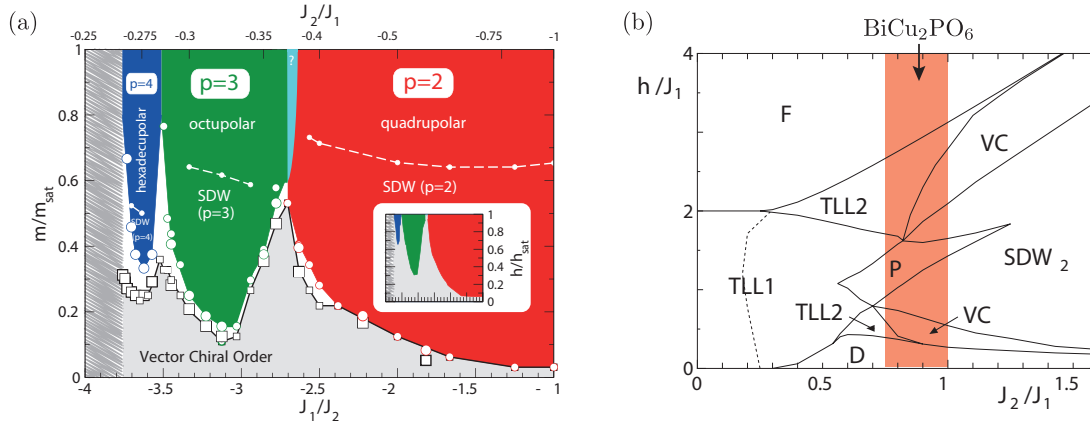


Figure 7.2: Phase diagram of the zigzag chain in an external magnetic field h , reproduced from [383] (a) and adapted from [164] (b), respectively. While the frustrating NNN coupling J_2 is generally antiferromagnetic, ferromagnetic (a) and antiferromagnetic (b) NN couplings J_1 need to be distinguished. The saturation magnetization and the saturating field are denoted by m_{sat} and h_{sat} , respectively. The phase diagram includes dimer (D), plateau (P), chiral (VC), spin-density wave (SDW_p), multipolar, n -component Tomonaga-Luttinger liquid (TLL_n), and fully polarized (F) phases. The cyan region marked with a question tag in (a) corresponds to an incommensurate nematic phase [163, 383]. The white region in (a) represents a metamagnetic magnetization jump, whereas the scribbled region has not been studied in the corresponding work [383]. The inset of (a) shows the same phase diagram as function of magnetic field h , rather than magnetization m . Note that the multipolar and incommensurate nematic phases are negligibly narrow in this representation [163, 383]. The parameter range corresponding to BiCu_2PO_6 (see parameter sets *A-C* in section 4.3.3) has been indicated in orange. (Reprinted figure (a) with permission from Ref. [383]. Copyright 2009 by the American Physical Society. Figure (b) adapted with permission from Ref. [164]. Copyright 2010 by the American Physical Society.)

The case of ferromagnetic nearest-neighbor (NN) coupling [see Fig. 7.2(a)]⁴ exhibits various phases which are characterized by algebraically-decaying multipolar spin correlations $M_p(r)$ of order p [240],

$$M_p(r) = \left\langle \left(\prod_{n=0}^{p-1} S_n^+ \right) \left(\prod_{n=0}^{p-1} S_{n+r}^- \right) \right\rangle .$$

These phases correspond to multi-magnon bound states [88, 163]. In addition, the longitudinal spin correlations $\langle S_i^z S_{i+r}^z \rangle$ are algebraically decaying as well (e. g., [240]). If the former correlations decay more slowly,⁵ the corresponding phase is termed multipolar [163] ($p = 2$: quadrupolar [240] or (n-type) nematic [163], $p = 3$: octupolar [240] or triatic [163], $p = 4$: hexadecupolar [240] or quartic [163]). In the other case, the phase is of spin-density wave type (SDW_p) [163, 164, 240]. Dashed lines indicate the crossover between these two regimes in Fig. 7.2(a). The transverse spin correlations decay exponentially [164, 383]. Only the SDW_p phases are relevant for the phase diagram as function of magnetic field (see Fig. 7.2, caption). These phases are gapless one-component Tomonaga-Luttinger liquids (TLLs) [163] in which the magnetization S_{tot}^z changes in steps of p [163, 164]. The finite-temperature properties of the corresponding phases emerging in two-dimensional arrays of coupled zigzag chains were studied in [345].

⁴Other relevant previous works include [163, 240].

⁵Inside the corresponding phases, exactly one of these two correlation functions decays slower than the inverse distance [240] (cf. section 7.7.3).

The SDW_2 phase also appears for antiferromagnetic (AFM) NN coupling [see Fig. 7.2(b)].⁶ The TLL1 phase is connected to the gapless phase of the Heisenberg chain, and therefore has algebraically decaying transverse and longitudinal spin correlations [164]. The former dominate to the left of the dashed line in Fig. 7.2(b), whereas the latter dominate to its right [164]. The TLL2 phase is a critical phase in which all correlation functions of interest, including the chiral correlations, decay algebraically [164]. The spin correlations are incommensurate and the two TLL components result from two inequivalent minima of the magnon⁷ dispersion [164]. If the densities of the two corresponding condensates become imbalanced due to magnon-magnon interactions, chiral order emerges [164]. Finally, a gapped (incompressible [136]) plateau phase appears at one-third of the saturation magnetization (e. g., [164]). The corresponding ground-state is triply-degenerate [301] with an “up-up-down” magnetic structure [302] and its excitations can be understood as domain walls with fractional spin $S_z = \frac{1}{3}$ [301]⁸.

The (vector-)chiral phase appearing for AFM NN couplings is of particular relevance for the rest of this chapter. This phase is a one-component TLL and hence gapless [164, 211, 255]. It is characterized by long-range order of the chirality [255] and the Z_2 -symmetry-breaking ground state is doubly degenerate [164]. As illustrated by its review earlier in this section, the chiral phase is a quantum correspondent of the spiral phase expected based on classical considerations [164]. It is therefore not surprising that its stability range grows rapidly with increasing spin [209]. The spin correlations decay algebraically at large distances, the transverse spin correlations being dominant compared to the longitudinal ones [164]. In the chiral phase observed at low magnetization, the decay exponent of the transverse spin correlations is close to one, whereas that of the longitudinal ones equals to two [164].

7.1.3 Frustrated ladder

The frustrated-ladder model was introduced in section 1.3.4, and is directly relevant for BiCu_2PO_6 (section 4.3.1). Whereas the zero-field phase diagram of the frustrated ladder is rather well-characterized (see section 1.3.4), much less is known about its field-induced phases.

In the strong-rung case, the VBS state consisting of a singlet on each rung bond is a good starting point for a bond-operator mean-field theory (BOMF) [384]. In this approximation, the minimum of the dispersion shifts from $q = \pi$ to an incommensurate wavevector at the Lifshitz⁹ point $J_2/J_1 = 1/4$ [384] [Fig. 7.3(a)]. The resulting double-well structure gives rise to additional singularities in the magnetic density-of-states (DOS) [384] [Fig. 7.3(b)]. A strong rung coupling results in short-range triplon-triplon interactions, which are negligible at low magnetization [384]. An analogous description is obtained for the regime close to saturation by considering individual rung-singlets in a fully-polarized vacuum [367, 384]. For non-interacting magnetic excitations, the magnetization curve is directly related with the DOS of the magnetic excitations [384]. Most importantly, any singularities in the DOS are reflected by $\partial M/\partial H$, as illustrated by the results reproduced in Fig. 7.3(c) [384]. The approximation of negligible interactions naturally holds at the magnetization onset, where the triplon-density is low [384], which

⁶Other relevant previous works related to the magnetic phase diagram of the frustrated zigzag ladder with AFM NN coupling include [211, 300, 302].

⁷The magnon picture arises close to saturation (e. g., [211]). For the low-field TLL2 phase it corresponds to the lower edge of the two-spinon continuum [164]. With explicit dimerization, the lowest-energy excitation is a triplet bound state of two spinons [410].

⁸Note that [301] considers the Ising limit.

⁹For a suitably-chosen chemical potential (magnetic field), the number of Fermi points changes from two to four at the Lifshitz point [384]. As explained in [384], this analogy with a Lifshitz transition (see [234]) justifies the name.

is why most magnetization curves of gapped systems exhibit a square-root-like onset, resulting from the parabolic minimum of the dispersion [401].¹⁰ By contrast, the appearance of the additional cusp singularities [Fig. 7.3(c)] observed in the incommensurate case depends on negligible interactions of the particles carrying the magnetization (triplons in case of the low-magnetization region) [384].

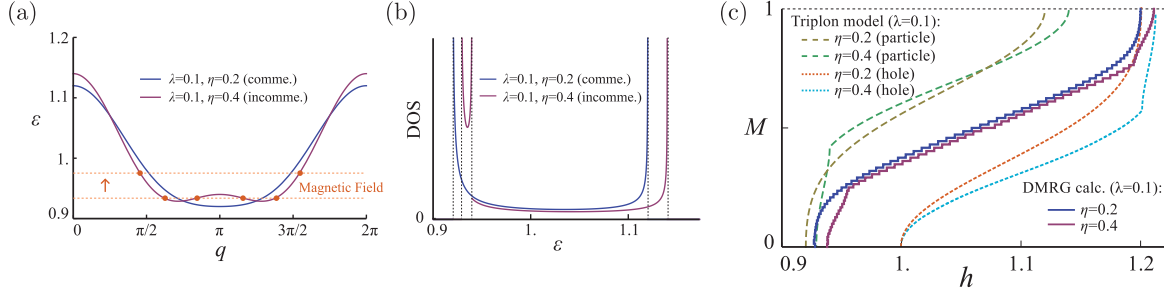


Figure 7.3: (a-b): Dispersion and density-of-states (DOS) of frustrated ladder, as obtained using BOMF [386]. (c): Magnetization curves, obtained using BOMF and DMRG [386]. The parameters λ and η correspond to J_1/J_\perp and J_2/J_1 , respectively. (Figures (a-c) reproduced with permission from [386]. Copyright 2015 Physical Society of Japan.)

Depending on the values of the exchange couplings, the frustrated ladder model exhibits several magnetization plateaux [387]. As expected, the one-third magnetization plateau of the zigzag chain (see section 7.1.2) is recovered in the limit of weak rung coupling [387]. In the strong-rung limit, quasispin operators involving singlet and triplet combinations of spins can be defined on each rung of the ladder [387]. This establishes a mapping between the strong-rung frustrated spin ladder with magnetization $\frac{1}{2}M + \frac{1}{2}$ and a zigzag chain with XXZ anisotropy and magnetization M , where the magnetizations are expressed relative to the saturation magnetization of the corresponding model [387]. Thus, the dimerization gap of the zigzag chain (at $M = 0$) gives rise to a magnetization plateau at $M = 1/2$ in the frustrated spin ladder [387].¹¹ Similarly, the one-third magnetization plateau ($M = \pm 1/3$) of the zigzag chain induces plateaux at $M = 1/3$ and $M = 2/3$ in the frustrated ladder [387].

Besides the work reviewed in the following subsection (section 7.1.4), the only detailed study of the (quantum) phase diagram of the frustrated spin ladder in a magnetic field known to the author focuses on the magnetization region close to saturation and predicts the existence of a chiral phase for the parameter regime relevant for BiCu_2PO_6 (cf. section 4.3.3) [367]. While these results corroborate the expected similarity between the zigzag chain and the frustrated ladder, they also show that the phase diagrams of the two systems are not identical [367].

7.1.4 Frustrated ladder with reduced symmetry

The Hamiltonian (4.1) proposed [401] for BiCu_2PO_6 is closely related to the frustrated-ladder model, but exhibits a reduced symmetry (see section 4.3.1). The excited states and the magnetization curve of the model were considered using exact diagonalization and DMRG within the context of a first-principles study of BiCu_2PO_6 [401]. Subsequent calculations were performed by A. Feiguin [74, 75, 77, 78, 131]: By calculating suitable correlation functions (analogous to those defined in section 7.7.1), the emergence of chiral order was shown and it was proposed that spiral order should appear in BiCu_2PO_6 at high

¹⁰A similar discussion applies to the regime close to saturation [367, 384].

¹¹A plateau at half-saturation magnetization is also observed in the diagonally-frustrated spin ladder [136].

magnetic fields. The regime above one-half saturation magnetization was identified with two essentially decoupled spin chains [131]. Moreover, the chiral order appeared to set in at a finite magnetization, in a manner reminiscent of a phase transition [77]. It has therefore been suggested that this corresponds to a phase transition from an, experimentally established [78], solitonic phase to a chiral phase [77].

7.2 Introduction

Previous numerical work related with the model Hamiltonian (4.1) was reviewed in section 7.1.4 (see also section 7.1.3). In particular, the present work was strongly influenced by calculations performed by A. Feiguin [78, 131].

The calculations presented in the remainder of this chapter are motivated by the following observations: (i) The previous works used parameter set A almost exclusively, despite the uncertainties associated with the model parameters (section 4.3.3). (ii) Although the effects of possible DM interactions (section 4.3.2) were considered [131] (see also [75, pp. 30,35]), no detailed reports of the results are known to the author (see also [77, p. 8] and [74, p. 140]). (iii) The influence of site-dependent g-factors appears not to have been investigated, nor was the effect of the symmetric anisotropy term proposed in conjunction with parameter set B [318] (cf. section 5.4.4). (iv) Questions remained regarding the numerical evidence for solitons [78] (see also [77, p. 7]), since similar delayed-onset behavior of the chiral correlations was reported in calculations performed for the zigzag chain and attributed to finite-size effects or convergence problems [383].

In the following, the BiCu_2PO_6 model Hamiltonian (4.1) is studied using DMRG on finite lattices with open boundaries (see sec. 1.4.3). Following previous work [78], I restrict myself to the case $\mathbf{H} \parallel b$ and the spin-quantization axis z is taken to coincide with the b direction of the crystal.

Section 7.3 discusses the ground-state degeneracy observed in the field-induced phases, which has important implications for the uniqueness of the expectation values measured using the eigenstates obtained by the calculations. *Inter alia*, these results are used in section 7.6 to reconsider the real-space spin textures—previously suggested as evidence for the formation of solitons [78]. The relation between ground-state degeneracy, chirality, and spiral order is at the focus of section 7.8.

After these rather general considerations, detailed results for parameter set A are presented in section 7.9 and interpreted in section 7.10. The small g-factor staggering (see section 5.2.1) is ignored at first, enabling efficient use of S_z^{tot} conservation.¹² The results confirm the existence of long-range chiral order (see [77]) and clarify the lower-field phase boundary of the chiral phase.

The effects of site-dependent g-factors, as well as those of varying the exchange couplings, are examined in section 7.11. An intermediate summary of these results is given in section 7.12. Subsequently, extensions of parameter set A by various DM terms are discussed in section 7.13, and the recently-proposed parameter set B is considered in detail in section 7.14.

The chapter concludes with a discussion (section 7.15). Open questions related to differences between the predictions of the model and experimental results reported for BiCu_2PO_6 are considered separately, in section 7.16.

¹²Although S_z^{tot} -conservation is preserved, the Zeeman term becomes non-trivial for site-dependent g-factors.

7.3 Ground-state degeneracy

DMRG calculations performed in this work for parameter set A with uniform g -factor, targeting the two lowest-energy states in each S_{tot}^z sector, indicate that the field-induced ground-states are two-fold degenerate within numerical accuracy for magnetizations M up to one half the saturation magnetization M_{sat} . This is consistent with exact-diagonalization (ED) calculations performed for systems with periodic boundary conditions.¹³

The discussion in the following subsections is a standard application of basic quantum-mechanics and group-theory knowledge to the frustrated-ladder system with $J'_2 \neq J_2$. While similar ideas appear throughout the abundant literature for the zigzag chain (see, e. g., [164, 291], and discussion in section 7.15), I am not aware of any detailed description of these straightforward-to-derive facts. Moreover, the presence of inequivalent magnetic sites requires a dedicated discussion for the model [401] considered in this work.

7.3.1 Symmetry associated with degeneracy

It will turn out instructive to identify the symmetry responsible for the ground-state degeneracy.

First, consider the spin-space symmetries of the Heisenberg Hamiltonian (4.1) for $\mathbf{H} \parallel b$. Details regarding the following discussion are summarized in appendix A.5.9.

- The system is invariant under $U(1)$ rotations about z . These are trivial for eigenstates with well-defined S_{tot}^z , since they correspond to a global phase factor.
- Time reversal \mathcal{T} is another important symmetry. For a system of N spin- $\frac{1}{2}$ particles, a possible representation reads $\mathcal{T} = 2^N \left(\prod_{i=1}^N S_i^y \right) K$ [389], where K denotes complex conjugation of the coefficients in the canonical S_z -basis. Unfortunately, $[\mathcal{T}, S_{\text{tot}}^z] \neq 0$.
- Similarly, the reflection symmetries R_x and R_y about the x and y axes in spin space, respectively, are incompatible with S_{tot}^z -conservation.
- The combination $R_y \mathcal{T} = K$ is trivial for eigenstates with real coefficients in the S_z -basis. Also, $R_x \mathcal{T} = -(-1)^{N/2 - S_{\text{tot}}^z}$ if the eigenstates have well-defined S_{tot}^z in addition, rendering this symmetry operator trivial as well.

To conclude, none of the spin-space symmetries could be identified as the origin of the ground-state degeneracy.

For even system sizes L , the only non-trivial crystal symmetry preserved by the *finite* ladder graph depicted in Fig. 4.4(b) is inversion, i. e., the interchange of the two ladder legs, followed by the reflection σ_b .¹⁴ For odd system sizes, the corresponding symmetry is σ_b .¹⁵ To get rid of this explicit system-size dependence, the appropriate symmetry shall be called P in the following. Note that being a crystal symmetry, P is unbroken by DM interactions or staggered g -tensors. Also, P involves a rotation by π

¹³System sizes up to $L = 10$ were considered using full-spectrum ED. The ground-state is found to be doubly-degenerate, except for special values of the magnetization $M/M_{\text{sat}} = 0, 0.25, 0.5, 0.75$.

¹⁴This is the same as the symmetry \mathcal{C}_{2z} defined in [401].

¹⁵This is the same as the symmetry \mathcal{P}_y defined in [401].

about the z -axis in spin space for odd system sizes. For simplicity, the following discussion therefore assumes an even system size, for which the symmetry P simply corresponds to a permutation of the lattice-site indices, $i \mapsto P(i)$. Note that this implies compatibility with S_{tot}^z -conservation, $[P, S_{\text{tot}}^z] = 0$.¹⁶ By considering transpositions of two spins in the S_z basis, a spin-space representation of P can be obtained,

$$P = \prod_{i \in I} \left(S_{P(i)}^+ S_i^- + S_{P(i)}^- S_i^+ + S_{P(i)}^+ S_i^+ S_{P(i)}^- S_i^- + S_{P(i)}^- S_i^- S_{P(i)}^+ S_i^+ \right) = \prod_{i \in I} 2 \left(\mathbf{S}_{P(i)} \cdot \mathbf{S}_i + \frac{1}{4} \right) \quad ,$$

where the set of compound indices I is chosen such that $|I| = L$ and $P(I) \cap I = \emptyset$.

Since P is a symmetry ($[\mathcal{H}, P] = 0$), any eigenstate $|\varphi\rangle$ with energy E gives rise to an eigenstate $P|\varphi\rangle$ with the same energy. If the state $|\varphi\rangle$ is non-degenerate, $P^2 = 1$ requires $P|\varphi\rangle = \pm|\varphi\rangle$, and all expectation values of local operators like S_i^z are invariant under P . For a degenerate state, $P|\varphi\rangle \neq \pm|\varphi\rangle$ and one can define P -even/odd states $|g/u\rangle = \frac{1}{\sqrt{2}}(|\varphi\rangle \pm P|\varphi\rangle)$ which satisfy $P|g/u\rangle = \pm|g/u\rangle$ and $\langle g|u\rangle = 0$. If two (orthogonal and normalized) eigenstates $|\varphi_1\rangle$ and $|\varphi_2\rangle$ form a degenerate doublet which is due to the symmetry P , both give rise to the same states $|g/u\rangle$ and basis-independence of the (partial) trace over $\text{span}\{|\varphi_1\rangle, |\varphi_2\rangle\} = \text{span}\{|g\rangle, |u\rangle\}$ implies that

$$\langle \varphi_1 | P | \varphi_1 \rangle + \langle \varphi_2 | P | \varphi_2 \rangle = \langle g | P | g \rangle + \langle u | P | u \rangle = 1 - 1 = 0 \quad . \quad (7.1)$$

By extending the ALPS full-spectrum ED code [49] (see appendix A.1 for technical details) to implement a bond-operator product measurement, expectation values of the P -operator could be computed. For periodic boundary conditions, the symmetry P connects sectors with different lattice momenta, i. e. , it does not commute with the group of translation and screw-axis symmetries. By performing full-spectrum ED calculations without explicit translation invariance, it could be shown that equation (7.1) is indeed satisfied by all the doublets. In accordance with the fact that no other non-trivial symmetry compatible with the S_{tot}^z quantum number could be identified, the maximal observed eigenspace dimension is two.

Another way to look at the same question is to diagonalize the Hamiltonian in a basis which is compatible with both S_{tot}^z -conservation and translation invariance.¹⁷ These data show that states form doublets if and only if their lattice momentum is not invariant under P , i. e. , the lattice momenta of doublets satisfy $k_1 = -k_2 \pmod{2\pi}$, and the lattice-momenta of non-degenerate states are integer multiples of π . Note that flipping the lattice momentum is precisely the effect of P .¹⁸ These observations prove that the observed ground-state degeneracy is due to the spatial symmetry P of the ladder graph.

7.3.2 Uniqueness of measurements

Consider an eigenstate $|\varphi\rangle$ obtained, e. g. , using the DMRG method. If this state belongs to a P -doublet, it can be expanded using the states $|g\rangle$ and $|u\rangle$ introduced in the preceding subsection. One can define states $|\pm\rangle = \frac{1}{\sqrt{2}}(|g\rangle \pm e^{i\phi}|u\rangle)$, which satisfy $P|\pm\rangle = |\mp\rangle$. For a suitable choice of ϕ , they are a

¹⁶The same holds for odd system sizes L .

¹⁷Using the reduced unit cell (see section 4.3.1).

¹⁸Consider a doublet of degenerate states $|k\rangle$ and $|-k\rangle$ with inequivalent lattice-momenta k and $-k$, respectively. Let T_a denote a translation by a lattice units. By definition, $T_a|k\rangle = \exp(-ik a)|k\rangle$. Since $P T_a P = T_{-a}$, we also have $T_a P|k\rangle = P T_{-a}|k\rangle = \exp(ik a)P|k\rangle$. Thus, $P|k\rangle$ is an eigenstate ($[P, \mathcal{H}] = 0$) which transforms according to a representation with lattice momentum $-k$. Since the states form a doublet, the only possibility is $P|k\rangle = |-k\rangle$ (up to a phase factor).

generalization of the translation-symmetry adapted states $|\pm k\rangle$ found in full-spectrum ED calculations with periodic boundary conditions (see section 7.8.1 for details). At sufficient distance from the boundaries, the open-boundary results are assumed to approximate the behavior of the infinite and/or periodic systems. I therefore use the notation $|\pm k\rangle$ rather than $|\pm\rangle$ in the following. By expanding the eigenstate $|\varphi\rangle$,

$$|\varphi\rangle = \cos \alpha |k\rangle + e^{i\theta} \sin \alpha |-k\rangle \quad ,$$

assuming translation-invariance of $|\pm k\rangle$, and applying the translation operator T_a ,

$$\begin{aligned} \langle \varphi | T_a A T_{-a} | \varphi \rangle &= \cos^2 \alpha \langle k | A | k \rangle + \sin^2 \alpha \langle -k | A | -k \rangle \\ &+ \sin \alpha \cos \alpha [\exp(-2i k a + i \theta) \langle k | A | -k \rangle + \exp(2i k a - i \theta) \langle -k | A | k \rangle] \quad , \end{aligned} \quad (7.2)$$

for any measurement operator A . Following the intuition that the behavior deep inside the bulk should not be altered by open boundary conditions, this result is expected to hold (approximately) for DMRG simulations of sufficiently large systems and operators A which are “local”, i. e., only involve sites far away from the system boundaries. Hence, A adopts a position-independent expectation value with superimposed oscillations at frequency $2k$. If A is expected to be position-independent, these rapid and (in this case, see [77, p. 6]) incommensurate oscillations can be averaged out. For instance, as pointed out in [112] (see also [164, p. 3] and [209, 255]), this is useful when calculating correlation functions $\langle \varphi | C_i C_{i+d} | \varphi \rangle$, which should not depend on the reference position i .¹⁹ Clearly, the oscillations can also be used to determine the ground-state lattice momentum k .²⁰

However, even after averaging-out of the $2k$ -oscillations, the result (7.2) still depends on α , which is unknown in general. A simplification arises if the operator A is P -invariant in addition, $P A P = A$. Then,

$$\langle \varphi | T_a A T_{-a} | \varphi \rangle = \langle \pm k | A | \pm k \rangle + \sin(2\alpha) \operatorname{Re} [\exp(-2i k a + i \theta) \langle k | A | -k \rangle] \quad ,$$

which is well-defined, i. e., independent of α , after averaging-out of the $2k$ -oscillations.

An alternative approach to get rid of the $2k$ -oscillations, which requires neither (approximate) translation-invariance nor P -invariance of A , is to solve for an orthonormal basis $\{|\varphi_1\rangle, |\varphi_2\rangle\}$ of the ground-state eigenspace. Basis-invariance of the (partial) trace then implies

$$\langle \varphi_1 | A | \varphi_1 \rangle + \langle \varphi_2 | A | \varphi_2 \rangle = \langle k | A | k \rangle + \langle -k | A | -k \rangle = \langle \pm k | (A + P A P) | \pm k \rangle \quad .$$

Note that tracing and averaging are not mutually exclusive.

The first approach requires explicit P -symmetrization of A , whereas the second approach symmetrizes A implicitly. Thus, only P -symmetrized measurements are well-defined in general. This limitation could be circumvented by adding a potential term which selects a unique ground state $|\pm k\rangle$ (e. g., a (small) uniform longitudinal DM interaction, which would be equivalent to the twist-field proposed in [300]), or by measuring²¹ $\langle \varphi_1 | A | \varphi_2 \rangle$. As will be confirmed later, the system has a tendency to form field-induced chiral order [77, 78, 131], which spontaneously breaks the symmetry P (see section 7.8). For this reason, the correlations in the maximally P -breaking states $|\pm k\rangle$ (see section 7.8.1) are of particular interest, and indeed accessible using the methods outlined above.

¹⁹In practice, the oscillatory contributions to the correlation functions are typically found to be weak.

²⁰This is different from analyzing boundary-induced Friedel oscillations as done, e. g., in [164].

²¹Even though the framework appears to provide the required methods, such measurements were not directly supported by the employed DMRG code [111] at the time.

7.3.3 Consequences for correlation functions

As detailed in the preceding subsection, only P -invariant operators yield well-defined measurements. It is important to be aware of the implications for calculations of site and bond correlation functions.

Consider the correlations between two nearest-neighbor (NN) bonds located on the same ladder leg. Assume the bonds to be non-overlapping, such that the corresponding measurement operators commute. The existence of two inequivalent Cu sites results in two types of NN bonds. Boundary effects are assumed negligible, i. e., the simulated system is taken to be sufficiently large in the case of open boundary conditions. Then, lattice translations are an approximate symmetry. Hence, consider states $|\pm k\rangle$ which are approximately translation invariant (see section 7.3.2). In this case, $C_2^b |\pm k\rangle \propto |\pm k\rangle$ should hold exactly for the infinite system and approximately in the large-but-finite case.²²

- The situation arising if the two considered bonds are of different type is illustrated in Fig. 7.4(a). The symmetry P maps the blue bonds onto the red bonds, which can be related to the blue ones using the approximate symmetries described above.²³ Thus, the measurement is (approximately) P -invariant and therefore well-defined.
- The other possibility is depicted in Fig. 7.4(b). Again, the solid blue bonds are mapped onto the solid red ones by the symmetry P . However, the aforementioned approximate symmetries only allow to relate the solid red bonds with the dashed blue bonds, which do not coincide with the initially considered ones.

The discussion for odd L is analogous and the results also apply to a single ladder leg, i. e., an isolated zigzag chain, when considering the (approximate) symmetry σ_b in place of P .

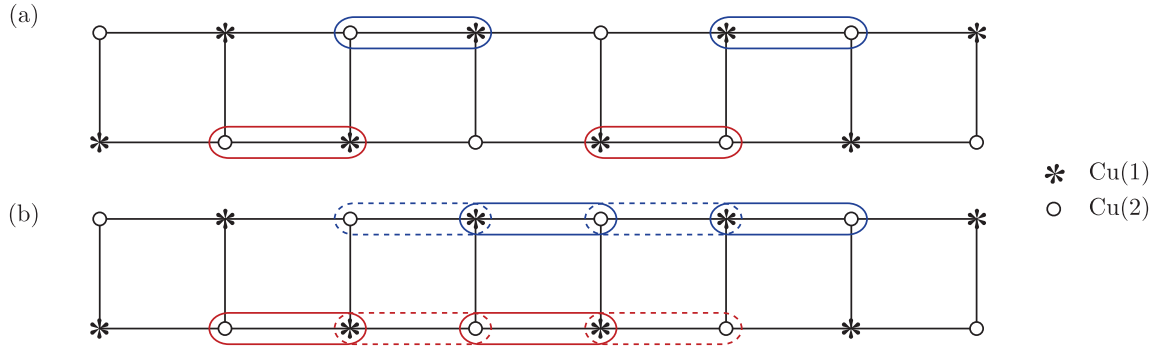


Figure 7.4: Examples of bond correlations and their transformation properties under the symmetry P for an even-length ladder ($L = 8$). See text for details.

A similar issue arises for NN-bond correlations involving bonds on opposite legs, except that the roles of odd and even distances are interchanged. By contrast, next-nearest neighbor (NNN) bonds and rung bonds do not exhibit such problems. In principle, spin-spin correlations could also be affected, even though this was not observed in practice.

²²The periodic system is symmetric under C_2^b and σ_b , $[C_2^b, \mathcal{H}] = [\sigma_b, \mathcal{H}] = 0$ and $[\sigma_b, C_2^b] = 0$. The argument made to prove $P|k\rangle \propto |-k\rangle$ in footnote 18 can be reiterated using σ_b instead of P , yielding $\sigma_b|k\rangle \propto |-k\rangle$. Since $P = C_2^b \sigma_b$, this implies $C_2^b|k\rangle = P\sigma_b|k\rangle \propto |k\rangle$, which completes the proof.

²³After accounting for bond-reversal due to P , the spin-space rotation associated with C_2^b does not affect any of the measurement operators considered in this chapter, except κ_{ij}^z which hence cannot be measured directly.

Neglecting the inequivalence of the two Cu sites increases the translation and reflection symmetry of the interaction graph. In the absence of incompatible DM interactions (D_1^b , D_4^b , and D_2^c), all correlation functions are well-defined and the subtleties discussed above do not need to be considered. The effect of a non-uniform g -factor is considered in a later section (section 7.11.3). It is generally small and tracing over the ground-state eigenspace does not appear to affect the results.²⁴ Meanwhile, e. g., the DM interactions D_1^b and D_4^b have manifest effects, which necessitate tracing over the ground-state doublet and are discussed in detail in sections 7.13 and 7.14. Yet, there always exists a distance parity (odd or even) for which the correlations obtained using the tracing and/or averaging scheme are well-defined, even in the most general case. This allows firm conclusions regarding the range and asymptotic behavior of the correlations.

7.4 Convergence

There are several parameters which control the accuracy of the DMRG calculations described in this chapter (see section 1.4.3 and references therein).

- First, the effects of finite system size L and open boundaries need to be accounted for. Ideally, L can be chosen large enough for both to be negligible. Although Fig. 5.4 suggests that this is the case for $L \gtrsim 64$, the influence of L upon the conclusions drawn from the calculations will be reconsidered carefully in the following.
- Secondly, the accuracy of the MPS ansatz depends on the bond dimension m . The energy variance $\langle \mathcal{H}^2 \rangle - \langle \mathcal{H} \rangle^2$ vanishes for an exact eigenstate (e. g., [111]). While generally preferable to, e. g., the truncation error (e. g., [350, p. 155]), this convergence indicator is not used in this work for technical reasons (see section A.1.5). Instead, the convergence of various quantities of interest as function of m is directly assessed (like in, e. g., [112]).
- Finally, the number of optimization sweeps s needs to be large enough for the variational solution to converge to a minimum (e. g., [111]). In the present work, it has been observed that correlation functions are sufficiently converged after $s = 24$ sweeps, whereas expectation values of position-dependent operators like S_i^z can require many more iterations to converge, especially for small bond dimensions m (see section A.1.7 for details).

7.5 Notation

For the sake of completeness, the parameters characterizing a certain DMRG calculation and the associated data analysis shall be reported along with the data. Besides the parameters determining the magnetic interactions (cf. section 4.3.3), the following choices play a role.

- The system size, expressed by the number of ladder rungs L .
- The MPS bond dimension m (section 1.4.3).
- The number of optimization sweeps s (section 1.4.3). Each sweep comprises two half-sweeps in opposite directions [111].

²⁴Probably because the properties associated with the two Cu sites (exchange couplings and g -tensors) are invariant under P which connects the two types of translationally-inequivalent nearest-neighbor leg bonds.

- The averaging parameter a : Correlation functions are averaged (cf. section 7.3) over reference sites/bonds contained within a subset of a ladder rungs located close to the center of the finite ladder system (see [111, 112] and section A.1.8 for details).
- Whether observables are traced over the complete ground-state eigenspace (“traced”) or a single lowest-energy state only (“ground-state only” or not mentioned).

To keep notation concise, the above symbols will be used consequently.

7.6 Spin textures

7.6.1 Triplon density

An expression for the triplon density within a finite-size ladder system was given in [136] and used in previous work ([74, p. 140] and [78]). Below, I re-iterate the steps leading to this result. This is done mainly for completeness, but also to illustrate an alternative interpretation in terms of localized triplons.

Bond-operator treatments of the simple spin ladder (section 1.3.2) identify the elementary magnetic excitations as triplons [152]—bosons with a hard-core constraint [146]. By approximating the rung-singlet (RS) ground state of the frustrated spin ladder (see section 1.3.4) by a valence-bond solid (VBS) with singlet bonds on the ladder rungs, a similar picture is obtained [179]. The boson creation and annihilation operators b_i^\dagger and b_i describing a magnetic excitation centered at ladder rung i are thus assumed to satisfy (see, e. g., [152])

$$\begin{aligned} [b_i, b_j] &= [b_i^\dagger, b_j^\dagger] = [b_i, b_j^\dagger] = 0 \quad \text{for } i \neq j \\ b_i^2 &= (b_i^\dagger)^2 = 0, \quad [b_i, b_i^\dagger] = 1 \quad . \end{aligned}$$

Following [136], the hard-core bosons $b_i^{(\dagger)}$ can be mapped onto spinless fermions $c_i^{(\dagger)}$ by means of the Jordan-Wigner transformation [193] (see [193, eqs. 31-32], [74, p. 9] and [111, eq. 11]),

$$c_j = e^{i\phi_j} b_j, \quad \text{where} \quad \phi_j = \pi \sum_{i=0}^{j-1} b_i^\dagger b_i \quad .$$

If the index i corresponds to a one-dimensional lattice, it is easy to verify that the operators c_i satisfy fermionic commutation relations and $c_j^\dagger c_j = b_j^\dagger b_j$.

The NN and NNN exchange interactions are expected to result in an effective triplon hopping amplitude t , such that the relevant Hamiltonian for a ladder consisting of L rungs becomes (see [136, p. 3] and [401, p. 9])

$$\mathcal{H}_{\text{triplon},0} = -t \sum_{r=0}^{L-1} c_{r+1}^\dagger c_r + \text{H. c.} \quad , \quad (7.3)$$

i. e., the triplons behave like non-interacting spinless fermions in one dimension [136].²⁵ Hence, the triplon density for a state with n_0 triplons is that of n_0 non-interacting fermions in a box [74, 136], i. e.

²⁵By considering the matrix elements in the Fock basis, $b_{j+1}^\dagger b_j = c_{j+1}^\dagger \exp(i\pi b_j^\dagger b_j) c_j = c_{j+1}^\dagger c_j$ (and accordingly for the H. c.). By contrast, $b_{j+2}^\dagger b_j = c_{j+2}^\dagger \exp(i\pi b_{j+1}^\dagger b_{j+1}) c_j$, which only equals $c_{j+2}^\dagger c_j$ upon restriction to the one-triplon sector.

[74, p. 140] (see also [136, 373]),

$$f(x) = \sum_{k=1}^{n_0} \frac{2}{L} \sin\left(\frac{\pi}{L+1} k x\right)^2 = \frac{1}{2L} + \frac{n_0}{L} - \frac{1}{2L} \frac{\sin\frac{(2n_0+1)\pi}{L+1} x}{\sin\frac{\pi}{L+1} x} .$$

The resulting oscillations can be regarded as Friedel oscillations [373].

Note that an onsite repulsion term has no effect for spinless fermions, such that the system described by $\mathcal{H}_{\text{triplon},0}$ corresponds to one (arbitrary since degenerate) spin-sector of the usual spin- $\frac{1}{2}$ Hubbard model in the limit $U \rightarrow \infty$. In finite systems, the latter exhibits Wigner oscillations, yielding density profiles consistent with $f(x)$ [373]. In general never-vanishing spin correlations suggest that, in addition to the hard-core constraint, triplons are generally subject to infinite-reach, although possibly weak, and tentatively repulsive [136, 208, 384] interactions (see [136, 208]). This motivates an alternative and intuitive picture of triplons being localized due to interactions.

7.6.2 Short-period oscillations and fits

As shown in Fig. 7.5, and noted in previous work (e. g. , [74, Fig. 6.12]), rapid oscillations are observed in the calculated spin textures. This motivates the following fit model for the longitudinal spin polarization [74, p. 143],

$$\langle S_{r,j}^z \rangle = A_{P(r),j}^{(u)} \left[1 + A_{P(r),j}^{(s)} \cos(qr + \phi_{P(r),j}) \right] f(r) , \quad (7.4)$$

where the indexing scheme corresponds to section 4.3.1, $P(r)$ denotes the parity (odd/even) of r (see section 4.3.1, cf. [74, p. 140]), and the envelope function $f(r)$ describes the triplon density (see section 7.6.1).

In principle, the NNN exchange couplings give rise to hopping terms of the type $b_{i+2}^\dagger b_i$ [401, p. 9] which should allow triplons to move past one another (cf. sec. 7.6.1). Nonetheless, the model (7.4) with the simple triplon-density $f(r)$ provides a good fit to the data ([78] and Fig. 7.5), suggesting that triplon-triplon interactions are extended and strong, effectively outweighing the effect of the NNN exchange couplings.

Intriguingly, the staggered components proportional to $A_{P(r),j}^{(s)}$ appear to disappear abruptly at $S_{\text{tot}}^z \sim 5$. This behavior has been noted in earlier works [74, 77, 78]. A technically more robust and direct method to estimate $A_{P(r),j}^{(u/s)} \approx A_j^{(u/s)}$ (up to normalization), is

$$A_j^{(u/s)} \approx \sum_r \frac{1}{2} (|\langle S_{r,j}^z \pm S_{r+1,j}^z \rangle| + |\langle S_{r,j}^z \pm S_{r-1,j}^z \rangle|) , \quad (7.5)$$

where the sum over r is taken over rungs inside the bulk, i. e. away from the boundaries ($L/4 \leq r \leq 3L/4$). The results of a systematic analysis of these quantities as function of system size L and MPS bond-dimension m are summarized in Fig. 7.6. The behavior of $A_j^{(u)}$ [Fig. 7.6(b)] shows that the ratio of the sublattice magnetizations remains fixed up to magnetizations $M \sim M_{\text{sat}}/2$. The sublattice magnetizations are different as a consequence of $J_2 \neq J_2'$ [77, p. 8]. As mentioned above, and noted previously [77], the staggered component $A_j^{(s)}$ [Fig. 7.6(a)] disappears in a way reminiscent of an order parameter. For fixed bond dimension m , this “transition” occurs at an approximately system-size independent magnetization (triplon density) (cf. [78]), and sharpens up with increasing system size. However, the

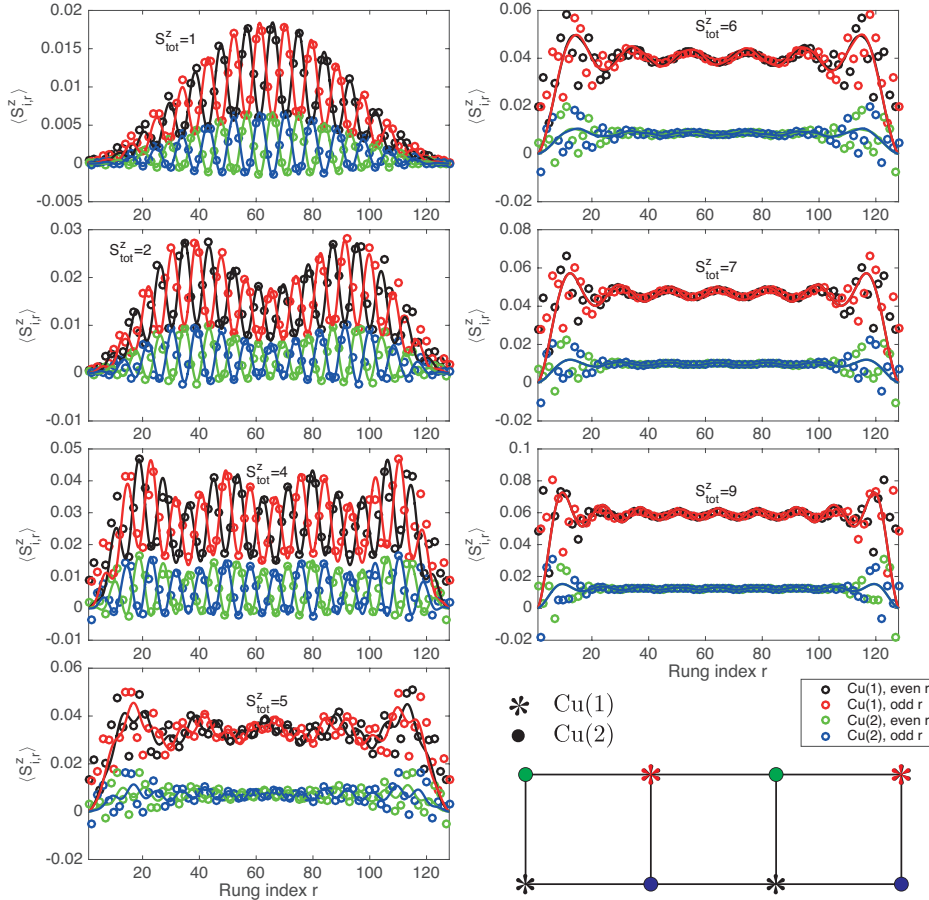


Figure 7.5: Calculated spin textures for a finite ladder with $L = 128$ rungs ($m = 512$, $s = 16$). The sub-panels correspond to the lowest-energy state in the respective S_{tot}^z sector. The color code is visualized at the bottom right. Solid lines are fits using the model (7.4). The calculations were performed using parameter set A with uniform g -factor. Equivalent results and fits were reported previously in [78] and [74, Fig. 6.12a].

staggered component $A_j^{(s)}$ is suppressed as the bond dimension m increases.²⁶ This is illustrated in Fig. 7.7(a). Consistently, the decay of the energy variance [Fig. 7.7(b)] appears to accelerate around $m = 512$, suggesting that the eigenstates in the sectors with low S_{tot}^z require correspondingly-large bond dimensions m to be accurately captured by the MPS ansatz.

To conclude, the calculations indicate that $A_j^{(s)}/A_j^{(u)} \rightarrow 0$ as $L \rightarrow \infty$ and $m \rightarrow \infty$, for magnetizations $M \lesssim \frac{1}{2}M_{\text{sat}}$. Please note that the behavior at $M \gtrsim M_{\text{sat}}/2$ is qualitatively different, and certainly deserves to be considered separately. However, this regime is unlikely to be relevant for the understanding of the high-field experiments on BiCu_2PO_6 and is thus beyond the focus of this work.

²⁶The apparent saturation of the suppression for the $L = 64$ data was identified as a boundary effect, by restricting the summation range in (7.5) even further.

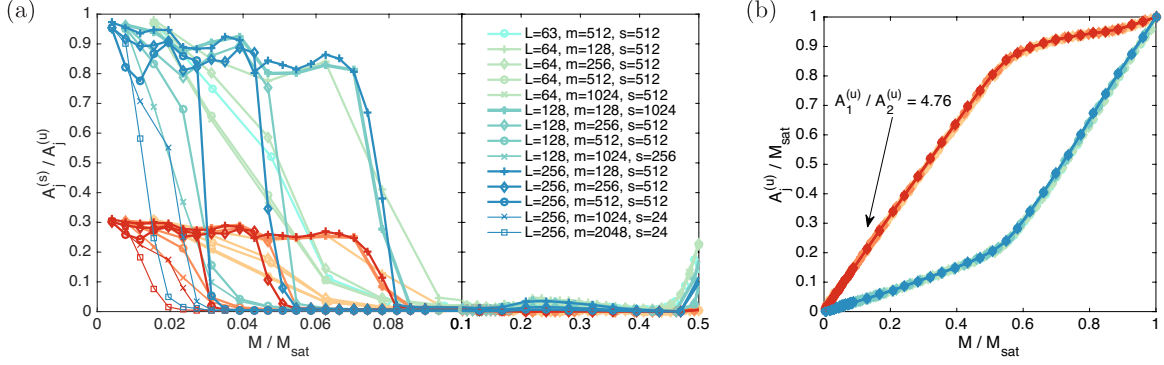


Figure 7.6: Staggered (a) and uniform (b) components of spin texture in S_{tot}^z -sector ground state, as obtained using DMRG, as function of $M/M_{\text{sat}} = S_{\text{tot}}^z/L$. Reddish colors correspond to Cu(1) sites, while bluish colors correspond to Cu(2) sites. Note the different abscissa scales in (a). The calculations were performed using parameter set A with uniform g-factor. The legend in (a) also applies to (b).

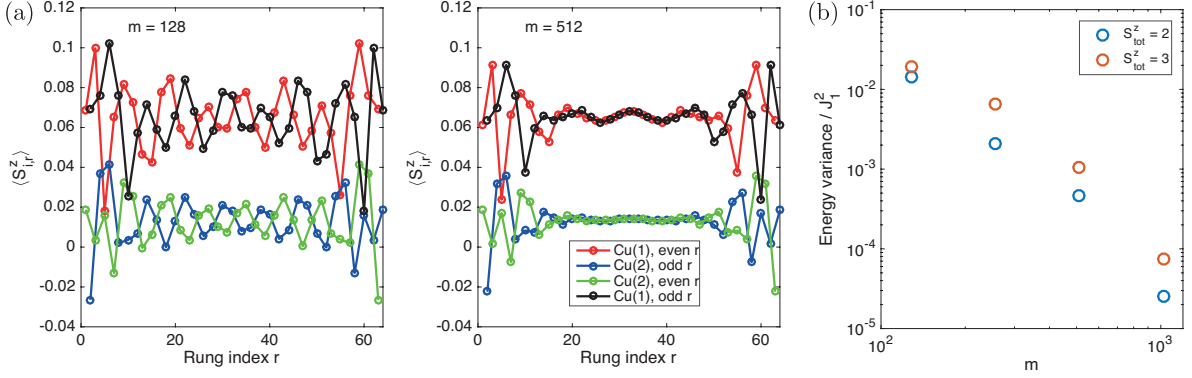


Figure 7.7: (a): Calculated spin textures in lowest-energy state of $S_{\text{tot}}^z = 5$ sector of a finite ladder with $L = 64$ rungs ($s = 512$), for different MPS bond dimensions m . (b): Energy variance of lowest-energy state of $S_{\text{tot}}^z = 2$ and $S_{\text{tot}}^z = 3$ sectors of the same system, as function of bond dimension m ($s = 512$). The calculations were performed using parameter set A with uniform g-factor.

7.6.3 Nature of short-period oscillations

This section attempts to clarify the origin of the rapid oscillations analyzed in section 7.6.2. Consistently with the preceding section, parameter set A with uniform g-factor is used as a representative choice.

First, the oscillation period shall be considered. As seen from Fig. 7.10(a), the spin correlations along the b direction correspond to a pitch angle $q \sim 0.6\pi$ (per ladder rung, i. e., over a distance of $b/2$), in agreement with previous results [78]. This is consistent with neutron scattering data [259, 316, 318].²⁷ Moreover, exact-diagonalization (ED) calculations show that the lowest-energy state with $S_{\text{tot}}^z = 1$ has

²⁷The data are reported in reciprocal lattice units (r. l. u.), which can correspond to π/b or $2\pi/b$. All references appear to use the same convention, and [259] suggests [259, pp. 127 and 132] that $1 \text{ r. l. u.} = 2\pi/a_i$ [259, 318], with a_i denoting the respective lattice constants. For the b -direction, this choice happens to be consistent with many theoretical works (e. g., [228]), despite the unit-cell doubling in BiCu_2PO_6 . The period of the measured dispersion along b is 2 r. l. u. [318], which is not obvious, since the doubled unit cell should result in back-folding at the boundary of the Brillouin zone of the crystal at 0.5 r. l. u. (see, e. g., [401, p. 10]). However, the two branches resulting due to zone-folding can be separated experimentally, as discussed in [318].

$k \sim \pm 0.6 \pi$.²⁸ To compare the above spatial periodicity with Fig. 7.5, one has to keep in mind that the decomposition of the ladder into four sub-units in these plots leads to *aliasing* of the spatial frequencies (an analogue of zone folding). Hence, the observed oscillation period of $\sim 5b$ is consistent with $2k \sim 1.2 \pi \hat{=} 0.2 \pi$.²⁹

Secondly, it is instructive to examine what happens upon tracing over the complete ground-state eigenspace (section 7.3). As illustrated in Fig. 7.8, the rapid oscillations are generally suppressed upon tracing over the ground-state doublet and only residual oscillations induced by the open boundaries remain.

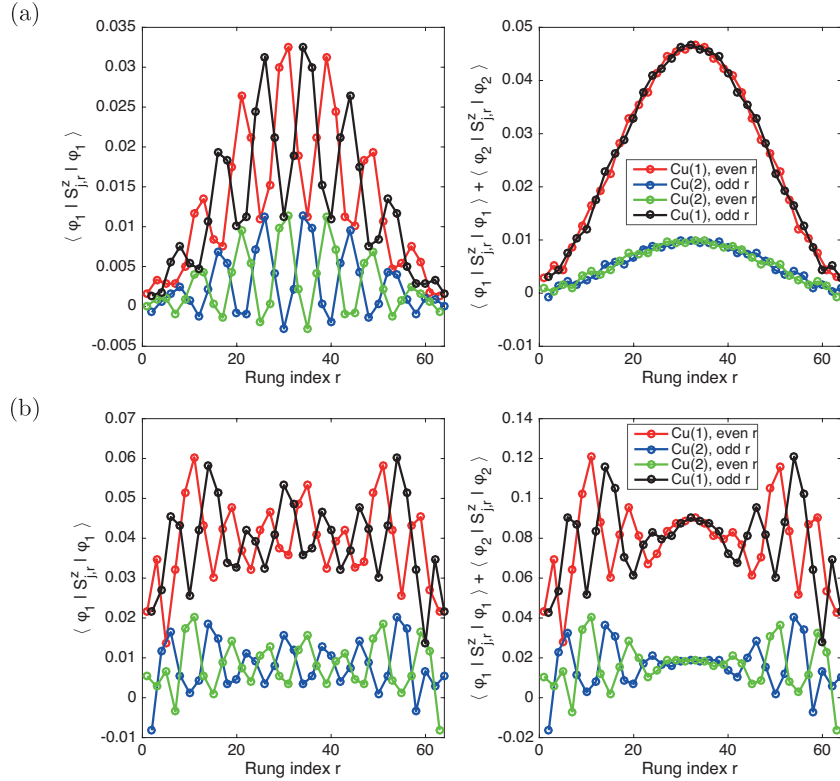


Figure 7.8: Calculated spin textures in lowest-energy state of a finite ladder with $L = 64$ rungs ($m = 512$, $s = 512$), for $S_{\text{tot}}^z = 1$ (a) and $S_{\text{tot}}^z = 3$ (b). The left panels show expectation values in the (ambiguous) ground-state, whereas the partial trace over the doubly-degenerate ground-state eigenspace is taken in the right panels.

7.6.4 Discussion

The envelope of the spin textures (cf. Fig. 7.5) is confirmed as the density profile arising due to free or, equivalently, localized triplons (see section 7.6.1 and references therein). Even though long-range interactions might stabilize a Wigner crystal of triplons, as proposed for the one-dimensional electron

²⁸The calculations performed in this work use the reduced unit cell [401] (cf. section 4.3.1) and yield a lattice momentum $\pm 0.39(5) \pi$ (L -weighted average over $10 \leq L \leq 16$), in agreement with the earlier calculations [401, Fig. 11]. However, transformation to the lattice-momentum convention corresponding to the original ladder graph involves an additional modulation with wave-vector π , resulting in $k \sim \pi \pm 0.4 \pi \pmod{2\pi}$.

²⁹Upon replacing $(J_2, J'_2) \mapsto \alpha (J_2, J'_2)$, correlations are commensurate with wavevector $k = \pi$ for $\alpha \lesssim \frac{1}{3}$ (calculations performed for $\alpha \in \{0, \frac{1}{3}, \frac{2}{3}, 1\}$, cf. section 7.11.2). Indeed, $A_j^{(s)} = 0$ in these cases, consistent with $2k = 0 \pmod{2\pi}$.

gas [352], the most likely scenario is that $f(r)$ approaches a constant in the thermodynamic limit. Also, field-induced order typically occurs in the transverse spin component (see section 7.1.1), as confirmed by the quasi long-range transverse spin correlations [77, p. 7] (cf. section 7.9).

Calculation results similar to those shown in Fig. 7.5 have been obtained earlier and were interpreted as evidence for the fractionalization of triplons into spin- $\frac{1}{2}$ solitons [74, 75, 77, 78, 131]. Fractionalization of triplons into two solitons is clearly revealed in calculations performed for the soliton-bearing compound CuGeO_3 , where the solitons are localized due to coupling to lattice degrees of freedom [132] (see section 8.7.3). Similarly, bound states with $S_z > 1$ formed by magnons in ferromagnetic systems result in an envelope wavefunction with longer modulation period [367]. Meanwhile, the envelopes of the spin texture for $S_{\text{tot}}^z = n$ obtained in this and previous [78] work are consistent with a state of n particles (see sections 7.6.1-7.6.2), which is compatible with ordinary triplons.

In section 7.6.3, it has been established that the rapid oscillations shown in Fig. 7.5 (i) have a period consistent with $2k$ and (ii) disappear at sufficient distance from the boundaries upon tracing over the ground-state doublet. These properties identify the observed oscillations as the result of ground-state degeneracy, as anticipated in equation (7.2).^{30,31} Thus, unless the ground-state degeneracy is explicitly lifted by modifying the Hamiltonian, well-defined correlation functions (section 7.3.3) are the most promising method to study the field-induced phases of the model.

7.7 Pertinent observables

The following subsections introduce a few standard concepts required for the comprehensible and reproducible discussion of the numerical calculations in later sections.

7.7.1 Definitions

All DMRG calculations are performed in the S_z -basis. The corresponding site-local observables are S_i^\pm and S_i^z , where i denotes a suitable site index in the following. Moreover, the following bond operators—two-site operators acting on magnetic bonds—are relevant for this work.

³⁰As shown in section 7.8.1, the states $|\pm k\rangle$ cannot be chosen to have real-valued coefficients in the S_z -basis. Meanwhile, the calculations reported in this section use real-valued arithmetic. Together with the disappearance of the oscillations with increasing L and m (section 7.6.2), and equation (7.2), this implies $\langle k | S_{i,r}^z | -k \rangle = 0$. Since the $S_{\text{tot}}^z = 1$ states also form a well-defined triplon branch [228, 401] (cf. section 8.7.3), site-dependent g-factors thus mainly admix states in the vicinity of each individual dispersion minimum, which suggests that they should not have any dramatic effects (to first order in perturbation theory).

³¹In section 7.6.3, the oscillation period was found to be consistent with $2k$ for $S_{\text{tot}}^z = 1$. Figure 7.5 shows that the oscillation period does not change with increasing S_{tot}^z . By contrast, the field-induced ground states obtained using exact diagonalization are consistent with $k(S_{\text{tot}}^z) = \pm S_{\text{tot}}^z k(S_{\text{tot}}^z = 1)$ (calculated in this work, relation checked to hold for even system sizes $6 \leq L \leq 16$ and $1 \leq |S_{\text{tot}}^z| \leq 4$), which indicates that triplon-triplon interactions are indeed responsible for the field-induced breaking of the reflection symmetry P and thus field-induced chirality, as described in Refs. [164, 404] (cf. [74, p. 125], see also section 7.8). Clearly, a minimum of the triplon dispersion at an incommensurate wave-vector (due to frustration) is a prerequisite (see [404]). While the “fan phase” discussed in [404] also exhibits $\langle S_i^z \rangle$ -textures with modulation wavenumber $2k$ [404], it should not exhibit long-range correlations of the longitudinal chirality [404]. This, as well as the expected ground-state lattice momentum $\pm k(S_{\text{tot}}^z) \in \{0, k(S_{\text{tot}}^z = 1)\}$ (bosons at both dispersion minima condense simultaneously [404]), is incompatible with the results obtained in the present work. Therefore, the discrepancies w. r. t. Fig. 7.5 are attributed to convergence problems, i. e., the MPS bond dimension is insufficient to fully account for the triplon-triplon interactions at $S_{\text{tot}}^z > 1$ [cf. Fig. 7.6(a)].

- The *dimer operator* or *dimerization strength* $D_{ij} = \mathbf{S}_i \cdot \mathbf{S}_j$, which is commonly used to detect dimerized phases, e. g., in the zigzag chain [443] (section 1.3.3) or the frustrated ladder [228] (section 1.3.4).
- The (*vector*) *chirality* κ_{ij} , used in many of the works reviewed in section 7.1 (e. g., [77])³²,

$$\kappa_{ij} = \mathbf{S}_i \times \mathbf{S}_j = \begin{pmatrix} \frac{1}{2i} (S_i^+ S_j^z - S_i^- S_j^z - S_i^z S_j^+ + S_i^z S_j^-) \\ \frac{1}{2} (S_i^z S_j^+ + S_i^z S_j^- - S_i^+ S_j^z - S_i^- S_j^z) \\ \frac{i}{2} (S_i^+ S_j^- - S_i^- S_j^+) \end{pmatrix} .$$

The *longitudinal spin correlations* are measured by the operator $S_i^z S_j^z$, whereas the *transverse spin correlations* are quantified using $\frac{1}{4} (S_i^+ S_j^- + S_i^- S_j^+) = \frac{1}{2} (S_i^x S_j^x + S_i^y S_j^y)$.

Guided by the phase diagram of the zigzag chain (section 7.1.2.1) and previous work (see section 7.1.4), dimerization and chirality are anticipated to characterize the field-induced phases of the considered model. Since the chiral order parameter cannot be measured directly, as detailed in section 7.8.1, it is imperative to consider correlations of the corresponding bond operators. Explicitly, the *dimer correlations* on two bonds (i, j) and (k, l) correspond to $D_{ij,kl} = D_{ij} D_{kl}$, while the (*vector*-) *chiral correlations* are given by $\kappa_{ij,kl}^{\alpha\alpha} = \kappa_{ij}^\alpha \kappa_{kl}^\alpha$ (see, e. g., [77, p. 8]).

7.7.2 Structure factors

When searching for (quasi) long-range order, the asymptotic long-distance behavior of the correlation functions is relevant. One possible approach, not followed in this work, consists in fitting the calculated correlation functions using analytical models (e. g., [164]).³³

Structure factors are a standard alternative and have also been used in previous work [77, 131]. Consider two site-dependent operators A_i and B_i , e. g., spin operators, with a compound index $i \in \{1, \dots, 2L\}$ for the sake of cleaner notation. Structure factors make use of the (discrete) Fourier transform and thereby allow model-free analyses of the correlation functions $C^{AB}(d) = \langle A_i B_{i+d} \rangle$. For the present example, Fourier analogues of the site operators are defined via $A_q = \sum_j \exp(i \mathbf{q} \cdot \mathbf{r}_j) A_j$, and similarly for B_q . For the ladder model, it is convenient to work with integer coordinates $\mathbf{r}_j = (\rho, i) \in \mathbb{N} \times \{1, 2\}$ (cf. $\mathbf{S}_{i,\rho}$ in section 4.3.1), which is compatible with previous work [77, p. 6] and the lattice-momentum units used in section 7.6.3. Following standard practice, the *structure factor* $S^{AB}(\mathbf{q})$ associated with the correlation function $C^{AB}(d)$ is defined as (cf., e. g., [379, p. 62] and [74, p. 143])

$$S^{AB}(\mathbf{q}) = \frac{1}{2L} \langle \varphi | A_q B_{-q} | \varphi \rangle = \frac{1}{2L} \sum_{j,d} \exp(i \mathbf{q} \cdot (\mathbf{r}_j - \mathbf{r}_{j+d})) \langle \varphi | A_j B_{j+d} | \varphi \rangle .$$

There are cases where the index j is one-dimensional and corresponds to a ladder rung, e. g., if only correlations along a single ladder leg are considered. Adaptation of the definition of $S^{AB}(\mathbf{q})$ then yields the *along-leg structure factor* $S_1^{AB}(q)$,

$$S_1^{AB}(q) = \frac{1}{L} \langle \varphi | A_q B_{-q} | \varphi \rangle = \frac{1}{L} \sum_{j,d} \exp(-i q d) \langle \varphi | A_j B_{j+d} | \varphi \rangle .$$

³²It appears that [418, eq. 7] can be considered a precursor to the definition of κ_{ij} .

³³Obviously, a suitable model needs to be developed. This may introduce bias by presuming, e. g., a certain type of order. Moreover, depending on the theoretical description, short-distance behavior, finite-size and/or boundary effects may not be captured by the model, which can become a problem if the accessible system sizes are limited.

Technical details regarding the computation of the structure factors are given in the appendix (section A.1.8). As discussed there, the relevant correlation functions are real-valued and symmetric, such that the corresponding structure factors are real. Finally, it is convenient to define the short-hand notations $S_{(1)}^{zz} = S_{(1)}^{S^z S^z}$ and $S_{(1)}^{+-} = \frac{1}{2}(S_{(1)}^{S^x S^x} + S_{(1)}^{S^y S^y})$.

7.7.3 Asymptotic behavior of correlation functions

As is well known, the asymptotic behavior of a correlation function is important to assess whether features correspond to actual instabilities of the system. The asymptotic behavior can be short-ranged (exponentially decaying), quasi long-ranged (algebraically decaying, i. e. , power law), or long-ranged (non-zero constant). Correlation functions $C^{AB}(d)$ decaying slower than d^{-1} with distance d clearly give rise to divergences in the structure factor $S_{(1)}^{AB}$. Due to the resemblance between the definition of the structure factor in section 7.7.2 and the simple fluctuation-dissipation theorem (A.12) (section A.5.3), such divergences typically indicate instabilities towards an ordered state (cf. [74, p. 125]).

Divergences in the structure factor can be detected conveniently by analyzing the scaling of the structure factor with the system size and extrapolating towards the thermodynamic limit—a procedure known as finite-size scaling (see, e. g. , [112]). In addition, visual inspection of linear and log-log plots (as in, e. g. , [164]) of the raw data is used to assess the asymptotic behavior of the correlation functions.

7.7.4 Number of required measurements

Through their definitions and manipulations involving angular-momentum algebra (see section A.1.9), all required correlators can be reduced to polynomials of order $n \leq 4$ in the spin operators which do not involve repeated lattice sites. Clearly, the number of required measurements is dominated by the fourth-order monomials and the measurements generally account for a significant fraction of the total computing time.

Besides allowing the use of real-valued arithmetic and generally faster calculations, S_{tot}^z conservation reduces the number of required fourth-order monomials from 3^4 to 3^2 , which is a significant improvement. For this reason, most calculations for larger system sizes L and higher bond dimensions m were performed using the S_{tot}^z -conserving model corresponding to parameter set A with site-independent g-factor.

7.8 Degeneracy, chirality and spiral structures

7.8.1 Chirality and degenerate ground states

The following section discusses the relationship between chirality and the symmetries introduced in section 7.3. Again (see section 7.3, note also discussion in section 7.15), the following arguments are all very basic, but nonetheless considered helpful for future readers. Assume a translation invariant Hamiltonian with real-valued matrix elements in the canonical S_z -basis. As shown in section 7.3, the ground-state eigenspace Ω is two-dimensional in the field-induced phase, and spanned by a pair of translation-invariant states $|\pm k\rangle$ with inequivalent lattice momenta $\pm k$. It can be shown (section A.5.10) that the longitudinal

chirality κ_{ij}^z ($i \neq j$) of a generic state $|\psi\rangle \in \Omega$ is extremal when $|\psi\rangle = |\pm k\rangle$ (up to global phase). Hence, the translation invariant states $|\pm k\rangle$ have *maximal (by magnitude) and opposite chirality*.

As discussed in section 7.3, the ladder model involves two subsets of nearest-neighbor (NN) leg bonds, related by the symmetry P . The aforementioned results imply³⁴ that the longitudinal chirality is nevertheless uniform on all leg bonds of a certain type (i. e. , all J_1 , J_2 , or J'_2 bonds, respectively).

Generalization for total chirality In the preceding argument, the existence of eigenstates with real-valued coefficients in the S_z -basis permitted conclusions about the chirality on an individual bond. For the more general case of a Hamiltonian respecting the P -symmetry, but including DM terms, this is no longer the case. However, one can still choose the states $|\pm k\rangle$ such that $P|\pm k\rangle = |\mp k\rangle$.³⁵ Consider instead the total chirality $\kappa_{\text{tot}}^z = \sum_{(i,j)} \kappa_{ij}^z$, where the sum runs over a translation- and P -invariant subset of bonds, e. g. , all nearest-neighbor leg bonds. Thus, $T_a \kappa_{\text{tot}}^z T_{-a} = \kappa_{\text{tot}}^z$ and $P \kappa_{\text{tot}}^z P = -\kappa_{\text{tot}}^z$. Finally, the total chirality of a general eigenstate $|\psi\rangle$ in the two-dimensional ground-state eigenspace, $|\psi\rangle = \cos \alpha |k\rangle + e^{i\theta} \sin \alpha |-k\rangle$, is

$$\langle \psi | \kappa_{\text{tot}}^z | \psi \rangle = \cos(2\alpha) \langle k | \kappa_{\text{tot}}^z | k \rangle + \text{Re } e^{i\theta} \sin(2\alpha) \langle k | \kappa_{\text{tot}}^z | -k \rangle .$$

Since the off-diagonal matrix element vanishes due to translation symmetry, the above proves that the states $|\pm k\rangle$ have extremal total chirality.

7.8.2 Symmetry breaking

Mathematically, any quantum superposition of the two states $|\pm k\rangle$ is a valid eigenstate. In general, this includes density-wave like states which break translation invariance (cf. section 7.6). Since the Hamiltonian is always linear and P -symmetric, other mechanisms must be responsible for selecting one of the maximally-chiral states $|\pm k\rangle$ (cf. section 7.8.1). For instance, the chiralities of neighboring ladders may be coupled due to magneto-elastic contributions to the DM interactions [304], yielding a model which is analogous to an Ising magnet (cf. [419]). Ordinary interladder couplings have a similar effect and the resulting analogy to an effective Ising model was already described in [419]. Another point of view, motivated by the ideas in [304, 356] and possible magnetoelastic effects in BiCu_2PO_6 (see section 8.7.5 and references therein), consists in considering the combined system of magnetic moments and the crystal lattice: Assume a lattice distortion due to magneto-elastic couplings, parametrized by some parameter δ . The two ground states in question are then $|\pm k, \pm \delta\rangle$. Thus, the entanglement between the spin system and the (classical) lattice degrees of freedom is expected to select one of the two states $|\pm k\rangle$.

Neglecting macroscopic quantum superpositions, the depth of the minima in the magnetic-excitation spectrum constitutes a potential barrier separating the two corresponding chiral ground states (see footnote 31 and references therein), as was already noted in [418, p. 389]. This barrier provides for ergodicity breaking (e. g. , [48]), which ultimately stabilizes the *chiral order* [419] corresponding to the state $|\pm k\rangle$.

If the interaction favoring the chiral order is compatible with crystal symmetry (or sufficiently weak), the chirally-ordered ground states $|\pm k\rangle$ should remain (approximately) translation-invariant. *Spiral order* can develop on top of chiral order by breaking of the *translation* symmetry [419, p. 565]. Since the chirally-ordered ground state is effectively non-degenerate after P -symmetry breaking, this type of order

³⁴ $\langle k | \kappa_{ij}^z | k \rangle = -\langle -k | \kappa_{ij}^z | -k \rangle = \langle k | (-P \kappa_{ij}^z P) | k \rangle$.

³⁵E. g. , given an eigenstate $|\varphi\rangle$, set $|k\rangle = \mathcal{P}_k(|\varphi\rangle)$ and $|-k\rangle = P |k\rangle$ (see section A.5.10).

appears by alteration of the ground state—similarly to how classical Néel order is known to emerge out of the highly-entangled singlet ground-state of a quantum antiferromagnet. The structure of the resulting ordered state is generally assumed to be determined by the *correlations* of the original eigenstate before the symmetry breaking. Thus, as usual (see, e.g., [74, p. 125]), instabilities towards magnetic order with wavevector q are equivalently characterized by either long-ranged (slowly decaying) spin-spin correlations with q -periodic oscillations, or a divergent susceptibility at wavevector q (cf. section 7.7.3).

Considering a typical spiral structure, it is clear that translations correspond to rotations in spin-space. Hence, in terms of spiral structures with *incommensurate* propagation vector, the translation symmetry of the states $|\pm k\rangle$ generates a *dense subset* of $U(1)$ (cf. [404], and also [419, p. 565]). Thus, the manifold of spiral states is endowed with an effective continuous $U(1)$ symmetry, as discussed in [404] for the zigzag chain. Of course, S_{tot}^z -conservation can independently provide for a continuous $U(1)$ -symmetry [404] (see also [419, p. 565]). A very similar situation arises for incommensurate charge-density waves and it is generally assumed that the spontaneous-symmetry breaking is that of a continuous $U(1)$ symmetry group in such cases (e.g., [457] or [299, p. 8]). Then, the Coleman theorem [97] (or extensions of the Mermin-Wagner theorem [45, 260]) rule out long-range magnetic order in $d \leq 2$ dimensions (cf., e.g., [68]). This aspect is revisited in section 7.16.

7.9 Results

The following results illustrate the behavior of the Heisenberg Hamiltonian (4.1) in the absence of DM interactions. Parameter set A (section 4.3.3) is used as a representative example, and a site-independent g -factor is assumed for computational efficiency. Since model and method coincide with previous works [74, 77, 131, 401], a significant overlap with those works is inevitable. Nonetheless, the documentation of results confirming the previous calculations is considered important in order to establish the validity of the numerical treatment and allow for a comprehensive and hence self-consistent presentation of the continuing work discussed in subsequent sections of this chapter.

7.9.1 Magnetization

The calculated magnetization $M(H)$ is shown in Fig. 7.9. It is converged as function of m and s and reproduces previous results [401]. The steps in the data are a finite-size effect. As discussed in [401], the square-root singularities close to onset and saturation are consistent with the simple picture reviewed in section 7.1.3. Meanwhile, this model also predicts additional cusps in $M(H)$ for strongly-frustrated systems like BiCu_2PO_6 [384], which are not observed in the calculations. By reconsidering the arguments leading to the prediction [384] (cf. section 7.1.3), the absence of cusps implies that triplon-triplon interactions are important already at low magnetizations—a conclusion which is consistent with recent neutron-scattering experiments [318].

7.9.2 Spin correlations

The calculated spin structure factors and spin correlations are generally consistent with previous results [77, Fig. 6] (see also [74, Fig. 6.13]) and their discussion in [77] (see also [74, pp. 143-144]).

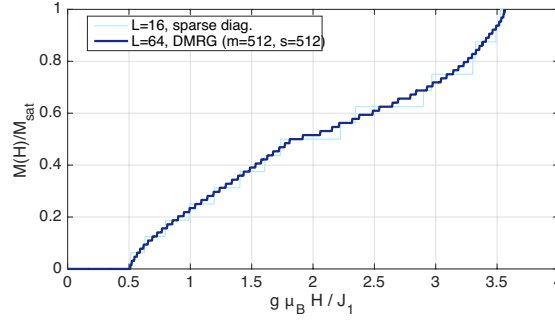


Figure 7.9: Calculated magnetization, reproducing the results [401, Fig. 12] of the original work for parameter set A [401].

The spin structure factors are shown in Fig. 7.10. The longitudinal spin correlations [Fig. 7.10(b)] exhibit rapidly-decaying incommensurate correlations (see [77, p. 6]), associated with the incommensurate minimum of the triplon dispersion (cf. sections 1.2 and 7.1.3), as well as trivial long-range features at wavevector $\mathbf{q} = (0, 0)$ due to the uniform magnetization (see [77, p. 8]). In addition, as noted in previous work [77, p. 8], the inequivalence $J_2 \neq J'_2$ leads to the preferential magnetization of one sublattice, giving rise to a long-range component at $\mathbf{q} = (\pi, \pi)$, which becomes maximal close to $M = \frac{1}{2}M_{\text{sat}}$.

The transverse spin correlations [Fig. 7.10(a)] are incommensurate and quasi long-ranged for $0 < M/M_{\text{sat}} < 0.5$ (see [77, p. 6]). Another region with quasi long-ranged transverse spin correlations is observed at higher magnetization. Finite-size scaling of the structure factors (Fig. 7.11) indicates that the decay of the transverse spin correlations is slow enough to give rise to a diverging susceptibility for magnetizations $0 < M/M_{\text{sat}} < 0.5$ (cf. section 7.7.3). This conclusion is consistent with direct inspection of the corresponding correlation functions (see Fig. 7.12 and section 7.12).

7.9.3 Dimerization

The dimerization strength on the different bonds in the system is shown Fig. 7.13. As noted in previous work [401] (see also [77, p. 6] and [74, p. 142]), the rung bonds (J_4) are strongest at low-to-intermediate magnetization, which is consistent with the rung-singlet phase suggested by the zero-field phase diagram of the frustrated ladder [228] (Fig. 1.4). Also, one observes that the J'_2 bonds are broken preferentially, as expected for $J'_2 < J_2$ (see [77, p. 8]).

The along-leg structure factors obtained from the dimer correlations of the rung and nearest-neighbor leg bonds are shown in Fig. 7.14. The dominant long-range components at $q = 0$ correspond to the dimerization strength shown in Fig. 7.13. In addition, rapidly-decaying correlations with $q = \pi$ are observed on the J_1 bonds. These are remnants of the columnar-dimer phase of the frustrated ladder [131, 228] (cf. section 1.3.4 and 5.4.3). Except for the static correlations at $q = 0$, the dimer correlations are generally short-ranged³⁶ for $0 \leq M/M_{\text{sat}} < 0.5$, in accordance with earlier calculations [77, 131]. This is confirmed by direct inspection of the correlation functions (see Fig. 7.15 for an example), which are generally consistent with previous work [131]. The dimer correlations on the next-nearest neighbor (NNN) bonds (structure factors not shown) closely resemble those on the J_1 and J_4 bonds in the re-

³⁶The statement refers to the component with the dominant weight, since the correlation functions generally contain algebraically-decaying components (see section 7.12).

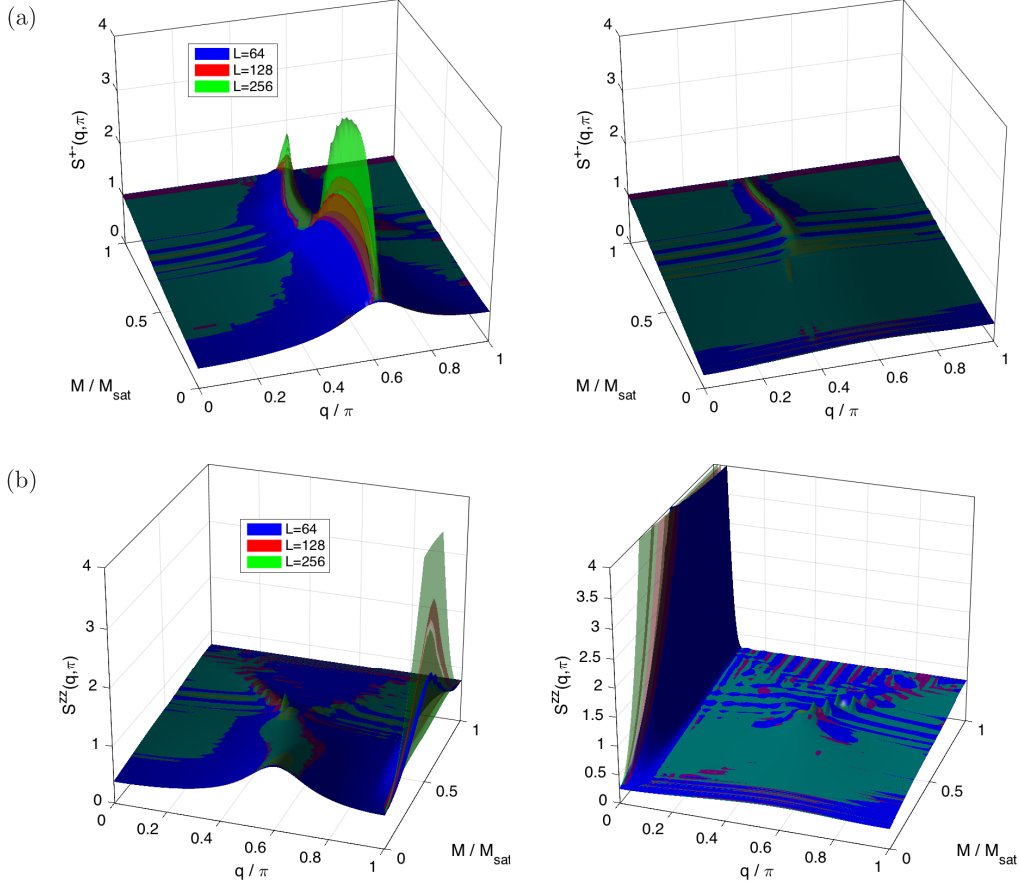


Figure 7.10: Structure factors $S^{+-}(q_{\parallel}, q_{\perp})$ (a) and $S^{zz}(q_{\parallel}, q_{\perp})$ (b) of transverse and longitudinal spin correlations, respectively ($m = 512$, $s = 512$, $a = 8$).

gion $0 < q < \pi$. Trivial long-range correlations appear at $q = \pi$ as a result of the alternation of the inequivalent J_2 and J'_2 bonds (see also Fig. 7.15).

7.9.4 Chirality

Consider the correlations of the longitudinal chirality κ_{ij}^z first (Fig. 7.16). Its correlation functions are generally consistent with previous results [77, Fig. 7] (see also [74, Fig. 6.14]) and their discussion in [74, 77]. The leg bonds exhibit uniform ($q = 0$) long-range correlations, whereas the rung correlations decay rapidly. Exemplary correlation functions are depicted in Fig. 7.18(a)³⁷ [see also Fig. 7.26(b)]. Note that a sufficient MPS bond-dimension m is crucial for the observation of long-range correlations of the longitudinal chirality. The appearance of long-range chiral correlations for $0 < M/M_{\text{sat}} < 0.5$ will be considered in section 7.10.2 in more detail. The absence of $q = \pi$ components in the correlations on the leg bonds is consistent with section 7.8.1. Trivial components with $q = \pi$ in the correlation functions for the NNN bonds (J'_2 and J_2) [Fig. 7.16(c-d)] arise due to the alternation of the corresponding bonds

³⁷Long-wavelength modulations result due to the wavefunction of the localized triplons (cf. section 7.6.1).

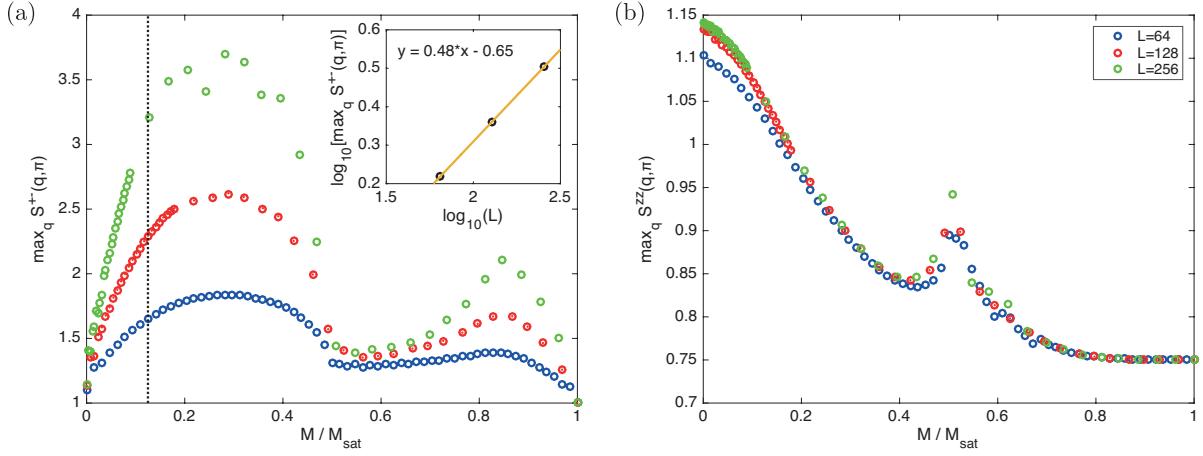


Figure 7.11: Maximal value $\max_q S^{+-}(q, \pi)$ of structure factors $S^{+-}(q, \pi)$ (a) and $S^{zz}(q, \pi)$ (b) for $0.5\pi \leq q \leq 0.7\pi$, as function of magnetization M/M_{sat} (cf. Fig. 7.10). The inset of (a) shows a power-law fit to the scaling behavior of $\max_q S^{+-}(q, \pi)$ with the system size L at $M/M_{\text{sat}} \approx 0.125$ (dotted line). Red dots, calculated with $L = 128$, $m = 1024$, and $s = 256$, confirm convergence with the MPS bond dimension m . The legend of (b) also applies to (a).

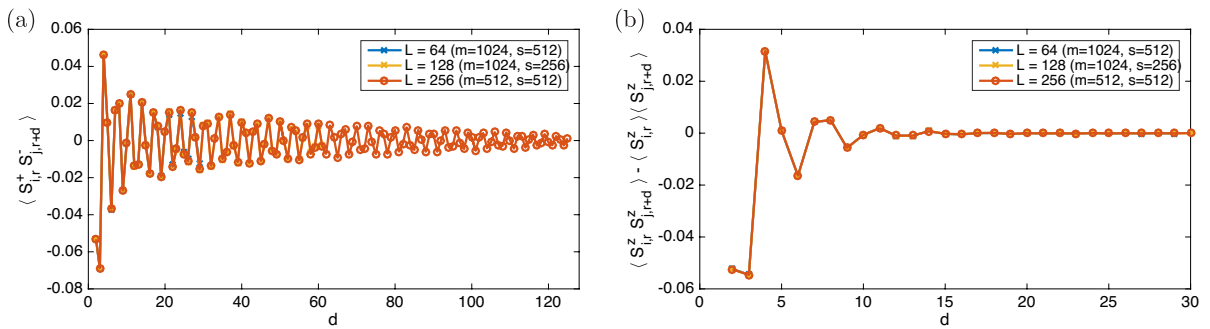


Figure 7.12: Transverse (a) and longitudinal (b) spin correlation functions measured along one leg of the ladder ($a = 8$). The distance in ladder units is denoted by d and the reference position corresponds to a Cu(1) site. The magnetization is $M/M_{\text{sat}} = S_{\text{tot}}^z/L = 5/64 \approx 0.078$.

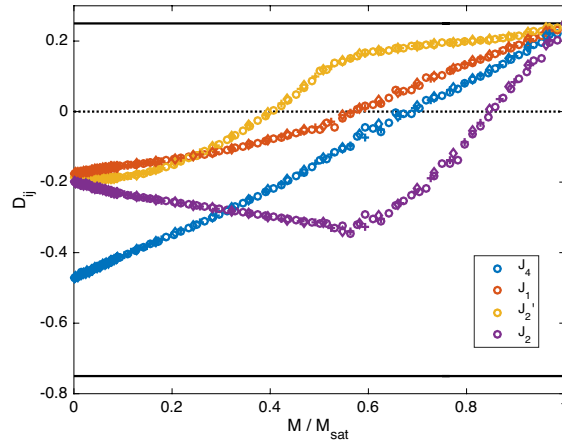


Figure 7.13: Dimerization strength as function of magnetization for the different bond types present in the system. System sizes are $L = 64$ (circles), $L = 128$ (crosses), and $L = 256$ (diamonds) [$m = 512$, $s = 512$]. Solid black lines indicate the limiting values for a system consisting of an isolated dimer.

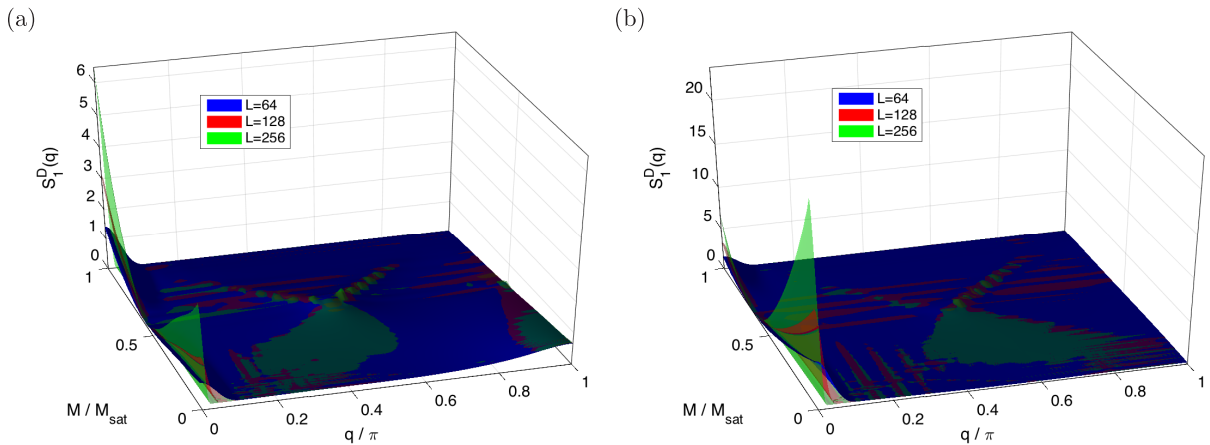


Figure 7.14: Along-leg structure factors of dimer correlations on the nearest-neighbor leg (a) and rung (b) bonds, corresponding to the exchange couplings J_1 and J_4 , respectively ($m = 512$, $s = 512$, $a = 8$).

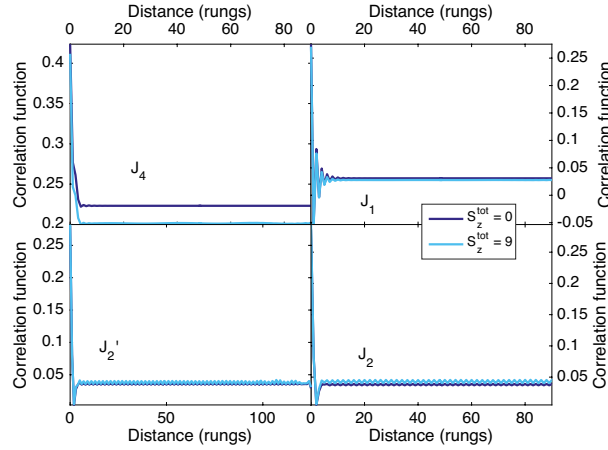


Figure 7.15: Dimer correlations for different types of bonds ($L = 256$, $m = 2048$, $a = 2$). Correlations are measured on one ladder leg for the J_1 (NN) and J_2/J_2' (NNN) bonds. The magnetization is $M/M_{\text{tot}} = S_{\text{tot}}^z/L$, with S_{tot}^z as indicated in the legend.

along each leg of the ladder.

The structure factors of the correlations of the transverse chirality κ_{ij}^x , or equivalently κ_{ij}^y , are shown in Fig. 7.17. The uniform component (at $q = 0$) remains short-ranged for $0 \leq M/M_{\text{sat}} \leq 0.5$. For $0 < M/M_{\text{sat}} < 0.5$ additional quasi long-ranged components are observed at incommensurate wavevectors [see also Fig. 7.18(b)]. In this magnetization range, the raw data are consistent with a power-law which decays slower or equally fast as the inverse distance and hence corresponds to an instability of the system (cf. section 7.7.3). Such oscillations have also been noted in previous works [255, 367] and an intuitive explanation for this behavior is given in section 7.10.3.

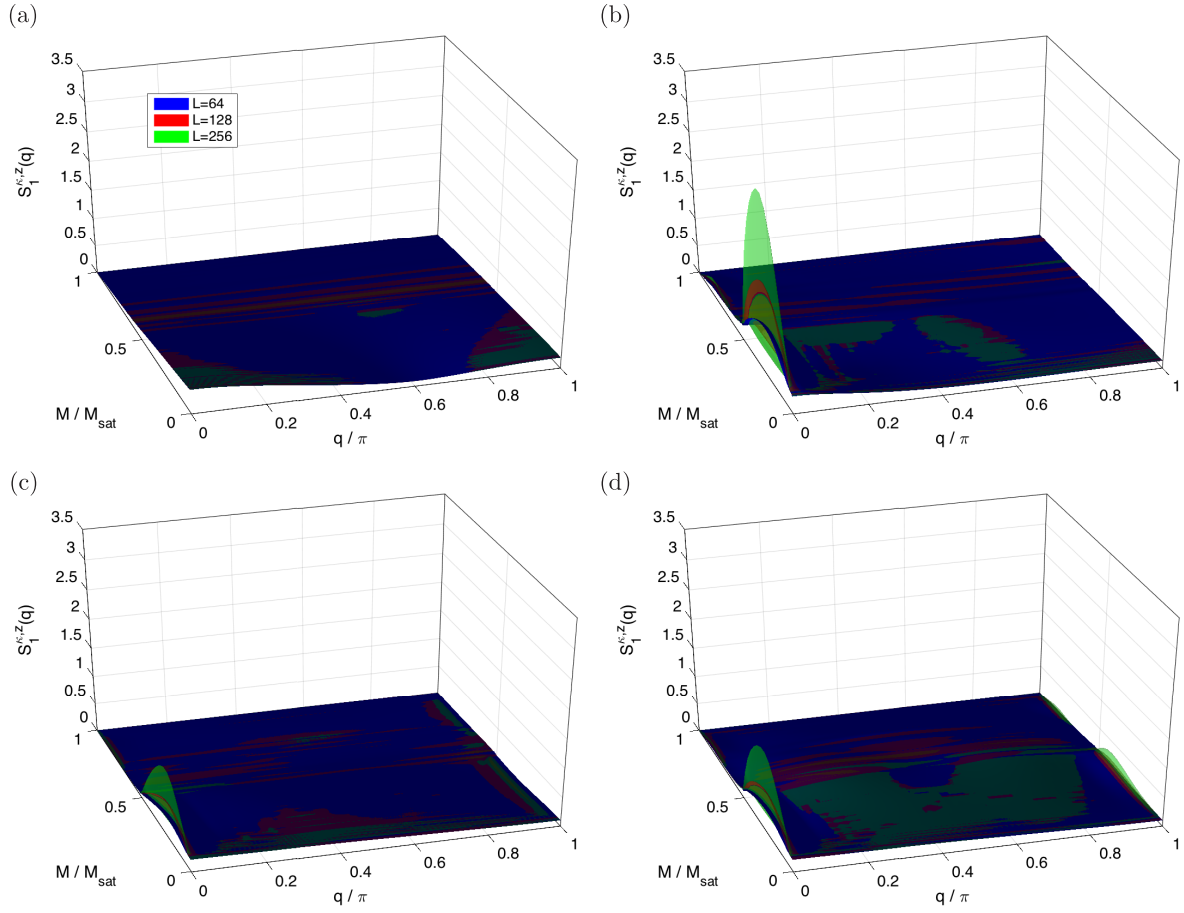


Figure 7.16: Along-leg structure factors of longitudinal chirality on rung bond J_4 (a), nearest-neighbor bond J_1 (b), and next-nearest neighbor bonds J'_2 (c) and J_2 (d) ($m = 512$, $s = 512$, $a = 8$). In (c) [(d)], the correlation functions are calculated using alternating pairs of equivalent and inequivalent bonds, with the reference bond fixed to a J'_2 [J_2] bond.

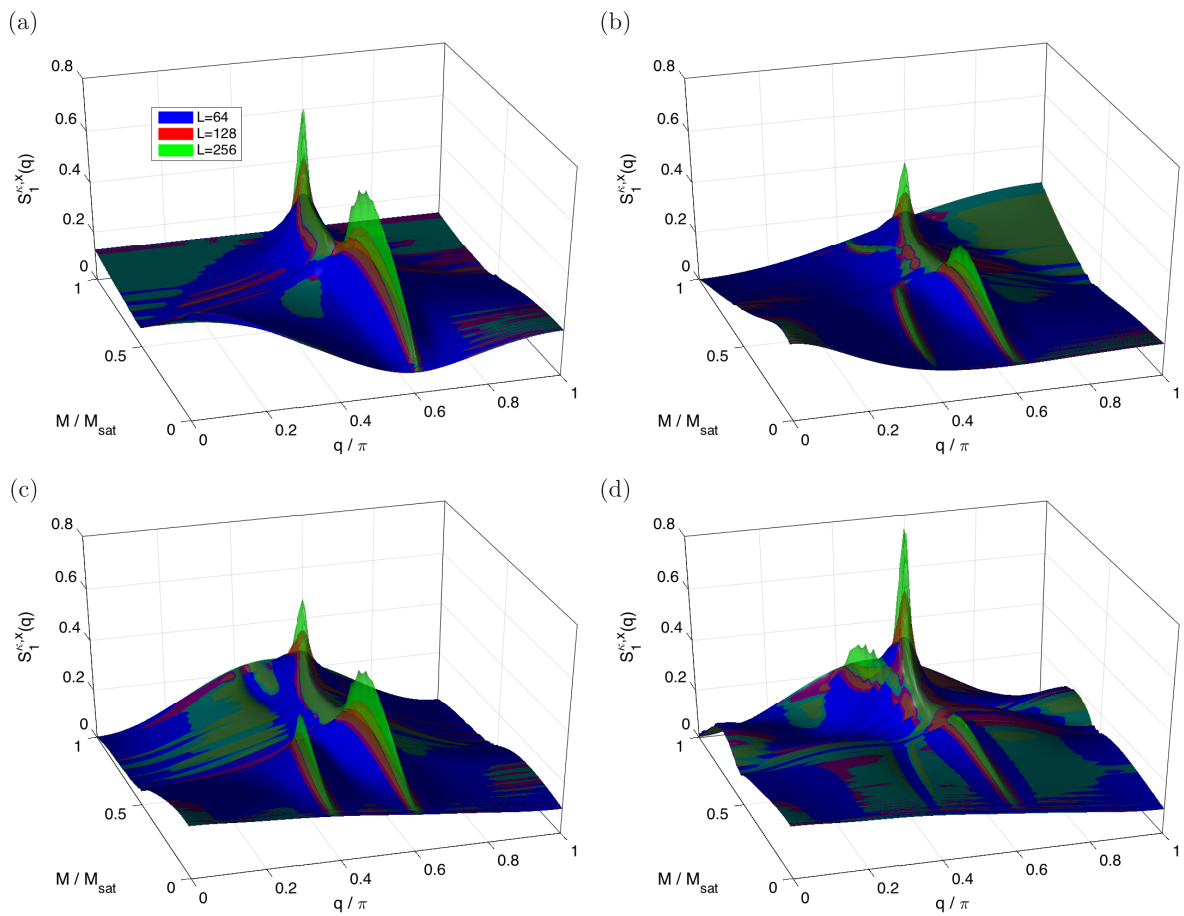


Figure 7.17: Along-leg structure factors of transverse chirality on rung bond J_4 (a), nearest-neighbor bond J_1 (b), and next-nearest neighbor bonds J'_2 (c) and J_2 (d) ($m = 512$, $s = 512$, $a = 8$). In (c) [(d)], the correlation functions are calculated using alternating pairs of equivalent and inequivalent bonds, with the reference bond fixed to a J'_2 [J_2] bond.

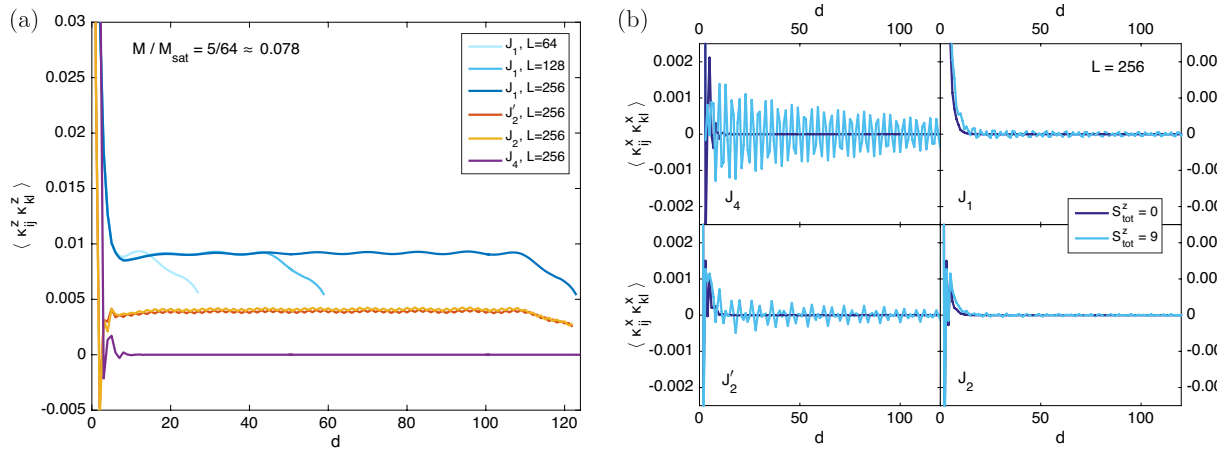


Figure 7.18: Correlations of longitudinal (a) and transverse (b) chirality on various bonds of the frustrated ladder model, as function of distance d (measured in units of nearest-neighbor bonds). For (b), the magnetization is $M/M_{\text{sat}} = S_{\text{tot}}^z/L$, with S_{tot}^z and L as indicated in the figure. The calculation parameters are $a = 8$ and $m = 512$ for (a), as well as $a = 2$ and $m = 2048$ for (b). The “ J_2' ” (“ J_2 ”) correlation functions are calculated using alternating pairs of equivalent and inequivalent bonds, with the reference bond fixed to a J_2' (J_2) bond. (Subfigure (a) is an extended version of a figure previously used in [312].)

7.10 Interpretation

In this section, the calculation results presented in section 7.9 are used to obtain a self-consistent picture of the field-induced phases of the considered model. Guided by the experimentally-accessible range of magnetic fields, the primary focus is on the phase adopted for magnetizations $0 < M/M_{\text{sat}} < 0.5$. As in the preceding section, parameter set A with site-independent g -factors is used.

7.10.1 Chiral order

The field range $0 < M/M_{\text{sat}} < 0.5$ is characterized by rapidly-decaying longitudinal spin correlations and quasi long-range transverse spin correlations. Moreover, the longitudinal chirality acquires a uniform expectation value on the leg bonds.³⁸ No dimerization tendency is observed for $M/M_{\text{sat}} \lesssim 0.5$. All these features are consistent with previous work [77, 131], as well as with the chiral phase of the zigzag chain reviewed in section 7.1.2.1. Therefore, consistently with the previous work [131], the corresponding phase of the frustrated ladder is referred to as the “*chiral phase*” from here on.

The slow decay of the transverse spin correlations reflects the fact that the chiral phase is unstable towards spiral order if the breaking of the remaining $U(1)$ symmetry is permitted [164] (see section 7.8.2 and previous discussion in [77, pp. 7-8]). Based on these results, a system consisting of suitably-coupled frustrated spin ladders with the considered exchange couplings is expected to adopt a spiral (helical) magnetic order in which the spiraling moments lie in a plane perpendicular to the magnetic field [77, 164]. The pitch angle along the leg direction is determined by the wavevector of the transverse spin correlations [164, p. 11]. Since the dominant transverse spin correlations are confirmed to be in the $q_{\perp} = \pi$ sector (see previous results in [77, Fig. 6b]), the magnetic structure on the two ladder legs differs by a phase of π , i. e., the AFM correlations required by the rung bonds are satisfied completely [131]. Thus, everything is fully consistent with previous work [74, 75, 77, 78, 131] and the corresponding spiral structure [77, 131] is visualized in Fig. 7.19(a).

7.10.2 Onset of chiral order

In previous work [74, 77, 131], a phase-transition-like onset of the chirality was observed (see [77, Fig. 7], and also [74, Fig. 6.14]). This observation is confirmed in the calculations performed in the context of this work. Moreover, comparison of results for different system sizes shows that the “critical magnetization” for the appearance of long-range chiral correlations is independent of system size (cf. [78]). Since the magnetization corresponds to the triplon density, this hints towards the importance of triplon-triplon interactions (cf. [78]). However, as implied in [78, pp. 141,144] and explicitly shown in the inset of Fig. 7.20(a), the onset of chirality coincides with the disappearance of the spurious $2k$ -oscillations in the spin texture (cf. Fig. 7.6 and section 7.6.3). Since the oscillations, measured by $A_j^{(s)}$ (section 7.6.2) were shown to disappear with increasing MPS bond dimension m , it makes sense to check the evolution of the chiral correlations with m . From the results depicted in Fig. 7.20(a) it becomes clear that what looked reminiscent of a phase transition for small m , turns into a smooth onset in the limit

³⁸This is confirmed by calculating the correlations of longitudinal chirality on nearest-neighbor leg bonds residing on opposite ladder legs.

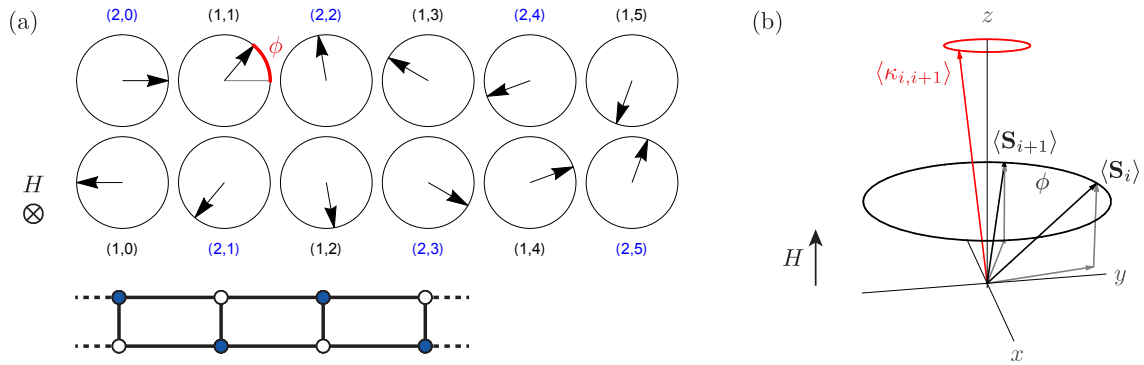


Figure 7.19: (a): Illustration of expected spiral structure, as proposed in previous work [74, Fig. 3a] (see text for details). The arrows represent the ordered moment $\langle \mathbf{S}_{i,r} \rangle$ on site (i, r) , where the indexing convention is consistent with section 4.3.1. For visualization purposes, a section of the corresponding ladder graph is depicted at the bottom (next-nearest neighbor bonds have been omitted for readability). Black/white [blue/blue] indices/vertices correspond to Cu(1) [Cu(2)] sites. (b): Spin canting in the spiral phase for two magnetic moments corresponding to a pair of sites which are nearest neighbors along the leg direction of the ladder. The two circles indicate the geometrical loci visited by the magnetic moments (black) and the chirality (red) upon propagation of the (incommensurate) magnetic structure along the ladder direction.

$m \rightarrow \infty$.³⁹ This strongly suggests that the chiral phase occupies the entire range of magnetizations between 0 and approximately $M_{\text{sat}}/2$. Note that similar delayed-onset behavior was already reported for the ferromagnetic zigzag chain, and convergence problems were proposed as one possible explanation [383].

Direct inspection of the correlation functions [Fig. 7.20(b)] confirms that long-range chiral correlations appear immediately as soon as the system gets magnetized. By comparing the top and bottom panels of Fig. 7.20(b), it further becomes evident that the chiral correlations are modulated by the wavefunction of the localized triplons (cf. section 7.6.1). Surprisingly, a minimum of two triplons is required to clearly establish long-range chiral correlations. While this observation does not affect the conclusions about the thermodynamic limit, it corroborates that triplon-triplon interactions are indeed essential to the formation of chiral correlations, as was conjectured in previous work [77, 78, 131] (albeit for solitons), and described earlier in, e. g., [404] (see also [367]).

Finally, besides confirming the somewhat pathological nature of states containing a single triplon, Fig. 7.21 shows that slowly-decaying transverse spin correlations develop concomitantly with the chirality as soon as the system gets magnetized. Therefore, as discussed in [419], the most promising scenario for observing two separate phase transitions corresponding to chiral order and spiral order is competition between thermal fluctuations and residual interactions required for the $U(1)$ -symmetry breaking (see section 7.8.2).

³⁹It has been checked that reducing the number of DMRG sweeps s from 512 to 24 does not affect the chiral correlations. Similarly, the data in Fig. 7.20(a) show that reducing the averaging range from $a = 8$ to $a = 2$ has negligible effect. Note that even after setting $a = 2$ and $s = 24$, the largest bond dimension reachable with reasonable effort was $m = 2048$.

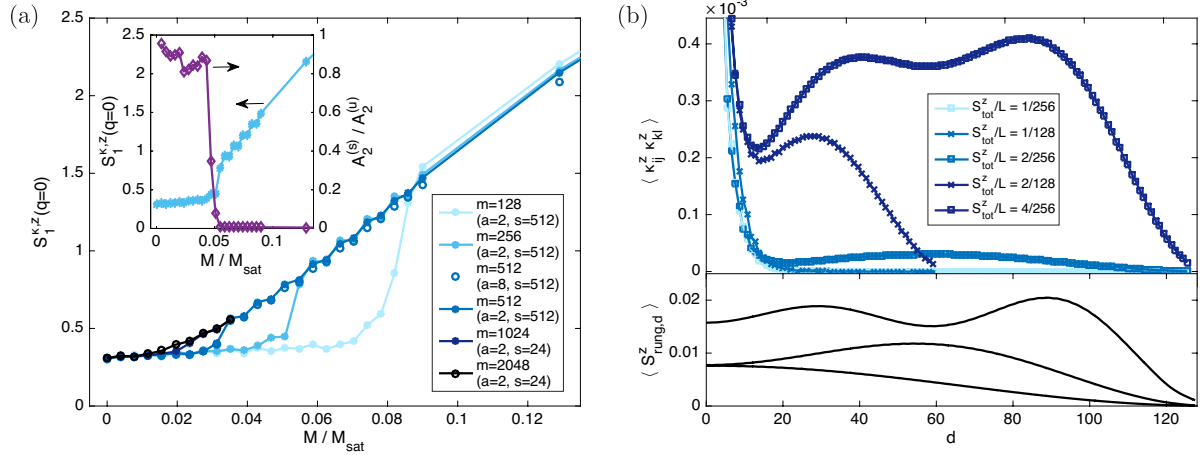


Figure 7.20: (a): Magnitude of uniform ($q = 0$) structure factor of longitudinal chirality on nearest-neighbor leg bonds as function of magnetization. The inset shows a comparison with data from Fig. 7.6(a) ($m = 256$, $L = 256$). (b): Correlations of longitudinal chirality on nearest-neighbor leg bonds as function of distance d (measured in units of nearest-neighbor bonds). The calculations used $a = 2$ and $m = 1024$ ($m = 2048$) for $L = 128$ ($L = 256$), and convergence with bond dimension m was checked. The bottom panel shows the spatial distribution of the calculated rung-magnetization, which equals the triplon density, for a system with $L = 256$ rungs and $S_{\text{tot}}^z = 1, 2, 3$. The position $d = 0$ corresponds to the reference position used to evaluate the correlation functions (approximately at the center of the ladder). A smoothing-spline interpolation was used to suppress short-period oscillations in $\langle S_{\text{rung},d}^z \rangle = \langle S_{1,d}^z + S_{2,d}^z \rangle$. (Subfigure (b) reused from [312].)

7.10.3 Spin canting

It is instructive to reconsider the correlations of the transverse chirality shown in Fig. 7.17. Key to an interpretation is the observation that their quasi long-ranged components resemble the transverse spin correlations [Fig. 7.10(a)]. In addition to the spiraling moments, the magnetic structure exhibits a small longitudinal component corresponding to the uniform magnetization, which results in a *canted spiral* structure [77, 78, 131]. The situation corresponding to the nearest-neighbor bond J_1 is illustrated in Fig. 7.19(b). The canting of the ordered moments gives rise to a small transverse chirality component, which delineates a spiral upon propagation of the magnetic structure along the ladder axis. This is in fact consistent with previous analytical results for the zigzag chain [255, eqs. 8-9]. Similarly, a spiraling

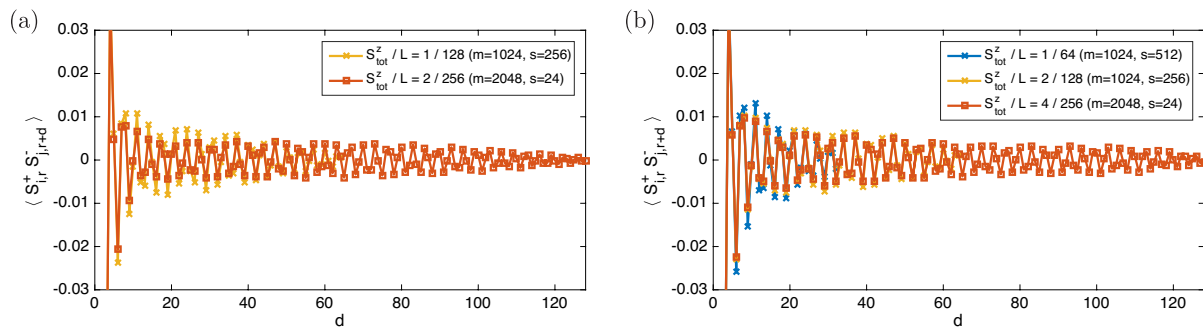


Figure 7.21: System-size dependence of transverse spin correlation functions close to the magnetization onset ($a = 2$).

transverse chirality component appears on the rung bonds.⁴⁰ Thus, once the $U(1)$ -symmetry associated with the transverse magnetic moments is broken, long-range correlations of the transverse chirality develop at the wavevector corresponding to the spiral pitch angle, i. e. , the maximum in the transverse spin structure factor. Conversely, a perturbation which enforces a transverse chirality with suitable (incommensurate) periodicity, would create a pinning potential which locks the transverse moments.

Thus, the slow decays of the correlations of the transverse chirality and the transverse spin correlations both correspond to the very same instability. This is corroborated by the similar asymptotic behavior of the transverse chiral and transverse spin correlations [see, e. g. , Fig. 7.26(b)]. In particular, the features in the correlations of the transverse chirality do not indicate any competing instabilities for $0 \leq M/M_{\text{sat}} < 0.5$. The conclusions reviewed in section 7.10.1 are therefore unaltered, except for the rather obvious amendment that the uniform longitudinal magnetization needs to be considered in addition to the planar-spiral component of the magnetic structure [Fig. 7.19(a)], as already pointed out in previous work [77, 78].

7.11 Influence of model parameters

In this section, the effect of varying various model parameters, especially the exchange couplings, is considered. Since the preceding results are largely independent of system size L (e. g. , Fig. 7.12)—at least within the chiral phase—, most of the following calculations use $L = 64$. The smaller system size also requires smaller bond dimensions m , where $m = 512$ was found to be well sufficient. Consistently with the preceding sections, parameter set A with site-independent g-factors is used as a starting point.

The purpose of this section is twofold. First, it serves as a sensitivity analysis, to make sure that the conclusions described above (and in previous work [74, 77]) do not depend on the precise values of the model parameters. Secondly, additional insights can be gained by considering certain limiting cases. The parametrization used for varying the exchange couplings is the same as in section 5.4.

7.11.1 Effect of the rung exchange

For $J_4 = 0$, the frustrated ladder corresponds to two decoupled zigzag chains. It therefore makes sense to compare the results with the phase diagram of the zigzag chain [164] [Fig. 7.2(b)] with an effective frustrating coupling of $(J_2 + J'_2) = 0.75 J_1$. The behavior inferred from inspection of the correlation functions⁴¹ and their structure factors, in a manner analogous to the preceding sections, is consistent with the following succession of field-induced phases (cf. [164]): (i) dimerized ground-state, (ii) TLL2 phase, (iii) VC phase, (iv) a narrow non-chiral phase with short-range transverse spin correlations (TLL1 with dominant longitudinal spin correlations or SDW_2 ⁴²), (v) $1/3$ -plateau (P), (vi) TLL1 phase with dominant

⁴⁰Modulation due to the presence of two inequivalent sites gives rises to two peaks in the structure factors for the leg bonds [Fig. 7.17(b-d)].

⁴¹I focus on the magnetization curves, the correlations of the transverse and longitudinal spin components, as well as the correlations of the longitudinal chirality, since these quantities contain most information and are predominantly studied in the literature (e. g. , [164]). Note, however, that the relatively small system size makes it difficult to reliably assess the range of the correlation functions. Except for the chiral correlations, whose long-range nature is rather easy to check, the correlations are therefore primarily classified depending on whether they decay faster than inverse distance or not.

⁴²Since S_{tot}^z of each chain changes in units of one, the TLL1 phase appears more likely [164].

longitudinal correlations, (vii) TLL2 phase. In addition, the TLL1 phase is interrupted⁴³ by a magnetization plateau at $M/M_{\text{sat}} = 1/2$, which is related to $J_2 \neq J_2'$ (see section 7.11.3) and will be discussed later (section 7.12). Except for this narrow additional phase, the observations are thus fully consistent with the phase diagram of the zigzag chain.

For $J_4/J_1 = 0.25$, the sequence of phase transitions is very similar, except for a few important differences: (i) The TLL2 phase at low magnetization is replaced by the VC phase. (ii) The TLL1 phase below the $1/3$ -plateau is not clearly established by the correlation functions, suggesting that it is either extremely narrow or absent. (iii) The $1/3$ -plateau is weakened by the rung coupling.

For even higher rung couplings ($J_4/J_1 \geq 0.5$), the chiral phase occupies the entire magnetization range $0 < M/M_{\text{sat}} < 0.5$.⁴⁴ Also, the dimer crystal present in the ground state of the zigzag chain melts, as already reported in [228] for the symmetric frustrated ladder ($J_2' = J_2$) and discussed in section 5.4.3 [Fig. 5.11(b)]. A (small) $1/2$ -plateau is always present. The phase diagram at $M/M_{\text{sat}} > 0.5$ is less clear (see section 7.12).

The evolution of magnetization and chiral correlations upon varying the rung coupling is summarized in Fig. 7.22.⁴⁵ The magnetization curves [Fig. 7.22(a)] show that the incompressible states [136] (plateau phases) become more stable in the limit $J_4 \rightarrow 0$. For the $1/3$ -plateau this result is intuitive: This phase corresponds to an “up-up-down” magnetic structure [164, 301], which is clearly incompatible with the antiferromagnetic rung coupling (see [387] for a more advanced treatment). The $1/2$ -plateau is considered in more detail later (see sections 7.11.3 and 7.12). Focusing on the chirality [Fig. 7.22(b)] in the magnetization range $0 < M/M_{\text{sat}} < 0.5$, it becomes evident that the TLL phases surrounding the chiral phase [cf. black arrows in Fig. 7.22(b)] are suppressed with increasing J_4 . While the extent of the chiral phase is limited by the $1/3$ -plateau at first, it occupies all the region up to $M_{\text{sat}}/2$ as the plateau disappears.⁴⁴ Since the rung coupling destabilizing the $1/3$ -plateau also binds spinons into triplons [228, 412], this suggests a description of the chiral phase in terms of triplons, which is consistent with the observations made in section 7.10.2 and previous work for the zigzag chain [164, 404].

The J_4 -dependence of the spin gap is shown the inset of Fig. 7.22(a), and is consistent with results reported for the symmetric frustrated spin ladder [228]. For $J_4/J_1 \lesssim 0.5$, the energy gain associated with spinon confinement (binding energy) and/or the kinetic energy gain due to the rung bonds outweighs the increased cost of breaking a rung bond (cf. [228]). This crossover is consistent with the transition from columnar-dimer to rung-singlet phase [228] (cf. Fig. 1.4).

Finally, the results presented in this subsection show that the chiral phase of the frustrated ladder is connected with the chiral phase of the zigzag chain in the parameter space of the exchange couplings. Thus, the chiral phase of the frustrated ladder emerges due to frustration within each ladder leg (see, e. g. , [164]). The rung coupling was also checked to have negligible influence on the wavevector of the incommensurate spin correlations, in accordance with [228] [cf. Fig. 1.4(c)]. Still, the role of the rung coupling is not solely limited to defining the relative phase of the spiral structures emerging on the two

⁴³Since dimer correlations and longitudinal spin correlations decay comparably fast on both sides of the plateau, it is not completely clear to which extent the two corresponding phases resemble each other.

⁴⁴While the data do not show any hints of additional, narrow phases, more detailed calculations are required to confirm the phase boundaries with certainty. See section 7.12 for a discussion.

⁴⁵Note that all results were obtained by targeting the two lowest-energy eigenstates of the full ladder model. Strictly speaking, the ground state may (the degeneracy associated with dimerization is likely lifted by the boundaries) be four-fold degenerate for $J_4 = 0$ [228]. However, it was argued earlier (section 7.3.3), and explicitly checked for parameter set *A*, that tracing over the ground-state multiplet can be omitted in favor of averaging over reference sites for the simple class of models considered here.

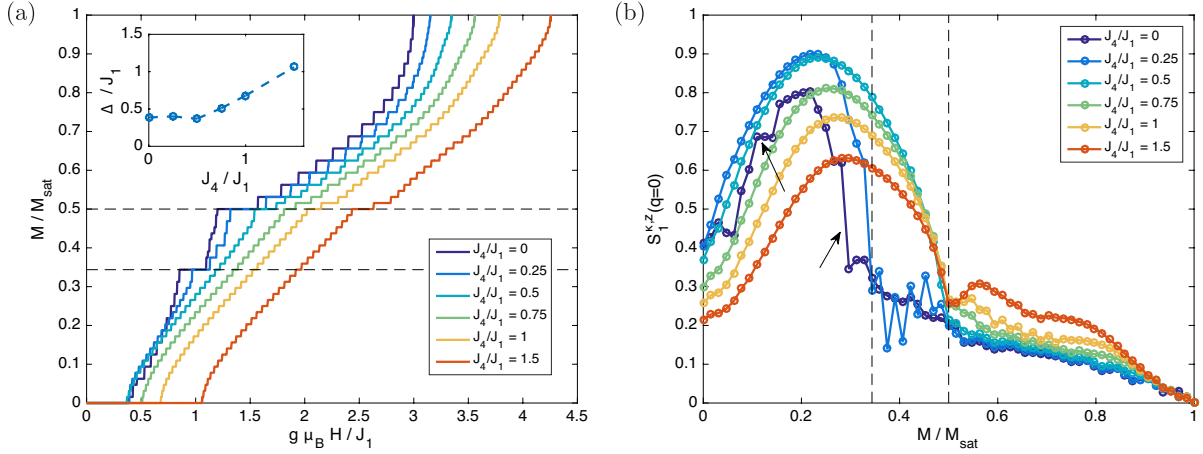


Figure 7.22: Magnetization (a) and uniform ($q = 0$) correlations of longitudinal chirality on the nearest-neighbor leg bonds (b) for parameter set A with varying rung coupling J_4 ($a = 8$, $m = 512$, traced over doublets). Black arrows indicate the limits of the low-field chiral phase for $J_4 = 0$, as estimated from inspection of the correlation functions of the transverse spin components and the longitudinal chirality. Dashed lines mark one-third (adjusted to $M/M_{\text{sat}} = 11/32$, which is closest to $1/3$ for an isolated leg) and one-half saturation magnetization. The inset of (a) shows the J_4 -dependence of the spin gap Δ .

legs of the ladder, as illustrated in Fig. 7.19(a). As shown above, the rung coupling also greatly extends the magnetization region occupied by the chiral phase. According to Fig. 7.22(b), the chiral correlations pass through a maximum at very small rung couplings $J_4/J_1 \sim 0.25$ already. This indicates that the chiral phase is stabilized predominantly by the weakening of the surrounding, competing phases.

7.11.2 Role of frustration

Sufficient frustration is a prerequisite for the appearance of field-induced chiral order in the zigzag chain [164] (see Fig. 7.2). At the same time, the rung coupling of the frustrated ladder enhances the stability range of the chiral phase (section 7.11.1). It is therefore interesting to examine the role of frustration for the appearance of chiral order in the frustrated ladder. This is done by performing calculations for parameter set A with modified next-nearest neighbor (NNN) couplings $(J'_2/J_1, J_2/J_1) = \alpha(0.5, 1)$, where $\alpha \in \{0, 1/3, 2/3, 1\}$. For the sake of a clearer discussion, the average frustration $J_F/J_1 = (J'_2 + J_2)/(2J_1) \in \{0, 0.25, 0.5, 0.75\}$ is used to refer to these parameter sets in the following.

For $J_F/J_1 \leq 0.25$, the behavior of the correlation functions is qualitatively consistent with the field-induced phase of the simple spin ladder (cf. section 7.1.1). The transverse chiral correlations exhibit quasi long-range contributions with wavevector π , which is compatible with spin-canting of the antiferromagnetically-ordered transverse magnetic moments (cf. section 7.10.3). Unlike suggested by the dashed line in Fig. 7.2, the transverse spin correlations dominate also for $J_F/J_1 = 0.25$. An additional phase with asymptotically dominant longitudinal-spin and dimer correlations appears at $M/M_{\text{sat}} \gtrsim 0.87$ for $J_F/J_1 = 0.25$.

Incommensurate correlations emerge between $J_F/J_1 = 0.25$ and $J_F/J_1 = 0.5$ [see Fig. 5.11(c)], and the corresponding models have a non-degenerate zero-field ground state, in agreement with the results reported in [228] (cf. Fig. 1.4). The phase diagram for $J_F/J_1 = 0.5$ is rather complicated. Magnetization

plateaux appear at $M/M_{\text{sat}} = 1/2$ and $M/M_{\text{sat}} = 2/3$ [Fig. 7.23(a)].⁴⁶ A $2/3$ -plateau is theoretically expected in the strong rung-coupling limit [387].⁴⁷ Increasing J_F moves the system away from this limit, explaining the disappearance of the plateau at larger values of J_F . The frustration-dependence of the spin gap Δ [Fig. 7.23(a), inset] is consistent with literature results for the (symmetric) frustrated spin ladder [228]. In addition, the magnetization curve exhibits cusps at low and high magnetization [black arrows in Fig. 7.23(a)]. These cusps reflect singularities in the magnetic density of states [384], as reviewed in section 7.1.3.

In addition to a chiral phase adjacent to the zero-field ground state,⁴⁴ chiral order is also observed between the $1/2$ -plateau and the $2/3$ -plateau [Fig. 7.23(b)]. The low-field chiral phase extends up to the cusp singularity in $M(H)$. This makes sense, since the cusp corresponds to a Lifshitz transition [384] (cf. section 7.1.3), such that the two-component Tomonaga-Luttinger-Liquid description used to describe the chiral phase of the zigzag ladder [164] is expected to break down [164, sec. VII.B]. The real-space texture of the dimerization strength on the J_1 bonds indicates that the following phase is dimerized. Note that the chiral phase occupies a smaller fraction of the magnetization region $0 < M/M_{\text{sat}} < 0.5$ than for parameter set *A* ($J_F/J_1 = 0.75$). Since negligible triplon-triplon interactions are assumed to explain the magnetization cusps [384] (cf. section 7.1.3), this observation corroborates the importance of triplon-triplon interactions for the chiral order (see section 7.10.2 and references therein).

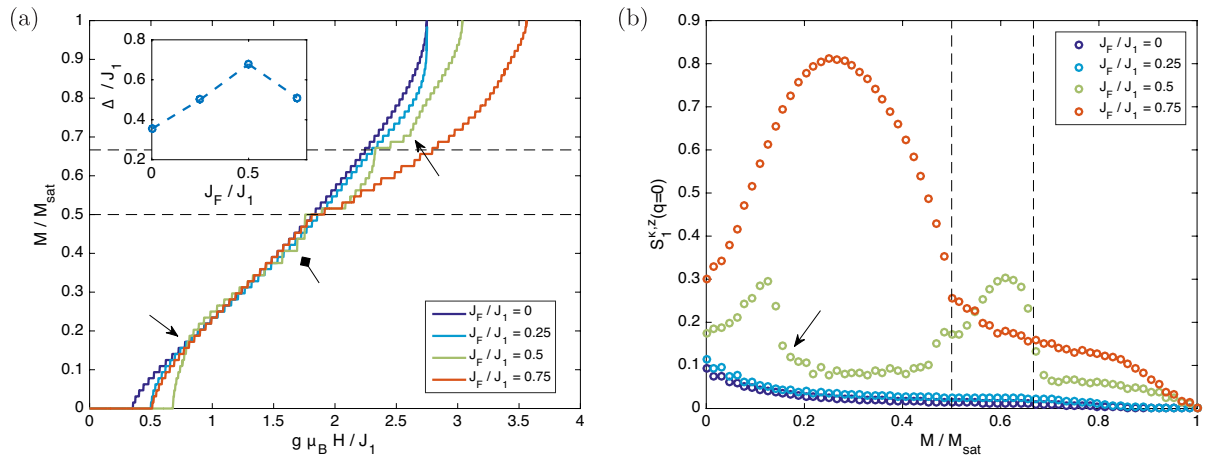


Figure 7.23: Magnetization (a) and uniform ($q = 0$) correlations of longitudinal chirality on the nearest-neighbor leg bonds (b) for parameter set *A* with varying frustration J_F , $J_2/J_2' = 2$ fixed ($a = 8$, $m = 512$, traced over doublets). Black arrows in (a) indicate cusp singularities, whereas the diamond-tip arrow illustrates the approximate location of a tentative $1/3$ -plateau. Black arrows in (b) mark the upper boundary of the low-field chiral phase for $J_F/J_1 = 0.5$, as estimated from inspection of the correlation functions of the transverse spin components and the longitudinal chirality. Dashed lines mark one-half and two-thirds of the saturation magnetization. The inset of (a) shows the J_F -dependence of the spin gap Δ .

To conclude, frustration is essential for the emergence of chiral order: In complete analogy with the zigzag chain (see, e. g., [164]), it induces incommensurate correlations which are a prerequisite for P -symmetry breaking (section 7.3) and hence the appearance of degenerate, chiral ground states (section

⁴⁶There are a few bigger magnetization steps at $S_{\text{tot}}^z/L \geq 22/64 \approx 1/3$ [diamond-tip arrow in Fig. 7.23(a)]. However, no evident changes are observed in the correlation functions.

⁴⁷The reference assumes equivalent magnetic sites. Note that the magnetization plateaux shown in [387, Fig. 1(b)] could be reproduced after adjusting the exchange couplings accordingly, which corroborates the validity of the calculations reported in this work.

7.8; note also the discussion in section 7.12). In addition, increasing frustration seems to further stabilize the chiral phase observed at $M/M_{\text{sat}} < 0.5$.

7.11.3 Relevance of reduced symmetry associated with inequivalent Cu sites

The presence of two inequivalent Cu sites results in two inequivalent next-nearest neighbor (NNN) couplings, J'_2 and J_2 (see section 4.3.1). In order to check to which extent the conclusions obtained before depend on this staggering of the NNN exchange couplings, the difference $\Delta J_F = (J_2 - J'_2)$ has been varied while keeping $(J_2 + J'_2)/(2J_1) = 0.75$ constant.

The calculated magnetization curves are shown in Fig. 7.24(a). As seen in Fig. 7.13, $J'_2 < J_2$ results in the preferential magnetization of the Cu(1) sublattice, which is associated with the J'_2 bonds (see also [77, p. 8]). However, at latest for $M > \frac{1}{2}M_{\text{sat}}$, the Cu(2) sublattice needs to be magnetized as well. Thus, ΔJ_F simplifies the magnetization process below $\frac{1}{2}M_{\text{sat}}$ and hampers it above $\frac{1}{2}M_{\text{sat}}$, which is clearly reflected by the magnetization curves. The $1/2$ -plateau [Fig. 7.24(a)], already noted in [401], appears to be stabilized by the reduced symmetry associated with the staggered NNN couplings (cf. [131]). The corresponding states exhibit dimer order on the J_1 bonds, the inspection of which suggests that a small $1/2$ -plateau persists also for $\Delta J_F = 0$. The occurrence of such a plateau in the frustrated ladder with equivalent NNN couplings is not unexpected, and has been explained in the strong rung-coupling limit [387] (cf. section 7.1.3). This is also consistent with the evolution of the $1/2$ -plateau at large rung couplings J_4 [Fig. 7.22(a)].

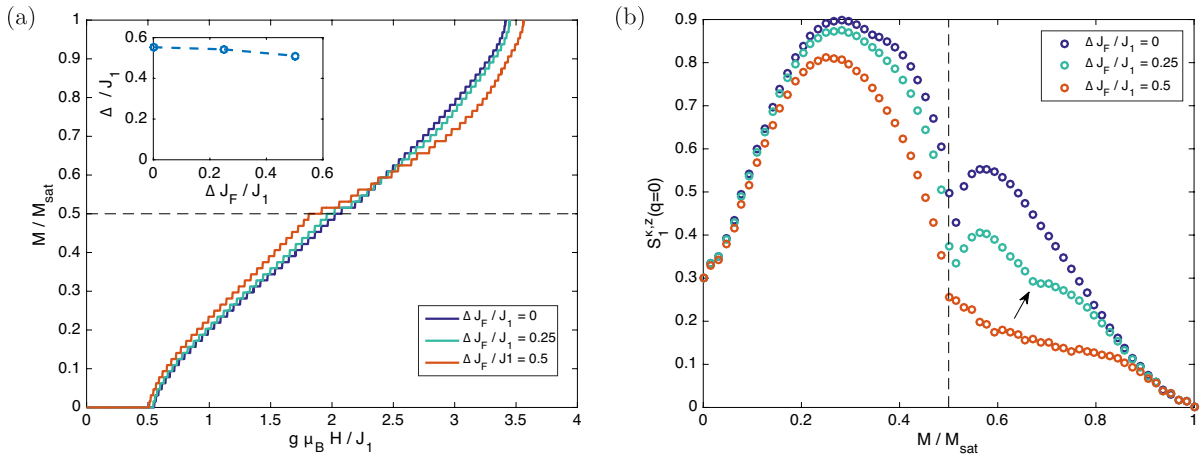


Figure 7.24: Magnetization (a) and uniform ($q = 0$) correlations of longitudinal chirality on the nearest-neighbor leg bonds (b) for parameter set A with varying difference of frustrating couplings $\Delta J_F = (J_2 - J'_2)$, $(J_2 + J'_2)/(2J_1) = 0.75$ fixed ($a = 8$, $m = 512$, traced over doublets). The dashed line marks one-half saturation magnetization. The inset of (a) shows the evolution of the spin gap Δ .

The correlation functions indicate chiral order for $0 < M/M_{\text{sat}} < 0.5$ in all cases [cf. Fig. 7.24(b)].⁴⁴ While chiral order is also observed at $M/M_{\text{sat}} > 0.5$ for $\Delta J_F/J_1 \leq 0.25$,⁴⁴ a non-chiral region appears for $\Delta J_F/J_1 = 0.5$. The suppression of chiral correlations around $\frac{2}{3}M_{\text{sat}}$ observed for $\Delta J_F/J_1 = 0.25$ [arrow in Fig. 7.24(b)] could not be related to any qualitative changes in the correlation functions and is therefore attributed to the proximity of the aforementioned non-chiral phase.

Besides $J'_2 \neq J_2$, the g-factors ($\mathbf{H} \parallel b$) can be site-dependent. To check the effect of non-uniform

g-factors, additional calculations were performed for parameter set A ,⁴⁸ using the g-factors obtained in section 5.2.1. Selected results are summarized in Fig. 7.25. As discussed in section 5.2.1, the site-dependent g-factor results in a non-vanishing magnetic susceptibility of the spin-liquid ground state [Fig. 7.25(a) inset], as anticipated in [207]. The low-field chiral phase and the $1/2$ -plateau are largely unaffected⁴⁴ [Fig. 7.25(b)]. Meanwhile, the site-dependent g-factor restores many features observed for $\Delta J_F/J_1 = 0.25$, such as an overall more linear field-dependence of the magnetization and a high-field chiral phase, including the depression of chiral correlations at $M/M_{\text{sat}} \approx \frac{2}{3}$. This is plausible, since $g_1 < g_2$ favors magnetization of the Cu(2) sublattice and hence counteracts the effect of $J'_2 < J_2$.

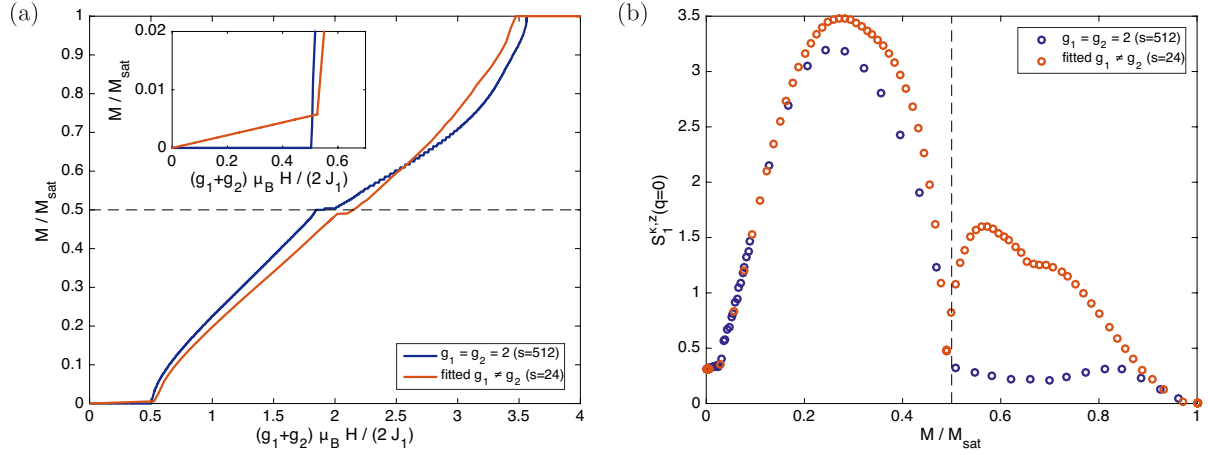


Figure 7.25: Magnetization (a) and uniform ($q = 0$) correlations of longitudinal chirality on the nearest-neighbor leg bonds (b) for parameter set A with uniform and site-dependent g-factors, see text for details ($L = 256$, $a = 2$, $m = 512$). The dashed line marks one-half saturation magnetization. The inset of (a) shows a magnified view of the same data.

Without inequivalent Cu sites, the wavevector of the transverse spin correlations is $\mathbf{q} = (q_{\parallel}, \pi)$. Inequivalence of the two Cu(i) sites corresponds to a modulation with wavevector $\mathbf{q}_{\text{stag}} = (\pi, \pi)$, giving rise to components with wavevectors $\mathbf{q} \pm \mathbf{q}_{\text{stag}} = (q_{\parallel} \pm \pi, 0)$ [cf. Fig. 7.10(a)]. Similar modulation products appear in other correlation functions (see section 7.9) and have been confirmed to be absent in calculations with equivalent Cu sites (i. e., $g_1 = g_2$ and $J_2 = J'_2$).

Chirality and ordered moments A naive estimate of the magnitude of the spiraling moments $m_{\perp,i}$ on the two Cu(i) sublattices can be obtained as follows. Consider parameter set A with uniform g-factors. Assuming classical moments, the maximal value of the chiral correlations on the NN bonds (at $M/M_{\text{sat}} \approx 0.25$), together with the pitch angle inferred from the transverse spin correlations [Fig. 7.10(a)], yields an average transverse ordered moment of $0.42 \hbar$. The proximity to a classical spin- $1/2$ ($\sqrt{0.42^2 + 0.125^2} \approx 0.44$) suggests that quantum effects are indeed small at this magnetization. The longitudinal chiralities on the next-nearest neighbor (NNN) bonds then yield the estimate $(|\kappa_{J_2}^z/\kappa_{J'_2}^z|)^{1/2} = m_{\perp,2}/m_{\perp,1} \approx 1.1$. Alternatively, consider the classical potential energy ϵ of the spiral structure per spin (cf. [419]),

$$\epsilon = J_1 m_{\perp,1} m_{\perp,2} \cos \phi + \frac{1}{2} (J'_2 m_{\perp,1}^2 \cos 2\phi + J_2 m_{\perp,2}^2 \cos 2\phi) .$$

⁴⁸Real-valued arithmetic without explicit S_{tot}^z -conservation is used to directly obtain the ground state as function of field. Still, the (exact) eigenstates have well-defined S_{tot}^z , justifying the use of the simplifications discussed in section 7.7.4.

For sufficiently strong frustration, all terms are negative. For a classical state, quantum fluctuations (kinetic energy) should not be relevant, and $J_2 \gtrsim J'_2$ implies $m_{\perp,2} \gtrsim m_{\perp,1}$, which is consistent with the numerical estimate. Taking the uncertainties of the NNN couplings into account (section 4.3.3), $m_{\perp,1} \sim m_{\perp,2}$ is generally expected for a field-induced spiral phase in BiCu_2PO_6 , as assumed in previous work [78].

7.12 Intermediate summary

The calculations presented above identify chiral order as a prevalent feature of the frustrated spin ladder. All correlation functions indicate an instability towards the formation of a spiral magnetic structure (sections 7.10.1 and 7.10.3), reproducing previous results for the particular case of parameter set A [77]. Specifically, given sufficient frustration, all calculations revealed a chiral phase between the zero-field ground state and one-half saturation magnetization (sections 7.11.1-7.11.3), which will be referred to as the C1 phase in the following. The C1 phase seems to be generally stabilized upon increasing frustration and rung exchange (sections 7.11.1 and 7.11.2). Except for the possibility of different ordered moments on the corresponding sublattices, the presence of two inequivalent Cu sites has negligible effects on the C1 phase (section 7.11.3).

The similarity to the phase diagram of the zigzag ladder in the limit of vanishing rung coupling shows that the C1 phase is connected to the chiral phase of the zigzag ladder (section 7.11.1). Consistently (see, e. g., [164]), it is characterized by (i) long-ranged chiral correlations, i. e., static chiral order, (ii) transverse spin correlations which decay slower or equally-fast as inverse distance, and (iii) longitudinal spin correlations which decay faster or equally-fast as inverse distance. This behavior is consistent with previous work [77] and illustrated in Fig. 7.26(b)⁴⁹. The dominant-weight components of many correlation functions decay exponentially fast, while the algebraically-decaying contributions are too small to be seen in a linear representation [see, e. g., Fig. 7.12(b)]. The evolution of the C1 phase is summarized in Fig. 7.26(a).

The long-range nature of the chiral correlations in the chiral phases can be identified rather reliably. For $J_F/J_1 \gtrsim 0.5$ and $J_4/J_1 \gtrsim 0.25$, no indication of additional phases below the C1 phase is found. This is confirmed by detailed calculations (section 7.10.2, see also 7.6.3) for the particular case of parameter set A . This strongly suggests that the C1 phase is the only field-induced phase which is relevant for the parameter regime corresponding to BiCu_2PO_6 (section 4.3.3).⁵⁰ It is generally conjectured that a C1 phase exists for all exchange couplings corresponding to the incommensurate region of the phase diagram of the frustrated ladder [cf. Fig. 7.26(a)]. If frustration and rung coupling are strong enough, the C1 phase is expected to occupy the entire magnetization range between the zero-field ground state and the $1/2$ -plateau. Based on the insights obtained in this work, it appears worthwhile to perform additional calculations for the frustrated ladder with $J'_2 = J_2$, as function of rung coupling and frustration, in order to check the aforementioned conjectures and thus clarify at least the corresponding part of the in-field phase diagram of the frustrated ladder. Such calculations should include a detailed consideration of the phase boundaries, analogous to section 7.10.2.

⁴⁹The slow modulations seen in some of the rapidly-decaying correlation functions are due to the triplon wavefunction discussed in section 7.6.1. Similar plots for the zigzag chain can be found in [164].

⁵⁰The dispersion minimum at $q^* = 0.574\pi$ [316] (in ladder units, see footnote 27) depends only weakly on J_4 and yields $J_F/J_1 \sim 1$ [228], suggesting the lower bound $J_F/J_1 \gtrsim 0.5$ (cf. [401, Fig. 6]), in accordance with [257]. Since no two-spinon continuum (cf. [385]) is reported [316, 318], the rung-singlet phase is assumed to be realized in BiCu_2PO_6 (note that a similar argument was made in [179, p. 3]).

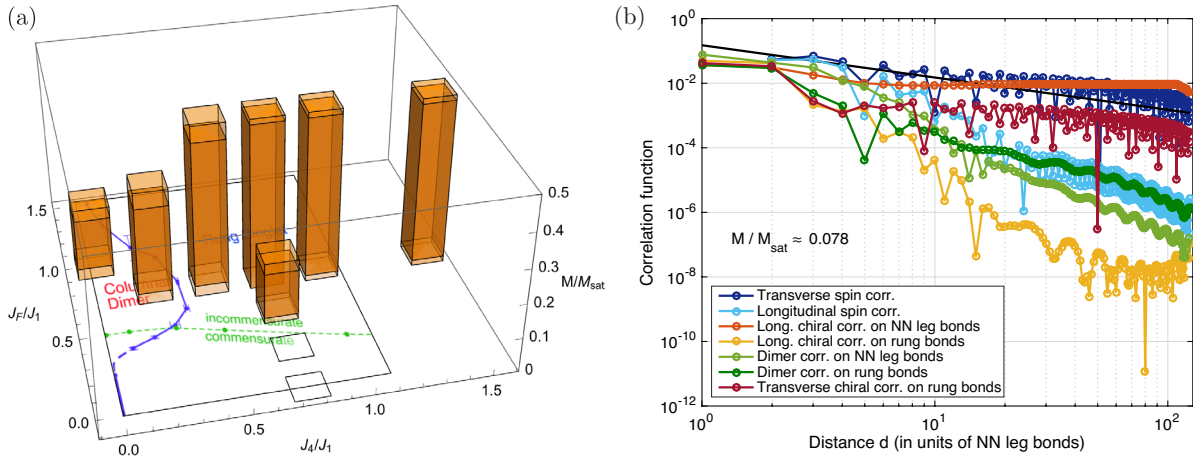


Figure 7.26: (a): Magnetization region occupied by the C1 phase, as function of exchange couplings ($J_2/J_2' = 2$ fixed; see parameter set A, section 4.3.3). The data are based on the calculations presented in sections 7.9, 7.11.1, and 7.11.2. Transparency is used to indicate uncertainties. The zero-field phase diagram [228] of the frustrated ladder (with $J_2' = J_2$) is included for comparison purposes (Adapted with permission from Ref. [228]. Copyright 2011 by the American Physical Society.). (b): Typical behavior of correlation functions in the C1 phase, calculated for parameter set A ($L = 256$, $m = 512$, $a = 8$). The black line decays like d^{-1} .

Various plateau phases are clearly visible in the magnetization curves. The $1/3$ -plateau appearing for weak rung coupling is known from the zigzag chain (see sections 7.11.1 and 7.1.2.1). Additional plateaux observed around $\frac{1}{2}M_{\text{sat}}$ (sections 7.11.1 and 7.11.3) and $\frac{2}{3}M_{\text{sat}}$ (section 7.11.2) are also consistent with earlier results for the frustrated ladder [131, 384, 401]. For sufficient frustration ($J_F/J_1 \gtrsim 0.5$) and rung coupling ($J_4/J_1 \gtrsim 0.5$), only a $1/2$ -plateau is observed. The rung-coupling dependence of this plateau (section 7.11.1) can be understood as a crossover: While a plateau is expected at large J_4 even in the symmetric frustrated-spin ladder [384] (cf. section 7.1.3), the presence of inequivalent NNN couplings becomes increasingly important for its stabilization at lower rung couplings (see [131] and section 7.11.3).

In addition to the C1 phase, a second chiral phase is generally observed above $\frac{1}{2}M_{\text{sat}}$. This phase is destabilized by the presence of inequivalent Cu sites (section 7.11.3), and its relation with the chiral phase appearing above the $1/3$ -plateau of the zigzag chain (see section 7.1.2.1) is unclear. Except for the TLL2 phase, the competing non-chiral phases of the frustrated ladder are generally accompanied by features in the structure factors of the longitudinal spin correlations and the dimer-dimer correlations [see, e. g., the fanning-out features at $M \gtrsim \frac{1}{2}M_{\text{sat}}$ in Figs. 7.10(b) and 7.14]. For the longitudinal spin correlations, this is illustrated in Fig. 7.27. Clearly, the sharp features disappear within the chiral phases. The TLL2 phase is only manifest for $J_4 = 0$ (see section 7.11.1) and its phase boundary towards the chiral phase is not completely clear. Whilst not relevant for the present work, computations of the entanglement entropy have been established as a convenient method for detecting the distinctive two-component nature of the TLL2 phase [164] and may prove useful in future work.

Lastly, it is evident [Fig. 7.27(c)] that the regimes $M \gtrsim \frac{1}{2}M_{\text{sat}}$ are fundamentally different. This is corroborated by the fact that the C1 phase is generally found to be more robust than its counterpart above the $1/2$ -plateau [see, e. g., Fig. 7.24(b)]. The peak at $(M/M_{\text{sat}}, q) = (\frac{1}{2}, \frac{\pi}{2})$ and its splitting above $\frac{1}{2}M_{\text{sat}}$ [Figs. 7.27(a) and 7.10(b)] has already been noted in earlier calculations performed for parameter set A [75, 131]. It has been proposed that, for $J_2' < J_2$, the regime $M > \frac{1}{2}M_{\text{sat}}$ corresponds to two essentially

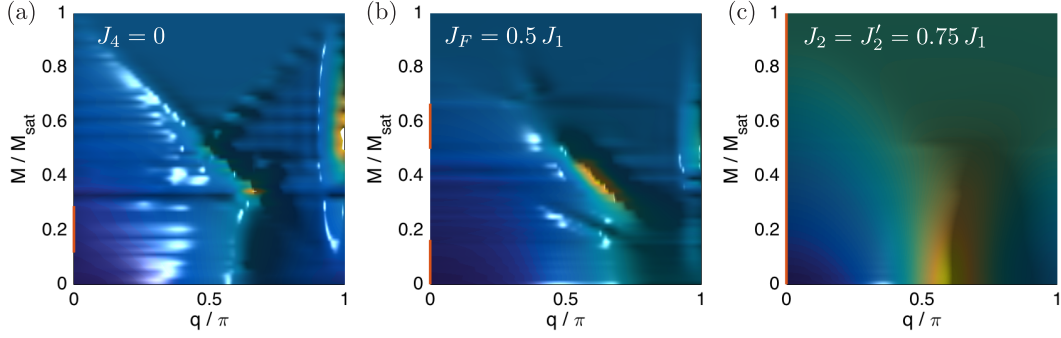


Figure 7.27: Structure factor $S^{zz}(q, \pi)$ of longitudinal spin correlations for parameter set A with individual couplings altered as indicated in the figure ($L = 64$, $a = 8$, $m = 512$). Rust-colored lines along the ordinate indicate the regions occupied by chiral phases (based on section 7.11).

decoupled spin chains formed by the Cu(2) sites [131]. The J_2 exchange coupling thus takes the role of a nearest-neighbor coupling, while the interjacent Cu(1) sites are fully polarized [131]. A byproduct of the present work supporting this scenario is shown in Fig. 7.28: (i) The intrasector gap Δ_{sec} vanishes for even system size L and odd S_{tot}^z . (ii) This even/odd-behavior⁵¹ is not observed in the chiral phases. (iii) The even/odd behavior is suppressed with increasing rung coupling. Note that only for an even-length system, the two ladder legs are equivalent [cf. Fig. 4.4(b)]. Whereas each leg carries the same magnetization for even S_{tot}^z by symmetry, an ambiguity arises in the case of decoupled legs and odd S_{tot}^z . Thus, the above observations are fully consistent with two effectively decoupled chains, as proposed in [131]. Despite these insights, it remains unclear what type of field-induced long-range order could develop out of these non-chiral phases. Simulations for larger system sizes could allow a more reliable determination of the asymptotic behavior of the corresponding correlation functions. However, since not corresponding to experimentally-accessible magnetizations for BiCu₂PO₆, these questions are left for future work.

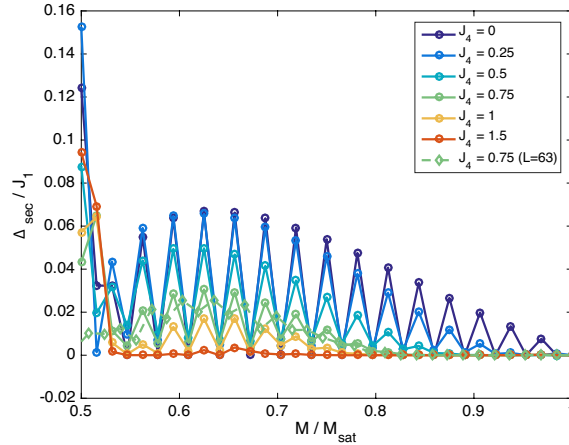


Figure 7.28: Energy difference Δ_{sec} between the two lowest-energy states in each S_{tot}^z -sector, as function of magnetization $M/M_{\text{sat}} = S_{\text{tot}}^z/L$, calculated for parameter set A with varying rung coupling J_4 (circles: $L = 64$, diamonds: $L = 63$; $m = 512$).

⁵¹Note that similar alternating features are observed in the magnetization curves [Fig. 7.24(a)].

7.13 Influence of individual DM interactions

In this section, the effect of extending the Hamiltonian (4.1) by symmetry-allowed DM terms (section 4.3.2) is examined. In analogy to section 5.4, the considerations are restricted to individual DM terms. As mentioned in section 7.2, similar calculations were attempted in the past [131]. The only available result is a brief comment in [131], which suggests that these early calculations were generally consistent with the data and conclusions presented below.

Most simulations presented in this subsection were performed with $L = 64$, $m = 128$, and $s = 24$ (cf. section 7.5). Although the bond dimension is low compared to the calculations reported in the preceding sections, additional calculations performed for parameter set B (section 7.14) show that it is sufficient for most magnetizations. This suggests that DM interactions yield less entangled ground states which are easier to capture by the MPS ansatz (see, e. g., [349, p. 16.4]). Since the magnetic field needs to be explicitly accounted for in the calculations, the g -factors cannot be fitted to the data in a manner analogous to section 5.4. Instead, they are fixed to the values obtained in section 5.2.1.

The results of the calculations are summarized in Fig. 7.29. Consider the magnetization curves first. The longitudinal DM terms D_1^b and D_4^b are found to have almost no effect on $M(H)$ within the range of experimentally-relevant magnetizations [Fig. 7.29(a,c)]. While not *a-priori* obvious, this is plausible given that these DM terms are S_{tot}^z -conserving.⁵² Accordingly, simple classical energy considerations (see end of this subsection) suggest that these DM interactions induce twist-distortions in a plane perpendicular to the magnetic field and thus should not affect the total magnetization. These observations are consistent with previous calculations for a simple spin ladder with a weak rung-DM interaction analogous to D_4^b [270]. The overall similar effects of D_1^b and D_4^b are not completely unexpected, since local spin-space rotations about the magnetic-field axis [15, 359] (cf. section 4.3.2) can be used to transform these interactions into one another, at the expense of additional XXZ anisotropies.

By contrast, the transverse DM terms mix states with different S_{tot}^z and are thus expected to allow for a field-induced deformation of the ground-state which results in a non-zero magnetization already well below the magnetic field required for closing the spin gap (e. g., [207, 270]; see also [74, pp. 125,134-135]). This is clearly reflected in the calculations [Fig. 7.29(e,g,i)].⁵³ In particular, transverse DM terms $\sim 0.3 J_1$ can reproduce the slope of the measured magnetization at fields below the critical field, which is consistent with the analysis of the finite-temperature susceptibility in section 5.4.

The right column of plots in Fig. 7.29 illustrates the evolution of the chiral order up to one-half saturation magnetization. Chiral phases, as inferred from the inspection of the correlation functions, are marked using gray shading.⁵⁴ All corresponding magnetization curves exhibit a distinct change of slope around 55 T, which corresponds to the field-induced suppression of the spin gap. Since the magnetic field is sampled uniformly, this change of slope is visible as a change in the density of data points in the plots showing the chiral correlations. Thus, the data admit the following conclusions: (i) a chiral phase appears in all considered cases, (ii) the chiral phase extends well beyond the magnetization range relevant

⁵²This obvious fact has already been noted in previous work [77, p. 3]. However, this observation alone is not a proof, since DM interactions can still deform the ground state *within* the $S_{\text{tot}}^z = 0$ sector (cf. [74, p. 125], but cf. [74, p. 132]).

⁵³Note that the apparently negligible effect of D_2^c in section 5.4 [Fig. 5.7(c)] resulted because the DM-induced changes were compensated by the fitting of the g -factors.

⁵⁴The drops observed in Fig. 7.29(b,d), as well as the step-like features seen in $M(H)$ [Fig. 7.29(a,c)], are attributed to slow convergence. This is substantiated by comparing with calculations for uniform g -factors (section A.1.10). Also due to convergence problems, the point at $M/M_{\text{sat}} \approx 0.16$ in Fig. 7.29(j) (marked by a cross) was recalculated using $s = 128$ iterations.

for the high-field experiments performed in this work, (iii) the onset of the chiral phase is consistent with the closing of the spin gap. While some DM terms clearly destabilize the chiral order at higher magnetizations, more accurate calculations are required to analyze the competing phases. Such studies are beyond the scope of the present work. The onset is considered in more detail in section 7.14 (for parameter set B).

Lastly, it is important to realize that the DM interactions represent a linear potential for the chirality, $\mathbf{D}_{ij} \cdot \boldsymbol{\kappa}_{ij}$. Thus, a DM term D_{ij}^α generally induces a small, static chirality κ_{ij}^α . For eigenstates with intrinsic chiral order $\langle \kappa_{ij}^\beta \rangle \neq 0$, this implies that the axis of the corresponding classical spiral order is *tilted* for $\alpha \neq \beta$, whereas DM-vector components with $\alpha = \beta$ alter the pitch angle of the spiral. Although the present, and rather obvious, discussion is driven by the numerical results, it should be noted that at least certain tilt-distortions were already proposed in previous work based on similar considerations (see section 7.15 for details). In terms of correlation functions, a DM interaction D_{ij}^α is thus expected to yield a long-ranged contribution to the correlation function of the α -component of the chirality, with a periodicity reflecting the staggering of the respective DM interaction. Indeed, the calculated correlation functions (not shown) are consistent with this expectation. For the J_1 bond, the implications for the magnetic structure are discussed in detail in section 7.14.

7.14 Special case: DM interaction on nearest-neighbor leg bond

As explained in section 7.13, DM interactions act as a potential for the chirality. Although chiral order is found to persist in the presence of small-to-moderate DM interactions, the ground state is altered in general. In this section, the effect of the DM interactions D_1^{ac} and D_1^b (section 4.3.2) associated with the nearest-neighbor (NN) bonds on the ladder legs is considered in more detail. These interactions are of particular interest, since they are an important ingredient of parameter set B , which was proposed to explain the measured dispersion of magnetic excitations in BiCu_2PO_6 [318] (cf. section 4.3.3).

In section 7.10.2, the onset of chiral order was shown to coincide with the closing of the spin gap if no DM interactions are present. While the results presented in the preceding section (section 7.13) are consistent with this scenario, additional calculations were made to check if this is indeed the case for parameter set B (section 7.14.1). These results are also used to discuss the effects of the DM interactions on the magnetic order (sections 7.14.2 and 7.14.3). For consistency with the literature [179, 318], as well as the analysis of the magnetic susceptibility in section 5.4.4, a uniform g -factor $g = 2$ is assumed.

Finally, as reviewed in section 1.1.2, additional symmetric anisotropy terms should be considered for superexchange interactions [318] (cf. also section 5.4.4). No such terms were included in the calculations reported in the preceding section (section 7.13), as is often the case in the literature (e. g., [15, 79, 82, 108, 136, 157, 219, 306, 450, 458]). Generally, the effect of these terms on the magnetic and thermal response functions was found to be negligible (section 5.4.4). The data in Fig. 7.30 corroborate that this conclusion remains valid in the presence of large magnetic fields. For the specific case of parameter set B , the DM vectors actually result in particularly small symmetric anisotropies [318] (cf. section 5.4.4, footnote 20), which are unlikely to be significant. Nonetheless, for the sake of consistency with the literature [179, 318, 377], these symmetric anisotropy terms are included in the calculations for parameter set B .

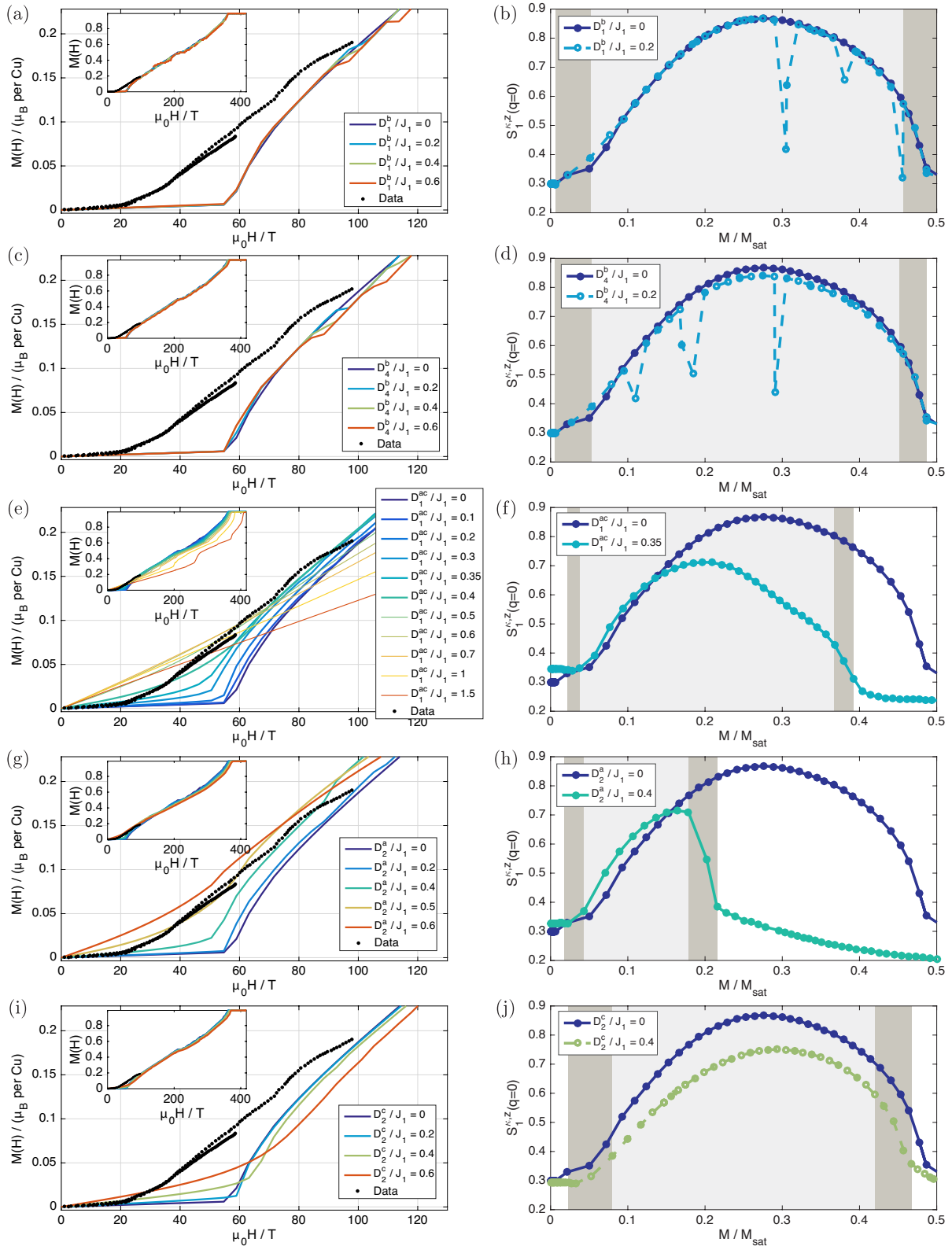


Figure 7.29: Magnetization curves and uniform ($q = 0$) correlations of longitudinal chirality on nearest-neighbor leg bonds, calculated for parameter set A including the site-dependent g -factors obtained in section 5.2.1 and augmented by various DM terms as indicated in the legends ($L = 64$, $m = 128$, $a = 8$, $s = 24$, traced; see text for additional details). For the models involving non-zero DM terms, regions with chiral order are indicated in the plots of the chiral correlations using gray shading (uncertainties in darker color). Experimental magnetization data sampled from the curves reported in [207] and [208] are included for comparison.

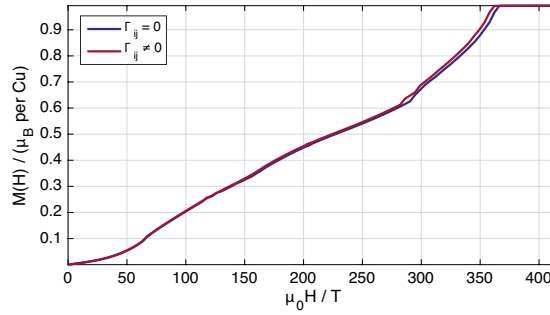


Figure 7.30: Calculated magnetization for parameter set A , including site-dependent g -factors obtained in section 5.2.1, augmented by a DM interaction $D_1^b = 0.4 J_1$ ($L = 64$, $m = 128$, $s = 24$, traced). The two curves were calculated with and without the symmetric anisotropy terms Γ_{ij} , respectively.

7.14.1 Field-induced chirality

The results obtained for parameter set B are analyzed in a manner analogous to the preceding sections, with a focus on the regime below half-saturation magnetization. The correlation functions are generally similar, except that (i) features related to the inequivalence of the two Cu sites (see section 7.11.3) are absent, as expected, and (ii) the wavevector of the transverse spin correlations is shifted towards $\pi/2$, as expected for a one-dimensional classical spiral with dominant uniform DM vector.

The most important aspects are illustrated in Fig. 7.31. Again, long-range order of the longitudinal chirality, resembling the C1 phase described in section 7.12, is observed almost throughout the entire magnetization region between gap closure and half saturation [Fig. 7.31(b)]. This chiral phase clearly extends beyond the range of experimentally accessible magnetizations. Additional calculations (Fig. 7.32) confirm the twofold degeneracy of the ground state in the chiral phase. Note that the chiral phase appears to be gapped, which could be a consequence of the DM interactions.⁵⁵ The details of the excitations and their softening in the vicinity of the phase boundaries are left for future research. In agreement with the results of section 7.13, the data also suggest that the onset of chiral order coincides with the closing of the spin gap.

Nonetheless, due to the relevance of parameter set B for BiCu_2PO_6 , more careful checks for the existence of possible additional phases at magnetizations below the chiral phase seemed appropriate. Corresponding results are shown in Fig. 7.33.⁵⁶ Clearly, the onset of chirality coincides with the closing of the spin gap, which manifests itself as a kink in the magnetization curve. This confirms that the regime below half saturation magnetization is dominated by the chiral phase and no other phases are expected at lower magnetizations.

⁵⁵As pointed out in [319, p. 63], DM interactions can—like site-dependent g -tensors—induce staggered effective magnetic fields [15, 306], which can, e. g., induce a gap in the otherwise gapless field-induced phase of the spin ladder [425]. Strictly speaking, the corresponding phase transition is expected to be replaced by a crossover in such a case [370] (see also [136], [74, pp. 125,136]).

⁵⁶The small long-wavelength modulation seen in the yellow ($\langle\langle S_{\text{tot}}^z \rangle\rangle \approx 3.1$) and orange ($\langle\langle S_{\text{tot}}^z \rangle\rangle \approx 5.4$) traces is attributed to triplon-triplon correlations, analogous to Fig. 7.20(b). The positions of the maxima are consistent with this hypothesis. However, no accompanying static S_z -texture is observed in this case, since the simple picture reviewed in section 7.6.1 breaks down due to absence of S_{tot}^z -conservation (cf. [74, p. 125]).

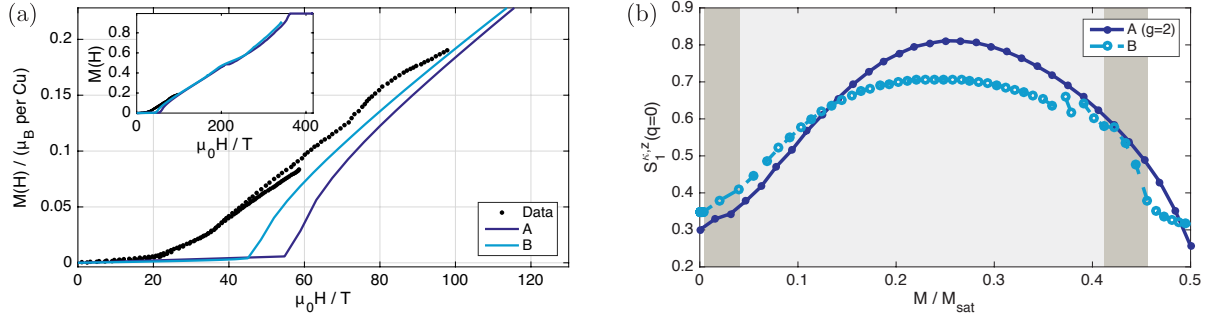


Figure 7.31: Magnetization curves (a) and uniform ($q = 0$) correlations of longitudinal chirality on nearest-neighbor leg bonds (b), calculated for parameter sets A ($m = 512$, $s = 512$, traced) and B ($L = 64$, $m = 128$, $s = 24$, traced). Experimental magnetization data sampled from the curves reported in [207] and [208] are included for comparison. For parameter set A , the site-dependent g -factors obtained in section 5.2.1 were used in (a) ($L = 256$), whereas a uniform g -factor $g = 2$ was assumed in (b) ($L = 64$)—as well as for parameter set B in general. Gray shading in (b) indicates regions with chiral order for parameter set B (uncertainties in darker color).

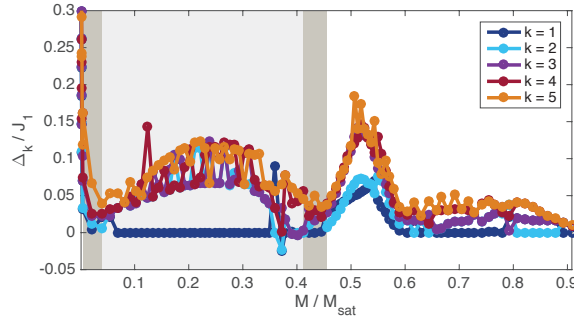


Figure 7.32: Excitation energy Δ_k of the k 'th excited state w.r.t. the ground-state energy ($L = 64$, $m = 128$, $s = 24$). The shaded regions correspond to Fig. 7.31(b).

7.14.2 Transverse component

Two principal effects of the transverse component of the DM vector on the nearest-neighbor leg bond, D_1^{ac} , could be identified. The first is of a rather technical nature. As discussed in section 7.10.3, spin canting yields a transverse chirality component which rotates along with the spiral structure [Fig. 7.19(b)]. Mismatch between finite system size and incommensurate wavevector then results in a net transverse chirality. This chirality is pinned⁵⁷ by D_1^{ac} (cf. section 7.13), which effectively breaks the $U(1)$ -symmetry associated with the propagation phase of the spiral (see sections 7.8.2 and 7.10.3). Thus, transverse spiraling magnetic moments appear in the simulations. Yet, these moments generally differ from those expected in a real spiral phase,⁵⁸ and are therefore not considered further. Since the pinning potential depends solely on the oscillating component of the chirality parallel to D_1^{ac} , κ_{ij}^x , reversal of the spiral orientation does not change the resulting $\langle \kappa_{ij}^x \rangle$ -texture, which implies that the oscillations do not disappear upon tracing over the ground-state doublet [Fig. 7.34(a)]. By contrast, the phase of the chirality component perpendicular to D_1^{ac} and to the external magnetic field ($\mathbf{H} \parallel b$), κ_{ij}^y , changes by π [Fig. 7.34(b)]. It

⁵⁷Note that the brief remark in the previous work [131] (see discussion in section 7.15) might also be referring to this effect.

⁵⁸The issues related to the ground-state degeneracy (sections 7.3 and 7.8.1) still apply. Moreover, quasi long-ranged components persist in the transverse spin correlations, indicating that couplings between ladders will generally increase the transverse ordered moments.

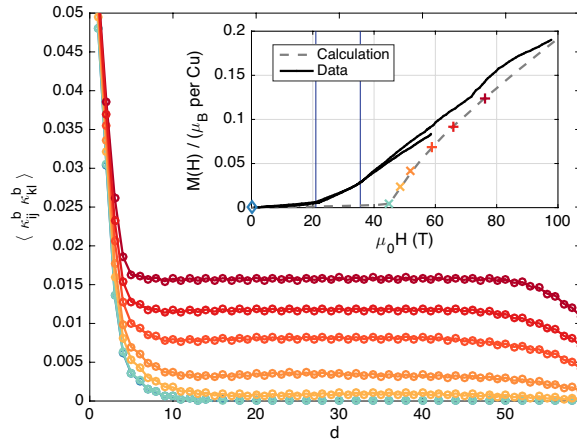


Figure 7.33: Correlations of longitudinal chirality on nearest-neighbor leg bonds as function of distance d , calculated for parameter set B ($L = 128$, $s = 24$, $a = 8$). The inset shows the magnetization curve from Fig. 7.31(a) (with magnetization data sampled from the curves reported in [207, 208]), along with symbols indicating the magnetizations at which the correlation functions shown in the main panel have been evaluated. The marker symbols encode the MPS bond dimension used in the respective calculations (crosses: $m = 512$, diamonds: $m = 256$, pluses: $m = 128$). The critical fields [207, 208] are marked by blue lines. (Updated version of a figure previously used in [312].)

is important to be aware of the aforementioned effects when analyzing quantities like the transverse spin correlations or the correlations of the transverse chirality, since both will contain long-ranged oscillating components. Note that, despite being a finite-size effect, the static moments do not necessarily disappear upon increasing the system size [Fig. 7.34(a)].

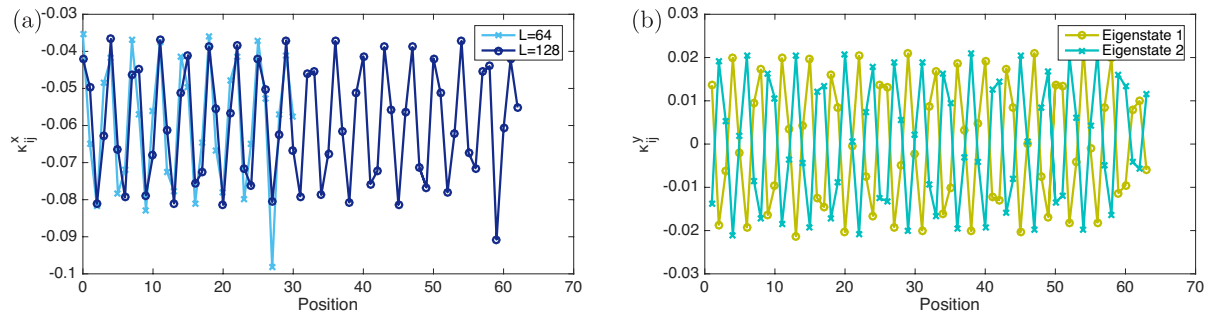


Figure 7.34: Spatial distribution of transverse chirality parallel (a) and orthogonal (b) to D_1^{ac} , for $M/M_{\text{sat}} \approx 0.12$. Calculations for $L = 128$ used $m = 256$ and $s = 24$, calculations for $L = 64$ used $m = 128$ and $s = 24$; data in (a) are traced over the ground-state doublet. The chirality is determined on the nearest-neighbor leg bonds. The abscissa enumerates bonds on one leg of the ladder, the origin corresponding to the central bond.

A second important effect of the transverse DM interaction D_1^{ac} is also manifest in Fig. 7.34(a): The DM term induces a uniform chirality-component antiparallel to D_1^{ac} , as expected when considering the DM interactions as a classical potential for the chirality (see section 7.13). In terms of the spiral structure discussed in section 7.10.1 [Fig. 7.19(a)], this corresponds to a tilt of the local spiral axis towards D_1^{ac} .⁵⁹

⁵⁹Upon increasing the magnetization within the chiral phase, oscillating long-range components appear in the longitudinal chiral correlations, too. However, even at $M/M_{\text{sat}} \approx 0.34$, the oscillation amplitude amounts to no more than 3% of the

The tilt angle α can be estimated as follows. First, κ_{ij}^x [Fig. 7.34(a)] is averaged, yielding mean $\bar{\kappa}^x$ and standard deviation $\delta(\bar{\kappa}^x)$. The square of the longitudinal chirality $(\bar{\kappa}^z)^2$ and its uncertainty $\delta[(\bar{\kappa}^z)^2]$ are obtained from the asymptotic behavior of the corresponding correlation function (cf., e. g., Fig. 7.33).⁶⁰ The same analysis is performed for the y -component of the chirality, yielding $(\bar{\kappa}^y)^2$. The estimates $(\bar{\kappa}^y)^2$ and $(\bar{\kappa}^z)^2$ incur a systematic error related to the decaying components of the correlation function. The deviation from the expectation $(\bar{\kappa}^y)^2 = 0$ is used to assess this systematic uncertainty. Finally, using the notation $|x|_y = \max\{x, y\}$, the nominal value α , as well as lower/upper bounds $\alpha_{l/u}$, are estimated according to

$$\alpha = \arctan \sqrt{\frac{|(\bar{\kappa}^x)^2|_0}{|(\bar{\kappa}^z)^2|_{0+}}} \quad \text{and} \quad \alpha_{u/l} = \arctan \sqrt{\frac{|(\bar{\kappa}^x)^2 \pm 2\bar{\kappa}^x \delta(\bar{\kappa}^x)|_0}{|(\bar{\kappa}^z)^2 \mp \delta[(\bar{\kappa}^z)^2] \mp (\bar{\kappa}^y)^2|_{0+}}}$$

Calculations have been performed for parameter set B , as well as for models derived from it by varying the rung coupling $J_4/J_1 \in \{0, 0.5, 0.75, 1, 1.5\}$. The transverse DM terms mix different S_{tot}^z -sectors and thus allow the system to be magnetized by “deformations” of the ground state before closing the spin gap (see section 7.13 and references therein). Hence, the magnetization curves (Fig. 7.35) indicate that the rigidity of the ground state decreases with decreasing rung coupling. For $J_4/J_1 \geq 0.5$, the correlation functions are consistent with a chiral phase analogous to the C1 phase (section 7.12) spanning the magnetization region from gap closure⁶¹ up to $M/M_{\text{sat}} = 0.41$ at least [see Fig. 7.37(a)]. Note, however, that the system is so deformable for $J_4/J_1 = 0.5$ that the spin gap closes very late, at $M/M_{\text{sat}} \approx 0.24$. A phase reminiscent of the C1-phase also seems to appear in an isolated ladder leg ($J_4/J_1 = 0$) for $0.25 \lesssim M/M_{\text{sat}} \lesssim 1/3$.⁶²

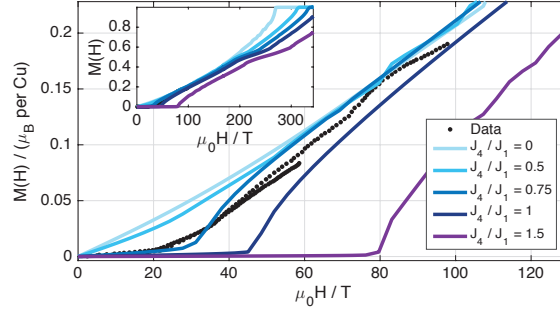


Figure 7.35: Calculated magnetization curves for parameter set B with varying rung coupling J_4 ($L = 64$, $m = 128$, $s = 24$, traced). Experimental magnetization data sampled from the curves reported in [207] and [208] are included for comparison.

The analysis of the DM-free models (see section 7.12) revealed a field-induced chiral phase (C1 phase), with chirality pointing predominantly parallel to the applied magnetic field, in accordance with previous

uniform component of the correlation function. In terms of the longitudinal chirality itself, the relative weight is a factor of two lower $[(f + g \cos(qr))^2 \propto f + 2g \cos(qr)]$ for $|g| \ll |f|$. It is therefore safe to neglect these oscillations, which corresponds to assuming complete independence between the longitudinal and the spiraling magnetization components.

⁶⁰To be precise, I calculate the mean and the standard deviation of the correlations of the longitudinal chirality on nearest-neighbor leg bonds at distances d satisfying $14 \leq d \leq 20$ ($30 \leq d \leq 42$) for $L = 64$ ($L = 128$).

⁶¹The delayed onset seen for $J_4/J_1 = 1.5$ [Fig. 7.37(a)] is attributed to slow convergence with MPS bond dimension m (see sections 7.10.2 and 7.14.1, and [383]).

⁶²Its identification is difficult because the longitudinal chirality is very small. The main evidence consists in a ground-state degeneracy at the tentative phase boundaries. Note that D_1^b breaks the symmetry of a leg with even length L (i. e., an odd number of NN bounds), which lifts the ground-state degeneracy within a possible C1 phase.

work [77, 131]. In terms of the anticipated magnetic order, this corresponds to a (canted) spiral in the plane perpendicular to the magnetic field [77, 78, 131] (cf. section 7.10). While it also appears in the isolated zigzag chain (e. g., [164]), this phase is stabilized by the rung couplings (section 7.12) and its occurrence is generally found to be unaffected by DM interactions (see above, sections 7.13 and 7.14.1, as well as brief remark in [131]). Neglecting the origin of the chirality for a moment and noting that D_1^{ac} is uniform on each ladder leg (Fig. 4.5), I thus arrive at the following picture: The rung coupling prefers the chirality of both ladder legs to point parallel (and along the applied magnetic field). By contrast, the DM interaction D_1^{ac} prefers an antiparallel alignment of chirality on the two ladder legs, which is incompatible with the rung coupling (cf. Fig. 7.19). Therefore, as the rung coupling decreases, the tilt angle of the spiral axis is expected to increase. Indeed, this is confirmed by calculations of the tilt angle following the method outlined above (Fig. 7.36).⁶³

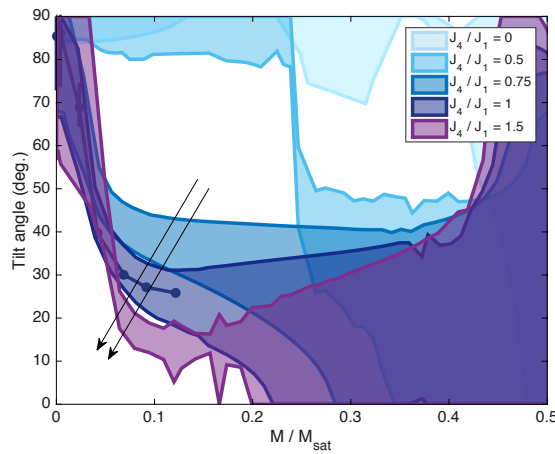


Figure 7.36: Tilt angles estimated from calculations for parameter set B with varying rung couplings J_4 . Shaded areas and error bars represent the angular ranges bounded by α_l and α_u (see text for details). If present, points indicate the nominal values of the tilt angle α . Calculation parameters: Generally $L = 64$, $m = 128$, $s = 24$; $J_4 = 0$ solved with $m = 512$; nominal parameters ($J_4 = 1$) solved with $m = 512$ for $M/M_{\text{sat}} \lesssim 0.14$; data at $M/M_{\text{sat}} \approx 0.38$ recalculated with $s = 128$ for $J_4/J_1 = 0.5$ due to slow convergence; data at $M/M_{\text{sat}} \approx 0.13$ recalculated with $s = 128$ for $J_4/J_1 = 0.75$ due to slow convergence; points calculated using nominal parameters and $L = 128$, $m = 256$, $a = 8$.

Note that the longitudinal chirality in the C1 phase is field-induced, as illustrated by Fig. 7.37(a), whereas the transverse chirality, which is responsible for the spiral-axis tilt in the C1 phase, is already present in the zero-field ground state [Fig. 7.37(b)]. Also, unlike its field-induced counterpart, this DM-induced chirality does not affect the ground-state degeneracy. Note that this is different from the DM-induced scalar chirality and ordered magnetic moments reported in [219] for a pyrochlore antiferromagnet. The opposite J_4 -dependence of the two phenomena supports a scenario with competition between DM-induced and field-induced chirality.

Finally, the dimer correlations in the zero-field ground states of all considered variants of parameter set B , including the isolated ladder leg ($J_4/J_1 = 0$), are not long-ranged, unlike suggested by the phase diagram of the frustrated ladder [228] (cf. section 1.3.4).⁶⁴ Similarly, the non-trivial long-range dimer

⁶³The uncertainty grows with the magnetization, since the quasi long-ranged component of the correlations of the transverse chirality and hence $\delta(\bar{\kappa}^x)$ increases. Calculations for larger system sizes should alleviate this issue.

⁶⁴Note that the static transverse moments, together with a tilted spiral axis, trivially give rise to oscillations of the dimerization which correspond to the projection of the transverse moments onto the longitudinal polarization and are ignored.

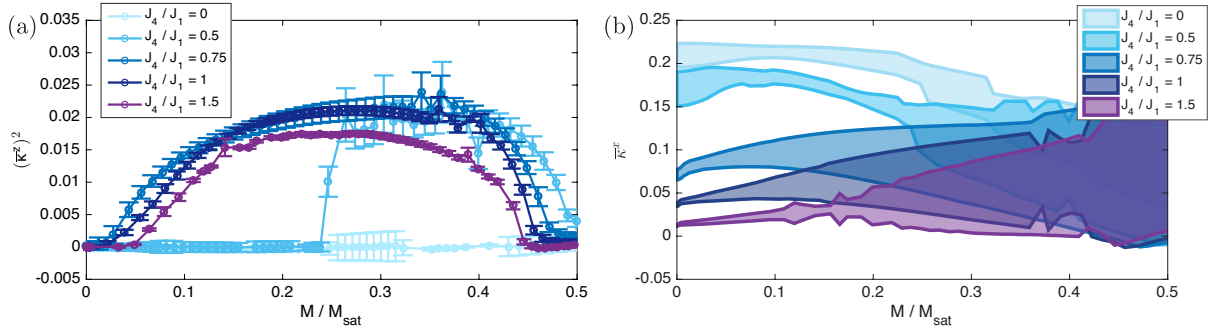


Figure 7.37: Squared longitudinal chirality $(\bar{\kappa}^z)^2$ (a) and transverse chirality $\bar{\kappa}^x$ (b) on the nearest-neighbor leg bond. The quantities and their uncertainties are estimated as described in the text. The calculation parameters correspond to Fig. 7.36.

correlations observed in zero field for parameter set *A* with $J_4/J_1 \leq 0.25$ [cf. Fig. 5.11(b), section 7.12, and Fig. 7.26(a)] are consistently absent in the C1 phase. This phenomenology strongly suggests that (non-trivial) dimerization and chirality are mutually exclusive,⁶⁵ independent of whether the latter is induced by a magnetic field or by DM interactions. Further analysis of the role of dimerization for the field-induced phases of the frustrated ladder is left for future work.

7.14.3 Longitudinal component

Before discussing the effect of the longitudinal component D_1^b of the DM vector on the nearest-neighbor (NN) leg bond, it helps to reconsider its symmetry (see Fig. 4.5): D_1^b alternates along each ladder leg with a phase shift of π between the two legs. As discussed in section 7.10.1, and in agreement with previous work [77, 131], the *field-induced* chirality (see last paragraph of section 7.13) in the frustrated ladder is uniform and parallel to the magnetic field, which is assumed to be applied along the *b*-axis of the crystal ($b \parallel z$). Thus, for a given choice of orientation of the field-induced chirality, the field-induced chirality points either parallel or antiparallel to the longitudinal component of the DM interaction. Following the intuition motivated in section 7.13, the field-induced chirality on a given NN bond is enhanced (reduced) whenever it is parallel (antiparallel) to D_1^b . The resulting situation is depicted in Fig. 7.38(b).

Since the corresponding NN bonds have shared endpoints, the only way to realize such a modulation of the chirality for a classical spiral structure [cf. Fig. 7.19(a)] consists of a modulation of the spiral pitch angle $[\Delta\varphi_{\pm}$ in Fig. 7.38(b)]. Consider, e. g., the oriented NN bond depicted in green [Fig. 7.38(b)]. Clearly, flipping the total chirality interchanges “long” and “short” bonds. Therefore, the staggering of the longitudinal chirality on the NN leg bonds—even though manifest in each individual eigenstate [Fig. 7.38(a)]—disappears upon tracing over the ground-state eigenspace, confirming that the longitudinal chirality on a single NN leg bond is not a well-defined observable (see section 7.3).

Remedy is possible by focusing on the rung bonds instead. As illustrated in Fig. 7.38(b), the alternating pitch angles on the NN leg bonds are expected to induce a twist on the rung bonds. Consider the classical longitudinal chirality κ^z of the oriented rung bond depicted in magenta [Fig. 7.38(b)]. In one of the

⁶⁵This is somewhat complementary to the conclusions drawn in previous work (see [78] and [74, pp. 141-142]).

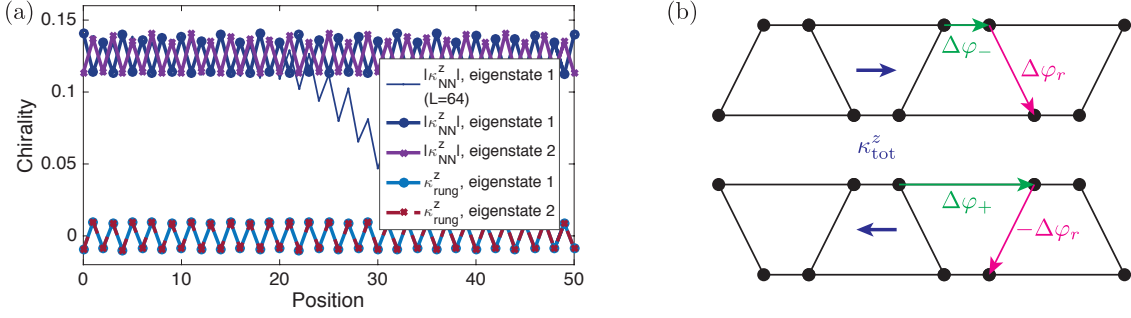


Figure 7.38: (a): Longitudinal chirality on the NN leg (κ_{NN}^z) and rung bonds (κ_{rung}^z), as function of the position along the ladder ($L = 128$, $m = 128$, $s = 24$, $a = 1$; and $L = 64$, $m = 512$, $s = 24$, $a = 1$). The system magnetization is $M/M_{\text{sat}} \approx 0.12$. The origin of the abscissa corresponds to the center of the ladder. (b): Schematic representation of the effect of D_1^b . The (total) field-induced chirality is indicated by the blue arrows (cf. section 7.8.1). The lengths of the leg bonds correspond to the magnitude of the longitudinal chirality. See text for details.

maximally-chiral states [top part of Fig. 7.38(b)],⁶⁶

$$\kappa^z \propto [(1, 0, 0) \times (\cos \Delta\varphi, \sin \Delta\varphi, 0)]_z \quad .$$

In the other maximally-chiral state, the spiral orientation is different, but also the difference of the propagation phases is inverted, such that

$$\kappa^z \propto [(1, 0, 0) \times (\cos \Delta\varphi, -\sin(-\Delta\varphi), 0)]_z \quad .$$

Hence, the longitudinal chirality induced on the rung bonds is independent of the eigenstates and thus a well-defined observable, as confirmed by the calculation results shown in Fig. 7.38(a).

7.14.4 Inferred magnetic structure

The expected effects of the transverse and longitudinal DM interactions on the NN leg bonds on the ordered magnetic structure have been identified for parameter set B . The conclusions are generally consistent with calculations performed for parameter set A with individual DM terms (section 7.13). The results of the two preceding subsections indicate that the ordered magnetic structure in the presence of D_1^{ac} and D_1^b can be described as a spiral resembling Fig. 7.19(a), except that the pitch angles and the rotation axes alternate along each ladder leg. Due to the symmetry C_2^b relating the two ladder legs (see section 4.2.1), the propagation of the spiraling moments is thus determined by two rotation matrices R_{\pm} corresponding to the “long” and “short” bonds in Fig. 7.38(b).

7.15 Discussion and conclusions

Detailed numerical studies of the frustrated spin ladder were performed.⁶⁷ The observed two-fold degeneracy of many field-induced ground states is related with a reflection symmetry of the ladder system

⁶⁶Complications arising due to spin canting (see sections 7.10.3 and 7.14.2) are neglected, such that the absolute propagation phase does not matter.

⁶⁷See section A.1.11 for computing resources used.

(section 7.3). For a translationally invariant system, the two-dimensional ground-state eigenspaces are spanned by states with lattice momenta $|\pm k\rangle$, which also happen to have maximal chirality (section 7.8.1). Note that the zigzag chain exhibits essentially the same symmetry [291]⁶⁸ and chiral order is known to break this spatial parity symmetry [88, 142, 164, 211, 291, 383]. Thus, the preceding results are not surprising after all. In particular, the chiral nature of the states $|\pm k\rangle$ is fully consistent with previous descriptions of the field-induced chiral phase of the zigzag ladder as an imbalanced condensation of magnetic excitations with incommensurate lattice momenta $\pm q$ [164, 404]—an idea which was also applied to the frustrated ladder, albeit in the regime close to saturation [367]. Clearly, suitable interactions are needed to stabilize a broken-symmetry chiral phase (see section 7.8.2). Moreover, if higher-dimensional couplings are present, field-induced chiral order is expected to give rise to a spiral magnetic structure (see sections 7.8.2, 7.10.1, and references therein).

The numerical calculations confirm the previously-reported [77, 131] appearance of a chiral phase (C1 phase) in the frustrated spin ladder, and the computed correlations are consistent with an incipient canted-spiral structure (cf. Fig. 7.19 and previous work [77, 131]). Furthermore, the dependence of the C1 phase upon the individual exchange couplings is established. Please refer to section 7.12 for a summary of the main results of this analysis.

A site-dependent g -tensor generally gives rise to a staggered component of the magnetic field (e. g. , [83, 306]). Certain types of staggered field were predicted to induce quantum criticality in the unfrustrated spin- $1/2$ ladder [425].⁶⁹ More commonly, the effect is limited to an induced antiferromagnetic magnetization component (e. g. , in the spin-1 chain NENP [13, 83, 140]), which can, e. g. , open a field-dependent excitation gap in an otherwise gapless spin- $1/2$ chain [15, 306]. Since the staggered field induced in BiCu_2PO_6 is inconsistent with the next-nearest neighbor exchange couplings, it is nonetheless important to check its effect upon the C1 phase. Corresponding calculations for the case $\mathbf{H} \parallel b$ indicate that the moderately site-dependent g -factors estimated in section 5.2.1 do not destabilize the C1 phase in the experimentally-relevant magnetization range (sections 7.11.3 and 7.13). This is consistent with the intuition that the induced *longitudinal* staggered magnetization should not interfere with the predominantly transverse spiraling moments. However, as noted previously [78] (see also [74, p. 145]), this is not necessarily the case for the transverse field components appearing for $\mathbf{H} \nparallel b$, and hence may contribute to the anisotropic phase diagram of BiCu_2PO_6 [207] (cf. section 4.5).

In the absence of DM interactions, the results suggest the appearance of a C1 phase for all choices of exchange couplings which give rise to incommensurate correlations (section 7.12). Generally, chirality and dimerization appear to compete (see end of section 7.14.2). The C1 phase is connected with the chiral phase of the zigzag ladder (section 7.11.1). For sufficient rung coupling, it spans the magnetization range between the field-induced closing of the spin gap and a plateau-phase at $M/M_{\text{sat}} \approx 1/2$ (section 7.12). Interestingly, the C1 phase is not destabilized by the inequivalence of the next-nearest neighbor (NNN) bonds, $J'_2 \neq J_2$ (section 7.11.3). Therefore, future work is proposed to verify the aforementioned conjectures regarding the stability region of the C1 phase by additional calculations for the frustrated ladder with equivalent NNN couplings (see section 7.12).

The occurrence of a C1 phase is found to be robust against weak-to-moderate DM interactions (see sections 7.13 and 7.14.1). Even though some DM interactions like D_2^c reduce its stability range, the C1

⁶⁸The authors of [291] discuss a discrete interaction-graph symmetry, which turns out to be equivalent to P after substituting the corresponding definitions.

⁶⁹Note that [425] is motivated by copper benzoate [107] and therefore assumes a staggered field which competes with the antiferromagnetic rung coupling. However, this is not the case for BiCu_2PO_6 .

phase extends beyond the range of experimentally accessible magnetizations for all considered choices of exchange couplings and DM interactions (sections 7.12, 7.13, and 7.14). In all cases, chiral order appears as soon as the spin gap has been closed by the applied magnetic field. Inclusion of a symmetric exchange anisotropy associated with the DM interactions (cf. section 1.1.2) appears not to alter these conclusions (section 7.14). The absence of additional phases between the spin-liquid ground state and the C1 phase is confirmed by detailed calculations for parameter sets A and B (sections 7.10.2 and 7.14.1).

Correlation functions calculated in the chiral phase suggest that the DM interactions affect the chirality in a manner consistent with the effects expected for a classical spiral magnetic structure (see section 7.13). For the DM interactions on the nearest-neighbor leg bond, which are believed to be dominant in BiCu_2PO_6 [318] (cf. section 4.3.3), these effects are described in detail in section 7.14. Since the DM interactions act like a potential for the chirality, they also induce static chirality in the spin-liquid ground state. However, due to the symmetry of the system (section 4.3.2), no net chirality emerges below the critical field required to close the spin gap.

Note that a qualitative remark regarding DM interactions in [131] suggests that the aforementioned robustness against DM interactions and the DM-induced perturbations of the spiral correlations were also observed in previous work (cf. sections 7.2 and 7.13). Also, certain types of DM-induced distortions were already considered in [74, pp. 138-140] (and [78])—motivated by classical energy considerations reported for a triangular-lattice antiferromagnet with uniform DM vector [411].

Technically, it is possible to estimate various quantities like transverse ordered moments and spiral tilt angles from the chirality and its correlations (see, e. g., section 7.14.2). However, these results are likely to change once a classical spiral structure is stabilized in the vicinity of higher-dimensional couplings. While not suited to study dynamical properties like the value of the spin gap (section A.5.5), a self-consistent combination of mean-field theory and DMRG, analogous to the treatment of the simple ladder reported in [64], may prove useful for quantitative studies of the field-induced ordered phases in future work. Future calculations focusing on the chiral order might also benefit from methods to select a maximally chiral state in the DMRG procedure (see sections 7.3.2 and 7.8.1, and references therein). Alternatively, the DMRG code could be extended to enable measurements of off-diagonal matrix elements of the chirality (see section 7.3.2). In both cases, the chirality could be measured directly rather than having to resort to its correlation functions, which would generally reduce the computational effort. Since the effects of the DM interactions upon the C1 phase are generally consistent with classical intuition, classical Monte-Carlo calculations might represent a complementary approach [90, 119].

7.16 Open questions regarding BiCu_2PO_6

The prediction of a spiral structure with distortions induced by the DM interactions, similar to the one proposed in previous work [78], is contrasted with high-field NMR data in chapter 8. The rest of this section is dedicated to the discussion of published magnetization and inelastic neutron scattering (INS) data.

As described in section 4.3.3, parameter set B was obtained by fitting the measured dispersion relations of the magnetic excitations in BiCu_2PO_6 to a bond-operator mean-field [317] (BOMF) theory with one-loop corrections [179, 318].⁷⁰ Experimentally, some excitation branches are found to bend towards lower energies and terminate upon entering certain regions of energy-momentum space [318]. This breakdown

⁷⁰Note that the model neglects the inequivalence of the Cu(1) and Cu(2) sites [179, 318].

of the quasi-particle description of the magnetic excitations is attributed to a two-triplon continuum and triplon-(two-triplon) processes which arise due to DM interactions [318]. While two-triplon scattering has been observed earlier [298], the bending down of the triplon mode before merging with the continuum is a remarkable feature, which is not captured by the BOMF theory [318]. Numerical calculations, e. g. , using dynamical DMRG [186] (cf. [385]), would allow to check whether all experimental observations are reproduced by the Hamiltonian proposed in [318] or if additional interactions need to be considered (cf. [179]).

The measured magnetization increases linearly with the magnetic field below the first critical field of BiCu_2PO_6 [207], which is related to the non-vanishing low-temperature magnetic susceptibility discussed in section 5.2.1. While this behavior can be reproduced by including a site-dependent g -factor and/or transverse DM interactions, as proposed in [207], the difference of the g -factors estimated in section 5.2.1 is insufficient to provide quantitative agreement. The data shown in Fig. 7.29 suggest transverse DM interactions of order $0.3 J_1$. This conclusion is consistent with fits to the temperature-dependent magnetic susceptibility (chapter 5) and the aforementioned INS results [318].

Nonetheless, it has to be noted that none of the calculated magnetization curves reproduces the measured magnetization (see Figs. 7.29 and 7.31). Most importantly, the critical field is overestimated, as already noted in [401, pp. 10-11] (see also [131]). This observation agrees with the exact-diagonalization calculations of magnetic and thermal response functions described in [401] and chapter 5 and strongly suggests that the frustrated-ladder model is incomplete. Note that the degeneracy of the triplet magnetic excitations is fully lifted in BiCu_2PO_6 already in zero field [318], which is only possible if DM interactions involving at least two different spatial directions are present [179]. Although desirable for the future, an exhaustive search over all combinations of different DM interactions, exchange couplings, and g -factors is not feasible within the scope of the present work (cf. section 6.8). Still, small perturbations of the individual parameters of the Hamiltonian (4.1) are expected to be approximately independent and their effects have been considered in the preceding subsections. The discrepancies between the calculated and the measured magnetization curves are therefore attributed to the presence of additional interactions.⁷¹

At magnetic fields well above the critical field, the calculated and measured magnetization curves generally approach each other [see, e. g. , Fig. 7.31(a)], which corroborates the exchange-energy scales proposed in the literature (cf. section 4.3.3; see also discussion in section 5.4.5 and references therein). Thus, the main differences are restricted to the region around the critical fields. Consider the results for parameter set B in more detail [Fig. 7.31(a)]. The critical field predicted by the calculation is of the order of 45 T, which is larger than the two experimentally observed critical fields $\mu_0 H_{c1} \simeq 20$ T and $\mu_0 H_{c2} \simeq 34$ T [207]. There is experimental evidence for the importance of interladder couplings in BiCu_2PO_6 (see section 5.3), and in fact parameter set B involves such interactions (see section 4.3.3), even though these had to be ignored for computational reasons (section 5.3). In this context, it is important to note that the BOMF theory used to explain the INS data predicts critical fields remarkably close to H_{c1} [318], whereas the calculations performed in this work appear more compatible with H_{c2} . On the other hand, the NMR data presented in chapter 8 indicate that the phase above H_{c2} corresponds to the C1 phase. Hence, similarly to the case of the two-triplon scattering reviewed above, calculations including the interladder couplings are needed to clarify which of the observed transitions are reproduced by the model (cf. [401, p. 11]). Answering this question is computationally expensive (see section 5.3) and therefore left for future work. However, the proposed interladder couplings [318] are fully compatible

⁷¹As pointed out in [401], since the square-root-like onset of the magnetization reflects the density of states (cf. section 7.1.3 and references therein), its absence suggests higher-dimensional interactions such as interladder couplings.

with the rung exchange, and therefore believed to have an effect similar to increasing the rung coupling in the magnetically ordered phases. Thus, the stabilization of the C1 phase with increasing rung coupling (section 7.12) suggests that interladder couplings alone are insufficient to explain the appearance of a second magnetic phase transition in BiCu_2PO_6 .⁷² Possible additional interactions are discussed in chapter 8 (section 8.7.5).

Besides the questions outlined above, future theoretical work should consider the effects of combinations of uniform and staggered magnetic fields with general orientations, as they are expected to appear for magnetic-field orientations $\mathbf{H} \nparallel b$ (see section 7.15 and references therein). Also, exhaustive scans of the corresponding parameter space might be able to identify a single model which is consistent with all experimental data.

Finally, the arguments given in section 7.8.2 suggest that interlayer, i. e. , three dimensional, couplings are a prerequisite for long-range magnetic order. Experimentally, the field-induced magnetic order remains stable up to temperatures $T \lesssim 10$ K [207], which coincides with the upper bound for the interlayer couplings obtained in first-principles calculations [401]. By contrast, no appreciable dispersion is observed along the a direction in INS experiments, suggesting that interlayer couplings are smaller ([316–318] and [259, p. 113]). It therefore remains unclear to which extent the long-range magnetic order realized in the field-induced phases of BiCu_2PO_6 depends on the three-dimensionality associated with the interlayer couplings.

⁷²Note that previous numerical evidence [77, 131] for the existence of a solitonic phase below the C1 phase could not be substantiated in this work (see sections 7.6.3 and 7.10.2).

8 BiCu₂PO₆: High-field nuclear magnetic resonance experiments

8.1 Introduction and previous results

Exemplary results of previous ³¹P-NMR experiments [74, 78] probing the intermediate-field phase in BiCu₂PO₆ are reproduced in Fig. 8.1. For the present work, the data obtained on pure BiCu₂PO₆ ($x = 0$) are of particular relevance. Peaks in the spin-lattice relaxation rate T_1^{-1} have been used to confirm [78] the phase boundaries reported earlier [207]. At the critical field H_{c1} , the line shape manifestly changes from a single peak to a complicated distribution with three peaks, which admits two main conclusions [74, 78]: (i) A long-range ordered magnetic structure can only give rise to a continuous distribution of internal magnetic fields if the propagation vector is incommensurate with the lattice [74, p. 133]. Note that some caution is required in the presence of disorder. However, incommensurate correlations are experimentally established in BiCu₂PO₆ (see section 4.1). (ii) The spectra are incompatible with a long-range ordered single- q structure (see [74, pp. 138-145] and discussion below).

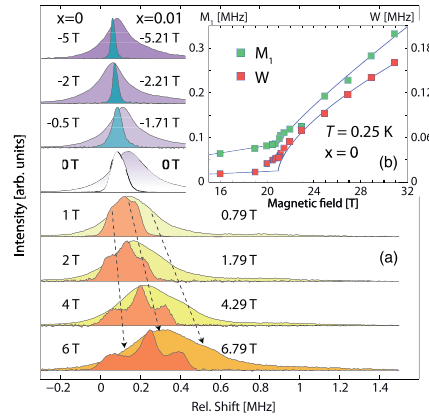


Figure 8.1: (a): Previously-obtained ³¹P-NMR spectra of Bi(Cu_{1-x}Zn_x)₂PO₆ [78]. The $x = 0$ ($x = 0.01$) compound was measured at $T = 0.25$ K ($T = 1.4$ K) and the corresponding data are shown in the foreground (background). The magnetic fields ($\mathbf{H} \parallel b$) are reported w.r.t. the corresponding critical fields of $\mu_0 H_{c1} = 20.96(7)$ T [$\mu_0 H_{c1} = 24.21(9)$ T], and shifts relate to the Larmor frequency of the ³¹P nuclei in a reference compound (see [308]). (b): First moment M_1 and standard deviation W of the spectra for the $x = 0$ compound [78]. Lines are guides to the eye. (Reprinted figures (a) and (b) with permission from Ref. [78]. Copyright 2013 by the American Physical Society.)

It appears worthwhile to reconsider argument (ii) in more detail. As discussed in section 1.5.9, the coupling between electronic and nuclear magnetic moments is typically linear. For a one-dimensional ordered magnetic structure with (one-dimensional) propagation vector q , the NMR shift ν is proportional to $\sin(qr + \varphi)$, where r is a spatial coordinate (cf. [74, p. 139]). For incommensurate q , this corresponds to $\nu(\alpha) = a \sin(\alpha)$ with α quasi-continuous and uniformly distributed in $[-\pi/2, \pi/2)$. The intensity $I(\nu_0)$ of the NMR spectrum at frequency ν_0 is hence given by the well-known *double-horn line shape*

(e. g. , [70]; cf. [74, p. 140]) [Fig. 8.2(a) inset],

$$I(\nu_0) = \int_{-\pi/2}^{\pi/2} d\alpha \delta(\nu(\alpha) - \nu_0) \propto \int_{-\pi/2}^{\pi/2} d\alpha \frac{1}{|\cos \alpha|} \delta(\alpha - \arcsin \frac{\nu_0}{a}) = \frac{[\nu_0 \in [-a, a]]}{\sqrt{1 - (\frac{\nu_0}{a})^2}}, \quad (8.1)$$

where $[x \in A] = 1$ (0) whenever $x \in A$ ($x \notin A$) [431]. By contrast, if q is commensurate and corresponds to a lattice period¹ p , the spectrum consists of p individual, discrete peaks (cf. [74, pp. 133,140]).

An extensive discussion of NMR line shapes expected in systems with incommensurate order can be found in [61], and the fact that one-dimensional sinusoidal spiral models cannot reproduce the three-peak line shape was shown in [74, pp. 138-140] (see also [78]). The following arguments enlarge the class of magnetic structures which can be excluded based on the three-peak shape of the NMR spectrum in the intermediate-field phase.

First, it is noted that (8.1) also holds for three-dimensional single- q structures. For a general three-dimensional multi- q structure, $\nu = \sum_k a_k \sin(\mathbf{q}_k \cdot \mathbf{r} + \varphi_k)$ needs to be histogrammed over $\mathbf{r} \in \mathbb{Z}^3$. The analysis of this general case is not straightforward. In fact, there exist multi- q scenarios which are consistent with the observed lineshapes [61], as illustrated in Fig. 8.2(a). Clearly, the $2q$ component gives rise to anharmonic² features [Fig. 8.2(b)], resulting in a histogram remarkably similar to the experimental data.³

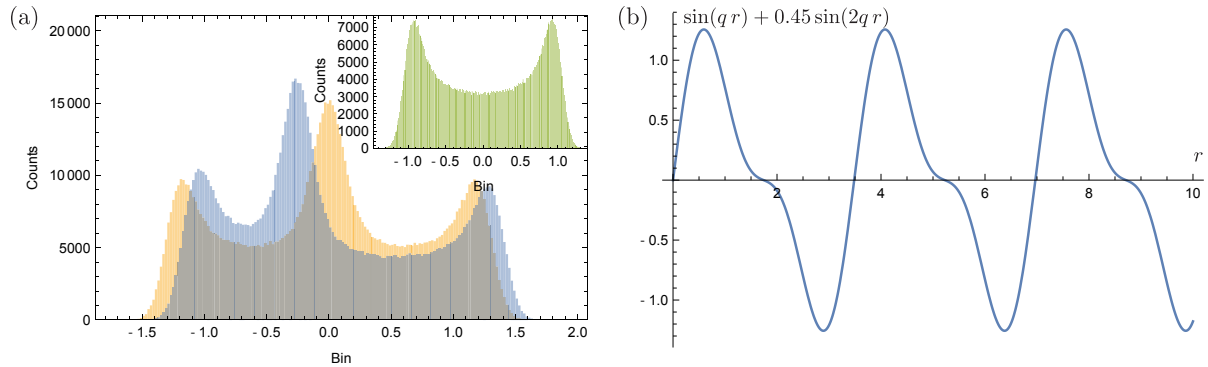


Figure 8.2: (a): Histograms of $\sin(qr) + 0.45 \sin(2qr + \varphi) + \delta$ with δ normal-distributed (standard deviation 0.1) and $q = 0.574 \pi$, for $\varphi = 0$ (yellow) and $\varphi = 0.5$ (blue). The inset shows a histogram of $\sin(qr) + \delta$ for comparison. (b): Spatial dependence of $\sin(qr) + 0.45 \sin(2qr)$ (as function of r).

Consider instead a general three-dimensional multi- q structure with commensurate modulations and distortions, i. e. , \mathbf{q}_k for $k \neq 0$ is either commensurate or differs by a commensurate wave-vector from \mathbf{q}_0 . If incommensurate wavenumbers appear only along one lattice direction, the full spectrum reduces to a superposition of a finite number of shifted spectra corresponding to the one-dimensional case. Consider this one-dimensional case without loss of generality. The commensurate components alone give rise to a discrete spectrum. The full spectrum is then obtained by convolution of this discrete spectrum with the

¹ $p = \min \{p \in \mathbb{N}^+ : qp = 0 \pmod{2\pi}\}$

²The term ‘‘anharmonic’’ (cf. [74, p. 140]) is used to refer to functions which do not satisfy the equation of motion of a harmonic oscillator.

³In fact, inspection of the model used to fit the spin textures shown in Fig. 7.5 shows that it corresponds to such a multi- q structure. Although this model was already developed in previous work and was used to motivate a phenomenological model for the NMR spectrum [74], the corresponding works resorted to the inclusion of a solitonic phase-variation to reach agreement with the experimental data (see [75, Figs. 18,20 and eqs. 30,31], [74, p. 145 and Fig. 6.15], and [78]).

spectrum due to the incommensurate components. Note that the convolution with the discrete spectrum corresponds to a superposition of shifted spectra. Thus, let all q_k be incommensurate without loss of generality. By assumption $q_k = q_0 + q_k^{(c)}$ with $q_k^{(c)}$ commensurate. Since q_0 is incommensurate, the phases $q_0 r$ and $q_k^{(c)} r$ are uncorrelated upon sampling over r . With \bar{p} the lowest common multiple of the lattice periods associated with all the commensurate components $q_k^{(c)}$, the histogramming over the commensurate and incommensurate phase terms can therefore be performed independently and the full histogram is a superposition of \bar{p} double-horn spectra. This argument shows that, at least under the aforementioned assumptions, the full spectrum corresponds to a superposition of shifted double-horn spectra, which is inconsistent with the NMR data acquired in the intermediate-field phase of BiCu_2PO_6 for general parameter values.

Based on the experimental evidence reviewed above, the intermediate-field phase was interpreted as a soliton-lattice phase and a phenomenological model based on solutions of the Sine-Gordon equation was used to explain the NMR line shape [74, 78]. Furthermore, numerical calculations [77, 131] (cf. section 7.2) indicated the appearance of a spiral phase at higher magnetic fields and it was conjectured [78] that this corresponds to the high-field phase observed [207] in BiCu_2PO_6 (cf. section 4.5). These conclusions motivated the experiments reported in the following, since spiral magnetic order should give rise to double-horn spectra like the one depicted in the inset of Fig. 8.2(a) (cf. [78, Fig. 3b]) and thus be easy to detect using NMR [74, pp. 139-140] (see also [78]).

The experiments were proposed (see [74, p. 156]) and initiated by F. Casola, and prepared and carried out in collaboration with T. Shiroka and F. Casola, using single crystals grown by S. Wang. Profs. H.-R. Ott and J. Mesot were responsible for the scientific lead and supervision of the project, and are further involved in ongoing efforts (see [312]) to publish the results presented in part II of this work. Note also that the data analysis presented in this chapter is generally inspired by previous work [74, 78]. Valuable experimental contributions were also made by A. P. Reyes and P. L. Kuhns. See Acknowledgments for more information.

8.2 Experimental details

Following the motivation outlined in section 8.1, ^{31}P NMR experiments in high magnetic fields were performed. For $\mathbf{H} \parallel b$, the magnetic field required to reach the high-field field-induced magnetic phase of BiCu_2PO_6 [cf. Fig. 4.6(a)] is $\mu_0 H_{c2} \geq 34$ T [207]. The experiments therefore required the use of the 45 T hybrid magnet at the National High Magnetic Field Laboratory (NHMFL) in Tallahassee (FL, USA), which combines a 12 T superconducting “outsert” magnet with a 33 T resistive insert magnet [269]. Two magnet times of 5 days each were dedicated to performing the experiments.⁴ Although the phase diagram indicates that a ^4He cryostat is in principle sufficient to study the field-induced phases of BiCu_2PO_6 , during the first magnet time it turned out to be prone to blockage by bubbles of diamagnetic ^4He which can accumulate in the system due to the large magnetic-field gradients in the vicinity of the magnet [2]. Later experiments therefore made use of a ^3He cryostat.

The sample and the experimental setup are depicted in Fig. 8.3. The somewhat unorthodox winding direction of the coil has been chosen because a low coil induction is preferred for bottom tuning (cf.

⁴Besides time constraints, the experiments are limited by the total energy budget allocated. In our case this amounted to 650 MWh for each magnet time, which allows for about 20 h of operation at maximum field.

section 3.2).⁵ In addition to the strongly-anisotropic phase diagram of BiCu_2PO_6 [207] [Fig. 4.6(a)], the NMR spectra recorded in the intermediate-field phase were found to be very sensitive to the sample alignment in previous work [74]. Therefore, a two-axis rotator was used in this work to carefully align the sample *in-situ* [Fig. 8.3(b)]. The details of this alignment procedure are summarized in section A.4.2. Additional measurements of magnetization and ^{31}P NMR performed at ETH Zürich further corroborate the alignment and the integrity of the sample used in the high-field experiments (see section A.4.3 for more information).

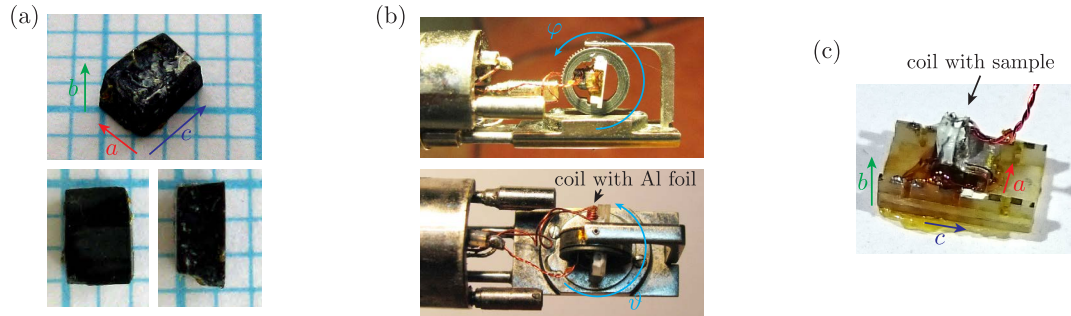


Figure 8.3: (a): Sample used in the high field experiments. (b): Two-axis rotator used at NHMFL, with sample mount. The two rotation angles φ and ϑ are indicated in the figure. The bottom panel also shows the separate coil containing the Al foil employed for the frequency calibration. (c): Sample mount consisting of G10 sample carrier, sample, and single-turn coil made from two layers of thin Cu wires. The white substance is a PTFE coating used to insulate the terminals of the coil. The sample has dimensions $2.9 \times 2.1 \times 1.35 \text{ mm}^3$ and mass 46.6 mg (measured by T. Shiroka). The approximate crystal directions indicated in (a) and (c) are consistent with earlier documentation (by S. Wang [3]), as well as the angular dependences of the NMR shift (see sections A.4.2 and A.4.3).

The applied magnetic field was determined from the resonance frequency of the ^{27}Al nuclei in a piece of aluminum foil located nearby the sample [Fig. 8.3(b) bottom].⁶ Besides varying the magnetic field, the influence of temperature on the high-field phase was explored. Since the only temperature sensor available at the time of the experiment exhibited strong magnetoresistance effects, the spin-lattice relaxation rate of ^{27}Al [378] was used as a secondary means of determining the temperature in the vicinity of the sample (see section A.4.1 for details).

8.3 Results

The best data obtained during the high-field experiments are summarized in Fig. 8.4. In accordance with previous work [74, p. 138], the relaxation rates T_1^{-1} were determined by stretched-exponential fits [363] to the recovery of the nuclear magnetization following a single saturating pulse.⁷ Unless stated

⁵The setup depicted in Fig. 8.3 corresponds to the one used during the second magnet time (in 2014). During the preceding magnet time (in 2013), a multi-turn coil and top tuning were used, which has the advantage of not imposing any frequency restrictions. However, at high magnetic fields, the output level of the available high-frequency power amplifier (250 W) was insufficient to invert the ^{31}P nuclei using reasonably short pulse widths.

⁶The effective gyromagnetic ratio is $\gamma_{^{27}\text{Al}} = 11.1122 \text{ MHz/T}$ [74, p. 33]. A different approach was chosen for the spectra measured at 14 K and 24 K (see end of section A.4.2). Generally, a systematic uncertainty results from the off-center position of the reference (see section A.4.5 for details).

⁷The associated relative uncertainty is estimated as 10%, based on previous experience [2] and in accordance with the results of repeated measurements of the ^{27}Al spin-lattice relaxation rate.

otherwise, T_1^{-1} was measured at a frequency close to the center of the NMR spectrum. All spectra, as well as the relaxation rates shown in Fig. 8.4(a), were recorded using the sample alignment documented in section A.4.2. The relaxation rates shown in Fig. 8.4(b) were obtained during an earlier magnet time and the sample was slightly misaligned during the corresponding measurements (see section A.4.4 for details).

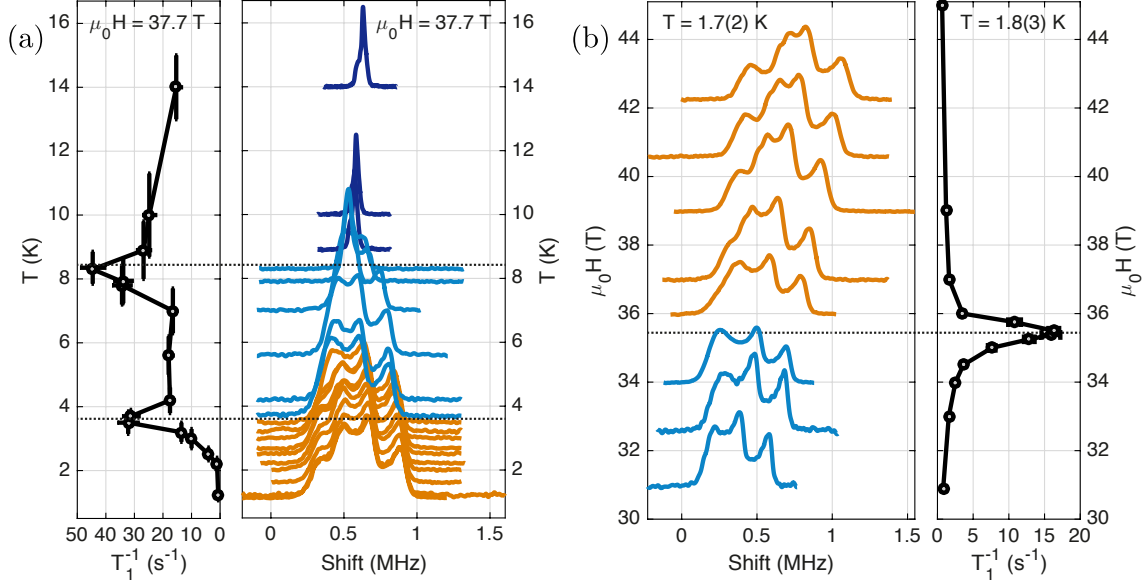


Figure 8.4: NMR spectra and spin-lattice relaxation rates T_1^{-1} of the ^{31}P nuclei in BiCu_2PO_6 , (a) as function of temperature T and (b) as function of magnetic field $\mu_0 \mathbf{H} \parallel b$. The ordinates of the baselines of the NMR spectra encode the corresponding temperatures and magnetic fields, respectively. The intensities are scaled to have a common maximum value. Colors distinguish different phases and dotted lines indicate the approximate locations of the peaks in the relaxation rates. Shifts are reported w. r. t. a standard ^{31}P reference [308] and are subject to a systematic field-calibration uncertainty which is expected to be common to all spectra shown in (a) and similar (i. e., correlated) for the spectra shown in (b) (see section A.4.5). (Updated version of a figure previously used in [312].)

With increasing magnetic field at low temperature [Fig. 8.4(b)], as well as upon decreasing temperature at high magnetic field [Fig. 8.4(a)], the ^{31}P -NMR spectra evolve from a single narrow line, characteristic of the (quantum) disordered regime [78] (cf. Fig. A.9), through the distinct three-peak structure of the intermediate-field phase [78] (cf. section 8.1), to a previously unreported four-peak spectrum in the high-field phase. Since the high-field phase is the primary focus of the present work, the shape of the NMR spectra at $H \gg H_{c2}$ is discussed first, in section 8.6. Afterwards, I briefly describe a few ideas regarding the intermediate-field phase (section 8.7), before concluding the chapter.

8.4 Phase boundaries

The NMR spectra depicted in Fig. 8.4 undergo distinct changes, which are accompanied by peaks in the spin-lattice relaxation rate T_1^{-1} . Such peaks are expected to arise due to the softening of the excitations in the vicinity of a phase transition (cf. section 1.5.8). They can therefore be used to map the phase boundaries, as done in previous work on the intermediate-field phase of BiCu_2PO_6 [74].

The transition temperatures $T_{c2} \approx 3.6$ K and $T_{c1} \approx 8.3$ K estimated from the temperature-dependence of T_1^{-1} at $\mu_0 H = 37.7$ T [Fig. 8.4(a)], as well as the critical field $\mu_0 H_{c2} \approx 35.5$ T obtained from the field-dependence at $T = 1.8(3)$ K [Fig. 8.4(b)], are compared with recently-reported [207, 208] phase diagrams of BiCu₂PO₆ in Fig. 8.5. The agreement with the literature is very good. Although T_1^{-1} decreases quickly upon reducing temperature, the data do not admit firm statements regarding the presence or magnitude of an excitation gap.

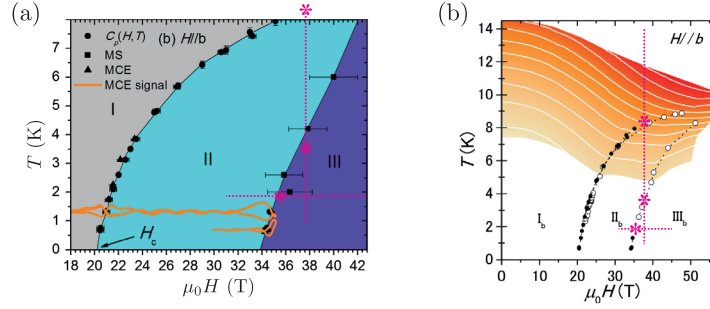


Figure 8.5: Comparison of phase boundaries deduced from the ³¹P-NMR spin-lattice relaxation rates T_1^{-1} shown in Fig. 8.4 (magenta asterisks) with the phase diagrams reported in Refs. [207] (a) and [208] (b). Dashed lines illustrate the temperature and magnetic-field ranges covered by the T_1^{-1} data shown in Fig. 8.4. (Reprinted figure (a) with permission from Ref. [207]. Copyright 2012 by the American Physical Society. Phase boundaries annotated with permission. Reprinted figure (b) with permission from Ref. [208]. Copyright 2014 by the American Physical Society. Phase boundaries annotated with permission.)

8.5 Analysis of NMR shift

If one assumes that the uniform component of the ordered magnetic structure does not break the rotation-symmetry C_2^b about the b -axis of the crystal (see section 4.2.2), the first moment of the NMR spectrum can be related with the sample magnetization [74, p. 133]. In this case, the NMR shift K , w. r. t. the ³¹P resonance frequency in BiZn₂PO₆, is given by (cf. section 6.5.1)

$$K/\gamma_{31\text{P}} = 2 \sum_{i=1}^2 \Lambda_i^{bb} m_{\parallel,i} + \sum_{i,k=1}^2 \left[D_{i,k}^{bb} + 2(l_D - l) \frac{\mu_0 \mu_B}{V} \right] g_i^{bb} m_{\parallel,i} . \quad (8.2)$$

Here, $m_{\parallel,i}$ denotes the uniform component of the longitudinal ordered moment on the Cu(i) site ($m_{\parallel,i} = -\langle S_{i,r}^{(k),z} \rangle$), which is assumed to be the same for all ladder units in the crystal. The shift K is expressed in frequency units and $\gamma_{31\text{P}}$ is the gyromagnetic ratio of the ³¹P nucleus [308]. The remaining notation is consistent with chapter 6. The matrices $\Lambda_i = A_i g_i$ describe the hyperfine couplings estimated in section 6.6.3 (see Fig. 6.2 for the coupling geometry). Correspondingly, $D_{i,k}$ (section 6.3.5) represents the dipolar coupling to all Cu(i) sites in the magnetic layer selected by $k \in \{1, 2\}$ (see section 6.2 for site-indexing conventions). Since there are two such sites per unit cell, the demagnetization correction (see section 6.3.2) involves a factor two. The demagnetization factors l and l_D correspond to the sample geometry and the summation region used to evaluate the dipole-coupling matrices (cf. section 6.3.2), respectively. The rather simple form of the expression for K is due to the fact that the b direction is a principal axis of the g -tensors g_i [74, p. 96] (cf. section 4.3.1). Finally, the four P sites present in BiCu₂PO₆ (see Fig. 6.1) are related by the symmetries σ_a and C_2^b , as will be discussed in more detail

below (section 8.6.2). Unless the hyperfine couplings are field-dependent, arguments analogous to those presented in section 8.6.2.5 show that the average NMR shifts of the four P sites are degenerate, which is why the P-site index was omitted in equation (8.2).

Clearly, a relation between $m_{\parallel,1}$ and $m_{\parallel,2}$ is needed in order to solve equation (8.2) for the magnetization $M = \frac{1}{2} \sum_i g_i^{bb} m_{\parallel,i}$. For parameter set A (see section 4.3.3), the smaller frustration of the Cu(1) sites results in a preferential magnetization of the Cu(1) sublattice [cf. Fig. 7.6(b), see also [77, p. 8]]. By contrast, the g-factors estimated in section 5.2.1 counteract this preference and yield a predominantly staggered longitudinal magnetic response in the spin-liquid phase (cf. Fig. 5.2). With increasing magnetization, these two effects compete, as illustrated in Fig. 8.6. Direct use of the curve obtained for parameter set A did not provide satisfactory results.⁸ However, this is not unexpected given the uncertainty regarding the model parameters (see sections 4.3.3 and 5.4.5), as well as the observation that the model generally appears to be incomplete (sections 5.5 and 7.16). In the absence of additional constraints, and in accordance with parameter set B deduced from inelastic neutron scattering [318], $m_{\parallel,1} \approx m_{\parallel,2}$ is therefore assumed in the following.

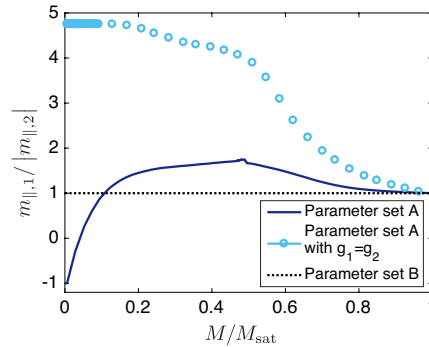


Figure 8.6: Ratio of sublattice magnetization calculated using DMRG for parameter set A with uniform ($L = 256$, $m = 128$, $s = 24$) and site-dependent g-factors estimated in section 5.2.1 ($L = 256$, $m = 512$, $s = 512$). The dotted line illustrates the behavior expected for parameter set B which assumes equivalent Cu sites.

The results of the analysis are summarized in Fig. 8.7. The new NMR data agree reasonably well with previous results [74]. Differences are attributed to different sample temperatures during the corresponding experiments. Indeed, a decrease of K at low temperature was reported in the intermediate-field phase [74, Fig. 6.8a]. Moreover, complete alignment of the sample was not possible during the measurements yielding the open circles (see section A.4.4).

Differences with published magnetization data [207, 208] are not unexpected given the significant uncertainties associated with the hyperfine couplings (sections 6.7 and A.4.4), as well as the arbitrariness of the assumption $m_{\parallel,1} = m_{\parallel,2}$. Accepting that the presence of two inequivalent Cu sites precludes a model-free estimation of the magnetization from the NMR data, the overall good qualitative agreement with the published magnetization data is nonetheless reassuring and corroborates that the assumptions made above are *approximately* correct.

All data shown in the inset of Fig. 8.7 were recorded following a careful sample alignment procedure (see section A.4.2). In particular, the data points at temperatures $T \leq 13.5$ K were measured without any intermittent changes of magnetic field or sample alignment. Therefore, the uncertainty of the rel-

⁸This remains the case when using the magnetization data from [207] to obtain an interpolation $H \mapsto M$ in order to work around the overestimated critical field (see [401] and section 7.12).

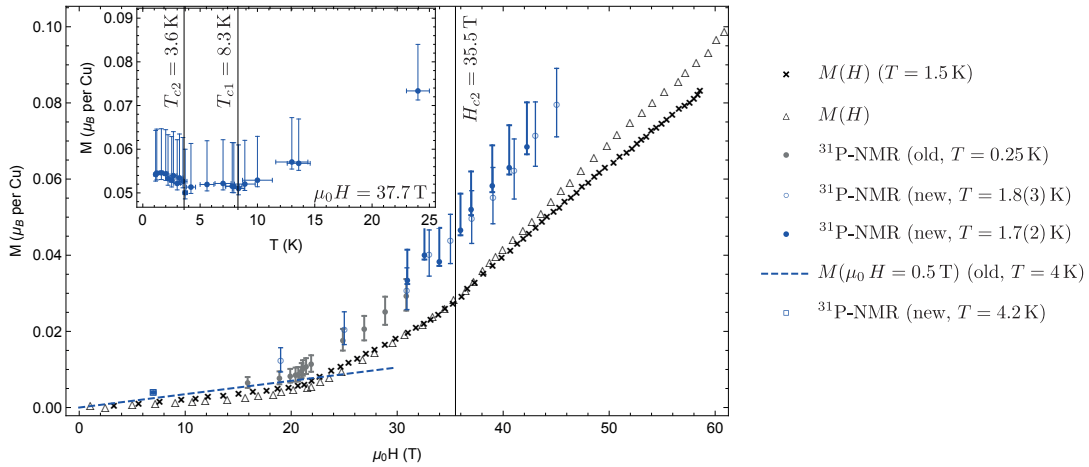


Figure 8.7: High-field magnetization estimated from analysis of ^{31}P -NMR shifts using equation (8.2). Previous NMR results (“old”) originate from Ref. [74, p. 134], whereas new results (“new”) correspond to the data shown in Fig. 8.4 (filled symbols) and Fig. A.9 (open symbols), respectively. A demagnetization factor $l = 0.55(10)$ is used for the high-field sample shown in Fig. 8.3(a) (“new”), while $l \approx 0.33(30)$ is assumed for the previous results. In addition to the demagnetization factors, the error bars also account for the field-calibration uncertainties estimated in section A.4.5. Low-field ^{31}P NMR [see Fig. A.7(a)] and magnetization [dashed line, extrapolated from $\mu_0 H = 0.5$ T; see Fig. 5.1(b) for data source and details] were measured at ETH Zürich. Magnetization values sampled from the curves reported in Refs. [207] (crosses) and [208] (triangles) are included for comparison. The inset shows the temperature dependence of the magnetization in the high-field phase.

ative temperature-induced changes is much smaller than suggested by the error bars. Note that under the assumptions made above, equation (8.2) predicts a linear relation between magnetization and NMR shift. Considering the inset of Fig. 8.7, the NMR shifts clearly pass through a minimum at both phase transitions—a behavior which remains to be explained. Furthermore, an increase of the NMR shift is observed outside the magnetically-ordered phases, which suggests that a gap towards magnetic excitations is either absent or comparable to the thermal energy scale. The preceding observations agree with previous measurements of the temperature-dependence of the ^{31}P -NMR shift at $H_{c1} < H < H_{c2}$ [74, Fig. 6.8a]. However, these features are not necessarily related to the net magnetization, since the peculiar temperature-dependence of the NMR shift may equally well indicate the breakdown of any of the assumptions made in the course of the above analysis.

8.6 Interpretation of NMR spectra in the high-field phase

In this section, I discuss the shape of the NMR spectra acquired in the high-field phase of BiCu_2PO_6 (orange data in Fig. 8.4) in more detail. The relation between the following subsections should become clear from the concluding discussion in section 8.6.6, which also summarizes the most important intermediate results.

8.6.1 Phenomenology

As seen in Fig. 8.4(b), the ^{31}P -NMR spectra develop a fourth peak in the high-field phase of BiCu_2PO_6 . The continuous appearance of the NMR spectra (see section 8.1 and references therein), numerical calculations [401] (see also chapter 7), and neutron scattering experiments [259, 316, 318], all indicate that correlations along the b -direction are incommensurate.

The line shape acquired at $\mu_0 H = 42.2$ T [Fig. 8.4(b)] is believed to be representative of the NMR spectrum well within the high-field phase ($H \gg H_{c2}$) and is therefore considered in more detail in the following. Qualitatively, the spectrum appears to consist of two superimposed double-horn spectra, similar to the one shown in the inset of Fig. 8.2. Such a shape was predicted earlier for the high-field phase [74, 78]. To illustrate the similarity, the measured spectrum is fitted using a superposition of two double-horn spectra, resulting in the black line shown in Fig. 8.8(a). The estimated widths of the two double-horn components are 0.2 MHz and 0.65 MHz, respectively.⁹ The average shift is the same for both components and amounts to 0.75 MHz. A Gaussian broadening of 0.11 MHz full-width at half-maximum (FWHM) is included. Hints of a fine structure in the narrow component of the spectrum are attributed to the strong angular-dependence of the NMR spectrum in the high-field phase.¹⁰

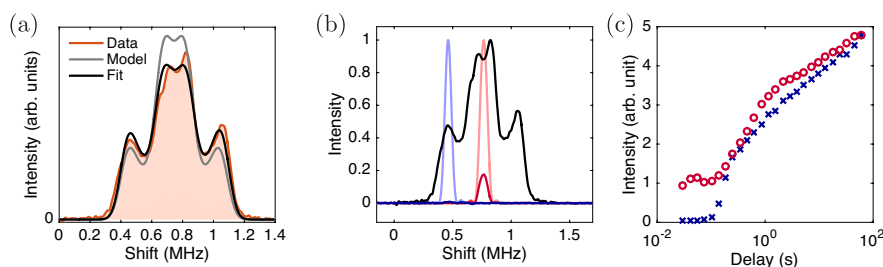


Figure 8.8: (a): Fit to, and resulting double-horn model for, the ^{31}P -NMR spectrum measured at $\mu_0 H = 42.2$ T [Fig. 8.4(b)]. See text for details. (b): Fourier transforms of ^{31}P -NMR echoes acquired 30 ms (dark colors) and 60 s (light colors) after a comb of 50 saturation pulses with 1 ms interpulse delay at $\mu_0 H = 42.2$ T and $T = 1.7(2)$ K. The black line shows the corresponding complete spectrum [cf. (a)]. Intensities are normalized to the maxima of the data acquired at 60 s delay. (c): Relaxation of nuclear magnetization corresponding to the data shown in (b). The intensities are rescaled to agree at large delays. (Subfigures (a) and (b) reused from [312].)

Note that the areas of the two fitted double-horn components have a ratio of approximately 2 : 3. However, there is no apparent physical reason why such a ratio should arise in BiCu_2PO_6 . For any single- q magnetic structure, each of the four P sites in BiCu_2PO_6 is expected to give rise to a double-horn spectrum (see section 8.1). Hence, as long as the magnetic unit cell coincides with the crystallographic one, intensity ratios of 0 : 1, 1 : 1, or 1 : 3 are expected. Visually, the deviation of the data from this prediction is not dramatic, as illustrated by the gray curve in Fig. 8.8(a), in which the relative intensities of the two components were adjusted to 1 : 1. Two possible origins for the relative reduction of the observed intensity of the narrow double-horn component of the spectrum are proposed.

First, the spectra were acquired by summing Fourier-transformed spin echoes obtained at different frequencies [91] and the bandwidth of each of the echoes was smaller than the width of the central double-horn contribution. The recorded signals were generally very strong and therefore prone to distortion by a possible non-linear response of the receiver electronics (signal compression), which can result in a

⁹These widths correspond to $2a$ in equation (8.1).

¹⁰Note that the fine-structure initially present in the blue trace disappeared after the alignment scan shown in Fig. A.6(b).

reduced amplitude of the central peak (see section A.4.6 for details).

Secondly, the nuclear-spin dynamics appear to be different for the two double-horn components. The colored data shown in Fig. 8.8(b) were acquired in the same experimental conditions and using the same NMR pulse sequence, consisting of a train of evenly-spaced pulses. Clearly, the nuclear magnetization is saturated in one case (blue data), but not in the other (red data).¹¹ Furthermore, the corresponding relaxation curves [Fig. 8.8(c)] cannot be fitted using stretched exponentials. This is not the case when using a single saturating pulse instead of the pulse train. Note that the spin-spin relaxation rate is most likely too short to explain this behavior (cf. Fig. A.9). A possible explanation might be spectral diffusion (e. g., [422, p. 30]), which could also explain the otherwise observed stretched-exponential recovery. In a classical spiral structure, phason-like sliding modes of the spiral might give rise to such effects.¹² However, additional experiments would be needed to study this behavior more systematically.¹³

8.6.2 General spiral structures

8.6.2.1 General symmetry considerations

Each unit cell of BiCu_2PO_6 contains four P sites (Fig. 6.1). Therefore, four double-horn contributions are expected to arise for a general single- q magnetic structure, or a sample which is misaligned along a general direction (see section 8.1; see also [75, Fig. 15]). The experimental procedure is assumed to guarantee the orientation $\mathbf{H} \parallel b$ to a good approximation (see sections 8.2 and A.4.2). It is further assumed that correlations along the b -direction are incommensurate (see section 8.6.1).

The symmetric appearance of the NMR spectrum reflects the fact that the average NMR shift is the same for all P sites (section 8.6.1), which indicates that the uniform longitudinal magnetizations $m_{\parallel,1}$ and $m_{\parallel,2}$ are equal for all ladder units. Since $m_{\parallel,i}$ merely defines the average NMR shift already analyzed in section 8.5, the corresponding $q = 0$ component of the magnetic structure is ignored in the following.

Guided by the dominant exchange couplings (see section 4.3.1), the magnetic order in BiCu_2PO_6 is believed to be defined by the one-dimensional ladder units. Thus, each ladder unit is assumed to adopt a general magnetic structure with incommensurate wavevector q_b (cf. [74, pp. 138-139]). Without loss of generality, this magnetic order is taken to have a net chirality along the b -direction, as suggested by numerical calculations (see chapter 7 and references therein). The magnetic structure may involve distortions like those expected to be induced by the DM terms (see sections 7.13 and 7.14.4). Although motivated by the anticipated spiral order (cf. chapter 7), these assumptions neither exclude various non-uniform components of the longitudinal magnetization (as long as their phase is locked to the spiraling moments), nor elliptical spirals.

While an extension of the discussion to other cases is possible, the antiferromagnetic interladder coupling J_i established by inelastic neutron scattering (INS) [316, 318]¹⁴ is anticipated to co-align the chiralities and phases of all ladder units within each bc plane (cf. [419] and Fig. 4.4). By contrast, not much is known about the couplings between the bc planes (see section 7.16). INS observed no dispersion along the a direction, indicating that interplane couplings are very weak [316, 318]. Meanwhile, the stacking

¹¹Note that the shortest delay is much smaller than T_1 of the narrow double-horn contribution.

¹²Assuming, e. g., that the two non-degenerate double-horn contributions are due to the P_l and P_{l+2} sites (Fig. 6.1).

¹³No additional measurements were performed in this work, since relaxation measurements are very time consuming and an influence of extrinsic factors like mechanical vibrations cannot be ruled out on millisecond time scales.

¹⁴Dispersion minima are observed at integer multiples of $2\pi/c$ [316, 318].

of the magnetic structure along the a direction is important for the NMR spectrum, because dipolar coupling between electronic moments and nuclear spins is not negligible in BiCu_2PO_6 (section 6.3.3).

The four P sites are connected by the crystal symmetries σ_a , σ_c , and C_2^b (see section 4.2.2, cf. [74, p. 105]). Of these symmetries, only C_2^b is preserved in a magnetic field $\mathbf{H} \parallel b$.¹⁵ If the magnetic structure is invariant under C_2^b (up to translations), the spectral contributions of the P_l and P_{l+2} sites are degenerate (cf. Fig. 6.1). For the structures considered here, this corresponds to two independent conditions: (i) The distortions of the (spiral) magnetic structure must be compatible with crystal symmetry, and (ii) the stacking order of the bc -planes must be (approximately) symmetric w. r. t. each individual bc plane (or most bc planes, see section 8.6.3.7).

8.6.2.2 Proposed magnetic structure for individual ladder

As discussed in chapter 7 and references therein, numerical calculations suggest the emergence of a field-induced spiral phase in BiCu_2PO_6 . The DM interactions are expected to induce distortions like tilting of the spiral axis (see section 7.14.2), as well as twisting, i. e., variations of the pitch angle (see section 7.14.3). For the sake of manageability, I assume that these distortions of the incommensurate spiral structure are compatible with the translation symmetry of the crystal lattice along the b -direction. I introduce a rung-index $\rho \in \mathbb{Z}$ which enumerates the rungs of the ladder unit under consideration. The four translationally-inequivalent $\text{Cu}(i)$ sites of the considered ladder are then indexed by $i \in \{1, 2\}$ and the rung-parity $p(\rho) \in \{0, 1\}$.¹⁶ Assuming planar spirals on each of the four sublattices,¹⁷ the magnetic structure is hence given by

$$\mathbf{m}_{i,\rho} = R(\alpha_{i,p(\rho)}, \gamma_{i,p(\rho)}) \begin{pmatrix} m_{\perp,i,p(\rho)} \cos(q_b \rho + \varphi_{i,p(\rho)}) \\ 0 \\ m_{\perp,i,p(\rho)} \sin(q_b \rho + \varphi_{i,p(\rho)}) \end{pmatrix},$$

where the angles α_{\dots} and γ_{\dots} parametrize the tilt of the spiral axis towards the a and c directions, respectively,

$$R(\alpha, \gamma) = R_a(\gamma)R_c(\alpha) = \begin{pmatrix} \cos \alpha & -\sin \alpha & 0 \\ \cos \gamma \sin \alpha & \cos \alpha \cos \gamma & -\sin \gamma \\ \sin \alpha \sin \gamma & \cos \alpha \sin \gamma & \cos \gamma \end{pmatrix}.$$

Here, $R_v(\vartheta)$ denotes the rotation with angle ϑ about the (oriented) axis \mathbf{v} , and $\mathbf{m}_{i,\rho} = -\langle \mathbf{S}_{i,\rho} \rangle$ is used in order to avoid the negative sign associated with the electron charge (cf. section 1.5.9).

Note that tilted-spiral models were already proposed and considered in previous work [74, 78]. The above equations represent a natural extension which incorporates the DM-induced distortions discussed in chapter 7.

¹⁵Note that \mathbf{H} is an axial vector. The other symmetries compatible with $\mathbf{H} \parallel b$ (σ_b and inversion) do not provide any additional information.

¹⁶In the notation of section 6.2, $p(\rho)$ corresponds to r , i to i , and $k = 1$.

¹⁷The irrelevance of the $q = 0$ component of the structure is justified in section 8.6.2.1. Certain types of longitudinal modulations (note that amplitude-modulated structures were reported for Zn-doped BiCu_2PO_6 [259, p. 174]) were also considered, but are omitted for readability.

8.6.2.3 Structural chirality

Strictly speaking, C_2^b is the only exact symmetry of BiCu_2PO_6 in a magnetic field, such that the two crystallographically equivalent bc planes depicted in Fig. 4.4 become inequivalent. Indeed, inspection of the crystal structure shows that the two types of bc planes have different *structural chirality*, as visualized by the black arrows in Fig. 4.4(a) (cf. section 4.2.2).¹⁸

Due to its chiral nature, the magnetic field can therefore, in principle, have different effects upon the two types of bc planes. In particular, the ordered moments and/or the orientation of the longitudinal chirality might be different for each of the two bc -planes. Such a situation could be favored if, e. g., magneto-elastic effects involving DM interactions [304, 356] give rise to a coupling between the chirality of the crystal structure and that of the magnetic moments. While this possibility appears interesting, it also implies that the hyperfine and dipolar couplings will deviate from those estimated from the low-field data (chapter 6), which precludes quantitative considerations. Nonetheless, if the C_2^b -symmetry discussed in section 8.6.2.1 is preserved, the aforementioned scenario would be qualitatively consistent with the observed NMR spectra.

8.6.2.4 Specialization to symmetric spiral

If structural effects like those proposed in section 8.6.2.3 are negligible, the ordered magnetic moments in the two types of bc planes are expected to be the same.

One possibility to obtain a partial lifting of spectral degeneracies, as observed in the experimental data (section 8.6.1), then corresponds to magnetic structures which spontaneously choose to satisfy the DM-induced spiral-axis tilt distortion on one ladder leg only. Such structures correspond to those considered in previous work [74, p. 130] (see also [78]). They were also considered in detail in the context of this work and found quantitatively consistent with the data. Meanwhile, heuristic potential-energy models for the classical spiral structure¹⁹ suggest that additional interactions are required to stabilize such a configuration. Since, in addition, the magnetic field does not lift the degeneracy of the two ladder legs, this scenario appears less likely than the hypothesis postulated in section 8.6.2.3.

The second possibility, which will be considered throughout the rest of this analysis, is that the DM interactions are fully satisfied, such that the distortions of the spiral-structure are compatible with the crystal symmetry, as suggested by the calculations in chapter 7. Since interladder couplings are anti-ferromagnetic [318] (cf. section 8.6.2.1), translation invariance along the c -direction is expected. Thus, the magnetic structure in each bc plane of the crystal (see Fig. 4.4) is fully constrained, and the only remaining degrees of freedom correspond to fixing the orientation of the chirality²⁰ and the propagation phase $\delta\varphi(s)$ for each of the bc planes (indexed by $s \in \mathbb{Z}$). The reference for the phases $\delta\varphi(s)$ is chosen such that it is consistent with translations along the a direction, as well as the reflection symmetry σ_c (Fig. 8.9), which is advantageous for the symmetry considerations in the following subsection.

¹⁸When looking along the b direction, the oriented $\text{Cu}(2)$ - $\text{Cu}(1)$ - $\text{Cu}(2)$ angles, measured from the leg towards the rung bond (and after projection into the ac plane), are close to 90° and close to 270° , respectively.

¹⁹The transverse DM components are assumed to provide a linear potential $\mathbf{D} \cdot \boldsymbol{\kappa}_\lambda$ for the classical chirality $\boldsymbol{\kappa}_\lambda$ on ladder leg λ (cf. section 7.13), whereas rung exchange and external field \mathbf{H} are modeled by terms proportional to $\boldsymbol{\kappa}_1 \cdot \boldsymbol{\kappa}_2$ and $\boldsymbol{\kappa}_i \cdot \mathbf{H}$, respectively.

²⁰The weak interlayer coupling [316, 318] (cf. section 8.6.2.1) may not be sufficient to co-align the net chiralities of the different bc planes.

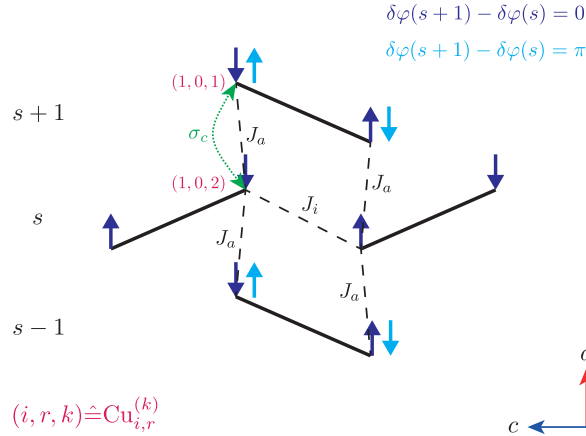


Figure 8.9: Schematic representation of a cut through an ac -plane of BiCu_2PO_6 (cf. Fig. 6.1). Rung bonds are indicated using thick black lines, interladder (J_i) and tentative interlayer bonds (J_a) using dashed black lines. Dark and light blue arrows show the magnetic structures obtained for the corresponding choices of $\delta\varphi(s)$. The (fractional) translation associated with the crystal symmetry σ_c (see section 4.2.2) can be chosen such that the symmetry relates the two sites connected by the green dotted line.

8.6.2.5 Symmetry considerations for linear coupling

The spectra of the two types of bc planes can only be related if the Zeeman term is assumed to be the only magnetic-field dependent term in the nuclear-spin Hamiltonian—besides the electronic spins, of course, which are usually replaced by the ordered magnetic moments in the spirit of an adiabatic approximation (see section 1.5.9). In particular, this means that the crystal structure, and hence the dipolar and hyperfine couplings, are taken not to be affected by the magnetic field. Although often made implicitly, this assumption is not unquestionable, especially when magnetoelastic effects might be present (cf. section 8.7.5). Nonetheless, it shall be adopted for the remainder of this discussion. The idea underlying the following arguments is that transformations of the hyperfine field $\mathbf{B}_h \mapsto \sigma_a \mathbf{B}_h$, $\mathbf{B}_h \mapsto \sigma_b \mathbf{B}_h$, or $\mathbf{B}_h \mapsto \sigma_c \mathbf{B}_h$ do not affect the shape of the resulting ^{31}P -NMR spectra (after histogramming). Note that throughout this subsection, all symmetries are represented by their matrices and all vectors, including magnetic field and ordered moments, are mathematically treated like polar vectors. To keep the following arguments reasonably compact, I specialize to the spiral structure defined in section 8.6.2.2.

- As depicted in Fig. 4.1(c), the $\text{Cu}(i)$ and P sites are located in common, equally-spaced ac planes [11], which can be labeled using a linear index $\rho \in \mathbb{Z}$. Consider thus a reference P_l site and a pair of $\text{Cu}(i)$ sites related by the σ_b -type reflection (cf. section 4.2.2) about the ac -plane containing the reference P_l site. No assumption about the relative displacement along the a and c directions is made. Using the ac -plane indexing, the ordered moments of the two $\text{Cu}(i)$ sites are $\mathbf{m}_{i,\rho}$ and $\mathbf{m}_{i,-\rho}$ (without loss of generality). The hyperfine field $\mathbf{B}_h^{(l)}$ created by these moments at the reference nucleus is

$$\mathbf{B}_h^{(l)} = \Lambda_-^{(l)} \mathbf{m}_{i,-\rho} + \Lambda_+^{(l)} \mathbf{m}_{i,\rho} \quad ,$$

with the generic coupling matrices $\Lambda_{\pm}^{(l)}$ describing the corresponding dipolar and/or hyperfine couplings (cf. section 1.5.9). Crystal symmetry mandates $\Lambda_{\pm}^{(l)} = \sigma_b \Lambda_{\mp}^{(l)} \sigma_b$. Note that $\sigma_b \mathbf{B}_h^{(l)}$ is

expected to give rise to the same NMR spectrum as $\mathbf{B}_h^{(l)}$, and

$$\sigma_b \mathbf{B}_h^{(l)} = \Lambda_-^{(l)} \sigma_b \mathbf{m}_{i,\rho} + \Lambda_+^{(l)} \sigma_b \mathbf{m}_{i,-\rho} \quad .$$

The substitution $\rho \mapsto -\rho$ corresponds to a change $q_b \mapsto -q_b$, which is equivalent to reversal of longitudinal chirality (cf. section 7.8.1). Meanwhile, $p(-\rho) = p(\rho)$ and hence $\sigma_b R(\alpha_{i,p(-\rho)}, \gamma_{i,p(-\rho)}) = R(-\alpha_{i,p(\rho)}, -\gamma_{i,p(\rho)}) \sigma_b$. This inversion of the tilt angles is consistent with chirality reversal (cf. section 7.13). Thus, $\sigma_b \mathbf{m}_{i,-\rho}$ corresponds to the same magnetic structure as $\mathbf{m}_{i,\rho}$, but with reversed chirality, which proves that, under the aforementioned assumptions, the ³¹P-NMR spectra are insensitive to the orientation of chirality.²¹

To prepare the discussion of the symmetries σ_a and σ_c , consider a crystal symmetry g ($g^2 = 1$) which relates P_l and $P_{l'}$ and for which $\mathbf{B}_h^{(l)}$ and $g \mathbf{B}_h^{(l)}$ give rise to the same contribution to the NMR spectrum. Generally, $\mathbf{B}_h^{(l)} = \sum_j \Lambda_j^{(l)} \mathbf{m}_j$ for some site-index j . The coupling matrices corresponding to different P sites are related through g : $\Lambda_{g(j)}^{(l')} = g \Lambda_j^{(l)} g$. Hence, $g \mathbf{B}_h^{(l)} = \sum_j \Lambda_j^{(l')} g \mathbf{m}_{g(j)}$. Therefore, the spectral contributions from the P_l and $P_{l'}$ sites are degenerate if $g \mathbf{m}_{g(j)}$ and \mathbf{m}_j describe the same magnetic structures (up to translation).

The following arguments are specific to the symmetric spiral structure introduced in section 8.6.2.4, such that the magnetic structure of each bc plane, indexed by $s \in \mathbb{Z}$, is defined by selecting a propagation phase $\delta\varphi(s)$ and an orientation of the longitudinal chirality $c(s) \in \{-1, 1\}$.

- The symmetry σ_c transforms the two types of bc planes into one another (see Fig. 8.9). For the assumed structure, it inverts the chirality and the γ_{\dots} -tilt angle, which is consistent with DM-induced distortions. The stacking order of the bc -planes is unaffected. By invoking the preceding result for σ_b , the spectral contributions of the P_l and P_{l+1} sites are found to be degenerate if there exist $b \in \{0, 1\}$, $d \in \mathbb{Z}$, and²² $\varphi_0 \in \mathbb{R}$ such that

$$\forall s \in \mathbb{Z} \quad : \quad \left[c(s + 2d + 1) = (-1)^b c(s) \right. \\ \left. \wedge \delta\varphi(s + 2d + 1) = (-1)^b \delta\varphi(s) + \varphi_0 \pmod{2\pi} \right] \quad . \quad (8.3)$$

- Similarly, σ_a connects the two types of bc planes and inverts the chirality. The tilt angles again transform consistently with crystal symmetry and hence with DM-induced distortions. In addition, the stacking order along a is inverted, such that the spectral contributions of the P_l and P_{l+3} sites are found to be degenerate if there exist $b \in \{0, 1\}$, $d \in \mathbb{Z}$, and²² $\varphi_0 \in \mathbb{R}$ such that

$$\forall s \in \mathbb{Z} \quad : \quad \left[c(-s + 2d + 1) = (-1)^b c(s) \right. \\ \left. \wedge \delta\varphi(-s + 2d + 1) = (-1)^b \delta\varphi(s) + \varphi_0 \pmod{2\pi} \right] \quad . \quad (8.4)$$

It is instructive to consider the simple choice $c(s) = (-1)^{su}$, where $u = 0$ ($u = 1$) corresponds to uniform (alternating) stacking of chirality. Clearly, both (8.3) and (8.4) require $b = u$.

²¹Some care is needed regarding the phases $\varphi_{i,p(\rho)}$. While the argument clearly holds for a uniform spiral [$\varphi_{i,p(\rho)} = 0 \forall i, p(\rho)$, without loss of generality for q_b incommensurate], it remains valid for the twisting-distortions induced by D_1^b and D_4^b (section 7.14.3), since “long” (“short”) bonds are mapped onto “long” (“short”) bonds in Fig. 7.38(b).

²²A constant phase offset is irrelevant for incommensurate q_b (cf. translation symmetry reviewed in section 7.8.2).

- Consider (8.3) first. If $u = 0$, $\delta\varphi$ has to be translation invariant. The simplest, but not the only,²³ solution is $d = 0 \Rightarrow \delta\varphi(s) = \frac{1}{2}q_a s$. For $u = 1$, one finds alternating stacking $\delta\varphi(s) = (-1)^s \delta\varphi_0 + \phi_0$ (with $\phi_0 \in \mathbb{R}$) instead.²³
- Condition (8.4) is simpler. One finds $\delta\varphi(-s + 2d + 1) = (-1)^u \delta\varphi(s) + \varphi_0$, with $\varphi_0 \in \{0, \pi\}$ [$\varphi_0 \in [0, 2\pi]$] for $u = 0$ [$u = 1$], which merely demands that the stacking order be symmetric about the a -direction while the values of $\delta\varphi(s)$ for even (or odd) s can be chosen arbitrarily.
- Lastly, the combination of (8.4) with the mono-layer ($d = 0$) solutions of (8.3) is considered. For $u = 0$, the resulting condition reads $\forall s : \frac{1}{2}q_a = q_a s \pmod{\pi}$ implying $q_a \in 2\pi\mathbb{Z}$. The case $u = 1$ yields $\varphi_0 = 2\phi_0$, which does not restrict any actual parameters of the structure. As expected, these results are consistent with the requirement of a -symmetric stacking obtained by considering $C_2^b = \sigma_a \sigma_c$ in section 8.6.2.1.

8.6.3 Explicit models

8.6.3.1 Possible spiral structure

As discussed earlier in this section (section 8.6), a variety of spiral structures which are compatible with an NMR spectrum consisting of two non-degenerate double-horn contributions (Fig. 8.8) exists. In particular, such spiral structures can involve twist (section 7.14.3) and tilt distortions (section 7.14.2). The model presented in the following focuses on the NMR data shown in Fig. 8.8(a), which were obtained at $\mu_0 H = 42.2$ T, corresponding to a magnetization $M/M_{\text{sat}} \approx 0.045$ [207]. Moreover, the model is motivated by inelastic neutron-scattering results which suggest that the DM interactions on the nearest-neighbor leg bonds are dominant [318] (cf. section 7.14).

Coupling effects between the twist and tilt distortions caused by D_1^b and D_1^{ac} , respectively, are expected to be of order $O(D_1^b D_1^{ac})$ and therefore neglected. In section 7.14.2, spiral-axis tilt angles $\alpha \sim 40^\circ$ were estimated from numerical calculations. An analogous treatment for the local deviation from purely antiferromagnetic correlations on the rung bond yields $\Delta\varphi_\pm = 101(2)^\circ \mp |\Delta\varphi_r|$ with $|\Delta\varphi_r| \approx 11^\circ$ [cf. Fig. 7.38(b)].²⁴ While these estimates are rather crude (see section 7.15), they suggest that the spiral-axis tilt is dominant. Furthermore, since the hyperfine couplings of the P nuclei only involve next-nearest neighbor Cu sites ([22] and [74, p. 105]; cf. Fig. 6.1), the twisting distortion mainly contributes through the altered rung correlations [$\Delta\varphi_r$ in Fig. 7.38(b)]. Increasing the rung coupling tends to decrease the tilt angles, as shown in Fig. 7.36, and is expected to have the same regularizing effect upon $\Delta\varphi_r$. Hence, interladder couplings are believed to affect both distortions similarly, such that the twist distortion can be neglected, which has the additional advantage of reducing the already abundant number of degrees of freedom of the model.

Focusing on tilt distortions of the spiral axes which are DM-induced and hence consistent with the crystal

²³Values $d \neq -1, 0$ give rise to analogous 3-layer, 5-layer, ..., stacking sequences.

²⁴The average pitch angle $0.55\pi \leq q \leq 0.57\pi$ of the spiral is obtained from the spin correlations calculated for parameter set B in chapter 7 (see section 7.6.3 or [78] for parameter set A , and [74, p. 114] for the doped case). Then, the asymptotic longitudinal chiral correlations on the leg bonds correspond to $m_\perp^4 \sin^2 q$, which yields $m_\perp = 0.0282(1)$. Finally, the asymptotic longitudinal chiral correlations on the rung bonds correspond to $m_\perp^4 \sin^2 \Delta\varphi_r \cos^2 \alpha$, giving $|\Delta\varphi_r| = 11.4(1)^\circ$. Note that the estimated $\Delta\varphi_+$ is consistent (within error) with the fact that the chirality is maximal for a pitch angle of 90° .

symmetry, the spiral structure introduced in section 8.6.2.4 is parametrized as

$$\mathbf{m}_{i,r}^{(k)}(x, y, z) = \begin{pmatrix} 0 \\ m_{\parallel,i} \\ 0 \end{pmatrix} + (-1)^{i+r+1} m_{\perp} R \left((-1)^{k+1} \alpha_{i,r}, \gamma_{i,r} \right) \begin{pmatrix} \cos(\varphi_{i,r,k}(x, y, z)) \\ 0 \\ \sin(\varphi_{i,r,k}(x, y, z)) \end{pmatrix}, \quad (8.5)$$

with $\alpha_{i,r} = (-1)^{i+r+1} \alpha_0$, $\gamma_{i,r} = (-1)^{i+r+1} \gamma_0$, and the propagation phase

$$\varphi_{i,r,k}(x, y, z) = 2\pi \mathbf{q}_{\parallel} \cdot \left(\begin{array}{c} c(s) \left(y - \frac{r}{2} \right) \\ z + (k-1)(-1)^i \left(r - \frac{1}{2} \right) \end{array} \right) + \delta\varphi(s),$$

where $s = 2x + (k-1)(2r-1)$, such that the chirality orientation $c(s) = \pm 1$ and the relative propagation phases $\delta\varphi(s)$ of the individual bc planes follow the conventions described in section 8.6.2.4. The Cu-site indexing corresponds to Fig. 6.1 (section 6.2; $\mathbf{m}_{i,r}^{(k)}(x, y, z) = -\langle \mathbf{S}_{i,r}^{(k)}(x, y, z) \rangle$) and \mathbf{q}_{\parallel} describes the propagation within each bc -plane (consistently with section A.2.2). The specialization to antiferromagnetic interladder couplings implies $\mathbf{q}_{\parallel} = (q_b, 0)$.²⁵ The same tilt angles are assumed for the Cu(1) and Cu(2) sites on each ladder leg, which is expected for the experimentally-suggested [318] DM interaction D_{\perp}^{ac} (cf. Fig. 4.5) and further reduces the number of free parameters.

8.6.3.2 Long-range order along the a -direction

First consider the case of three-dimensional long-range order,²⁶ and focus on the two possible choices of parallel or antiparallel alignment of chirality in neighboring bc -planes, i. e., $u = 0$ or $u = 1$, respectively, in $c(s) = (-1)^{s u}$ (cf. sections 8.6.2.5 and 8.6.3.1). The requirements for symmetry-induced spectral degeneracies for both cases have been worked out in section 8.6.2.5.

In the case $u = 1$, the constraints imposed by a spectral degeneracy due to σ_c are more restrictive than those corresponding to σ_a . A possible stacking order giving rise to two non-degenerate double-horn contributions is given by $\delta\varphi(s) = (-1)^s \frac{1}{2} q_a s + \frac{1}{2} (1 - (-1)^s) \phi_0$. However, it appears that opposite linear propagation of the two types of bc planes would require a coupling between next-nearest neighbor bc planes. Since this is inconsistent with the layered crystal structure of BiCu₂PO₆ (see section 4.3.1), the corresponding magnetic structures are not considered further.

For $u = 0$, the constraints imposed by σ_c are less restrictive than those imposed by σ_a , and possible stacking orders giving rise to two non-degenerate double-horn contributions to the NMR spectrum are given by $\delta\varphi(s) = \frac{1}{2} q_a s$ with a low-symmetry q_a , i. e., $-\frac{1}{2} q_a \neq \frac{1}{2} q_a \pmod{2\pi} \Leftrightarrow q_a \notin 2\pi\mathbb{Z}$. Such a structure is plausible, since interlayer couplings between adjacent bc planes should be sufficient for its stabilization.

8.6.3.3 Long-range order along the a -direction: Quantitative model

Consider the three-dimensional long-range ordered magnetic structure proposed in section 8.6.3.2 (for $u = 0$). The symmetry arguments made in the preceding sections imply that the spectral contributions

²⁵By considering an individual classical rung dimer with Heisenberg exchange, an average relative propagation phase of π between the two ladder legs is found energetically optimal, at least for total tilt angles below 45° .

²⁶Note that only antiferromagnetic interladder coupling J_i (cf. section 8.6.2.1) is compatible with long-range order along the a direction (cf. Fig. 8.9).

of the P sites associated with the two types of bc planes are degenerate. I therefore focus on the P_l sites ($l = 1, 3$) located in the $k = 1$ bc -plane at $x = 0$. An analytic expression for the full width $w^{(l)}$ of the double-horn contribution arising from these P_l sites can be obtained. As in the preceding sections, an antiferromagnetic interladder coupling is used. Due to the various trigonometric functions in eqs. (8.1) and (8.5), a formulation using complex phasors $z^{(l)}$ is convenient, such that $w^{(l)} = 4\gamma_{31P} \mu_B |z^{(l)}|$ and

$$\begin{aligned}
z^{(l)} &= z_h^{(l)} + z_d^{(l)} \\
z_d^{(l)} &= \frac{1}{2} \sum_{j,r',k} \exp\left(i\Delta\delta_{j,r',k}^{(l)}\right) \left[\mathbf{A}_{j,r',k,1}^{(l)} - i\mathbf{A}_{j,r',k,3}^{(l)} \right] \\
z_h^{(l)} &= \sum_{j \in \{1,2\}} (-1)^{j+1} m_{\perp,j} \left[\cos \gamma_{j,r_0} \left(\Lambda_j^{bc} \sin q_0 + \Lambda_j^{bb} \sin \alpha_{j,r_0} \cos q_0 \right) \right. \\
&\quad \left. + i \left(\Lambda_j^{ba} \cos \alpha_{j,r_0} + \Lambda_j^{bc} \sin \alpha_{j,r_0} \sin \gamma_{j,r_0} \right) \sin q_0 + i \Lambda_j^{bb} \sin \gamma_{j,r_0} \cos q_0 \right] \\
\mathbf{A}_{j,r,k}^{(l)} &= (-1)^{j+r+1} m_{\perp,j} \hat{\mathbf{B}} \cdot M_{j,r,k,\mathbf{q}}^{(l)} g_{j,k} R \left((-1)^{k+1} \alpha_{j,r}, \gamma_{j,r} \right) \\
\Delta\delta_{i,r',k}^{(l)} &= -r_0\pi + 2\pi q_a (k-1) \left(r' - \frac{1}{2} \right) + 2\pi q_b \frac{1-r_0-r'}{2} \\
q_0 &= (-1)^{r_0} \pi q_b \\
\mathbf{q} &= 2\pi (q_a, q_b, 0) \\
\alpha_{j,p} &= (-1)^{j+p+1} \alpha_0 \\
\gamma_{j,p} &= (-1)^{j+p+1} \gamma_0 \quad .
\end{aligned} \tag{8.6}$$

Here, r_0 denotes the parity of the rungs to which the P_l site couples through hyperfine couplings (cf. r -index in Fig. 6.1) and the dipole-coupling matrices $M_{j,r,k,\mathbf{q}}^{(l)}$ are defined according to equation (6.2) (section 6.3.1). The hyperfine couplings Λ_i were estimated in section 6.6.3 and the g-tensors in section 5.2.1. The notation is generally consistent with chapters 5 and 6.

8.6.3.4 Long-range order along the a -direction: Candidate solutions

The results (8.6) allow for quantitative comparisons with the observed NMR spectrum described in section 8.6.1. Within the considered subclass of possible magnetic structures, each structure is determined by the choice of q_a , q_b , $m_{\perp,1}$, $m_{\perp,2}$, α_0 , and γ_0 .

To reduce the set of candidate solutions further, $q_b = 0.574$ is fixed based on inelastic neutron scattering [316, 318], and consistently with numerical calculations (cf. chapter 7 and references therein). Note that the primary goal is to show that solutions *exist*. Meanwhile, there is a large number of models which yield NMR spectra consisting of two double-horn contributions. Ultimately, the experiment only constrains the widths $w^{(1)}$ and $w^{(3)}$ of these two contributions, such that the model for the magnetic structure is highly underconstrained. Therefore, the parameters obtained in the following are unlikely to be related to those of the actual magnetic structure. Set $m_{\perp,1} = m_{\perp}$ and $m_{\perp,2} = f m_{\perp}$. Since the Cu moments in BiCu_2PO_6 have spin-1/2, physical solutions must satisfy $m_{\perp,i} \leq \frac{1}{2}$. Furthermore, the arguments presented in section 7.11.3 suggest that $f \sim 1$. Then, for each choice of $q_a \in [0, 1)$ and $(\alpha_0, \gamma_0) \in [-90^\circ, 90^\circ]^2$, the two remaining parameters (m_{\perp}, f) are fully constrained by the experimental data.

A candidate magnetic structure obtained following this approach is depicted in Fig. 8.10. To check (8.6),

the NMR spectrum shown in Fig. 8.10(c) [and Fig. 8.8(a)] was calculated independently. A computer program was written to evaluate equations (6.5) and (6.1) directly on a finite lattice.²⁷ The program estimates the uniform component of the magnetic structure and corrects for the demagnetization tensor of the sample. The magnetic structure is specified by a callback function returning $\mathbf{m}_{i,r}^{(k)}(x, y, z)$, which coincides with equation (8.5) in the present case.²⁸ Note that the same program has been used to test the symmetry arguments discussed in the preceding sections for selected example cases.

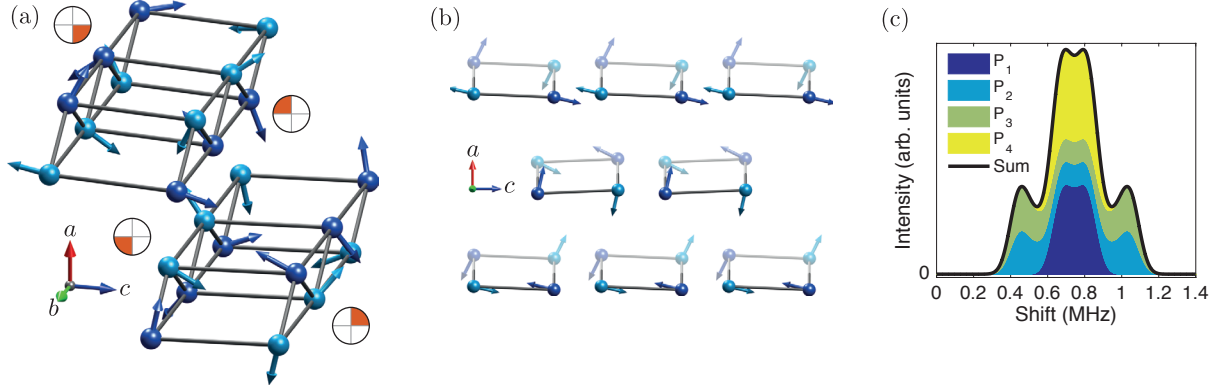


Figure 8.10: (a), (b): Magnetic spiral structure proposed for the high-field magnetic phase of BiCu_2PO_6 ($\mathbf{H} \parallel b$). Intraladder bonds are indicated by gray cylinders and Cu moments $\mathbf{m}_{i,r}^{(k)}(x, y, z) = -\langle \mathbf{S}_{i,r}^{(k)}(x, y, z) \rangle$ by arrows. The black-orange symbols indicate the orientation of the DM-induced spiral-axis tilt (perpendicular to the b -direction) of the spiral structure realized on each of the four ladder legs shown (cf. Fig. 4.5). Panel (b) shows two adjacent ac planes, the more distant one being represented using fainter colors. (c): Simulated line shape [gray line in Fig. 8.8(a)], illustrating the double-horn contributions from the individual P sites. The hyperfine couplings listed in Tab. 6.2 (Group 1) and the g-tensors obtained in section 5.2.1 are used. A Gaussian broadening of 0.11 MHz (FWHM) is applied. The parameters of this particular solution are $q_b = 0.574 \cdot 2\pi/b$, $q_a = 0.5 \cdot 2\pi/a$, $\alpha_0 = 4^\circ$, $\gamma_0 = -10^\circ$, $m_{\perp,1} = 0.483 \hbar$, $m_{\perp,2} = 0.95 m_{\perp,1}$, and $m_{\parallel} = 0.034(1) \hbar$. (Updated version of a figure previously used in [312].)

8.6.3.5 Long-range order along the a -direction: Parameter uncertainties

The results of the preceding subsection (section 8.6.3.4) demonstrate that the NMR spectrum observed in the high-field phase of BiCu_2PO_6 (see section 8.6.1) is quantitatively consistent with a spiral magnetic structure. On the other hand, the large uncertainties of the coupling parameters describing the g-tensors and hyperfine interactions (sections 5.2.1 and 6.7), raise questions about the significance of this result.

²⁷Conceptually, such simulations of NMR spectra, including the use of periodic boundaries to efficiently account for the dipolar couplings, are standard practice and have also been used in previous work (see, e. g., [75, pp. 26,28], [74, Figs. 6.11(a-c), 6.15], and [78]).

²⁸For efficiency reasons, the model is evaluated only once and periodic boundaries are used along a and c . The program is implemented in MATLAB and performance-critical parts like dipole sums are either reduced to dense linear-algebra operations on large matrices or accelerated using (automatically-generated) C code, in addition to parallel evaluation. Dipole sums are typically performed over spheres with radius 50 \AA , which corresponds to ~ 5000 unit cells. See footnote 27 for related previous work.

The parameter uncertainties are accounted for by considering perturbations of the nominal solutions,

$$\begin{aligned} g_i^{\alpha\beta} &\mapsto g_i'^{\alpha\beta} = g_i^{\alpha\beta} \left(1 + \delta g_i^{\alpha\beta}\right) \\ \Lambda_i^{b\beta} &\mapsto \Lambda_i'^{b\beta} = \sum_{\alpha} \Lambda_i^{b\alpha} \left(1 + \delta \Lambda_i^{b\alpha}\right) (g_i^{-1} g_i')^{\alpha\beta} \quad . \end{aligned} \quad (8.7)$$

Following the discussion in sections 5.2.1 and 6.6.4, the ranges of the sixteen allowed deviation parameters are restricted according to $|\delta g_i^{\alpha\beta}| \leq 0.1$ and $|\delta \Lambda_i^{b\alpha}| \leq 0.25$ ($|\delta \Lambda_i^{ba}| \leq 0.1$ for fit group 2). Note that this uncertainty model is quite generic, since it also includes parameter sets which violate some of the assumptions made during the estimation of the nominal parameter values.

Generally, the parameters of the candidate magnetic structures are found to be very sensitive to the coupling parameters. This can be understood by reconsidering the position of the ^{31}P nuclei (Fig. 6.1). For $\mathbf{H} \parallel b$, the antiferromagnetic interladder coupling [318] and the approximate σ_c symmetry of the crystal (see section 4.3.2) suggest that the b -projections of the hyperfine fields created by the oscillating a and b components of the ordered moments on the Cu(1) and Cu(2) sites nearly cancel each other. Since the corresponding hyperfine couplings are dominant (cf. Tabs. 6.2 and 6.3), this enhances the relative uncertainty of the net hyperfine field at the P site.

In principle, the coupling parameters could be sampled randomly, according to a suitable distribution. Together with the model for the magnetic structure (8.6), the set of candidate solutions could then be analyzed using statistical methods. However, such an approach is computationally expensive and unlikely to be of practical use given the strong sensitivity to the model parameters expected based on the preceding discussion. Instead, one- and two-parameter variations parametrized according to equation (8.7) with $\delta \Lambda_i^{b\alpha} \in \{0, \pm 0.1, \pm 0.25\}$ and $\delta g_i^{\alpha\beta} \in \{0, \pm 0.1\}$ are considered.²⁹ This procedure corresponds to a discretized second-order expansion in the coupling parameters. For each variation of the coupling parameters, candidate solutions are obtained analogously to section 8.6.3.4.

Even the simplified treatment outlined above produces large sets of candidate magnetic structures. Since the primary intention is to check consistency with experimental data, a representative, plausible solution is obtained for each variation of the coupling parameters by selecting the candidate which is most compatible with $f = 1$ ($m_{\perp,2} = f m_{\perp,1} \approx m_{\perp,1}$, see end of section 7.11.3). For the coupling parameters of fit group 1 (fit group 2) (cf. section 6.6.3), the representative solutions satisfy $|1 - f| < 0.11$ ($|1 - f| < 0.44$), $-7^\circ \leq \alpha_0 \leq 12^\circ$ ($-6^\circ \leq \alpha_0 \leq 10^\circ$), $-24^\circ \leq \gamma_0 \leq 5^\circ$ ($1^\circ \leq \gamma_0 \leq 24^\circ$), and $0.2 \hbar \leq m_{\perp,i} < 0.5 \hbar$ ($0.17 \hbar \leq m_{\perp,i} < 0.5 \hbar$). The magnitude of the total tilt angle is below 25° in both cases and q_a assumes values between 0.2 and 0.85.³⁰

The somewhat large deviation from $f = 1$ observed for fit group 2 can be interpreted as indirect evidence corroborating the correctness of the peak assignments yielding fit group 1 (cf. section 6.6.3). Either way, the orders of magnitude of the remaining parameters seem plausible, especially for the hyperfine couplings of fit group 1. In this sense, the considered class of spiral models is quantitatively consistent with the NMR data presented in section 8.6.1. However, due to the vast number of possible solutions, the significant uncertainties of the coupling parameters, and the fact that the considered class of models is not even the most general one, no further analysis of the set of possible magnetic structures is attempted.

²⁹This yields 945 possible parameter variations, which are sampled exhaustively. For the hyperfine couplings of fit group 2, $\delta \Lambda_i^{ba} \in \{0, \pm 0.1\}$ is used in accordance with section 6.7.

³⁰Note that changing $q_a \mapsto -q_a$ merely interchanges the spectral contributions of the P_1 and P_3 sites. Without loss of generality, $w^{(3)} > w^{(1)}$ is assumed.

8.6.3.6 Short-range order along the a -direction: Random walk

Once q_b , as well as the tilt angles α_{\dots} and γ_{\dots} , are fixed, the spiral structure proposed in section 8.6.3.1 is fully constrained within each bc plane of the crystal (up to the ordered moments). The remaining degrees of freedom merely correspond to the stacking of these bc planes, *viz.* the choice of chirality $c(s)$ and propagation phase $\delta\varphi(s)$ of each bc plane (indexed by $s \in \mathbb{Z}$).

On the other hand, the summation formula (A.5) (re-derived following [292, 438] in section A.2.2) suggests that the dipolar field created by the neighboring bc planes decays rapidly with distance, so that short-range order along the a -direction might be sufficient to explain the observed NMR spectra. Let the matrix $M_{i,r,k,q_{\parallel}}^{(l)}(x)$ describe the dipolar coupling of the Cu _{i,r} ^(k) moments in the bc -plane intersecting the unit cells with a -coordinate $x \in \mathbb{Z}$ with the P _{l} -site in unit cell $(0, 0, 0)$ (see section 6.2 for notation). This convention allows the above matrices to be calculated using equation (A.5) (see section A.2.2 and references therein). The expressions (8.6) can be generalized to obtain the width $w^{(l)} = 4\gamma_{31P} \mu_B |z^{(l)}|$ of the double-horn contribution to the NMR spectrum created by the P _{l} ($l = 1, 3$) sites in the bc -plane with $s = 0$. After some algebra, I obtain the following result

$$\begin{aligned}
z^{(l)} &= e^{i\delta\varphi(0)} z_h^{(l)} + z_d^{(l)} \\
z_d^{(l)} &= \sum_s e^{i\delta\varphi(s)} z_d^{(l)}(s) \\
z_d^{(l)}(s = 2x + t) &= \frac{1}{2} \sum_{j,r} (-1)^{j+r+1} m_{\perp,j} \exp\left(i\Delta\delta_{j,r,t+1}^{(l)}\right) \\
&\quad \hat{\mathbf{B}} \cdot M_{j,r,t+1,c(s)q_{\parallel}}^{(l)}(x) g_{j,t+1} R\left((-1)^t c(s) \alpha_{j,r}, c(s) \gamma_{j,r}\right) (1, 0, -i)^T \\
\Delta\delta_{i,r',k}^{(l)} &= -r_0\pi + 2\pi c(2x + (k-1)(2r-1)) q_b \frac{1-r_0-r'}{2} \\
z_h^{(l)} &= \sum_{j \in \{1,2\}} (-1)^{j+1} m_{\perp,j} \left[\cos(c(0) \gamma_{j,r_0}) \left(\Lambda_j^{bc} \sin q_0 + \Lambda_j^{bb} \sin(c(0) \alpha_{j,r_0}) \cos q_0 \right) \right. \\
&\quad \left. + i \left(\Lambda_j^{ba} \cos(c(0) \alpha_{j,r_0}) + \Lambda_j^{bc} \sin(c(0) \alpha_{j,r_0}) \sin(c(0) \gamma_{j,r_0}) \right) \sin q_0 \right. \\
&\quad \left. + i \Lambda_j^{bb} \sin(c(0) \gamma_{j,r_0}) \cos q_0 \right] \\
q_{\parallel} &= 2\pi (q_b, 0) \\
q_0 &= (-1)^{r_0} \pi c(0) q_b \quad .
\end{aligned} \tag{8.8}$$

The transformation properties of the individual objects imply that $z_d^{(l)}(s) \mapsto -z_d^{(l)}(s)$ upon changing $c(s) \mapsto -c(s)$. Similarly, $z_h^{(l)} \mapsto -z_h^{(l)}$ upon changing $c(0) \mapsto -c(0)$. Therefore, the equations (8.8) can be recast as

$$z^{(l)} = \sum_{s \in \mathbb{Z}} c(s) e^{i\delta\varphi(s)} z^{(l)}(s) \quad , \tag{8.9}$$

for suitably defined $z^{(l)}(s)$. Here, $z^{(l)}(s)$ is independent of $c(s)$ and $\delta\varphi(s)$. After choosing $\delta\varphi(s) = \frac{1}{2}q_a s$ and $c(s) = 1$, the result (8.6) is recovered. However, the formulation (8.9) is clearly more powerful. Most notably, the distribution of the widths of double-horn contributions in a sample with disordered stacking along the a direction is identified with the radial end-point distribution of a two-dimensional random walk with step sizes $|z^{(l)}(s)|$.

8.6.3.7 Short-range order along the a -direction: Range of dipolar couplings

Equation (8.8) can be used to estimate the step sizes $|z^{(l)}(s)|$. Results for the candidate solution from Fig. 8.10 are shown in Fig. 8.11. Clearly, the contributions of the individual bc planes to the hyperfine field at the P site decay rapidly with distance. This has two consequences: (i) It is sufficient if the stacking order assumed in section 8.6.3.4 is realized only locally, on length scales corresponding to a few unit cells, and for a majority of reference lattice planes; and (ii) the random-walk averaging of equation (8.9) required to calculate the NMR spectrum for disordered stacking configurations converges rapidly with the number of considered bc planes.

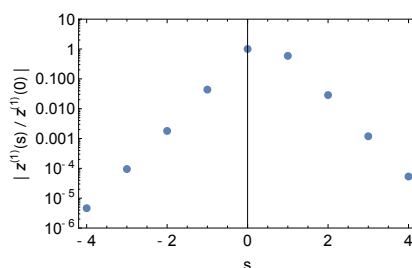


Figure 8.11: Hyperfine-field contributions $|z^{(l)}(s)|$ from individual bc planes (indexed by $s \in \mathbb{Z}$, see section 8.6.3.6 for notation). The parameters of the magnetic structure correspond to Fig. 8.10.

8.6.3.8 Short-range order along the a -direction: Results

A systematic quantitative survey of disordered-stacking scenarios analogous to the analysis performed for certain classes of three-dimensional long-range ordered magnetic structures (sections 8.6.3.4 and 8.6.3.5) is beyond the scope of this work. Instead, two particular examples of short-range stacking order are considered in order to illustrate the qualitative features of the resulting NMR spectra.

The distributions assumed in the following for $c(s)$ and $\delta\varphi(s)$ (see section 8.6.3.6) are symmetric w. r. t. the a direction and do not distinguish between the two types of bc -planes (corresponding to even and odd s). Therefore, after ensemble-averaging over disorder realizations, the NMR spectra of all P-sites are expected to be degenerate, which is why the P_1 site is considered without loss of generality.

Perhaps the most obvious disordered-stacking scenario is that the interlayer couplings are too weak to establish any relation between the magnetic structures of the individual bc planes. In such a case, other mechanisms like pinning of the magnetic structure by defects may dominate and the phases $\delta\varphi(s)$ are expected to be uniformly distributed in $[0, 2\pi)$. Because of the special form of (8.9), the choice of $c(s)$ does not matter as long as it is uncorrelated with $\delta\varphi(s)$. The resulting spectrum is depicted in Fig. 8.12(a) and is clearly inconsistent with the salient features of the measured data (section 8.6.1).

However, there exist disordered-stacking scenarios yielding NMR spectra which are consistent with the experimental results. One such structure is obtained by assuming parallel chirality in all bc planes, i. e. , $c(s) = 1$, and a discrete uniformly-distributed relative stacking phase $\delta\varphi(s) - \delta\varphi(s - 1) \in \{-\delta, \delta\}$. Such a stacking could arise due to geometrical frustration of the interlayer couplings, which is not inconceivable considering the crystal structure of BiCu_2PO_6 . In fact, such couplings have been reported in first-principles calculations focusing on the related compound BiMn_2PO_6 [289]. Setting $\delta = \pi/2$ for analogy with section 8.6.3.4, the spectrum shown in Fig. 8.12(b) is obtained. Clearly, this spectrum

is qualitatively consistent with the data and quantitative agreement could be reached by tweaking the parameters slightly. Note that, after summing up the contributions from all P sites, the final spectrum is unaltered even if the two stacking phases occur with different probabilities. The striking similarity between Fig. 8.12(b) and Fig. 8.10(c) is not accidental. In fact, the data shown in Fig. 8.11 (section 8.6.3.7) show that the sum over lattice planes appearing in the calculation of the width of the NMR spectrum in the case of three-dimensional long-range order is dominated by the two bc planes directly adjacent to the considered P site.

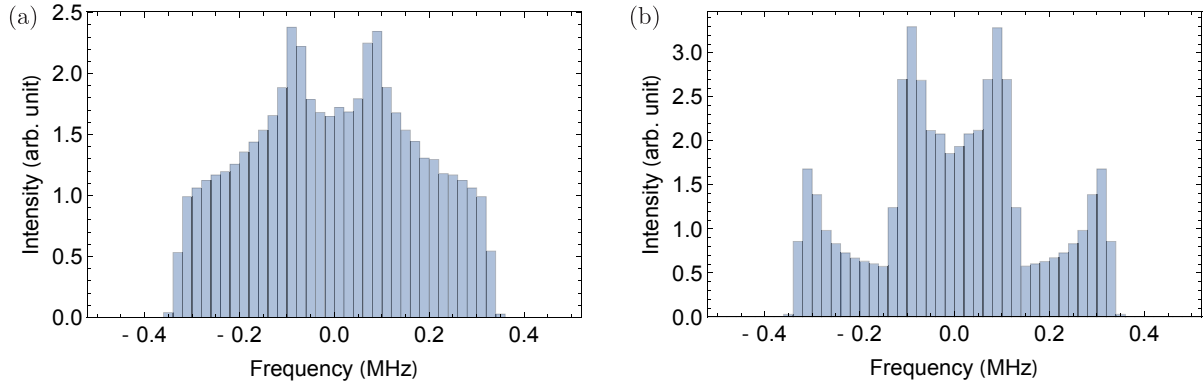


Figure 8.12: Calculated NMR spectra for $\delta\varphi(s)$ uniformly distributed in $[0, 2\pi)$ (a) and $\delta\varphi(s) - \delta\varphi(s-1)$ uniformly-distributed in $\{-\frac{1}{2}\pi, \frac{1}{2}\pi\}$ (b). Terms with $-10 \leq s \leq 10$ were considered in the random-walk averaging of $|z^{(l)}|$ [equation (8.9)], sampling $2 \cdot 10^4$ disorder realizations. An intrinsic Gaussian broadening of 1.7% (FWHM of broadening w. r. t. full line-width of double-horn contribution) was assumed for each individual disorder realization. The remaining parameters correspond to Fig. 8.10.

8.6.4 High-temperature line shape

To conclude the analysis of the experimental results, a short comment regarding the NMR spectra measured at high magnetic field and high temperature seems appropriate. As seen in Fig. 8.4(a), the NMR lines measured outside the magnetically-ordered high-field phase exhibit a shoulder-like feature on the low-frequency side.

The finite geometry of the sample is expected to affect the line shape through the position-dependence of the demagnetizing field [Fig. 8.13(a)] (see also section 6.3.4). While the resulting line-width is consistent with the data, the overall line shape is not [red dotted line in Fig. 8.13(b)],³¹ indicating that the low-frequency shoulder must have a different origin. It has been checked by additional experiments that no such features are observed in low magnetic fields (section A.4.3). Thus, the low-frequency shoulder is either an extrinsic experimental effect of the high-field NMR setup, or due to a field-induced change of the properties of the sample.

Experimentally, such distortions of the line shape can be caused by field inhomogeneity. While the field-inhomogeneity of the high-field magnet system alone appears insufficient [125], the observed effect might be caused by field inhomogeneities created by the sample environment (cryostat and NMR probe) (cf. [134, 294]). On the other hand, no such features were observed at $H < H_{c1}$ during earlier

³¹Note that the discrepancy between calculated and observed line shape persists when tilts of the box-shaped sample of the order of 15° are included in the model.

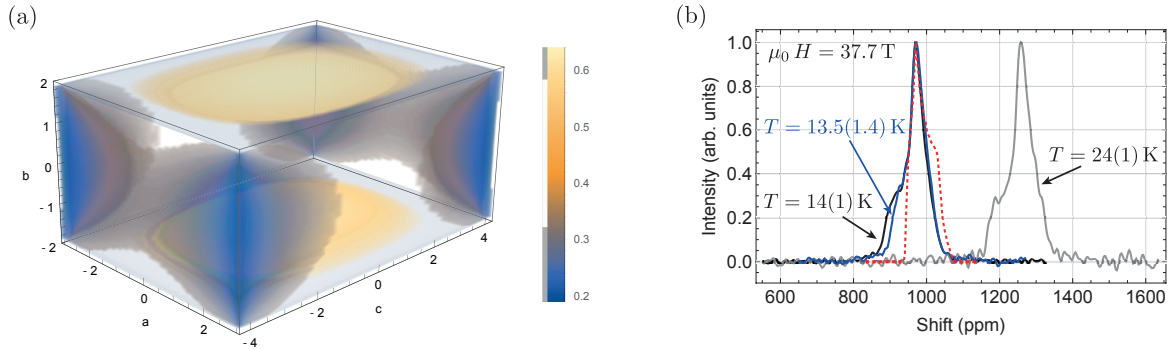


Figure 8.13: (a): Distribution of demagnetization factors within a box-shaped sample with dimensions $(a, b, c) \propto (3.1, 2, 4.1)$, for a field applied along the b direction (calculated according to [194]). (b): Comparison of NMR data (solid lines) with the line shape calculated from the results shown in (a) (dotted line). See text for details.

high-field measurements (see section A.4.4).³² The data depicted in blue and black/gray in Fig. 8.13(b) were measured before and after a scan of the sample rotation angle [cf. Fig. A.6(b)], respectively. By contrast, intermittent changes of temperature and field ramps during the temperature scan summarized in Fig. 8.4(a) did not seem to affect the high-temperature line shape. This suggests that the distortion of the high-temperature line shape is due to the sample environment, which has changed slightly during the aforementioned alignment scan.

Meanwhile, a field-induced structural distortion of the crystal cannot be completely excluded. In the latter scenario, the line shape might reflect domain walls. This possibility is exciting, since it could correspond to the elusive chiral phase without long-range magnetic order [21, 68, 419] (cf. sections 7.1.2 and 7.8.2). Ultimately, only additional high-field experiments can clarify the nature of the high-field high-temperature phase.

8.6.5 Multiferroicity

Ferroelectric behavior is often observed in materials exhibiting spiral magnetic order [81]. Indeed, recent high-field experiments on BiCu_2PO_6 observed the appearance of electric polarization at H_{c2} [188]. For $\mathbf{H} \parallel b$, the polarization is orthogonal to \mathbf{H} and predominantly directed along the a direction of the crystal [188]. While the ac -component of the electric polarization shows an order-parameter-like onset starting at H_{c2} , the b -component appears discontinuously at H_{c1} and then passes through a peak at H_{c2} [188].³³ These results [188] suggest that BiCu_2PO_6 is an improper magnetic ferroelectric [81]. It appears worthwhile to discuss the implications of the aforementioned experimental findings for the possible magnetic structures considered in the preceding sections.

- In a Ginzburg-Landau treatment of electric polarization \mathbf{P} and magnetization \mathbf{M} , the lowest-order coupling between the two order parameters is given by the so-called Lifshitz invariant $P_i(\mathbf{r}) M_j(\mathbf{r}) \partial_k M_l(\mathbf{r})$ [278]. Re-iterating the derivations outlined in Ref. [278] for orthorhombic

³²The magnetic field range was restricted due to technical reasons during the second magnet time (see section A.4.2).

³³Note that a biasing electric field was applied in the experiment [188], such that the b -component most likely reflects the behavior of the electric susceptibility.

bic symmetry, the polarization arising due to improper ferroelectricity is

$$\mathbf{P} = \chi_e \sum_{i \neq j} \gamma_{ij} (M_i \partial_j M_j - M_j \partial_j M_i) \mathbf{e}_i \quad , \quad (8.10)$$

where χ_e denotes the (anisotropic) electric susceptibility in the absence of magnetism [278]. Under the assumption of a magnetic structure

$$\mathbf{M}(\mathbf{r}) = M_1 \mathbf{e}_1 \cos \mathbf{Q} \cdot \mathbf{r} + M_2 \mathbf{e}_2 \sin \mathbf{Q} \cdot \mathbf{r} + M_3 \mathbf{e}_3 \quad , \quad (8.11)$$

the simple relation $\mathbf{P} \propto \chi_e M_1 M_2 (\mathbf{e}_3 \times \mathbf{Q})$ commonly stated in the literature (e. g. , [81]) is recovered [278], provided that \mathbf{e}_3 [278] and $\mathbf{Q} - (\mathbf{Q} \cdot \mathbf{e}_3) \mathbf{e}_3$ point along principal axes of the crystal.³⁴ The preceding considerations suggest that $\mathbf{P} \parallel c$ for the spiral structures considered in section 8.6.3.3 [$\mathbf{Q} = (q_a, q_b, 0)$], which is not fully consistent with the measured [188] polarization.

While the result (8.10) seems generic in nature, its derivation relies on a continuum description of the electric and magnetic fields in the crystal [278]. In order to justify equation (8.11), the microscopic magnetic field needs to be averaged over length scales corresponding to the lattice constants. However, the spatial period corresponding to the wavevector \mathbf{Q} is comparable to the lattice constants, too. It is therefore not particularly alarming if this macroscopic model fails to describe the multiferroic behavior of BiCu₂PO₆.

- Microscopic considerations for a superexchange configuration suggest that

$$\mathbf{P} \propto \mathbf{e}_{ij} \times (\mathbf{S}_i \times \mathbf{S}_j) \quad , \quad (8.12)$$

where \mathbf{e}_{ij} connects the magnetic moments \mathbf{S}_i and \mathbf{S}_j [199]. Applying this result to the leg bonds of BiCu₂PO₆ and the magnetic structure considered in section 8.6.3.3, the net polarization is predicted to vanish as a result of the symmetry of the individual ladder units (see also [404]). A net chirality could only result on the interlayer bonds in this case. However, these bonds are expected to be very weak [318] and equation (8.12) suggests that $\mathbf{P} \parallel c$. An alternative possibility is that the magnetic structure breaks the symmetry of the individual ladder units (see section 8.6.2.4).

- Another microscopic model has been obtained through perturbation theory for the Hubbard model, yielding

$$\delta n_i = n_i - 1 = \sum_{jk} 8 \frac{t_{ij} t_{jk} t_{ki}}{U^3} [\mathbf{S}_i \cdot (\mathbf{S}_j + \mathbf{S}_k) - 2 \mathbf{S}_j \cdot \mathbf{S}_k] \quad , \quad (8.13)$$

where n_i is the charge density on lattice site i and the sum extends over all triangles (i, j, k) [68]. Application of (8.13) to the frustrated ladder model for BiCu₂PO₆ (cf. section 4.3.1) and assuming that the system is not dimerized, as suggested by numerical calculations (cf. section 7.15 and references therein), merely predicts a charge redistribution among the Cu(1) and Cu(2) sites due to $J'_2 \neq J_2$. Again, no net polarization emerges due to the C_2^b -symmetry of the individual ladder units.

From a more abstract point of view, the magnetic field $\mathbf{H} \parallel b$ lifts all symmetries except σ_b and C_2^b , and the latter is broken by the magnetic structure proposed in section 8.6.3.3. Thus, from a symmetry perspective, any orientation of $\mathbf{P} \perp \mathbf{H}$ is permitted.

³⁴Note that the preceding condition differs slightly from the one given in [278].

Furthermore, it should be noted that neither of the two aforementioned microscopic theories [68, 199] appears to have considered the effect of DM interactions, which might explain the unexpected orientation of the electric polarization. Also, the reported magnitude of the electric polarization in BiCu_2PO_6 ($\sim 30 \mu\text{Cm}^{-2}$ [188]) is one order of magnitude smaller than, e. g. , in TbMnO_3 [81]. Thus, multiferroicity may simply be a result of a small perturbation on top of an almost symmetric spiral structure like the one described in section 8.6.3.3. Finally, calculations indicate that the field-induced spiraling moments appear in the plane perpendicular to the magnetic field (see section 7.10 and references therein). Hence, the magnetic structure on all ladder units is expected to follow the external magnetic field upon slight misalignment of the sample. Via equation (8.12) this could then give rise to a measurable net electric polarization.

8.6.6 Discussion

The NMR spectrum measured in the high-field phase can be described using two double-horn components [Fig. 8.8(a)] (section 8.6.1). This is generally consistent with the conclusions from calculations performed for the frustrated-ladder model, which indicate the emergence of field-induced spiral order (see [78] and chapter 7).

Assuming a spiral structure and antiferromagnetic interladder couplings, as indicated by inelastic neutron scattering [316], constrains the class of possible magnetic structures within each bc plane of the crystal (section 8.6.2.2). The remaining degrees of freedom are associated with the details of the magnetic structure, as well as the stacking along the a -direction, where magnetic interactions are weak [316].

In order to obtain two non-degenerate double-horn contributions for $\mathbf{H} \parallel b$, as observed experimentally (section 8.6.1), the magnetic structure must break one of the symmetries connecting the four types of P sites in the BiCu_2PO_6 crystal (see section 8.6.2). Three possible scenarios have been considered:

1. Strictly speaking, the magnetic field itself already reduces the corresponding symmetry group from $Z_2 \times Z_2$ to Z_2 (section 8.6.2.1). Thus, the two types of bc planes in the crystal become inequivalent in a magnetic field due to their chiral *structure* (section 8.6.2.3). If there is any coupling between this structural chirality and the magnetic moments, the two types of layers may adopt different magnetic orders. However, neither the magnetic Hamiltonian (4.1), nor the nuclear-spin Hamiltonian, contain corresponding interaction terms, which is why this scenario has not been explored further.
2. By assuming that the symmetry-allowed couplings between magnetic and structural chirality invoked in scenario 1 are indeed negligible, which is compatible with field-independent hyperfine interactions, the entire zero-field space group of the crystal can be used to analyze the spectral degeneracies in the high-field phase (section 8.6.2.5). Assuming a single- \mathbf{q} magnetic structure with magnetic unit cell equal to the crystallographic one, the symmetries relevant for spectral degeneracies are σ_a , σ_c and C_2^b (see section 8.6.2.1). Since they generate a group isomorphic to $Z_2 \times Z_2$, exactly two of these symmetries need to be broken in order to obtain two non-degenerate double-horn contributions.

One possibility discussed in section 8.6.2.4 is that the spiral exhibits distortions, e. g. , tilts of the spiral axes, which are incompatible with the crystal symmetry, like the structures proposed and considered in previous work [78]. While such behavior may be relevant for $\mathbf{H} \nparallel b$, there is no experimental or theoretical evidence for its appearance in the case $\mathbf{H} \parallel b$. Therefore, the following

symmetry discussion (section 8.6.2.5) is specialized to the case that any distortions of the spiral structure are compatible with crystal symmetry (section 8.6.2.4). Such distortions are expected to be induced by DM interactions (see sections 7.13 and 7.14). In addition, under these assumptions, the spectral contribution of each P site is found to be invariant under global chirality reversal (section 8.6.2.5).

An explicit parametrization of the spiral structure anticipated for dominant DM interactions on the nearest-neighbor bond (see [318]) is given in section 8.6.3.1. The subsequent discussion focuses on this subclass of magnetic structures.

- a) If long-range order along the a direction is assumed (section 8.6.3.2), quantitative features of the NMR spectrum can be expressed in closed form (section 8.6.3.3). In particular, plausible magnetic structures which are quantitatively consistent with the measured data are obtained (Fig. 8.10). Based on systematic considerations of variations of the NMR coupling parameters, it is argued that this observation is robust against parameter uncertainties (section 8.6.3.5).
- b) The explicit model from section 8.6.3.3 is extended to include arbitrary stacking configurations along the a direction (section 8.6.3.6). In this case, the calculation of the NMR spectra corresponds to a random-walk averaging. Two illustrative models are considered in section 8.6.3.8. Most importantly, a scenario with parallel chirality but fixed relative stacking angle with randomly-chosen sign is also shown to be consistent with the experimentally observed spectrum (Fig. 8.11). This is related to the fact that the dipole field at the ^{31}P nucleus is dominated by the contributions of the two adjacent magnetic layers, which is why the line shape is mainly determined by the short-range stacking order (section 8.6.3.7). Meanwhile, contributions from stacking defects might explain the broadening of the NMR spectra in the high-field phase [cf. Fig. 8.8(a)].

To summarize the conclusions: (i) The ^{31}P -NMR spectra in the high-field phase ($H \gg H_{c2}$) are qualitatively consistent with two non-degenerate double-horn contributions and therefore a single- q structure which partially lifts the symmetry of the four P sites (see sections 8.1 and 8.6.1). (ii) Even within a strongly restricted subset of all possible spiral structures,³⁵ there exist many candidate solutions which yield quantitative agreement with the measured NMR spectrum (section 8.6.3). This conclusion is robust against parameter uncertainties (section 8.6.3.5) and has been validated by symmetry arguments (section 8.6.2) and explicit modeling of the NMR spectrum (sections 8.6.3.3 and 8.6.3.4). (iii) While quantitative agreement might also be achievable for amplitude-modulated structures, numerical calculations strongly suggest that the field-induced order in BiCu_2PO_6 is chiral (see [78] and section 7.15). (iv) Chirality is generally believed to be a prerequisite for multiferroic behavior (e. g., [81, 199]), which has been observed in BiCu_2PO_6 [188] (cf. section 8.6.5). Thus, while the precise magnetic structure cannot be inferred from the NMR data, the preceding arguments strongly suggest that the high-field field-induced magnetic order in BiCu_2PO_6 is of the spiral type.

³⁵For instance, the spiral-axis tilts were assumed to result from the DM interaction D_1^{ac} and to be equal for both Cu sites. In general, many other DM-induced distortions are possible (cf. section 8.6.3.1). Also, other types of symmetry-breaking structures exist, such as those enumerated above, and the ordering-wavenumber q_b may deviate from the minimum of the dispersion of the magnetic excitations [228].

8.7 Intermediate-field phase

8.7.1 Phenomenology of NMR spectra for $H_{c1} \leq H \leq H_{c2}$

The ^{31}P -NMR spectra obtained in the intermediate-field phase (light blue data in Fig. 8.4), appear asymmetric when compared to previous reports [78] (cf. Fig. 8.1). On the other hand, the experiments reported herein were the first to allow for an *in-situ* alignment of the sample (see section 8.2). In previous work, the sample was visually aligned *ex-situ*, and the NMR coil was mainly supported by the wires connecting it to the NMR probe [3] (cf. [74, Fig. 2.7d]). A small residual misalignment, possibly enhanced by magnetic torque (see section A.4.2), can therefore not be excluded. This hypothesis is supported by the following observations: (i) Asymmetric spectra were also observed during previous high-field experiments [74, Fig. 6.8b]. (ii) The spectrum acquired at $\mu_0 H = 25$ T with a slightly misaligned sample (Fig. A.9) qualitatively resembles the previous spectra. Moreover, the narrow central peak develops a fine structure as the magnetic field approaches H_{c2} (Fig. A.9), and a similar fine structure is present in earlier data collected at 31 T [74, Fig. 6.7]. (iii) By contrast, a line shape with at most three peaks is observed throughout the entire intermediate-field phase in the measurements reported in Fig. 8.4, corroborating the correct alignment of the sample during the corresponding experiments.

Furthermore, the above discussion suggests that the spectra acquired at lower magnetic fields (e. g. , $\mu_0 H \approx 25$ T) might resemble previous data more closely. If this is true,³² the persisting asymmetry of the spectra upon increasing temperature towards the phase boundary T_{c1} in high field [Fig. 8.4(a)], indicates that the corresponding transition may be different from the field-induced one at H_{c1} and low temperature.

8.7.2 Models for the NMR spectrum

As reviewed in section 8.1 (see also [74, pp. 138-140]), the three-peak NMR spectra observed in the intermediate phase appear inconsistent with generic single- \mathbf{q} magnetic structures. By contrast, multi- \mathbf{q} structures can yield similar spectra {[61] and Fig. 8.2(a)}. More generally, the three-peak structure of the spectrum suggests an anharmonic (in the sense of section 8.1) propagation of the magnetic structure. For instance, the spatial variation of the hyperfine field shown in Fig. 8.2(b) is *almost* sinusoidal. This explains the appearance of the lower- and upper-frequency peaks, which resemble a double-horn spectrum [Fig. 8.2(a) inset], whereas the additional saddle points seen in Fig. 8.2(b) give rise to a third peak (see [61], cf. [74, p. 145] and [78]).

Phenomenologically, almost sinusoidal structures resembling the multi- \mathbf{q} scenario described above can be constructed by replacing the linear propagation phase $u = \mathbf{q} \cdot \mathbf{r}$ of a single- \mathbf{q} magnetic structure by the Jacobi amplitude $\text{am}(u, k)$ [61, 432]—an approach used successfully in previous work [78]. However, the corresponding models predict equal intensities for the low- and high-frequency peaks, which is inconsistent with the data obtained at $H \lesssim H_{c2}$ (section 8.7.1). By contrast, the multi- \mathbf{q} structure mentioned above essentially corresponds to the inclusion of higher harmonics like $\cos(\mathbf{q} \cdot \mathbf{r})^2$, and such hyperfine-field configurations are known to generate intensity distributions with lower symmetry [61, e. g. Fig. 12].

Although phenomenological models providing a good fit to the NMR spectra measured in the intermediate-field phase are likely to exist, the search for such models needs to be guided by physical intuition. How-

ever, unlike the high-field chiral phase discussed in section 8.6, the intermediate-field phase appears not to be captured by the current theoretical models for BiCu_2PO_6 (section 7.16), which is why no further attempts to analyze the NMR spectra obtained in the intermediate-field phase have been made.

8.7.3 Solitons

In previous work, the phenomenological description of the NMR spectra using the Jacobi elliptic functions (cf. section 8.7.2) was interpreted as evidence for the formation of a field-induced soliton lattice [78]. A heuristic reason is that the Jacobi amplitude appears in solutions of the sine-Gordon equation [274] which describe lattice arrangements of solitons [61].

Solitons are topologically non-trivial solutions of differential equations, usually the equations of motion of a (quantum) field theory [105, 331]. The concept has also been applied to condensed-matter systems (e. g., [56, 61, 65, 243, 265, 285, 332]). Asymptotically, solitons often correspond to different homogeneous vacua [105] and thus can be considered as domain walls or *defects* [265]. Since the domains separated by a single domain wall have infinite extent, the energy barrier to destroy an isolated soliton is infinite, which stabilizes the soliton [265]. Excitations are soliton-antisoliton (bound) states, *viz.* domains [265]. The potential energy is proportional to the surface of these domains, which is why soliton-antisoliton pairs are typically confined in systems of dimension larger than one (e. g., [225]). The one-dimensional (Ising) magnet is a well-known example for such behavior (see [182, 225, 417] and [265, pp. 320]). Here, a single spin-flip corresponding to a spin-1 excitation fractionalizes into two domain walls called spinons (see, e. g., [265, Fig. 64]; cf. section 1.3.1).

The reference to differential equations in the definition of the soliton presumes a *continuum* description of the system. While this is trivial for slowly-varying magnetic structures like long-wavelength spirals, the large wavevector of the spin correlations in BiCu_2PO_6 (see chapter 7 and references therein) represents a problem. Possible work-arounds might build on Haldane's mapping of the quantum Heisenberg antiferromagnet onto the non-linear σ model (see [103] for a review), or the bosonization treatment of the vector-chiral phase of the zigzag chain [164]. Please note that, even though the sine-Gordon equation often appears in effective low-energy theories obtained by bosonization [360, 425], the resulting solitons still correspond to, e. g., *magnons* in the spin system [56].

The zigzag-chain (cf. section 1.3.3) material CuGeO_3 [174, 336] is a famous soliton-bearing compound (see previous discussion in [74, pp. 128 ff]). Due to the presence of magnetoelastic couplings, this system is theoretically described by the so-called spin-Peierls model, which has been studied both analytically [71, 139, 286, 407, 456] and numerically [110, 132, 262, 407]. The field-induced magnetic solitons carry spin- $1/2$ and are localized by associated lattice distortions (lattice solitons) [132]. Clearly, the three-dimensional nature of the system, either due to the phonon field or magnetic interchain couplings, as well as the slow dynamics of the quasi-classical lattice degrees of freedom³⁶ are essential for understanding the finite-temperature phase transition and the details of the ordered structure (see [110, 200, 375, 407, 456]). For this particular example, the longitudinal spin texture of the soliton lattice was characterized theoretically [456] and confirmed by subsequent NMR experiments [174].

Clearly, an analogous theoretical treatment for BiCu_2PO_6 would be desirable. As described in section 7.16, the numerical calculations performed in this work did not provide any clear evidence of solitonic behavior. In particular, the spectrum of states obtained using exact diagonalization (see Fig. 8.14 for a

³⁶The lattice degrees of freedom are treated in an adiabatic approximation (e. g., [132]).

reproduction of previous results [401]) confirms a well-defined triplon mode [401], whereas fractional excitations like spinons typically give rise to a continuum [227]. This is consistent with inelastic neutron scattering experiments on BiCu_2PO_6 which only report a two-triplon continuum [316, 318].

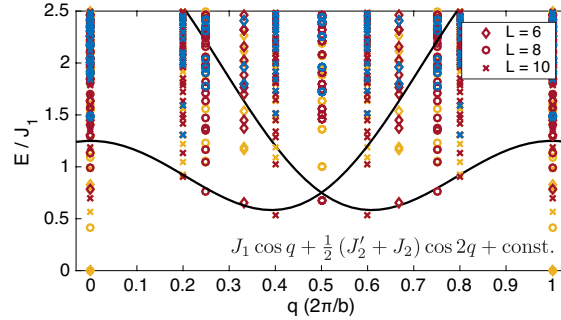


Figure 8.14: Energies and lattice momenta of excited states with $S_{\text{tot}}^z = 0$ (yellow), $S_{\text{tot}}^z = 1$ (red), and $S_{\text{tot}}^z = 2$ (blue) relative to the energy of the $q = 0$ ground state, as obtained using full-spectrum exact diagonalization for parameter set A (see section 4.3.3) and different system sizes L (cf. section 7.5). The expression for the solid line is stated in the figure, and is based on the expressions derived in Refs. [228, 401]. Following [401], the results were obtained using the reduced unit cell and back-folded to the Brillouin zone of the original frustrated-ladder model (cf. section 4.3.1). Unsurprisingly, this reproduces the previous results published in Ref. [401].

In CuGeO_3 , solitons separate domains corresponding to different dimerized ground states of the zigzag chain [285, 286]. By contrast, the zero-field ground-state of BiCu_2PO_6 is not dimerized (see section 7.15). The only degenerate ground state captured by the frustrated ladder model considered in chapter 7 is the chirally-ordered one, which corroborates that the solitons might nonetheless (see previous work [74, 78]) be related with the spiral structure proposed for the high-field field-induced phase [78] (cf. section 8.6). This idea is described in more detail in the following subsection (section 8.7.4).

8.7.4 The limit $H \gtrsim H_{c2}$

The evolution of the ^{31}P -NMR spectrum upon approaching the phase transition at H_{c2} from above is illustrated in Fig. 8.15. The high-field spectra become increasingly asymmetric upon approaching H_{c2} [see also Fig. 8.4(b)]. As the relative intensity of the two lower-frequency peaks is reduced, their splitting decreases until they finally merge at H_{c2} .³⁷ Meanwhile, the two higher-frequency peaks appear largely unaffected, except for a slight narrowing, which remains to be explained.

In the model constructed for the high-field phase (section 8.6), each P site in the crystal gives rise to a symmetric double-horn contribution to the NMR spectrum [cf. Fig. 8.2(a) inset]. Quite intuitively, the relative intensity of the two peaks of each of these contributions can become imbalanced if the spiral phase becomes non-linear [74, p. 140]. Such non-linearly propagating spirals may be related to solitons (see section 8.7.3 and references therein). However, given the short wavelength of the spin correlations, a picture based on discontinuous *defects* and their statistical distributions might be more appropriate. Besides the shape of the ^{31}P -NMR data, the relevance of defects is corroborated experimentally by an increased magnetic entropy in the intermediate-field phase [208]. As discussed in [208], this is also consistent with the long-range spiral magnetic order proposed [78] for the high-field phase (cf. section 8.6).

³⁷Note that, despite the misalignment, the spectra shown in Fig. A.9 exhibit qualitatively similar behavior.

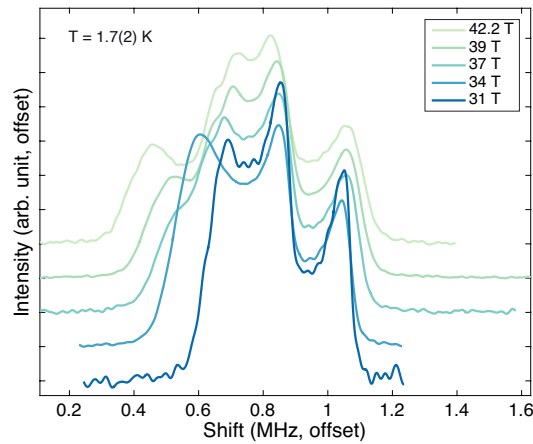


Figure 8.15: Subset of the ^{31}P -NMR spectra shown in Fig. 8.4(b), measured at the magnetic fields indicated in the legend. The areas of the spectra are normalized and the data are offset horizontally and vertically for clarity.

In the following, possible defects of the spiral magnetic structure discussed in section 8.6.6 are considered. Note that this discussion is by no means exhaustive.³⁸ Stacking defects along the a direction (cf. section 8.6.3.6) are one possibility. Moreover, for $\mathbf{H} \parallel b$, the spiral-axis tilts induced by transverse DM interactions (Fig. 4.5) compete with the rung and interladder exchange couplings (section 7.14.2), which might give rise to an instability in combination with additional interactions.³⁹ However, it is easy to see that every individual one-dimensional array of P sites running along the b -direction in the BiCu_2PO_6 crystal gives rise to a symmetric double-horn contribution. Being extended along the ladder units, i. e., along the b direction, the defects proposed above therefore cannot explain the asymmetric distortion of the NMR spectra. Moreover, the NMR spectra are sensitive to the dipole fields created by the neighboring bc planes (section 8.6.3.7). Thus, the weak field-dependence of the two higher-frequency peaks (Fig. 8.15) indicates that (short-range) spiral correlations and stacking order are preserved in the corresponding spatial regions, which further suggests that defects are extended along the a direction.

The implications of the observed loss of electric polarization at H_{c2} [188] depend on the assumed scenario (cf. section 8.6.5). If the polarization arises due to the magnetic chirality on the interlayer bonds, stacking defects would in principle be sufficient to destroy it. However, these defects should be “healed” by a biasing electric field, which is inconsistent with the reported results [188]. The electric polarization could also appear through a symmetry-breaking lattice distortion, caused, e. g., by inverse DM interaction [81, 356] (cf. [304]). In this case, knowledge of the lattice distortion is required to draw firm conclusions. Lastly, the electric polarization could be due to the longitudinal chirality of the magnetic structure (section 8.6.5). In this case, the experimental observations [188] (cf. section 8.6.5) suggest that the net longitudinal chirality is lost within each individual ladder unit. This implies that the defects (i) intersect the ladder units, and (ii) change the longitudinal chirality. In combination with the above discussion of the NMR spectra, this last scenario seems most likely. Two points of view appear possible: chiral defects whose chirality is opposite to that of the long-range ordered background [141], or domain walls separating regions with opposite chirality. Note that both scenarios are compatible with NMR, since the ^{31}P spectra are expected to be insensitive to the choice of chirality in the spiral phase

³⁸For instance, competition between different DM-induced distortions and/or various symmetric exchange couplings might give rise to an instability and associated domain walls.

³⁹Note that no instabilities were observed for the isolated ladder model considered in chapter 7.

(section 8.6.2.5). Furthermore, the second-order nature of the phase transition at H_{c2} [208] would then suggest that the solitons of the intermediate-field phase are chiral as well (cf. [46]; “spiral” or “twisted” solitons were previously proposed to explain magnetic order in doped BiCu_2PO_6 [424, pp. 133-134]), which could explain the finite dielectric susceptibility observed [188] for $H > H_{c1}$ (cf. section 8.6.5).⁴⁰

The asymmetry of the NMR spectra implies that the distribution of defects is non-uniform along the ladder units. In principle, the expressions given in section 8.6.3 can be used to identify the spatial regions corresponding to the low- and high-frequency edges of the NMR spectrum. However, in the present case, such analyses are hampered by the uncertainties regarding the coupling parameters and the ordered magnetic structure (see section 8.6.3.5). Furthermore, the hyperfine couplings of each ^{31}P nucleus (see Fig. 6.1) involve Cu sites whose distance along the b direction is comparable to the period of the spiral structure. Hence, there is little hope that the structure of the defects can be inferred using ^{31}P NMR alone.

8.7.5 Magnetoelastic couplings

The experimental data obtained in the intermediate- [78] and high-field field-induced phases of BiCu_2PO_6 suggest the appearance of defects in the magnetic structure (see [78] and sections 8.7.3-8.7.4). Often such defects are stabilized by magnetoelastic effects (see section 8.7.3 and references therein). Observations corroborating the importance of such effects in BiCu_2PO_6 are reviewed below.

- Both field-induced transitions give rise to measurable features in the magnetostriction [207].
- The temperature dependences of the thermal conductivities measured along all crystal directions exhibit a local minimum which roughly coincides with the maximum of the magnetic specific heat [325, Fig. 5.7]. The thermal conductivity, including the one measured perpendicular to the magnetic layers, is suppressed by a magnetic field $\mathbf{H} \parallel b$ [284]. A similar, strong suppression of the lattice contribution to the thermal conductivity is observed in high magnetic fields $\mathbf{H} \parallel a$, and explained by the resonant scattering of phonons, involving transitions between thermally-populated excited magnetic states with $S = 1$ triplons and $S = 1$ two-triplon bound states [190]. The suppression is maximal at H_{c1} , and even stronger than predicted by the resonant-scattering model, which is attributed to the combination of non-resonant scattering with critical magnetic fluctuations [190].
- First-principles calculations showed a strong dependence of the next-nearest neighbor exchange coupling upon the orientation of the PO_4 tetrahedra [401] (cf. Fig. 4.1). The influence of the superexchange angle on the nearest-neighbor bonds is expected to give rise to magnetoelastic effects as well [190]. DM interactions can also give rise to magnetoelastic couplings [304, 356] (see also [190]), which appears particularly relevant given the suspected chiral nature of the field-induced phases (cf. section 7.8.2).
- The lattice contributions to the specific heat of BiCu_2PO_6 , BiZn_2PO_6 , and BiMn_2PO_6 are all very similar [217, 289]. Yet, the specific heat of BiZn_2PO_6 can be described using a model based on acoustic phonons only at temperatures $T \gtrsim 200$ K [289]. Deviations at lower temperatures are interpreted as evidence for an anomalous lattice softening [289].

⁴⁰Note that the spectra observed upon misalignment in the intermediate-field phase [Figs. A.9 and A.6(a)] are indeed reminiscent of those observed in the high-field phase.

- The two types of magnetic layers present in the BiCu_2PO_6 crystal become inequivalent upon application of a magnetic field (section 8.6.2.3). Thus, field-induced changes of the lattice are generally allowed. The possibility of magnetoelastic couplings, based on structural aspects, was also pointed out in [377].
- Finally, the numerical calculations performed in this work predict only a single phase transition and it is unlikely that the inclusion of interladder couplings alone will change this conclusion (see section 7.16). Similarly, quantitative differences between the calculated and measured magnetic susceptibilities might be related to magnetoelastic effects [377].

9 Conclusions and Outlook

Inspired by the intriguing variety of field-induced phases in BiCu_2PO_6 [207] (cf. section 4.5), the frustrated ladder model proposed [257, 401] to describe its properties was investigated numerically (see chapter 7). A field-induced chiral phase, previously reported in [77, 78, 131], appears as a ubiquitous feature of this model, provided that frustration and rung exchange are not too weak (see section 7.12). The effect of DM interactions is studied in detail and found to be consistent with classical expectations (sections 7.13 and 7.14). In particular, the chiral phase is robust against moderate DM interactions. A short comment in [131] suggests that this is in agreement with previous work (cf. section 7.2). On the other hand, detailed calculations reveal no additional phases between the spin-liquid ground state and the field-induced chiral phase of the frustrated spin ladder (sections 7.10.2 and 7.14.1), which suggests that additional interactions need to be considered in order to explain the diversity of field-induced phases in BiCu_2PO_6 , even for $\mathbf{H} \parallel b$ (see section 7.16). Please refer to sections 7.15 and 7.16 for more complete discussions of the numerical calculations, as well as the differences between published experimental data and the predictions of the frustrated-ladder model.

High-field ^{31}P -NMR experiments ($\mathbf{H} \parallel b$) were performed (see sections 8.1 and 8.2) in order to test the prediction of a field-induced chiral phase ([78] and section 7.15). The phase boundaries determined from the spin-lattice relaxation rates agree with previously-published [207, 208] results (see section 8.4). The NMR shifts generally reflect the behavior of the bulk magnetization and exhibit an interesting temperature dependence in the high field phase (see section 8.5). However, the complicated couplings between the ^{31}P nuclei and the Cu spins prevent firm quantitative conclusions. Although outside the focus of this work, $^{63,65}\text{Cu}$ NMR might be better suited for studying the longitudinal magnetization [74, p. 156]. Speculating that the on-site hyperfine coupling might be rather isotropic, this would also allow to check for a modulation of the longitudinal ordered moments in both field-induced phases (cf. [74, p. 156]). As pointed out in [74, p. 156], such a modulation was observed, e. g., in conjunction with the soliton lattice in CuGeO_3 [174] (cf. section 8.7.3).

On the other hand, the hyperfine couplings of the ^{31}P site are sensitive to the transverse ordered magnetic moments and their correlations [74, p. 117] (cf. chapter 6). Since interladder couplings are known to be relevant in BiCu_2PO_6 (see section 5.3 and references therein), field-induced chirality is expected to give rise to a more conventional spiral magnetic order [78] (cf. section 7.8). Indeed, the ^{31}P -NMR spectra obtained in the high-field field-induced phase at $H > H_{c2}$ ($\mu_0 H_{c2} \approx 35.5$ T) are qualitatively consistent with the aforementioned prediction (see section 8.6.1). Note that the observed intensities are somewhat different from the expected ones. While this is believed to be of experimental origin (section 8.6.1), it should be mentioned that an accidental agreement with the theoretical expectations cannot be excluded with certainty. However, the chiral nature of the high-field phase is corroborated by independent reports of multiferroic behavior [188] (cf. section 8.6.5). Moreover, explicit models of spiral magnetic structures reproduce the NMR spectra for plausible parameter values (section 8.6.3.4). Although quantitative estimates are hampered by the uncertainties of the hyperfine couplings and g-tensors (see section 6.8), the existence of plausible candidate magnetic structures appears robust against variations of these parameters (section 8.6.3.5). A detailed discussion of these arguments can be found in section 8.6.6. To summarize, based on the results and considerations presented in the preceding

chapter, I conclude that BiCu_2PO_6 indeed (see [78]) adopts a spiral magnetic structure with DM-induced distortions at $H \gg H_{c2}$ ($\mathbf{H} \parallel b$) and low temperature.

Regarding the intermediate-field phase realized for $H_{c1} < H < H_{c2}$, the new data resemble previous results [78] and are consistent with a non-linear propagation of the magnetic structure, as proposed earlier [74, 78] (cf. section 8.7). Accordingly, the asymmetric appearance of the NMR spectra observed upon approaching H_{c2} from above is interpreted as evidence for the formation of defects in the spiral magnetic structure (see section 8.7.4). This corroborates that the intermediate-field phase is a precursor of the high-field spiral, as suggested in previous work [78]. Indeed, the features observed in the magnetization [207] and the specific heat [207, 208] are more pronounced for the phase transition at H_{c1} than for the one at H_{c2} . Similarly, a non-zero electric susceptibility first appears at H_{c1} [188] and the magnetic excitations become soft at H_{c1} ([190] and [74, p. 136]), as predicted in [179, 318].

According to the aforementioned results, the spin gap becomes very small¹ at H_{c1} and chiral order emerges at H_{c2} . By contrast, numerical calculations predict that both events occur simultaneously (see section 7.16). Thus, additional interactions are required to explain the stabilization of the defects in BiCu_2PO_6 . Future experimental and theoretical work should focus on identifying the defects and characterizing the interactions responsible for their stabilization. As argued in section 8.7.5, magnetoelastic couplings are a promising candidate, known to induce dimerization and associated solitons in certain classes of ladder models—at least in zero magnetic field [210, 290]. Note that for the frustrated spin-ladder models studied numerically in this work, dimerization and chirality appear to compete (see section 7.15), which might explain the appearance of an additional phase transition.

Besides neutron-scattering surveys of the phonons, magnetoelastic effects can be studied through high-field measurements of elastic constants [5] (ultrasound; e. g. , [271, 365]). Indirect evidence might also be obtained from experiments under pressure (cf. [455]). Any lattice distortions in the field-induced phases of BiCu_2PO_6 could also be detected using diffraction techniques (X-rays or neutrons), or NMR, by making use of the quadrupole moments of the $^{63,65}\text{Cu}$ and ^{209}Bi nuclei.²

From an NMR perspective, it could appear desirable to reduce the uncertainties of various model parameters. For the hyperfine couplings and g-tensors, this topic was discussed in a previous chapter (section 6.8). The magnetic interactions might be constrained further by extending the magnetization measurements to even higher fields. As pointed out in [319, pp. 84,108], characterizing the hyperfine couplings of ^{209}Bi with the electronic magnetic moments on the Cu sites could provide indirect information about the DM interactions in BiCu_2PO_6 . In the end, the usefulness of such campaigns is questionable, since many coupling parameters are likely to be field dependent, especially if magnetoelastic effects are present. It therefore appears more promising to focus on the phenomenology of the NMR spectra in the field-induced phases observed in even higher (pulsed) fields, as well as for other orientations of the magnetic field, i. e. , $\mathbf{H} \nparallel b$ [208] (the latter was already proposed in [74, p. 156]). Moreover, the dynamical properties of the field-induced phases, including the thermally disordered regime (see section 8.6.4) which might exhibit chiral order [68, 419] (cf. section 7.1.2), are an interesting topic to address in future work, e. g. , through systematic investigations of the ^{31}P spin-lattice relaxation rates (see previous work [74, 78] for corresponding experiments and detailed discussions) at different positions within the spectrum (cf. section 8.6.1).

To conclude, numerical calculations identify field-induced chirality as an essential feature of the phase

¹Note that the spin gap might not close completely due to DM interactions ([190, 370] and [74, pp. 125,136]).

²Note that only the $^{63,65}\text{Cu}$ resonance has been reported so far [74, p. 156].

diagram of the frustrated spin ladder below half-saturation magnetization (see [367] for the regime close to saturation). Combined with the experimental data, convincing evidence for a field-induced spiral phase [78] in BiCu_2PO_6 is provided. Defects appear to play a role at intermediate magnetic fields ([78] and section 8.7), and their properties remain to be clarified through additional experiments. Field-induced chiral phases were reported in other frustrated systems (e. g. , [143]). Similarly, spiral phases with multiferroic properties have been observed in other zigzag-chain materials, like LiCuVO_4 [120, 147, 279] and the example of a solitonic phase in CuGeO_3 was reviewed in section 8.7.3. What sets BiCu_2PO_6 apart from many other compounds is the challenging *combination* of the following aspects: (i) A spin-liquid ground state [258] with (ii) a field-induced chiral phase (proposed in [78], confirmed in this work), including multiferroicity [188], (iii) a ladder geometry [257] consisting of pairs of (iv) zigzag-chain units with antiferromagnetic nearest-neighbor (NN) interactions [217], which are expected to give rise to different field-induced phases (e. g. , [164, 383]) than the ferromagnetic NN interactions present in, e. g. , LiCuVO_4 [70, 249, 280], (v) a highly anisotropic phase diagram [207], (vi) important DM interactions [316], and (vii) the appearance of defects or static solitons in the field-induced phases ([78, 208] and this work).

Acknowledgments

First of all, I am grateful to my thesis supervisor Prof. Dr. Joël François Mesot for giving me the opportunity to pursue this work in his research group, as well as for his continued trust and support—both, personally and scientifically. I am also deeply indebted to Prof. Dr. Hans Rudolf Ott, who was always available to discuss ideas and provide valuable advice. Furthermore, I also thank Prof. Dr. Thomas C. Schulthess for agreeing to review this thesis as a co-examiner. Moreover, I thank my current and previous colleagues, Lukas Korosec, Nicolò Barbero, Dr. Francesco Casola, Dr. Toni Shiroka, and Dr. Krunoslav Prša, for sharing hard work and enjoyable moments alike. Privately, I thank my parents, Susana, and my friends for their support and patience during the past years.

Besides his active involvement in most of the projects reported herein, Toni's (Dr. Toni Shiroka) hands-on collaboration was particularly indispensable to the success of the strenuous high-field NMR experiments on BiCu_2PO_6 . The same applies to the superior experimental and moral support provided by Dr. Arneil P. Reyes and Dr. Philip L. Kuhns of the National High Magnetic Field Laboratory (NHMFL, Tallahassee, FL, USA). The crystals used in the experiments were grown by Dr. Shuang Wang (Paul-Scherrer Institute and EPF Lausanne). The experiments were initially proposed by Francesco (Dr. Francesco Casola), who also contributed actively during the first series of high-field experiments and before. I thank Francesco for getting me interested in this project, and helping me to get started during the experiments and their preparation. Representing a continuation, the present work clearly overlaps with his previous work. In particular, the refined analyses of the g -tensors and hyperfine couplings in chapters 5 and 6 build on previous ideas and data [74, 75]. Also, the analysis and interpretation of the high-field NMR data in chapter 8 is strongly inspired by Francesco's previous work [74, 78]. Moreover, I acknowledge S. Zvyagin for communicating preliminary results of his high-field ESR experiments.

I further thank Prof. Dr. Adrian E. Feiguin (Northeastern University, Boston) for sharing his unpublished results [131] associated with the work published in [74, 77, 78]. These previous results [77, 131] served as a general guidance for the detailed calculations reported in chapter 7. I further acknowledge the access to the computing resources of the Swiss National Supercomputing Centre (CSCS), kindly provided by the Paul-Scherrer Institute (PSI). Moreover, the technical support of Michele Dolfi and the ALPS user community was very helpful.

The presentation of the results in part II of this work also benefited from synergies with ongoing collaborative publication efforts (see, in particular, [312]).

With regard to part I, I especially thank Prof. Ott for taking care of the operation of the dilution refrigerator during various test runs. I also thank Toni, Nicolò (Nicolò Barbero), Lukas (Lukas Korosec), Francesco, W. Bachmann, and M. Baer for various technical contributions (see chapter 3, especially sections 3.4, 3.5.1, and 3.5.2 for details/examples), as well as many helpful discussions and general assistance in the lab. I also acknowledge the general support of H.-R. Aeschbach in various technical matters. Furthermore, I thank our secretary, Gaby Strahm, for handling vast amounts of associated paperwork. The present work generally benefited from the excellent support infrastructure provided by ETH Zürich—especially the mechanical workshop of the physics department, as well as FIRST-Lab. Important engineering and technical contributions, in particular by Walter Bachmann and Sandro Loosli

(FIRST-Lab), were already acknowledged in chapter 3. I also thank Reinhardt Microtech AG (Wangs, Switzerland) for technical advice regarding the fabrication of the microstrip lines described in section 3.5.3. Related to the work presented in chapter 3, I thank Dr. Marek Bartkowiak (PSI), Prof. Dr. Vesna Mitrović (Brown University, Providence), Dr. Philip L. Kuhns (NHMFL), Dr. Arneil P. Reyes (NHMFL), Dr. Patrick Hautle (PSI), Dr. Ben van den Brandt (PSI), Peter Märki, Dr. Sarah Hellmüller, Dr. Yves Acremann, Dr. Lars Steffen, and Dr. Julian O. Piatek (EPF Lausanne) for various discussions and technical advice. I further thank SP Devices Sweden AB for loaning the radio-processor device initially used for the work reported in chapter 2, as well as for their rapid response to technical issues encountered during development and testing. I also acknowledge the help of Prof. Dr. Guiseppa Allodi (Università di Parma) with various issues related to NMR software [26].

While the corresponding projects are not part of this thesis, I also enjoyed collaborating with Dr. Marisa Medarde (PSI), Prof. Dr. Johan Chang (Universität Zürich), Dr. Niels B. Christensen (Technical University of Denmark), Prof. Dr. L. Udby (University of Copenhagen), Prof. Dr. Christof Niedermayer (PSI), Dr. Tatsuo Goko (PSI), Dr. Robert Scheuermann (PSI), and many other scientists involved in those research efforts. I further appreciate various discussions with Prof. Dr. Henrik Rønnow (EPF Lausanne) and Prof. Dr. Christian Rüegg (PSI).

A Appendix

A.1 Technical aspects of calculations

The methodology described in the following subsections is considered standard practice. Nonetheless, it appears that a detailed documentation might be useful for possible future continuation work.

A.1.1 Units

I measure J_1 in temperature units and write the exchange Hamiltonian as $J_1 \tilde{\mathcal{H}}$. All numerical methods are applied to $\tilde{\mathcal{H}}$, including an additional Zeeman term where applicable. Thus, the applied magnetic field is effectively measured in units of J_1/μ_B . In this convention, the Boltzmann weight of an eigenstate of $\tilde{\mathcal{H}}$ with energy ϵ is $\exp(-J_1\epsilon/T)$.

A.1.2 Additional details

Most of the full-spectrum exact diagonalization calculations used ALPS release 2.2.b3-r7462 [49] and the parallel version of Intel MKL [181]. Updated revisions of the code were used in later calculations (DMRG and doped models). Lattice graphs and required operators were described using XML files. The simulations were primarily controlled using the Python [326] interface to ALPS [49]. MPI-Bash [281] was used to distribute parts of the DMRG calculations. Whenever possible, real-valued arithmetic was used. The results were post-processed using custom MATLAB [250] routines.

A.1.3 Exact-diagonalization performance

The official versions of the diagonalization applications of ALPS [49] (*fulldiag* and *sparsediag*) are single-threaded and do not support distributed memory. *Fulldiag* uses external BLAS/LAPACK [59, 226] libraries for the linear algebra routines and hence can make some use of multiple processing cores. Distributed storage could be incorporated with moderate effort by using ScaLAPACK [346] instead. Still, serial execution paths, related to matrix setup and measurement, limit the obtainable speed-up using the current implementation (Amdahl's law [29]). The largest system size solved with full-spectrum diagonalization was $L = 10$, taking 18 d and 6 GiB of (random-access) memory (on the Euler cluster). For sparse diagonalization, the largest system size ($L = 16$) needed 75 d and 182 GiB of memory (using translation invariance and “fat nodes” of the Brutus cluster). Different sectors of the Hamiltonian have been solved in parallel by independent jobs. The indicated run-time is the total CPU time consumed by these jobs. The calculation time was minimized by making use of the $S_{\text{tot}}^z \leftrightarrow -S_{\text{tot}}^z$ symmetry of the Hamiltonian. Given an eigenbasis $\{|n\rangle\}_n$ of the $S_{\text{tot}}^z = s$ sector, an eigenbasis for the $S_{\text{tot}}^z = -s$ sector is given by $\{P|n\rangle\}_n$, where $P = \prod_{i,u} \sigma_{i,u}^x$ flips all spins in the S_z -basis and the product is a tensor product. Here, σ_{\dots}^i (with $i = x, y, z$) denotes the Pauli matrices [434]. The matrix elements $\langle Pm | A | Pn \rangle =$

$\langle m | P A P | n \rangle$ need to be transformed accordingly [$\sigma^x \sigma^k \sigma^x = (2\delta_{xk} - 1)\sigma^k$]. The lack of translation invariance made the calculations for the inhomogeneous systems (section 5.2.4) particularly demanding. For these calculations, the code was modified to represent the sparse Hamiltonian matrix using a list format during the setup phase, before switching to a compressed storage format for the diagonalization step. Even so, the calculations for $L = 16$ took 5 days per S_z -sector and required about 600 GiB of memory (“fat nodes” of the Brutus cluster). No further attempts at performance optimization were made. Although the exponential scaling of the Hilbert-space dimension ultimately clearly limits the applicability of any diagonalization code, it appears that a generic matrix-free implementation of the sparse-diagonalization application (e. g., [130, p. 541]) might be a nice feature for the future.

A.1.4 Site-dependent g-tensors

As discussed in section A.5.3, there are two computational approaches to obtaining the matrices C_{ij} .

The first method corresponds to equation (A.11) and requires the matrix-elements of the sublattice spin operators. As discussed in the corresponding section, these operators are block-diagonal in a basis which respects translation symmetry. I have extended ALPS [49] with a “matrix-block measurement” to accommodate such measurements. The new option `MEASURE_SUM_MATRIX_BLOCK[<label>]=A` instructs ALPS to measure the complex-valued matrix elements $\langle m | A_{i,\Sigma} | n \rangle$ for all eigenstates $|m\rangle$ and $|n\rangle$ within a given symmetry sector. Here, A denotes a site-operator and $A_{i,\Sigma} = \sum_p A_{i,p}$ its sub-lattice sum. For the subsequent numerical evaluation of equation (A.11), it is favorable to rewrite

$$\frac{e^{-\beta E_m} - e^{-\beta E_n}}{-\beta(E_m - E_n)} = e^{-\beta E_{\text{avg}}} \frac{\sinh \beta h}{\beta h} ,$$

where $E_{\text{avg}} = 1/2(E_m + E_n)$ and $h = 1/2(E_m - E_n)$. The expression $\sinh x/x$ is numerically stable for $x \rightarrow 0$, and only the continuous continuation at $x = 0$ needs to be handled separately.

The second method is based on equation (A.13). For a Zeeman term of the form $-h S_{j,\Sigma}^\sigma$, I obtain (cf. section A.1.1)

$$\frac{1}{h} \langle S_{i,\Sigma}^\rho \rangle \approx J_1 C_{ij}^{\rho\sigma}(T) .$$

The field h has to be chosen small enough to remain in the linear-response regime, but large enough to avoid numerical errors. The gap between the ground state and the first excited state is ~ 1 in simulation units (section A.1.1) and the first excited state has $S_{\text{tot}}^z = 1$ (see section 5.2.3), such that the field h required to close the gap is ~ 1 (cf. section 7.9.1). For each choice of j and σ , I therefore run simulations with $h \in \{0.017, 0.034, 0.051\}$, calculate $\langle S_{i,\Sigma}^\rho \rangle(h)$, and finally perform a linear regression to obtain $C_{ij}^{\rho\sigma}(T)$. In real units, $h = 0.05$ corresponds to $B = 0.05 \frac{k_B 140 \text{ K}}{\mu_B} \approx 10 \text{ T}$ (for parameter set A). To make sure that the linear response regime is maintained, the R^2 -value (section A.6.1) of the regression fits is monitored. For the calculations reported in section 5.2.1, $1 - R^2 \leq 1.1 \cdot 10^{-6}$.

The methods described above were validated through application to the simple-dimer example considered in section A.5.3. While the matrix-block measurement does not rely on a suitable choice of the field h , the second approach is more efficient for larger systems. For the fits reported in section 5.2.1, the two methods agree up to about 1%.

A.1.5 DMRG calculations

Recently, the ALPS libraries [49] have been extended by an implementation of DMRG using the MPS formulation [111]. Calculations used SVN revisions 7584, 7666, and 7669 (see also section A.1.6). The two-site optimization algorithm [111] was used. Larger bond dimensions m (up to 2048) benefited from nested OpenMP [396] parallelization, allowing both the MPS code as well as the BLAS library [59] (Intel MKL [181]) to make use of multiple processor cores [111]. The evaluation of the energy-variance was found to be very time-consuming and was therefore omitted for most calculations reported herein. The measurements (cf. section 7.7.4) are implemented using the *MEASURE_LOCAL_AT* functionality of the ALPS MPS applications [111]. The measurement strings are generated by a Python [326] script, which parses the output of the ALPS *printgraph* utility [49] to obtain the required vertex indices. A set of custom MATLAB [250] scripts is used to post-process and analyze the simulation output.

A.1.6 Notes for ALPS users

A few minor issues were encountered while using ALPS and were fixed either by the author of this work or members of the ALPS collaboration. As of SVN revision 7669 [28], the only change not propagated back into the ALPS project concerns the *MEASURE_LOCAL_AT* feature of the MPS application, which truncates the imaginary parts of all calculated expectation values. However, the code adjustments required to change this behavior are very straightforward.

A.1.7 Convergence measures for spin texture

As a simple check, one can verify that the solution is consistent with the symmetries of the system [6]. The P -symmetry introduced in section 7.3 allows to construct a criterion to assess the convergence of the spin textures $\langle S_z^i \rangle$. Since all expectation values calculated by tracing over the ground-state eigenspace, which is either one- or two-dimensional, need to be P -invariant, I define the P -asymmetry

$$a_P = \frac{L}{S_{\text{tot}}^z} \min \left(\max_i \left| \langle \varphi_1 | S_i^z | \varphi_1 \rangle - \langle \varphi_1 | S_{P(i)}^z | \varphi_1 \rangle \right|, \right. \\ \left. \frac{1}{2} \max_i \left| \langle \varphi_1 | S_i^z | \varphi_1 \rangle + \langle \varphi_2 | S_i^z | \varphi_2 \rangle - \langle \varphi_1 | S_{P(i)}^z | \varphi_1 \rangle - \langle \varphi_2 | S_{P(i)}^z | \varphi_2 \rangle \right| \right),$$

where $|\varphi_1\rangle$ and $|\varphi_2\rangle$ are the two lowest-energy eigenstates found using the DMRG method (sorted by ascending energy). While correlation functions converge quickly with the number of optimization sweeps s , a_P decreases more slowly with s . For system size $L = 64$ and parameter set A with uniform g -factors, $a_P \approx 0$ is satisfied for $s = 512$, which has been used in most calculations.

For practical reasons, only one lowest-energy eigenstate was targeted in the calculations for larger systems. While not a necessary convergence criterion, the “naive” asymmetry measure

$$a_P^{(1)} = \frac{L}{S_{\text{tot}}^z} \max_i \left| \langle \varphi_1 | S_i^z | \varphi_1 \rangle - \langle \varphi_1 | S_{P(i)}^z | \varphi_1 \rangle \right|$$

is considered instead, and is found to decrease with increasing bond dimension m and increasing number of optimization sweeps s .¹ Generally, convergence is slower for smaller values of S_{tot}^z .

¹This does not necessarily suggest that the DMRG algorithm converges towards the representations $|g\rangle$ and $|u\rangle$ of the

A.1.8 Calculation of structure factors

There are a few not necessarily obvious technical aspects concerning the computation of the structure factors, which should be mentioned in the following.

- First, instead of summing over all “source” sites j in the expressions for the structure factors (section 7.7.2), the sum is restricted to a subset of indices defined by the parameter a (see section 7.5). Such an approach was used before, e. g., in [111, 112] (see also [164, 209, 255]). The normalization factor L^{-1} is adjusted accordingly.² This lowers the computational effort, while still reducing possible spurious oscillations (see section 7.3).
- Only half of the possible distances d need to be considered when calculating $C^{AB}(d) = \langle A_i B_{i+d} \rangle$. Consider the case of a one-dimensional linear index, without loss of generality. As demonstrated in section 7.3.3 (footnote 22), the approximate symmetry σ_b has essentially the same effect as P , such that

$$\langle k | A_i B_{i+d} | k \rangle = \langle k | \sigma_b^2 A_i B_{i+d} \sigma_b^2 | k \rangle = \langle -k | \sigma_b A_i \sigma_b \sigma_b B_{i+d} \sigma_b | -k \rangle \quad .$$

The symmetry σ_b corresponds to a spatial reordering of the ladder graph, combined with a spin-space rotation by π about the spin quantization axis $z \parallel b$. Besides the spatial component of the symmetry, $i \mapsto R(i)$, the operators introduced in section 7.7.1 transform trivially, i. e., up to signs which cancel from all relevant correlation functions (section 7.7.1). Therefore,

$$\langle k | A_i B_{i+d} | k \rangle = \langle -k | A_{R(i)} B_{R(i)-d} | -k \rangle \quad .$$

This proves that, after performing the partial trace over the ground-state eigenspace³ (cf. section 7.3), $C^{AB}(d) = C^{AB}(-d)$, for the combinations of operators A and B considered in this work.

- The Fourier transformation requires knowledge of $C^{AB}(d)$ for all distances d . At small distances, sites/bonds can overlap or coincide. These cases need special consideration, the corresponding expressions are summarized in section A.1.9. Note that the bond correlations for two bonds (i, j) and (j, k) with one overlapping site are not Hermitian, yielding complex-valued expectation values in general. However, for two bonds of the same type (i. e., NN or NNN leg bonds), reflection about j , which corresponds to the approximate symmetry σ_b , transforms the measurement operator into its Hermitian conjugate. Since σ_b is closely related to P (section 7.3.3, footnote 22), the partial trace over the ground-state eigenspace is then expected to be a real number. The anti-Hermitian part is also irrelevant for real-valued eigenstates (in the canonical S_z -basis). Since either of these two conditions (tracing or real-valued eigenstates) is always satisfied for the calculations reported in this work, the corresponding correlation functions (see section 7.7.1) are taken to be real-valued.
- To avoid spurious oscillations in the structure factors, which arise as a consequence of the system boundaries, a windowing function (Blackman window) is applied before the Fourier transform,

symmetry group $\{1, P\} \simeq Z_2$ (cf. section 7.3) for large m and s , since, e. g., convergence towards $|\pm k\rangle$ would result in the same observations if $\langle k | S_i^z | k \rangle = \langle -k | S_i^z | -k \rangle$ was satisfied accidentally.

²As discussed in section 7.3, this procedure may result in averaging of two different types of bonds, e. g., for the NN leg bonds. Note that the number of such bonds is imbalanced for even a , which is why a weighted average is used to avoid artifacts resulting from incomplete cancellation.

³For special cases, e. g., parameter set A with site-independent g -factor, the trace was found not to affect the results for $L = 64$. Therefore, only one eigenstate was targeted in some of the corresponding calculations performed for larger system sizes L .

as appears to be common practice (e. g., [444]). In addition, the correlation functions are zero-padded over a distance of 1000 lattice units in each direction, in order to obtain an interpolation in momentum space.

A.1.9 Useful identities for correlation functions

When calculating bond correlations between bonds (i, j) and (k, l) , it is possible that one or two sites coincide. In the former case, the following expressions (checked using Mathematica [448] and DiracQ [449]) are helpful

$$\begin{aligned}\kappa_{ij}^x \kappa_{jk}^x &= -\frac{1}{4} (S_i^y S_k^y + S_i^z S_k^z) + \frac{i}{2} (S_i^z S_j^x S_k^y - S_i^y S_j^x S_k^z) \\ \kappa_{ij}^y \kappa_{jk}^y &= -\frac{1}{4} (S_i^x S_k^x + S_i^z S_k^z) + \frac{i}{2} (S_i^z S_j^y S_k^x - S_i^x S_j^y S_k^z) \\ \kappa_{ij}^z \kappa_{jk}^z &= -\frac{1}{4} (S_i^x S_k^x + S_i^y S_k^y) + \frac{i}{2} (S_i^y S_j^z S_k^x - S_i^x S_j^z S_k^y) \\ D_{ij}^z D_{jk}^z &= \frac{1}{4} D_{ik} - \frac{i}{2} \sum_{\alpha, \beta, \gamma} \epsilon_{\alpha, \beta, \gamma} S_i^\alpha S_j^\beta S_k^\gamma \quad .\end{aligned}$$

In the latter,

$$\begin{aligned}\kappa_{ij}^\alpha \kappa_{ij}^\alpha &= \frac{1}{8} - \frac{1}{2} S_i^\alpha S_k^\alpha \\ D_{ij} D_{ij} &= \frac{3}{16} - \frac{1}{2} D_{ij} \quad .\end{aligned}$$

A.1.10 Convergence problems with longitudinal DM vectors

Note that the longitudinal DM terms obviously conserve S_{tot}^z (see also [77, p. 2]), even though this is not explicitly accounted for in the calculations presented in section 7.13. In combination with the low bond dimension and iteration count, this is likely to give rise to convergence problems. The drops observed in Fig. 7.29(b,d), as well as the step-like features in $M(H)$ [Fig. 7.29(a,c)], are attributed to such effects. This is corroborated by the generally good agreement of the remaining data with the results obtained for the DM-free case.

Neglecting the site-dependent g-factor allows for efficient calculations using S_{tot}^z -conservation.⁴ The results of this approach are depicted in Fig. A.1. The correlation functions are consistent with chiral order for $1 \leq S_{\text{tot}}^z < L/2$, which is compatible with the phase boundaries obtained in sections 7.10.2 and 7.14 (see also Fig. 7.29). The magnitude of the chiral correlations also turns out to be comparable [Fig. A.1(b,d)]. Hence, the effect of the site-dependent g-factors upon the chiral order appearing below half-saturation magnetization is again found to be negligible. Thus, the fact that the calculations obtained using S_{tot}^z -conservation and larger MPS bond-dimension m are well-behaved, shows that the glitches seen earlier are due to convergence problems and should disappear upon increasing the bond dimension m and/or the number of optimization sweeps s . Due to limited computational resources, more detailed calculations were only performed for parameter set B (cf. section 7.14).

⁴Otherwise, several S_{tot}^z sectors would need to be solved for each applied field (see also footnote 12 in chapter 7).

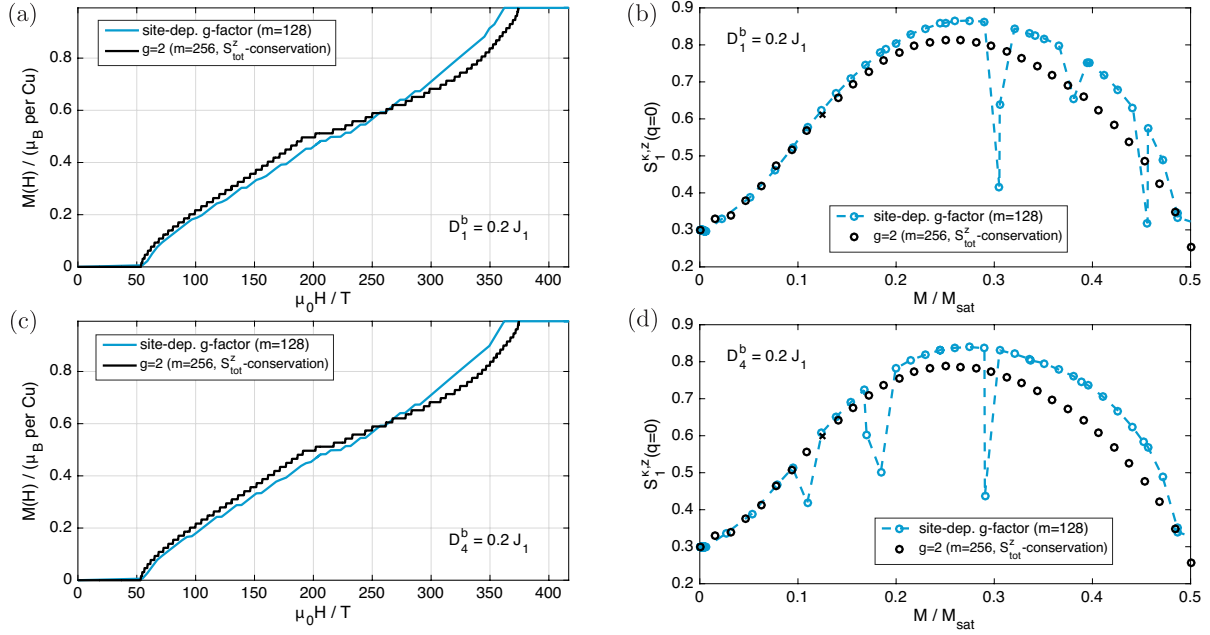


Figure A.1: Magnetization (a,c) and uniform ($q = 0$) correlations of longitudinal chirality (b,d), calculated for parameter set *A* augmented by longitudinal DM terms, $D_1^b = 0.2 J_1$ and $D_4^b = 0.2 J_1$, respectively ($L = 64$, $s = 24$, traced; remaining calculation parameters listed in legend). Data represented in blue-green color are identical with Fig. 7.29(a-d). The black data at $M/M_{\text{sat}} = 0.125$ [indicated by a cross in (b,d)] were calculated with $m = 512$ and $s = 64$ due to slow convergence.

A.1.11 Computing resources

Calculations were performed on the Brutus and Euler clusters of ETH Zürich, as well as on Piz Dora at the Swiss National Supercomputing Center (CSCS). Table A.1 summarizes the resources consumed on each of these systems. The rightmost column indicates the minimum waiting time resulting from the queue limits.⁵ The above numbers do not include queue waiting times or failed runs. For calculations requiring nodes with large amounts of memory (RAM), such as sparse diagonalization calculations, the number of parallel jobs was often limited by the available resources rather than by the queue limits.

System	CPU hours	Min. time (days)
Euler (ETH)	220007	191
Brutus (ETH)	106919	17
Piz Dora (CSCS)	75240 ⁶	n/a

Table A.1: Overview of computing resources used in this work. See text for details.

⁵For non-shareholders, these amount to 48 and 256 CPU cores per user, for Euler and Brutus, respectively. No such limits applied on Piz Dora, where a fixed compute budget within the context of the PSI allocation was agreed upon instead.

A.2 Dipole sums

A.2.1 Magnetic field inside a uniformly-magnetized volume

In this section, a macroscopic continuum magnetostatics description is used to calculate the magnetic field within a sample volume Ω with surface $\partial\Omega$ and uniform magnetization \mathbf{M} . Note that there is nothing novel about this section. For instance, similar treatments can be found in [194, 277] and are likely to have guided the following arguments, most of which are based on general electrodynamics knowledge, as it can be found, e. g., in [184]. Using the magnetic “charge” density $\rho_M = -\nabla \cdot \mathbf{M}$ [184],

$$\mathbf{B} = \mu_0 (\mathbf{H} + \mathbf{M}) \quad \begin{array}{l} \nabla \cdot \mathbf{B} = 0 \\ \Rightarrow \end{array} \quad \nabla \cdot \mathbf{H} = -\nabla \cdot \mathbf{M} \quad \begin{array}{l} \mathbf{H} = -\nabla \Phi_M \\ \Rightarrow \end{array} \quad \nabla^2 \Phi_M = -\rho_M \quad .$$

The introduction of the magnetostatic potential Φ_M is justified since $\nabla \times \mathbf{H} = 0$ [184]. Assume that there exists an isomorphism $\mathbf{u} : \mathbb{R}^3 \rightarrow \mathbb{R}^3$, which maps the surface of the unit sphere $\partial B(1)$ onto the surface of the sample $\partial\Omega$. I parametrize $\partial B(1)$ using spherical coordinates (θ, ϕ) and require that the surface normal of the induced parametrization of $\partial\Omega$ points outwards. As derived in section A.5.6, the magnetostatic potential at $\mathbf{x}_0 \in \Omega$ is then given by (cf. [277, eq. 8])

$$\Phi_M(\mathbf{x}_0) = \int_0^\pi d\theta \int_0^{2\pi} d\phi \frac{\mathbf{M} \cdot \left(\frac{\partial \mathbf{u}}{\partial \theta} \times \frac{\partial \mathbf{u}}{\partial \phi} \right)}{4\pi |\mathbf{x}_0 - \mathbf{u}(\theta, \phi)|} \quad . \quad (\text{A.1})$$

The field $\mathbf{H} = -\nabla \Phi_M$ is called *demagnetizing field* or *demagnetization*, and is given by $\mathbf{H}(\mathbf{x}_0) = -\mathcal{M}^\Omega(\mathbf{x}_0) \mathbf{M}$ [277], with the *demagnetization tensor* $\mathcal{M}^\Omega(\mathbf{x}_0)$ (e. g., [277]), which is defined as (cf. [277, eq. 9])

$$-\mathcal{M}_{ij}^\Omega(\mathbf{x}_0) = \int_0^\pi d\theta \int_0^{2\pi} d\phi \frac{\left(\frac{\partial \mathbf{u}}{\partial \theta} \times \frac{\partial \mathbf{u}}{\partial \phi} \right)_j}{4\pi |\mathbf{x}_0 - \mathbf{u}(\theta, \phi)|^3} (\mathbf{x}_0 - \mathbf{u}(\theta, \phi))_i \quad . \quad (\text{A.2})$$

The demagnetization tensor has several useful properties [277],⁷

$$\begin{aligned} \text{Tr } \mathcal{M}^\Omega(\mathbf{x}_0) &= 1 \\ \mathcal{M}^\Omega(\mathbf{x}_0) &= \mathcal{M}^\Omega(\mathbf{x}_0)^T \\ \int_\Omega d\mathbf{x}_0 \mathcal{M}_{kk}^\Omega(\mathbf{x}_0) &\geq 0 \quad . \end{aligned}$$

Consider $\mathbf{x}_0 = 0$ (without loss of generality), and a scaling of the sample by a factor s , i. e., $\mathbf{u} \mapsto s\mathbf{u}$. Clearly, $\mathbf{H}(\mathbf{x}_0) \mapsto \mathbf{H}(\mathbf{x}_0)$, which demonstrates that, as is well known, the demagnetizing field within a finite-size sample depends on the shape of the sample, but not on its size (cf. [438]).

Examples The following two sample geometries are relevant for the present work.

- *Sphere*: For a sphere S of radius R , centered around $\mathbf{x}_0 = 0$, $\mathbf{u}(\theta, \phi) = R(\sin \theta \cos \phi, \sin \theta \sin \phi, \cos \theta)$ and equation (A.2) yields $\mathcal{M}_{ij}^S(\mathbf{x}_0) = \frac{1}{3} \delta_{ij}$ (see, e. g., [184, p. 198]).

⁷For domains satisfying the assumptions made in its derivation, the first identity also easily follows from equation (6.4), as well as the observation that each partial lattice sum is traceless and $\text{Tr } \mathcal{M}_{ij}^S(0) = 1$.

- *Box*: Consider a cuboid sample Γ with principal axes coincident with the coordinate system and edge lengths $2a, 2b, 2c$. The demagnetization tensor at an arbitrary reference point $\mathbf{r} = (x, y, z)$ within the sample is [194]

$$\mathcal{M}_{zz}^{\Gamma}(\mathbf{r}) = \frac{1}{4\pi} \sum_{s_x, s_y, s_z \in \{-1, 1\}} \arctan f(s_x x, s_y y, s_z z) \quad (\text{A.3})$$

$$\text{with } f(x, y, z) = \frac{(a-x)(b-y)}{(c-z)\sqrt{(a-x)^2 + (b-y)^2 + (c-z)^2}}$$

$$\mathcal{M}_{xz}^{\Gamma}(\mathbf{r}) = -\frac{1}{4\pi} \sum_{s_x, s_y, s_z \in \{-1, 1\}} s_x s_y s_z \log |g(s_x x, s_y y, s_z z)| \quad (\text{A.4})$$

$$\text{with } g(x, y, z) = (b-y) + \sqrt{(a-x)^2 + (b-y)^2 + (c-z)^2} \quad ,$$

where the expressions for the remaining elements can be obtained by cyclic permutation. Note that in the special case of a cube and $\mathbf{r} = 0$, the result reduces to the demagnetization tensor of a sphere.

When performing dipole-lattice sums directly, a straightforward decomposition scheme is $\mathbb{Z}^3 = \cup_{L \in \mathbb{N}} (\partial B_{\infty}(L) \cap \mathbb{Z}^3)$, where $\partial B_{\infty}(L)$ denotes the surface of the l_{∞} -ball with radius L , centered around the origin. Using the lattice constants of BiCu_2PO_6 [11], this corresponds to a demagnetization tensor $\mathcal{M}^{\Gamma}(0) = \text{diag}(0.142453, 0.552269, 0.305278)$ (in the a, b, c basis).

A.2.2 Efficient evaluation

The following derivation closely follows the original publications [292, 438]. Its main purpose is to illustrate the method and re-state the relevant results in a form consistent with the notation used in this work. See section 6.3.2 for additional context.

Infinite plane Consider a tetragonal lattice with lattice constants a, b, c . Generalization to other geometries should be straightforward (see [438]). The coupling matrix describing the dipole field created by an individual bc -plane with two-dimensional magnetic propagation vector $\mathbf{q}_{\parallel} = (q_b, q_c)$ is

$$M_{\mathbf{q}_{\parallel}} = \sum_{(y,z) \in \mathbb{Z}^2} \frac{\mu_0}{4\pi \rho^3} (3\hat{\rho}\hat{\rho}^T - 1) \exp(2\pi i \mathbf{q}_{\parallel} \cdot (y, z)) \quad .$$

Here, $\boldsymbol{\rho} = \mathbf{r} - \mathbf{r}_0$ with $\mathbf{r} = (ax, by, cz)$ and $\mathbf{r}_0 = (ax_0, by_0, cz_0)$. Assume $x \neq x_0$, as is the case when calculating the magnetic field generated by the Cu moments at the P sites in BiCu_2PO_6 . As re-derived in section A.5.7, closely following [292, 438], the sum can be recast as

$$M_{\mathbf{q}_{\parallel}} = \frac{\mu_0 \pi}{abc} \sum_{\boldsymbol{\mu} \in \mathbb{Z}^2} e^{2\pi i (\mathbf{q}_{\parallel} - \boldsymbol{\mu}) \cdot (y_0, z_0)} \mathbf{v}_{\mathbf{q}_{\parallel}, \boldsymbol{\mu}} \mathbf{v}_{\mathbf{q}_{\parallel}, \boldsymbol{\mu}}^T \frac{\exp\left(-2\pi a (bc)^{-\frac{1}{2}} \|\mathbf{q}_{\parallel} - \boldsymbol{\mu}\|_{bc} |x - x_0|\right)}{\|\mathbf{q}_{\parallel} - \boldsymbol{\mu}\|_{bc}} \quad , \quad (\text{A.5})$$

and

$$\mathbf{v}_{\mathbf{q}_{\parallel}, \boldsymbol{\mu}} = \left(\frac{a^{\frac{1}{2}}}{(bc)^{\frac{1}{4}}} \|\mathbf{q}_{\parallel} - \boldsymbol{\mu}\|_{bc} \operatorname{sgn}(x - x_0), \quad i \frac{a^{\frac{1}{2}} c^{\frac{1}{4}}}{b^{\frac{3}{4}}} (q_b - \mu_1), \quad i \frac{a^{\frac{1}{2}} b^{\frac{1}{4}}}{c^{\frac{3}{4}}} (q_c - \mu_2) \right)$$

$$\|\mathbf{q}_{\parallel} - \boldsymbol{\mu}\|_{bc} = \sqrt{\frac{c}{b} (q_b - \mu_1)^2 + \frac{b}{c} (q_c - \mu_2)^2} \quad .$$

The resulting sum over $\boldsymbol{\mu}$ converges exponentially, as do all its derivatives with respect to $x \neq x_0$ (cf. [292, 438]). Note that the expression for $M_{\mathbf{q}_{\parallel}}$ has a removable singularity at $\mathbf{q}_{\parallel} \in \mathbb{Z}^2$ (see section A.5.7 for details). Therefore, whenever $\mathbf{q}_{\parallel} = \boldsymbol{\mu}$, the corresponding summand vanishes.

Three-dimensional lattice The preceding results can be used to calculate the coupling matrix $M_{\mathbf{q}}$ describing the field created by a three-dimensional dipole lattice with magnetic propagation vector $\mathbf{q} = (q_a, q_b, q_c)$ [cf. (6.2) in section 6.3.1],

$$M_{\mathbf{q}} = \sum_x e^{2\pi i q_a x} M_{\mathbf{q}_{\parallel}}(x) \quad .$$

Exponential convergence of the series involved justifies the interchange of the summation over $\boldsymbol{\mu}$ and x after substituting equation (A.5). Introducing $\lceil x \rceil = \min \{k \in \mathbb{Z} \mid k \geq x\}$ and $\lfloor x \rfloor = \max \{k \in \mathbb{Z} \mid k < x\}$ and splitting $\sum_x = \sum_{x < x_0} + \sum_{x > x_0}$ (note that $x \neq x_0$), gives (cf. [438, eq. 24])

$$M_{\mathbf{q}} = \frac{\mu_0 \pi}{abc} \sum_{\boldsymbol{\mu} \in \mathbb{Z}^2} \frac{e^{2\pi i (\mathbf{q}_{\parallel} - \boldsymbol{\mu}) \cdot (y_0, z_0)}}{\|\mathbf{q}_{\parallel} - \boldsymbol{\mu}\|_{bc}}$$

$$\left[\left(\mathbf{v}_{\mathbf{q}_{\parallel}, \boldsymbol{\mu}} \mathbf{v}_{\mathbf{q}_{\parallel}, \boldsymbol{\mu}}^T \right)_{x < x_0} \exp\left(-2\pi a (bc)^{-\frac{1}{2}} \|\mathbf{q}_{\parallel} - \boldsymbol{\mu}\|_{bc} (x_0 - \lfloor x_0 \rfloor)\right) \frac{\exp(2\pi i q_a \lfloor x_0 \rfloor)}{1 - \exp(-2\pi \tilde{q}^*)} \right. \quad (\text{A.6})$$

$$\left. + \left(\mathbf{v}_{\mathbf{q}_{\parallel}, \boldsymbol{\mu}} \mathbf{v}_{\mathbf{q}_{\parallel}, \boldsymbol{\mu}}^T \right)_{x > x_0} \exp\left(-2\pi a (bc)^{-\frac{1}{2}} \|\mathbf{q}_{\parallel} - \boldsymbol{\mu}\|_{bc} (\lceil x_0 \rceil - x_0)\right) \frac{\exp(2\pi i q_a \lceil x_0 \rceil)}{1 - \exp(-2\pi \tilde{q})} \right] \quad ,$$

with $\tilde{q} = a(bc)^{-\frac{1}{2}} \|\mathbf{q}_{\parallel} - \boldsymbol{\mu}\|_{bc} - i q_a$ and

$$\left(\mathbf{v}_{\mathbf{q}_{\parallel}, \boldsymbol{\mu}} \right)_{x \gtrless x_0} = \left(\pm \frac{a^{\frac{1}{2}}}{(bc)^{\frac{1}{4}}} \|\mathbf{q}_{\parallel} - \boldsymbol{\mu}\|_{bc}, \quad i \frac{a^{\frac{1}{2}} c^{\frac{1}{4}}}{b^{\frac{3}{4}}} (q_b - \mu_1), \quad i \frac{a^{\frac{1}{2}} b^{\frac{1}{4}}}{c^{\frac{3}{4}}} (q_c - \mu_2) \right) \quad .$$

Note that this result corresponds to an infinite-slab shaped sample with demagnetization tensor $\operatorname{diag}(1, 0, 0)$ ⁸ [438]. No convergence error estimates are needed in practice, since the remaining sum over $\boldsymbol{\mu}$ quickly converges (cf. [292, 438]) to within machine precision in most cases.

A.3 Angular dependence of NMR shift

A.3.1 Experimental details

The convention for the rotation angles used in previous work [74] is illustrated in Fig. A.2(a). After choosing an orthonormal reference frame which is fixed to the NMR probe ($x \parallel a$, $y \parallel b$, $z \parallel c$), the

⁸This can be seen by considering the slab as a degenerate box and using the corresponding limits of (A.3).

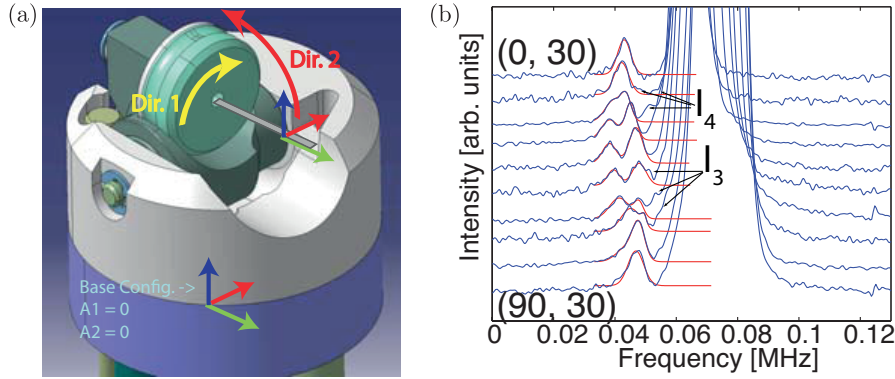


Figure A.2: (a): Parametrization of the sample orientation (figure reproduced from [75, Fig. 2c]). The two angles α_1 and α_2 parametrize the rotations indicated by the bent arrows. The order of the rotations is determined by the depicted mechanism (described in [364]). The configuration shown corresponds to $(\alpha_1, \alpha_2) = (0, 0)$. In this configuration, the blue, red, and green arrows coincide with the b , a , and c directions of the crystal, respectively [75]. (b): ^{31}P -NMR spectra as function of α_1 for $\alpha_2 = 30^\circ$ (reproduced figure from [74, Fig. 5.7b] and annotated I_4). The curves are offset vertically and the labels correspond to (α_1, α_2) , where α_1 was sampled uniformly [74, Fig. 5.8].

combined effect of the two-axis rotator mechanism upon arbitrary positions \mathbf{r} is $\mathbf{r} \mapsto R\mathbf{r}$, R being a rotation with coordinate representation

$$R = R[-\alpha_2, \mathbf{e}_x] R[-\alpha_1, \mathbf{e}_z] \quad ,$$

where $R[\beta, \mathbf{v}]$ is the mathematically positive rotation around \mathbf{v} by an angle β . Rotating the sample according to $\mathbf{r} \mapsto R\mathbf{r}$ is equivalent to transforming the applied magnetic field as $\mathbf{B}_{\text{ext}} \mapsto R^T \mathbf{B}_{\text{ext}}$ with (cf. [74, pp. 105 ff.])

$$\begin{aligned} R^T &= R[-\alpha_1, \mathbf{e}_z]^T R[-\alpha_2, \mathbf{e}_x]^T = R[\alpha_1, \mathbf{e}_z] R[\alpha_2, \mathbf{e}_x] \\ &= \begin{pmatrix} \cos \alpha_1 & -\sin \alpha_1 & 0 \\ \sin \alpha_1 & \cos \alpha_1 & 0 \\ 0 & 0 & 1 \end{pmatrix} \begin{pmatrix} 1 & 0 & 0 \\ 0 & \cos \alpha_2 & -\sin \alpha_2 \\ 0 & \sin \alpha_2 & \cos \alpha_2 \end{pmatrix} . \end{aligned}$$

In addition to the NMR resonance frequencies obtained in [74, Fig. 5.10], reported w. r. t. the resonance frequency of a powder sample [74, p. 99] of BiZn_2PO_6 [74, Fig. 5.5] (see also [75, pp. 4-5], [74, pp. 99-100], as well as section A.4.3), possible additional satellite peaks were observed for particular orientations in the weakly-doped sample [74, p. 108] [cf. I_3 and I_4 in Fig. A.2(b)].

A.3.2 Hyperfine-coupling parameter fits

See Figs. A.3-A.4.

A.4 High-field NMR experiments

The following subsections provide supplemental information for the high-field NMR experiments described in chapter 8. Please see section 8.1 for context and collaborators involved.

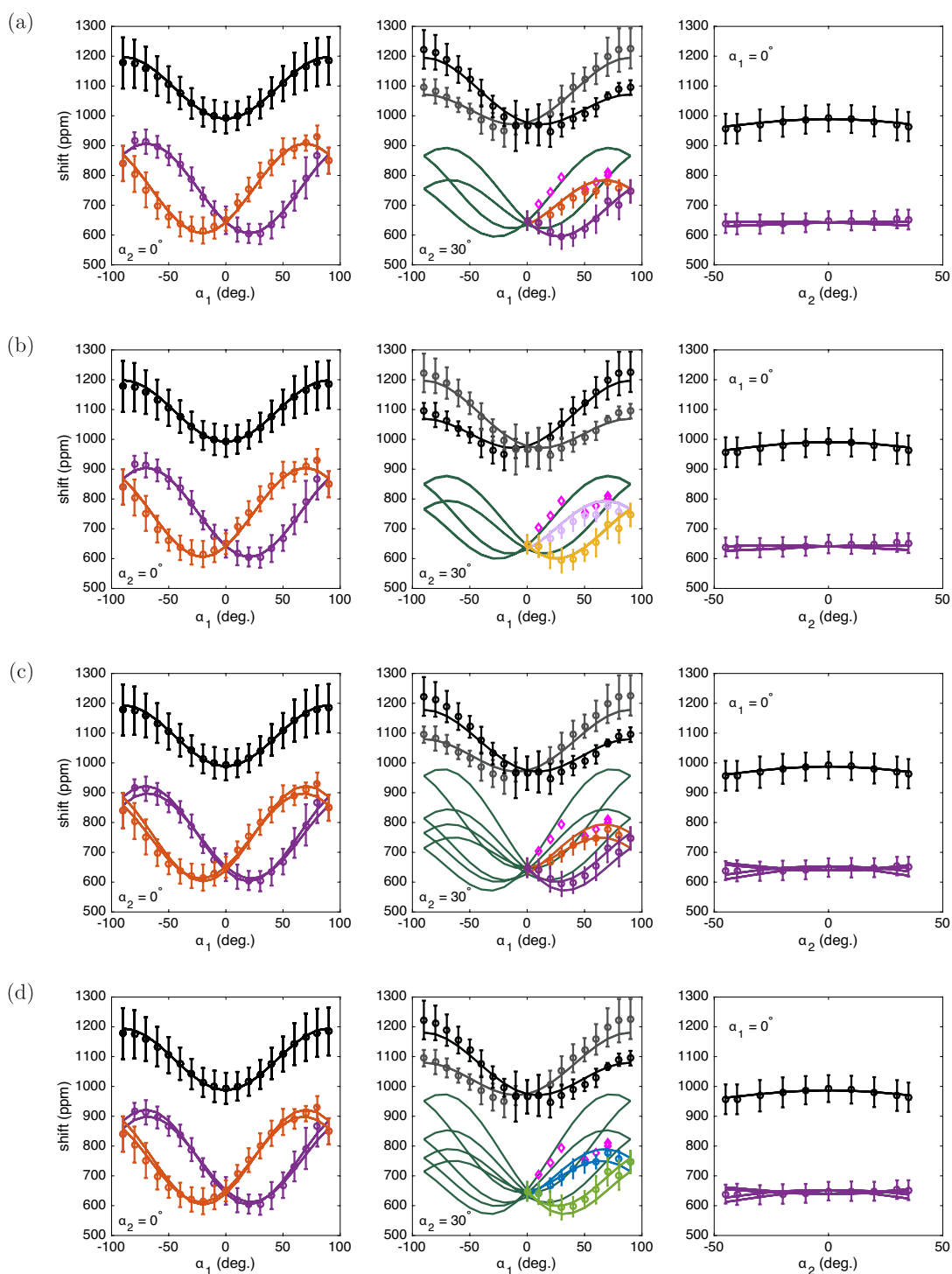


Figure A.3: Plausible hyperfine-coupling parameter fits. See section 6.6.3 for details. The individual sub-figures correspond to different peak assignments, as listed in Tab. 6.1. Experimental data from [74] (see section 6.6.1).

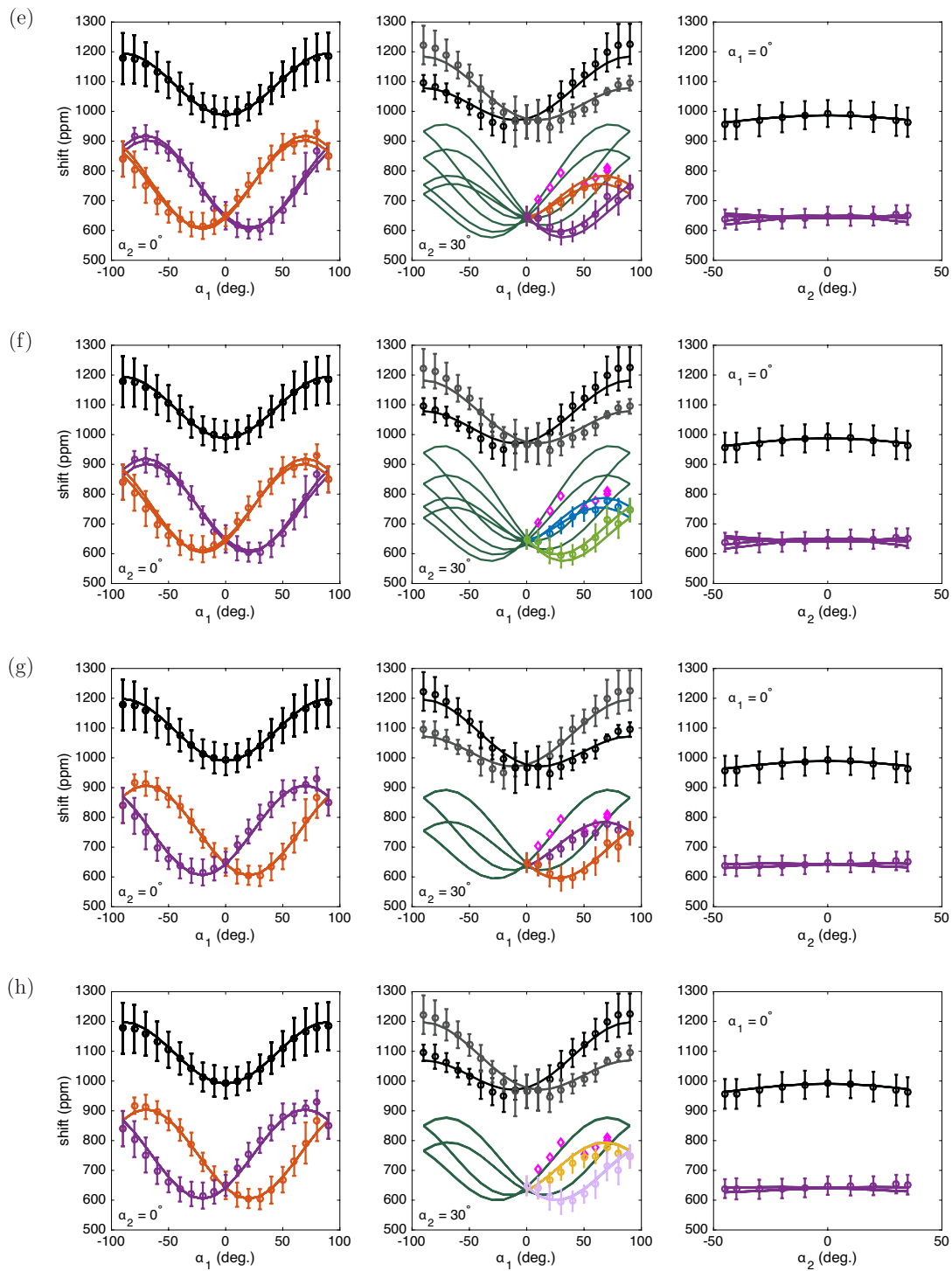


Figure A.3: (continued) Plausible hyperfine-coupling parameter fits. See section 6.6.3 for details. The individual sub-figures correspond to different peak assignments, as listed in Tab. 6.1. Experimental data from [74] (see section 6.6.1).

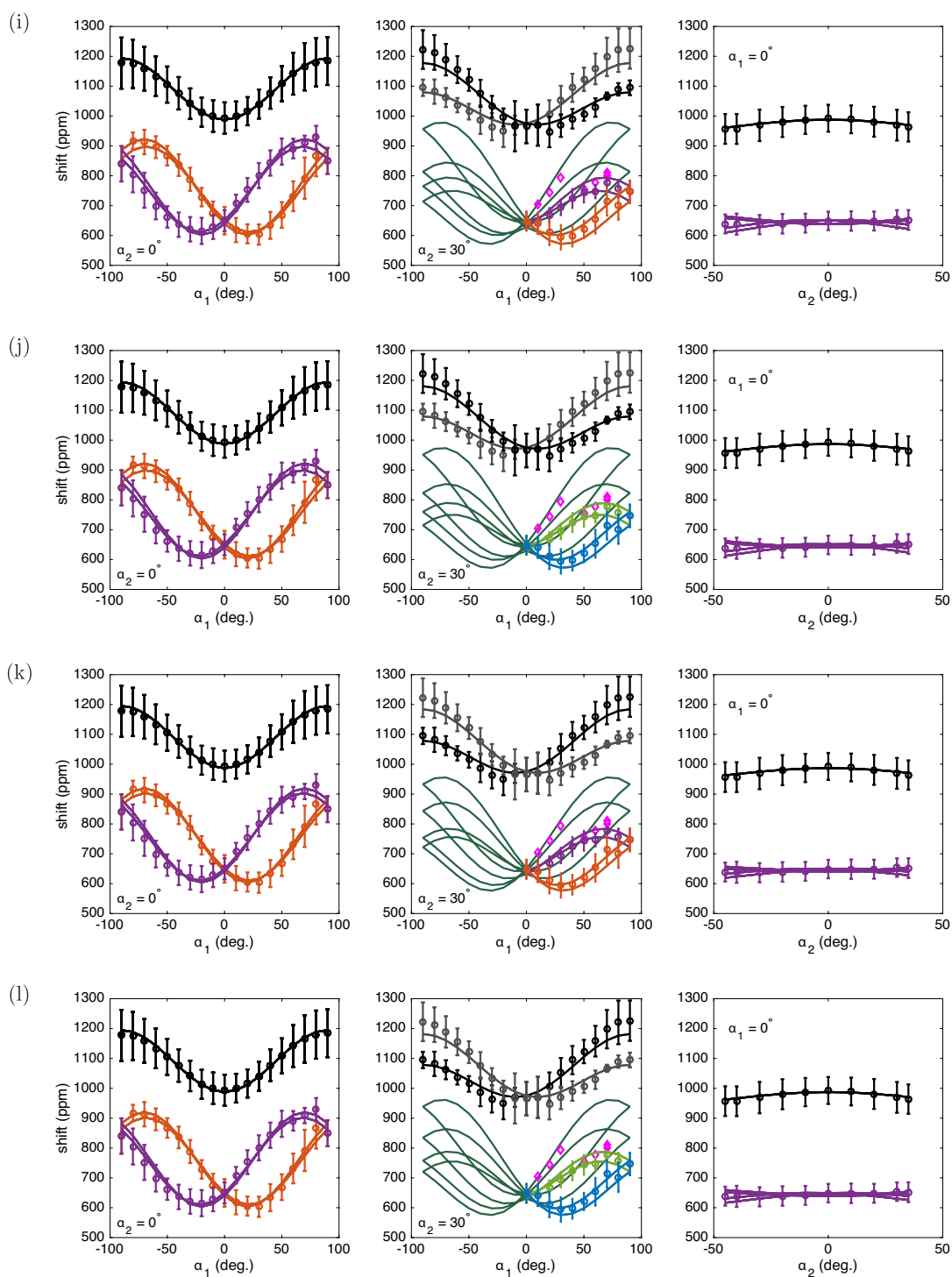


Figure A.3: (continued) Plausible hyperfine-coupling parameter fits. See section 6.6.3 for details. The individual sub-figures correspond to different peak assignments, as listed in Tab. 6.1. Experimental data from [74] (see section 6.6.1).

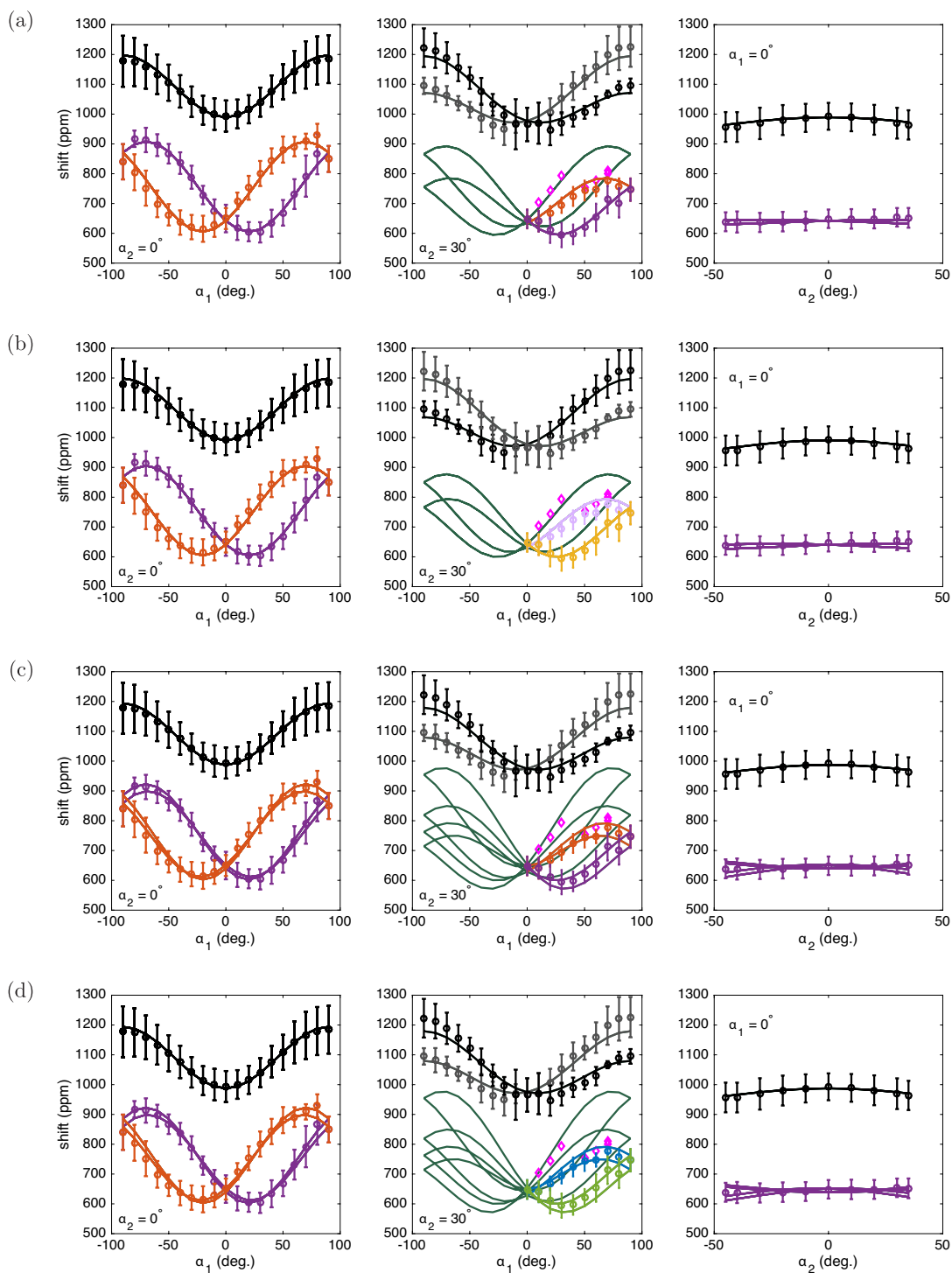


Figure A.4: Plausible hyperfine-coupling parameter fits for “uniform” model (model C_0 of section 5.2.1). See section 6.6.4 for details. The individual sub-figures correspond to different peak assignments, as listed in Tab. 6.1. Experimental data from [74] (see section 6.6.1).

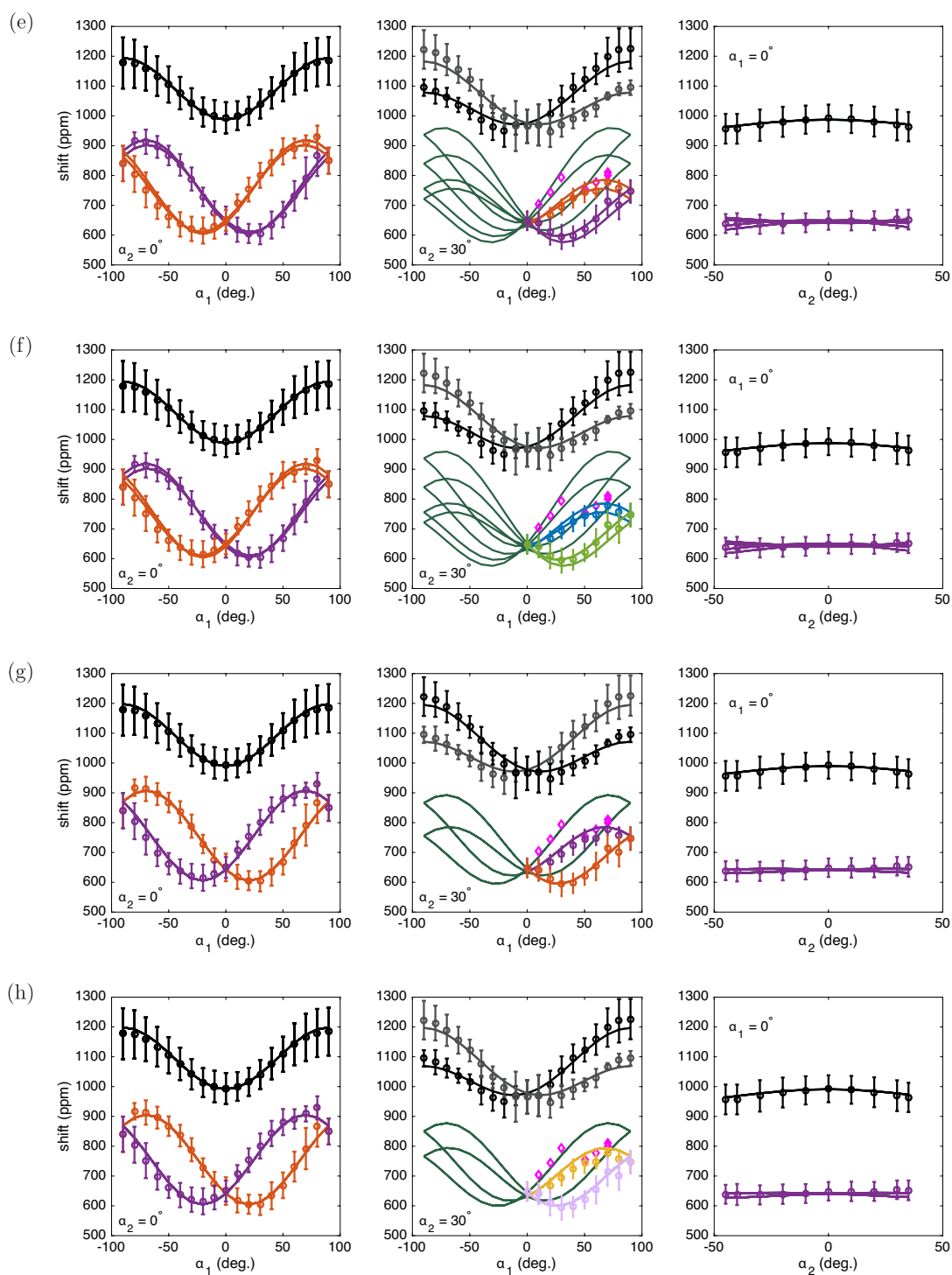


Figure A.4: (continued) Plausible hyperfine-coupling parameter fits for “uniform” model (model C_0 of section 5.2.1). See section 6.6.4 for details. The individual sub-figures correspond to different peak assignments, as listed in Tab. 6.1. Experimental data from [74] (see section 6.6.1).

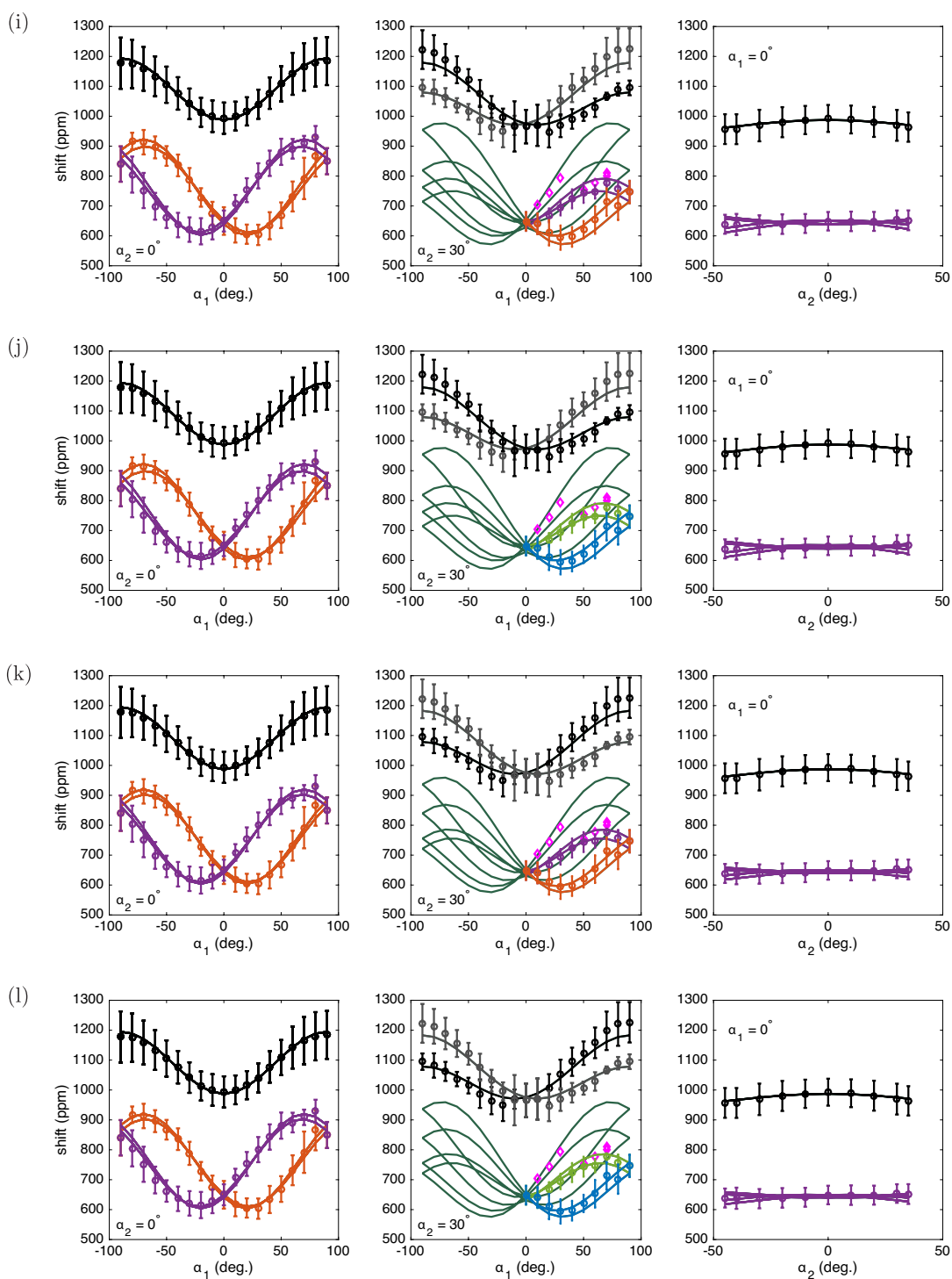


Figure A.4: (continued) Plausible hyperfine-coupling parameter fits for “uniform” model (model C_0 of section 5.2.1). See section 6.6.4 for details. The individual sub-figures correspond to different peak assignments, as listed in Tab. 6.1. Experimental data from [74] (see section 6.6.1).

A.4.1 Thermometry

For most measurements targeting temperature-dependences, the spin-lattice relaxation rate of ^{27}Al in aluminum foil [378] was used to work around the high magnetoresistance of the Cernox temperature sensor installed on the NMR probe.⁹ For the data shown in Fig. 8.4(a), this method was followed in most cases, in particular in the vicinity of the phase boundaries. The uncertainty of the measured relaxation times T_1 is estimated as 10% (see footnote 7 in section 8.3). In some cases more than one T_1 -measurement was performed and the resulting temperatures were averaged, enlarging the error bars to encompass all individual estimates.

As a byproduct, the relaxation-rate measurements provide the systematic error $\delta T(T)$ of the temperature measured using the Cernox sensor down to 1.6 K. The steady-state temperature of the ^3He -cryostat is expected to be field-independent, which was used to determine $\delta T(T)$ at $(T, \mu_0 H) = (0.7(1) \text{ K}, 42.9 \text{ T})$. By assuming that $\delta T(T = 0.7 \text{ K})$ at $\mu_0 H = 37.7 \text{ T}$ is comparable, linear interpolation was used to determine the sample temperatures below 1.6 K.

For the data points measured at 14 K and 24 K, the magnetoresistance of the Cernox sensor was deemed negligible and a constant uncertainty of 1 K was assumed instead.

A.4.2 Sample alignment

The approximate crystal orientation of the sample documented by the sample grower, S. Wang, was used as a starting point for the sample alignment. An NMR probe with two-axis rotator [cf. Fig. 8.3(b)] was used. In accordance with the angular dependence reported earlier [74, Fig. 5.10] (cf. Fig. 6.3), the configuration $\mathbf{H} \parallel b$ corresponds to a saddle point. After optimizing the rotation angles φ and ϑ in $\mu_0 H = 15.2 \text{ T}$ using a superconducting magnet with room temperature bore [Fig. A.5(a-b)],¹⁰ the NMR probe was transferred to the high-field magnet. Note that the tank circuit used for tuning of the NMR probe (see section 8.2) needed to be reconfigured for the high-field measurements, which limited the magnetic-field range in the experiment to $\mu_0 H \gtrsim 31 \text{ T}$.

At this point, it is important to note a peculiarity of the miniature two-axis rotator developed by A. P. Reyes (NHMFL). The device involves a sophisticated cogwheel-based transmission, which results in significant backlash of the mechanism, especially for the ϑ degree of freedom [2]. For this reason, the ϑ -mechanism was initially detached from its drive shaft and locked into place using GE 7031 varnish. Indeed, a highly-symmetric lineshape was observed in the high-field phase using this initial sample orientation [black trace in Fig. A.5(d)]. Since the spectra acquired afterwards in the intermediate-field phase looked different from previous results [78] (cf. Fig. 8.1), a scan of φ was performed in the intermediate-field phase [Fig. A.5(c)]. The small sensitivity of the spectrum w. r. t. φ suggested that the differences were not caused by misalignment. However, the symmetric line shape observed initially in the high-field phase could not be reproduced during subsequent variation of φ [Fig. A.5(d)], indicating that the two-axis rotator failed to return to its initial configuration. This is attributed to a loosening of the ϑ mechanism.

The aforementioned observations indicate that the decoupling of the two rotation angles is not perfect. This issue, as well as the backlash of the mechanism, can be circumvented to some extent by strictly

⁹A ruthenium oxide thermometer installed on the same probe failed during the experiment.

¹⁰The larger relative variation of the NMR shift with ϑ [comparing with Fig. A.7(b)] is attributed to the coupling of the angular degrees of freedom discussed below. The proximity of the applied field to H_{c1} [207] might play a role as well.

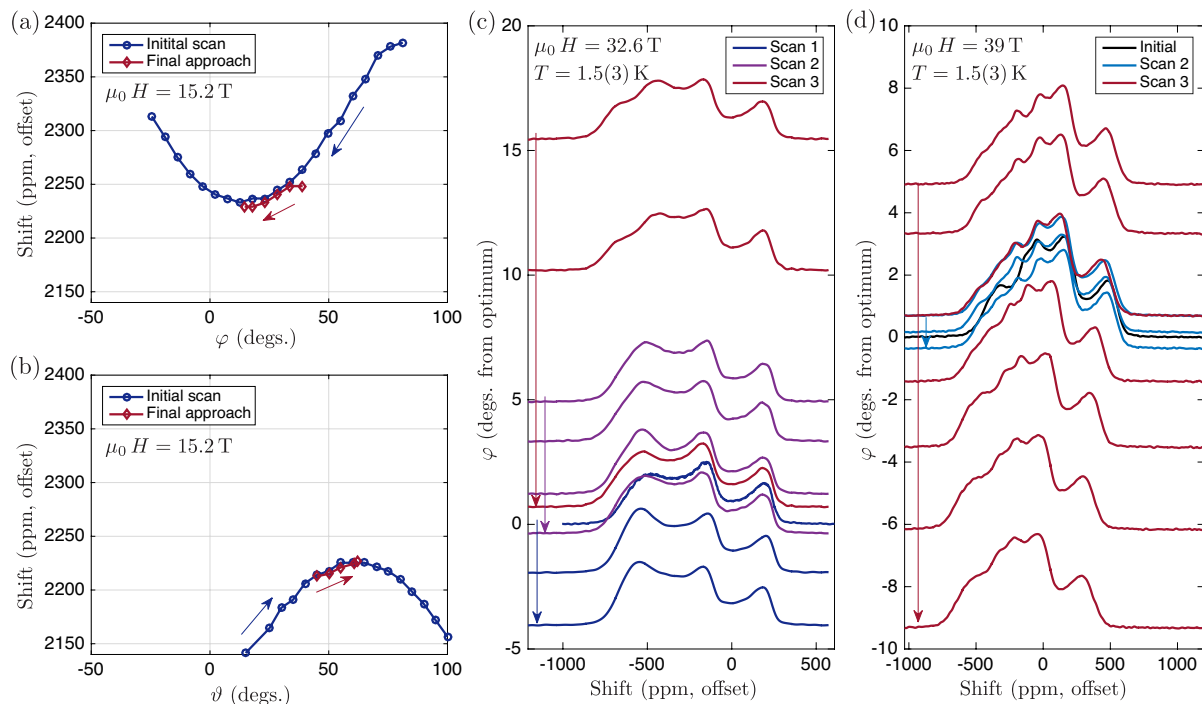


Figure A.5: (a),(b): ^{31}P -NMR shifts measured during sample alignment in superconducting magnet (ambient temperature). (c),(d): ^{31}P -NMR spectra measured during angular scans in the intermediate-field (c) and the high-field (d) field-induced phases. Arrows indicate the directions along which the angles were varied. Note that the NMR shifts are uncalibrated.

following a certain protocol when adjusting the angles, in order to ensure that the teeth of the transmission gears always mesh in the same way [2]. However, in practice, the precision of the rotator is limited. Furthermore, the anisotropy of the high-field magnetization [207] [cf. Fig. 4.6(b)] implies that the configuration $\mathbf{H} \parallel b$ is unstable and slight misalignment results in a torque trying to coalign the magnetic field with the a -direction. For these reasons, the backlash of the rotator mechanism posed a significant challenge for the experiment.

In order to re-align the sample, the ϑ -mechanism was reconnected. To save magnet time, and because the data shown in Fig. A.5 corroborated the correctness of the initial alignment, φ was returned to its initial configuration and ϑ was optimized in the intermediate-field phase [Fig. A.6(a)]. Checking of φ was deferred until the end of the magnet time. Fortunately, the angular dependence finally recorded in the high-field phase [Fig. A.6(b)] corroborated the correct alignment of φ .

The NMR shifts in Fig. A.6 are reported w. r. t. the ^{31}P -NMR frequency [308], as obtained from the resonance frequency of the ^{27}Al reference (see section 8.2). Note that the friction of the rotator device results in significant heating of the NMR probe. To conserve energy, the magnet was temporarily ramped down during the thermal relaxation of the system before acquiring the red data in Fig. A.6(b). The data were offset by -50 ppm to compensate for the resulting difference in magnetic field. The same offset was applied to the line shapes measured afterwards at $T = 14$ K and $T = 24$ K [Figs. 8.4(a) and 8.13].

The data reported in Fig. A.6 confirm the correct alignment. Strictly speaking, this method of sample alignment is an iterative procedure. However, the fact that the angular scans are highly symmetric about

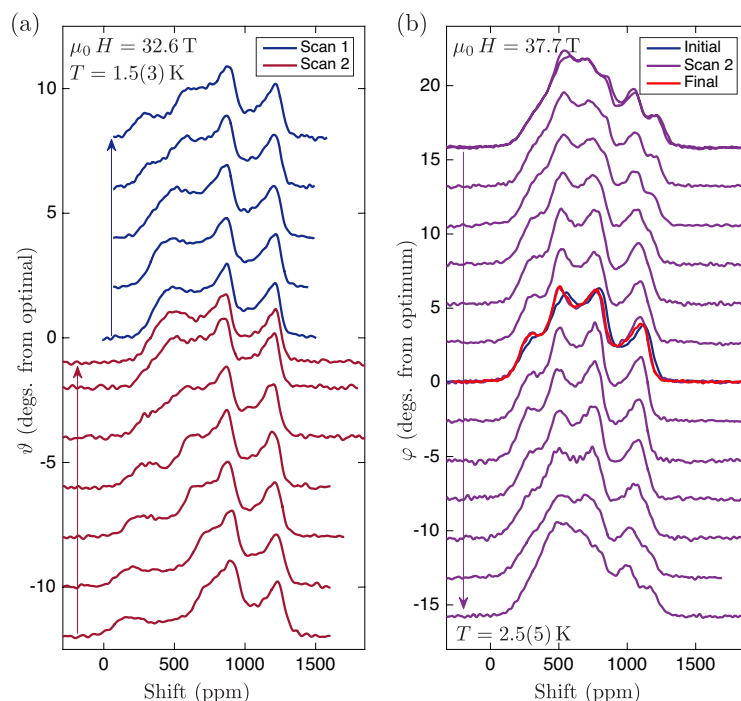


Figure A.6: ^{31}P -NMR spectra measured during angular scans in the intermediate-field (a) and the high-field (b) field-induced phases. Arrows indicate the directions along which the angles were varied.

the initial configurations of both angles indicates that the sample configuration during the experiment was very close to the fixed-point $\mathbf{H} \parallel b$. This is further corroborated by the additional measurements described in section A.4.3.

A.4.3 Post-experiment checks

Although the results presented in section A.4.2 corroborate the correct alignment of the sample during the high-field experiments, the different shape of the NMR lines measured in the intermediate-field phase provided the motivation to perform additional measurements to double-check the orientation of the crystal. The data shown in Fig. A.7(b) confirm the orientation of the b axis depicted in Fig. 8.3. The apparent offset between the old (see caption of Fig. 8.3 for data source) and new data is discussed at the end of this subsection.

In accordance with similar comparisons in previous work ([74, Fig. 5.9b inset] and [22, Fig. 1]), the NMR shift mirrors the temperature dependence of the magnetization measured previously [see Fig. A.7(a) for results and data source] (see section 6.4 for notation). Temperature and field dependence of the magnetization measured after the high-field experiments also compare favorably with the previous data (see Fig. A.8)¹¹ and the magnetic response is found to be linear up to $\mu_0 H = 7$ T at least (Fig. A.8 inset), in agreement with previous work [74, p. 99].

The evolution of the NMR line from a Gaussian to a Lorentzian shape illustrated in the inset of Fig. A.7(a)

¹¹The maximum difference is 2.5%. The noise in the new measurement is attributed to the different measurement technique (RSO vs. DC SQUID).

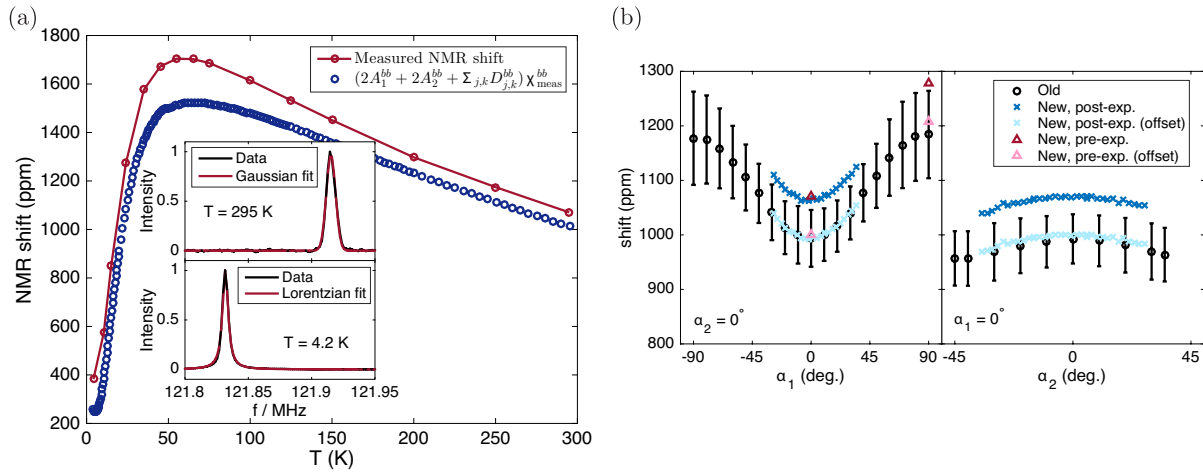


Figure A.7: (a): Comparison of ^{31}P -NMR shift measured on high-field NMR sample (at $\mu_0 H = 7.0667$ T) with magnetization data [see Fig. 5.1(b) for data source and details]. The inset shows representative NMR lines and fits. See [74, Fig. 5.9] for equivalent analyses of previous NMR data. (b): Comparison of angular rotation patterns obtained using the high-field NMR sample (colored data, $\mu_0 H \approx 7$ T) with previous data from [74] (black) (cf. Fig. 6.3). The light-colored data have been offset by -70 ppm. Data on the high-field sample acquired before (triangles) and after (crosses) the high-field experiments are shown. The error bars correspond to the line width [74, Fig. 5.8] (taken as full-width at half-maximum for the new data) and are of comparable magnitude for previous and new data (only drawn once for clarity). As in the previous work [74], shifts in (a) and (b) were determined by fitting a Voigtian line shape (cf. [74, p. 102]) and are expressed relative to the resonance frequency of ^{31}P in BiZn_2PO_6 [75, pp. 4-5] (cf. section 6.6.1).

has already been documented in previous work [74, Fig. 5.9]. The apparent narrowing of the line at low temperature is compatible with a reduction of the dipolar broadening due to the reduced magnetization—although partially compensated by the Lorentzian broadening which is attributed to dynamical effects [74, p. 110]. Moreover, the slight asymmetry of the NMR line measured at high temperature [Fig. A.7(a) inset] is consistent with a shoulder at high frequency, as expected from the dipole lineshape depicted in Fig. 8.13. The linewidth observed at high temperature (full-width at half-maximum of 70 ppm) is roughly consistent with that expected for the dipole lineshape (approx. 80 ppm, cf. section 6.3.4). In agreement with the evolution of the sample shape from oblate to prolate upon rotation from $\mathbf{H} \parallel \mathbf{b}$ to $\mathbf{H} \parallel \mathbf{a}$ [cf. Fig. 8.3(a)], the asymmetry of the lines corresponding to the red data in Fig. A.7(b) changes sign. Meanwhile, the distinct features of the dipole line shape appear to be smeared-out, hinting at the presence of dynamical phenomena (cf. [74, p. 110]). Thus, besides the offset of the shifts, everything is consistent with previous results [74] and theoretical expectations.

As noted above, offsetting the data by 70 ppm yields very good agreement between old [74] and new data [light-colored points in Fig. A.7(b)]. This is most probably related to the NMR shift of ^{31}P in BiZn_2PO_6 : The numbers reported in [75, pp. 4-5] (cf. Fig. 6.3), which are used in this work, correspond to a relative shift of -57 ppm w. r. t. the nominal ^{31}P Larmor frequency [308] and thus differ from the 10 ppm reported in [22]. Also, [74, Fig. 5.5] and [75, Fig. 1] suggest a very small shift. Assuming an error in [75] hence results in an offset of 10 ppm $- (-57 \text{ ppm}) \approx 70$ ppm, which could explain the differences observed in Fig. A.7(b).^{12,13} However, partial inspection of the available old data indicates

¹²Since the data used in section 6.6 were assumed to be reported as relative shifts [74, Fig. 5.10] w. r. t. non-magnetic BiZn_2PO_6 (see sections 6.6.1 and A.3.1), this offset is irrelevant for the hyperfine-coupling parameters estimated in this work.

¹³While such an offset affects the results shown in Fig. 8.7, the changes are too small to change the qualitative appearance

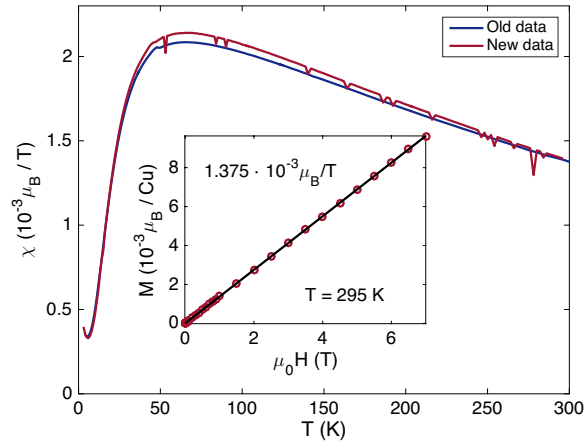


Figure A.8: Comparison of the magnetic susceptibility measured on the high-field sample with previous data [see Fig. 5.1(b) for data source and details]. The inset shows the field-dependence of the magnetization at $T = 295$ K along with a linear fit (without intercept). The (red) data were measured by T. Shiroka using a Quantum Design MPMS XL magnetometer with RSO option. The temperature-dependence was measured in $\mu_0 H = 0.5$ T after zero-field cooling.

that not all previous measurements are consistent with this hypothesis, which might be related to the following issue.

The old data were supposedly measured using approximately cubic samples [74, Fig. 5.4d and p. 99] and, consistently, a spherical summation scheme has been used for the dipolar couplings in [74, p. 106], as well as in this work (see sections 6.3.5 and 6.6). However, the oblate shape of the high-field sample [Fig. 8.3(a)] (aspect ratio 4.3 : 3.1 : 2) should result in a demagnetization factor $l \approx 0.55$ for magnetic fields applied along the short edge (cf. section A.2.1), which corresponds to a demagnetization-induced shift of about -60 ppm (cf. section 6.3.2).¹⁴ Note that the correct calibration of the new data is corroborated by the good agreement of the data acquired before and after the high-field experiments [triangles and crosses in Fig. A.7(b)]. Even more worrying than the apparent absence of this additional shift, which could be related to field-calibration issues,¹⁵ is the excellent agreement after offsetting the data, which is unexpected, since the anisotropic demagnetization tensor of a non-cubic sample should give rise to a different curvature of the angular dependences shown in Fig. A.7(b).¹⁶ This suggests that some of the

of the figure. Correspondingly, the estimate for m_{\parallel} in Fig. 8.10 would change only insignificantly to $0.33(1) \hbar$.

¹⁴By considering a large-but-finite cubic sample and extending it along the in-plane directions in order to approximate an oblate sample geometry, it becomes clear that the far-field created by the added dipole moments points opposite to the magnetization, in agreement with the expressions in section 6.3.2. Therefore, the dipole field inside a flat sample is reduced w. r. t. a cubic sample, which results in *smaller* NMR shifts.

¹⁵In this work, the Al foil used for the field calibration was measured separately from the sample (section 8.2), whereas in the previous measurements it was placed inside the same coil as the sample [74, Fig. 5.4d]. Simple estimates, made by approximating the sample as a point-like dipole and/or using the analytical result from Ref. [121], suggest that the stray field created by the sample can give rise to NMR shifts of the order of 100 ppm in the worst case (aluminum foil located on top or bottom face of the sample). Another possibility is that the field of the magnet was drifting during the measurements. This typically happens soon after a magnetic-field change.

¹⁶The demagnetization factor changes to $l \approx 0.29$ for fields applied along the intermediate-length edge of the high-field sample. The total excursion of the angular dependence of the high-field sample in the ab -plane should therefore be about 70 ppm larger than for a cubic sample, whereas the observed difference is of order 15 ppm. Note that the demagnetization corrections are not sufficient to invert the oscillation in the ab plane, hence not jeopardizing the assignment of the crystal axes. Correct assignment of the axes is further corroborated by the magnetization (Fig. A.8) and the agreement of the phase

samples used in previous work [74, 75] may not have been cubic. In principle, different sample shapes could be accounted for in the analysis of section 6.6. However, this is not attempted at this moment, since the exact experimental conditions during the previous measurements are not known to me.

To conclude, the new data confirm the integrity and the alignment of the sample used in the high-field experiments. While a sample-dependence cannot be fully excluded, differences with previous data [74, 75] suggest a problem with the magnetic-field calibration in previous measurements. However, as seen in section 6.7, the uncertainties estimated for the hyperfine couplings are generally large, so that these issues merely underline the importance of the *qualitative* arguments discussed in section 8.6.

A.4.4 Additional data

As mentioned in section 8.3, the sample was slightly misaligned during the first magnet time, as result of a technical problem with the φ -mechanism of the two-axis rotator. Whereas the relaxation-rate data in Fig. 8.4(b) corroborate the approximate alignment of the sample, the line shapes shown in Fig. A.9 are clearly different from those depicted in Fig. 8.4(b).

The spin-lattice relaxation rates reported in Fig. 8.4(b) were determined close the central (i. e., highest-amplitude) peaks of the spectra. Only one measurement of the spin-spin relaxation rate T_{2g}^{-1} was performed, at $\mu_0 H = 39$ T and again close to the central peak of the spectrum. The decay of the spin-echo amplitude with interpulse delay was fitted to a relaxation of the form $\exp(-(T/T_{2g})^2)$, yielding the value indicated in Fig. A.9.

A.4.5 Field calibration

During the experiments yielding the relaxation rates shown in Fig. 8.4(b) and the line shapes depicted in Fig. A.9, the ^{27}Al field-calibration reference was placed inside the same coil as the sample. To assess the effect of the stray field created by the sample, the shifts obtained from ^{27}Al -NMR were compared with ^{63}Cu -NMR performed on the NMR coil itself [426]. Moreover, since the coil is orthogonal to the external magnetic field and surrounds the sample, the stray field can also be estimated from the linewidth of the ^{63}Cu resonance. For data obtained at $\mu_0 H \approx 39$ T, such considerations indicate an uncertainty of ± 30 ppm—yet, an actually even larger systematic error caused by the stray field of the sample cannot be fully excluded. In addition, problems with the cryostat required frequent and unscheduled ramping of the magnetic field (see remark about bubbles in section 8.2). Therefore, a primary field calibration was not possible for all measurements. Instead, the data were interpolated to obtain an effective relation between the field indicated by the high-field magnet system and the calibrated field at the sample.¹⁷ The final relative uncertainty of the reported shifts is estimated as ± 100 ppm.

To avoid the aforementioned problems, the reference sample was placed inside a separate coil during subsequent experiments, as shown in Fig. 8.3(b). Like this, the ^{27}Al line is unperturbed by the stray field of the sample and the field can be determined to less than ± 25 ppm. The drawback is a radial displacement of the reference by approximately 5(2) mm w. r. t. the center of field, where the sample was located. This results in a systematic error between 25 ppm and 125 ppm, the off-center magnetic field being larger [125]. The total error interval for the shifts thus ranges from 0 ppm to 150 ppm.

boundaries observed in the high-field experiments with the phase diagram of BiCu_2PO_6 [207] (see Fig. 8.5 in section 8.4).

¹⁷A simple experimental test indicates a field-setting accuracy of around 60 ppm, in accordance with [2].

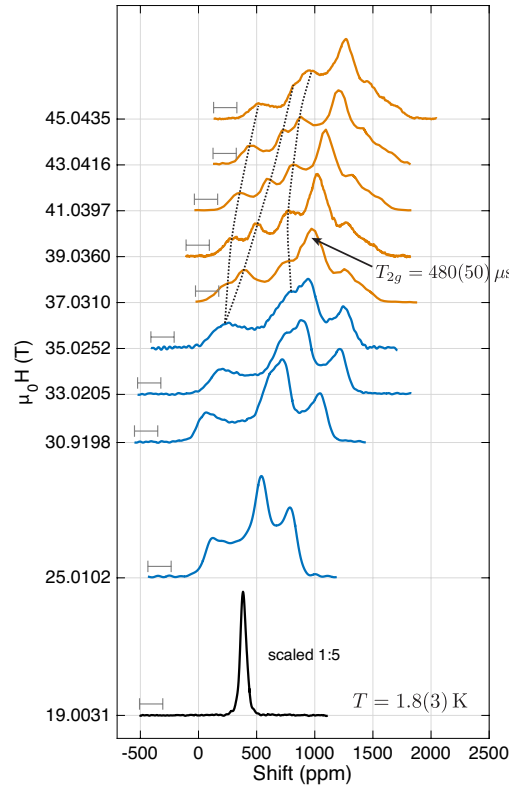


Figure A.9: ^{31}P -NMR spectra of BiCu_2PO_6 , as function of magnetic field $\mu_0 H$ ($H \parallel b$). The ordinates of the baselines of the NMR spectra encode the corresponding magnetic fields. The intensities are normalized to their area. Colors distinguish different phases [analogous to Fig. 8.4(b)]. Shifts are reported w.r.t. a standard ^{31}P reference [308]. Dashed lines are guides to the eye. The estimated total field-calibration uncertainty (see section A.4.5) is indicated by gray bars. See text for details.

As outlined above, none of the two approaches is fully satisfactory. A possible solution consists in mounting the calibration reference in a vertically-offset location (cf. [74, Fig. 2.7d]) and then displacing the entire cryostat to center the desired NMR coil within the high-field magnet. Such a technique was used at LNCMI Grenoble [3] (see also [74, p. 133]), where the experiments reported in Ref. [74] were performed, and the uncertainty of the reported shifts is empirically assumed as ± 40 ppm. For data acquired at ETH Zürich, the calibration uncertainties are typically of the order of 10 ppm or better (cf., e. g., Fig. A.7).

A.4.6 Effect of signal compression on NMR spectrum

Strictly speaking, signal compression affects the time-domain signal $s(t)$ in a non-uniform fashion. The (rephased) frequency-domain spectra $\hat{s}(\omega) = \int s(t)e^{i\omega t} dt$ obtained from full spin-echoes are typically real and non-negative. This is exact for Gaussian and Lorentzian lines, and approximately correct for the $\sin(\omega)/\omega$ -like spectra expected while scanning a broad line (cf. [91]). Therefore, the area in frequency domain can be approximated as $\int \hat{s}(\omega) d\omega \propto s(0)$, where $t = 0$ is assumed to coincide with the center of the rephased (see, e. g., [229, pp. 102 ff.], section 1.5.6, or [74, appendix D.2]) spin echo, which normally has maximal signal amplitude. Thus, the area under the NMR spectrum is generally expected

to be reduced due to signal compression.

Considering $\hat{s}(\omega)$ itself, the overall amplitude reduction competes with the broadening of the time-domain signal, which sharpens-up the spectrum. Which of the two effects wins, generally depends on the details of the electronics. A simple result can be obtained if one assumes the compression to occur after the signal has been down-converted to zero intermediate-frequency (IF). The compressed signal is modeled as $s_c(t) = s(t) - \alpha|s(t)|s(t)$ ($\alpha \geq 0$). For zero IF, the aforementioned standard NMR spectra correspond to Gaussian, exponential, and box-shaped time-domain signals $s(t)$, respectively. At zero IF, $s(t) \geq 0$ for a properly-phased signal and thus the intensity obtained from the compressed signal is $\hat{s}_c(\omega) = \hat{s}(\omega) - \alpha \int s(t)^2 e^{i\omega t} dt$. Now, if $s(\omega)$ is real-valued and non-negative, Bochner's theorem [429] shows that $s(t)$ is a symmetric positive-definite (s. p. d.) function, which implies that $s(t)^2$ is s. p. d. as well. This finally shows that the Fourier-transform of $s(t)^2$ must be real-valued and non-negative, proving that $\hat{s}_c(\omega) \leq \hat{s}(\omega)$. Even though the box-shaped signal is not s. p. d., the argument clearly survives, at least in the ideal case for which $\exists c : \forall t : s(t)^2 = c s(t)$. Finally, the zero-IF argument made above also applies if compression occurs in a high-frequency component in a way which affects only the low-frequency envelope of the signal and not the carrier-wave itself.¹⁸

A.5 Derivations

A.5.1 Formal derivation of superexchange interaction

In order to obtain an effective spin model (see section 1.1.1), the high-energy sectors Ω_e with $e > 0$ need to be removed from the description, yielding an effective Hamiltonian $\mathcal{H}_{\text{eff}} = P_0 \mathcal{H}_0 P_0 + \mathcal{V}_{\text{eff}}$, where P_e shall denote the projector onto Ω_e . A formal framework for the construction of such effective Hamiltonians is described in [374] and is applied in the following. The notation is adopted from this reference. While the final result and its physical origin in virtual hopping processes contributing at second order in perturbation theory are clearly well-known [31], it appears instructive to re-derive the result using the formalism presented in [374].

Ref. [374] characterizes an effective Hamiltonian $\mathcal{H}_S = \mathcal{H}_0 + \mathcal{W}_S$ through a set of properties which it should satisfy [374, section II]. Following [374], repeated substitution of [374, eq. 31] into [374, eq. 32], keeping terms up to second order in \mathcal{V} , yields¹⁹

$$\mathcal{W}_S = \langle \mathcal{V} \rangle + \langle \mathcal{V} h_0 (\langle \mathcal{V} \rangle - \mathcal{V}) \rangle = \langle \mathcal{V} \rangle - \langle \mathcal{V} h_0 (\mathcal{V}) \rangle .$$

Using the definitions from [374] then results in the familiar expression

$$\mathcal{V}_{\text{eff}} = P_0 \mathcal{W}_S P_0|_{\Omega_0} = \left(P_0 \mathcal{V} P_0 - \sum_{e \neq 0} \frac{P_0 \mathcal{V} P_e \mathcal{V} P_0}{e} \right) \Big|_{\Omega_0} \quad (\text{A.7})$$

describing the effective interactions within the ground-state sector Ω_0 of \mathcal{H}_0 .

For the considered Hubbard model at half filling, \mathcal{V} connects the ground-state sector Ω_0 with the sector Ω_U of excited states having exactly one doubly-occupied site, such that $\mathcal{V}_{\text{eff}} = -U^{-1} P_0 \mathcal{V}^2|_{\Omega_0}$. Also,

¹⁸This is not a very strict assumption, since non-linear response on timescales corresponding to the carrier frequency would mainly generate higher harmonics of the signal, which are typically filtered out by the receiving electronics of the NMR spectrometer.

¹⁹In order to have $\mathcal{H}_S = \mathcal{H}_0$ (and hence $\mathcal{V}_{\text{eff}} = 0$) in the limit $\mathcal{V} \rightarrow 0$ [374, eq. 9], one needs $\langle S \rangle = 1$ [374, eq. 27].

$P_0 = \prod_k p_k$ with $p_k = (2 - n_k)$ is a straightforward choice in this case. With the notation $\langle i, j \rangle'$ for summation over directed bonds, and using $(p_k + a) c_{j\sigma}^{(\dagger)} = c_{j\sigma}^{(\dagger)} (p_k + (-)\delta_{jk} + a)$, I obtain

$$\begin{aligned} P_0 \mathcal{V}^2 |\{\sigma_i\}_i\rangle &= \sum_{\substack{\langle i, j \rangle', \sigma \\ \langle i', j' \rangle', \sigma'}} \left(\prod_k p_k \right) t_{ij} t_{i'j'} c_{i\sigma}^\dagger c_{j\sigma} c_{i'\sigma'}^\dagger c_{j'\sigma'} |\{\sigma_i\}_i\rangle \\ &= \sum_{\substack{\langle i, j \rangle', \sigma \\ \langle i', j' \rangle', \sigma'}} t_{ij} t_{i'j'} c_{i\sigma}^\dagger c_{j\sigma} c_{i'\sigma'}^\dagger c_{j'\sigma'} \left(\prod_{k \in \{i, j, i', j'\}} (1 - \delta_{ki} + \delta_{kj} - \delta_{ki'} + \delta_{kj'}) \right) |\{\sigma_i\}_i\rangle . \end{aligned}$$

Non-zero contributions only arise for $(i, j) = (j', i')$, and a bit of algebra gives

$$P_0 \mathcal{V}^2 |\{\sigma_i\}_i\rangle = 2 \sum_{\langle i, j \rangle', \sigma, \sigma'} |t_{ij}|^2 c_{i\sigma}^\dagger c_{j\sigma} c_{j'\sigma'}^\dagger c_{i'\sigma'} |\{\sigma_i\}_i\rangle ,$$

which actually coincides with [31, eq. 18]. Hence it is not surprising that, by comparing the matrix elements in the $\{|\{\sigma_i\}_i\rangle\}$ basis, one finds $c_{i\sigma}^\dagger c_{j\sigma} c_{j'\sigma'}^\dagger c_{i'\sigma'} \Big|_{\Omega_0} = (-2\mathbf{S}_i \cdot \mathbf{S}_j + \frac{1}{2}) \Big|_{\Omega_0}$, and the final result follows, in full agreement with [31].

A.5.2 Transformation properties of DM vectors

I encountered somewhat confusing statements regarding the transformation properties of the DM vector \mathbf{D} in the literature (see, e. g. , [108, 179], [74, p. 49], and [259, p. 127]). To clarify this issue, I will briefly re-derive the transformation rules for \mathbf{D} . Consider a crystal symmetry R which transforms vectors $\mathbf{x} \mapsto R\mathbf{x}$. In the presence of spin-orbit coupling, the spin operators need to be transformed accordingly, $\mathbf{S}_i \mapsto \det(R) (R^{-1})^T \mathbf{S}_i$.²⁰ Crystal symmetries preserve distances and angles, so that R is orthogonal.²¹ Consider now the graph G formed by *oriented* (cf. [377, sec. IV.A]) magnetic bonds $b = (b_1, b_2)$ connecting the vertices b_i . The symmetry R induces an automorphism of G by mapping $b \mapsto R(b) = (R(b_1), R(b_2))$. Hence,

$$\mathcal{H}_{\text{DM}} = \sum_{b \in G} \mathbf{D}_b \cdot (\mathbf{S}_{b(1)} \times \mathbf{S}_{b(2)}) \mapsto \sum_{b \in G} \det(R) (R^T \mathbf{D}_b) \cdot (\mathbf{S}_{R(b(1))} \times \mathbf{S}_{R(b(2))}) .$$

While there exists a unique $\tilde{b} \in G$ for which $\{\tilde{b}_1, \tilde{b}_2\} = \{R(b_1), R(b_2)\}$, the orientations of $R(b)$ and \tilde{b} may differ. Let $\sigma_R(b) = 1$ whenever $R(b)$ and \tilde{b} have the same orientation and -1 otherwise. Then,

$$\mathcal{H}_{\text{DM}} \mapsto \sum_{\tilde{b} \in G} \sigma_R(b) \det(R) (R^T \mathbf{D}_b) \cdot (\mathbf{S}_{\tilde{b}(1)} \times \mathbf{S}_{\tilde{b}(2)}) .$$

Requiring invariance of \mathcal{H}_{DM} under R thus corresponds to

$$\mathbf{D}_b \mapsto \sigma_R(b) \det(R) R^T \mathbf{D}_b \stackrel{!}{=} \mathbf{D}_{\tilde{b}} . \quad (\text{A.8})$$

²⁰As is well known, $(R\mathbf{u}) \times (R\mathbf{v}) = \det(R) (R^{-1})^T (\mathbf{u} \times \mathbf{v})$.

²¹In accordance with Wigner's theorem (see section 1.4.4 and references therein).

The effective transformation rule (A.8) is, in fact, essentially equivalent to those given in the literature (see, e. g. , [259, p. 127]) and allows to relate the elements of DM vectors on equivalent bonds to one-another, as well as to derive symmetry constraints on \mathbf{D}_b whenever $\tilde{b} = b$ for some R , up to orientation (see, e. g. , [275]). Note also that the preceding discussion merely reflects a personal preference for closed mathematical formulations, whereas the corresponding concepts are clearly well known and generally considered, more or less explicitly, by other authors (see, e. g. , [377]).

A.5.3 Method to account for site-dependent g -tensors

In the following, I derive a suitable, extended form of the fluctuation-dissipation theorem (e. g. , [353, p. 300]) in order to address the problem outlined in section 1.4.5. Furthermore, I illustrate how this can be combined with the calculation techniques discussed in section 1.4. Although clearly a straightforward application of elementary (quantum) statistical mechanics, the corresponding results are needed for the analyses described in chapter 5. Note also that site-dependent g -tensors and their effects are a standard topic and have been discussed in various previous works (see, e. g. , [15] and [74]).

Example: Dimer To illustrate the problem, it is sufficient to consider a simple dimer formed by two spins \mathbf{S}_1 and \mathbf{S}_2 with anti-ferromagnetic (AFM) exchange coupling $\mathcal{H}_0 = J \mathbf{S}_1 \cdot \mathbf{S}_2$, subjected to small uniform and staggered external magnetic fields $H_u \mathbf{e}_z$ and $H_s \mathbf{e}_z$, respectively. The Hamiltonian of this toy model reads

$$\mathcal{H} = J \mathbf{S}_1 \cdot \mathbf{S}_2 - H_u (S_1^z + S_2^z) - H_s (S_1^z - S_2^z) \quad .$$

Focus on the limit $T \searrow 0$. The ground state $|0\rangle$ is non-degenerate, and converges towards the usual singlet for $H_s \rightarrow 0$. The expectation values of staggered and uniform magnetization are straightforward to obtain,

$$\langle 0 | S_1^z + S_2^z | 0 \rangle = 0 \quad \langle 0 | S_1^z - S_2^z | 0 \rangle = \frac{2H_s}{\sqrt{J^2 + 4H_s^2}} = \frac{2H_s}{J} + \mathcal{O}(H_s^3) \quad .$$

Thus, both the uniform and the staggered susceptibilities converge to constant values, 0 and $\frac{2}{J}$, respectively, as $T \searrow 0$. If one had assumed a site-dependent g -factor, a uniform external field would give rise to non-zero uniform *and* staggered field components, each of which would give rise to a uniform *and* a staggered magnetization response (cf. [15, sec. VIII.B] and [74, p. 51]). From the above expressions, it is clear that in the limit $T \searrow 0$ the *uniform* susceptibility tends to zero for $g_1 = g_2 = g$ and towards $\frac{2\mu_B^2 g^2}{J}$ if $g_1 = -g_2 = g$.

For reasons which will become clear later, I assume that the magnetic field applied to each sub-lattice can be controlled independently, $\mathcal{H} = -\sum_{i,p} \mathbf{B}_i \cdot \boldsymbol{\mu}_{i,p} + \mathcal{H}_0$. I begin to calculate the (average) susceptibility

of sub-lattice i w. r. t. the field B_j ,

$$\begin{aligned} \chi_{ij}^{\rho\sigma} &= \frac{1}{N} \frac{\partial}{\partial B_j^\sigma} \left\langle \sum_p \mu_{i,p}^\rho \right\rangle \Big|_{B_j^\sigma=0} = \frac{1}{\beta N} \frac{\partial}{\partial B_j^\sigma} \frac{\partial}{\partial B_i^\rho} \log Z \Big|_{B_i^\rho=B_j^\sigma=0}, \quad Z = \text{Tr} \exp(-\beta\mathcal{H}) \\ &= \frac{1}{\beta N} \left(\frac{\partial_{B_i^\rho} \partial_{B_j^\sigma} Z}{Z} - \frac{\partial_{B_i^\rho} Z}{Z} \frac{\partial_{B_j^\sigma} Z}{Z} \right) \Big|_{B_i^\rho=B_j^\sigma=0}, \end{aligned} \quad (\text{A.9})$$

with $\beta^{-1} = k_B T$ and for a system consisting of N unit cells. Clearly, $\chi_{ij}^{\rho\sigma} = \chi_{ji}^{\sigma\rho}$. The main difficulty arises during the evaluation of the 2nd derivative, as discussed in the following.

For a matrix-valued function $t \mapsto A(t)$,

$$\partial_t \exp A = \partial_t \sum_{n=0}^{\infty} \frac{1}{n!} A^n = \sum_{n=1}^{\infty} \frac{1}{n!} \sum_{k=0}^{n-1} \left(\prod_{l=0}^{k-1} A \right) (\partial_t A) \left(\prod_{l=k+1}^{n-1} A \right),$$

which is different from $\partial_t A \exp A$ in the general case $[\partial_t A, A] \neq 0$. Still, the cyclic property of the trace, $\text{Tr} AB = \text{Tr} BA$, implies

$$\partial_t \text{Tr} \exp A = \text{Tr} \partial_t \exp A = \text{Tr} (\partial_t A) \exp A.$$

However, such a complete reordering is not possible anymore for expressions of the form

$$\begin{aligned} \partial_t \text{Tr} B \exp A(t)|_{t=t_0} &= \text{Tr} \partial_t B \exp A \\ &= \text{Tr} \left[B \partial_t \sum_{k=0}^{\infty} \frac{1}{k!} A^k \right] = \sum_{k=1}^{\infty} \frac{1}{k!} \sum_{l=0}^{k-1} \text{Tr} \left[B \left(\prod_{j=0}^{l-1} A \right) (\partial_t A|_{t=t_0}) \left(\prod_{j=l+1}^{k-1} A \right) \right] \\ &= \sum_n \sum_{k=1}^{\infty} \frac{1}{k!} \sum_{l=0}^{k-1} \langle n | B A^l (\partial_t A) A^{k-l-1} | n \rangle \\ &= \sum_{m,n} \sum_{k=1}^{\infty} \frac{1}{k!} \sum_{l=0}^{k-1} \langle n | B A^l | m \rangle \langle m | (\partial_t A) A^{k-l-1} | n \rangle \\ &= \sum_{m,n} \langle n | B | m \rangle \langle m | (\partial_t A) | n \rangle \sum_{k=1}^{\infty} \frac{1}{k!} \sum_{l=0}^{k-1} E_m^l E_n^{k-l-1} \\ &\stackrel{[448]}{=} \sum_{m,n} \langle n | B | m \rangle \langle m | (\partial_t A|_{t=t_0}) | n \rangle \frac{e^{E_m} - e^{E_n}}{E_m - E_n}, \end{aligned} \quad (\text{A.10})$$

for an orthonormal eigenbasis $\{|n\rangle\}_n$ of $A(t_0)$ with eigenvalues E_n . In order not to overload the notation, the evaluated-at symbol $\cdot|_{t=t_0}$ was not repeated constantly throughout the derivation. The naive result $\partial_t \text{Tr} B \exp A(t)|_{t=t_0} = \text{Tr} B (\partial_t A) \exp A|_{t=t_0} = \text{Tr} (\partial_t A) B \exp A|_{t=t_0}$ is recovered whenever $[B, A]|_{t=t_0} = 0$ or $[\partial_t A, A]|_{t=t_0} = 0$.

Returning to the original problem,

$$\begin{aligned} \frac{\partial}{\partial B_i^\rho} \frac{\partial}{\partial B_j^\sigma} Z \Big|_{B_i^\rho = B_j^\sigma = 0} &= -\beta \mu_B g_j^{\sigma\tau} \sum_p \frac{\partial}{\partial B_i^\rho} \text{Tr} S_{j,p}^\tau \exp(-\beta \mathcal{H}) \Big|_{B_i^\rho = B_j^\sigma = 0} \\ &= -\beta \mu_B^2 g_j^{\sigma\tau} g_i^{\rho\eta} \sum_{p,q} \sum_{m,n} \langle n | S_{j,p}^\tau | m \rangle \langle m | S_{i,q}^\eta | n \rangle \frac{e^{-\beta E_m} - e^{-\beta E_n}}{E_m - E_n} , \end{aligned}$$

for an eigenbasis $\{|n\rangle\}_n$ of the zero-field Hamiltonian $\mathcal{H}_{zf} = \mathcal{H}|_{\mathbf{B}_i=0 \forall i}$ with eigenvalues E_n . I further define the sub-lattice spin $\mathbf{S}_{i,\Sigma} = \sum_p \mathbf{S}_{i,p}$ and obtain

$$\begin{aligned} \chi_{ij}^{\rho\sigma} &= \frac{1}{N} \mu_B^2 g_i^{\rho\eta} \beta \underbrace{\left(\frac{1}{Z} \sum_{m,n} \langle n | S_{i,\Sigma}^\eta | m \rangle \langle m | S_{j,\Sigma}^\tau | n \rangle \frac{e^{-\beta E_m} - e^{-\beta E_n}}{-\beta (E_m - E_n)} - \langle S_{i,\Sigma}^\eta \rangle \langle S_{j,\Sigma}^\tau \rangle \right)}_{C_{ij}^{\eta\tau}} (g_j^T)^{\tau\sigma} \\ &= \frac{\mu_B^2}{N} (g_i C_{ij} g_j^T)^{\rho\sigma} , \end{aligned} \tag{A.11}$$

where the averages are evaluated using the density matrix $\exp(-\beta \mathcal{H}_{zf}) / \text{Tr} \exp(-\beta \mathcal{H}_{zf})$.

Sanity check Consider the special case $g_i = g_j = g \forall i, j = 1 \dots s$, and calculate the total longitudinal susceptibility χ ,²²

$$\begin{aligned} \chi^{\alpha\alpha} &= \frac{1}{s} \sum_{i,j} \chi_{ij}^{\alpha\alpha} \\ &= \frac{\beta \mu_B^2}{sN} \left(\frac{1}{Z} \sum_{m,n} \langle n | g^{\alpha\eta} S_{\text{tot}}^\eta | m \rangle \langle m | g^{\alpha\tau} S_{\text{tot}}^\tau | n \rangle \frac{e^{-\beta E_m} - e^{-\beta E_n}}{-\beta (E_m - E_n)} - \langle g^{\alpha\eta} S_{\text{tot}}^\eta \rangle^2 \right) . \end{aligned}$$

If \mathcal{H}_{zf} conserves $g^{\alpha\eta} S_{\text{tot}}^\eta$, one can chose a compatible eigenbasis for which $\langle m | g^{\alpha\eta} S_{\text{tot}}^\eta | n \rangle \propto \delta_{m,n}$. Then,

$$\begin{aligned} \chi^{\alpha\alpha} &= \frac{\beta \mu_B^2}{sN} \left(\sum_{m,n} \langle n | g^{\alpha\eta} S_{\text{tot}}^\eta | m \rangle \langle m | S_{\text{tot}}^z | n \rangle \frac{e^{-\beta E_n}}{Z} - \langle g^{\alpha\eta} S_{\text{tot}}^\eta \rangle^2 \right) \\ &= \frac{\beta \mu_B^2}{sN} \left(\langle (g^{\alpha\eta} S_{\text{tot}}^\eta)^2 \rangle - \langle g^{\alpha\eta} S_{\text{tot}}^\eta \rangle^2 \right) , \end{aligned}$$

where I used the limit

$$\lim_{E_m \rightarrow E_n} \frac{e^{-\beta E_m} - e^{-\beta E_n}}{-\beta (E_m - E_n)} = \frac{-\beta e^{-\beta E_n}}{-\beta} .$$

If α also happens to be a principal axis of g ,

$$\chi^{\alpha\alpha} = \frac{\beta \mu_B^2 (g^{\alpha\alpha})^2}{sN} \left(\langle (S_{\text{tot}}^\alpha)^2 \rangle - \langle S_{\text{tot}}^\alpha \rangle^2 \right) \tag{A.12}$$

and one recovers the usual fluctuation-dissipation theorem (cf. , e. g. , [353, p. 300]).

²²A similar expression was stated in [13, eq. 2.20].

Example: Dimer (continued) Reconsider now the simple dimer system. Using eq. (A.11), one finds

$$\lim_{T \searrow 0} \chi_{ij}^{zz} = \mu_B^2 g_i g_j \left(\sum_{m \neq 0} 2 \operatorname{Re} \langle 0 | S_i^z | m \rangle \langle m | S_j^z | 0 \rangle \frac{1}{E_m - E_0} + \beta \underbrace{\langle 0 | S_i^z | 0 \rangle^2}_{=0} \right) .$$

I specialize to the problematic case $g_1 = -g_2 = g$ and calculate the uniform susceptibility

$$\begin{aligned} \lim_{T \searrow 0} \chi &= \chi_{11}^{zz} + \chi_{22}^{zz} + \chi_{12}^{zz} + \chi_{21}^{zz} \\ &= 2\mu_B^2 g^2 \sum_{m \neq 0} \frac{|\langle 0 | (S_1^z - S_2^z) | m \rangle|^2}{E_m - E_0} . \end{aligned}$$

The ground state $|0\rangle = \frac{1}{\sqrt{2}} (|\uparrow\downarrow\rangle - |\downarrow\uparrow\rangle)$ (energy $E_0 = -\frac{3J}{4}$) has non-zero matrix elements with $|1\rangle = \frac{1}{\sqrt{2}} (|\uparrow\downarrow\rangle + |\downarrow\uparrow\rangle)$ (energy $E_1 = \frac{J}{4}$) only, yielding the correct zero-temperature limit

$$\lim_{T \searrow 0} \chi = \frac{2\mu_B^2 g^2}{J} .$$

By contrast, the simple fluctuation-dissipation theorem (A.12) would have suggested $\chi \propto \beta$ in the low-temperature limit.

A high-temperature expansion of (A.11) gives

$$\begin{aligned} \chi_{ij}^{\rho\sigma} &= \frac{1}{N} \mu_B^2 g_i^{\rho\eta} g_j^{\sigma\eta} \beta \left(\frac{1}{Z} \sum_{m,n} \langle n | S_{i,\Sigma}^\eta | m \rangle \langle m | S_{j,\Sigma}^\tau | n \rangle - \langle S_{i,\Sigma}^\eta \rangle \langle S_{j,\Sigma}^\tau \rangle \right) (g_j^T)^{\tau\sigma} + \mathcal{O}(\beta^2) \\ &= \frac{1}{N} \mu_B^2 g_i^{\rho\eta} g_j^{\sigma\eta} \beta \left(\langle S_{i,\Sigma}^\eta S_{j,\Sigma}^\tau \rangle - \langle S_{i,\Sigma}^\eta \rangle \langle S_{j,\Sigma}^\tau \rangle \right) (g_j^T)^{\tau\sigma} + \mathcal{O}(\beta^2) . \end{aligned}$$

The first summand corresponds to the result obtained by neglecting the non-commutativity of the operators in (A.10). Indeed, this easier-to-evaluate expression is found to represent a reasonable approximation to the susceptibility at moderate to high temperatures.

Method The expression (A.11) can be evaluated in two different ways.

1. Once the eigenstates have been obtained, the 3×3 matrices $C_{ij}(T)$ can be evaluated in $\mathcal{O}(2^{3sN})$ time using the definition (A.11) and the sparsity of the sub-lattice spin operator matrices. This is comparably expensive to diagonalizing a general symmetric matrix (see, e. g., [168, p. 42-22]).
2. Alternatively, one can set $g_i = 1 \forall i$ and apply a field $\mathbf{B}_j \parallel \mathbf{e}_\sigma$ selectively to one of the sub-lattices. If the field is small enough to yield a linear response, equation (A.11) gives

$$\langle S_{i,\Sigma}^\rho \rangle = \mu_B C_{ij}^{\rho\sigma} B_j^\sigma . \quad (\text{A.13})$$

For each of the $3s$ independent choices of j and σ , at least one full diagonalization needs to be performed to calculate the left hand side and thus $C_{ij}(T)$.

Note that in both cases, the thermal averaging is performed after the diagonalization step. However, the form of (A.11) implies that the work that needs to be repeated at each temperature is $\mathcal{O}(2^{2sN})$ for the first approach, whereas it is only $\mathcal{O}(2^{sN})$ in the second case. Once the $C_{ij}(T)$ are known, the total susceptibility per unit cell for any choice of g -tensors is obtained according to

$$\chi(T) = \frac{\mu_B^2}{N} \sum_{i,j} g_i C_{ij}(T) g_j^T . \quad (\text{A.14})$$

A few simplifications arise if the system exhibits additional symmetries:

- Since the sub-lattice spin operator $S_{i,\Sigma}$ is translation invariant, it is block diagonal in a basis which respects translation invariance (see [215] and section 1.4.4). While this does not improve the scaling, it can be used to speed up method 1.
- For $SU(2)$ -symmetric exchange interactions $C_{ij}^{\alpha\beta} = \delta_{\alpha\beta} C_{ij}^{zz}$, which reduces the amount of calculations required. Although $[S_{j,\Sigma}^z, H] \neq 0$ in general, such that the extended fluctuation-dissipation theorem (A.11) must be used, each simulation run remains computationally efficient, since S_{tot}^z is conserved. The expression for the susceptibility becomes

$$\chi^{\alpha\beta} = \mu_B^2 \sum_{ij} C_{ij}^{zz}(T) [g_i g_j^T]^{\alpha\beta} . \quad (\text{A.15})$$

A.5.4 Empirical model for specific heat

See section 5.2.2 for context. By writing (see, e. g., [353, p. 89])

$$C_M = \frac{1}{k_B T^2} \left(\frac{Z_2}{Z_0} - \left(\frac{Z_1}{Z_0} \right)^2 \right) , \quad (\text{A.16})$$

with

$$Z_m = \sum_n E_n^m e^{-\beta E_n} = \int dE \rho_0(E) E^m e^{-\beta E} ,$$

where $\{E_n\}_{n \in \mathbb{N}}$ describes the spectrum of \mathcal{H} , one sees that, as is generally known, C_M is determined by the density of states $\rho_0(E) = \sum_n \delta(E - E_n)$. The proposed ‘‘toy-model’’ density of states is

$$\rho'(E) = \delta(E - E_0) + \sum_{n \neq 0} \frac{1}{2\tilde{D}} \Theta(\tilde{D} - |E - E_n|) .$$

The magnetic specific heat of this model can be obtained from

$$\begin{aligned} Z'_m &= E_0^m e^{-\beta E_0} + \sum_{n \neq 0} \int dE \frac{1}{2\tilde{D}} \Theta(\tilde{D} - |E - E_n|) E^m e^{-\beta E} \\ &= E_0^m e^{-\beta E_0} + \sum_{n \neq 0} \frac{1}{2\beta^{m+1} \tilde{D}} \int_{\beta(\epsilon - \tilde{D})}^{\beta(\epsilon + \tilde{D})} dt t^m e^{-t} \\ &= E_0^m e^{-\beta E_0} + \sum_{n \neq 0} \frac{1}{2\beta^{m+1} \tilde{D}} \left[-\Gamma(m+1, \beta(E_n + \tilde{D})) + \Gamma(m+1, \beta(E_n - \tilde{D})) \right] , \end{aligned}$$

where $\Gamma(a, z) = \int_z^\infty dt t^{a-1} e^{-t}$ is the incomplete gamma function [430]. The resulting expression for C_M is then evaluated numerically.

A.5.5 Mean-field description of interladder couplings

The in-plane interladder coupling J_i can be treated using standard mean-field theory, and a similar model was applied to BiCu_2PO_6 [218]. The following argument is inspired by [64, 192]. Clearly, the meaningfulness of the results will be limited, since the system remains low-dimensional. The Hamiltonian \mathcal{H} is augmented by the interladder coupling, yielding

$$\mathcal{H} = \mathcal{H}_0 + J_i \sum_{i,r} \mathbf{S}_{i,r} \cdot \mathbf{S}_{\bar{i},r,\text{NN}} \quad ,$$

where $\mathbf{S}_{i,r}$ and $\mathbf{S}_{i,r,\text{NN}}$ correspond to the $\text{Cu}(i)$ site on the reference ladder and a neighboring ladder, respectively. I use the notation \bar{i} to indicate the index complementary to i , i. e. , $\bar{1} = 2$ and $\bar{2} = 1$, and assume antiferromagnetic $J_i > 0$, as suggested by inelastic neutron scattering [316]. I further assume $\mathbf{H} \parallel b$ for simplicity of notation (see section 4.3.1), and call the corresponding g-factors g_1 and g_2 . Let χ_i denote the mean-field susceptibility of the $\text{Cu}(i)$ site, and $\chi_{ij}^{(0)}$ be the bare susceptibility of the $\text{Cu}(i)$ sites for magnetic fields applied to the $\text{Cu}(j)$ sites. Then,

$$\chi_i H = \chi_{ii}^{(0)} H + \chi_{i\bar{i}}^{(0)} H + \chi_{ii}^{(0)} h_i + \chi_{i\bar{i}}^{(0)} h_{\bar{i}} \quad ,$$

with the mean fields

$$h_i = -\frac{J_i}{\mu_B^2 g_1 g_2} \chi_{\bar{i}} H \quad .$$

These equations imply

$$\begin{pmatrix} \chi_1 \\ \chi_2 \end{pmatrix} = \left[1 + \frac{J_i}{\mu_B^2 g_1 g_2} \begin{pmatrix} \chi_{12}^{(0)} & \chi_{11}^{(0)} \\ \chi_{22}^{(0)} & \chi_{21}^{(0)} \end{pmatrix} \right]^{-1} \begin{pmatrix} \chi_1^{(0)} \\ \chi_2^{(0)} \end{pmatrix} \quad ,$$

where $\chi_i^{(0)} = \chi_{i1}^{(0)} + \chi_{i2}^{(0)}$. Finally,

$$\chi_1 = \frac{\mu_B^2 g_1 g_2}{J_i} \frac{\left(\frac{\mu_B^2 g_1 g_2}{J_i} + \chi_{21}^{(0)} \right) \chi_1^{(0)} - \chi_{11}^{(0)} \chi_2^{(0)}}{\left(\frac{\mu_B^2 g_1 g_2}{J_i} + \chi_{12}^{(0)} \right) \left(\frac{\mu_B^2 g_1 g_2}{J_i} + \chi_{21}^{(0)} \right) - \chi_{11}^{(0)} \chi_{22}^{(0)}} \quad ,$$

which reduces to the usual mean-field expression in the case of two equivalent Cu sites (cf. , e. g. , [192, eq. 20a]),

$$\chi_1 = \frac{\chi_1^{(0)}}{1 + \frac{J_i}{\mu_B^2 g^2} \chi_1^{(0)}} \quad .$$

According to this result, if $\chi_1(T)$ is exponentially suppressed at low temperature, this behavior is unchanged by J_i . Thus, within the mean-field treatment, J_i cannot affect the spin gap. At the same time, it is known that the two-dimensional Heisenberg model has no spin gap [253]. This contradiction confirms that the mean-field approach is not particularly sound for this system, as anticipated initially. This is partly because the mean-field approach only considers the longitudinal mean-field, whereas the neglected $S^+ S^-$ -terms provide a mechanism for triplon hopping, which reduces the energy of the triplons (see, e. g. , [401]).

The case of two inequivalent $\text{Cu}(i)$ sites is slightly less obvious. Results obtained using the g-tensors estimated in section 5.2.1 are therefore shown in Fig. A.10. Besides generally reducing the magnetic

response, as expected for an AFM coupling, J_i also affects the zero-temperature limit. However, the thermal energy scale governing the suppression of the magnetic response at low temperature is clearly unaffected by J_i . This example concludes the argument why a standard mean-field treatment of interlayer couplings is not sufficient.

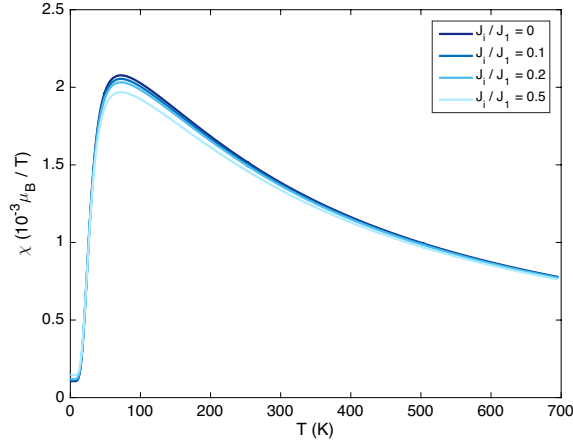


Figure A.10: Magnetic susceptibilities obtained by applying the mean-field corrections arising due to the interlayer coupling J_i to the results obtained in section 5.2.1 (for $\mathbf{H} \parallel b$).

A.5.6 Derivation of (A.1)

Please refer to section A.2.1 for an explanation of the purpose of this section and its relation with previous work. In complete analogy to electrostatics, the magnetostatic potential can be represented as (see, e. g. , [184, p. 196])

$$\Phi_M(\mathbf{r}_0) = \int d^3r \frac{\rho_M(\mathbf{r})}{4\pi|\mathbf{r}_0 - \mathbf{r}|} . \quad (\text{A.17})$$

Obviously, ρ_M is only nonzero at the surface of the sample, where it exhibits a δ -like singularity. The main task consists in determining the correct form of this singularity.

Without loss of generality, $\mathbf{r}_0 = 0$. Using \mathbf{u} and assuming spherical coordinates $\mathbf{u}(\theta, \phi)$, yields a parametrization of \mathbb{R}^3 , $\mathbf{r}(r, \theta, \phi) = r \mathbf{u}(\theta, \phi)$, such that

$$\int_{\mathbb{R}^3} d^3x f(\mathbf{x}) = \int_0^\infty dr r^2 \int_0^\pi d\theta \int_0^{2\pi} d\phi \left| \mathbf{u}(\theta, \phi) \cdot \left(\frac{\partial \mathbf{u}}{\partial \theta} \times \frac{\partial \mathbf{u}}{\partial \phi} \right) \right| f(r \mathbf{u}(\theta, \phi)) .$$

The δ -distribution which “selects” the surface $\partial\Omega$ is therefore

$$\delta_{\partial\Omega}(r, \theta, \phi) = \frac{\left\| \frac{\partial \mathbf{u}}{\partial \theta} \times \frac{\partial \mathbf{u}}{\partial \phi} \right\|}{\left| \mathbf{u}(\theta, \phi) \cdot \left(\frac{\partial \mathbf{u}}{\partial \theta} \times \frac{\partial \mathbf{u}}{\partial \phi} \right) \right|} \delta(r - 1) .$$

Applying the divergence theorem for \mathbf{M} to a thin box containing the sample surface, and making use of the assumption about the orientation of the surface described by $\mathbf{u}(\theta, \phi)$, gives

$$\rho_M(\mathbf{r}) = \mathbf{M} \cdot \hat{\mathbf{n}}(\mathbf{r}) \delta_{\partial\Omega}(r, \theta, \phi) ,$$

where $\hat{\mathbf{n}}(\mathbf{r}) \propto (\partial_\theta \mathbf{u} \times \partial_\phi \mathbf{u})$ denotes the unit surface normal. Substituting this result into (A.17) finally yields (A.1).

A.5.7 Derivation of (A.5)

Please refer to section A.2.2 for an explanation of the purpose of this section and its relation with previous work. Define differential operators $\nabla_{(0)} = (\partial_{ax_{(0)}}, \partial_{by_{(0)}}, \partial_{cz_{(0)}})$ and $\nabla'_{(0)} = (\partial_{x_{(0)}}, \partial_{y_{(0)}}, \partial_{z_{(0)}}) = T \nabla_{(0)}$, where $T = \text{diag}(a, b, c)$. For an arbitrary magnetic moment \mathbf{m} (see, e. g., [184, pp. 196-197]),

$$\frac{1}{\rho^3} (3(\hat{\boldsymbol{\rho}} \cdot \mathbf{m})\hat{\boldsymbol{\rho}} - \mathbf{m}) = -\nabla \frac{\mathbf{m} \cdot \boldsymbol{\rho}}{\rho^3} = \nabla \left(\mathbf{m} \cdot \nabla \frac{1}{\rho} \right) = T^{-1} \nabla'_0 \left(\mathbf{m} \cdot T^{-1} \nabla'_0 \frac{1}{\rho} \right) .$$

Thus (cf. section A.2.2),

$$M_{\mathbf{q}_{\parallel}} \mathbf{m} = \frac{\mu_0}{4\pi} T^{-1} \nabla'_0 \left(\mathbf{m} \cdot T^{-1} \nabla'_0 \text{FT}_2 \left[\frac{1}{\rho} \right] (q_b, q_c) \right) , \quad (\text{A.18})$$

with

$$\text{FT}_2 \left[\frac{1}{\rho} \right] (x, q_b, q_c) = \sum_{(y,z) \in \mathbb{Z}^2} \frac{\exp(2\pi i \mathbf{q}_{\parallel} \cdot (y, z))}{\underbrace{\sqrt{a^2 (x - x_0)^2 + b^2 (y - y_0)^2 + c^2 (z - z_0)^2}}_{g((y,z))}} .$$

The following manipulations in this section essentially re-enact the treatment described in Refs. [292, 438] (cf. section A.2.2). First, one writes (cf. [438, eq. 18])

$$\text{FT}_2 \left[\frac{1}{\rho} \right] (x, q_b, q_c) = \sum_{\boldsymbol{\lambda} \in \mathbb{Z}^2} g(\boldsymbol{\lambda}) = \int d^2 \sigma f(\boldsymbol{\sigma}) g(\boldsymbol{\sigma}) ,$$

where $f(\boldsymbol{\sigma}) = \sum_{\boldsymbol{\lambda} \in \mathbb{Z}^2} \delta(\boldsymbol{\sigma} - \boldsymbol{\lambda})$. The idea [292, 438] is to make use of the Plancherel theorem [315] for the Fourier transform on $L^2(\mathbb{R}^d)$ which states that (cf. [438, eq. 19])

$$\int f(\mathbf{x})^* g(\mathbf{x}) d^d x = \int F(\mathbf{k})^* G(\mathbf{k}) d^d k ,$$

where $F = \mathcal{F}_d[f]$ and $G = \mathcal{F}_d[g]$ denote the continuous Fourier transforms of f and g , respectively, $\mathcal{F}_d[f](\mathbf{k}) = \int f(\mathbf{x}) e^{2\pi i \mathbf{k} \cdot \mathbf{x}} d^d x$.

Following [292], the function $\mathcal{F}_2[f]$ is calculated using the Poisson summation formula [435], which states that

$$\sum_{x=-\infty}^{\infty} f(x) = \sum_{k=-\infty}^{\infty} \hat{f}(k) ,$$

for a suitable function f and its continuous Fourier transform $\hat{f} = \mathcal{F}_1[f]$. In the following, this result is assumed to generalize to sums over \mathbb{Z}^2 and Dirac combs (see [292, appendix 2]). The same applies to the various interchanges of limits which are used throughout the following argument. Hence (cf. [292, appendix 2]),

$$f(\boldsymbol{\sigma}) = \sum_{\boldsymbol{\lambda} \in \mathbb{Z}^2} \delta(\boldsymbol{\sigma} - \boldsymbol{\lambda}) = \sum_{\boldsymbol{\mu} \in \mathbb{Z}^2} \int d^2 \lambda e^{2\pi i \boldsymbol{\mu} \cdot \boldsymbol{\lambda}} \delta(\boldsymbol{\sigma} - \boldsymbol{\lambda}) = \sum_{\boldsymbol{\mu} \in \mathbb{Z}^2} e^{2\pi i \boldsymbol{\mu} \cdot \boldsymbol{\sigma}} ,$$

and therefore (cf. [292, eq. A.11]),

$$\mathcal{F}_2[f](\mathbf{h}) = \int d^2 \sigma \exp(2\pi i \mathbf{h} \cdot \boldsymbol{\sigma}) \sum_{\boldsymbol{\lambda} \in \mathbb{Z}^2} \delta(\boldsymbol{\sigma} - \boldsymbol{\lambda}) = \sum_{\boldsymbol{\mu} \in \mathbb{Z}^2} \int d^2 \sigma \exp(2\pi i (\mathbf{h} + \boldsymbol{\mu}) \cdot \boldsymbol{\sigma}) = \sum_{\boldsymbol{\mu} \in \mathbb{Z}^2} \delta(\mathbf{h} + \boldsymbol{\mu}) .$$

Note that the preceding result corresponds to the usual definition of the reciprocal lattice as the Fourier transform of the direct-space lattice (e. g. , [397]; see also [292, end of appendix 1]).

The other expression to consider is (cf. [438, eq. 22])

$$\begin{aligned} \mathcal{F}_2 [g] (\mathbf{h}) &= \int d^2 \sigma \frac{\exp(2\pi i (\mathbf{h} + \mathbf{q}_{\parallel}) \cdot \boldsymbol{\sigma})}{\sqrt{a^2 (x - x_0)^2 + b^2 (\sigma_1 - y_0)^2 + c^2 (\sigma_2 - z_0)^2}} = \frac{1}{bc} \int d^2 \tilde{\sigma} \frac{\exp(2\pi i (\mathbf{h} + \mathbf{q}_{\parallel}) \cdot \boldsymbol{\sigma})}{\sqrt{a^2 (x - x_0)^2 + \tilde{\sigma}^2}} \\ &= \frac{e^{2\pi i (\mathbf{h} + \mathbf{q}_{\parallel}) \cdot (y_0, z_0)}}{bc} \int d^2 \tilde{\sigma} \frac{\exp(2\pi i \tilde{\mathbf{h}} \cdot \tilde{\boldsymbol{\sigma}})}{\sqrt{a^2 (x - x_0)^2 + \tilde{\sigma}^2}} , \end{aligned}$$

where $\tilde{\boldsymbol{\sigma}} = (b(\sigma_1 - y_0), c(\sigma_2 - z_0))$ and $\tilde{\mathbf{h}} = (1/b(h_1 + q_{\parallel,1}), 1/c(h_2 + q_{\parallel,2}))$. The integral can be evaluated using polar coordinates (r, φ) [448],

$$\begin{aligned} \int d^2 \tilde{\sigma} \frac{\exp(2\pi i \tilde{\mathbf{h}} \cdot \tilde{\boldsymbol{\sigma}})}{\sqrt{a^2 (x - x_0)^2 + \tilde{\sigma}^2}} &= \int_0^{\infty} dr r \int_0^{2\pi} d\varphi \frac{\exp(2\pi i |\tilde{\mathbf{h}}| r \cos \varphi)}{\sqrt{a^2 (x - x_0)^2 + r^2}} = 2\pi \int_0^{\infty} dr \frac{r J_0(2\pi |\tilde{\mathbf{h}}| r)}{\sqrt{a^2 (x - x_0)^2 + r^2}} \\ &= \frac{\exp(-2\pi a |\tilde{\mathbf{h}}| |x - x_0|)}{|\tilde{\mathbf{h}}|} , \text{ provided } x \neq x_0 . \end{aligned}$$

Lastly (cf. [438, eq. 23]),

$$\begin{aligned} \text{FT}_2 \left[\frac{1}{\rho} \right] (x, q_b, q_c) &= \int d^2 \mathbf{h} \sum_{\boldsymbol{\mu} \in \mathbb{Z}^2} \delta(\mathbf{h} + \boldsymbol{\mu}) \frac{e^{2\pi i (\mathbf{h} + \mathbf{q}_{\parallel}) \cdot (y_0, z_0)}}{bc} \frac{\exp(-2\pi a |\tilde{\mathbf{h}}| |x - x_0|)}{|\tilde{\mathbf{h}}|} \\ &= \sum_{\boldsymbol{\mu} \in \mathbb{Z}^2} \frac{e^{2\pi i (\mathbf{q}_{\parallel} - \boldsymbol{\mu}) \cdot (y_0, z_0)}}{\sqrt{bc}} \frac{\exp(-2\pi a (bc)^{-\frac{1}{2}} \|\mathbf{q}_{\parallel} - \boldsymbol{\mu}\|_{bc} |x - x_0|)}{\|\mathbf{q}_{\parallel} - \boldsymbol{\mu}\|_{bc}} , \end{aligned}$$

where I introduced the “ bc -norm”,

$$\|(y, z)\|_{bc}^2 = bc \left(\frac{y^2}{b^2} + \frac{z^2}{c^2} \right) .$$

Substituting into (A.18) then yields the result (A.5).

Note that ferromagnetic configurations $(\mathbf{q}_{\parallel} \in \mathbb{Z}^2)$ need special consideration, since $\mathcal{F}_2 [g] (-\mathbf{q}_{\parallel})$ reduces to the Coulomb potential of the infinite lattice in this case and diverges. However, since only the derivative $\nabla'_0 \text{FT}_2 \left[\frac{1}{\rho} \right] (x, q_b, q_c)$ is ultimately needed, one could have worked with $\nabla'_0 g$ instead of g , the Fourier transform of which has no singularity at $\mathbf{q}_{\parallel} \in \mathbb{Z}^2$. This is in fact the approach taken in [438] and, while not a rigorous proof, justifies why the result (A.5) is assumed to be valid for all \mathbf{q}_{\parallel} .

A.5.8 Weighted linear regression

The weighted least-squares regression [17] is a very well known and established regression method, and the following formulae are solely re-stated for the purpose of completeness. Consider a model $\tilde{\mathbf{y}}(\tilde{\mathbf{x}})$,

which is proposed to describe a set of n measurements (y_i, x_i) . Let the model parameters be described by a vector $\mathbf{p} \in \mathbb{R}^m$, and the measurements be arranged in vectors $\mathbf{x}, \mathbf{y} \in \mathbb{R}^n$. For a linear model, the predictions of the model can be represented as

$$\tilde{\mathbf{y}} = B(\mathbf{x}) \mathbf{p} + \mathbf{b}(\mathbf{x}) \quad ,$$

with $B(\mathbf{x}) \in \mathbb{R}^{n \times m}$ and $\mathbf{b}(\mathbf{x}) \in \mathbb{R}^n$. Let W be a diagonal matrix whose entries correspond to the weighting factors of the observations y_i . The weighted least-squares parameter estimate is then, formally,

$$\min_{\mathbf{p} \in \mathbb{R}^m} \left| \sqrt{W} (B \mathbf{p} + \mathbf{b} - \mathbf{y}) \right|^2 \Rightarrow \mathbf{p} = C (\mathbf{y} - \mathbf{b}) \quad ,$$

where $C = (B^T W B)^{-1} B^T W$ (cf. , e. g. , [17, section 3]). If the covariance matrix of the observations is V (i. e. , the expectation $E[(y_i - b_i)(y_j - b_j)] = V_{ij}$), standard linear error propagation yields the covariance matrix of the parameters (e. g. , [17, p. 46]),

$$V^{(p)} = C V C^T = (B^T V^{-1} B)^{-1} \quad ,$$

where the usual assumption $W = V^{-1}$ was used. Thus, the parameters p_i , as well as their uncertainties $V_{ii}^{(p)}$ and covariances $V_{ij}^{(p)}$, can be estimated directly and without the need for an initial guess.

A.5.9 Discrete spin-space symmetries

See section 7.3.1 for context.

The anti-unitary operator \mathcal{T} satisfies $\mathcal{T} \mathbf{S}_i \mathcal{T}^{-1} = -\mathbf{S}_i$ by construction (cf. section 7.3.1). Since the magnetic field \mathbf{B} transforms as $\mathcal{T} \mathbf{B} \mathcal{T}^{-1} = -\mathbf{B}$, the Hamiltonian (4.1) is time-reversal invariant, $\mathcal{T} \mathcal{H} \mathcal{T}^{-1} = \mathcal{H}$ (even if DM interactions are present).

Since spin is invariant under inversion, the (unitary²³) operator corresponding to R_y should satisfy

$$R_y \mathbf{S}_i R_y^\dagger = \text{diag}(-1, 1, -1) \mathbf{S}_i \quad ,$$

which, as is easy to check, admits the choice $R_y = 2^N \prod_{i=1}^N S_i^y$ (N even). Analogously, $R_x = 2^N \prod_{i=1}^N S_i^x$.

K is a symmetry of the DM-free Hamiltonian if the y -component of the magnetic field is zero. For a K -invariant state $|v\rangle$ with well-defined S_{tot}^z and N even, one can write

$$R_x \mathcal{T} |v\rangle = 4^N \left(\prod_{i=1}^N S_i^x S_i^y \right) K |v\rangle = (2i)^N \left(\prod_{i=1}^N S_i^z \right) K |v\rangle = -(-1)^{N/2 - S_{\text{tot}}^z} |v\rangle \quad .$$

A.5.10 Longitudinal chirality and degenerate ground states

Please refer to section 7.8.1 for context. Use the assumptions made in section 7.8.1, and choose a state $|\varphi\rangle \in \Omega$ with real-valued coefficients in the S_z -basis. It has also been shown that an alternative basis

²³Wigner's theorem (see section 1.4.4 and refs. therein).

of Ω is given by a pair of translation-invariant states $|\pm k\rangle$ with inequivalent lattice-momenta $\pm k$ (cf. section 7.3.1). Translation-invariant states $|\pm k\rangle$ can be obtained by projection onto the corresponding irreducible representations of the translation group (e. g. , [214, p. 24])

$$|\pm k\rangle = \mathcal{P}_{\pm k}(|\varphi\rangle) = \frac{1}{L} \sum_a \exp(\pm i k a) T_a |\varphi\rangle \quad .$$

Here, L denotes the number of rungs constituting the system.

Let K denote complex conjugation of the coefficients in the S_z -basis (cf. section 7.3). By construction, $K |\pm k\rangle = |\mp k\rangle$. Being different quantum states, $|k\rangle$ and $|-k\rangle$ hence cannot be equivalent to any state with real-valued coefficients. In particular, the states $|\pm k\rangle$ defined above are both non-trivial.

The symmetry P defined in section 7.3 implies that $P |\pm k\rangle$ is a degenerate eigenstate with lattice-momentum $\mp k$ (footnote 18 in section 7.3.1), such that $P |\pm k\rangle = p |\mp k\rangle$ with $p = \pm 1$ (note that $P^2 = 1$). Hence, after restriction to Ω , one has $K = p P$.

Expanding $|\pm k\rangle$ using the P -even and P -odd states $|g\rangle$ and $|u\rangle$ introduced in section 7.3, both of which have real-valued coefficients, and invoking $K |\pm k\rangle = |\mp k\rangle$ yields

$$|\pm k\rangle = p^{\frac{1}{2}(1\pm 1)} (\alpha |g\rangle \pm \beta |u\rangle) \quad ,$$

where one of the coefficients is real and the other purely imaginary. Combined with $\langle k | -k \rangle = \langle g | u \rangle = 0$, this implies

$$|\pm k\rangle = \frac{1}{\sqrt{2}} (|g\rangle \pm i p' |u\rangle) \quad ,$$

with $p' = \pm 1$ and up to global phase factors.

Finally, the longitudinal chirality $\kappa_{ij}^z = \frac{i}{2}(S_i^+ S_j^- - S_i^- S_j^+)$ ($i \neq j$) of a generic state $|\psi\rangle = (\cos \alpha |g\rangle + e^{i\theta} \sin \alpha |u\rangle) \in \Omega$ is given by

$$\langle \psi | \kappa_{ij}^z | \psi \rangle = 0 + \sin(2\alpha) \operatorname{Re} e^{i\theta} \langle g | \kappa_{ij}^z | u \rangle \quad .$$

Since $\langle g | \kappa_{ij}^z | u \rangle \in i\mathbb{R}$, the chirality is extremal for $\alpha = \pm \frac{\pi}{4} \pmod{\pi}$ and $\theta = \pm \frac{\pi}{2} \pmod{\pi}$. This condition is equivalent to $|\psi\rangle = |\pm k\rangle$ (up to global phase).

A.6 Miscellaneous

A.6.1 Goodness-of-fit measures

In statistics, for a set of measurements (x_i, y_i) , and a model $f(x_i)$ with predictor variables x_i , the goodness of fit can be quantified using the so-called R^2 value (e. g. , [268]),

$$R^2 = 1 - \frac{\sum_i (y_i - f(x_i))^2}{\sum_i (y_i - \bar{y}_i)^2} \quad .$$

The advantage of R^2 over χ^2 is that it is invariant upon rescaling of the y -axis (i. e. , a change of units; cf. , e. g. , [305]). In order to compare different models, it makes sense to include the number of degrees of freedom, which motivates the definition of the so-called adjusted R^2 value, \bar{R}^2 (e. g. , [268]),

$$\bar{R}^2 = 1 - \frac{\sum_i (y_i - f(x_i))^2}{\sum_i (y_i - \bar{y}_i)^2} \frac{n-1}{n-p-1} \quad ,$$

where n denotes the number of data points and p the number of degrees of freedom in the model.

Bibliography

- ¹Private communication with Marek Bartkowiak.
- ²Private communication with P. L. Kuhns and A. P. Reyes.
- ³Private communication with Francesco Casola.
- ⁴Private communication with Peter Märki.
- ⁵Private communication with H.-R. Ott.
- ⁶Private communication with Michele Dolfi.
- ⁷C. A. R. de A. Melo and R. E. de Souza, “FPGA-based Digital Direct-Conversion Transceiver for Nuclear Magnetic Resonance Systems”, in 25th Symposium on Integrated Circuits and Systems Design (SBCCI), Brasilia, Brazil (2012), pp. 1–5, <http://dx.doi.org/10.1109/SBCCI.2012.6344427>.
- ⁸A. Abragam, *The Principles of Nuclear Magnetism* (Clarendon Press, Oxford, UK, 1961), ISBN: 9780198512363.
- ⁹A. Abragam and B. Bleaney, *Electron paramagnetic resonance of transition ions*, International series of monographs on physics (Clarendon Press, Oxford, UK, 1970), ISBN: 978-0198512509.
- ¹⁰A. Abragam and M. H. L. Pryce, “Theory of the nuclear hyperfine structure of paramagnetic resonance spectra in crystals”, *P. Roy. Soc. A-Math. Phys.* **205**, 135–153 (1951), <http://dx.doi.org/10.1098/rspa.1951.0022>.
- ¹¹F. Abraham, M. Ketatni, G. Mairesse, and B. Mernari, “Crystal structure of a new bismuth copper oxyphosphate: BiCu_2PO_6 ”, *Eur. J. Solid State Inorg. Chem.* **31**, 313–323 (1994), <http://dx.doi.org/10.1002/chin.199448018>.
- ¹²D. Aerts and M. S. de Bianchi, “The extended Bloch representation of quantum mechanics and the hidden-measurement solution to the measurement problem”, *Ann. Phys.* **351**, 975–1025 (2014), <http://dx.doi.org/10.1016/j.aop.2014.09.020>.
- ¹³I. Affleck, “Theory of Haldane-gap antiferromagnets in applied fields”, *Phys. Rev. B* **41**, 6697–6702 (1990), <http://dx.doi.org/10.1103/PhysRevB.41.6697>.
- ¹⁴I. Affleck and F. D. M. Haldane, “Critical theory of quantum spin chains”, *Phys. Rev. B* **36**, 5291–5300 (1987), <http://dx.doi.org/10.1103/PhysRevB.36.5291>.
- ¹⁵I. Affleck and M. Oshikawa, “Field-induced gap in Cu benzoate and other $S = \frac{1}{2}$ antiferromagnetic chains”, *Phys. Rev. B* **60**, 1038–1056 (1999), <http://dx.doi.org/10.1103/PhysRevB.60.1038>.
- ¹⁶I. Affleck, T. Kennedy, E. H. Lieb, and H. Tasaki, “Rigorous Results on Valence-Bond Ground States in Antiferromagnets”, *Phys. Rev. Lett.* **59**, 799–802 (1987), <http://dx.doi.org/10.1103/PhysRevLett.59.799>.
- ¹⁷A. C. Aitken, “IV.—On Least Squares and Linear Combination of Observations”, *Proc. R. Soc. Edinb.* **55**, 42–48 (1936), <http://dx.doi.org/10.1017/S0370164600014346>.
- ¹⁸H. Akimoto and D. Candela, “Small Birdcage Resonator for Low Temperature NMR Experiments”, *J. Low Temp. Phys.* **121**, 791–796 (2000), <http://dx.doi.org/10.1023/A:1017529425563>.

- ¹⁹M. C. Al-Edani and K. S. Dubey, “Boundary Scattering and Phonon Conductivity: Application to GaAs”, *Phys. Status Solidi B* **87**, K47–K52 (1978), <http://dx.doi.org/10.1002/pssb.2220870161>.
- ²⁰M. C. Al-Edani and K. S. Dubey, “Phonon Conductivity of InSb and GaAs”, *Phys. Status Solidi B* **86**, 741–750 (1978), <http://dx.doi.org/10.1002/pssb.2220860238>.
- ²¹K. A. Al-Hassanieh, C. D. Batista, G. Ortiz, and L. N. Bulaevskii, “Field-Induced Orbital Antiferromagnetism in Mott Insulators”, *Phys. Rev. Lett.* **103**, 216402 (2009), <http://dx.doi.org/10.1103/PhysRevLett.103.216402>.
- ²²L. K. Alexander, J. Bobroff, A. V. Mahajan, B. Koteswararao, N. Laflorencie, and F. Alet, “Impurity effects in coupled-ladder BiCu_2PO_6 studied by NMR and quantum Monte Carlo simulations”, *Phys. Rev. B* **81**, 054438 (2010), <http://dx.doi.org/10.1103/PhysRevB.81.054438>.
- ²³N. G. Alexopoulos and C. M. Krowne, “Characteristics of Single and Coupled Microstrips on Anisotropic Substrates”, *IEEE Trans. Microwave Theory Tech.* **26**, 387–393 (1978), <http://dx.doi.org/10.1109/TMTT.1978.1129399>.
- ²⁴A. A. Aligia, C. D. Batista, and F. H. L. Eßler, “Numerical method for detecting incommensurate correlations in the Heisenberg zigzag ladder”, *Phys. Rev. B* **62**, 3259–3263 (2000), <http://dx.doi.org/10.1103/PhysRevB.62.3259>.
- ²⁵R. J. Allen and N. S. Nahman, “Analysis and Performance of Superconductive Coaxial Transmission Lines”, *Proc. IEEE* **52**, 1147–1154 (1964), <http://dx.doi.org/10.1109/PROC.1964.3302>.
- ²⁶G. Allodi, A. Banderini, R. De Renzi, and C. Vignali, “HyReSpect: A broadband fast-averaging spectrometer for nuclear magnetic resonance of magnetic materials”, *Rev. Sci. Instrum.* **76**, 083911 (2005), <http://dx.doi.org/10.1063/1.2009868>.
- ²⁷D. P. Almond and M. J. Lea, “A co-axial transmission line for use in a dilution refrigerator”, *Cryogenics* **14**, 225 (1974), [http://dx.doi.org/10.1016/0011-2275\(74\)90196-9](http://dx.doi.org/10.1016/0011-2275(74)90196-9).
- ²⁸*ALPS subversion repository*, <https://alps.comp-phys.org/svn/alps1/trunk/alps>.
- ²⁹G. M. Amdahl, “Validity of the single processor approach to achieving large scale computing capabilities”, in *Proceedings of the April 18-20, 1967, Spring Joint Computer Conference, Atlantic City, New Jersey, USA, AFIPS '67 (Spring) (1967)*, pp. 483–485, <http://dx.doi.org/10.1145/1465482.1465560>.
- ³⁰P. M. Andersen, N. S. Sullivan, B. Andraka, J. S. Xia, and E. D. Adams, “Population Difference Thermometry for Ultra-Low Temperatures”, *J. Low Temp. Phys.* **89**, 715–718 (1992), <http://dx.doi.org/10.1007/BF00694124>.
- ³¹P. W. Anderson, “New Approach to the Theory of Superexchange Interactions”, *Phys. Rev.* **115**, 2–13 (1959), <http://dx.doi.org/10.1103/PhysRev.115.2>.
- ³²P. W. Anderson, “Resonating valence bonds: A new kind of insulator?”, *Mater. Res. Bull.* **8**, 153–160 (1973), [http://dx.doi.org/10.1016/0025-5408\(73\)90167-0](http://dx.doi.org/10.1016/0025-5408(73)90167-0).
- ³³S. M. Anlage, “High Temperature Superconducting Radio Frequency Coils for NMR Spectroscopy and Magnetic Resonance Imaging”, in *Microwave Superconductivity*, edited by H. Weinstock and M. Nisenoff, NATO Science Series (Series E: Applied Sciences), vol 375 (Springer, Dordrecht, Netherlands, 2001), ISBN: 978-94-010-0450-3, pp. 337–352, http://dx.doi.org/10.1007/978-94-010-0450-3_13.
- ³⁴A. Antonakos, S. Wang, E. Liarokapis, and K. Conder, “Low temperature Raman study of the spin ladder compound BiCu_2PO_6 ”, *J. Phys. Conf. Ser.* **400**, 032004 (2012), <http://dx.doi.org/10.1088/1742-6596/400/3/032004>.

- ³⁵*Application Note: Waveform averaging*, 11-0699 B (SP Devices, Sept. 19, 2014).
- ³⁶ARM Limited, *AMBA[®] AXI4-Stream Protocol Specification*, <http://infocenter.arm.com>, issue D.
- ³⁷ARM Limited, *AMBA[®] AXITM and ACETM[™] Protocol Specification*, version 1.0, <http://infocenter.arm.com>.
- ³⁸“Space group 62”, in *International Tables for Crystallography*, Vol. A: Space-group symmetry, edited by M. I. Aroyo, 2nd online edition (International Union of Crystallography, 2016), ISBN: 978-0-470-97423-0, <http://dx.doi.org/10.1107/9780955360206000114>, pp. 354-355.
- ³⁹V. Arp, J. H. Wilson, L. Winrich, and P. Sikora, “Thermal Expansion of Some Engineering Materials from 20 to 293°K”, *Cryogenics* **2**, 230–235 (1962), [http://dx.doi.org/10.1016/0011-2275\(62\)90057-7](http://dx.doi.org/10.1016/0011-2275(62)90057-7).
- ⁴⁰H. A. Atwater, “Tests of Microstrip Dispersion Formulas”, *IEEE Trans. Microwave Theory Tech.* **36**, 619–621 (1988), <http://dx.doi.org/10.1109/22.3561>.
- ⁴¹I. J. Bahl, *Fundamentals of RF and Microwave Transistor Amplifiers* (John Wiley & Sons, Inc., Hoboken, NJ, USA, 2008), ISBN: 9780470462348, <http://dx.doi.org/10.1002/9780470462348>, section 18.2.4.
- ⁴²L. Balents, “Spin liquids in frustrated magnets”, *Nature* **464**, 199–208 (2010), <http://dx.doi.org/10.1038/nature08917>.
- ⁴³V. Bargmann, “Note on Wigner’s Theorem on Symmetry Operations”, *J. Math. Phys.* **5**, 862–868 (1964), <http://dx.doi.org/10.1063/1.1704188>.
- ⁴⁴E. C. S. Barretto, “Integrated Ultrasonic-Photonic Devices”, PhD thesis (Technical University of Denmark (DTU), Kgs. Lyngby, Denmark, 2011), ISBN: 87-92062-69-5, [http://orbit.dtu.dk/en/publications/integrated-ultrasonicphotonic-devices\(b950586b-7767-40e2-92ff-a6e3bb8b2a0e\).html](http://orbit.dtu.dk/en/publications/integrated-ultrasonicphotonic-devices(b950586b-7767-40e2-92ff-a6e3bb8b2a0e).html) (retrieved 19.09.2013).
- ⁴⁵V. G. Baryakhtar and D. A. Yablonskii, “On the Criterion of the Magnetic Ordering Existence in Non-Collinear Structures”, *Phys. Status Solidi B* **72**, K95–K98 (1975), <http://dx.doi.org/10.1002/pssb.2220720170>.
- ⁴⁶V. G. Bar’yakhtar, V. A. L’vov, and D. A. Yablonskii, “Inhomogeneous magnetoelectric effect”, *JETP Lett.* **37**, 673–675 (1983), http://www.jetpletters.ac.ru/ps/1499/article_22895.shtml.
- ⁴⁷M. T. Batchelor, X.-W. Guan, N. Oelkers, K. Sakai, Z. Tsuboi, and A. Foerster, “Exact Results for the Thermal and Magnetic Properties of Strong Coupling Ladder Compounds”, *Phys. Rev. Lett.* **91**, 217202 (2003), <http://dx.doi.org/10.1103/PhysRevLett.91.217202>.
- ⁴⁸C. D. Batista and G. Ortiz, “Algebraic approach to interacting quantum systems”, *Adv. Phys.* **53**, 1–82 (2004), <http://dx.doi.org/10.1080/00018730310001642086>.
- ⁴⁹B. Bauer, L. D. Carr, H. G. Evertz, A. Feiguin, J. Freire, S. Fuchs, L. Gamper, J. Gukelberger, E. Gull, S. Guertler, A. Hehn, R. Igarashi, S. V. Isakov, D. Koop, P. N. Ma, P. Mates, H. Matsuo, O. Parcollet, G. Pawłowski, J. D. Picon, L. Pollet, E. Santos, V. W. Scarola, U. Schollwöck, C. Silva, B. Surer, S. Todo, S. Trebst, M. Troyer, M. L. Wall, P. Werner, and S. Wessel, “The ALPS project release 2.0: open source software for strongly correlated systems”, *J. Stat. Mech: Theory Exp.* **2011**, P05001 (2011), <http://dx.doi.org/10.1088/1742-5468/2011/05/P05001>.
- ⁵⁰P. Beck, “Molecular dynamics of metal oxides with induced electrostatic dipole moments”, PhD thesis (Universität Stuttgart, Stuttgart, Germany, 2012), <http://dx.doi.org/10.18419/opus-5085>.

- ⁵¹M. Beleggia and M. De Graef, “On the computation of the demagnetization tensor field for an arbitrary particle shape using a Fourier space approach”, *J. Magn. Magn. Mater.* **263**, L1–L9 (2003), [http://dx.doi.org/10.1016/S0304-8853\(03\)00238-5](http://dx.doi.org/10.1016/S0304-8853(03)00238-5).
- ⁵²R. Berman, E. L. Foster, and J. M. Ziman, “Thermal conduction in artificial sapphire crystals at low temperatures. I. Nearly perfect crystals”, *P. Roy. Soc. A-Math. Phys.* **231**, 130–144 (1955), <http://dx.doi.org/10.1098/rspa.1955.0161>.
- ⁵³H. Bethe, “Zur Theorie der Metalle”, *Zeitschrift für Physik* **71**, 205–226 (1931), <http://dx.doi.org/10.1007/BF01341708>.
- ⁵⁴C. M. Bhandari and G. S. Verma, “Role of Longitudinal and Transverse Phonons in Lattice Thermal Conductivity of GaAs and InSb”, *Phys. Rev.* **140**, A2101–A2104 (1965), <http://dx.doi.org/10.1103/PhysRev.140.A2101>.
- ⁵⁵K. Binder and D. W. Heermann, *Monte Carlo Simulation in Statistical Physics: An Introduction* (Springer, Berlin Heidelberg, Germany, 2010), ISBN: 978-3-642-03163-2, <http://dx.doi.org/10.1007/978-3-642-03163-2>.
- ⁵⁶A. R. Bishop, “Solitons in Condensed Matter Physics”, *Physica Scripta* **20**, 409–423 (1979), <http://dx.doi.org/10.1088/0031-8949/20/3-4/016>.
- ⁵⁷D. Björklund, “Implementation of a Software-Defined Radio Transceiver on High-Speed Digitizer/Generator SDR14”, available online, MSc Thesis (Linköpings universitet, Linköping, Sweden, 2012), <http://urn.kb.se/resolve?urn=urn:nbn:se:liu:diva-78213>.
- ⁵⁸R. D. Black, T. A. Early, P. B. Roemer, O. M. Mueller, A. Mogro-Campero, L. G. Turner, and G. A. Johnson, “A High-Temperature Superconducting Receiver for Nuclear Magnetic Resonance Microscopy”, *Science* **259**, 793–795 (1993), <http://dx.doi.org/10.1126/science.8430331>.
- ⁵⁹*BLAS (Basic Linear Algebra Subprograms)*, <http://www.netlib.org/blas/>.
- ⁶⁰B. Bleaney, “The Spin Hamiltonian of a Γ_8 Quartet”, *P. Phys. Soc.* **73**, 939–942 (1959), <http://dx.doi.org/10.1088/0370-1328/73/6/413>.
- ⁶¹R. Blinc, “Magnetic resonance and relaxation in structurally incommensurate systems”, *Phys. Rep.* **79**, 331–398 (1981), [http://dx.doi.org/10.1016/0370-1573\(81\)90108-3](http://dx.doi.org/10.1016/0370-1573(81)90108-3).
- ⁶²B. Blümich, “Stochastic NMR Spectroscopy”, *Bull. Magn. Reson.* **7**, 5–26 (1985), http://www.weizmann.ac.il/ISMAR/sites/ISMAR/files/bulletin/BMR_07_005_026_1985.pdf.
- ⁶³J. Bobroff, N. Laflorencie, L. K. Alexander, A. V. Mahajan, B. Koteswararao, and P. Mendels, “Impurity-Induced Magnetic Order in Low-Dimensional Spin-Gapped materials”, *Phys. Rev. Lett.* **103**, 047201 (2009), <http://dx.doi.org/10.1103/PhysRevLett.103.047201>.
- ⁶⁴P. Bouillot, C. Kollath, A. M. Läuchli, M. Zvonarev, B. Thielemann, Ch. Rüegg, E. Orignac, R. Citro, M. Klanjšek, C. Berthier, M. Horvatić, and T. Giamarchi, “Statics and dynamics of weakly coupled antiferromagnetic spin- $\frac{1}{2}$ ladders in a magnetic field”, *Phys. Rev. B* **83**, 054407 (2011), <http://dx.doi.org/10.1103/PhysRevB.83.054407>.
- ⁶⁵S. Brazovskii, Yu. I. Latyshev, S. I. Matveenko, and P. Monceau, “Recent views on solitons in Density Waves”, *J. Phys. IV France* **131**, 77–80 (2005), <http://dx.doi.org/10.1051/jp4:2005131017>.
- ⁶⁶C. Buchal, J. Hanssen, R. M. Mueller, and F. Pobell, “Platinum wire NMR thermometer for ultralow temperatures”, *Rev. Sci. Instrum.* **49**, 1360–1361 (1978), <http://dx.doi.org/10.1063/1.1135588>.
- ⁶⁷A. D. Buckingham and I. Love, “Theory of the Anisotropy of Nuclear Spin Coupling”, *J. Magn. Reson.* **2**, 338–351 (1970), [http://dx.doi.org/10.1016/0022-2364\(70\)90104-6](http://dx.doi.org/10.1016/0022-2364(70)90104-6).

- ⁶⁸L. N. Bulaevskii, C. D. Batista, M. V. Mostovoy, and D. I. Khomskii, “Electronic orbital currents and polarization in Mott insulators”, *Phys. Rev. B* **78**, 024402 (2008), <http://dx.doi.org/10.1103/PhysRevB.78.024402>.
- ⁶⁹R. Bursill, G. A. Gehring, D. J. J. Farnell, J. B. Parkinson, T. Xiang, and C. Zeng, “Numerical and approximate analytical results for the frustrated spin- $\frac{1}{2}$ quantum spin chain”, *J. Phys.: Condens. Matter* **7**, 8605–8618 (1995), <http://dx.doi.org/10.1088/0953-8984/7/45/016>.
- ⁷⁰N. Büttgen, K. Nawa, T. Fujita, M. Hagiwara, P. Kuhns, A. Prokofiev, A. P. Reyes, L. E. Svistov, K. Yoshimura, and M. Takigawa, “Search for a spin-nematic phase in the quasi-one-dimensional frustrated magnet LiCuVO_4 ”, *Phys. Rev. B* **90**, 134401 (2014), <http://dx.doi.org/10.1103/PhysRevB.90.134401>.
- ⁷¹A. I. Buzdin, M. L. Kulić, and V. V. Tugushev, “Spin-Peierls systems in magnetic field: Phase transition from dimerized to soliton lattice state”, *Solid State Commun.* **48**, 483–487 (1983), [http://dx.doi.org/10.1016/0038-1098\(83\)90859-1](http://dx.doi.org/10.1016/0038-1098(83)90859-1).
- ⁷²D. Candela and D. R. McAllaster, “Platinum NMR thermometry in high magnetic fields”, *Cryogenics* **31**, 94–98 (1991), [http://dx.doi.org/10.1016/0011-2275\(91\)90252-R](http://dx.doi.org/10.1016/0011-2275(91)90252-R).
- ⁷³L. Capriotti, D. J. Scalapino, and S. R. White, “Spin-Liquid versus Dimerized Ground States in a Frustrated Heisenberg Antiferromagnet”, *Phys. Rev. Lett.* **93**, 177004 (2004), <http://dx.doi.org/10.1103/PhysRevLett.93.177004>.
- ⁷⁴F. Casola, “Aspects of quantum magnetism in quasi one-dimensional materials: an NMR study”, PhD thesis (ETH Zürich, Zürich, Switzerland, 2013), <http://dx.doi.org/10.3929/ethz-a-010005724>.
- ⁷⁵F. Casola and A. Feiguin, “ BiCu_2PO_6 : complete NMR study”, Internal report (40 pages), Feb. 2012.
- ⁷⁶F. Casola, T. Shiroka, S. Wang, K. Conder, E. Pomjakushina, J. Mesot, and H.-R. Ott, “Direct Observation of Impurity-Induced Magnetism in a Spin- $\frac{1}{2}$ Antiferromagnetic Heisenberg Two-Leg Spin Ladder”, *Phys. Rev. Lett.* **105**, 067203 (2010), <http://dx.doi.org/10.1103/PhysRevLett.105.067203>.
- ⁷⁷F. Casola, T. Shiroka, A. Feiguin, S. Wang, M. S. Grbić, M. Horvatić, S. Krämer, S. Mukhopadhyay, C. Berthier, H.-R. Ott, H. M. Rønnow, Ch. Rüegg, and J. Mesot, “Field-induced quantum soliton lattice in a frustrated two-leg spin-1/2 ladder”, e-print (2012), arXiv:1211.5522v1 [cond-mat.str-el].
- ⁷⁸F. Casola, T. Shiroka, A. Feiguin, S. Wang, M. S. Grbić, M. Horvatić, S. Krämer, S. Mukhopadhyay, K. Conder, C. Berthier, H.-R. Ott, H. M. Rønnow, Ch. Rüegg, and J. Mesot, “Field-Induced Quantum Soliton Lattice in a Frustrated Two-Leg Spin-1/2 Ladder”, *Phys. Rev. Lett.* **110**, 187201 (2013), <http://dx.doi.org/10.1103/PhysRevLett.110.187201>.
- ⁷⁹O. Cépas, K. Kakurai, L. P. Regnault, T. Ziman, J. P. Boucher, N. Aso, M. Nishi, H. Kageyama, and Y. Ueda, “Dzyaloshinski-Moriya Interaction in the 2D Spin Gap System $\text{SrCu}_2(\text{BO}_3)_2$ ”, *Phys. Rev. Lett.* **87**, 167205 (2001), <http://dx.doi.org/10.1103/PhysRevLett.87.167205>.
- ⁸⁰H.-Y. Chen, Y. Kim, P. Nath, and C. Hilty, “An ultra-low cost NMR device with arbitrary pulse programming”, *J. Magn. Reson.* **255**, 100–105 (2015), <http://dx.doi.org/10.1016/j.jmr.2015.02.011>.
- ⁸¹S.-W. Cheong and M. Mostovoy, “Multiferroics: a magnetic twist for ferroelectricity”, *Nat. Mater.* **6**, 13–20 (2007), <http://dx.doi.org/10.1038/nmat1804>.
- ⁸²A. L. Chernyshev, “Effects of an external magnetic field on the gaps and quantum corrections in an ordered Heisenberg antiferromagnet with Dzyaloshinskii-Moriya anisotropy”, *Phys. Rev. B* **72**, 174414 (2005), <http://dx.doi.org/10.1103/PhysRevB.72.174414>.

- ⁸³M. Chiba, Y. Ajiro, H. Kikuchi, T. Kubo, and T. Morimoto, “Transverse staggered moment in the Haldane-gap antiferromagnet $[\text{Ni}(\text{C}_2\text{H}_8\text{N}_2)_2\text{NO}_2(\text{ClO}_4)]$ observed by proton nuclear magnetic resonance”, *Phys. Rev. B* **44**, 2838–2841 (1991), <http://dx.doi.org/10.1103/PhysRevB.44.2838>.
- ⁸⁴*Chicago Manual of Style 15th ed. Style Sheet*, <http://msupress.org/wp-content/uploads/2012/12/ContagionStyleSheet.pdf> (dated 14.09.2010, retrieved 04.11.2017).
- ⁸⁵R. Chitra and T. Giamarchi, “Critical properties of gapped spin- $\frac{1}{2}$ chains and ladders in a magnetic field”, *Phys. Rev. B* **55**, 5816–5826 (1997), <http://dx.doi.org/10.1103/PhysRevB.55.5816>.
- ⁸⁶R. Chitra, S. Pati, H. R. Krishnamurthy, D. Sen, and S. Ramasesha, “Density-matrix renormalization-group studies of the spin-1/2 Heisenberg system with dimerization and frustration”, *Phys. Rev. B* **52**, 6581–6587 (1995), <http://dx.doi.org/10.1103/PhysRevB.52.6581>.
- ⁸⁷K.-Y. Choi, J. W. Hwang, P. Lemmens, D. Wulferding, G. J. Shu, and F. C. Chou, “Evidence for Dimer Crystal Melting in the Frustrated Spin-Ladder System BiCu_2PO_6 ”, *Phys. Rev. Lett.* **110**, 117204 (2013), <http://dx.doi.org/10.1103/PhysRevLett.110.117204>.
- ⁸⁸A. V. Chubukov, “Chiral, nematic, and dimer states in quantum spin chains”, *Phys. Rev. B* **44**, 4693–4696 (1991), <http://dx.doi.org/10.1103/PhysRevB.44.4693>.
- ⁸⁹F. Cinti, A. Rettori, M. G. Pini, M. Mariani, E. Micotti, A. Lascialfari, N. Papinutto, A. Amato, A. Caneschi, D. Gatteschi, and M. Affronte, “Two-Step Magnetic Ordering in Quasi-One-Dimensional Helimagnets: Possible Experimental Validation of Villain’s Conjecture about a Chiral Spin Liquid Phase”, *Phys. Rev. Lett.* **100**, 057203 (2008), <http://dx.doi.org/10.1103/PhysRevLett.100.057203>.
- ⁹⁰F. Cinti, A. Cuccoli, and A. Rettori, “Vector chiral spin liquid phase in quasi-one-dimensional incommensurate helimagnets”, *Phys. Rev. B* **83**, 174415 (2011), <http://dx.doi.org/10.1103/PhysRevB.83.174415>.
- ⁹¹W. G. Clark, M. E. Hanson, F. Lefloch, and P. Ségransan, “Magnetic resonance spectral reconstruction using frequency-shifted and summed Fourier transform processing”, *Rev. Sci. Instrum.* **66**, 2453–2464 (1995), <http://dx.doi.org/10.1063/1.1145643>.
- ⁹²J. des Cloizeaux and M. Gaudin, “Anisotropic Linear Magnetic Chain”, *J. Math. Phys.* **7**, 1384–1400 (1966), <http://dx.doi.org/10.1063/1.1705048>.
- ⁹³J. des Cloizeaux and J. J. Pearson, “Spin-Wave Spectrum of the Antiferromagnetic Linear Chain”, *Phys. Rev.* **128**, 2131–2135 (1962), <http://dx.doi.org/10.1103/PhysRev.128.2131>.
- ⁹⁴P. Cofrancesco, G. Moiraghi, P. Mustarelli, and M. Villa, “A new NMR duplexer made with quadrature couplers”, *Meas. Sci. Technol.* **2**, 147–149 (1991), <http://dx.doi.org/10.1088/0957-0233/2/2/010>.
- ⁹⁵M. H. Cohen and F. Reif, “Quadrupole Effects in Nuclear Magnetic Resonance Studies of Solids”, in *Solid State Physics, Advances in Research and Applications*, Vol. 5, edited by F. Seitz and D. Turnbull (Academic Press, New York, NY, USA, 1957), ISBN: 978-0-12-607705-6, pp. 321-438, [http://dx.doi.org/10.1016/S0081-1947\(08\)60105-8](http://dx.doi.org/10.1016/S0081-1947(08)60105-8).
- ⁹⁶C. Cohen-Tannoudji, J. Dupont-Roc, and G. Grynberg, *Atom-Photon Interactions: Basic Processes and Applications* (Wiley-VCH Verlag GmbH, Weinheim, Germany, 2004), ISBN: 9780471293361, <http://dx.doi.org/10.1002/9783527617197>.
- ⁹⁷S. Coleman, “There are no Goldstone Bosons in Two Dimensions”, *Commun. Math. Phys.* **31**, 259–264 (1973), <http://dx.doi.org/10.1007/BF01646487>.
- ⁹⁸M. S. Conradi, “Low-Temperature NMR Techniques”, *Concepts Magn. Reson.* **5**, 243–262 (1993), <http://dx.doi.org/10.1002/cmr.1820050304>.

- ⁹⁹R. J. Corruccini and J. J. Gniewek, *Thermal Expansion of Technical Solids at Low Temperatures*, National Bureau of Standards Monograph 29 (National Bureau of Standards, United States Department of Commerce, USA, 1961), <http://nvlpubs.nist.gov/nistpubs/Legacy/MONO/nbsmonograph29.pdf>.
- ¹⁰⁰H. Cory, “Dispersion Characteristics of Microstrip Lines”, *IEEE Trans. Microwave Theory Tech.* **29**, 59–61 (1981), <http://dx.doi.org/10.1109/TMTT.1981.1130287>.
- ¹⁰¹T. S. Cubitt, D. Perez-Garcia, and M. M. Wolf, “Undecidability of the spectral gap”, *Nature* **528**, 207–211 (2015), <http://dx.doi.org/10.1038/nature16059>.
- ¹⁰²E. Dagotto and T. M. Rice, “Surprises on the Way from One- to Two-Dimensional Quantum Magnets: The Ladder Materials”, *Science* **271**, 618–623 (1996), <http://dx.doi.org/10.1126/science.271.5249.618>.
- ¹⁰³J. Dai and W.-M. Zhang, “Quantum Nonlinear σ Model for Arbitrary Spin Heisenberg Antiferromagnets”, *Phys. Rev. Lett.* **95**, 167205 (2005), <http://dx.doi.org/10.1103/PhysRevLett.95.167205>.
- ¹⁰⁴E. Dalgaard and J. Linderberg, “Calculations of g tensors for electron spin resonance in the energy weighted maximum overlap model”, *J. Chem. Phys.* **65**, 692–696 (1976), <http://dx.doi.org/10.1063/1.433082>.
- ¹⁰⁵R. F. Dashen, B. Hasslacher, and A. Neveu, “Nonperturbative methods and extended-hadron models in field theory. II. Two-dimensional models and extended hadrons”, *Phys. Rev. D* **10**, 4130–4138 (1974), <http://dx.doi.org/10.1103/PhysRevD.10.4130>.
- ¹⁰⁶D. E. Demco, P. V. Hecke, and J. S. Waugh, “Phase-Shifted Pulse Sequence for Measurement of Spin-Lattice Relaxation in Complex Systems”, *J. Magn. Reson.* **16**, 467–470 (1974), [http://dx.doi.org/10.1016/0022-2364\(74\)90230-3](http://dx.doi.org/10.1016/0022-2364(74)90230-3).
- ¹⁰⁷D. C. Dender, P. R. Hammar, D. H. Reich, C. Broholm, and G. Aeppli, “Direct Observation of Field-Induced Incommensurate Fluctuations in a One-Dimensional $S = 1/2$ Antiferromagnet”, *Phys. Rev. Lett.* **79**, 1750–1753 (1997), <http://dx.doi.org/10.1103/PhysRevLett.79.1750>.
- ¹⁰⁸V. E. Dmitrienko, E. N. Ovchinnikova, J. Kokubun, and K. Ishida, “Dzyaloshinskii–Moriya Interaction: How to Measure Its Sign in Weak Ferromagnets?”, *JETP Letters* **92**, 383–387 (2010), <http://dx.doi.org/10.1134/S0021364010180050>.
- ¹⁰⁹E. R. Dobrovinskaya, L. A. Lytvynov, and V. Pishchik, *Sapphire*, Material, Manufacturing, Applications (Springer Science+Business Media, LLC, New York, NY, USA, 2009), ISBN: 978-0-387-85694-0, <http://dx.doi.org/10.1007/978-0-387-85695-7>.
- ¹¹⁰A. Dobry and J. A. Riera, “Soliton width in the incommensurate phase of spin-Peierls systems”, *Phys. Rev. B* **56**, R2912–R2915 (1997), <http://dx.doi.org/10.1103/PhysRevB.56.R2912>.
- ¹¹¹M. Dolfi, B. Bauer, S. Keller, A. Kosenkov, T. Ewart, A. Kantian, T. Giamarchi, and M. Troyer, “Matrix product state applications for the ALPS project”, *Comput. Phys. Commun.* **185**, 3430–3440 (2014), <http://dx.doi.org/10.1016/j.cpc.2014.08.019>.
- ¹¹²M. Dolfi, B. Bauer, S. Keller, and M. Troyer, “Pair correlations in doped Hubbard ladders”, *Phys. Rev. B* **92**, 195139 (2015), <http://dx.doi.org/10.1103/PhysRevB.92.195139>.
- ¹¹³F. D. Doty, “Probe Design and Construction”, in *Encyclopedia of Magnetic Resonance*, eds. in chief R. K. Harris and R. E. Wasylshen (John Wiley & Sons, Ltd., Chichester, UK, 2007), ISBN: 9780470034590, <http://dx.doi.org/10.1002/9780470034590.emrstm0414.pub2>, posted on-line 15th December 2007.

- ¹¹⁴M. S. Dresselhaus, *Solid State Physics. Part III: Magnetic Properties of Solids*, lecture notes, Massachusetts Institute of Technology (MIT), Cambridge, MA, USA, 1999, <http://web.mit.edu/course/6/6.732/www/6.732-pt3.pdf> (retrieved 17.03.2017, index at <http://web.mit.edu/course/6/6.732/www/texts.html>).
- ¹¹⁵K. S. Dubey and G. S. Verma, “Phonon Conductivity of InSb and GaAs in the Temperature Range 2–300 °K”, *Phys. Rev. B* **4**, 4491–4498 (1971), <http://dx.doi.org/10.1103/PhysRevB.4.4491>.
- ¹¹⁶I. E. Dzyaloshinskii, “Theory of Helicoidal Structures in Antiferromagnets. I. Nonmetals”, *Sov. Phys. JETP* **19**, 960–971 (1964), <http://www.jetp.ac.ru/cgi-bin/e/index/e/19/4/p960?a=list>.
- ¹¹⁷I. Dzyaloshinsky, “A thermodynamic theory of “weak” ferromagnetism of antiferromagnetics”, *J. Phys. Chem. Solids* **4**, 241–255 (1958), [http://dx.doi.org/10.1016/0022-3697\(58\)90076-3](http://dx.doi.org/10.1016/0022-3697(58)90076-3).
- ¹¹⁸A.-M. A. El-Sherbiny, “Exact Analysis of Shielded Microstrip Lines and Bilateral Fin Lines”, *IEEE Trans. Microwave Theory Tech.* **29**, 669–675 (1981), <http://dx.doi.org/10.1109/TMTT.1981.1130427>.
- ¹¹⁹M. Elhajal, B. Canals, R. Sunyer, and C. Lacroix, “Ordering in the pyrochlore antiferromagnet due to Dzyaloshinsky-Moriya interactions”, *Phys. Rev. B* **71**, 094420 (2005), <http://dx.doi.org/10.1103/PhysRevB.71.094420>.
- ¹²⁰M. Enderle, C. Mukherjee, B. Fåk, R. K. Kremer, J.-M. Broto, H. Rosner, S.-L. Drechsler, J. Richter, J. Malek, A. Prokofiev, W. Assmus, S. Pujol, J.-L. Raggazzoni, H. Rakoto, M. Rheinstädter, and H. M. Rønnow, “Quantum helimagnetism of the frustrated spin- $\frac{1}{2}$ chain LiCuVO₄”, *Europhys. Lett.* **70**, 237–243 (2005), <http://dx.doi.org/10.1209/epl/i2004-10484-x>.
- ¹²¹R. Engel-Herbert and T. Hesjedal, “Calculation of the magnetic stray field of a uniaxial magnetic domain”, *J. Appl. Phys.* **97**, 074504 (2005), <http://dx.doi.org/10.1063/1.1883308>.
- ¹²²R. R. Ernst, “Magnetic Resonance with Stochastic Excitation”, *J. Magn. Reson.* **3**, 10–27 (1970), [http://dx.doi.org/10.1016/0022-2364\(70\)90004-1](http://dx.doi.org/10.1016/0022-2364(70)90004-1).
- ¹²³G. Eska, “Comment on Pulsed NMR Thermometry at Very Low Temperatures”, *J. Low Temp. Phys.* **73**, 207–219 (1988), <http://dx.doi.org/10.1007/BF00681977>.
- ¹²⁴G. Eska, J. Peters, E. N. Smith, and E. Syskakis, “Pulsed NMR experiments on alkali metals at millikelvin temperatures”, *Phys. Lett. A* **136**, 509–512 (1989), [http://dx.doi.org/10.1016/0375-9601\(89\)90307-1](http://dx.doi.org/10.1016/0375-9601(89)90307-1).
- ¹²⁵*Estimated Magnetic Field Profiles along Bore & Mid-plane*, National High Magnetic Field Laboratory, Tallahassee, FL, USA, https://nationalmaglab.org/images/users/dc_field/searchable_docs/cell15_field_profiles.pdf (retrieved 23.04.2016, index at <https://nationalmaglab.org/user-facilities/dc-field/instruments-dcfield/resistive-magnets/45-tesla-2>).
- ¹²⁶P. P. Ewald, “Die Berechnung optischer und elektrostatischer Gitterpotentiale”, *Ann. Phys.* **369**, 253–287 (1921), <http://dx.doi.org/10.1002/andp.19213690304>.
- ¹²⁷J. Fabian, *Spin-orbit coupling in solids*, lecture notes, Universität Regensburg, Regensburg, Germany, 2008, http://www.physik.uni-regensburg.de/forschung/fabian/pages/mainframes/lecturenotes/lecturenotes_files/Spin-orbit-coupling-in-solids.pdf (retrieved 24.01.2017, index at http://www.physik.uni-regensburg.de/forschung/fabian/pages/index_teaching.html).
- ¹²⁸L. D. Faddeev and L. A. Takhtajan, “What is the spin of a spin wave?”, *Phys. Lett. A* **85**, 375–377 (1981), [http://dx.doi.org/10.1016/0375-9601\(81\)90335-2](http://dx.doi.org/10.1016/0375-9601(81)90335-2).

- ¹²⁹R. Faraji-Dana and Y. L. Chow, “The Current Distribution and AC Resistance of a Microstrip Structure”, *IEEE Trans. Microwave Theory Tech.* **38**, 1268–1277 (1990), <http://dx.doi.org/10.1109/22.58653>.
- ¹³⁰H. Fehske, R. Schneider, and A. Weiße, eds., *Computational Many-Particle Physics* (Springer, Berlin Heidelberg, Germany, 2008), ISBN: 978-3-540-74686-7, <http://dx.doi.org/10.1007/978-3-540-74686-7>.
- ¹³¹A. E. Feiguin, “DMRG study of BCPO”, internal report (5 pages), Feb. 2012.
- ¹³²A. E. Feiguin, J. A. Riera, A. Dobry, and H. A. Ceccatto, “Numerical study of the incommensurate phase in spin-Peierls systems”, *Phys. Rev. B* **56**, 14607–14613 (1997), <http://dx.doi.org/10.1103/PhysRevB.56.14607>.
- ¹³³A. E. Feiguin and S. R. White, “Finite-temperature density matrix renormalization using an enlarged Hilbert space”, *Phys. Rev. B* **72**, 220401(R) (2005), <http://dx.doi.org/10.1103/PhysRevB.72.220401>.
- ¹³⁴*Field distribution plot done by NMR*. National High Magnetic Field Laboratory, Tallahassee, FL, USA, https://nationalmaglab.org/images/users/dc_field/magnets/45tesla/cell15_distributionplot.jpg (retrieved 09.03.2017, index at <https://nationalmaglab.org/user-facilities/dc-field/instruments-dcfield/resistive-magnets/45-tesla-2>).
- ¹³⁵R. Finger and A. R. Kerr, “Microwave Loss Reduction in Cryogenically Cooled Conductors”, *Int. J. Infrared Millimeter Waves* **29**, 924–932 (2008), <http://dx.doi.org/10.1007/s10762-008-9394-1>.
- ¹³⁶J.-B. Fouet, F. Mila, D. Clarke, H. Youk, O. Tchernyshyov, P. Fendley, and R. M. Noack, “Condensation of magnons and spinons in a frustrated ladder”, *Phys. Rev. B* **73**, 214405 (2006), <http://dx.doi.org/10.1103/PhysRevB.73.214405>.
- ¹³⁷M. Fowler and M. W. Puga, “Dimer gas model for tetracyanoquinodimethane (TCNQ)”, *Phys. Rev. B* **18**, 421–428 (1978), <http://dx.doi.org/10.1103/PhysRevB.18.421>.
- ¹³⁸R. Freeman, “Selective Excitation in High-Resolution NMR”, *Chem. Rev.* **91**, 1397–1412 (1991), <http://dx.doi.org/10.1021/cr00007a006>.
- ¹³⁹M. Fujita and K. Machida, “Magnetic structure in a soliton lattice state of a spin-Peierls system under applied fields”, *J. Phys. C: Solid State Phys.* **21**, 5813–5823 (1988), <http://dx.doi.org/10.1088/0022-3719/21/34/015>.
- ¹⁴⁰N. Fujiwara, T. Goto, S. Maegawa, and T. Kohmoto, “Spin fluctuation and static properties of the local moments in the Haldane-gap system $\text{Ni}(\text{C}_2\text{H}_8\text{N}_2)_2\text{NO}_2(\text{ClO}_4)$ studied by ^1H NMR”, *Phys. Rev. B* **47**, 11860–11869 (1993), <http://dx.doi.org/10.1103/PhysRevB.47.11860>.
- ¹⁴¹S. Furukawa, M. Sato, Y. Saiga, and S. Onoda, “Quantum Fluctuations of Chirality in One-Dimensional Spin-1/2 Multiferroics: Gapless Dielectric Response from Phasons and Chiral Solitons”, *J. Phys. Soc. Jpn.* **77**, 123712 (2008), <http://dx.doi.org/10.1143/JPSJ.77.123712>.
- ¹⁴²S. Furukawa, M. Sato, and S. Onoda, “Chiral Order and Electromagnetic Dynamics in One-Dimensional Multiferroic Cuprates”, *Phys. Rev. Lett.* **105**, 257205 (2010), <http://dx.doi.org/10.1103/PhysRevLett.105.257205>.
- ¹⁴³V. O. Garlea, A. Zheludev, K. Habicht, M. Meissner, B. Grenier, L.-P. Regnault, and E. Ressouche, “Dimensional crossover in a spin-liquid-to-helimagnet quantum phase transition”, *Phys. Rev. B* **79**, 060404(R) (2009), <http://dx.doi.org/10.1103/PhysRevB.79.060404>.

- ¹⁴⁴W. Geertsma and D. Khomskii, “Influence of side groups on 90° superexchange: A modification of the Goodenough-Kanamori-Anderson rules”, *Phys. Rev. B* **54**, 3011–3014 (1996), <http://dx.doi.org/10.1103/PhysRevB.54.3011>.
- ¹⁴⁵T. Giamarchi and A. M. Tsvelik, “Coupled ladders in a magnetic field”, *Phys. Rev. B* **59**, 11398–11407 (1999), <http://dx.doi.org/10.1103/PhysRevB.59.11398>.
- ¹⁴⁶T. Giamarchi, Ch. Rüegg, and O. Tchernyshyov, “Bose-Einstein condensation in magnetic insulators”, *Nat. Phys.* **4**, 198–204 (2008), <http://dx.doi.org/10.1038/nphys893>.
- ¹⁴⁷B. J. Gibson, R. K. Kremer, A. V. Prokofiev, W. Assmus, and G. J. McIntyre, “Incommensurate antiferromagnetic order in the $S=1/2$ quantum chain compound LiCuVO_4 ”, *Physica B* **350**, e253–e256 (2004), <http://dx.doi.org/10.1016/j.physb.2004.03.064>.
- ¹⁴⁸G. Giovannetti, V. Hartwig, V. Viti, G. Gaeta, R. Francesconi, L. Landini, and A. Benassi, “Application of Undersampling Technique for the Design of an NMR Signals Digital Receiver”, *Concepts Magn. Reson.* **29B**, 107–114 (2006), <http://dx.doi.org/10.1002/cmr.b.20065>.
- ¹⁴⁹R. M. Golding and L. C. Stubbs, “The evaluation of the hyperfine interaction tensor components in molecular systems”, *Proc. R. Soc. Lond. A* **354**, 223–244 (1977), <http://dx.doi.org/10.1098/rspa.1977.0065>.
- ¹⁵⁰R. M. Golding and L. C. Stubbs, “Higher order hyperfine terms in the spin Hamiltonian”, *Proc. R. Soc. Lond. A* **362**, 525–536 (1978), <http://dx.doi.org/10.1098/rspa.1978.0148>.
- ¹⁵¹J. B. Goodenough, *Magnetism and the Chemical Bond*, edited by F. A. Cotton, Interscience Monographs on Chemistry, Volume I (John Wiley & Sons, Inc., New York-London, 1963).
- ¹⁵²S. Gopalan, T. M. Rice, and M. Sigrist, “Spin ladders with spin gaps: A description of a class of cuprates”, *Phys. Rev. B* **49**, 8901–8910 (1994), <http://dx.doi.org/10.1103/PhysRevB.49.8901>.
- ¹⁵³A. C. Gossard and A. M. Portis, “Observation of Nuclear Resonance in a Ferromagnet”, *Phys. Rev. Lett.* **3**, 164–166 (1959), <http://dx.doi.org/10.1103/PhysRevLett.3.164>.
- ¹⁵⁴D. D. Grieg and H. F. Engelmann, “Microstrip—A New Transmission Technique for the Kilomegacycle Range”, *Proc. IRE* **40**, 1644–1650 (1952), <http://dx.doi.org/10.1109/JRPROC.1952.274144>.
- ¹⁵⁵E. L. Hahn, “Spin Echoes”, *Phys. Rev.* **80**, 580–594 (1950), <http://dx.doi.org/10.1103/PhysRev.80.580>.
- ¹⁵⁶A. S. Hall, N. McN. Alford, T. W. Button, D. J. Gilderdale, K. A. Gehring, and I. R. Young, “Use of High Temperature Superconductor in a Receiver Coil for Magnetic Resonance Imaging”, *Magn. Reson. Med.* **20**, 340–343 (1991), <http://dx.doi.org/10.1002/mrm.1910200218>.
- ¹⁵⁷Z. Hao, Y. Wan, I. Rousochatzakis, J. Wildeboer, A. Seidel, F. Mila, and O. Tchernyshyov, “Destruction of valence-bond order in a $S = \frac{1}{2}$ sawtooth chain with a Dzyaloshinskii-Moriya term”, *Phys. Rev. B* **84**, 094452 (2011), <http://dx.doi.org/10.1103/PhysRevB.84.094452>.
- ¹⁵⁸S. Hashimoto, K. Kose, and T. Haishi, “Comparison of Analog and Digital Transceiver Systems for MR Imaging”, *Magn. Reson. Med. Sci.* **13**, 285–291 (2014), <http://dx.doi.org/10.2463/mrms.2013-0114>.
- ¹⁵⁹E. E. Hassan, “Field Solution, Polarization, and Eigenmodes of Shielded Microstrip Transmission Line”, *IEEE Trans. Microwave Theory Tech.* **34**, 845–852 (1986), <http://dx.doi.org/10.1109/TMTT.1986.1133456>.

- ¹⁶⁰C. J. Hasselwander, Z. Cao, and W. A. Grissom, “gr-MRI: A software package for magnetic resonance imaging using software defined radios”, *J. Magn. Reson.* **270**, 47–55 (2016), <http://dx.doi.org/10.1016/j.jmr.2016.06.023>.
- ¹⁶¹A. Hehn, N. van Well, and M. Troyer, “High-temperature series expansion for spin-1/2 Heisenberg models”, *Comput. Phys. Commun.* **212**, 180–188 (2017), <http://dx.doi.org/10.1016/j.cpc.2016.09.003>.
- ¹⁶²J. Heiserman, “Thermal grounding of a transmission line in a dilution refrigerator”, *Cryogenics* **22**, 243–244 (1982), [http://dx.doi.org/10.1016/0011-2275\(82\)90121-7](http://dx.doi.org/10.1016/0011-2275(82)90121-7).
- ¹⁶³T. Hikihara, L. Kecke, T. Momoi, and A. Furusaki, “Vector chiral and multipolar orders in the spin- $\frac{1}{2}$ frustrated ferromagnetic chain in magnetic field”, *Phys. Rev. B* **78**, 144404 (2008), <http://dx.doi.org/10.1103/PhysRevB.78.144404>.
- ¹⁶⁴T. Hikihara, T. Momoi, A. Furusaki, and H. Kawamura, “Magnetic phase diagram of the spin- $\frac{1}{2}$ anti-ferromagnetic zigzag ladder”, *Phys. Rev. B* **81**, 224433 (2010), <http://dx.doi.org/10.1103/PhysRevB.81.224433>.
- ¹⁶⁵H. D. W. Hill and R. E. Richards, “Limits of measurement in magnetic resonance”, *J. Phys. E: Sci. Instrum.* **1**, 977–983 (1968), <http://dx.doi.org/10.1088/0022-3735/1/10/202>.
- ¹⁶⁶O. Hirsch, G. Scheler, and C. Jäger, “Spectrometer for stochastic solid-state nuclear magnetic resonance spectroscopy”, *Rev. Sci. Instrum.* **72**, 1734–1741 (2001), <http://dx.doi.org/10.1063/1.1340563>.
- ¹⁶⁷A. Hobeika, T. M. Haard, E. M. Hoskinson, and R. E. Packard, “Development of a computer-based pulsed NMR thermometer”, *Physica B* **329–333**, Proceedings of the 23rd International Conference on Low Temperature Physics, Hiroshima, Japan, 1610–1611 (2003), [http://dx.doi.org/10.1016/S0921-4526\(02\)02424-9](http://dx.doi.org/10.1016/S0921-4526(02)02424-9).
- ¹⁶⁸L. Hogben, ed., *Handbook of Linear Algebra*, Discrete Mathematics and Its Applications (Chapman & Hall/CRC, Boca Raton, FL, USA, 2006), ISBN: 9781420010572, <http://dx.doi.org/10.1201/9781420010572>.
- ¹⁶⁹P. C. Hohenberg, “Existence of Long-Range Order in One and Two Dimensions”, *Phys. Rev.* **158**, 383–386 (1967), <http://dx.doi.org/10.1103/PhysRev.158.383>.
- ¹⁷⁰M. G. Holland, “Thermal Conductivity of Several Optical Maser Materials”, *J. Appl. Phys.* **33**, 2910–2911 (1962), <http://dx.doi.org/10.1063/1.1702584>.
- ¹⁷¹M. G. Holland, “Phonon Scattering in Semiconductors From Thermal Conductivity Studies”, *Phys. Rev.* **134**, A471–A480 (1964), <http://dx.doi.org/10.1103/PhysRev.134.A471>.
- ¹⁷²D. Homentcovschi, “An Analytical Approach to the Analysis of Dispersion Characteristics of Microstrip Lines”, *IEEE Trans. Microwave Theory Tech.* **39**, 740–743 (1991), <http://dx.doi.org/10.1109/22.76442>.
- ¹⁷³M. Horno, “Calculation of Quasi-Static Characteristics of Microstrip on Anisotropic Substrate Using Mapping Method”, in 1980 IEEE MTT-S International Microwave symposium (Washington, DC, USA) Digest (1980), pp. 450–452, <http://dx.doi.org/10.1109/MWSYM.1980.1124318>.
- ¹⁷⁴M. Horvatić, Y. Fagot-Revurat, C. Berthier, G. Dhalenne, and A. Revcolevschi, “NMR Imaging of the Soliton Lattice Profile in the Spin-Peierls Compound CuGeO_3 ”, *Phys. Rev. Lett.* **83**, 420–423 (1999), <http://dx.doi.org/10.1103/PhysRevLett.83.420>.
- ¹⁷⁵D. I. Hoult and R. E. Richards, “Critical factors in the design of sensitive high resolution nuclear magnetic resonance spectrometers”, *Proc. R. Soc. Lond. A* **344**, 311–340 (1975), <http://dx.doi.org/10.1098/rspa.1975.0104>.

- ¹⁷⁶D. I. Hoult and R. E. Richards, “The Signal-to-Noise Ratio of the Nuclear Magnetic Resonance Experiment”, *J. Magn. Reson.* **24**, 71–85 (1976), [http://dx.doi.org/10.1016/0022-2364\(76\)90233-X](http://dx.doi.org/10.1016/0022-2364(76)90233-X).
- ¹⁷⁷C. Huan, S. S. Kim, L. Phelps, J. S. Xia, D. Candela, and N. S. Sullivan, “A Novel Design of a Low Temperature Preamplifier for Pulsed NMR Experiments of Dilute ^3He in Solid ^4He ”, *J. Low Temp. Phys.* **158**, 692–696 (2010), <http://dx.doi.org/10.1007/s10909-009-9984-x>.
- ¹⁷⁸J. Hubbard, “Electron correlations in narrow energy bands”, *Proc. R. Soc. Lond. A* **276**, 238–257 (1963), <http://dx.doi.org/10.1098/rspa.1963.0204>.
- ¹⁷⁹K. Hwang and Y. B. Kim, “Theory of triplon dynamics in the quantum magnet BiCu_2PO_6 ”, *Phys. Rev. B* **93**, 235130 (2016), <http://dx.doi.org/10.1103/PhysRevB.93.235130>.
- ¹⁸⁰E. K. Insko, M. A. Elliott, J. C. Schotland, and J. S. Leigh, “Generalized Reciprocity”, *J. Magn. Reson.* **131**, 111–117 (1998), <http://dx.doi.org/10.1006/jmre.1997.1355>.
- ¹⁸¹*Intel Math Kernel Library (MKL)*, <https://software.intel.com/en-us/intel-mkl>.
- ¹⁸²N. Ishimura and H. Shiba, “Dynamical Correlation Functions of One-Dimensional Anisotropic Heisenberg Model with Spin 1/2.—I. Ising-Like Antiferromagnets”, *Prog. Theor. Phys.* **63**, 743–758 (1980), <http://dx.doi.org/10.1143/PTP.63.743>.
- ¹⁸³A. I. Ivanov, A. N. Luk’yanov, B. A. Merisov, A. V. Sologubenko, and G. Ya. Khadjai, “Thermal conductivity of a GaAs single crystal grown in microgravity”, *Low Temp. Phys.* **28**, 462–464 (2002), <http://dx.doi.org/10.1063/1.1491187>.
- ¹⁸⁴J. D. Jackson, *Classical Electrodynamics*, 3rd edition (John Wiley & Sons, Inc., Hoboken, NJ, USA, 1998), ISBN: 978-0-471-30932-1.
- ¹⁸⁵A. Jànossy, L.-C. Brunel, and J. R. Cooper, “ Gd^{3+} ESR determination of the local spin susceptibility in $\text{Gd:YBa}_2\text{Cu}_3\text{O}_y$ high-temperature superconductors”, *Phys. Rev. B* **54**, 10186–10191 (1996), <http://dx.doi.org/10.1103/PhysRevB.54.10186>.
- ¹⁸⁶E. Jeckelmann, “Dynamical density-matrix renormalization-group method”, *Phys. Rev. B* **66**, 045114 (2002), <http://dx.doi.org/10.1103/PhysRevB.66.045114>.
- ¹⁸⁷B.-G. Jeon, B. Koteswararao, C. B. Park, K. Hoon Kim, G. J. Shu, F. C. Chou, S. C. Riggs, and S. B. Chung, *High-Field Thermal Conductivity of a Frustrated Two-Leg Spin Ladder BiCu_2PO_6* , Research Report 222 (National High Magnetic Field Laboratory, Tallahassee, FL, USA, 2014), <https://legacywww.magnet.fsu.edu/mediacenter/publications/reports/2014annualreport/2014-NHMFL-Report222.pdf>.
- ¹⁸⁸B.-G. Jeon, B. Koteswararao, K. Hoon Kim, J. W. Kim, G. J. Shu, and F. C. Chou, *Multiferroicity in a Frustrated Spin Ladder BiCu_2PO_6 At High Magnetic Field*, Research Report 223 (National High Magnetic Field Laboratory, Tallahassee, FL, USA, 2014), <https://legacywww.magnet.fsu.edu/mediacenter/publications/reports/2014annualreport/2014-NHMFL-Report223.pdf>.
- ¹⁸⁹B.-G. Jeon, B. Koteswararao, C. B. Park, G. J. Shu, S. C. Riggs, E. G. Moon, S. B. Chung, F. C. Chou, and K. H. Kim, *Giant Suppression of Phononic Heat Transport in a Quantum Magnet BiCu_2PO_6* , Research Report 269 (National High Magnetic Field Laboratory, Tallahassee, FL, USA, 2015), <https://legacywww.magnet.fsu.edu/mediacenter/publications/reports/2015annualreport/2015-NHMFL-Report269.pdf>.
- ¹⁹⁰B.-G. Jeon, B. Koteswararao, C. B. Park, G. J. Shu, S. C. Riggs, E. G. Moon, S. B. Chung, F. C. Chou, and K. H. Kim, “Giant suppression of phononic heat transport in a quantum magnet BiCu_2PO_6 ”, *Sci. Rep.* **6**, 36970 (2016), <http://dx.doi.org/10.1038/srep36970>.

- ¹⁹¹Jmol: an open-source Java viewer for chemical structures in 3D, <http://www.jmol.org/>.
- ¹⁹²D. C. Johnston, M. Troyer, S. Miyahara, D. Lidsky, K. Ueda, M. Azuma, Z. Hiroi, M. Takano, M. Isobe, Y. Ueda, M. A. Korotin, V. I. Anisimov, A. V. Mahajan, and L. L. Miller, “Magnetic Susceptibilities of Spin-1/2 Antiferromagnetic Heisenberg Ladders and Applications to Ladder Oxide Compounds”, e-print (2000), arXiv:cond-mat/0001147v1 [cond-mat.str-el].
- ¹⁹³P. Jordan and E. Wigner, “Über das Paulische Äquivalenzverbot”, *Zeitschrift für Physik* **47**, 631–651 (1928), <http://dx.doi.org/10.1007/BF01331938>.
- ¹⁹⁴R. I. Joseph and E. Schlömann, “Demagnetizing Field in Nonellipsoidal Bodies”, *J. Appl. Phys.* **36**, 1579–1593 (1965), <http://dx.doi.org/10.1063/1.1703091>.
- ¹⁹⁵R. Kaiser, “Coherent Spectrometry with Noise Signals”, *J. Magn. Reson.* **3**, 28–43 (1970), [http://dx.doi.org/10.1016/0022-2364\(70\)90005-3](http://dx.doi.org/10.1016/0022-2364(70)90005-3).
- ¹⁹⁶T. A. Kaplan, “Single-Band Hubbard Model with Spin-Orbit Coupling”, *Z. Phys. B - Cond. Mat.* **49**, 313–317 (1983), <http://dx.doi.org/10.1007/BF01301591>.
- ¹⁹⁷M. Kasal, J. Halánek, V. Husek, M. Villa, U. Ruffina, and P. Cofrancesco, “Signal processing in transceivers for nuclear magnetic resonance and imaging”, *Rev. Sci. Instrum.* **65**, 1897–1902 (1994), <http://dx.doi.org/10.1063/1.1144840>.
- ¹⁹⁸V. Kataev, J. Baier, A. Möller, L. Jongen, G. Meyer, and A. Freimuth, “Orbital order in the low-dimensional quantum spin system TiOCl probed by ESR”, *Phys. Rev. B* **68**, 140405(R) (2003), <http://dx.doi.org/10.1103/PhysRevB.68.140405>.
- ¹⁹⁹H. Katsura, N. Nagaosa, and A. V. Balatsky, “Spin Current and Magnetoelectric Effect in Noncollinear Magnets”, *Phys. Rev. Lett.* **95**, 057205 (2005), <http://dx.doi.org/10.1103/PhysRevLett.95.057205>.
- ²⁰⁰D. Khomskii, W. Geertsma, and M. Mostovoy, “Elementary excitations, exchange interaction and spin-Peierls transition in CuGeO₃”, *Czech. J. Phys.* **46**, 3239–3246 (1996), <http://dx.doi.org/10.1007/BF02548136>.
- ²⁰¹S. Kilgore, C. Gaw, H. Henry, D. Hill, and D. Schroder, “Electromigration of Electroplated Gold Interconnects”, *Mater. Res. Soc. Symp. Proc.* **863**, B8.30.1–B8.30.6 (2005), <http://dx.doi.org/10.1557/PROC-863-B8.30>.
- ²⁰²R. W. P. King, “The Propagation of Signals Along a Three-Layered Region: Microstrip”, *IEEE Trans. Microwave Theory Tech.* **36**, 1080–1086 (1988), <http://dx.doi.org/10.1109/22.3635>.
- ²⁰³M. Kirschning and R. H. Jansen, “Accurate model for effective dielectric constant of microstrip with validity up to millimetre-wave frequencies”, *Electron. Lett.* **18**, 272–273 (1982), <http://dx.doi.org/10.1049/el:19820186>.
- ²⁰⁴C. Kittel, *Introduction to Solid State Physics*, 8th edition (John Wiley & Sons, Inc., Hoboken, NJ, USA, 2004), ISBN: 978-0-471-41526-8.
- ²⁰⁵M. Kobayashi, “Frequency Dependent Characteristics of Microstrips on Anisotropic Substrates”, *IEEE Trans. Microwave Theory Tech.* **30**, 2054–2057 (1982), <http://dx.doi.org/10.1109/TMTT.1982.1131377>.
- ²⁰⁶M. Kobayashi, “Longitudinal and Transverse Current Distributions on Microstriplines and Their Closed-Form Expression”, *IEEE Trans. Microwave Theory Tech.* **33**, 784–788 (1985), <http://dx.doi.org/10.1109/TMTT.1985.1133127>.

- ²⁰⁷Y. Kohama, S. Wang, A. Uchida, K. Prša, S. Zvyagin, Y. Skourski, R. D. McDonald, L. Balicas, H. M. Rønnow, Ch. Rüegg, and M. Jaime, “Anisotropic Cascade of Field-Induced Phase Transitions in the Frustrated Spin-Ladder System BiCu_2PO_6 ”, *Phys. Rev. Lett.* **109**, 167204 (2012), <http://dx.doi.org/10.1103/PhysRevLett.109.167204>.
- ²⁰⁸Y. Kohama, K. Mochizuki, T. Terashima, A. Miyata, A. DeMuer, T. Klein, C. Marcenat, Z. L. Dun, H. Zhou, G. Li, L. Balicas, N. Abe, Y. H. Matsuda, S. Takeyama, A. Matsuo, and K. Kindo, “Entropy of the quantum soliton lattice and multiple magnetization steps in BiCu_2PO_6 ”, *Phys. Rev. B* **90**, 060408(R) (2014), <http://dx.doi.org/10.1103/PhysRevB.90.060408>.
- ²⁰⁹A. K. Kolezhuk and I. P. McCulloch, “Field-controlled spin current in frustrated spin chains”, *Condens. Matter Phys.* **12**, 429–434 (2009), <http://dx.doi.org/10.5488/CMP.12.3.429>.
- ²¹⁰A. K. Kolezhuk and H.-J. Mikeska, “Non-Haldane Spin-Liquid Models with Exact Ground States”, *Phys. Rev. Lett.* **80**, 2709–2712 (1998), <http://dx.doi.org/10.1103/PhysRevLett.80.2709>.
- ²¹¹A. Kolezhuk and T. Vekua, “Field-induced chiral phase in isotropic frustrated spin chains”, *Phys. Rev. B* **72**, 094424 (2005), <http://dx.doi.org/10.1103/PhysRevB.72.094424>.
- ²¹²L. Korosec, “Development and Testing of a New NMR Spectrometer; First NMR Studies on RNiO_3 Perovskites”, MSc Thesis (ETH Zürich, Zürich, Switzerland, 2014).
- ²¹³J. G. Korvink and A. Greiner, *Semiconductors for Micro- and Nanotechnology: An Introduction for Engineers* (Wiley-VCH Verlag GmbH, Weinheim, Germany, 2002), <http://dx.doi.org/10.1002/3527600221>.
- ²¹⁴Y. Kosmann-Schwarzbach, *Groups and Symmetries, From Finite Groups to Lie Groups*, trans. by S. Frank Singer, Universitext (Springer Science+Business Media, LLC, New York, NY, USA, 2009), ISBN: 978-0-387-78866-1, <http://dx.doi.org/10.1007/978-0-387-78866-1>.
- ²¹⁵G. F. Koster, “Matrix Elements of Symmetric Operators”, *Phys. Rev.* **109**, 227–231 (1958), <http://dx.doi.org/10.1103/PhysRev.109.227>.
- ²¹⁶G. F. Koster and H. Statz, “Method of Treating Zeeman Splittings of Paramagnetic Ions in Crystalline Fields”, *Phys. Rev.* **113**, 445–454 (1959), <http://dx.doi.org/10.1103/PhysRev.113.445>.
- ²¹⁷B. Koteswararao, S. Salunke, A. V. Mahajan, I. Dasgupta, and J. Bobroff, “Spin-gap behavior in the two-leg spin-ladder BiCu_2PO_6 ”, *Phys. Rev. B* **76**, 052402 (2007), <http://dx.doi.org/10.1103/PhysRevB.76.052402>.
- ²¹⁸B. Koteswararao, A. V. Mahajan, L. K. Alexander, and J. Bobroff, “Doping effects in the coupled, two-leg spin ladder BiCu_2PO_6 ”, *J. Phys.: Condens. Matter* **22**, 035601 (2010), <http://dx.doi.org/10.1088/0953-8984/22/3/035601>.
- ²¹⁹V. N. Kotov, M. Elhadj, M. E. Zhitomirsky, and F. Mila, “Dzyaloshinsky-Moriya-induced order in the spin-liquid phase of the $S = 1/2$ pyrochlore antiferromagnet”, *Phys. Rev. B* **72**, 014421 (2005), <http://dx.doi.org/10.1103/PhysRevB.72.014421>.
- ²²⁰G. Koutroulakis, “Unravelling the mysteries of unconventional superconductivity with NMR: The curious case of CeCoIn_5 ”, PhD thesis (Brown University, Providence, RI, USA, 2011), <https://repository.library.brown.edu/studio/item/bdr:11206/>.
- ²²¹J. Krupka, R. G. Geyer, M. Kuhn, and J. H. Hinken, “Dielectric Properties of Single Crystals of Al_2O_3 , LaAlO_3 , NdGaO_3 , SrTiO_3 , and MgO at Cryogenic Temperatures”, *IEEE Trans. Microwave Theory Tech.* **42**, 1886–1890 (1994), <http://dx.doi.org/10.1109/22.320769>.

- ²²²L. Krämer, E. Di Napoli, M. Galgon, B. Lang, and P. Bientinesi, “Dissecting the FEAST algorithm for generalized eigenproblems”, *J. Comput. Appl. Math.* **244**, 1–9 (2013), <http://dx.doi.org/10.1016/j.cam.2012.11.014>.
- ²²³P. L. Kuhns, S.-H. Lee, C. Coretsopoulos, P. C. Hammel, O. Gonen, and J. S. Waugh, “A low temperature NMR probe for use in a dilution refrigerator”, *Rev. Sci. Instrum.* **62**, 2159–2162 (1991), <http://dx.doi.org/10.1063/1.1142332>.
- ²²⁴A. Kushino, S. Kasai, S. Kohjiro, S. Shiki, and M. Ohkubo, “Development of Superconducting Coaxial Cables for Cryogenic Detectors”, *J. Low Temp. Phys.* **151**, 650–654 (2008), <http://dx.doi.org/10.1007/s10909-008-9721-x>.
- ²²⁵B. Lake, A. M. Tselik, S. Notbohm, D. A. Tennant, T. G. Perring, M. Reehuis, C. Sekar, G. Krabbes, and B. Büchner, “Confinement of fractional quantum number particles in a condensed-matter system”, *Nat. Phys.* **6**, 50–55 (2010), <http://dx.doi.org/10.1038/nphys1462>.
- ²²⁶LAPACK — *Linear Algebra PACKage*, <http://www.netlib.org/lapack/>.
- ²²⁷A. Lavarélo and G. Roux, “Spinon excitation spectra of the J_1 - J_2 chain from analytical calculations in the dimer basis and exact diagonalization”, *Eur. Phys. J. B* **87**, 229 (2014), <http://dx.doi.org/10.1140/epjb/e2014-50472-x>.
- ²²⁸A. Lavarélo, G. Roux, and N. Laflorencie, “Melting of a frustration-induced dimer crystal and incommensurability in the J_1 - J_2 two-leg ladder”, *Phys. Rev. B* **84**, 144407 (2011), <http://dx.doi.org/10.1103/PhysRevB.84.144407>.
- ²²⁹M. H. Levitt, *Spin Dynamics*, Basics of Nuclear Magnetic Resonance, 2nd edition (John Wiley & Sons, Ltd., Chichester, UK, 2008), ISBN: 978-0-470-51117-6.
- ²³⁰S. Liang, B. Doucot, and P. W. Anderson, “Some New Variational Resonating-Valence-Bond-Type Wave Functions for the Spin- $\frac{1}{2}$ Antiferromagnetic Heisenberg Model on a Square Lattice”, *Phys. Rev. Lett.* **61**, 365–368 (1988), <http://dx.doi.org/10.1103/PhysRevLett.61.365>.
- ²³¹X. Liang and W. Weimin, “A radio-frequency source using direct digital synthesis and field programmable gate array for nuclear magnetic resonance”, *Rev. Sci. Instrum.* **80**, 124703 (2009), <http://dx.doi.org/10.1063/1.3271379>.
- ²³²X. Liang, S. Binghe, M. Yueping, and Z. Ruyan, “A digital magnetic resonance imaging spectrometer using digital signal processor and field programmable gate array”, *Rev. Sci. Instrum.* **84**, 054702 (2013), <http://dx.doi.org/10.1063/1.4803007>.
- ²³³E. Lieb, T. Schultz, and D. Mattis, “Two Soluble Models of an Antiferromagnetic Chain”, *Ann. Phys.* **16**, 407–466 (1961), [http://dx.doi.org/10.1016/0003-4916\(61\)90115-4](http://dx.doi.org/10.1016/0003-4916(61)90115-4).
- ²³⁴I. M. Lifshitz, “Anomalies of electron characteristics of a metal in the high pressure region”, *Sov. Phys. JETP* **11**, 1130–1135 (1960), <http://www.jetp.ac.ru/cgi-bin/e/index/e/11/5/p1130?a=list>.
- ²³⁵W. Low, “Paramagnetic Resonance in Solids”, in *Solid State Physics*, Advances in Research and Applications, Vol. 2, edited by F. Seitz and D. Turnbull (Academic Press, New York and London, 1960), ISBN: 978-0-12-607702-5, III. Paramagnetic Resonance Spectra of the Transition Elements in Single Crystals (pp. 76-148), [http://dx.doi.org/10.1016/S0081-1947\(08\)60713-4](http://dx.doi.org/10.1016/S0081-1947(08)60713-4).
- ²³⁶P. Löwenborg, *Digital Time-Interleaved ADC Mismatch Error Correction Embedded into High-Performance Digitizers*, Whitepaper 13-1004 (Signal Processing Devices Sweden AB, 2013), https://spdevices.com/images/stories/white_papers/13-1004_adx_and_digitizers.pdf.

- ²³⁷C. S. Lue, S. C. Chen, C. N. Kuo, and F. C. Chou, “⁵¹V NMR study of the spin-gap compound BiCu₂VO₆: A microscopic probe of magnetic interactions”, *Phys. Rev. B* **80**, 092407 (2009), <http://dx.doi.org/10.1103/PhysRevB.80.092407>.
- ²³⁸H. D. Lüke, “The Origins of the Sampling Theorem”, *IEEE Commun. Mag.* **37**, 106–108 (1999), <http://dx.doi.org/10.1109/35.755459>.
- ²³⁹A. Luther and I. Peschel, “Calculation of critical exponents in two dimensions from quantum field theory in one dimension”, *Phys. Rev. B* **12**, 3908–3917 (1975), <http://dx.doi.org/10.1103/PhysRevB.12.3908>.
- ²⁴⁰A. M. Läuchli, J. Sudan, and A. Läuscher, “The frustrated ferromagnetic S = 1/2 Heisenberg chain in a magnetic field – How multipolar spin correlations emerge from magnetically ordered states”, *J. Phys. Conf. Ser.* **145**, 012057 (2009), <http://dx.doi.org/10.1088/1742-6596/145/1/012057>.
- ²⁴¹C. K. Majumdar and D. K. Ghosh, “On Next-Nearest-Neighbor Interaction in Linear Chain. I”, *J. Math. Phys.* **10**, 1388–1398 (1969), <http://dx.doi.org/10.1063/1.1664978>.
- ²⁴²C. K. Majumdar and D. K. Ghosh, “On Next-Nearest-Neighbor Interaction in Linear Chain. II”, *J. Math. Phys.* **10**, 1399–1402 (1969), <http://dx.doi.org/10.1063/1.1664979>.
- ²⁴³K. Maki and P. Kumar, “Magnetic solitons in superfluid ³He”, *Phys. Rev. B* **14**, 118–127 (1976), <http://dx.doi.org/10.1103/PhysRevB.14.118>.
- ²⁴⁴L. G. Maloratsky, “Reviewing The Basics Of Microstrip Lines”, *Microwaves & RF* **March 2000**, 79–88.
- ²⁴⁵M. Marin, S. Barkeshli, and P. H. Pathak, “Efficient Analysis of Planar Microstrip Geometries Using a Closed-Form Asymptotic Representation of the Grounded Dielectric Slab Green’s Function”, *IEEE Trans. Microwave Theory Tech.* **37**, 669–679 (1989), <http://dx.doi.org/10.1109/22.18838>.
- ²⁴⁶W. Marshall, “Antiferromagnetism”, *Proc. R. Soc. Lond. A* **232**, 48–68 (1955), <http://dx.doi.org/10.1098/rspa.1955.0200>.
- ²⁴⁷B. R. Martin and G. Shaw, *Particle Physics*, 3rd edition, Manchester Physics Series (John Wiley & Sons, Ltd., Chichester, UK, 2008), ISBN: 978-0-470-03293-0.
- ²⁴⁸T. Masuda, A. Zheludev, H. Kageyama, and A. N. Vasiliev, “BiCu₂VO₆ : A new narrow-band spin-gap material”, *Europhys. Lett.* **63**, 757–763 (2003), <http://dx.doi.org/10.1209/epl/i2003-00467-y>.
- ²⁴⁹T. Masuda, M. Hagihala, Y. Kondoh, K. Kaneko, and N. Metoki, “Spin Density Wave in Insulating Ferromagnetic Frustrated Chain LiCuVO₄”, *J. Phys. Soc. Jpn.* **80**, 113705 (2011), <http://dx.doi.org/10.1143/JPSJ.80.113705>.
- ²⁵⁰*MathWorks MATLAB*, <https://www.mathworks.com/products/matlab.html>.
- ²⁵¹T. Matsubara and H. Matsuda, “A Lattice Model of Liquid Helium, I”, *Prog. Theor. Phys.* **16**, 569–582 (1956), <http://dx.doi.org/10.1143/PTP.16.569>.
- ²⁵²M. Matsumoto, B. Normand, T. M. Rice, and M. Sgrist, “Magnon Dispersion in the Field-Induced Magnetically Ordered Phase of TlCuCl₃”, *Phys. Rev. Lett.* **89**, 077203 (2002), <http://dx.doi.org/10.1103/PhysRevLett.89.077203>.
- ²⁵³M. Matsumoto, C. Yasuda, S. Todo, and H. Takayama, “Ground-state phase diagram of quantum Heisenberg antiferromagnets on the anisotropic dimerized square lattice”, *Phys. Rev. B* **65**, 014407 (2001), <http://dx.doi.org/10.1103/PhysRevB.65.014407>.

- ²⁵⁴R. A. Matula, “Electrical Resistivity of Copper, Gold, Palladium, and Silver”, *J. Phys. Chem. Ref. Data* **8**, 1147–1298 (1979), <http://dx.doi.org/10.1063/1.555614>.
- ²⁵⁵I. P. McCulloch, R. Kube, M. Kurz, A. Kleine, U. Schollwöck, and A. K. Kolezhuk, “Vector chiral order in frustrated spin chains”, *Phys. Rev. B* **77**, 094404 (2008), <http://dx.doi.org/10.1103/PhysRevB.77.094404>.
- ²⁵⁶D. McMorrow and H. Rønnow, *Spec1d*, version April 2001, <https://www.ill.eu/html/instruments-support/computing-for-science/cs-software/all-software/matlab-ill/spec1d/>.
- ²⁵⁷O. Mentré, E. Janod, P. Rabu, M. Hennion, F. Leclercq-Hugeux, J. Kang, C. Lee, M.-H. Whangbo, and S. Petit, “Incommensurate spin correlation driven by frustration in BiCu_2PO_6 ”, *Phys. Rev. B* **80**, 180413(R) (2009), <http://dx.doi.org/10.1103/PhysRevB.80.180413>.
- ²⁵⁸O. Mentré, E. M. Ketatni, M. Colmont, M. Huvé, F. Abraham, and V. Petricek, “Structural Features of the Modulated $\text{BiCu}_2(\text{P}_{1-x}\text{V}_x)\text{O}_6$ Solid Solution; 4-D Treatment of $x = 0.87$ Compound and Magnetic Spin-Gap to Gapless Transition in New Cu^{2+} Two-Leg Ladder Systems”, *J. Am. Chem. Soc.* **128**, 10857–10867 (2006), <http://dx.doi.org/10.1021/ja0631091>.
- ²⁵⁹P. L. H. Merchant, “Excitations and Criticality in Quantum Magnets”, PhD thesis (University College London, London, UK, 2012), <http://discovery.ucl.ac.uk/id/eprint/1388128>.
- ²⁶⁰N. D. Mermin and H. Wagner, “Absence of Ferromagnetism or Antiferromagnetism in One- or Two-Dimensional Isotropic Heisenberg Models”, *Phys. Rev. Lett.* **17**, 1133–1136 (1966), <http://dx.doi.org/10.1103/PhysRevLett.17.1133>.
- ²⁶¹N. Metropolis, A. W. Rosenbluth, M. N. Rosenbluth, A. H. Teller, and E. Teller, “Equation of State Calculations by Fast Computing Machines”, *J. Chem. Phys.* **21**, 1087–1092 (1953), <http://dx.doi.org/10.1063/1.1699114>.
- ²⁶²Y. Meurdesoif and A. Buzdin, “Soliton structure in spin-Peierls systems”, *Phys. Rev. B* **59**, 11165–11168 (1999), <http://dx.doi.org/10.1103/PhysRevB.59.11165>.
- ²⁶³U. Meyer-Baese, “Multirate Signal Processing”, in *Digital Signal Processing with Field Programmable Gate Arrays*, 1st edition (reprint) (Springer, Berlin Heidelberg, Germany, 2001), ISBN: 978-3-662-04613-5, pp. 143–207, http://dx.doi.org/10.1007/978-3-662-04613-5_5.
- ²⁶⁴C. A. Michal, K. Broughton, and E. Hansen, “A high performance digital receiver for home-built nuclear magnetic resonance spectrometers”, *Rev. Sci. Instrum.* **73**, 453–458 (2002), <http://dx.doi.org/10.1063/1.1433950>.
- ²⁶⁵H.-J. Mikeska and M. Steiner, “Solitary excitations in one-dimensional magnets”, *Adv. Phys.* **40**, 191–356 (1991), <http://dx.doi.org/10.1080/00018739100101492>.
- ²⁶⁶H.-J. Mikeska, U. Neugebauer, and U. Schollwöck, “Spin ladders with nonmagnetic impurities”, *Phys. Rev. B* **55**, 2955–2963 (1997), <http://dx.doi.org/10.1103/PhysRevB.55.2955>.
- ²⁶⁷N. P. Mikhin, N. F. Omelaenko, A. V. Polev, E. Ya. Rudavskii, and V. A. Shvarts, “Thermomagnetic relaxation in two-phase solid ^3He – ^4He mixtures at ultralow temperatures”, *Low Temp. Phys.* **24**, 845–851 (1998), <http://dx.doi.org/10.1063/1.593522>.
- ²⁶⁸J. Miles, “R Squared, Adjusted R Squared”, in *Wiley StatsRef: Statistics Reference Online* (John Wiley & Sons, Ltd., 2014), ISBN: 9781118445112, <http://dx.doi.org/10.1002/9781118445112.stat06627>, re-published on-line 29th September 2014.
- ²⁶⁹J. R. Miller, “The NHMFL 45-T Hybrid Magnet System: Past, Present, and Future”, *IEEE Trans. Appl. Supercond.* **13**, 1385–1390 (2003), <http://dx.doi.org/10.1109/TASC.2003.812673>.

- ²⁷⁰S. Miyahara, J.-B. Fouet, S. R. Manmana, R. M. Noack, H. Mayaffre, I. Sheikin, C. Berthier, and F. Mila, “Uniform and staggered magnetizations induced by Dzyaloshinskii-Moriya interactions in isolated and coupled spin-1/2 dimers in a magnetic field”, *Phys. Rev. B* **75**, 184402 (2007), <http://dx.doi.org/10.1103/PhysRevB.75.184402>.
- ²⁷¹S. Mombetsu, T. Murazumi, K. Hiura, S. Yamazaki, Y. Shimizu, H. Hidaka, T. Yanagisawa, H. Amitsuka, S. Yasin, S. Zherlitsyn, and J. Wosnitzer, “High Magnetic Field Study of Elastic Constants of the Cage-structure Compound SmBe_{13} ”, *J. Phys. Conf. Ser.* **683**, 012032 (2016), <http://dx.doi.org/10.1088/1742-6596/683/1/012032>.
- ²⁷²K. Momma and F. Izumi, “VESTA 3 for three-dimensional visualization of crystal, volumetric and morphology data”, *J. Appl. Crystallogr.* **44**, 1272–1276 (2011), <http://dx.doi.org/10.1107/S0021889811038970>.
- ²⁷³F. Momo, A. Sotgiu, L. Testa, and A. Zanin, “Digital frequency synthesizers for nuclear magnetic resonance spectroscopy”, *Rev. Sci. Instrum.* **65**, 3291–3292 (1994), <http://dx.doi.org/10.1063/1.1144567>.
- ²⁷⁴L. Mondaini, “The Rise of Solitons in Sine-Gordon Field Theory: From Jacobi Amplitude to Guder-mannian Function”, *J. Appl. Math. Phys.* **2**, 1202–1206 (2014), <http://dx.doi.org/10.4236/jamp.2014.213141>.
- ²⁷⁵T. Moriya, “Anisotropic Superexchange Interaction and Weak Ferromagnetism”, *Phys. Rev.* **120**, 91–98 (1960), <http://dx.doi.org/10.1103/PhysRev.120.91>.
- ²⁷⁶T. Moriya, “New Mechanism of Anisotropic Superexchange Interaction”, *Phys. Rev. Lett.* **4**, 228–230 (1960), <http://dx.doi.org/10.1103/PhysRevLett.4.228>.
- ²⁷⁷R. Moskowitz and E. Della Torre, “Theoretical Aspects of Demagnetization Tensors”, *IEEE Trans. Magn.* **2**, 739–744 (1966), <http://dx.doi.org/10.1109/TMAG.1966.1065973>.
- ²⁷⁸M. Mostovoy, “Ferroelectricity in Spiral Magnets”, *Phys. Rev. Lett.* **96**, 067601 (2006), <http://dx.doi.org/10.1103/PhysRevLett.96.067601>.
- ²⁷⁹M. Morigal, M. Enderle, R. K. Kremer, J. M. Law, and B. Fåk, “Ferroelectricity from spin super-currents in LiCuVO_4 ”, *Phys. Rev. B* **83**, 100409(R) (2011), <http://dx.doi.org/10.1103/PhysRevB.83.100409>.
- ²⁸⁰M. Morigal, M. Enderle, B. Fåk, R. K. Kremer, J. M. Law, A. Schneidewind, A. Hiess, and A. Prokofiev, “Evidence of a Bond-Nematic Phase in LiCuVO_4 ”, *Phys. Rev. Lett.* **109**, 027203 (2012), <http://dx.doi.org/10.1103/PhysRevLett.109.027203>.
- ²⁸¹*MPI-Bash*, Los Alamos National Security, LLC (LANS), <https://github.com/lanl/MPI-Bash/>.
- ²⁸²S. M. Musa and M. N. O. Sadiku, “Calculating the Capacitance of Shielded Microstrip Lines”, *Proceedings of the COMSOL Conference 2007, Boston, MA, USA*, 61–64 (2007).
- ²⁸³S. M. Musa and M. N. O. Sadiku, “Using finite element method to calculate capacitance, inductance, characteristic impedance of open microstrip lines”, *Microwave Opt. Technol. Lett.* **50**, 611–614 (2008), <http://dx.doi.org/10.1002/mop.23164>.
- ²⁸⁴H. Nagasawa, T. Kawamata, K. Naruse, M. Ohno, Y. Matsuoka, H. Sudo, Y. Hagiya, M. Fujita, T. Sasaki, and Y. Koike, “Thermal Conductivity in the Frustrated Two-Leg Spin-Ladder System BiCu_2PO_6 ”, *J. Phys. Conf. Ser.* **568**, 042012 (2014), <http://dx.doi.org/10.1088/1742-6596/568/4/042012>.

- ²⁸⁵T. Nakano and H. Fukuyama, “Solitons in Spin-Peierls Systems and Applications to Polyacetylene”, *J. Phys. Soc. Jpn.* **49**, 1679–1691 (1980), <http://dx.doi.org/10.1143/JPSJ.49.1679>.
- ²⁸⁶T. Nakano and H. Fukuyama, “Dimerization and Solitons in One-Dimensional XY-Z Antiferromagnets”, *J. Phys. Soc. Jpn.* **50**, 2489–2499 (1981), <http://dx.doi.org/10.1143/JPSJ.50.2489>.
- ²⁸⁷N. D. Narakidze, D. V. Shaykhtudinov, K. M. Shirokov, N. I. Gorbatenko, and S. G. Yanvarev, “Development and implementation of the NMR-spectrometer on the basis of the National Instruments technologies”, *IOP Conf. Series: Materials Science and Engineering* **177**, 012112 (2017), <http://dx.doi.org/10.1088/1757-899X/177/1/012112>.
- ²⁸⁸G. C. do Nascimento, M. Engelsberg, and R. E. de Souza, “Digital NMR imaging system for ultralow magnetic fields”, *Meas. Sci. Technol.* **3**, 370–374 (1992), <http://dx.doi.org/10.1088/0957-0233/3/4/006>.
- ²⁸⁹R. Nath, K. M. Ranjith, B. Roy, D. C. Johnston, Y. Furukawa, and A. A. Tsirlin, “Magnetic transitions in the spin- $\frac{5}{2}$ frustrated magnet BiMn_2PO_6 and strong lattice softening in BiMn_2PO_6 and BiZn_2PO_6 below 200 K”, *Phys. Rev. B* **90**, 024431 (2014), <http://dx.doi.org/10.1103/PhysRevB.90.024431>.
- ²⁹⁰A. A. Nersesyan and A. M. Tselik, “One-Dimensional Spin-Liquid without Magnon Excitations”, *Phys. Rev. Lett.* **78**, 3939–3942 (1997), <http://dx.doi.org/10.1103/PhysRevLett.79.1171>.
- ²⁹¹A. A. Nersesyan, A. O. Gogolin, and F. H. L. Eßler, “Incommensurate Spin Correlations in Spin-1/2 Frustrated Two-Leg Heisenberg Ladders”, *Phys. Rev. Lett.* **81**, 910–913 (1998), <http://dx.doi.org/10.1103/PhysRevLett.81.910>.
- ²⁹²B. R. A. Nijboer and F. W. De Wette, “On the calculation of lattice sums”, *Physica* **23**, 309–321 (1957), [http://dx.doi.org/10.1016/S0031-8914\(57\)92124-9](http://dx.doi.org/10.1016/S0031-8914(57)92124-9).
- ²⁹³T. Nikuni, M. Oshikawa, A. Oosawa, and H. Tanaka, “Bose-Einstein Condensation of Dilute Magnons in TlCuCl_3 ”, *Phys. Rev. Lett.* **84**, 5868–5871 (2000), <http://dx.doi.org/10.1103/PhysRevLett.84.5868>.
- ²⁹⁴*NMR line*. National High Magnetic Field Laboratory, Tallahassee, FL, USA, https://nationalmaglab.org/images/users/dc_field/magnets/45tesla/cell15_nmrline.jpg (retrieved 09.03.2017, index at <https://nationalmaglab.org/user-facilities/dc-field/instruments-dcfield/resistive-magnets/45-tesla-2>).
- ²⁹⁵K. Nomura and K. Okamoto, “Critical properties of $S=1/2$ antiferromagnetic XXZ chain with next-nearest-neighbour interactions”, *J. Phys. A: Math. Gen.* **27**, 5773–5788 (1994), <http://dx.doi.org/10.1088/0305-4470/27/17/012>.
- ²⁹⁶K. Nomura, J. Morishige, and T. Isoyama, “Extension of the Lieb–Schultz–Mattis theorem”, *J. Phys. A: Math. Theor.* **48**, 375001 (2015), <http://dx.doi.org/10.1088/1751-8113/48/37/375001>.
- ²⁹⁷B. Normand and F. Mila, “Absence of effective spins $\frac{1}{2}$ induced by nonmagnetic impurities in a class of low-dimensional magnets”, *Phys. Rev. B* **65**, 104411 (2002), <http://dx.doi.org/10.1103/PhysRevB.65.104411>.
- ²⁹⁸S. Notbohm, P. Ribeiro, B. Lake, D. A. Tennant, K. P. Schmidt, G. S. Uhrig, C. Hess, R. Klingeler, G. Behr, B. Büchner, M. Reehuis, R. I. Bewley, C. D. Frost, P. Manuel, and R. S. Eccleston, “One- and Two-Triplon Spectra of a Cuprate Ladder”, *Phys. Rev. Lett.* **98**, 027403 (2007), <http://dx.doi.org/10.1103/PhysRevLett.98.027403>.
- ²⁹⁹J. Okamoto, “Theoretical study of charge density waves in transition metal materials”, PhD thesis (Columbia University, New York, NY, USA, 2014), <https://doi.org/10.7916/D8N0155M>.
- ³⁰⁰K. Okunishi, “On Calculation of Vector Spin Chirality for Zigzag Spin Chains”, *J. Phys. Soc. Jpn.* **77**, 114004 (2008), <http://dx.doi.org/10.1143/JPSJ.77.114004>.

- ³⁰¹K. Okunishi and T. Tonegawa, “Fractional S^z excitation and its bound state around the $1/3$ plateau of the $S = 1/2$ Ising-like zigzag XXZ chain”, *Phys. Rev. B* **68**, 224422 (2003), <http://dx.doi.org/10.1103/PhysRevB.68.224422>.
- ³⁰²K. Okunishi and T. Tonegawa, “Magnetic Phase Diagram of the $S=1/2$ Antiferromagnetic Zigzag Spin Chain in the Strongly Frustrated Region: Cusp and Plateau”, *J. Phys. Soc. Jpn.* **72**, 479–482 (2003), <http://dx.doi.org/10.1143/JPSJ.72.479>.
- ³⁰³J. R. Olson, “Thermal conductivity of some common cryostat materials between 0.05 and 2 K”, *Cryogenics* **33**, 729–731 (1993), [http://dx.doi.org/10.1016/0011-2275\(93\)90027-L](http://dx.doi.org/10.1016/0011-2275(93)90027-L).
- ³⁰⁴S. Onoda and N. Nagaosa, “Chiral Spin Pairing in Helical Magnets”, *Phys. Rev. Lett.* **99**, 027206 (2007), <http://dx.doi.org/10.1103/PhysRevLett.99.027206>.
- ³⁰⁵OriginLab, *Algorithms (Linear Regression)*, <http://www.originlab.com/doc/Origin-Help/LR-Algorithm> (retrieved 06.04.2017).
- ³⁰⁶M. Oshikawa and I. Affleck, “Field-Induced Gap in $S = 1/2$ Antiferromagnetic Chains”, *Phys. Rev. Lett.* **79**, 2883–2886 (1997), <http://dx.doi.org/10.1103/PhysRevLett.79.2883>.
- ³⁰⁷R. P. Owens, J. E. Aitken, and T. C. Edwards, “Quasi-Static Characteristics of Microstrip on an Anisotropic Sapphire Substrate”, *IEEE Trans. Microwave Theory Tech.* **24**, 499–505 (1976), <http://dx.doi.org/10.1109/TMTT.1976.1128887>.
- ³⁰⁸T. Parella, *eNMR, NMR Periodic Table*, BRUKER Analytik GmbH, <http://www.bruker-nmr.de/guide/eNMR/chem/NMRnuclei.html> (accessed 28.02.2017). According to this source, the nominal resonance frequency of the ^{31}P nucleus in a magnetic field of 11.744 T is 202.404 MHz.
- ³⁰⁹R. Pässler, “Non-Debye heat capacity formula refined and applied to GaP, GaAs, GaSb, InP, InAs, and InSb”, *AIP Advances* **3**, 082108 (2013), <http://dx.doi.org/10.1063/1.4818273>.
- ³¹⁰P. Pérez, A. Santos, and J. J. Vaquero, “Potential use of the undersampling technique in the acquisition of nuclear magnetic resonance signals”, *Magn. Reson. Mater. Phys., Biol. Med.* **13**, 109–117 (2001), <http://dx.doi.org/10.1007/BF02668159>.
- ³¹¹M. Pikulski, T. Shiroka, H.-R. Ott, and J. Mesot, “A firmware-defined digital direct-sampling NMR spectrometer for condensed matter physics”, *Rev. Sci. Instrum.* **85**, 093906 (2014), <http://dx.doi.org/10.1063/1.4896351>.
- ³¹²M. Pikulski et al., “Field-induced chirality driving the magnetic order in frustrated low-dimensional spin systems”, latest circulated version (27.12.2016) of unpublished manuscript with supplemental material (2016), incorporating suggestions, corrections, and improvements by H.-R. Ott, T. Shiroka, A. P. Reyes, and J. Mesot.
- ³¹³A. B. Pippard, “Metallic Conduction at High Frequencies and Low Temperatures”, in *Advances in Electronics and Electron Physics*, Vol. 6, edited by L. Marton (Academic Press, Inc., New York, NY, USA, 1954), ISBN: 978-0-12-014506-5, pp. 1-45, [http://dx.doi.org/10.1016/S0065-2539\(08\)60130-4](http://dx.doi.org/10.1016/S0065-2539(08)60130-4).
- ³¹⁴B. Pirvu, F. Verstraete, and G. Vidal, “Exploiting translational invariance in matrix product state simulations of spin chains with periodic boundary conditions”, *Phys. Rev. B* **83**, 125104 (2011), <http://dx.doi.org/10.1103/PhysRevB.83.125104>.
- ³¹⁵M. Plancherel, “Contribution à l’étude de la représentation d’une fonction arbitraire par des intégrales définies”, *Rend. Circ. Matem. Palermo* **30**, 289–335 (1910), <http://dx.doi.org/10.1007/BF03014877>.

- ³¹⁶K. W. Plumb, Z. Yamani, M. Matsuda, G. J. Shu, B. Koteswararao, F. C. Chou, and Y.-J. Kim, “Incommensurate dynamic correlations in the quasi-two-dimensional spin liquid BiCu_2PO_6 ”, *Phys. Rev. B* **88**, 024402 (2013), <http://dx.doi.org/10.1103/PhysRevB.88.024402>.
- ³¹⁷K. W. Plumb, K. Hwang, Y. Qiu, L. W. Harriger, G. E. Granroth, G. J. Shu, F. C. Chou, Ch. Rüegg, Y. B. Kim, and Y.-J. Kim, “Giant Anisotropic Interactions in the Copper Based Quantum Magnet BiCu_2PO_6 ”, e-print (2014), arXiv:1408.2528v1 [cond-mat.str-el].
- ³¹⁸K. W. Plumb, K. Hwang, Y. Qiu, L. W. Harriger, G. E. Granroth, A. I. Kolesnikov, G. J. Shu, F. C. Chou, Ch. Rüegg, Y. B. Kim, and Y.-J. Kim, “Quasiparticle-continuum level repulsion in a quantum magnet”, *Nat. Phys.* **12**, 224–230 (2016), <http://dx.doi.org/10.1038/nphys3566>.
- ³¹⁹K. W. Plumb, “Inelastic Neutron Scattering Studies of Novel Quantum Magnets”, PhD thesis (University of Toronto, Toronto, Ontario, Canada, 2014), <http://hdl.handle.net/1807/68319>.
- ³²⁰F. Pobell, *Matter and Methods at Low Temperatures*, 3rd edition (Springer, Berlin Heidelberg, Germany, 2007), ISBN: 978-3-540-46360-3, <http://dx.doi.org/10.1007/978-3-540-46360-3>.
- ³²¹E. Polizzi, “Density-matrix-based algorithm for solving eigenvalue problems”, *Phys. Rev. B* **79**, 115112 (2009), <http://dx.doi.org/10.1103/PhysRevB.79.115112>.
- ³²²L. Pollack, E. N. Smith, J. M. Parpia, and R. C. Richardson, “Determination of the Electric Field Gradient and Relaxation Time Measurements in Scandium Metal at Very Low Temperature”, *J. Low Temp. Phys.* **87**, 753–772 (1992), <http://dx.doi.org/10.1007/BF00118333>.
- ³²³P. Poshala, *Why Oversample when Undersampling can do the Job?*, Application Report SLAA594A (Texas Instruments, July 2013), <http://www.ti.com/lit/pdf/slaa594>.
- ³²⁴D. M. Pozar, *Microwave Engineering*, 3rd edition (John Wiley & Sons, Inc., Hoboken, NJ, USA, 2005), ISBN: 0-471-44878-8.
- ³²⁵N. Prasai, “Spin-Phonon Coupling and Magnetic Heat Transport in Low-Dimensional Quantum Antiferromagnets”, PhD thesis (University of Miami, Miami, FL, USA, 2015), http://scholarlyrepository.miami.edu/oa_dissertations/1421.
- ³²⁶*Python*, <https://www.python.org>.
- ³²⁷X. Qin, S. Jie, L. Jianqi, and L. Gengying, “Compensation for unknown acquisition delay caused by digital receiver without external synchronization in NMR and MRI”, *Magn. Reson. Mater. Phys., Biol. Med.* **18**, 217–224 (2005), <http://dx.doi.org/10.1007/s10334-005-0121-9>.
- ³²⁸I. Radosavljevic, J. S. O. Evans, and A. W. Sleight, “Synthesis and Structure of Bismuth Copper Vanadate, BiCu_2VO_6 ”, *J. Solid State Chem.* **141**, 149–154 (1998), <http://dx.doi.org/10.1006/jssc.1998.7931>.
- ³²⁹N. F. Ramsey, “Electron Coupled Interactions between Nuclear Spins in Molecules”, *Phys. Rev.* **91**, 303–307 (1953), <http://dx.doi.org/10.1103/PhysRev.91.303>.
- ³³⁰J. C. Rautio and V. Demir, “Microstrip Conductor Loss Models for Electromagnetic Analysis”, *IEEE Trans. Microwave Theory Tech.* **51**, 915–921 (2003), <http://dx.doi.org/10.1109/TMTT.2003.808693>.
- ³³¹D. B. Reeves, *An introduction to topological defects in field theories*, <http://www.dartmouth.edu/~dbr/topdefects.pdf> (dated 07.03.2014, retrieved 18.06.2015).
- ³³²M. J. Rice, A. R. Bishop, J. A. Krumhansl, and S. E. Trullinger, “Weakly Pinned Fröhlich Charge-Density-Wave Condensates: A New, Nonlinear, Current-Carrying Elementary Excitation”, *Phys. Rev. Lett.* **36**, 432–435 (1976), <http://dx.doi.org/10.1103/PhysRevLett.36.432>.

- ³³³T. M. Rice, S. Gopalan, and M. Sigrist, “Superconductivity, Spin Gaps and Luttinger Liquids in a Class of Cuprates”, *Europhys. Lett.* **23**, 445–449 (1993), <http://dx.doi.org/10.1209/0295-5075/23/6/011>.
- ³³⁴P. C. Riedi, “Magnetic studies with zero field NMR”, *Hyperfine Interact.* **49**, 335–355 (1989), <http://dx.doi.org/10.1007/BF02405148>.
- ³³⁵I. D. Robertson, *Microstrip lines (2008)*, http://prof-robertson.com/index_files/MICROSTRIP.pdf (retrieved 16.08.2013, available via https://web.archive.org/web/20120131040300/http://prof-robertson.com/index_files/MICROSTRIP.pdf).
- ³³⁶H. M. Rønnow, M. Enderle, D. F. McMorrow, L.-P. Regnault, G. Dhahlenne, A. Revcolevschi, A. Hoser, K. Prokes, P. Vorderwisch, and H. Schneider, “Neutron Scattering Study of the Field-Induced Soliton Lattice in CuGeO_3 ”, *Phys. Rev. Lett.* **84**, 4469–4472 (2000), <http://dx.doi.org/10.1103/PhysRevLett.84.4469>.
- ³³⁷B. Rosas, *The Design & Test of Broadband Launches up to 50 GHz on Thin & Thick Substrates*, Technical Article (Southwest Microwave, Inc., USA), available via <http://mpd.southwestmicrowave.com/resources/> (retrieved 16.08.2013).
- ³³⁸C. Rose and M. J. Gans, “A Dielectric-Free Superconducting Coaxial Cable”, *IEEE Trans. Microwave Theory Tech.* **38**, 166–177 (1990), <http://dx.doi.org/10.1109/22.46427>.
- ³³⁹I. Rosu, *Microstrip, Stripline, and CPW Design*, http://www.qsl.net/va3iul/Microstrip_Stripline_CPW_Design/Microstrip_Stripline_and_CPW_Design.pdf (retrieved 13.08.2013).
- ³⁴⁰Ch. Rüegg, K. Kiefer, B. Thielemann, D. F. McMorrow, V. Zapf, B. Normand, M. B. Zvonarev, P. Bouillot, C. Kollath, T. Giamarchi, S. Capponi, D. Poilblanc, D. Biner, and K. W. Krämer, “Thermodynamics of the Spin Luttinger Liquid in a Model Ladder Material”, *Phys. Rev. Lett.* **101**, 247202 (2008), <http://dx.doi.org/10.1103/PhysRevLett.101.247202>.
- ³⁴¹N. RUIPENG, D. YIDONG, Y. GUANG, and L. GENGYING, “A digital receiver with fast frequency- and gain-switching capabilities for MRI systems”, *Magn. Reson. Mater. Phys., Biol. Med.* **22**, 333–342 (2009), <http://dx.doi.org/10.1007/s10334-009-0182-2>.
- ³⁴²S. Sachdev and K. Damle, “Low Temperature Spin Diffusion in the One-Dimensional Quantum $O(3)$ Nonlinear σ Model”, *Phys. Rev. Lett.* **78**, 943–946 (1997), <http://dx.doi.org/10.1103/PhysRevLett.78.943>.
- ³⁴³J. J. Sakurai and J. Napolitano, *Modern Quantum Mechanics*, 2nd edition (Addison-Wesley, San Francisco, CA, USA, 2010), ISBN: 978-0-8053-8291-4.
- ³⁴⁴A. W. Sandvik, “An Introduction to Quantum Monte Carlo Methods”, in *Strongly Correlated Magnetic and Superconducting Systems: Proceedings of the El Escorial Summer School Held in Madrid, Spain, 15-19 July 1996*, edited by G. Sierra and M. A. Martín-Delgado (Springer, Berlin Heidelberg, Germany, 1997), ISBN: 978-3-540-49734-9, pp. 109-135, <http://dx.doi.org/10.1007/BFb0104635>.
- ³⁴⁵M. Sato, T. Hikihara, and T. Momoi, “Spin-Nematic and Spin-Density-Wave Orders in Spatially Anisotropic Frustrated Magnets in a Magnetic Field”, *Phys. Rev. Lett.* **110**, 077206 (2013), <http://dx.doi.org/10.1103/PhysRevLett.110.077206>.
- ³⁴⁶*ScaLAPACK — Scalable Linear Algebra PACKage*, <http://www.netlib.org/scalapack/>.
- ³⁴⁷D. Schmidiger, K. Yu. Povarov, S. Galeski, N. Reynolds, R. Bewley, T. Guidi, J. Ollivier, and A. Zheludev, “Emergent Interacting Spin Islands in a Depleted Strong-Leg Heisenberg Ladder”, *Phys. Rev. Lett.* **116**, 257203 (2016), <http://dx.doi.org/10.1103/PhysRevLett.116.257203>.

- ³⁴⁸U. Schollwöck, Th. Jolicœur, and T. Garel, “Onset of incommensurability at the valence-bond-solid point in the $S=1$ quantum spin chain”, *Phys. Rev. B* **53**, 3304–3311 (1996), <http://dx.doi.org/10.1103/PhysRevB.53.3304>.
- ³⁴⁹U. Schollwöck, “DMRG: Ground States, Time Evolution, and Spectral Functions”, in *Emergent Phenomena in Correlated Matter*, edited by E. Pavarini, E. Koch, and U. Schollwöck, Modeling and Simulation Vol. 3, Schriften des Forschungszentrums Jülich (Forschungszentrum Jülich GmbH, Jülich, Germany, 2013), ISBN: 978-3-89336-884-6, <http://hdl.handle.net/2128/5389>, pp. 16.1-16.34.
- ³⁵⁰U. Schollwöck, “The density-matrix renormalization group in the age of matrix product states”, *Ann. Phys.* **326**, 96–192 (2011), <http://dx.doi.org/10.1016/j.aop.2010.09.012>.
- ³⁵¹H. J. Schulz, “Phase diagrams and correlation exponents for quantum spin chains of arbitrary spin quantum number”, *Phys. Rev. B* **34**, 6372–6385 (1986), <http://dx.doi.org/10.1103/PhysRevB.34.6372>.
- ³⁵²H. J. Schulz, “Wigner Crystal in One Dimension”, *Phys. Rev. Lett.* **71**, 1864–1867 (1993), <http://dx.doi.org/10.1103/PhysRevLett.71.1864>.
- ³⁵³F. Schwabl, *Statistical Mechanics*, trans. by W. Brewer, 2nd edition (Springer, Berlin Heidelberg, Germany, 2006), ISBN: 978-3-540-36217-3, <http://dx.doi.org/10.1007/3-540-36217-7>.
- ³⁵⁴T. Scott and M. Giles, “Dislocation Scattering in Teflon at Low Temperatures”, *Phys. Rev. Lett.* **29**, 642–643 (1972), <http://dx.doi.org/10.1103/PhysRevLett.29.642>.
- ³⁵⁵C. Senatore, *Switzerland winds up superconductivity*, <http://www.unige.ch/communication/press-release/2016/CdP080616EN.html> (dated 08.06.2016, accessed 01.04.2017.; also available via <https://web.archive.org/web/20160924183540/http://www.unige.ch/communication/press-release/2016/CdP080616EN.html>).
- ³⁵⁶I. A. Sergienko and E. Dagotto, “Role of the Dzyaloshinskii-Moriya interaction in multiferroic perovskites”, *Phys. Rev. B* **73**, 094434 (2006), <http://dx.doi.org/10.1103/PhysRevB.73.094434>.
- ³⁵⁷J. K. N. Sharma, “Heat conductivities below 1° K. I”, *Cryogenics* **7**, 141–156 (1967), [http://dx.doi.org/10.1016/S0011-2275\(67\)80054-7](http://dx.doi.org/10.1016/S0011-2275(67)80054-7).
- ³⁵⁸B. S. Shastry and B. Sutherland, “Excitation Spectrum of a Dimerized Next-Neighbor Antiferromagnetic Chain”, *Phys. Rev. Lett.* **47**, 964–967 (1981), <http://dx.doi.org/10.1103/PhysRevLett.47.964>.
- ³⁵⁹L. Shekhtman, O. Entin-Wohlman, and A. Aharony, “Moriya’s Anisotropic Superexchange Interaction, Frustration, and Dzyaloshinsky’s Weak Ferromagnetism”, *Phys. Rev. Lett.* **69**, 836–839 (1992), <http://dx.doi.org/10.1103/PhysRevLett.69.836>.
- ³⁶⁰D. G. Shelton, A. A. Nersesyan, and A. M. Tsvelik, “Antiferromagnetic spin ladders: Crossover between spin $S=1/2$ and $S=1$ chains”, *Phys. Rev. B* **53**, 8521–8532 (1996), <http://dx.doi.org/10.1103/PhysRevB.53.8521>.
- ³⁶¹N. Shibata and C. Hotta, “Boundary effects in the density-matrix renormalization group calculation”, *Phys. Rev. B* **84**, 115116 (2011), <http://dx.doi.org/10.1103/PhysRevB.84.115116>.
- ³⁶²C. Shih, R.-B. Wu, S.-K. Jeng, and C. H. Chen, “A Full-Wave Analysis of Microstrip Lines by Variational Conformal Mapping Technique”, *IEEE Trans. Microwave Theory Tech.* **36**, 576–581 (1988), <http://dx.doi.org/10.1109/22.3551>.
- ³⁶³T. Shiroka, F. Casola, V. Glazkov, A. Zheludev, K. Prša, H.-R. Ott, and J. Mesot, “Distribution of NMR Relaxations in a Random Heisenberg Chain”, *Phys. Rev. Lett.* **106**, 137202 (2011), <http://dx.doi.org/10.1103/PhysRevLett.106.137202>.

- ³⁶⁴T. Shiroka, F. Casola, J. Mesot, W. Bachmann, and H.-R. Ott, “A two-axis goniometer for low-temperature nuclear magnetic resonance measurements on single crystals”, *Rev. Sci. Instrum.* **83**, 093901 (2012), <http://dx.doi.org/10.1063/1.4748861>.
- ³⁶⁵B. S. Shivaram, V. W. Ulrich, P. Kumar, and V. Celli, “High-field ultrasound measurements in UPt_3 and the single-energy-scale model of metamagnetism”, *Phys. Rev. B* **91**, 115110 (2015), <http://dx.doi.org/10.1103/PhysRevB.91.115110>.
- ³⁶⁶A. A. Shubin and S. A. Dikanov, “Determination of Hyperfine Tensor Components from Nuclear Frequencies at Canonical Orientations of the g -Tensor”, *J. Magn. Reson.* **155**, 100–105 (2002), <http://dx.doi.org/10.1006/jmre.2002.2509>.
- ³⁶⁷I. T. Shyiko, I. P. McCulloch, J. V. Gumenjuk-Sichevska, and A. K. Kolezhuk, “Double zigzag spin chain in a strong magnetic field close to saturation”, *Phys. Rev. B* **88**, 014403 (2013), <http://dx.doi.org/10.1103/PhysRevB.88.014403>.
- ³⁶⁸S. Singh and A. Marwaha, “Electromagnetic Wave Analysis of Waveguide and Shielded Microstripline”, *Proceedings of the COMSOL Conference in Bangalore (2012)*, <https://www.comsol.de/paper/electromagnetic-wave-analysis-of-wave-and-shielded-stripline-14079>.
- ³⁶⁹P. Sipilä, R. F. Schulte, G. Wachutka, and F. Wiesinger, “Digital Multiband Receiver for Magnetic Resonance”, *Concepts Magn. Reson.* **35B**, 210–220 (2009), <http://dx.doi.org/10.1002/cmr.b.20149>.
- ³⁷⁰J. Sirker, A. Weisse, and O. P. Sushkov, “Consequences of spin-orbit coupling for the Bose-Einstein condensation of magnons”, *Europhys. Lett.* **68**, 275–281 (2004), <http://dx.doi.org/10.1209/epl/i2004-10179-4>.
- ³⁷¹C. P. Slichter, *Principles of Magnetic Resonance*, 3rd edition, corrected, Springer Series in Solid-State Sciences Vol. 1 (Springer, Berlin Heidelberg, Germany, 1996), ISBN: 978-3-642-08069-2, <http://dx.doi.org/10.1007/978-3-662-09441-9>.
- ³⁷²A. Smerald and N. Shannon, “Angle-resolved NMR: Quantitative theory of ^{75}As T_1 relaxation rate in BaFe_2As_2 ”, *Phys. Rev. B* **84**, 184437 (2011), <http://dx.doi.org/10.1103/PhysRevB.84.184437>.
- ³⁷³S. A. Söffing, M. Bortz, I. Schneider, A. Struck, M. Fleischhauer, and S. Eggert, “Wigner crystal versus Friedel oscillations in the one-dimensional Hubbard model”, *Phys. Rev. B* **79**, 195114 (2009), <http://dx.doi.org/10.1103/PhysRevB.79.195114>.
- ³⁷⁴C. E. Soliverez, “General theory of effective Hamiltonians”, *Phys. Rev. A* **24**, 4–9 (1981), <http://dx.doi.org/10.1103/PhysRevA.24.4>.
- ³⁷⁵E. Sørensen, I. Affleck, D. Augier, and D. Poilblanc, “Soliton approach to spin-Peierls antiferromagnets: Large-scale numerical results”, *Phys. Rev. B* **58**, R14701–R14704 (1998), <http://dx.doi.org/10.1103/PhysRevB.58.R14701>.
- ³⁷⁶R. Speight, A. Wong, P. Ellis, P. T. Bishop, T. I. Hyde, T. J. Bastow, and M. E. Smith, “ ^{59}Co NMR study of the allotropic phase transformation in small ferromagnetic cobalt particles”, *Phys. Rev. B* **79**, 054102 (2009), <http://dx.doi.org/10.1103/PhysRevB.79.054102>.
- ³⁷⁷L. Splinter, N. A. Drescher, H. Krull, and G. S. Uhrig, “Minimal model for the frustrated spin ladder system BiCu_2PO_6 ”, *Phys. Rev. B* **94**, 155115 (2016), <http://dx.doi.org/10.1103/PhysRevB.94.155115>.
- ³⁷⁸J. J. Spokas and C. P. Slichter, “Nuclear Relaxation in Aluminum”, *Phys. Rev.* **113**, 1462–1472 (1959), <http://dx.doi.org/10.1103/PhysRev.113.1462>.

- ³⁷⁹G. L. Squires, *Introduction to the Theory of Thermal Neutron Scattering*, 3rd edition (Cambridge University Press, Cambridge, UK, 2012), ISBN: 978-1-107-64406-9.
- ³⁸⁰M. Stoudenmire, *Periodic vs Open or Infinite Boundary Conditions for DMRG, Which Should You Choose?*, <http://itensor.org/docs.cgi?page=articles/periodic> (dated 28.04.2014, retrieved 01.02.2017).
- ³⁸¹S. P. Strong and A. J. Millis, “Competition between Singlet Formation and Magnetic Ordering in One-Dimensional Spin Systems”, *Phys. Rev. Lett.* **69**, 2419–2422 (1992), <http://dx.doi.org/10.1103/PhysRevLett.69.2419>.
- ³⁸²J. Su and S. Y. Huang, “The Design and Implementation of a Compact NMR System”, in 2015 IEEE MTT-S International Microwave Workshop Series on Advanced Materials and Processes for RF and THz Applications (IMWS-AMP), Suzhou, China (2015), pp. 1–3, <http://dx.doi.org/10.1109/IMWS-AMP.2015.7325038>.
- ³⁸³J. Sudan, A. Lüscher, and A. M. Läuchli, “Emergent multipolar spin correlations in a fluctuating spiral: The frustrated ferromagnetic spin- $\frac{1}{2}$ Heisenberg chain in a magnetic field”, *Phys. Rev. B* **80**, 140402(R) (2009), <http://dx.doi.org/10.1103/PhysRevB.80.140402>.
- ³⁸⁴T. Sugimoto, M. Mori, T. Tohyama, and S. Maekawa, “Lifshitz Transition Induced by Magnetic Field in Frustrated Two-Leg Spin-Ladder Systems”, e-print (2014), arXiv:1409.4280v2 [cond-mat.str-el].
- ³⁸⁵T. Sugimoto, M. Mori, T. Tohyama, and S. Maekawa, “Effects of frustration on magnetic excitations in a two-leg spin-ladder system”, *Phys. Rev. B* **87**, 155143 (2013), <http://dx.doi.org/10.1103/PhysRevB.87.155143>.
- ³⁸⁶T. Sugimoto, M. Mori, T. Tohyama, and S. Maekawa, “Lifshitz Transition Induced by Magnetic Field in Frustrated Two-Leg Spin-Ladder Systems”, in Proc. 2nd Int. Symp. Science at J-PARC — Unlocking the Mysteries of Life, Matter and the Universe —, Tsukuba, Ibaraki, Japan, JPS Conf. Proc. 8, 034005 (2015), <http://dx.doi.org/10.7566/JPSCP.8.034005>.
- ³⁸⁷T. Sugimoto, M. Mori, T. Tohyama, and S. Maekawa, “Magnetization plateaus by reconstructed quasispinons in a frustrated two-leg spin ladder under a magnetic field”, *Phys. Rev. B* **92**, 125114 (2015), <http://dx.doi.org/10.1103/PhysRevB.92.125114>.
- ³⁸⁸N. S. Sullivan, “NMR at Very Low Temperatures: Population Difference Thermometry”, *Bull. Magn. Reson.* **18**, 258–264 (1996), https://www.weizmann.ac.il/ISMAR/sites/ISMAR/files/bulletin/BMR_18_258-264_1996.pdf.
- ³⁸⁹K. Sun, *Physics 620: Condensed Matter Physics (Fall 2012), section 5.7: time-reversal symmetry for spin-1/2 and Kramers doublet*, lecture notes, University of Michigan, Ann Arbor, MI, USA, http://www-personal.umich.edu/~sunkai/teaching/Fall_2012/chapter5_part2.pdf (retrieved 30.01.2017, index at http://www-personal.umich.edu/~sunkai/teaching/Fall_2012/phys620.html).
- ³⁹⁰O. F. Syljuåsen and A. W. Sandvik, “Quantum Monte Carlo with directed loops”, *Phys. Rev. E* **66**, 046701 (2002), <http://dx.doi.org/10.1103/PhysRevE.66.046701>.
- ³⁹¹K. Takeda, “A highly integrated FPGA-based nuclear magnetic resonance spectrometer”, *Rev. Sci. Instrum.* **78**, 033103 (2007), <http://dx.doi.org/10.1063/1.2712940>.
- ³⁹²K. Takeda, “OPENCORE NMR: Open-source core modules for implementing an integrated FPGA-based NMR spectrometer”, *J. Magn. Reson.* **192**, 218–229 (2008), <http://dx.doi.org/10.1016/j.jmr.2008.02.019>.

- ³⁹³K. Takeda, “Chapter 7 - Highly Customized NMR Systems Using an Open-Resource, Home-Built Spectrometer”, in *Annual Reports on NMR Spectroscopy*, Vol. 74, edited by G. A. Webb (Elsevier Ltd., Oxford, UK, 2011), ISBN: 978-0-08-097072-1, pp. 355-393, <http://dx.doi.org/10.1016/B978-0-08-097072-1.00007-8>.
- ³⁹⁴W. Tang and W. Wang, “A single-board NMR spectrometer based on a software defined radio architecture”, *Meas. Sci. Technol.* **22**, 015902 (2011), <http://dx.doi.org/10.1088/0957-0233/22/1/015902>.
- ³⁹⁵W. Tang, H. Sun, and W. Wang, “A digital receiver module with direct data acquisition for magnetic resonance imaging systems”, *Rev. Sci. Instrum.* **83**, 104701 (2012), <http://dx.doi.org/10.1063/1.4755089>.
- ³⁹⁶*The OpenMP API specification for parallel programming*, <http://www.openmp.org/>.
- ³⁹⁷D. Thompson, “The reciprocal lattice as the Fourier transform of the direct lattice”, *Am. J. Phys* **64**, 333–334 (1996), <http://dx.doi.org/10.1119/1.18243>.
- ³⁹⁸M. Tian, H. Liu, and Z. Chen, “Application of Software Defined Radio in 500MHz NMR Spectrometers”, in 9th International Conference on Electronic Measurement & Instruments, ICEMI '09, Beijing, China (IEEE, 2009), ISBN: 978-1-4244-3864-8, pp. 1-800 - 1-804, <http://dx.doi.org/10.1109/ICEMI.2009.5274048>.
- ³⁹⁹M. D. Tiwari, D. N. Talwar, and Bal. K. Agrawal, “Phonon conductivity of GaAs”, *Solid State Commun.* **9**, 995–997 (1971), [http://dx.doi.org/10.1016/0038-1098\(71\)90447-9](http://dx.doi.org/10.1016/0038-1098(71)90447-9).
- ⁴⁰⁰M. Troyer and U.-J. Wiese, “Computational Complexity and Fundamental Limitations to Fermionic Quantum Monte Carlo Simulations”, *Phys. Rev. Lett.* **94**, 170201 (2005), <http://dx.doi.org/10.1103/PhysRevLett.94.170201>.
- ⁴⁰¹A. A. Tsirlin, I. Rousochatzakis, D. Kasinathan, O. Janson, R. Nath, F. Weickert, C. Geibel, A. M. Läuchli, and H. Rosner, “Bridging frustrated-spin-chain and spin-ladder physics: Quasi-one-dimensional magnetism of BiCu₂PO₆”, *Phys. Rev. B* **82**, 144426 (2010), <http://dx.doi.org/10.1103/PhysRevB.82.144426>.
- ⁴⁰²B. G. Turrell, G. Eska, N. Masuhara, and E. Schuberth, “Nuclear Spin-Lattice Relaxation in Metals at Low Temperatures”, *J. Low Temp. Phys.* **70**, 151–172 (1988), <http://dx.doi.org/10.1007/BF00683249>.
- ⁴⁰³S. V. Tyablikov, *Methods in the Quantum Theory of Magnetism* (Springer Science+Business Media, LLC, New York, NY, USA, 1967), ISBN: 978-1-4899-7182-1, <http://dx.doi.org/10.1007/978-1-4899-7182-1>.
- ⁴⁰⁴H. T. Ueda and K. Totsuka, “Magnon Bose-Einstein condensation and various phases of three-dimensional quantum helimagnets under high magnetic field”, *Phys. Rev. B* **80**, 014417 (2009), <http://dx.doi.org/10.1103/PhysRevB.80.014417>.
- ⁴⁰⁵H. Ueda and S. Onoda, “Symmetry-protected topological phases and transition in a frustrated spin- $\frac{1}{2}$ XXZ chain”, *Phys. Rev. B* **90**, 214425 (2014), <http://dx.doi.org/10.1103/PhysRevB.90.214425>.
- ⁴⁰⁶H. Ueda and S. Onoda, “Vector-spin-chirality order in a dimerized frustrated spin- $\frac{1}{2}$ chain”, *Phys. Rev. B* **89**, 024407 (2014), <http://dx.doi.org/10.1103/PhysRevB.89.024407>.
- ⁴⁰⁷G. S. Uhrig, F. Schönfeld, J.-P. Boucher, and M. Horvatić, “Soliton lattices in the incommensurate spin-Peierls phase: Local distortions and magnetizations”, *Phys. Rev. B* **60**, 9468–9476 (1999), <http://dx.doi.org/10.1103/PhysRevB.60.9468>.

- ⁴⁰⁸S. Utsuzawa, S. Mandal, and Y.-Q. Song, “Transformer-coupled NMR Probe Technology”, in *eMagRes*, Vol. 2 (John Wiley & Sons, Ltd., 2013), ISBN: 9780470034590, pp. 185-192, <http://dx.doi.org/10.1002/9780470034590.emrstm1322>.
- ⁴⁰⁹M.-A. Vachon, G. Koutroulakis, V. F. Mitrović, A. P. Reyes, P. Kuhns, R. Coldea, and Z. Tylczynski, “Anisotropic transferred hyperfine interactions in Cs_2CuCl_4 ”, *J. Phys.: Condens. Matter* **20**, 295225 (2008), <http://dx.doi.org/10.1088/0953-8984/20/29/295225>.
- ⁴¹⁰L. Vanderstraeten, J. Haegeman, F. Verstraete, and D. Poilblanc, “Quasiparticle interactions in frustrated Heisenberg chains”, *Phys. Rev. B* **93**, 235108 (2016), <http://dx.doi.org/10.1103/PhysRevB.93.235108>.
- ⁴¹¹M. Y. Veillette, J. T. Chalker, and R. Coldea, “Ground states of a frustrated spin- $\frac{1}{2}$ antiferromagnet: Cs_2CuCl_4 in a magnetic field”, *Phys. Rev. B* **71**, 214426 (2005), <http://dx.doi.org/10.1103/PhysRevB.71.214426>.
- ⁴¹²T. Vekua and A. Honecker, “Quantum dimer phases in a frustrated spin ladder: Effective field theory approach and exact diagonalization”, *Phys. Rev. B* **73**, 214427 (2006), <http://dx.doi.org/10.1103/PhysRevB.73.214427>.
- ⁴¹³I. B. Vendik, O. G. Vendik, and S. S. Gevorgian, “Effective Dielectric Permittivity of r-Cut Sapphire Microstrip”, in 24th European Microwave Conference, Cannes, France (IEEE, 1994), pp. 395–400, <http://dx.doi.org/10.1109/EUMA.1994.337241>.
- ⁴¹⁴I. B. Vendik and E. T. Kalendarov, “CAD Model of Effective Dielectric Constant of Microstrip Line on M-Cut Sapphire Substrate”, *International Journal of Microwave and Millimeter-Wave Computer-Aided Engineering* **5**, 402–405 (1995), <http://dx.doi.org/10.1002/mmce.4570050606>.
- ⁴¹⁵I. B. Vendik, O. G. Vendik, S. S. Gevorgian, M. F. Sitnikova, and E. Olsson, “A CAD Model for Microstrips on r-Cut Sapphire Substrates”, *International Journal of Microwave and Millimeter-Wave Computer-Aided Engineering* **4**, 374–383 (1994), <http://dx.doi.org/10.1002/mmce.4570040407>.
- ⁴¹⁶M. Villa, F. Tian, P. Cofrancesco, J. Halánek, and M. Kasal, “High-resolution digital quadrature detection”, *Rev. Sci. Instrum.* **67**, 2123–2129 (1996), <http://dx.doi.org/10.1063/1.1147025>.
- ⁴¹⁷J. Villain, “Propagative spin relaxation in the Ising-like antiferromagnetic linear chain”, *Physica* **79B**, 1–12 (1975), [http://dx.doi.org/10.1016/0378-4363\(75\)90101-1](http://dx.doi.org/10.1016/0378-4363(75)90101-1).
- ⁴¹⁸J. Villain, “A magnetic analogue of stereoisomerism : application to helimagnetism in two dimensions”, *J. Phys. France* **38**, 385–391 (1977), <http://dx.doi.org/10.1051/jphys:01977003804038500>.
- ⁴¹⁹J. Villain, “Chiral Order in Helimagnets”, in Proceedings of the 13th IUPAP Conference on Statistical Physics, Technion-Israel Institute of Technology, Haifa, Israel, Vol. 2, edited by D. Cabib, C. G. Kuper, and I. Riess, executive editor C. Weil, *Ann. Isr. Phys. Soc.* **2** (1978), ISBN: 0-85274-356-4, pp. 565-568.
- ⁴²⁰*Virtex-6 Family Overview*, DS150 (v2.4), Product Specification, Xilinx, Inc. (Jan. 19, 2012), https://www.xilinx.com/support/documentation/data_sheets/ds150.pdf.
- ⁴²¹M. Van de Voorde, “Results of physical tests on polymers at cryogenic temperatures”, *Cryogenics* **16**, 296–302 (1976), [http://dx.doi.org/10.1016/0011-2275\(76\)90321-0](http://dx.doi.org/10.1016/0011-2275(76)90321-0).
- ⁴²²R. E. Walstedt, *The NMR Probe of High- T_c Materials*, Springer Tracts in Modern Physics 228 (Springer, Berlin Heidelberg, Germany, 2008), ISBN: 978-3-540-75564-7, <http://dx.doi.org/10.1007/978-3-540-75565-4>.

- ⁴²³S. Wang, E. Pomjakushina, T. Shiroka, G. Deng, N. Nikseresht, Ch. Rüegg, H. M. Rønnow, and K. Conder, “Crystal growth and characterization of the dilutable frustrated spin-ladder compound $\text{Bi}(\text{Cu}_{1-x}\text{Zn}_x)_2\text{PO}_6$ ”, *J. Cryst. Growth* **313**, 51–55 (2010), <http://dx.doi.org/10.1016/j.jcrysgro.2010.09.074>.
- ⁴²⁴S. Wang, “Synthesis, crystal growth and physical properties of the frustrated spin ladder material BiCu_2PO_6 ”, PhD thesis (École Polytechnique Fédérale de Lausanne, Lausanne, Switzerland, 2013), <http://dx.doi.org/10.5075/epfl-thesis-5891>.
- ⁴²⁵Y.-J. Wang, F. H. L. Essler, M. Fabrizio, and A. A. Nersesyan, “Quantum criticalities in a two-leg antiferromagnetic $S = \frac{1}{2}$ ladder induced by a staggered magnetic field”, *Phys. Rev. B* **66**, 024412 (2002), <http://dx.doi.org/10.1103/PhysRevB.66.024412>.
- ⁴²⁶W. W. Warren and W. G. Clark, “Knight Shift and Nuclear Spin-Lattice Relaxation Rate in Solid and Liquid Copper”, *Phys. Rev. B* **1**, 24–30 (1970), <http://dx.doi.org/10.1103/PhysRevB.1.24>.
- ⁴²⁷A. G. Webb, “Advances in Probe Design for Protein NMR”, in *Annual Reports on NMR Spectroscopy*, Vol. 58, edited by G. A. Webb (Elsevier Ltd., Oxford, UK, 2006), ISBN: 978-0-12-505458-4, pp. 1-50, [http://dx.doi.org/10.1016/S0066-4103\(05\)58001-3](http://dx.doi.org/10.1016/S0066-4103(05)58001-3).
- ⁴²⁸J. A. Weil and J. R. Bolton, “Zeeman Energy (g) Anisotropy”, in *Electron Paramagnetic Resonance, Elementary Theory and Practical Applications*, 2nd edition (John Wiley & Sons, Inc., Hoboken, NJ, USA, 2006), ISBN: 9780470084984, pp. 85-117, <http://dx.doi.org/10.1002/9780470084984.ch4>.
- ⁴²⁹E. W. Weisstein, *Bochner’s Theorem*. From MathWorld—A Wolfram Web Resource, <http://mathworld.wolfram.com/BochnersTheorem.html> (accessed 04.03.2017).
- ⁴³⁰E. W. Weisstein, *Incomplete Gamma Function*. From MathWorld—A Wolfram Web Resource, <http://mathworld.wolfram.com/IncompleteGammaFunction.html> (accessed 06.04.2017).
- ⁴³¹E. W. Weisstein, *Iverson Bracket*. From MathWorld—A Wolfram Web Resource, <http://mathworld.wolfram.com/IversonBracket.html> (accessed 04.03.2017).
- ⁴³²E. W. Weisstein, *Jacobi Amplitude*. From MathWorld—A Wolfram Web Resource, <http://mathworld.wolfram.com/JacobiAmplitude.html> (accessed 10.03.2017).
- ⁴³³E. W. Weisstein, *Natural Norm*. From MathWorld—A Wolfram Web Resource, <http://mathworld.wolfram.com/NaturalNorm.html> (accessed 19.12.2016).
- ⁴³⁴E. W. Weisstein, *Pauli Matrices*. From MathWorld—A Wolfram Web Resource, <http://mathworld.wolfram.com/PauliMatrices.html> (accessed 18.09.2017).
- ⁴³⁵E. W. Weisstein, *Poisson Sum Formula*. From MathWorld—A Wolfram Web Resource, <http://mathworld.wolfram.com/PoissonSumFormula.html> (accessed 29.12.2016).
- ⁴³⁶E. W. Weisstein, *Riemann Series Theorem*. From MathWorld—A Wolfram Web Resource, <http://mathworld.wolfram.com/RiemannSeriesTheorem.html> (accessed 27.12.2016).
- ⁴³⁷S. Wessel and S. Haas, “Magnetic field induced ordering in quasi-one-dimensional quantum magnets”, *Eur. Phys. J. B* **16**, 393–396 (2000), <http://dx.doi.org/10.1007/s100510070194>.
- ⁴³⁸F. W. de Wette and G. E. Schacher, “Internal Field in General Dipole Lattices”, *Phys. Rev.* **137**, A78–A91 (1965), <http://dx.doi.org/10.1103/PhysRev.137.A78>.
- ⁴³⁹H. A. Wheeler, “Transmission-Line Properties of a Strip on a Dielectric Sheet on a Plane”, *IEEE Trans. Microwave Theory Tech.* **25**, 631–647 (1977), <http://dx.doi.org/10.1109/TMTT.1977.1129179>.

- ⁴⁴⁰S. R. White, R. M. Noack, and D. J. Scalapino, “Resonating Valence Bond Theory of Coupled Heisenberg Chains”, *Phys. Rev. Lett.* **73**, 886–889 (1994), <http://dx.doi.org/10.1103/PhysRevLett.73.886>.
- ⁴⁴¹S. R. White, “Density Matrix Formulation for Quantum Renormalization Groups”, *Phys. Rev. Lett.* **69**, 2863–2866 (1992), <http://dx.doi.org/10.1103/PhysRevLett.69.2863>.
- ⁴⁴²S. R. White, “Minimally Entangled Typical Quantum States at Finite Temperature”, *Phys. Rev. Lett.* **102**, 190601 (2009), <http://dx.doi.org/10.1103/PhysRevLett.102.190601>.
- ⁴⁴³S. R. White and I. Affleck, “Dimerization and incommensurate spiral spin correlations in the zigzag spin chain: Analogies to the Kondo lattice”, *Phys. Rev. B* **54**, 9862–9869 (1996), <http://dx.doi.org/10.1103/PhysRevB.54.9862>.
- ⁴⁴⁴S. R. White, I. Affleck, and D. J. Scalapino, “Friedel oscillations and charge density waves in chains and ladders”, *Phys. Rev. B* **65**, 165122 (2002), <http://dx.doi.org/10.1103/PhysRevB.65.165122>.
- ⁴⁴⁵E. T. Whittaker, “On the Functions which are represented by the Expansions of the Interpolation-Theory”, *Proc. R. Soc. Edinb.* **35**, 181–194 (1915), <http://dx.doi.org/10.1017/S0370164600017806>. Similar results have been obtained by other authors, including C. E. Shannon; H. Nyquist; V. A. Kotelnikov; H. Raabe; and I. Someya, see [238] for a review.
- ⁴⁴⁶E. Wigner, *Gruppentheorie und ihre Anwendung auf die Quantenmechanik der Atomspektren*, reprint of the 1931 original edition (Springer Fachmedien Wiesbaden GmbH, Wiesbaden, Germany, 1977), ISBN: 978-3-663-02555-9, <http://dx.doi.org/10.1007/978-3-663-02555-9>.
- ⁴⁴⁷K. Wittel and R. Manne, “Atomic Spin-Orbit Interaction Parameters from Spectral Data for 19 Elements”, *Theoret. Chim. Acta (Berl.)* **33**, 347–349 (1974), <http://dx.doi.org/10.1007/BF00551162>.
- ⁴⁴⁸*Wolfram Mathematica*, <https://www.wolfram.com/mathematica/>.
- ⁴⁴⁹J. G. Wright and B. S. Shastry, “DiracQ: A Package for Algebraic Manipulation of Non-Commuting Quantum Variables”, *Journal of Open Research Software* **3**, e13 (2015), <http://dx.doi.org/10.5334/jors.cb>.
- ⁴⁵⁰Q. Xia and P. S. Riseborough, “One-dimensional Dzyaloshinski–Moriya antiferromagnets in an applied field”, *J. Appl. Phys.* **63**, 4141–4143 (1988), <http://dx.doi.org/10.1063/1.340521>.
- ⁴⁵¹T. Yildirim, A. B. Harris, A. Aharony, and O. Entin-Wohlman, “Anisotropic spin Hamiltonians due to spin-orbit and Coulomb exchange interactions”, *Phys. Rev. B* **52**, 10239–10267 (1995), <http://dx.doi.org/10.1103/PhysRevB.52.10239>.
- ⁴⁵²A. Yoshimori, “A New Type of Antiferromagnetic Structure in the Rutile Type Crystal”, *J. Phys. Soc. Jpn.* **14**, 807–821 (1959), <http://dx.doi.org/10.1143/JPSJ.14.807>.
- ⁴⁵³S. Yucel, N. Alexander, and A. Honig, “A superconducting coaxial transmission line for dilution refrigerators”, *Rev. Sci. Instrum.* **59**, 2276–2278 (1988), <http://dx.doi.org/10.1063/1.1139947>.
- ⁴⁵⁴J. Yun, J. Yu, T. Hongyan, and L. Gengying, “A complete digital radio-frequency source for nuclear magnetic resonance spectroscopy”, *Rev. Sci. Instrum.* **73**, 3329–3331 (2002), <http://dx.doi.org/10.1063/1.1497500>.
- ⁴⁵⁵S. Zabihzadeh, *AC-measurements of specific heat in BCPO*, TP4 project report, supervised by J. Larrea and H. M. Ronnow (Laboratory for Quantum Magnetism, École Polytechnique Fédérale de Lausanne, Lausanne, Switzerland, 2010), <https://infoscience.epfl.ch/record/151958>.
- ⁴⁵⁶J. Zang, S. Chakravarty, and A. R. Bishop, “Interchain coupling effects and solitons in CuGeO_3 ”, *Phys. Rev. B* **55**, R14705–R14708 (1997), <http://dx.doi.org/10.1103/PhysRevB.55.R14705>.

- ⁴⁵⁷S.-S. Zhang, N. Kaushal, E. Dagotto, and C. D. Batista, “Spin-orbit interaction driven dimerization in one dimensional frustrated magnets”, e-print (2017), arXiv:1703.03881v1 [cond-mat.str-el].
- ⁴⁵⁸J. Z. Zhao, X. Q. Wang, T. Xiang, Z. B. Su, and L. Yu, “Effects of the Dzyaloshinskii-Moriya Interaction on Low-Energy Magnetic Excitations in Copper Benzoate”, *Phys. Rev. Lett.* **90**, 207204 (2003), <http://dx.doi.org/10.1103/PhysRevLett.90.207204>.
- ⁴⁵⁹A. A. Zvyagin and S.-L. Drechsler, “Magnetic ordering of weakly coupled frustrated quantum spin chains”, *Phys. Rev. B* **78**, 014429 (2008), <http://dx.doi.org/10.1103/PhysRevB.78.014429>.

(page removed in online version)

(page removed in online version)